DETERMINATION OF OXIDATION MECHANISMS OF FERRITIC-MARTENSITIC ALLOYS IN SUPERCRITICAL WATER

by

Pantip Ampornrat

A dissertation submitted in partial fulfillment
of the requirements for the degree of
Doctor of Philosophy
(Nuclear Engineering and Radiological Sciences)
in The University of Michigan
2011

Doctoral Committee:

Professor Lumin Wang, Co-Chair
Professor Gary S. Was, Co-Chair
Professor J. Wayne Jones
Assistant Research Scientist Kai Sun

To my parents and grandparents

ACKNOWLEDGEMENT

I would like to thank my advisor Dr. Gary S. Was and co-advisor Dr. Lumin Wang, for their guidance and support for entire time I worked on this thesis. I would also like to thank the members of my dissertation committee, Dr. Wayne Jones and Dr. Kai Sun for their helpful insight as I completed this thesis.

I would also like to thank my colleagues and friends, Elaine West, Deepak Kumar, Gaurav Gupta, Micah Hackett, Josh McKinley, Anne Campbell, Michael McMurtrey, Cheng Xu, Gokce Gulsoy, Kale Stephenson, Tyler Moss, Janelle Wharry, Efrain Hernandez-Rivera, Jonathan Wierschke, Weixing Li, Guang Ran, Liang Chen, Stephen Raiman, Shyam Dwaraknath, William Lai, Jan Michalicka and Jeremy Bischoff for their support and fruitful discussion.

I would also like to thank research staffs who assisted me in lab and gave me very helpful suggestions, Chi Bum Bahn, Sebastien Teysseyre, Yanbin Chen, Zhijie Jiao, Alex Flick, Haiping Sun, John Mansfield and NERS staffs, Peggy Gramer, Caroline Joaquin, Cherilyn Davis, Edward Birdsall and Pam Derry.

I would also like to thank my friends outside working area, Phongphaeth Pengvanich, Niravun Pavenayotin, Yimprayoon's family, Rhatarporn Kessom, Chetwana Rungwanitchakul, Anupap Somboonsavatdee, Naruemol Sigha-Dong, Chanokruthai Choenarom, Yuko Kobayashi, Ning Ying Jeab, Bo Fai Ying, Godaiko's staffs, The old siam's staffs and a lot of friends who have been being with me along this journey.

Lastly, I would like to express my deep appreciation to my parents, grandparents and my family members for their patience, understanding and support they have given to me the entire time.

I would also like to thank the Thai Government and Thailand Institute of Nuclear Technology who supported me the full scholarship for Ph.D. study.

This work was supported by US Department of Energy under I-NERI project contract number 3F-01041.

TABLE OF CONTENTS

DEDICATION ii

ACKNOWLEDMENTS iii

LIST OF FIGURES viii

LIST OF TABLES xxi

LIST OF APPENDICES xxiv

ABSTRACT xxv

CHAPTER

1. INTRODUCTION 1

2. BACKGROUND 8

2.1 Supercritical Water 9
2.2 Ferritic-martensitic Alloys 15
2.2.1 Development and Composition Design 15
2.2.2 Phase Constitution 21
2.2.3 Microstructure of F-M Alloys 24
2.3 Oxidation of Ferritic-martensitic Alloys in SCW Environment 27
2.3.1 Overview of Oxidation of F-M alloys 27
2.3.1a Fundamental of Oxidation 27
2.3.1b Oxidation Rate 31
2.3.1c Oxide Structure 34
2.3.2 Effects of Alloy Composition and Microstructure 35
2.3.2a Chromium Content 35
2.3.2b Minor Alloying Elements 39
2.3.2c Alloy Microstructure 41
2.3.3 Environmental Effects on Oxidation of Ferritic-martensitic Alloys 42
2.3.3a Oxidation in Steam 43
2.3.3b Oxidation in Gas 46
2.3.3c Oxidation in SCW 47
2.4 Conclusion 53

2.5 Objective, Significant of Study and Approaches 53

3. EXPERIMENT 94

3.1 Alloy Composition and Process Condition 94
3.2 Sample Preparation for Exposure Experiments 96
3.3 Supercritical Water Test Facilities 98
3.4 Exposure Experiments and Test Conditions 103
3.4.1 Sample Installation in Autoclave 103
3.4.2 Operation of SCW Systems 103
3.4.3 Water Chemistry 105
3.4.4 Experimental Conditions 106
3.5 Oxidation Rate Measurements 107
3.6 Sample Preparation for Characterizations 108
3.6.1 Cross-sectional SEM Sample Preparation 109
3.6.2 Cross-sectional TEM Sample Preparation by Focused Ion Beam 109
3.7 Microstructural Characterization 114
3.7.1 Scanning Electron Microscopy 114
3.7.2 X-ray Diffraction 115
3.7.3 Transmission Electron Microscopy 117
3.7.4 Energy Dispersive Spectroscopy 120
3.8 Error Analysis 124

4. EXPERIMENTAL RESULTS 151

4.1 Oxidation Rate 152
4.1.1 Time-dependence of Oxidation Rate 152
4.1.2 Temperature-dependence of Oxidation Rate 154
4.1.3 Dissolved Oxygen Effect 157
4.2 Surface Oxide 158
4.2.1 Surface Oxide Morphology 158
4.2.2 Surface Oxide Phase 160
4.2.3 XPS Analysis of Surface Oxide 161
4.3 Oxide Scale Structure and Composition 163
4.3.1 Outer Oxide 164
4.3.2 Inner Oxide 164
4.3.3 Transition Layer and Cr-enriched Oxide 165
4.3.4 Alloy Effect on Oxide Structure at 600°C 167
4.4 Microstructure of Alloy and Oxide 168
4.4.1 Alloy Microstructure 168
4.4.2 HCM12A Oxidized in 400°C Deaerated SCW 169
4.4.3 HCM12A Oxidized in 500°C Deaerated SCW 172
4.4.4 HCM12A Oxidized in 500°C SCW Containing 300 ppb DO 174
4.4.5 HCM12A Oxidized in 600°C Deaerated SCW 175
4.4.6 T91 Oxidized in 600°C Deaerated SCW 179
4.4.7 HT-9 Oxidized in 600°C Deaerated SCW 181

4.4.8 9Cr-ODS Oxidized in 600°C Deaerated SCW 183

5. DISCUSSION 293

5.1 Time and Temperature Dependence of the Weight Gain and Oxide Growth 294
5.1.1 Time Dependence of the Weight Gain and Oxide Growth 294
5.1.2 Temperature Dependence of the Weight Gain and Oxide Growth 297
5.1.3 Determination of Location of Original Alloy Substrate and Mass Balance Equation 304
5.1.4 Determination of Rate Limiting Process from Diffusion Coefficient 309
5.2 Formation of Oxide Structure 318
5.2.1 Determination of Oxygen Partial Pressure at Inner oxide-Outer oxide-Alloy Interfaces 318
5.2.2 Formation of Outer Oxide 327
5.2.3 Formation of Inner Oxide 329
5.2.4 Formation of Transition Layer 337
5.3 Oxidation Mechanism 347
5.3.1 Defect Formation in Oxide 347
5.3.2 Summary of Oxidation Mechanisms 355

6. CONCLUSION 388

7. FUTURE WORK 392

LIST OF FIGURES

Figure

1.1 Schematic diagram of the Generation IV SCWR concept 6

2.1 Phase diagram for water [1]. 59

2.2 (a) Variation in the density of water with temperature showing the drop in density at critical region (350-400°C) [5]. (b) Plots of density vs. temperature for SCW as a function of pressure [6]. (Note that the large filled circles indicate values for HCl solution in the SCWO.) 60

2.3 Plots of viscosity vs. temperature for SCW as a function of pressure [6]. (Note that the large filled circles indicate values for HCl solution in the SCWO.) 61

2.4 (a) Plots of static dielectric constant as a function of temperature [12]..... 62

2.5 Ionic products as functions of temperature and pressure. [5] 63

2.6 Thermo-physical properties of SCW at pressure 25 MPa [1]. 64

2.7 The water trimer consists of three water molecules. Each water monomer acts as a single hydrogen bond donor and accepter. [21] 65

2.8 Development of ferritic alloys for boilers. (a) Schematic diagram shows development of F-M alloys that are classified into four generations based on alloying elements and creep strength [22]. (b) History of improvement of creep strength of F-M alloys and austenitic alloys [24]. 66

2.9 Relation between allowable metal temperature at 49 MPa of allowable stress and relative material cost [22]. 67

2.10 General concept of alloy composition design for heat resistant alloy [22]..... 68

2.11 Alloy design for HCM12A [27]..... 69

2.12 Phase diagram of Fe-C-Cr alloys showing the effect of chromium on the constitution of Fe-Cr-C alloys containing 0.1% C [23, 32]; note that $(CrFe)_4C$ is a $M_{23}C_6$ carbide. 70

2.13 The Schaeffler-Schneider diagram represent the correlation between the phases present to the chromium and nickel equivalent in 9-12%Cr alloys [23]. 71

2.14 Optical micrograph shows a ferrite stringer in HCM12A microstructure. [34] 72

2.15 Effect of tempering temperature on hardness of a 12Cr-0.14C alloy [23, 37] 73

2.16 Schematic diagram of the microstructure of normalized and tempered F-M alloys. 74

2.17 Ellingham/Richardson diagram shows plot of free energy with temperature for various oxides [50]. 75

2.18 Phase diagram of Fe-O [47]. 76

2.19 Effect of Cr addition on the corrosion rate of alloy at 1000^{o}C [47]. 77

2.20 Schematic representation of all possible component of oxide layers on Fe-Cr alloy [47]. 78

2.21 Schematic diagram of oxide structure formed on 9Cr-1Mo steel exposed in air at 400-600°C [59] 79

2.22 Oxidation of 1Cr, 10Cr, 10Cr-6.52Co and 12Cr in Ar-50%H_2O at 550-650°C reported by Zurek et al. (a) Oxidation rate, (b) Composition profiles of 10Cr-6.52Co exposed at 600°C, and (c) Composition profiles of 12%Cr exposed at 625°C. Both composition profiles show enrichment of Cr at the alloy/oxide interface. [62] 80

2.23 Schematic illustration of oxidation rate as function of Cr content for commercial ferritic alloys in steam with the temperature range of 550-650C. Arrows indicate qualitative changes of critical Cr-content by additions of Si, Co, and Mn respectively. [63] 81

2.24 Effects of steam pressure: Plots of oxidation rate constants of F-M alloys HCM2S, NF616 and HCM12A versus steam pressure tested at (a) 600°C and (b) 700°C. The Arrhenius plots of kp measured at (c) 10 MPa and (d) 2 MPa or lower show changes in activation energies trend. [75] 82

2.25 Effect of water vapor and steam composition: Scales formed on Fe-10Cr alloy after exposure in (a) Ar-20%O_2, (b) Ar-4%H_2-7%H_2O, and (c) Ar-7%H_2O and at 900°C for 72 hours, and (d) weight gain. [76] 83

2.26 Depth profiles of P91 after oxidation in N_2- 1 vol%$^{16}O_2$- 2 vol%$H_2{}^{18}O_2$ at 650°C. The profile after (a) 1 h, (b) 7 h, and 30 h show ^{16}O in the inner layers, and ^{18}O from water molecules distribute in the outer layers. [77] 84

2.27 Temperature effect of oxidation in dry air: (a) Double logarithmic plot of weight gain and temperature of HT-9 tested in dry air at 600-950°C. (b) The partial

dissolution of grain structure in the internal selective oxidation zone. Grain boundaries are outline with Cr-rich/Fe oxide. [74] 85

2.28 Potential-pH diagram for iron in supercritical aqueous solution at 400°C and P = 50 MPa. The diagram shows the approximate regions in potential-pH space for the operation of SCWO reactors and SCW thermal power plants. [6] 86

2.29 Oxidation rates of three alloy classes as represented by 625 (Ni-based alloy), D9 (austenitic alloy), and HCM12A (F-M alloy). The samples were tested in 500°C deaerated SCW (25 ppb O_2) for 1026 hours. [88] 87

3.1 Scanning electron microscope image for the microstructure of T91. 134

3.2 Optical micrograph of HCM12A [5]. 135

3.3 Scanning electron microscope image for HT-9. 136

3.4 SEM images of microstructure of 9Cr-ODS [6]. 137

3.5 Geometry of corrosion coupon before polishing. 138

3.6 (a) Positions of width and legth measurement of corrosion coupon. 139

3.7 Schematic diagram of the multi-sample SCW system. High pressure parts of the system are showed in highlighted. 140

3.8 The multi-sample SCW system in high temperature corrosion laboratory, ... 141

3.9 Test vessel of the multi-sample SCW system and corrosion coupons suspended inside the test vessel. 142

3.10 Plots of temperature and pressure control during an experiment at 500°C deaerated SCW for 10 hours. 143

3.11 Conductivity and DO of experiments in deaerated SCW at (a) 400°C (151 hours), (b) 500°C (182 hours), (c) 600°C (191 hours). 144

3.12 Conductivity and DO of experiments in 500°C SCW containing 300 ppb for 182 hours. 145

3.13 A schematic diagram of interactions of ion beam with the target material. 146

3.14 Mechanical polishing steps for cross section TEM preparation; (a) a small sample was cut from the exposed corrosion coupon, (b) sample was cut into 1x2x1 mm, (c) oxide surface was protected by gluing it with M-bond™ to silicon, (d) side view of the sample glued with silicon, (e) polished top (side A) and bottom (side B) sides, (f) polished front (side C) and back (side D) sides, (g) glued on Mo TEM grid with M-bong™, (f) finished sample 147

3.15 Cross section TEM sample preparation in FIB; (a) and (b) Side and top view of sample after mechanical polishing show mechanical damages, ... 148

3.16 Geometries of (a) the 3° glancing angle XRD compare to (b) the standard theta-2theta XRD. 149

4.1 Plots of the time-dependence of weight gain of T91, HCM12A, HT-9, and 9Cr-ODS exposed in deaerated SCW at 400 and 500°C. (Note that the unit of oxidation rate constant from fitting equation is $mg/dm^2/h$.) 200

4.2 Plots of the time-dependence of oxide thickness of (a) T91, (b) HCM12A and (c) HT-9 exposed in deaerated SCW at 500°C. (Note that the unit of oxidation rate constant from fitting equation is μm/h.) 202

4.3 Temperature-dependence of weight gain and total oxide thickness of T91, HCM12A, HT-9, and 9Cr-ODS exposed in deaerated SCW at 400, 500 and 600°C. The weight gain was normalized to 182 hours. 203

4.4 Temperature-dependence of oxide layer thickness of T91, HCM12A, HT-9, 9Cr-ODS exposed in deaerated SCW at 400, 500 and 600°C. The oxide thickness was normalized to 182 hours. 204

4.5 Dissolved oxygen effect on the weight gain and total oxide thickness of T91, HCM12A, and HT-9 in 500°C SCW containing <10 (deaerated), 100 and 300 ppb DO concentration. The weight gain was normalized to 182 hours. 205

4.6 Dissolved oxygen effect on the oxide layer thickness of T91, HCM12A, and HT-9 in 500°C SCW containing <10 (deaerated), 100 and 300 ppb DO concentration. The weight gain was normalized to 182 hours. 206

4.7 SEM images showing morphology of oxide on T91, HCM12A, and HT-9 corrosion coupon exposed in 400^{o}C deaerated SCW for 151.5 hours. 207

4.8 SEM images showing morphology of oxide on T91, HCM12A, and HT-9 corrosion coupon exposed in 500^{o}C deaerated SCW for 1 hour. 208

4.9 SEM images showing morphology of oxide on T91, HCM12A, and HT-9 corrosion coupon exposed in 500^{o}C deaerated SCW for 10 hours. 208

4.10 SEM images showing morphology of oxide on T91, HCM12A, and HT-9 corrosion coupon exposed in 500^{o}C deaerated SCW for 182.2 hours (T91 and HCM12A) and 195 hours (HT-9). 208

4.11 SEM images showing morphology of oxide on T91 and HCM12A corrosion coupon exposed in 500^{o}C SCW containing 100 ppb DO concentration for 236 hours. 209

4.12 SEM images showing morphology of oxide on T91, HCM12A, and HT-9 corrosion coupon exposed in 500°C SCW containing 300 ppb DO concentration for 182 hours. 209

4.13 SEM images showing morphology of oxide on T91, HCM12A, HT-9, and 9Cr-ODS corrosion coupon exposed in 600°C deaerated SCW for 191 hours. 210

4.14 SEM images showing microcracks on (a) surface oxide and (b) cross section of HCM12A exposed in 600°C deaerated SCW for 191 hours. Cross sectional BSE image shows a crack penetrates across outer and inner oxide layers. 211

4.15 Glancing angle XRD spectrum of alloy T91, HCM12A, and HT-9 before exposure in SCW showing iron phase (BCC). 212

4.16 The XRD spectra of the outer oxide layer of T91 tested in SCW at 400, 500, and 600°C deaerated SCW, and at 500°C containing 100 and 300 ppb DO concentration. 213

4.17 The XRD spectra of the outer oxide layer of HCM12A tested in SCW at 400, 500, and 600°C deaerated SCW, and at 500°C containing 100 and 300 ppb DO concentration. 214

4.18 The XRD spectra of the outer oxide layer of HT-9 tested in SCW at 400, 500, and 600°C deaerated SCW, and at 500°C containing 100 and 300 ppb DO concentration. 215

4.19 The XPS spectra from T91 exposed in 500°C SCW under (a) deaerated condition, and (b) 100 ppb DO concentration. Peak fitting of Fe2P is shown on the left side, and O1S is shown on the right side. 216

4.20 The XPS spectra from HCM12A exposed in 500°C SCW under (a) deaerated condition, and (b) 100 ppb DO concentration. Peak fitting of Fe2P is shown on the left side, and O1S is shown on the right side. 217

4.21 Corrosion coupon cross-section BSE image and composition profile of T91, HCM12A, and HT-9 tested in 400°C deaerated SCW, 151.5 hours. 218

4.22 Corrosion coupon cross-section BSE image and composition profile of T91 and HCM12A (exposure time 182.2 hours), and HT-9 (exposure time 195 hours) tested in 500°C deaerated SCW. 219

4.23 Corrosion coupon cross-section BSE image and composition profile of HCM12A exposed in 500°C deaerated SCW for (a)1, (b) 10 and (c) 477 hours. 220

4.24 Corrosion coupon cross-section BSE image and composition profile of T91 and HCM12A tested in 500°C and 100 ppb SCW, 236 hours. 221

4.25 Cross-section BSE images and composition profiles of alloys T91, HCM12A and HT-9 in 500C SCW containing 300 ppb dissolved oxygen, exposure time 182 hours. 222

4.26 Corrosion coupon cross-section BSE image and composition profile of T91 tested in 600^{o}C deaerated SCW, 191 hours. 223

4.27 Corrosion coupon cross-section BSE image and composition profile of HCM12A tested in 600^{o}C deaerated SCW, 191 hours..... 224

4.28 Corrosion coupon cross-section BSE image and composition profile of HT-9 tested in 600^{o}C deaerated SCW, 191 hours. 225

4.29 Corrosion coupon cross-section BSE image and composition profile of 9Cr-ODS tested in 600^{o}C deaerated SCW, 191 hours..... 226

4.30 BSE images showing oxide structure of a) T91, b) HCM12A, c) HT-9 and d) 9Cr-ODS exposed in 600°C SCW for 191 hours. 227

4.31 Cross section BSE images of etched T91 exposed in 600C deaerated SCW for 191 hours. The image shows Cr-rich $M_{23}C_6$ outline PAG boundaries..... 228

4.32 BSE image and elemental mapping of 9Cr-ODS exposed in 600°C SCW for 191 hour. The maps show Cr-enriched oxide at transition/alloy interface..... 229

4.33 Comparison of oxide thickness formed on T91, HCM12A, HT-9 and 9Cr-ODS exposed in 600°C deaerated SCW for 191 hours. 230

4.34 TEM images showing microstructure of HCM12A before exposure in SCW. (a) and (b) Martensite laths, and SAED from a lath (circled) in (a) from (c) $[\bar{1}11]$ and (d) $\bar{1}13$ zone axes exhibited BCC structure of Fe. 231

4.35 TEM images showing precipitate particles of Cr-rich $M_{23}C_6$ in pre-oxidized HCM12A. (a) The particles outline the PAG boundary, (b) a particle at lath boundary, and (c) clusters of precipitates inside alloy matrix..... 232

4.36 (a) BF and (b) DF of Cr-rich $M_{23}C_6$ precipitates, and (c) SAED of the precipitates from $[\bar{1}12]$ zone axes exhibiting FCC structure. 233

4.37 TEM image showing precipitate particles of V-Nb compound in pre-oxidized HCM12A. 234

4.38 TEM image showing precipitate particles of Cu in pre-oxidized HCM12A. 235

4.39 TEM images of microstructure of pre-oxidized T91 showing (a) the martensite laths, and (b) cluster of Cr-rich $M_{23}C_6$ precipitates. 236

4.40 (a) Bright field and (b) HAADF images of oxides formed on HCM12A exposed in 400°C deaerated SCW for 151 hours. The images show two distinct layers of oxide. 237

4.41 TEM image of oxides formed on HCM12A exposed in 400°C deaerated SCW for 151 hours present magnetite grains in the outer layer. (a) Bright field image, and SAED of a magnetite grain (circled) from (b) [011] and (c) $[\bar{1}12]$ directions. 238

4.42 TEM images of oxides formed on HCM12A exposed in 400°C deaerated SCW for 151 hours. (a) BF and (b) HAADF images of inner layer oxide shows precipitates and microcracks in the layer, (c) SAED from the inner oxide shows ring pattern, and (d) DF image exhibits grain size of the inner oxide < 100 nm. 239

4.43 Indexing SAED pattern from the inner oxide of HCM12A exposed in 400°C deaerated SCW for 151 hours. The pattern exhibited FCC spinel structure. 240

4.44 TEM images of oxides formed on HCM12A exposed in 400°C deaerated SCW for 151 hours. (a) - (d) Precipitate particles of Cr-rich $M_{23}C_6$ observed in the inner layer oxide. (e) SAED of precipitate from fcc $[\bar{1}23]$ zone axis. 241

4.45 Composition mapping of oxides formed on HCM12A exposed in 400°C deaerated SCW for 151 hours. (a) HAADF image and composition maps of (b) Fe, (c) O, (d) Cr, (e) V, and (f) Cu. The results show Cr, V and Cu precipitated in the inner layer oxide. 242

4.46 HRTEM images of oxides formed on HCM12A exposed in 400°C deaerated SCW for 151 hours. (a) Interface of magnetite grains and Fourier transformed image (right), (b) the outer-inner oxides interface, and (c) the inner oxide – alloy interface. 243

4.47 Images of oxides formed on HCM12A exposed in 500°C deaerated SCW for 182 hours. (a) Cross sectional BSE image shows oxide layers in (b) – (c). HAADF images of (b) outer layer oxide, (c) inner layer oxide, and (d) transition layer and alloy substrate. 244

4.48 TEM images of the outer layer oxide formed on HCM12A exposed in 500°C deaerated SCW for 182 hours. (a) HAADF image shows magnetite grains with voids inside the grain. (b) SAED pattern from [011] zone axis. 245

4.49 TEM images of the inner layer oxide formed on HCM12A exposed in 500°C deaerated SCW for 182 hours. (a) HAADF and (b) BF images shows morphology of the inner oxide that consisted of small grains of $(Fe,Cr)_3O_4$, precipitates, and microcracks. (c) SAED pattern from the inner oxide exhibited FCC spinel structure. 246

4.50 TEM images of the inner layer oxide formed on HCM12A exposed in 500°C deaerated SCW for 182 hours. (a) BF and (b) DF image shows small grain size of Fe-Cr spinel structure oxides. 247

4.51 (a) and (b) TEM images of precipitate particles in the inner layer oxide formed on HCM12A exposed in 500°C deaerated SCW for 182 hours. (c) SAED from a particle in (a) exhibited FCC structure of $Cr_{23}C_6$ with a = 10.69 Å. 248

4.52 Composition maps of an interface of the inner oxide - transition layer of HCM12A exposed in 500°C deaerated SCW for 182 hours. (a) HAADF image, and composition maps of (b) all elements, (c) Fe, (d) O, (e) Cr, (f) Cu and (g) V. 249

4.53 Images of the transition layer formed on HCM12A exposed in 500°C deaerated SCW for 182 hours. (a) and (b) HAADF images. (c) and (d) BF and DF images show oxide formation in the layer. (e) and (f) SAED patterns taken from transition layer. 250

4.54 Indexing SAED pattern from the transition layer of HCM12A exposed in 500°C deaerated SCW for 182 hours. The pattern exhibited BCC structure (bright spots) of alloy matrix from $[\bar{1}11]$ zone axis, and polycrystal of FCC spinel structure (ring pattern) from the oxides. 251

4.55 TEM images of oxides formed on HCM12A exposed in 500°C SCW containing 300 ppb DO for 182 hours. (a) outer oxide, (b) inner oxide, (c) transition layer, and (d) transition layer and alloy interface. 252

4.56 HAADF images of oxides formed on HCM12A exposed in 500°C SCW containing 300 ppb DO for 182 hours. (a) outer oxide, (b) inner oxide, (c) transition layer and alloy interface. 253

4.57 (a) BF and (b) DF images of inner oxide formed on HCM12A exposed in 500°C SCW containing 300 ppb DO for 182 hours. The images show small grain size of oxides in this layer. 254

4.58 Composition maps of the inner oxide formed on HCM12A exposed in 500°C SCW containing 300 ppb DO for 182 hours. (a) HAADF image, and composition maps of (b) Fe, (c) O, (d) Cr, (e) Cu, (f) V and (g) Nb. 255

4.59 Transition layer formed on HCM12A exposed in 500°C SCW containing 300 ppb DO for 182 hours. (a) HAADF image shows distinct morphology of transition layer from inner oxide and alloy substrate, (b) – (d) SAED from the transition layer exhibits two DP. The bright spots are DP of alloy from (b) $[\bar{1}11]$, (c) $[\bar{1}12]$ and (d) $[\bar{1}13]$ zone axes and the ring pattern diffracted from spinel oxide. 256

4.60 Images of oxides formed on HCM12A exposed in 600°C deaerated SCW for 191 hours. (a) Cross sectional SEM image shows oxide layers in (b) – (c). TEM images

of (b) outer layer oxide, (c) inner layer oxide, (d) transition layer and (e) porous Cr-rich region..... 257

4.61 (a) BF image of a magnetite grain in the outer layer and (b) SAED from $[\bar{1}14]$ direction..... 258

4.62 Comparison of microstructure of transition layer and alloy substrate on HCM12A exposed in 600°C deaerated SCW for 191 hours. BF images of (a) transition layer, (b) alloy, (c) interface of transition layer and alloy, and (d) HAADF images of the interface..... 259

4.63 HAADF image presents the detailed microstructure of transition layer of HCM12A exposed in 600°C deaerated SCW for 191 hours..... 260

4.64 Images of transition layer of HCM12A exposed in 600°C deaerated SCW for 191 hours. (a) BF image shows area of analysis in red-dashed box and SAED in circled area, (b) SAED pattern of intra-lath exhibited two diffraction sets of Fe BCC (bright spots) and FCC spinel structure of oxide (weak spots). DF image taken from (c) bright spot #1 shows lath structure, and (d) weak spots #2 shows formation of oxide grains..... 261

4.65 (a) Indexing SAED pattern from intra-lath of the transition layer of HCM12A exposed in 600°C deaerated SCW for 191 hours. The pattern exhibited three DP; (b) BCC structure from $[012]$ of alloy matrix (a=2.90 Å), and FCC spinel structure from (c) $[013]$ and (d) $[\bar{2}33]$ from the oxides (a=8.50±0.01 Å)..... 262

4.66 TEM images of Cr_2O_3 formed in the transition layer of HCM12A exposed in 600°C deaerated SCW for 191 hours. (a) HAADF image shows dark strips (arrows) of Cr_2O_3 between laths, (b) BF shows Cr_2O_3 strip at transition layer- alloy interface, and (c) SAED pattern can be indexed as the $[241]$ zone axis with $R\bar{3}C$ of Cr_2O_3. 263

4.67 HAADF images of interface of transition layer and alloy substrate of HCM12A exposed in 600°C deaerated SCW for 191 hours. (a) Cr_2O_3 formed at the interface, and (b) the interface without Cr_2O_3..... 264

4.68 Composition maps of the transition layer of HCM12A exposed in 600°C deaerated SCW for 191 hours. (a) HAADF image and composition maps of (b) Fe-Cr-O-Cu, (c) Fe, (d) O, (e) Cr, (f) Cu, (g) V, (h) Nb, (i) Mo and (j) W.. 265

4.69 (a) DF and (b) BF images show morphology of porous Cr-rich oxide formed between transition layer and alloy of HCM12A exposed in 600°C deaerated SCW for 191 hours..... 266

4.70 Series of TEM images verifying porosity of the Cr-rich oxide of HCM12A exposed in 600°C deaerated SCW for 191 hours. Specimen was first focused (a) and was tilted to 9.9° (b). Both images showed different morphology of pore (arrows), which

confirmed that the pores are exist. (c) Under-focused and (d) over-focused images show fringes at pore and crack's edge (arrows). 267

4.71 Indexing SAED of porous Cr-rich oxide formed on HCM12A exposed in 600°C deaerated SCW for 191 hours. The DP exhibited FCC spinel structure of a = 8.48 Å. 268

4.72 Comparison of EDS spectrum of alloy, transition layer and porous Cr-rich oxide from HCM12A exposed in 600°C deaerated SCW for 191 hours. 269

4.73 HAADF images T91 exposed in 600°C deaerated SCW for 191 hours. (a) Inner oxide - transition layer – alloy substrate. (b) Typical structure of transition layer of T91 that consisted of Cr-rich Fe-Cr oxide at lath boundaries and at transition - alloy interface. Small oxide grains embedded in the laths. 270

4.74 HAADF images of interface of transition layer and alloy of T91 exposed in 600°C deaerated SCW for 191 hours. (a) shows that Cr-rich Fe-Cr oxide formed at lath/ subgrain boundaries of alloy (perpendicular to the interface) and an oxide strip formed in the middle of lath (interface). (b) Continuous Cr-rich Fe-Cr oxide at the interface of transition layer and alloy substrate..... 271

4.75 HAADF images of the inner oxide – transition layer interface of T91 exposed in 600°C deaerated SCW for 191 hours. (a) shows z-contrast and difference in morphology of the transition layer and the inner oxide. Cr-rich Fe-Cr oxide strips can be observed in the inner oxide (white lines). (b) High magnification of the interface. (c) Pores in the inner layer oxide..... 272

4.76 Characterization of Cr-rich strip of T91 exposed in 600°C deaerated SCW for 191 hours. (a) BF image shows of Cr-rich strip at interface of transition layer and alloy. (b) and (c) SAED from circled area in (a) exhibit FCC structure with a ~ 8.20 Å from (b) [011] and (c) $[\bar{1}22]$ directions. (d) BF and (e) DF images from SAED in (b). 273

4.77 HAADF image and composition line scan across Cr-rich oxide at the interface of transition and alloy substrate of T91 exposed in 600°C deaerated SCW..... 274

4.78 Composition maps of the transition layer of T91 exposed in 600°C deaerated SCW for 191 hours. (a) HAADF image and composition maps of (b) Fe-Cr-O, (c) Fe, (d) O, (e) Cr, (f) Cu, (g) Ni and (h) Si..... 275

4.79 TEM images of HT-9 exposed in 600°C deaerated SCW for 191 hours. (a) Alloy substrate, (b) interface of alloy and inner oxide, and (c) inner layer oxide..... 276

4.80 HAADF images of interface of alloy and inner layer oxide of HT-9 exposed in 600°C deaerated SCW for 191 hours. (a) Images show characteristic of the interface that consisted of Cr-rich oxide region, pores, and transition region. (b) Transition region formed between alloy and inner oxide. 277

4.81 HAADF image of inner layer oxide of HT-9 exposed in 600°C deaerated SCW for 191 hours. (a) The inner oxide consisting of spinel structure oxide, pores and precipitates. (b) SAED from the inner oxide exhibits spinel structure. (c) and (d) Major precipitate type is Ni-rich particle. (e) and (f) Composition line scan shows Ni, Fe and O enriched in the particle (circled). 278

4.82 Composition maps of Cr-rich oxide region at interface of inner oxide and alloy on HT-9 exposed in 600°C deaerated SCW for 191 hours. (a) HAADF image and composition maps of (b) Fe, (c) O, (d) Cr, (e) Ni, (f) Si and (g) V. (W and Ti are omitted from this) 279

4.83 Composition maps of Cr-rich oxide region at interface of inner oxide and alloy on HT-9 exposed in 600°C deaerated SCW for 191 hours. (a) HAADF image and composition maps of (b) Fe, (c) O, (d) Cr, (e) Ni, (f) Mo and (g) V. 280

4.84 (a) and (b) Composition line scans of Cr-rich oxide region at interface of inner oxide and alloy on HT-9 exposed in 600°C deaerated SCW for 191 hours. The scans show Cr-rich spinel oxide at the interface with Fe:Cr:O of approximately 1:2:4. 281

4.85 SAED pattern of Cr-rich oxide region at interface of inner oxide and alloy on HT-9 exposed in 600°C deaerated SCW for 191 hours. The pattern exhibits spinel structure. 282

4.86 HAADF image of inner layer oxide, transition layer and alloy substrate of 9Cr-ODS exposed in 600°C deaerated SCW for 191 hours. 283

4.87 Characteristic of transition layer formed on 9Cr-ODS exposed in 600°C deaerated SCW for 191 hours. (a) HAADF image of transition layer. (b) BF image of intra-lath in the transition layer shows lattice fringes of small oxide grains. 284

4.88 HAADF images of 9Cr-ODS exposed in 600°C deaerated SCW for 191 hours. (a) Interface of transition layer and alloy, and (b) small precipitates of Ti in the alloy substrate. (c) Interface of inner oxide and transition layer, and (d) high magnification image shows large pore in the inner oxide. 285

4.89 Composition maps of transition layer of 9Cr-ODS exposed in 600°C deaerated SCW for 191 hours. (a) HAADF image and composition maps of (b) all elements, (c) Fe, (d) O, (e) Cr and (f) W. The results show Cr-rich oxide at lath boundaries and W-rich particles as a major precipitate in the transition layer. 286

4.90 Composition maps show W, Ti and Y enriched precipitates formed in transition layer of 9Cr-ODS exposed in 600°C deaerated SCW for 191 hours. (a) HAADF image and composition maps of (b) all elements, (c) Fe, (d) O, (e) Cr, (f) W, (g) Ti and (h) Y. 287

4.91 HAADF images and composition line scans across (a) the Cr-rich oxide and (b) the W-rich particle in the transition layer of 9Cr-ODS exposed in 600°C deaerated SCW for 191 hours. 288

4.92 (a) and (b) BF images illustrate Cr-rich oxide bands in the transition layer of 9Cr-ODS exposed in 600°C deaerated SCW for 191 hours. (c) SAED from a Cr-rich oxide band in (d). The pattern from [112] exhibits FCC structure with a = 8.92 Å, and (e) DF image from the pattern in (c)..... 289

4.93 Schematic diagram of oxides formed on (a) T91, (b) HCM12A, (c) HT-9 and (d) 9Cr-ODS alloy exposed in 600°C deaerated SCW for 191 hours..... 290

5.1 Plot of natural logarithmic of weight gain and 1/T of T91, HCM12A, HT-9 and 9Cr-ODS. 366

5.2 Plot of natural logarithmic of oxide thickness and 1/T of T91 tested in 400, 500 and 600°C deaerated SCW. The thickness was normalized to 182 hours. 367

5.3 Plot of natural logarithmic of oxide thickness and 1/T of HCM12A tested in 400, 500 and 600°C deaerated SCW. The thickness was normalized to 182 hours..... 368

5.4 Plot of natural logarithmic of oxide thickness and 1/T of HT-9 tested in 400, 500 and 600°C deaerated SCW. The thickness was normalized to 182 hours. 369

5.5 Plots of diffusivity of Fe in Fe_3O_4 as a function of oxygen partial pressure. 370

5.6 Plots of diffusivity of O in Fe_3O_4 as a function of oxygen partial pressure at 550°C. 370

5.7 Plots of diffusivity of Fe in Fe_3O_4, Fe_2CrO_4, $Fe_{1.8}Cr_{1.2}O_4$ as a function of oxygen partial pressure at 400, 500 and 600°C..... 371

5.8 Comparison of the diffusion coefficients of Fe and O in Fe_3O_4 and $FeCr_2O_4$. The data was obtained from the experiment with poly-crystal. 372

5.9 Calculated diffusing distance of Fe and O in Fe_3O_4 compared with outer oxide thickness. 373

5.10 Calculated diffusing distance of O in $FeCr_2O_4$ and Fe in Fe_2CrO_4 compared with inner oxide thickness. 373

5.11 A BSE image of HCM12A illustrating position of oxygen partial pressure determined by the oxidation rate equation. The alloy was exposed in 500°C deaerated SCW for 182 hours. 374

5.12 Predominance diagram of the Fe-Cr-O system at 400°C. M is Fe and Cr. 375

5.13 Predominance diagram of the Fe-Cr-O system at 500°C. M is Fe and Cr. 376

5.14 Predominance diagram of the Fe-Cr-O system at 600°C. M is Fe and Cr. 377

5.15 Plot of $P_{O_2}^{trans-inner}$, $P_{O_2}^{inner-outer}$ and $P_{O_2}^{outer-water}$ versus relative position in total oxide of T91, HCM12A, HT-9 and 9Cr-ODS exposed in 400-600°C SCW. 378

5.16 Crystallographic models of spinel structure showing (a) two types of sub-lattice that contain A^{2+} in tetrahedral site and B^{3+} in octahedral sites [70]. (b) Unit cell of spinel with tetrahedral sites (blue) and octahedral sites (pink). 379

5.17 Cross section BSE images of (a) T91, (b) HCM12A, (c) HT-9 and (d) 9Cr-ODS show pore formation in inner oxide at i) the interface inner oxide and transition layer, and ii) in the inner oxide 380

5.18 SEM cross section images of etched samples of (a) T91 and (b) HCM12A exposed in 600°C SCW for 191 hours. BSE images of HCM12A exposed in (c) 500°C SCW for 182 hours and (d) 600°C SCW for 191 hours 381

5.19 (a) Schematic diagram of oxide layer formed on HCM12A exposed in 600°C SCW. (b) Model of reactions and transport processes of ions involved in the growth of the outer oxide (Fe_3O_4), the inner oxide ($Fe_{3-x}Cr_xO_4$, assumed x = 1), and the transition layer. 382

LIST OF TABLES

Table

2.1 Effects of alloying addition on the constitution of steel containing 9-12% Cr [23, 33]. 55

2.2 Precipitation in normalized and tempered, aged, and creep rupture tested F-M alloys [23]. 56

2.3 Classification of electrical conductor for oxides, sulfides, and nitrides [44, 48] 57

2.4 Standard free energies of reaction [49]. 58

3.1 Composition of F-M alloys; T91, HCM12A, HT-9, and 9Cr-ODS. 125

3.2 Heat treatment of F-M alloys; T91, HCM12A, HT-9, and 9Cr-ODS. 126

3.3 Dimension, surface area, and weight of corrosion coupons tested in each experiment. 127

3.4 Specifications for main components of the multi-sample SCW test facility 128

3.5 Summary of SCW experimental conditions 129

3.6 Summary of sample characterization by the analysis techniques 130

3.7 Summary of reflections from cubic systems 131

3.8 List of characteristic X-ray energies of major compositions in four F-M alloys and oxide 132

3.9 Relations for calculation of error for two or more quantities which have individual errors 133

4.1 The time-dependence of weight gain of T91, HCM12A, HT-9, and 9Cr-ODS exposed in deaerated SCW at 400 and 500°C. 186

4.2 The time-dependence of oxide thickness of T91, HCM12A, HT-9 exposed in deaerated SCW at 400 and 500°C 187

4.3 Relations of weight gain vs. time fitted by parabolic, power and logarithmic equation. 188

4.4 Oxidation rate constant and power from the power equation ($w = k_w t^n$ and $x = k_x t^n$) of time-dependence of oxidation rate determined from weight gain at 400 and 500°C, and oxide thickness at 500°C deaerated SCW..... 189

4.5 The temperature-dependence of weight gain of T91, HCM12A, HT-9, and 9Cr-ODS exposed in deaerated SCW at 400, 500 and 600°C. 190

4.6 The temperature-dependence of oxide thickness of T91, HCM12A, HT-9, and 9Cr-ODS exposed in deaerated SCW at 400, 500 and 600°C. (continued on next page) 191

4.7 Dissolved oxygen effects on weight gain of T91, HCM12A, and HT-9 exposed at 500°C SCW containing <10 ppb (deaerated), 100 ppb, and 300 ppb DO concentration. 193

4.8 Dissolved oxygen effects on oxide thickness of T91, HCM12A, and HT-9 exposed at 500°C SCW containing <10 ppb (deaerated), 100 ppb, and 300 ppb DO concentration. 194

4.9 The XPS results of surface oxide formed on T91 and HCM12A exposed in 500°C SCW under deaerated condition and containing 100 ppb DO. 195

4.10 Compositions of the inner oxide ($(Fe,Cr)_3O_4$) of T91, HCM12A, HT-9, and 9Cr-ODS exposed in SCW. The data was determined in EDS of SEM. 196

4.11 Summary of microstructure characterizations of the oxides formed on HCM12A exposed in 400 and 500°C deaerated SCW, and in 500°C containing 300 ppb DO SCW for 188, 182.2, and 182 hour, respectively. 197

4.12 Summary of the microstructure of oxides formed on T91, HCM12A, HT-9 and 9Cr-ODS exposed in 600°C deaerated SCW for 191 hours..... 198

5.1 Comparison of oxidation rate constants and powers determined from weight gain of F-M alloys in SCW from this thesis and from literature. 358

5.2 Activation energies determined from weight gain and oxide thickness of T91, HCM12A, HT-9 and 9Cr-ODS, and from literature data. 359

5.3 Frequency factor (D_o) and activation energy (Q) of Fe, Cr and O in Fe_3O_4, Cr_2O_3 and miscellaneous oxides 360

5.4 Diffusion coefficients of Fe, Cr and O in Fe-Cr spinel oxide and Cr_2O_3. 361

5.5 Calculation of Cr concentration in inner oxide from the oxide thicknesses. The results agree with Cr concentration from experiments. 362

5.6 Calculation of thickness of alloy that was consumed to produce the inner oxide (h_{alloy})..... 363

5.7 List of parameters in equations 5.5 and 5.17, and calculated values at 400, 500 and 600°C. 364

5.8 Oxygen partial pressure of T91, HCM12A and HT-9 determined by oxidation rate equation..... 365

LIST OF APPENDICES

Appendix

I. Standard diffraction patterns from JCPDS 394

II. Analysis of X-ray diffraction pattern 400

III. Derivation of defect concentration in spinel structure oxide 404

ABSTRACT

DETERMINATION OF OXIDATION MECHANISMS OF

FERRITIC-MARTENSITIC ALLOYS IN SUPERCRITICAL WATER

by

Pantip Ampornrat

Co-Chairs: Lumin Wang and Gary S. Was

The objective of this thesis is to understand the oxidation mechanisms of ferritic-martensitic (F-M) alloys in supercritical water (SCW). The alloys are proposed as candidate materials for structural materials in SCW-cooled concept of Gen-IV nuclear reactors. The alloys should be able to withstand severe environment of SCW, which exists above 374.14°C and pressure of 22.09 MPa. The approaches of this study include; i) determine the effects of SCW temperature on the oxidation rate, ii) determine the diffusion processes in oxide in terms of diffusion species and mechanisms and iii) understand the structure of the various oxide phases and their formation. Research has been conducted in three major steps including SCW exposure experiment, sample analysis, and determination of the oxidation mechanisms.

Microstructure of oxide formed on four F-M alloys; T91, HCM12A, HT-9 and 9Cr-ODS, exposed in 400 – 600°C SCW consisted of two oxide layers and a transition layer. The outer oxide consisted of dense columnar grains of magnetite (Fe_3O_4). The inner oxide consisted of small equiaxed grains of Fe-Cr spinel oxide $Fe_{3-x}Cr_xO_4$, where x ~ 0.7-1 depends on alloy type. The transition layer consisted of grain boundary oxides of chromia and chromite, and fine oxide grains of a spinel structure precipitated inside laths.

SCW temperature and alloy type have influence on oxidation. The oxidation rate increased exponentially as a function of temperature. The oxidation rate followed trend of Cr content in alloy in which HCM12A and HT-9 with high Cr exhibited lower oxidation rate than T91. The 9Cr-ODS exhibited relatively good oxidation resistance compare to T91 with a similar Cr content. This reflects an effect of Y_2O_3 nano particles.

Interpretation of the oxidation rate reveals that; i) the power relation of the oxidation shows that the oxidation occurred by a diffusion controlled mechanism, ii) the activation energy of oxidation, which is lower than that of lattice diffusions of Fe and O in oxide suggests the occurrence of short circuit diffusion along grain boundaries and defects in the oxide, and iii) the rate limiting mechanism is Fe diffusion.

The original alloy surface is at the outer – inner oxide interface. Formation of the outer oxide occurs by outward diffusion of Fe ions. Transport of Fe ions in the outer oxide is dominated by a vacancy diffusion mechanism. Formation of the inner oxide occurs by inward diffusion of oxygen, and micropores occur as a result of outward diffusion of Fe ions to the outer oxide. Transport of Fe ions through the inner layer occurs by cation vacancies in most of the layer, and the interstitial diffusion dominates near the transition layer – inner oxide interface. Oxygen transport occurred primarily by the short-circuit diffusion.

CHAPTER 1

INTRODUCTION

The demand of energy increases rapidly as the world's population grows. However, simply expanding energy usage with present production options will continue to have adverse environmental impacts and potential long-term consequences from global climate change. Nuclear energy is one of the power generation options that provides clean, safe, and cost effective with non greenhouse gas emitting. The Generation IV nuclear reactors initiative has been developed based on advanced reactor design knowledge. Goals of this development are to improve sustainability, economics, safety and reliability, and to minimize nuclear waste. In order to approach these goals, the Generation IV reactors have been designed with a sustainability fuel cycle and high thermal efficiency by operating at higher temperatures and pressures, and different operating environments [1]. One of major concerns is their reliability, which is partially determined by the suitability of structural materials being used under such operating environments.

The supercritical water-cooled reactor (SCWR) is one of six concepts of the Generation IV nuclear reactors initiative [1]. The SCWR is basically light water reactor that operates in supercritical water (SCW) regime with a direct once-through cycle, Figure 1.1. Operation above the critical pressure eliminates coolant boiling, so the coolant remains single-phase throughout the system. The SCWR features two fuel cycle

options; the first is an open cycle with a thermal neutron spectrum reactor, and the second is a closed cycle with a fast-neutron spectrum reactor and full actinide recycle. In both options, the reactor will be operated at temperatures up to 620°C (and up to 700-840^{o}C for <30 seconds under off-normal conditions), pressure greater than 22 MPa (3,200 psi) and to neutron doses of 15-30 dpa of energy greater than 1 MeV [1, 2]. The most important requirement is structure materials that can withstand the SCW environment and the radiation field. Material degradations can occur during the services included; corrosion, stress corrosion cracking, reduction of creep strength, and material instability during irradiation (swelling and void formation). Therefore, understand these behaviors under the SCW condition are critical for development of the SCWR.

Ferritic-martensitic (F-M) alloys are proposed as candidate materials for in-core and core structural support components in the SCWR [1]. The F-M alloys have been considered because of their experiences in fossil SCW power plants and high temperature applications. The F-M alloys exhibited good performance of high temperature strength and creep resistance, high thermal conductivity, low swelling and activation under irradiation, low susceptibility to stress corrosion cracking (SCC) and modest corrosion resistance. While F-M alloys exhibit good resistance to SCC compared to austenitic and Ni-based alloys, their behavior following irradiation is unknown and corrosion resistance is limited. Further, the corrosion behavior under the SCW condition must be investigated in order to determine if these alloys can withstand the proposed operating environment of an SCWR.

Four types of F-M alloys; T91, HCM12A, HT-9, and oxide dispersive strengthening (ODS) containing 9 wt% of Cr, were studied in this thesis. However, only

three of them including T91, HCM12A, and 9Cr-ODS have been selected for the SCWR application. Alloy T91 has a nominal composition of 9Cr-1MoVNb and has been extensively used for header and steam pipes in ultra SCW fossil plants operating up to 593°C [3]. Alloy HCM12A with a nominal composition of 11Cr-0.5Mo-2WVNbCu has been used for thick wall pipes of fossil plant boilers [4]. Alloy HT-9 (12Cr-1MoVW) is an early generation F-M alloy that contains highest Cr content among the tested alloys. Due to its low creep strength [5], HT-9 was not selected as candidate material for the SCWR. The ODS alloy includes yttria (Y_2O_3) or titania (Ti_2O_3) dispersion aimed to increase the creep strength. The nominal composition of 9Cr ODS studied in this thesis is 9Cr-2WTi-0.35Y_2O_3.

While much attention is focused on mechanical properties, corrosion resistance of F-M alloys could be a major concern for their applications in the SCWR. Corrosion can cause numerous problems including; metal loss and loss of strength due to scaling of alloy, decrease of thermal conductivity of the structural materials, changes of surface chemistry, and reduction in component lifetime. Furthermore, soluble corrosion products can increase radioactivity level in the reactor coolant that affects the accessibility and safe maintenance, and insoluble corrosion products can build up on parts of the reactor primary system, which will block the coolant path and create high radiation field in some particular areas. The practical issues of corrosion protection methods focused on the kinetics of oxidation reaction, methods of slowing the reactions, and the means for controlling its morphology. These methodologies do need a fundamental understanding of the oxidation mechanisms. Especially in the SCW condition, there is very limited data

on the oxidation mechanism. This subject becomes a priority research that needs to be conducted on the SCWR project.

The oxidation of iron-based alloys at high temperature has been studied extensively in various environments such as in air, gas, and steam. However, information of oxidation in the SCW environment is still restricted. Most of the available data of different materials were reported from experiments in supercritical water oxidation waste disposal systems and from experiences in fossil fuel power plants. Very limited data on oxidation in low conductivity and deaerated condition that will be used in a SCWR.

At high temperature, the oxidation rates of the F-M alloys are relatively high compared to those of austenitic alloys that contain higher concentrations of Cr. Kinetics of oxidation can be expressed as a parabolic function of time. Oxides formed on the alloys consisted of multi-layer scales, and the types of scale depend on specific oxidation conditions of temperature and oxygen partial pressure. In pure iron, the order of oxide layer from the outermost surface is hematite (Fe_2O_3), magnetite (Fe_3O_4), and wustite (FeO). Addition of chromium concentration results in the formation of a Cr-rich oxide, such as a spinel structure oxide $Fe(Fe,Cr)_2O_4$, along with the Fe oxides. Further increasing the Cr concentration (> 12%) produces chromia (Cr_2O_3) scale. The oxidation mechanism has been known to dominate by the diffusion of either anions or cations through the scales. Formation of Cr-rich oxide and chromia slow down ionic transport. As a result, the oxidation rate decreases in the alloy that contains higher Cr concentration.

The preliminary study of oxidation of F-M alloys in SCW [6] showed that at least three layers of oxides including; an outer layer oxide of magnetite, an inner oxide of Fe-Cr spinel oxide, and a transition layer formed at the interface of inner oxide and alloy

substrate. Oxidation is believed to be controlled by at least two processes; growth of a magnetite layer by outward diffusion of Fe ions to the oxide - water interface, and inner Fe-Cr oxide layer growth by inward diffusion of oxygen to the oxide-metal interface. Transformation of the alloy into an oxide occurs in the transition layer, which also influences the oxidation resistance. The information from these results is sufficient to provide some insight into the oxidation mechanism. However, specific details of the microstructure and phase structure in each layer, especially in transition layer, are needed to fully understand the underlying physical principles.

The broad objective of this thesis is to understand the oxidation mechanisms of F-M alloys in SCW. In order to achieve this goal, research has been conducted in three major areas; i) SCW exposure experiments, ii) sample analysis, and iii) determination of oxidation mechanisms. The second chapter of this thesis will cover the background literature including SCW properties, the F-M alloys, the oxidation of F-M alloys, and will state the specific thesis objective and approach. Chapter 3 will describe the experimental procedures, the apparatus and the analysis techniques. Chapter 4 will present the results of oxidation rates, oxide morphology, composition, microstructure and phase. Chapter 5 will discuss the results by explanation of the oxide structures, formation of oxide scales, and determination of oxidation mechanisms. Recommendations for the future directions of the work will be given at the end of this chapter. Finally, Chapter 6 will state the conclusions of this thesis.

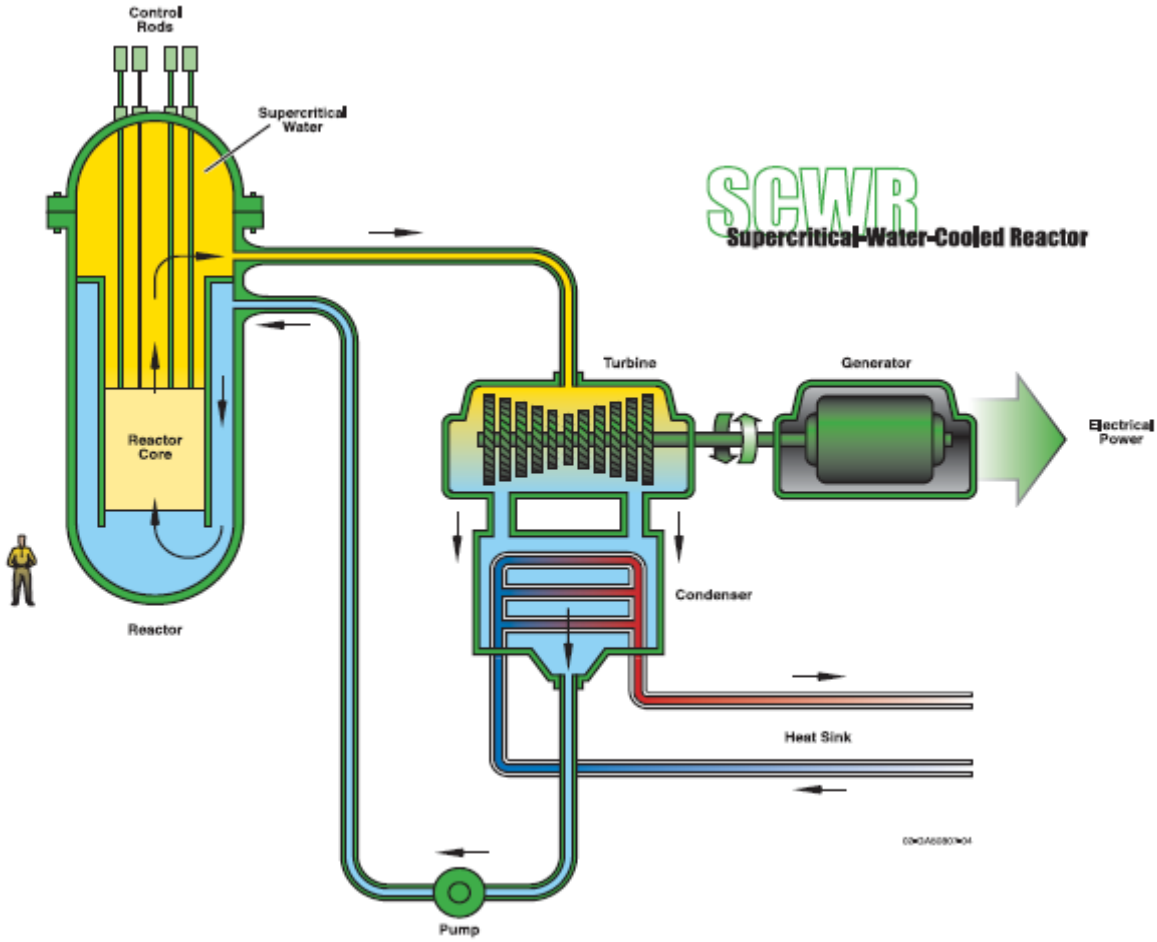

Figure 1.1 Schematic diagram of the Generation IV SCWR concept

BIBLIOGRAPHY

1. *A Technology Roadmap for Generation IV Nuclear Energy Systems*. 2002 U.S. DOE Nuclear energy research advisory committee and the Generation IV international forum.
2. Oka, Y. and e. al., *Systems design of direct-cycle supercritical-water-cooled fast reactors.* Nuclear Technology, 1995. **109**: p. 1-10.
3. Masuyama, F., *New Developments in Steels for Power Generation Boilers*, in *Advanced Heat Resistance Steels for Power Generation*, R.V.a.J.W. Nutting, Editor. 1999, IOM Communications Ltd.: London. p. 33-48.
4. Sawagari, Y., et al. *Development of a High Strength 12Cr Steel (HCM12A).* in *The 1994 Conference on Materials for Advanced Power Engineering*. 1994. Liege, Belgium: Kluwer Academic Publisher.
5. Klueh, R.L. and D.R. Harries, *High chromium ferritic and martensitic steels for nuclear applications*. 2001, PA, U.S.A.: ASTM.
6. Ampornrat, P. and G.S. Was, *Oxidation of ferritic-martensitic alloys T91, HCM12A and HT-9 in supercritical water.* Journal of Nuclear Materials, 2007. **371**(1-3): p. 1-17.

CHAPTER 2

BACKGROUND

This chapter presents the fundamental knowledge and literature data necessary for understanding the oxidation mechanisms of F-M alloys in SCW environments. First of all, the fundamental knowledge of SCW will be described in terms of physical and chemical properties that affect the oxidation. The discussion will be focused on the water property changing from liquid, gas, subcritical and SCW states. The effects of temperature and pressure on the SCW properties also will be reviewed. Following the SCW section, the characteristic of F-M alloys will be discussed starting from alloy design, constitution, phase transformation, microstructure, and properties of the alloys. The next section addresses the oxidation of F-M alloys and is focused on the influence of the alloy composition and microstructure, and the exposure environment on the oxidation mechanism, which are demonstrated through results of oxidation rate and oxide microstructure. Finally, the thesis objective and approach are presented at the end of this chapter.

2.1 Supercritical Water

Similar to metals, water can exist as a solid, liquid or depending on temperature and pressure. At high temperature water usually presents in a gaseous state, but it can transform into a phase called “supercritical water” if high pressure is applied. The phase diagram of water is shown in Figure 2.1 [1]. In fact, SCW is also discovered in nature on the ocean floor where superheated water vents from the Earth’s crust with temperature around 400°C and the water pressure exceeds water vapor pressure. This water contains dissolved mineral, mostly sulfides, from the crust so it forms into a black chimney-like structure, called “black smoker” [2]. For pure water, SCW exhibits chemical and physical properties intermediate between liquid and gas. The primary characteristics of SCW include [3];

- It behaves like dense gas,
- It has solubility approaching that of the liquid state,
- Diffusivity of SCW approaches the gas phase.

In order to understand the corrosion / oxidation mechanisms in SCW, the properties of SCW need to be clarified. This review will state some properties that define the oxidation of the alloys using available literature data of the SCWO and the SCW fossil power plants.

SCW exists above a super-critical point at temperature 374.14°C and pressure of 22.09 MPa with density of 14.13 mol/cm^3 [4]. Under this condition, the SCW exhibits unique properties that can be classified into; i) macroscopic properties including density, viscosity, diffusivity, dielectric constant, ionic products, and thermodynamic properties,

and ii) microscopic property such as hydrogen bonding. These parameters change continuously with the variations of temperature and pressure. The properties of SCW will be stated in both specific values and their trends compared to the sub-critical water and the gaseous states.

Density of SCW is ~0.1 g/cm^3, which is intermediate between the liquid (~1 g/cm^3) and the gaseous phases (< 0.001 g/cm^3). As a point of comparison, the SCW density is approximately equivalent to that of nitrogen gas of 0.1 g/cm^3 at 25°C and a pressure of 10 MPa. However, the SCW density changes as functions of temperature and pressure, Figure 2.2. Figure a) shows variation of water density from 250 to 600°C [5]. The density decreases dramatically in temperature range of ~350 - 400°C where the critical point located. The density drops to ~0.1 to 0.6 MPa (depends on pressure) at 400°C and gradually reduces as temperature increases. Figure b) shows plots of the density as a function of pressure from temperature 400 to 550°C [6]. Each plot corresponds to one pressure, which varied from 20 to 60 MPa (200-600 bar). The density gradually decreases as temperature increases, but the pressure has a great impact in which the density increases as the pressure increases. Hence it is important to indicate both temperature and pressure when referring to the density of SCW.

Viscosity of SCW also depends on its temperature and pressure. The viscosity decreases as temperature increases from ~400 – 550°C for the pressure of 30 – 60 MPa, Figure 2.3 [6]. However, the viscosity slightly increases as a function of temperature at a pressure of 20 MPa. From the same figure, the viscosity is directly dependent on the pressure of SCW. Note that the viscosity and the density of SCW exhibit almost similar trends of temperature and pressure dependences.

The viscosity is also related to the diffusivity of the species of interests (e.g. O_2 and H^+), following an estimation of Walden-type equation;

$$D\eta = \text{constant}, \qquad (2.1)$$

where D is the diffusivity of the species interest, and η is the dynamic viscosity of the medium. Note that this equation indicates in inverse relationship between diffusivity and viscosity [6]. If the viscosity decreases, the diffusivity of interest species increases. Therefore both viscosity and diffusivity can serve as guides to determining the transport properties of the SCW medium, for example, the rate at which reactants are transferred to the metal surface. As a result, the mass-transport controlled reaction rate can be predicted using these parameters. Based on equation (2.1), the diffusivity of reactants in SCW tends to increase at higher temperature, but decreases as the pressure increases.

Dielectric constant, which determines the extent to which ions are stabilized in condensed media, is one of the SCW properties that has been reported widely [6-12]. Dielectric constant of SCW decreases strongly with increasing temperature and decreasing pressure, Figure 2.4. Plot in Figure (a) shows the static dielectric constant as a function of temperature from 0 to ~550°C. This figure demonstrates that the dielectric constant decreases from $\varepsilon \sim 80$ for the liquid phase to the range of 2 to 30 for the SCW, which is in a similar range of organic solvent of low parity (e.g. hexane $\varepsilon = 1.8$ and methanol $\varepsilon = 32.6$). As a result, the low parity organic substances that do not dissolve in water under liquid phase can be dissolved in the SCW. In the same time, the solubility of high polar ion, i.e. corrosion product, increase under the SCW condition. From the same figure, there are significant drops of the dielectric constant at the critical point for the plots of pressure 20-30 MPa. Figures (b) and (c) show variations of the dielectric constant

as functions of temperature and pressure in the SCW regime, which exhibit the similar trend as mentioned above. The reason for the decrease of dielectric constant at high temperature is that electrolytes (e.g. HCl, NaCl, NaOH) are very poorly ionized under the SCW condition [6]. This is a most important point because the SCW begin to acquire the gas-like properties at above the critical point. Accordingly, supercritical aqueous systems may be described as the interface between the liquid and the gas phases in many properties, including the corrosion.

The ionic product of water (K_w) is determined from activities of the ion, e.g. hydronium (H_3O^+) and hydroxide ion (OH^-), remain in the water. The ionic product is another property that varies rapidly with temperature in the sub-critical and the SCW regimes. According to a report by Marshall and Franck [13], the ionic products gradually increases with temperature and reaches a maximum near 300°C, then rapidly drops with the further increase in temperature to the SCW regime. Figure 2.5 represents plots of the ionic products as a function of temperature [5]. Each plot corresponds to the ionic products under a pressure. It is found that the K_w in the range of 200-300°C is ~2 order of magnitude higher than that of the SCW temperature. Similar to the other properties, the rapid changes of K_w occurred at the sub-critical temperature. However, the K_w increases as the pressure increases. This property confirms that the SCW acts as a low polar solvent. The low polar nature and low density of the SCW allows virtually all small organics and permanent gases (i.e. O_2 and N_2) to be fully miscible in the SCW [7].

An important aspect of the ionic products is that it represents a direct correlation with the pH of the SCW. An estimation of the pH from the ionic products can be written as [6];

$$pH = \frac{pK_w}{2}, \qquad (2.2)$$

where, pK_w is the negative log of the ionic products of water (pK_w = -log K_w). As from this equation, trend of pH of SCW is expected to follow the similar trend of ionic products. Aside this, there are attempts to present the relationship of the pH and the electrochemical potential (E) by a Pourbaix diagram for the subcritical and the SCW regions [14-17]. The Pourbaix diagrams in this region will be discussed later in Section 2.3.3c.

Thermal conductivity of SCW also follows the similar trend of density and viscosity, Figure 2.6. The thermal conductivity decreases tremendously in subcritical region and drops ~5 times of that of liquid phase. However, the specific heat increases as a peak at the subcritical region. These thermal properties should not have any significant effects on the corrosion behavior.

In the microscopic aspect, the chemical reactivity between water molecules in terms of hydrogen bonding in subcritical and SCW regions has been studied extensively. This characteristic becomes an interest because the changes of hydrogen bonding can play an important role in the macroscopic properties, e.g. influence on the dielectric constant [8], density and viscosity. The studies have been performed using several techniques includes X-ray diffraction (XRD), Raman spectroscopy, Infrared spectroscopy (IR), nuclear magnetic resonance (NMR) and neutron diffraction compared to a molecular dynamics simulation [8, 18-20]. The hydrogen bonding of water molecules can be classified into trimers, dimers, and monomers, which correspond to the bonding of three, two and single molecules, respectively. Figure 2.7 demonstrates a water trimer that consists of three water molecules whereas each water monomer acts as a single hydrogen

bond donor and accepter [21]. Matsubayashi et al. [18] found that the strength of hydrogen bonding reaches a plateau value at high temperature and the hydrogen bonding persists in SCW. Ikushima et al. [8] found that in subcritical region dimers and / or trimers are predominant, but dimers, in part, might be broken into monomers due to large fluctuations of the structure. Thus their conclusion was that monomers, dimers, and trimers dominate in low density SCW. At higher density, more complex structure of water molecules could exist. The results agreed with molecular dynamics simulations [19, 20].

In summary, the properties of water including density, viscosity, dielectric constant and ionic products change dramatically when the water transform from liquid or gas phases to the subcritical region. These properties dropped from those of liquid (of $T < 374°C$ and $P < 22$ MPa) to very low values, which are close to the properties of the gas phase. The only property that increases is the diffusivity of reactants in SCW phase. Therefore, SCW possesses properties that are intermediate between the liquid and the gaseous states. The best description for SCW is that it behaves like dense gas. In the SCW region, temperature and pressure play important roles on its properties. SCW properties (density, viscosity, dielectric constant and ionic products) decrease strongly with increasing temperature and decreasing pressure.

2.2 Ferritic-martensitic Alloys

F-M alloys (as referred to as steels) are proposed as candidate materials for the SCWR because of their experiences in fossil SCW power plants and in high temperature applications. The F-M alloys exhibited good performance of high temperature strength and creep resistance, high thermal conductivity, stability under irradiation, and low susceptibility to SCC. However, the disadvantage of F-M alloys is their low corrosion resistance at high temperature when compared with austenitic and Ni-based alloys. This section describes the background and characteristics of F-M alloys that is necessary for understanding their behavior during the oxidation under SCW environment. The reviews consisted of development, constitution, and process conditions of the F-M alloys.

2.2.1. Development and Composition Design

The history of power plants and progress in heat resistant alloys were thoroughly summarized by Masuyama [22], and Klueh and Harries [23]. Primarily the alloy development has been conducted in order to supply the power industry requirements for alloys that can withstand high temperature and high pressure environment. For example, at present the steam temperature of 600°C of modern fossil power plant with swing load or sliding pressure demand functions has been utilized, and the goal for the future power plants is to increase temperature up to 630 to 650°C to improve thermal efficiency [24]. Likewise, the nuclear power industry also requires similar types of materials for the future generation of reactors.

The 9-12% Cr alloys were invented around 1912-1913 in Europe and the U.S. by discovering that the alloys containing 12-13%Cr did not rust [23]. The initial purpose was to use them for steam turbine blades. Later in 1970s, the 9% and 12% Cr transformable alloys with lower carbon content (0.1% max) and additions of Mo, W, V, Nb, N and other elements were developed for higher creep rupture strengths combined with good oxidation and corrosion resistance at elevated temperatures. The development of F-M alloys can be classified into at least four generations based on the improvement of creep rupture strength, Figure 2.8. Since four alloys studied in this thesis were developed in different generations of F-M alloys, the background of alloy design and their properties will be stated in this section.

The alloy design has been preformed based on the requirements of the industry and the problems occurred with the previous generation alloys. For the supercritical conditions, the major concerns for materials involved;

- High temperature strength: allowable stress is used to represent the high temperature strength characteristic of heat resistant alloys, and is often determined by creep rupture strength under actual operating conditions.
- High temperature corrosion and oxidation: high temperature corrosion and oxidation is a major factor affecting the life of superheater tubes, and the corrosion rate increases as the temperature goes up. In general, the increase of Cr content improves the corrosion resistance of alloys.
- Thermal fatigue: thermal and creep fatigue can cause substantial damage to the header, main steam pipes and valves because of frequent start and stop operation of the power plants. The accident can occur with low thermal conductivity alloys

such as austenitic alloys since the thermal stress can arise during start and stop processes. Therefore the F-M alloys must be employed.

- Economy: both high temperature strength and economy must be considered in the selection of materials. In general, high alloying element materials exhibit better creep rupture strength, but they are highly cost. Figure 2.9 shows the relationship between the allowable temperature at an allowable stress of 49 MPa and the relative material cost for the plant components [22].

The ferritic alloys can be classified into; carbon alloys (C-Mn, etc.), low alloy steels (0.5%Mo~2.25%Cr-1%Mo), intermediate alloy steels (5-10%Cr) and high alloy steels (12%Cr martensitic alloys and 12-18%Cr ferritic alloys of the AISI400 series). Ferritic alloy with Cr composition of 2%, and 9 - 12% are particularly high in strength and they are widely used. Composition design for these alloys was conducted to improve; i) the creep strength through solid solution strengthening, precipitation strengthening, and microstructural stabilization, and ii) the oxidation resistance through addition of Cr.

Much research has been conducted in order to understand the effects of alloying elements on 9-12%Cr F-M alloys. Figure 2.10 demonstrates the general composition design for F-M alloys. These alloying elements can be classified into seven groups based on their effects [22, 25, 26];

1) *Cr* is important for oxidation and corrosion resistance, precipitate strengthening, and phase stabilization. Service temperature is partially determined from the corrosion resistance, alloys containing Cr 9 and 12% can withstand service at temperatures ~625 and 650°C, respectively [27]. Cr and C can form precipitates of $M_{23}C_6$ and M_7C_3 (M is metal elements), which are important for precipitate strengthening. Cr

also stabilizes ferrite formation and provides a small effect on solid solution strengthening. Although Cr content does not exhibit a significant effect on the strength, high strength is likely to be obtained near 2% and 9-12%. The strength declines at compositions between these two regions. The reason for this remains unclear. [22]

2) *Mo, W and Re* form into solid solution with alloy matrix. Thus these elements create the solid solution strengthening effect. The combination of Mo and W is effective for strength improvement. W has adverse effects on corrosion resistance.

3) *V, Nb, Ti and Ta* react with either C or N (or both) to form precipitates of carbides, nitrides, or carbonitrides. The precipitates distribute in the alloy matrix or at boundaries to yield a strengthening effect. V and Nb will give an optimum effect with 0.2% and 0.05%, respectively. V was reported to decrease the corrosion resistance.

4) *C and N* create effects on both precipitate strengthening and microstructure stabilization. Both elements are austenite formers so they inhibit a formation of δ-ferrite. They also combine with other elements (Cr, V, Nb, etc.) to form precipitates, thus they affect precipitate strengthening. However if C content exceeds ~0.1%, the adverse effect on the creep strength can occur. An optimum concentration of N is ~0.05%.

5) *B* improves alloy toughness and enhances grain boundary strength. It promotes formation of carbides such as $M_{23}C_6$ (M is metal).

6) *Si and Mn* have effects on microstructure stabilization. Si promotes ferrite that causes brittleness. At the same time Si can promote lave phase that reduces toughness. Mn has an opposite effect to Si by promote austenite formation. Both elements should be balanced in order to obtain optimum results for the strength.

7) *Ni, Cu, and Co* are all austenite formers. They inhibit the formation of δ-ferrite by decreasing the Cr equivalent. If Cu and/or Co are added, the tempering temperature can be increased. Cu solubility is low, however, its precipitates can strengthen alloy, but can play a role on precipitate coarsening and lave phase growth [26].

Four of F-M alloys studied in this thesis also were designed upon the mentioned criteria. Figure 2.8 a) and b) show development of F-M alloys with addition of alloying elements to improve the creep strength [22, 24]. The early generation of ferritic alloys developed in 1940 consisted of 2.25Cr-1Mo (T22) and 9Cr-1Mo (T9) with only 35 - 50 MPa 10^5 h creep rupture strength at 600°C. The first generation consisted of HCM9M, EM12, Tempaloy F-9, HT91, and HT9 with Cr content of 2.25, 8 and 12%, Mo 0.5 to 2%, and additional elements of V, Nb, and W. Alloy HT-9 was designed [23] to have a composition of 12%Cr, 1%Mo, and small amount of V (0.30%), and W (0.52%). The second generation of F-M alloy has higher creep strength up to ~100 MPa including HCM2S (2.25%Cr), T91 (9%Cr) and HCM12 (12%Cr). T91 was produced with a nominal composition of 9Cr-1MoVNb contains ~9% Cr and major alloying elements of Mo (1%), V (0.22%), and Nb (0.08%).

The increase in creep strength was achieved by substituting Mo with W and addition of Cu. As a result, the third generation with creep strength up to 140 MPa consisted of NF616 (9%Cr, also called T92), E911 (12%Cr, TB12), and HCM12A (11%Cr, T122). Alloy HCM12A was developed in this generation with a design composition of 0.1C-11Cr-2W-0.4Mo-1Cu-V,Nb [27]. Figure 2.11 shows alloy design of HCM12A. The good strength was accomplished by substitution of W for a part of Mo for solid solution strengthening. Addition of slight amount of Cu less than 2% was added in

order to suppress δ-ferrite formation (instead of using C) and to increase tempering temperature. The optimum amounts of precipitate strengthening elements (V and Nb) were added. The content of C was reduced in order to improve the weldability.

At the same time as the conventional F-M alloys, ODS F-M alloys have been developed since 1960 for cladding materials of fast reactors [23, 26, 28]. To increase creep strength of F-M alloys up to temperature ~650°C, a new approach has been applied by adding nano-size particles of either titania (Ti_2O_3) or yttria (Y_2O_3) into the alloy matrix. These oxides dispersive will yield an effect of precipitate strengthening on the alloy. Initial compositions of ODS ferritic alloys consisted of 12-17% Cr with Mo, Ti, Ti_2O_3 and Y_2O_3. However, the major problem for ODS alloy that prevent them for being used is the anisotropy of mechanical properties owing to the process of producing these alloys. Therefore, during the past 10 years ODS alloy development programs have been focused on solving this problem, and to use a 9-11%Cr, 2-3%W base with yttria dispersive [29-31]. These recent compositions are still questioned due to their low Cr concentration, which will result in low corrosion resistance [26].

Up till now, the F-M alloys have been utilized for gas turbines, steam power plants, boiler components and turbine components in fossil power plants. Recently, the alloys were proposed for the Generation IV nuclear reactor concepts. The development of the new generation F-M alloys will be focused on the reduced-activation alloys, the ODS alloys, and the nano-particle strengthening alloys. Meanwhile, the researches involved mechanical and oxidation mechanisms have to be conducted in order to improve the next generation alloys.

2.2.2. Phase Constitution

This section will describe the phase formation and the process conditions that yield the optimum alloy phase and microstructure of the designed compositions to achieve good creep strength and corrosion resistance. The phase formation of F-M alloys consisted of three major processes; austenitizing, transformation to martensite, and tempering. The austenite phase transforms to martensite during cooling or quenching to ambient temperature, and the alloys are subsequently tempered to obtain a good combination of strength, ductility, and toughness.

The phase transformation of F-M alloys can be determined from a phase diagram of Fe-Cr-C, where C is fixed to 0.1% (by weight), Figure 2.12 [23, 32]. The composition was heated up to a temperature range of ~800 – 1450°C in which the austenite phase (γ) is stable. An austenitizing temperature depends on an initial ratio of Fe and Cr, so the temperature range reduces to ~850 – 1200°C for 9-12% Cr. Aside from this, the austenitizing temperature can be varied by adding austenite and ferrite stabilizing elements. The austenite stabilizers including C, N, Ni, Mn, Cu, and Co have an effect on the increase of austenitizing temperature. In this aspect, the higher austenitizing temperature are required to reduce formation of δ ferrite, and to dissolve carbides of the MC type (M is V, Nb, Ti, or Ta), resulting in coarser prior austenite (PAG) grain sizes and reductions of toughness and creep ductility.

The ferrite phase can be stabilized when Cr, Mo, Nb, V, W, Si, Ti, and Al are added. The ferrite phase inhibits austenite grain growth, but it adversely influences the strength and the toughness. These ferrite forming elements also remove C and/or N from solution as insoluble carbides or nitrides. The solubility of these compounds is limited

therefore they usually remain as precipitate particles, which are important to control austenite grain growth and to increase precipitate strengthening. However, ferrite phase causes brittleness of the alloys. The forming of this phase can be prevented by use of an appropriate amount of an austenite forming elements. Usually Ni is selected due to its effectiveness and fewer adverse effects. The effect of alloying elements on the change in δ ferrite content is shown in Table 2.1 [23, 33].

Following the cooling or quenching from an austenitizing temperature to an ambient temperature, the austenite phase should fully transform to martensite (α′). However, addition of Ni affects the phase constitution in which austenite and δ ferrite can be stable. The phase constitution can be predicted by a Ni and Cr equivalent diagram, called a Schaeffler-Schneider diagram, Figure 2.13 [23]. Generally, Ni and Cr are used as austenite and ferrite stabilizers because other elements have some restrictions, for example, exceed C decreases toughness and impairs weldability [23]. Both elements need to be balanced in order to achieve optimum properties of the alloy. The Schaeffler-Schneider diagram is a plot of Ni equivalent wt.% [(%Ni) + 30(%C) + 0.5(%Mn)] vs. Cr equivalent wt.% [(%Cr) + (%Mo) +1.5(%Si) +0.5(%Nb)] and predicts the constitution of an alloy based on the values of Ni and Cr equivalents of alloying elements in the alloy. From this diagram, composition of T91 transforms into a fully martensite phase. HCM12A consisted of martensite and δ ferrite phases. HT-9 consisted of three phases of austenite, martensite, and δ ferrite. These predictions are consistent with the experimental observation. HT-9 was reported to consist of martensite laths with high dislocation density, small amount of austenite in the form of islands, and δ ferrite grains with low

dislocation density [23]. Likewise, small amount of δ ferrite was observed along with martensite in HCM12A, Figure 2.14 [34].

Tempering treatment is required for F-M alloys in order to improve toughness by refining the microstructure. Martensite transformed from austenite is very brittle thus this phase is not desirable. After tempering, the martensite partially transformed into ferrite and cementite thus the tempered martensite structure exhibits enhanced toughness. To avoid re-austenitizing, the tempering in martensite should be performed at temperature below Ac_1, where Ac_1 is the temperature at which α transforms to γ [23, 35]. Since the effect of some alloying elements, e.g. Ni, Mn, and Cu, lower the Ac_1 temperature, the concentrations of these elements are limited. As a result, re-austenitizing is very sensitive to temperature. The microstructure is an important fact describes the tempering effect in these alloys. Formation of two types of precipitates, $M_{23}C_6$ and MX, are changed as a function of temperature [36]. In T92 (9Cr-0.5Mo1.8WVNb) and HCM12A, the matrix analyses showed that Cr and V content had decreased during tempering because of precipitation of $M_{23}C_6$ and MX, respectively.

Results of the microstructure changes during tempering affect the hardness of alloys, Figure 2.15 [23, 37]. A summary of the microstructure changes in different tempering temperatures is listed as following [23, 37];

- < 350^{o}C, A fine dispersion of M_3C (Fe_3C) precipitate forms and grows to a dendrite morphology and then to plate-like distribution.
- ~450-500^{o}C, fine needles of M_2X nucleate primarily on the dislocations within the martensite lath and retard to the softening.

- 500-550^{o}C, the M_7C_3 and M_2X phases coarsen and resulted in rapid decrease in hardness.
- >550^{o}C, the M_7C_3 and M_2X phases are replaced by Cr-rich $M_{23}C_6$ precipitates, which nucleate on the martensite lath and PAG boundaries. The dislocation density decreases relatives to “as-quenched” martensite.
- ≥650^{o}C, the $M_{23}C_6$ precipitates at the tempered lath martensite boundaries grow, leading to further reduction in dislocation density.
- ≥750^{o}C, the sub-cell within the martensite laths grow into equiaxed sub-grains with little or no trace of the original lath martensite structure. Growth of $M_{23}C_6$ precipitates continues, but clearly defined dislocation networks may be present.

2.2.3. Microstructure of F-M Alloys

Microstructure of F-M alloys in normalized and tempered condition consisted of two major features, the matrix and the precipitates. Figure 2.16 demonstrates a schematic diagram of the microstructure of F-M alloys. Largest structure in F-M alloy is the PAG (prior austenite grain) that exhibits an austenite grain formed during austenitizing process. The austenitizing temperature and time, and alloying elements affect the size of PAG as mentioned earlier. Inside each PAG, the grain is divided into several packets that contain well aligned martensite laths. A packet is a region in which the laths have the same habit plane and orientation [38]. The equiaxed sub-grains, which formed during tempering distribute along with the martensite lath. Sizes of martensite laths and sub-grains depend on the tempering temperature and time, which is independent of PAG size.

Precipitate particles are also an important characteristic of F-M alloy. Precipitate types depend on tempering temperature and alloying elements. These precipitates locate mainly at boundaries of PAG and packet, which help to indicate the boundaries, Figure 2.16. Sometimes the precipitates located at lath or subgrain boundaries and in lath matrix. For the normalized and tempered alloy, major precipitate types are $M_{23}C_6$ and MX. The $M_{23}C_6$ is metal rich carbide, where M is a combination of metal elements, majorly Cr, Fe, and Mo. This precipitate type is in equiaxed and elongate shape. Another type of precipitate usually found in alloy that contains V, Nb, Ti and Ta is MX phase, where M could be these four elements and X is either C or N or CN. Possible compounds of the MX are VC, VN, Nb(CN), Ta(CN) and TiN/TiC, which could form at tempering temperature greater than 550°C [23]. The MX precipitates locate both at the boundaries and inside the martensite laths.

In addition, the precipitate can form if alloy is exposed to high temperature (550-650°C) during service, thermal aging, or in a creep test. The laves phase can form by two metal elements, which usually are Fe, Mo, W, Cu, etc. For example, a lave phase of Cr(V,Nb)N (Z-phase) was observed in fractures of HCM12A from a tube rupture accident after 30,000 hours exposure at 58 MPa/ 610°C and after 12,000 hours at 45 MPa/ 660°C [39]. The formation of laves phase can cause an adverse effect to alloy strength by remove the solid solution strengthening elements from the matrix. In HCM12A case, it was found that formation of the Z-phase had lead to an almost complete dissolution of MX nitrides. Thus the Z-phase was responsible for the breakdown in creep stability of the HCM12A tube. In addition to the formation of new precipitate phases, coarsening of $M_{23}C_6$, MX, and lave phase possible occurred in which

the coarsening increases as function of temperature and stress applied. Table 2.2 is a list of precipitate possible form in normalized and tempered, aged, and creep-rupture tests of the F-M alloys.

Microchemistry at the PAG, packet and lath boundaries is one of interesting aspects because oxidation can take place at these boundaries. Measurement of grain boundary segregation in the F-M alloys, however, is challenging because these alloys have a lot of precipitates at the boundaries. After tempering, it was found that P concentration at the PAG boundaries was two orders of magnitude higher than those in matrix of HT-9 [23]. Segregation of P, Cr, and Si was observed at PAG boundaries of 9Cr and 9Cr-1Mo alloys after tempering. Z. Lu et al. summarized the grain boundary enrichment of Cr in normalized and tempered alloys T91, HCM12A and HT-9 [40-42]. They reported that only HCM12A and HT-9 exhibited Cr enrichment at PAG boundaries. After aging, alloying elements included P, Cr, Mo, and Si were observed to segregate at the boundaries [23].

Most of the PAG and packet boundaries are either randomly oriented or high angle boundaries, and the lath and subgrain boundaries are predominantly low angle grain boundaries [43]. Precipitates of $M_{23}C_6$ and MX are expected to be formed more easily around the PAGBs because the high angle boundaries of PAG act as the faster diffusion paths during the tempering.

2.3 Oxidation of Ferritic-martensitic Alloys in SCW Environment

As candidate materials in the SCWR, F-M alloys are required to withstand the severe environment of SCW at high temperature and high pressure. The F-M alloys generally exhibit good corrosion resistance in the steam generators of conventional fossil power plants. These alloys are superior to that of carbon and low-alloy steels, however, are inferior to that of the austenitic and Ni-based alloys. The reason for this drawback is their differences in composition and microstructure, such as low Cr concentration that is important for corrosion resistance. The oxidation of F-M alloys will be reviewed in this section by focusing on the effects of alloy compositions and microstructure on the kinetics and structure of oxidation in a temperature range of 400-600°C. The overview of oxidation of F-M alloys is described first, followed by the effects of alloy composition and microstructure.

2.3.1. Overview of Oxidation of F-M Alloys

2.3.1a Fundamental of Oxidation

Oxidation is a reaction between a metal and oxygen from environment. The reaction occurs due to the thermodynamic instability of the metal when exposed to the environment. Therefore, the oxidation mechanism depends on both metal substrate and environment, and each system behaves differently. The major parameters that can affect oxidation include alloy composition, microstructure, temperature, activity of oxygen in the environment, etc. The fundamentals of oxidation have been studied extensively, however, the understanding of mechanisms of each individual oxidation alloy will need to be clarified.

There are four major processes, as described elsewhere [44-49], which lead to oxidation;

- Dissociation of oxygen from the environment
- Adsorption of oxygen on the surface and nucleation of oxide
- Transport of oxygen ions inward and metal ions outward from the alloy
- Formation of oxides.

In order to understand the oxidation mechanisms of F-M alloys in SCW, the above processes should be studied thoroughly. The mechanism involving the dissociation of oxygen from the SCW are reviewed in section 2.1. Following the dissociation of oxygen atoms from water molecules, the adsorption of oxygen onto the alloy surface occurs. Parameters influencing the process of adsorption and initial oxidation involve crystal orientation and defect structure of surface, and possible include impurities on surface and in environment. The formation of oxide compounds occurs by the formation the formation of separate nuclei [44], or an amorphous layer due to the extra abundance of oxygen present [48]. The latter case is particularly common for oxides which have oxygen to metal ratio greater than 1. In this stage the oxide thickness is less than 100 nm and the process occurs in a short period of time, which depends on the conditions of surface and environment.

The transports of oxygen anions toward the alloy substrate and metal cations outward occur via solid-state diffusion mechanisms. The driving force for diffusion is the difference in chemical potential between two adjacent regions. Diffusion is assisted by the defect structure of the oxide, which can be classified into three types; the metal-excess (n-type) and metal-deficit (p-type) semiconductors, and the amphoteric oxides

[44]. The metal-excess or n-type semiconductor oxides have free electrons or negative charges as the major charge carriers. They may have either metal ions access ($M_{a+y}X_b$) or missing oxygen ions (M_aX_{b-y}) in the compounds so the total net is positive charge. The metal-deficit or p-type semiconductor oxides have electron holes or positive charges as the major charge carrier. Cations vacancies are the dominate defects in this oxide type resulted in the total net of negative charge. The amphoteric oxides show non-stoichiometry with either a deficient of cations or a deficient of anions. For example, chromium oxide (Cr_2O_3) is a cation-excess oxide ($Cr_{2+x}O_3$) at low oxygen partial pressure and a cation-deficient oxide ($Cr_{2-x}O_3$) at high oxygen partial pressure. Thus the diffusion mechanism in the chromia scale depends on the oxygen activity. A list of oxide of each type is presented in Table 2.3 [44, 48].

The reaction between a metal (M) and oxygen gas (O_2) can be written as,

$$M(s) + O_2(g) = MO_2(s) \qquad (2.3)$$

Thermodynamically, an oxide will form on the surface of a metal when the oxygen potential in the environment is greater than the oxygen partial pressure in equilibrium with the oxide [49]. This equilibrium oxygen pressure, also called the dissociation pressure of the oxide in equilibrium with the metal, is determined from the standard free energy of formation of the oxide. The standard free energy of oxidation can be written as;

$$\Delta G^0 = -RT \ln p(O_2) \qquad (2.4)$$

where $p(O_2)$ is the oxygen partial pressure, R is the gas constant, T is the temperature (K). This equation allows the determination of the oxygen partial pressure in equilibrium with the oxide from the standard free energy, which is represented by

Ellingham/Richardson diagram, Figure 2.17 [50]. The addition standard free energies of reaction are listed in Table 2.4 [49].

For the oxidation systems that are more complicated than a single metal and a single oxidizing gas, the determination of phase formation can be achieved by other types of diagram. Normally the oxidizing temperature is fixed to a particular value, and the phases are determined from various parameters, i.e., the gas pressure and ratio of alloy compositions. These diagrams included the predominance diagram and the Pourbaix potential-pH diagram, which will be used in this thesis. However, it is important to emphasize limitations of the diagrams [44], for example;

- Each area on the diagram is labeled with the predominance phase that is stable under the specific conditions of pressure and temperature. Other phases may also be stable in that area, but with small amounts.
- The diagrams are for the equilibrium situation.
- Microstructures and microchemistries can create situations that differ from that of the bulk reactant phases.
- The diagrams are based on thermodynamic data and do not show rates of reaction.

From the four major steps in the oxidation process, ones can construct a series of experiments to determine the oxidation mechanism of a particular system. Measurement of the oxidation rate leads to an understanding of the diffusion of ions during oxidation. Characterization of the oxide structure permits the understanding of oxide formation in both macroscopic and microscopic levels. Both behaviors also relate to each other. Reviews of oxidation of F-M alloys in SCW will be focused on these two behaviors involving to the determination of oxidation mechanisms.

2.3.1b Oxidation Rate

Oxidation rate is a way to describe the oxidation resistance of alloys. It also reveals the oxidation mechanism and defines the rate controlling process. There are several methods to determine the oxidation rate including measurement of; a) the amount of metal consumed by measure weight or thickness losses of metal, b) the amount of oxygen consumed by measure weight gain or amount of oxygen used, and c) the amount of oxide produced by measure oxide weight or oxide thickness. In this thesis, the oxidation rates were determined by measurements of both weight gain and oxide thickness.

The oxidation rate can be represented by simple formula described by logarithmic, inverse logarithmic, parabolic, and linear equations [44]. In most cases, the oxidation rates of either pure iron or alloys in isothermal exposure are usually expressed as the Tammann parabolic equation [51, 52];

$$\frac{dh}{dt} = \frac{k''_{ph}}{h}. \qquad (2.5)$$

Integrating eqn. 2.5 yields: $h^2 = k'_{ph}t + h_0^2$.

Assuming $h_0 = 0$, $h^2 = k'_{ph}t$, (2.6)

where, h is the total oxide thickness (original parameter x is changed to h to match with parameter in this thesis), t is the oxidation time, h_0 is the initial oxide thickness (at $t = 0$), and $k'_{ph} = 2k''_{ph}$ is the parabolic rate constant of oxide thickness. Likewise, the oxidation rate determined from the weight gain can be expressed as the Pilling-Bedworth equation;

$$w^2 = k'_{pw}t, \qquad (2.7)$$

where, w is the weight gain and k'_{pw} is the parabolic rate constant determined from weight gain.

The parabolic equations describe diffusion controlled reactions. Most of the works reported on oxidation kinetics of F-M alloys follow the parabolic relation. However, there are many cases in which the oxidation rate deviated from this relation. For instance, the exponent of oxidation rate equation of T22 (2.25 Cr alloy) in steam varied from 0.46, 0.49, 0.62 and 0.83 at 500, 550, 600 and 650°C, respectively [53]. The main reason could arise from changes in oxidation mechanisms. Moreover, the following condition are necessary for which the theory is valid [44]; a) one type of defect dominates the oxide, b) the thermodynamic equilibrium are established, c) the oxide scale shows small deviation from stoichiometry, d) the oxidant solubility, oxide evaporation, and other processes at interface are negligible, and e) the scale is thick compared with distances over which space charge effects occur. Due to these limitations, the power relation is applied for the oxidation rate in thesis. Starts with $\frac{dh}{dt} = k_h'' \frac{1}{x^{m_h - 1}}, m_h \approx 1.5$, the power law of the oxidation rate can be expressed as;

$$h^{m_h} = k_h' t \ , \qquad (2.8)$$

or, $$h = k_h t^{n_h}, \qquad (2.9)$$

likewise, $$w^{m_w} = k_w' t \ , \qquad (2.10)$$

or, $$w = k_w t^{n_w}, \qquad (2.11)$$

where, w is the weight gain (mg/dm^2), h is the oxide thickness (μm), k_x and k_w are the oxidation rate constants determined from oxide thickness (μm/h) and weight gain (mg/dm^2/h) , respectively ($k = (k')^{1/m}$), t is the time (hours), and n_h and n_w are the exponent on weight gain and thickness, respectively, and $n = 1/m$.

Temperature has a great effect on the oxidation rate. For alloys where the oxidation rate is diffusion limited, increasing in temperature resulted in an increase of the ion diffusivities thus the oxidation rate will increase. The relation of oxidation rate and temperature can be described as an exponential relation, called an Arrhenius equation;

$$k' = k'_0 \exp(-Q / RT), \qquad (2.12)$$

where *k'* and k'_0 are the oxidation rate constants (mg/dm^2/h), *Q* is the activation energy of oxidation (J/mol), *R* is the gas constant (8.314 J/mol-K) and *T* is temperature (K). Substitute eqn. 2.12 into eqn. 2.8 and 2.10;

$$h^{m_h} = k'_{0h} e^{-\frac{Q}{RT}} t,$$

$$h = k_{eff,h} t^{n_h} e^{-\frac{n_h Q}{RT}}, \qquad (2.13)$$

likewise,

$$w^{m_w} = k'_{0w} e^{-\frac{Q}{RT}} t,$$

$$w = k_{eff,w} t^{n_w} e^{-\frac{n_w Q}{RT}}, \qquad (2.14)$$

where $k_{eff,h}$ and $k_{eff,w}$ are the effective oxidation rate constant from thickness and weight gain, respectively. The $k_{eff,h}$ and $k_{eff,w}$ are defined as $k_{eff} = (k'_0)^n$. For a constant exposure time the activation energy for oxidation, *Q*, can be obtained from the slope of a plot of *ln h* vs. *1/T*, and *ln w* vs. *1/T*. The importance of determination of the activation energy is that it can be used to determine the rate controlling mechanism of oxidation. The activation energy of oxidation will be compared with the activation energy of ion diffusions in a medium to describe the rate controlled mechanism.

2.3.1c Oxide Structure

Oxide structure of the F-M alloys has the fundamental mechanism close to that of pure Fe due to their high concentration of Fe (~90%). However, the effect of alloying elements plays an important role in the oxidation mechanisms. The formation of oxides depends on the oxidation conditions of temperature and oxygen partial pressure. A phase diagram of Fe-O is shown in Figure 2.18 [47]. From this diagram, the oxide phases, ordered from low oxygen concentration to high, consisted of wustite (FeO), magnetite (Fe_3O_4), and hematite (Fe_2O_3). This leads to a formation of three layer oxide structure of pure iron. The outermost layer is Fe_2O_3, followed by Fe_3O_4 and FeO, respectively. The temperature also has a great effect on the oxide phase. At temperature below 570°C, magnetite phase is stable for oxygen concentration below ~23.4 wt% (51.38 at%). The wustite phase becomes stable at temperature of above 570°C. This temperature (570°C) called wustite point. Addition of some alloying elements, such as Cr, can shift the wustite point to a higher temperature.

It is also necessary to briefly explain selective oxidation. Selective oxidation (sometimes called selective internal oxidation) is the formation of oxide particles within the matrix of alloy. In the alloy with different compositions, oxidation can preferentially occur with some elements based on thermodynamic stability. If the free energy of formation of an oxide of alloying element ‘A’ is low enough, the solute atoms ‘A’ can react with the inward diffusion oxygen to form an oxide AO. However, the oxide can be further oxidized with other elements if the oxygen partial pressure increases to yield another level of thermodynamic stability.

The addition of alloying elements will affect the oxide types forming on the alloy substrate. Some alloying elements can form an oxide that can slow down the diffusion of anions or cations, called ‘protective oxide’, which has the effect of decreasing further oxidation. The main reason is that these oxides have structures with low concentrations of defects so that the diffusion coefficients are very low. The protective oxides included Cr_2O_3, Al_2O_3, and SiO_2. Moreover, formation of oxides of these alloying elements and other base metal elements, i.e. $FeCr_2O_4$, will cause a decrease in the diffusivities of ions. In order to understand this behavior, the effect of alloying elements on the oxide structure, and the oxide structure of F-M alloys will be discussed together in next section.

2.3.2. Effects of Alloy Composition and Microstructure

2.3.2a Chromium Content

In F-M alloys, Cr has the most impact on the oxidation resistance, the phase stability, and precipitate strengthening. Cr has influence on oxidation mechanisms of the F-M alloy, which affects both reduction of oxidation rate and changes of oxide microstructure. Ideally, Cr is added into steel in order to form a protective oxide, chromia (Cr_2O_3), because chromia can moderate the diffusivity of oxygen [54]. However, the formation of chromia will occur with relatively high Cr concentration, and also in a particular environment of oxygen partial pressure and temperature [55, 56]. The effect on the oxidation rate of alloy when Cr is added is demonstrated briefly in Figure 2.19 [47], which shows the oxidation rate at 1000°C. Addition of small amount of Cr content (< 5% by weight), the oxidation rate decreases sharply with the increasing of Cr content. The oxidation rate gradually drops from Cr content ~5-12%, and rapidly drops at Cr

greater than 12%. The most effective Cr concentration occurs when Cr is greater than ~22%, where chromia scale becomes stable. For the F-M alloys, the Cr is in a range of 9-12% in which the effect from Cr concentration is intermediate between poor and excellent oxidation resistances, and the effect is expected to be observed in this thesis.

Chromium also affects the sequence and types of oxides. Addition of a small percent of Cr content results in the formation of Fe-Cr spinel oxide ($(Fe,Cr)_3O_4$) in the inner part of the scale. With an increase of Cr, Fe-Cr spinel oxide becomes larger, and the corresponding FeO layer becomes thinner relative to Fe_3O_4. The main reason is Fe^{2+} ions are blocked by the spinel oxide [47]. Since the Fe ions are more mobile than the Cr ions, the outer oxide can still consist of the iron oxide, especially after long oxidation times. Schematic diagram of scales form on Fe-Cr alloys is shown in Figure 2.20 [47]. The sequence of oxide layers from the outermost surface consists of Fe_2O_3, Fe_3O_4, FeO, Fe-Cr spinel, and possible, Cr_2O_3 at the interface of scale/alloy. If the alloy contains Cr greater than ~20%, chromia scale (Cr_2O_3) forms at the outermost layer and becomes a protective oxide. Indeed, the oxide structure could deviate from this diagram based on the concentrations of Cr, other alloying elements, the temperature, and most important, the oxygen partial pressure in environment. In section 2.3.3, we will observe a lot of effects from the environment of steam, gas, and SCW, which are mostly driven by the oxygen partial pressure.

Since Cr is a major alloying element in four F-M alloys studied in this thesis, the effect of Cr, in a range of 9-12%, on the oxidation mechanism is important. The oxidation rate of these alloys generally follows the power law behavior with a variation of the exponent ‘n’ as described previously. Among the literature, there was no report of a

significant effect of Cr concentration on the value of 'n'. The major effect is on the oxidation kinetic constant (*k*) in which an increase in Cr content results in a decrease of the oxidation kinetic constant. The oxide structure of F-M alloys was shown by experimental results as three distinct oxide layers [57-61]. The innermost layer was a $(Fe,Cr)_3O_4$. The intermediate layer was porous magnetite (Fe_3O_4) followed by a compact thinner layer of hematite (Fe_2O_3). Defects in oxide scales usually found in Fe_3O_4 and at each interface.

Formation of the chromia scale in F-M alloys occurs only at a certain condition of environment (gas or steam), oxygen partial pressure, and temperature, which will be reviewed in the environmental effect section. The chromia scale in these alloys is not easily detected due to their small fraction on the scale. However, a thin layer of chromia can be detected by high resolution analysis techniques such as X-ray photoelectron spectroscopy (XPS), IR, and TEM techniques. Reports by Zurek et al. [62], Greef et al. [59], and Sánchez et al. [56] revealed formation of Cr_2O_3 at the alloy/oxide interface of F-M alloys. A work by Greef reported an additional Cr_2O_3 region at the interface of oxide and alloy substrate of a 9Cr-1Mo alloy exposed in air at 400-600°C [59]. They reported that the ratio between these oxides is temperature dependence. Below 400ºC the oxide layer consists mainly of Fe_2O_3 and a small amount of Cr_2O_3. Between 400ºC and 600ºC the oxide layer consists of a mixture of FeO, Fe_2O_3 and Cr_2O_3 and above 600ºC the layer consists mainly of Cr_2O_3. Figure 2.21 shows a schematic diagram of oxide structure formed on 9Cr-1Mo exposed in air at 400-600°C proposed by Greef el. al.[59].

Zurek et al. [63] observed anomalous temperature dependence behavior in a 10Cr-6.52Co alloy, and a 12Cr alloy exposed in steam of Ar-50%H_2O at 550-650°C. Figure

2.22a shows comparison of oxidation rate of four alloys, 1Cr, 10Cr, 10Cr-6.52Co, and 12Cr, tested in this research. They found that oxidation rates of 10Cr-6.52Co and 12Cr alloys do not steadily increase with increasing temperature. For the 10Cr-6.52Co, the oxidation rate increased with increasing temperature from 500 to 600°C, but decreased at 625°C. Similar behavior was observed in the 12Cr alloy, which the oxidation rate decreased with increasing temperature from 500 to 600°C and gradually increased at temperature 625°C. Characterization of 1Cr and 10Cr alloys (normal temperature dependent) showed three layers structure of Fe_3O_4 in an outer layer, Fe_3O_4+$(Fe,Cr)_3O_4$ in an inner layer, and a transition layer consisted of FeO and Cr_2O_3. In the alloys that exhibited anomalous temperature dependence, a small layer of ~1 μm of Cr_2O_3 was observed at the alloy/oxide interface, Figure 2.22b. This concluded that the presence of a chromia layer, even in a small fraction, results in a decrease in the oxidation rate. The effect of Cr content on the oxidation kinetic constant is represented in Figure 2.23 [62], which shows that the addition of Cr can result in a sharp drop of the oxidation rate. This critical Cr content also substantially differs as a function of temperature and other alloying elements.

The fact that F-M alloys usually contain Cr in the form of precipitate particles of $M_{23}C_6$ brought interest in the behavior of these precipitates during the oxidation. Since $M_{23}C_6$ contains high amount of Cr, dissociation of the particles will yield the Cr to the alloy. The formation of protective layer in a two-phase alloy was considered by Wang et al. [64]. They discovered that for protective behavior of multiphase alloys to be maintained, the ratio of volume fraction of second phase precipitates to precipitate size is a critical parameter. This reveals that the precipitate size also plays an important role in

the protective oxide formation. Durham et al. [65] conducted experiments to study the factors affecting chromium carbide precipitate dissociation during the oxidation. The work had been conducted on ferrous alloys with Cr concentration of 15%, which the nominal Cr content in matrix is ~11% and the rest of Cr contributed to carbide precipitates. The results of oxidation at 850°C in pure oxygen showed that the precipitate dissolution is slower for coarse carbides (3 μm) than that for fine carbides (1 μm). Therefore the chromia layer can form in the latter case. Moreover, addition of Si to an alloy with Cr < 15% leads to chromia formation by concerting the alloy matrix to ferrite (with more rapid chromium diffusion) and/ or by forming a thin sub-layer of SiO_2 at the scale base. However, the environment conditions in which the dissociation of carbide can occur should be further studied.

2.3.2b Minor Alloying Elements

Effects of minor alloying elements are not widely studied as they exhibited less influence on the oxidation of F-M alloys than that of Cr, and it is difficult to isolate an effect of single element. However, some of alloying elements are reported to have favorable or adverse effects on the oxidation resistance. The alloying element group that enhances the oxidation resistance consisted of Si, Co, Ti, Y, and Pd. The adverse element group consisted of V, Nb and W. Ni was reported to exhibit both good and bad effects to the oxidation resistance. Meanwhile, the influence of some elements cannot be determined separately because they have a combined effect.

Comparison of the relative oxidation rates of 9Cr alloys, including 9Cr1Mo, T91 (9Cr-1MoVNb) and T92 (9Cr-0.5Mo1.8WVNb), was conducted in steam at 520-620°C by Mongomery and Karlsson [66]. Both T91 and T91 contain alloying elements of V,

Nb, W and Ni. The results showed that the 9Cr1Mo exhibited better oxidation resistance than T91 and T92. The author stated that one of alloying elements in T91 and T92, V, Nb, W or Ni, is detrimental to oxidation resistant.

Another work by Lepingle et al. [67] also reported the results agreed with Mongomery and Karlsson [66]. This work compared four new developed alloys with T91 and HCM12A. The new developed alloys contain 11.5% Cr and different concentration of Si, Mn, Mo and W. The study found that Si is benefit to oxidation resistance. However, the effects of Mn, Mo and W cannot be distinguished. The authors concluded that the effects are complex and that the alloying elements cannot be considered separately. Instead these elements exhibit a joint influence on the oxidation resistance.

Influence of Si on the oxidation resistance was tested by Abe et al., and Hurst and Cowen [68, 69]. They proved that the addition of Si improves the oxidation resistance in steam oxidation at 600 and 650°C. However, amount of Si is limited in the alloy because Si can promote carbide agglomeration. The allowable maximum Si content is ~0.5% in the alloys [68]. Co was also reported to have an influence in chromia formation as mentioned in section 2.3.2a [62]. In the same work of Abe [68], effect of Ti and Y also reported to further improve the oxidation resistance. This result also consistent with the results from ODS alloys that contain Ti and Y.

Ti and Y are the alloying elements in the ODS alloys in a form of Ti_2O_3 and Y_2O_3 nano particles. The ODS alloys usually exhibit better oxidation resistance than the conventional F-M alloys with the same Cr concentration. The oxide structure formed on 9Cr-ODS alloys exhibited three layer structure of an outer oxide, an inner oxide, and a diffusion layer [70]. It was found that the ODS alloy has a large diffusion layer and a thin

inner oxide layer. Detailed microstructure indicates the formation of Y-Cr-rich oxides along grain boundaries in the diffusion layer near the metal-oxide interface may act to block cation diffusion outward. Thus the net conversion of metal to spinel appears to be driven by oxygen diffusion into the metal rather than cation diffusion to the oxide. This resulted in the reduction of oxidation rate in the ODS alloys.

Work conducted by Peraldi and Pint [71] reported the effect of Ni in diffusivity of Cr in Fe-Cr-Ni alloys. The results showed that Ni promotes the diffusion of Cr, which implies an indirect effect in the increase of corrosion resistance. Addition of Ni also delays spallation of the protective oxide in this alloy.

2.3.2c Alloy Microstructure

Microstructure is one of important factors affects the oxidation of F-M alloys. This included crystal structure of martensite, grain structure, and grain size. First of all, martensite and tempered-martensite have a structure of body-centered tetragonal, which has the lattice parameter close to that of BCC. The diffusivities of anions of oxygen and cations of metals tend to be higher in the BCC structure of F-M alloys than the FCC of austenitic alloys. The complex microstructure of F-M alloy grains that consists of PAG, packets, laths, sub-grains, and precipitates also creates large amount of grain boundaries. These boundaries are the short circuit diffusion paths for diffusions of ions inward and outward the alloy matrix. Therefore compared to the clean and simple microstructure of austenitic alloys, the F-M alloys have inferior microstructure than that of the austenitic alloys.

There is a question about the effect of alloy grain size on the corrosion resistance. Basically oxygen diffusion along grain boundary of alloy could lead to an increase of the

oxidation rate. However, many reports showed that alloys with a fine grain microstructure exhibit better oxidation resistance than those with a coarse grain microstructure. In $2^1/_4$ Cr-1Mo alloy, the effect of grains size on oxidation rate at 550°C in air was studied by R. K. Raman et al. [72], and at 500-600°C in air by Trindade et al. [73]. Both works found that the oxidation rate decreased with increasing grain size, which was varied in ranges of 16-59 μm (Raman) and 4-75 μm (Trindade). These are results from reduction in grain boundary area in the large grain alloy, which decreases the short circuit diffusion paths.

In alloys that contain higher amounts of Cr (5-20%), the effect of grain size was found to be opposite from that of low Cr alloys. Increasing the grain size of the alloy leads to a decrease in the oxidation rate. This could result from the different diffusion mechanisms. In high Cr alloys, Cr diffuses through the short circuit diffusion paths of grain boundaries to the bulk oxide. These Cr associated with Fe and O to form Fe-Cr spinel oxides, which affect the reduction of oxidation rate. Therefore the oxidation rate of a small grain size alloy is lower than a large grain size alloy. The assumption agreed with observations of thick layer of the inner spinel oxide ($(Fe,Cr)_3O_4$) on these alloys [71, 74].

2.3.3. Environmental Effects on Oxidation of Ferritic-martensitic Alloys

In the SCWR, operating temperature is ranging from 280-620°C in normal condition and up to 700-840°C for less than 30 seconds in abnormal condition with an operating pressure approximately 25 MPa. Under these severe conditions, SCW behaves intermediate between aqueous solution and gas so that the oxidation of F-M alloys is unpredictable. Mechanisms of oxidation of these alloys in different environment

including steam and dry gas at high temperature are reviewed in this section. The oxidation behavior in SCW from research groups that conducts studies on the same environment and material is also summarized.

2.3.3a Oxidation in Steam

Steam is vaporized water at high temperature, which is simply differentiated from SCW in a term of pressure of the system. Aside this fact, the transformation of water phase causes dramatically changes in chemical and physical properties of water as described in section 2.1. However, oxidation in steam environment can give some ideas about oxidation that affected from the water molecules, which will be benefit in understanding of the oxidation in SCW. In this section, the oxidation of F-M alloys in steam environment will be reviewed by focusing the effects of pressure and steam composition on the oxidation of F-M alloys.

Effect of steam pressure on oxidation rate of HCM12A, NF616 (9Cr, also called T92), and HCM2S (2.2Cr) was studied by Y.S. Yi et al. [75]. The steam pressures were verified between 1 and 10 MPa with a temperature range of 560-700°C. The results of oxidation rate showed a clear negative effect on the oxidation rate in a temperature range of 570-600°C. At 600°C, the parabolic oxidation rate constant (K_p) decreased by about half as the pressure was increased from 1 to 10 MPa for all the alloys. Meanwhile, there were no significant effects found at 620°C or higher. Figure 2.24a and b show plots of the parabolic oxidation rate constant as a function of pressure for 600 and 700°C cases. In addition to the oxidation rate constant, the activation energies of oxidation were also calculated from the temperature dependence of oxidation rate. Apparently, the activation energies changed at around 600°C for NF616 and HCM12A, Figure 2.24c and d. The

activation energy of HCM12A was as low as 40 kJ/mol in the temperature range from 620 to 700°C. This work revealed that an increase of steam pressure, which also resulted in an increase of water density, has an effect on oxidation rate reduction. However, detailed mechanisms were not explained in the article.

The water vapor was found to have a significant effect on the oxidation mechanisms. A set of experiments was conducted on Fe-Cr alloys containing 10% and 20% Cr with isothermal oxidation at 900 and 1500°C in Ar-20%O_2, Ar-7%H_2O and Ar-4%H_2-7%H_2O by Essuman el al. [76]. These environments corresponded to high, medium and low oxygen partial pressure, respectively. The results showed that the water vapor is the source of oxygen in the formation of internal selective oxide in which Cr exhibits a higher tendency to become internally oxidized than in the Ar-O_2 environment. Figure 2.25 presents weight change and scales formed on 10Cr alloy after exposure in Ar-20%O_2, Ar-7%H_2O and Ar-4%H_2-7%H_2O. Characterization indicated that chromia scale form on a sample exposed in Ar-20%O_2, a three-layer structure oxide formed on Ar-7%H_2O sample, and internal selective oxidation formed Fe-Cr spinel oxide in Ar-4%H_2-7%H_2O. The formation of oxides led to different behaviors of the oxidation rate. The results indicated that the presence of H_2O in the test gas can affect the oxidation behavior not only by modifying the transport process and void formation in the oxide scale but also by affecting transport process in the alloy.

A mechanism for internal selective oxidation can be accounted from effects of hydrogen atoms dissociated from water molecule. The enhanced solubility of hydrogen has been proposed as; rapid diffusion of hydrogen into the specimen shifts the H–O–H_2O equilibrium at the surface such that a meta-stably high concentration of oxygen exists

there and results in an increased inward flux of oxygen. A possible mechanism for enhanced diffusion involves rapidly diffusing hydrogen interstitials expanding the iron lattice enough that the diffusivity of oxygen is increased. This mechanism can explain the behavior of Fe-Cr alloys in which Fe-rich oxide always observed in wet gases, while protective Cr-rich oxide formed under dry gas condition. [76]

In an environment that contains both water vapor and oxygen, the scale grows with a competitive adsorption between oxygen and water vapor molecules on external and internal surfaces of the oxides. This subject was studied by Ehlers et al. [77] and Bertrand et al. [78] by an isotope O^{18} tracer technique. Ehlers et al. [77] conducted short term (100 h) oxidation 9%Cr alloy (P91) at 650°C in N_2–O_2–H_2O gas mixtures containing a relatively low oxygen level of 1%. The H_2O^{18}-tracer was used in the gas mixture with subsequent analyses of oxide scale composition and tracer distribution. It was found that the transition from protective, Cr-rich oxide formation into non-protective mixed oxide scales is governed by the ratio $H_2O(g)/O_2$ ratio rather than the absolute level of $H_2O(g)$. The results of the tracer studies in combination with the data obtained from experiments involving in situ gas changes clearly illustrated in Figure 2.26. This indicated that penetration of water vapor molecules triggers the enhanced oxidation and sustains the high growth rates of the Fe-rich spinel oxide formed in atmospheres with high $H_2O(g)/O_2$ ratios. The formation of the non-protective Fe-rich oxide scales is suppressed in atmospheres with low $H_2O(g)/O_2$ -ratios, and the healing of any such scale is promoted.

Another important phenomenon observed in the oxidation in environment contains water vapor is the formation of volatile species of oxidation products. The

reaction of oxide and water molecules results in the volatility of oxides following generalized reaction [79];

$$MO_x + nH_2O(g) + mO_2(g) = MO_{(x+n+2m)}H_{(2n)}(g). \qquad (2.15)$$

According to this equation, the formation could occur at the oxide/water interface or inside the scales where water molecule can permeate. The possible volatile species included $Fe(OH)_2$, $CrO_2(OH)_2$, SiO(OH), and $Al(OH)_3$ [53, 79, 80]. However, the concentration of initial elements (metal oxide and water) and temperature are important factors that needed to be considered. (Note that another volatile oxidation product of Cr is CrO_3 forms at temperature above 1,000°C, which is out of an interested temperature range of this thesis.) The formation of volatile oxidation products can remove the surface oxide, resulted in reduction of the protective ability of the protective scales. If the volatile products formed inside scale, they will diffuse outward to the oxide/gas interface and will leave pores or cracks on the oxide layer [81, 82]. High gas pressure can also cause the breakage of oxide scales.

2.3.3b Oxidation in Gas

Much work has been done to describe the oxidation of F-M alloys in gas environment such as in air and in pure oxygen. The oxidation in dry gas exhibits results different from oxidation in steam. In austenitic alloys, the oxidation in dry air results in less oxidation rate than that in the water vapor [83]. This is a result of formation of protective oxide of chromia layer as described in the previous section. An interesting study will be reviewed in this section involves the oxidation of HT-9 in dry air at 600-950°C that was tested by Vélez for her Ph.D. thesis [74]. This study used the same heat of HT-9 as our current study so that the effect of dry air can be compared with SCW

directly. The isothermal experiments were conducted at temperature from 600-950°C. The oxidation rates determined from weight gain showed strong effects from the temperature dependence, and the relation could be divided into at least two segments, Figure 2.27. These results exhibited a complex behavior in which several different kinetics and mechanisms are simultaneously active. The oxide structure also depended on the test temperature, which exhibited transition of scale from protective to non-protective. In all temperatures, the oxide scales consisted of two layers, an outer layer with Fe rich oxide and an inner layer with grainy texture features of Cr rich oxide. A selective internal oxide also formed at the alloy/oxide interface. At 600-850°C, thin oxide scales formed continuously on the surface with no spallation. At 850-863°C, spallation was observed resulted in a change of parabolic oxidation rate to linear relation. Samples tested at 875-950°C exhibited a double layer structure, and internal selective oxidation layer with Cr and O enriched at grains boundaries, Figure 2.27. Thus a Cr/Fe-rich oxide film developed along the substrate grain boundaries immediately adjacent to the oxide/substrate interface due to the inward diffusion of oxygen which reacts with the iron and chromium of the base metal.

2.3.3c Oxidation in SCW

The oxidation in SCW has been studied in both SCWO and the SCWR. One of primary objectives is to explore materials that can withstand an aggressive environment of the SCW in both systems. In the SCWO system (mixture of water, oxygen (or air), CO_2 and organic compound waste), the organic compound will be dissolved in the SCW resulting in the water of strong acidity level. Therefore, the SCWO system is highly aggressive. In this section, the information from the SCWO studies that will be benefit to

an understanding of the oxidation in SCW will be included. Effects of major parameters of the alloy and the SCW conditions generally followed the review previously mentioned in this chapter. However, they will be restated in this section with the studies conducted in SCW.

There are attempts to construct a Pourbaix diagram of iron in the subcritical and SCW regions in order to predict the corrosion/oxidation of materials used in the SCWO and SCWR systems [14, 15, 17]. The Pourbaix diagram presents the relationship of electrochemical potential (E) and pH, thus is useful for representing the thermodynamic equilibrium in metal - water system. It shows reactions and reaction products that will be present when system equilibrium has been attained, assuming that all appropriate reactions have been included [46].

Kriksunov and Macdonald [6, 17] constructed the Pourbaix diagrams of iron at temperature 300-500°C under pressures of 30, 50 and 100 MPa. Figure 2.28 is a Pourbaix diagram of iron at 400°C and 50 MPa. The dotted lines (a) and (b) correspond to the equilibrium conditions for the H_2/H_2O and O_2/H_2O reactions, respectively, both corresponding to unit gas fugacity. The other lines correspond to Fe/Fe^{2+} (Line 1), Fe/Fe_3O_4 (Line 13), Fe_3O_4/Fe_2O_3 (Line 12), Fe^{2+}/Fe_3O_4 (Line 14), and Fe^{2+}/Fe_2O_3 (Line 10). Note that no stability regions appear for Fe^{3+} and $HFeO^{2-}$ because the thermodynamic data indicate that these ionic species are so unstable at temperatures above the critical temperature that they can be ignored in the present analysis. Note also the extensions of Lines 12 and 13 into the Fe^{2+} stability field; these extensions define the conditions for the formation of Fe_3O_4 and Fe_2O_3 as metastable phases (potentials above Lines 13 and 12, respectively), which are responsible for any passivity that iron may

exhibit in SCW environments. This diagram shows that the condition in SCWO is more aggressive than that in SCWR. The potential and pH range of the SCWR giving the oxide phases of Fe_3O_4 and Fe_2O_3 are stable.

Research involving the structural component materials in the SCWR has been conducted in many countries including the U.S.A., Japan, Korea, China, and European countries [3]. There are several research groups that are focusing on the oxidation of F-M alloys including University of Wisconsin and Penn State University that are collaborating with the University of Michigan thought NERI and I-NERI programs. The alloys studied in the SCW condition consisted of 9-12% Cr F-M, ODS F-M, austenitic, Ni-based, zirconium, and INCOLOY alloys. The studies showed that the major parameters affecting the oxidation in SCW are; the alloy class and the SCW temperature, whereas the minor parameters included the dissolved oxygen concentration, the SCW pressure, and the surface modification of the alloy.

Among the listed alloys, Zircaloy-2 and Zircaloy-4 exhibited extremely high oxidation rate with spallation over period of time, however, with newly development of the model zirconium alloys, Zr-Fe-Cr and Zr-Cu-Mo exhibited improved corrosion resistance [84, 85]. The austenitic alloys exhibited good oxidation resistance [86], but the spallation was observed in 800H [87]. Corrosion pitting was observed in alloy 304NG tested at 550°C, 25 MPa, 1000 hours exposure [80]. The author suggested that the volatilization of $CrO_2(OH)_2$ is a major mechanism of the pitting and nodular oxidation [80]. Ni-based alloys showed very small oxidation rate, but the corrosion pitting was observed in alloy 625 [88]. An example of comparison of the oxidation rates of three

alloy classes is shown in Figure 2.29 whereas the Ni-based alloy (625) exhibited the lowest weight gain, followed by D9 (austenitic alloy) and HCM12A (F-M alloy) [88].

The F-M alloys have been studied extensively since the starting of the Generation IV initiative. The alloys tested including T91, T92 (NF616), HCM12A, HT-9, and advanced ODS F-M alloys [88-91]. The studies showed that F-M alloys revealed high oxidation rate in the SCW. Cr concentration plays an important role on the oxidation rate. The oxide structure consisted of two layers of oxide in which the oxide types depend on the condition of SCW (dissolved oxygen and temperature). The outer oxide could be Fe_3O_4 or Fe_2O_3 or both types. The inner oxide usually is Fe-Cr oxide with a spinel structure $(Fe, Cr)_3O_4$. Pores are always observed in both outer and inner oxides. Another layer formed at the inner oxide/alloy interface. This layer sometimes called “diffusion layer”, “internal oxidation layer”, “selective oxidation layer”, and or “transition layer” due to non-uniform oxide morphology and concentration gradients of oxygen and metal elements. In this thesis, this layer will be called as a transition layer.

Temperature has a great effect on the oxidation rate and the oxide structure. For alloys where the oxidation rate is diffusion limited, an increase in SCW temperature resulted in an increase of the ion diffusivities and the oxidation rate, eqn 2.12. Reports from Ampornrat and Was [90] showed that the oxidation of F-M alloys increased exponentially from 400 to 600°C. If the oxide grows very fast, thick oxide tends to spall off. Aside this, the type of oxide formed varies depend on the temperature, which was described in section 2.3.1c.

Effect of SCW pressure was studied by Watanabe et al. [92]. The SCW pressure is directly dependence to the density of water similar to the work of Y.S. Yi et al. for the

oxidation in steam [75]. However, the oxidation in SCW could be different from that in steam because of the chemical and physical properties of SCW. Watanabe et al. performed experiments on the Ni-based alloys B-2 and C-276 and the austenitic steel 316 under conditions of 400°C with a pressure range of 25-60 MPa and at 360°C with 25 MPa (subcritical water). The water contained 0.01 mol/kg of sulfuric acid and 0.025 mol/kg of oxygen. The results showed that the change from subcritical to supercritical and the change from high pressure to low pressure are both accompanied by decreases in the density, which has the effect of lowering the corrosion rate similar to the density effect in steam. However, these alloys exhibited a dissolution reaction or, sometimes, a spallation in SCW. Therefore the effects cannot be compared directly to the F-M alloys.

Most of the alloys will exhibit an increase in oxidation rate at high oxygen concentration. However, the oxidation rate tends to decrease at an intermediate level of oxygen concentration of ~100-300 ppb. The results from T91 and HCM12A in 500C SCW showed this behavior [80, 90]. This observation are consistent with the objective of combined water chemistry control [93] in which the addition of small amounts of oxygen enhances the formation of the hematite crystal between the magnetite grains and reduce the oxidation rate [88].

Surface modified and grain boundary engineering of alloys had been studied by Dr. T.R. Allen's group at the University of Wisconsin [87, 89]. The objective is to improve the oxidation resistance of alloys in SCW. Because the dissolved oxygen concentration has been shown to affect the growth of the oxide layer, studies have been initiated to implant oxygen into the surface to modify the growth during exposure to SCW. The surface of HT-9 was implanted with 40 kV oxygen ions to a dose of $3x10^{17}$

ions/cm^2. The depth of the modified surface was ~0.15 μm. Results from an exposure test in 500°C, 25 ppb DO and 505 hours showed that the surface modified HT-9 exhibited lower weight gain than the un-modified HT-9. This result may be related to the preferred orientation of the oxide grains that form early in the exposure, resulting in a denser textured oxide layer thus reduced the oxidation rate at a longer exposure time. Meanwhile, the grain boundary engineering on INCOLOY 800H improved the protective oxidation behavior by enhancing spallation resistance and reducing oxidation rate. Spallation resistance correlates with a reduction in texture of the oxide layers.

Extensive studies of the oxidation mechanisms in SCW have been reported in several articles. A review by Zhang et al. [80] purposed that the oxidation mechanism in SCW has a strong influence of water molecules. The major evidence is volatile oxidation products of Cr, Al, and Si with H_2O including $CrO_2(OH)_2$, $Al(OH)_3$, and $SiO(OH)_2$. This mechanism is proven by a nodular oxidation on 304NG austenitic alloys that contains 19.4%Cr. On the surface, pitting first occurred because of vaporization of $CrO_2(OH)_2$. The Cr concentration in this alloy is high enough to compensate the loss of Cr on the surface. However, the diffusion of Cr at grain boundary area is higher than in grain interior, so the pitting with Cr depletion was formed on the surface. Iron from the base metal disuse across the film and react with the oxygen or water to form an oxide island of Fe_3O_4 just above the film.

Tan et al. [94] reported the mechanism of void formation in magnetite scale on the HCM12A alloy. The author proposed that the pores can form at a location where a critical vacancy concentration occur at which the vacancies start to collapse into pores. The critical vacancy concentration corresponds to the threshold in the diffusion

coefficient of iron in magnetite layer, which changes from interstitial to vacancy mode. Therefore, determination of oxygen and iron gradients as a function of depth from the oxide/water interface can predict the location of pores. Experimental results agreed with theoretical calculation from this assumption. The location of pore formation is found to be roughly dependent upon oxygen partial pressure but not upon the exposure time.

2.4 Conclusion

Among the research reviewed here, there are a number of subjects involving the oxidation mechanisms of F-M alloys in SCW that are not well understood. First is the fact that the SCW behaves differently from the water in liquid or gaseous phases. The questions arose that how the SCW affects to the oxidation mechanisms, and will the oxidation behavior in SCW be similar to that of steam. Second, the complex microstructure and microchemistry of the F-M alloys are noted to employ a major role on the oxidation mechanisms. The effects of alloying elements and microstructure of these alloys should be investigated. Evolution of alloy microstructure during the oxidation is needed to be understood. Finally, the parallel studies with the similar alloys and environments suggested that the oxidation rate in SCW is relatively high, and the detailed mechanisms are not quite well understood. Therefore the oxidation mechanisms of the F-M alloys in SCW should be determined through the experimental results of the oxidation rate and the oxide microstructure.

2.5 Objective, Significant of Study and Approach

The objective of this thesis is to understand the mechanism of oxidation of F-M alloys in SCW. The results will be used to determine the application of these alloys in the SCWR. Furthermore, the knowledge can serve as a guide to improving the oxidation resistance of these alloys in a particular SCW environment. In order to achieve this goal, the research has been conducted following these steps; i) understand the effects of SCW on oxidation rate, including temperature and dissolved oxygen concentration, ii) characterize the effects of alloy microstructure and alloying elements of F-M alloys, iii) describe the formation and evolution of oxide scales, and finally, iv) propose the oxidation mechanisms of F-M alloys in SCW based on the experimental results of the oxidation rate and the oxide microstructure.

Table 2.1 Effects of alloying addition on the constitution of steel containing 9-12% Cr [23, 33].

Element	Change in δ-ferrite content, % per mass % of alloy addition
N	-220
C	-210
Ni	-20
Co	-7
Cu	-7
Mn	-6
W	+3
Mo	+5
Si	+6
Cr	+14
V	+18
Al	+54

Table 2.2 Precipitation in normalized and tempered, aged, and creep rupture tested F-M alloys [23].

Precipitate phase	Crystal structure and lattice parameter	Typical composition	Distribution of precipitates
$M_{23}C_6$	fcc a = 1.066 nm	$(Cr_{16}Fe_6Mo)C_6$, $(Cr_4Fe_{12}Mo_4Si_2WV)C_6$	Coarse particles at PAG and lath boundaries and fine intra-lath particles
MX	fcc a = 0.444-0.447 nm	NbC, NbN, VN, (CrV)N, Nb(CN) and (NbV)C	Undissolved particles and fine precipitates at lath boundaries
M_2X	Hexagonal a = 0.478 nm c = 0.444 nm	Cr_2N, Mo_2C and W_2C	Lath boundaries (Cr_2N and Mo_2C), PAG boundaries (Mo_2C), intra-lath (Mo_2C and W_2C), δ ferrite in duplex alloys ($Cr_2(CN)$ and $(CrMo_2)_2CN$))
Z-phase	Tetragonal a = 0.286 nm c =0.739 nm	(CrVNb)N	Large plate-like particles in the matrix after creep straining at 600°C
η-carbide	Diamond cubic a = 1.07-1.22 nm	M_6C, $(Fe_{39}Cr_6Mo_4Si_{10})C$	PAG and lath boundaries, and intra-lath
Vanadium carbide	fcc a = 0.420nm	V_4C_3	Low number density in matrix
Laves	Hexagonal a = 0.474 nm c = 0.773 nm	Fe_2Mo, Fe_2W and $Fe_2(MoW)$	PAG and lath boundaries, and intra-lath, δ ferrite in duplex alloys
Chi (χ)	bcc a = 0.892 nm	$M_{18}C$ or $Fe_{35}Cr_{12}Mo_{10}C$	Intra-lath, δ ferrite in duplex alloys

Table 2.3 Classification of electrical conductor for oxides, sulfides, and nitrides [44, 48]

Metal-excess semiconductors (n-type) BeO, MgO, CaO, SrO, BaO, BaS, ScN, CeO2, ThO_2, UO_3, TiO_2, TiS_2, TiN, ZrO_2, V_2O_5, VN,Mo_2O_5, Ta_2O_5, MoO_3, WO_3, WS_2, MnO_2, Fe_2O_3, ZnO, CdO, CdS, Al_2O_3, Tl_2O_3, In_2O_3, SiO_2, SnO_2, PbO_2, and at low oxygen partial pressure Cr_2O_3
Metal-deficit semiconductors (p-type) $FeCr_2O_4$, FeO UO_2, $MgCr_2O_4$, $FeCr_2O_4$, $CoCr_2O_4$, $ZnCr_2O_4$, WO_2, MoS_2, MnO_2, Mn_3O_4, Mn_2O_3, FeO, FeS, NiO, NiS, CoO, Co_3O_4, PdO, Cu_2O, Cu_2S, Ag_2O, $CoAl_2O4$, $NiAl_2O_4$, GeO, SnS, Sb_2S_3, and at high oxygen partial pressure Cr_2O_3
Amphoteric conductors TiO, Ti_2O_3, VO, Cr_2O_3, MoO_2, OsS_2, IrO_2, RuO_2

Table 2.4 Standard free energies of reaction [49].

(The free energies referred to pure metal.)

Reaction	ΔG° $A + BT$ (J mol^{-1})	
	A	B
$\frac{4}{3}Al(l) + O_2 = \frac{2}{3}Al_2O_3$	−565,900	128
$\frac{1}{2}Si + O_2 = \frac{1}{2}SiO_2$	−451,040	86.8
$Mn + \frac{1}{2}O_2 = MnO$	−412,304	72.8
$Zn + \frac{1}{2}O_2 = ZnO$	−356,190	107.9
$\frac{2}{3}Cr + \frac{1}{2}O_2 = \frac{1}{3}Cr_2O_3$	−373,420	86
$\frac{23}{6}Cr + C = \frac{1}{6}Cr_{23}C_6$	−68,533	−6.45
$\frac{7}{27}Cr_{23}C_6 + C = \frac{23}{27}Cr_7C_3$	−42,049	−11.9
$\frac{3}{7}Cr_7C_3 + C = \frac{2}{7}Cr_3C_2$	−13,389	−0.84
$2Cr + \frac{1}{2}N_2 = Cr_2N$	−108,575	138
$Cr_2N + \frac{1}{2}N_2 = 2CrN$	−133,890	174
$Fe + \frac{1}{2}O_2 = FeO$	−264,890	65.4
$3FeO + \frac{1}{2}O_2 = Fe_3O_4$	−312,210	125.1
$2Fe_3O_4 + \frac{1}{2}O_2 = 3Fe_2O_3$	−249,450	140.7
$Fe + \frac{1}{2}S_2 = FeS$	−150,247	52.6
$3Fe + C = Fe_3C$	29,037	−28.0
$Co + \frac{1}{2}O_2 = CoO$	−233,886	70.7
$3CoO + \frac{1}{2}O_2 = Co_3O_4$	−183,260	148.1
$Ni + \frac{1}{2}O_2 = NiO$	−234,345	84.3
$H_2 + \frac{1}{2}O_2 = H_2O$	−246,440	54.8
$H_2 + \frac{1}{2}S_2 = H_2S$	−180,580	98.8
$O_2 + \frac{1}{2}S_2 = SO_2$	−362,420	72.4
$CO + \frac{1}{2}O_2 = CO_2$	−282,420	86.8
$2CO = CO_2 + C$	−170,700	174.5

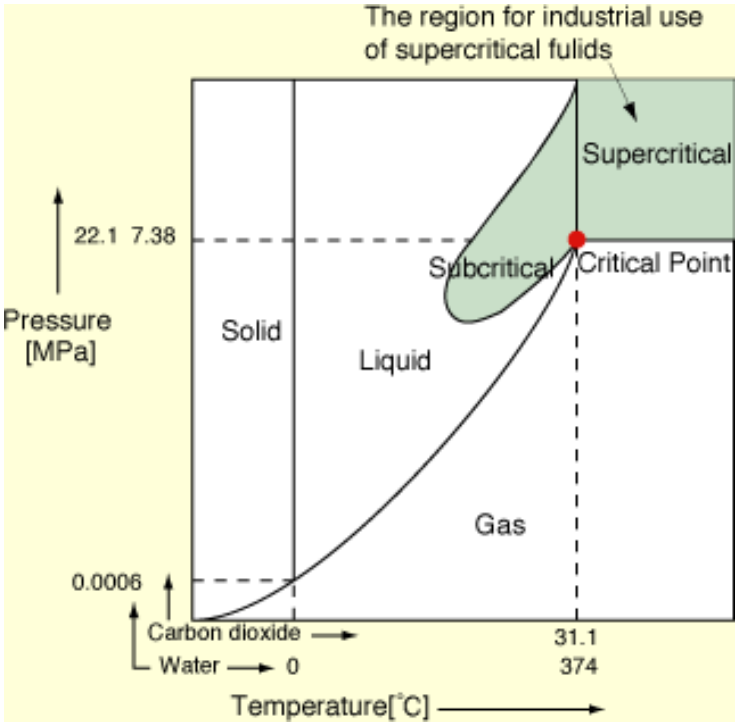

Figure 2.1 Phase diagram for water [1].

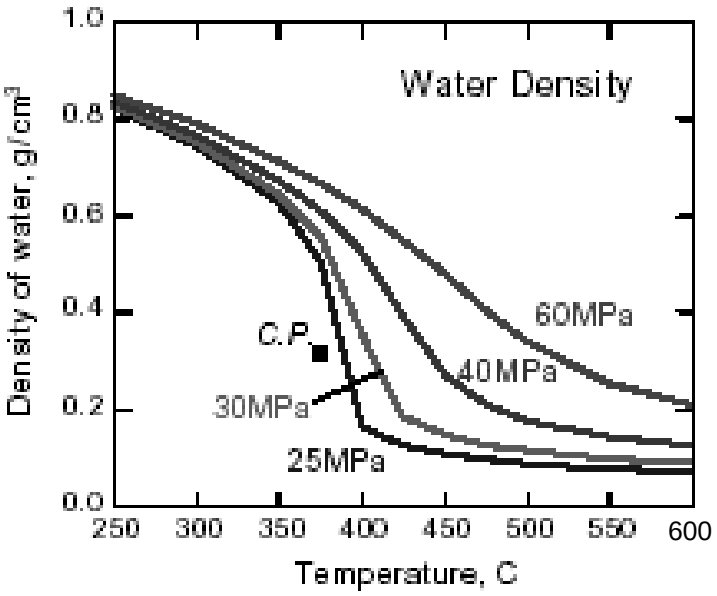

(a)

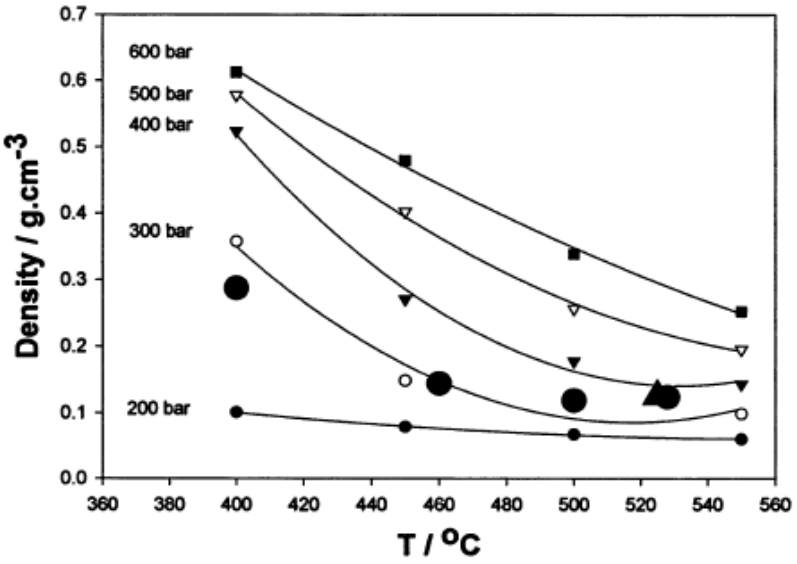

(b)

Figure 2.2 (a) Variation in the density of water with temperature showing the drop in density at critical region (350-400°C) [5]. (b) Plots of density vs. temperature for SCW as a function of pressure [6]. (Note that the large filled circles indicate values for HCl solution in the SCWO.)

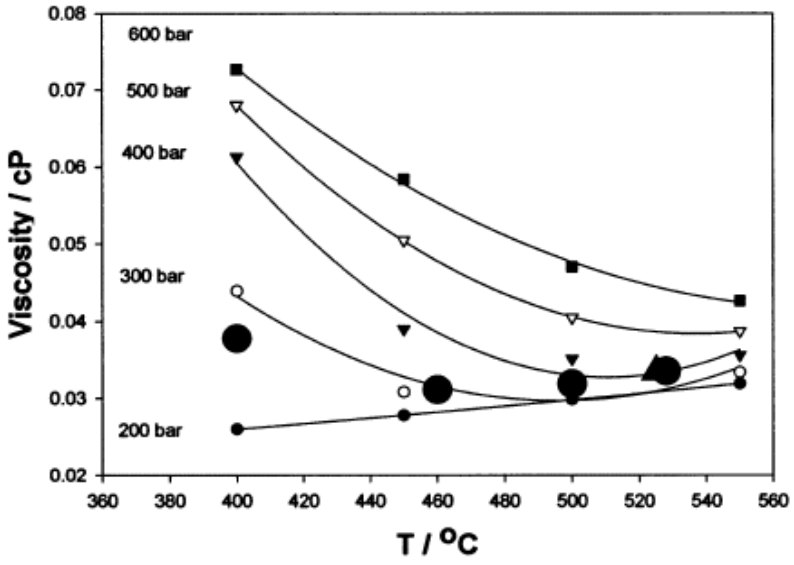

Figure 2.3 Plots of viscosity vs. temperature for SCW as a function of pressure [6]. (Note that the large filled circles indicate values for HCl solution in the SCWO.)

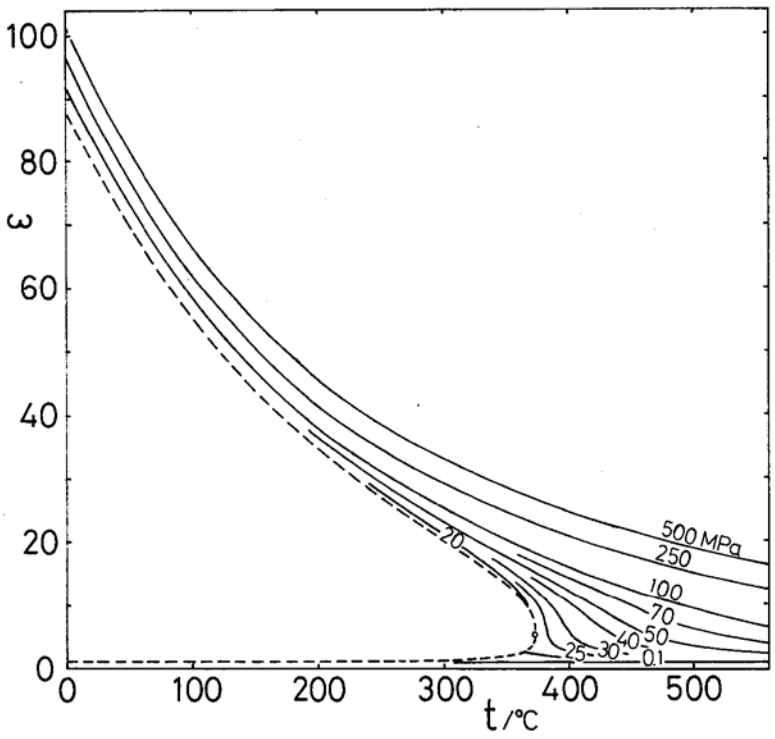

(a)

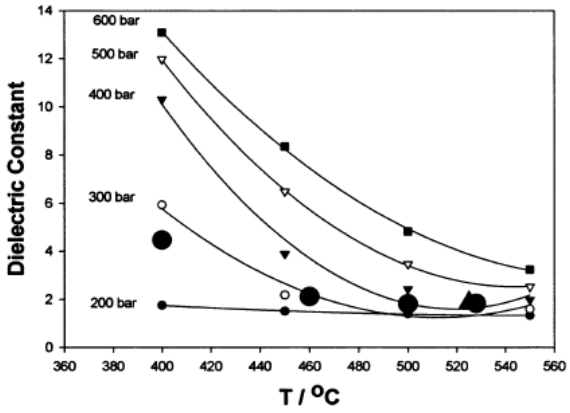

(b)

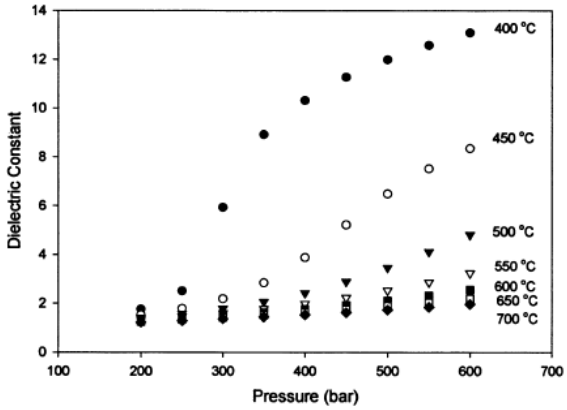

(c)

Figure 2.4 (a) Plots of static dielectric constant as a function of temperature [12].

(b) Plots of static dielectric constant as a function of temperature in sub-critical and SCW regimes [6].

(c) Variation of the dielectric constant of water over a range of pressure [6].

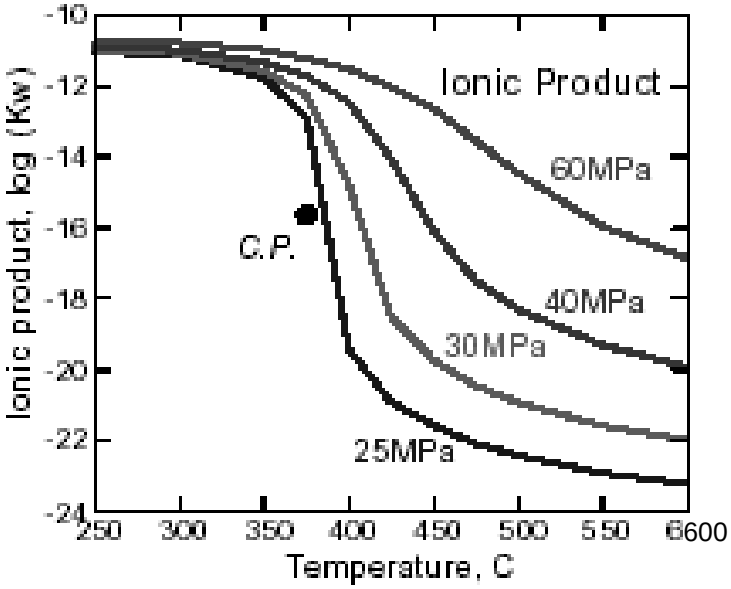

Figure 2.5 Ionic products as functions of temperature and pressure. [5]

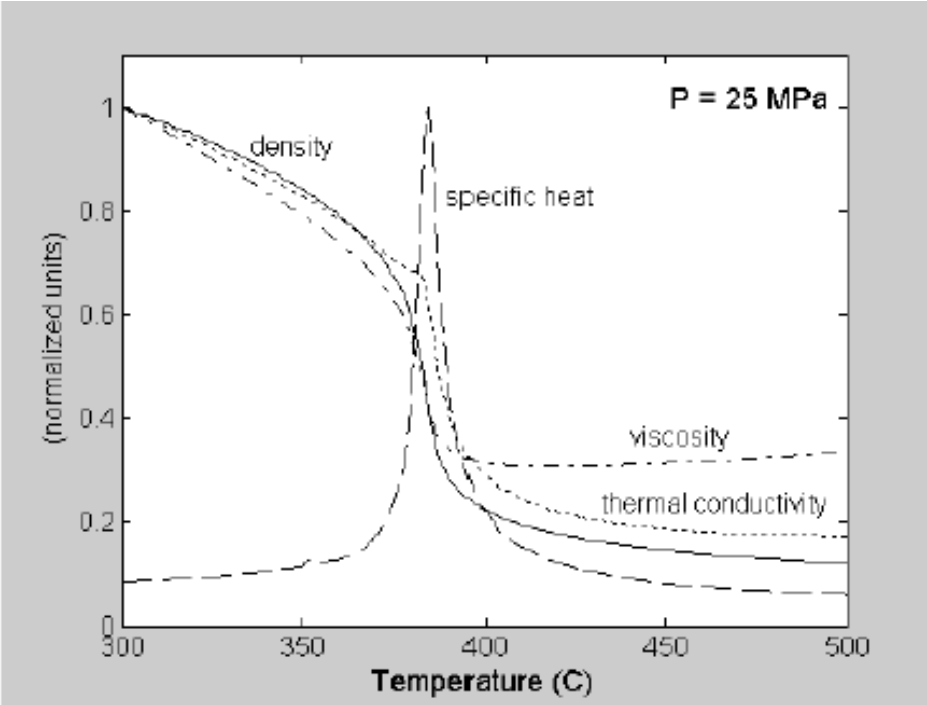

Figure 2.6 Thermo-physical properties of SCW at pressure 25 MPa [1].

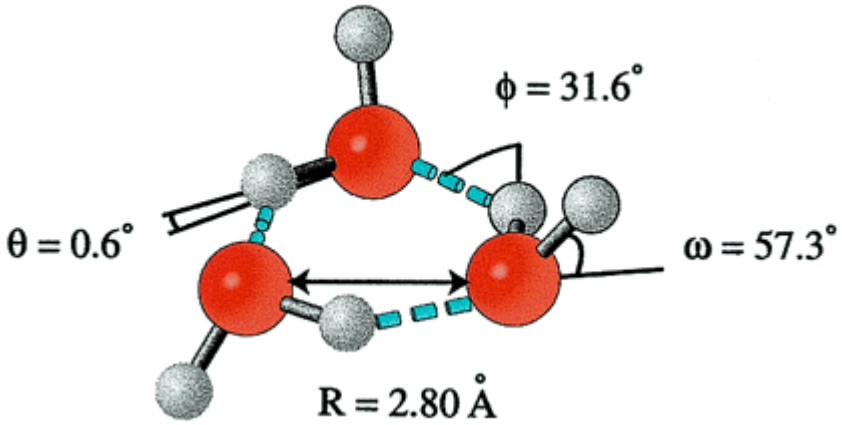

Figure 2.7 The water trimer consists of three water molecules. Each water monomer acts as a single hydrogen bond donor and accepter. [21]

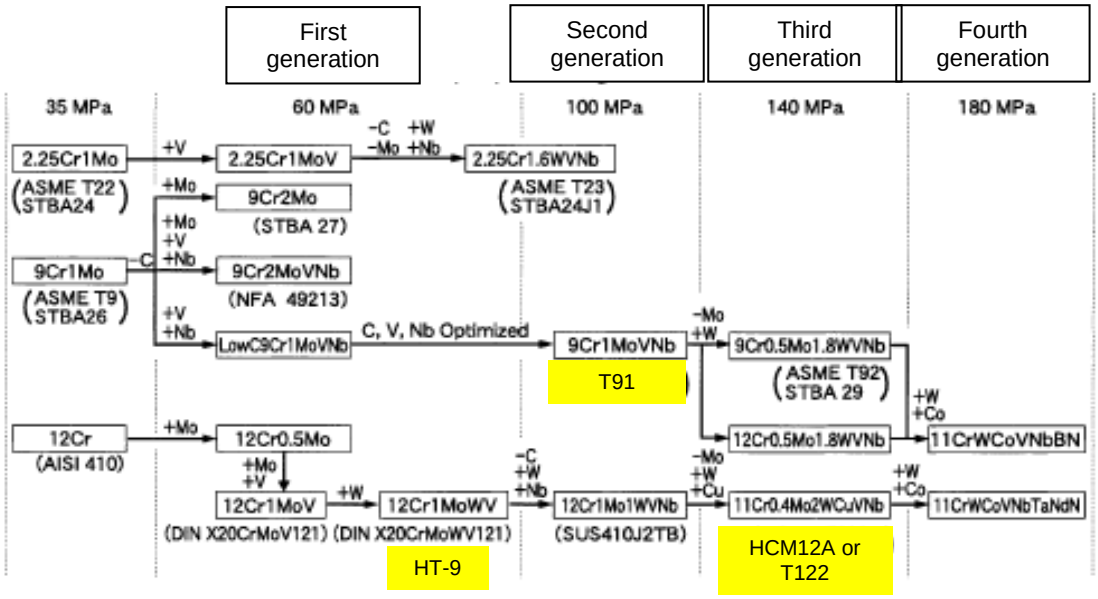

(a)

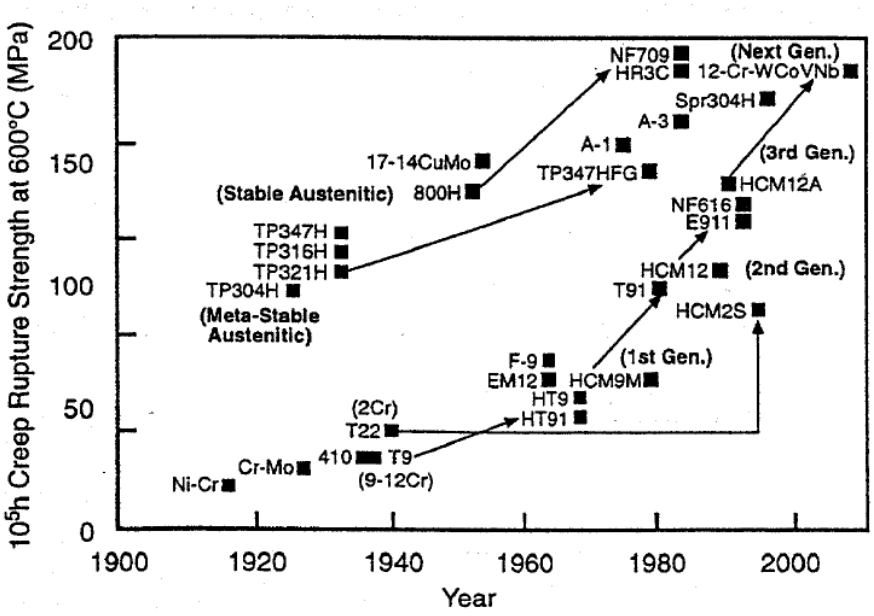

(b)

Figure 2.8 Development of ferritic alloys for boilers. (a) Schematic diagram shows development of F-M alloys that are classified into four generations based on alloying elements and creep strength [22]. (b) History of improvement of creep strength of F-M alloys and austenitic alloys [24].

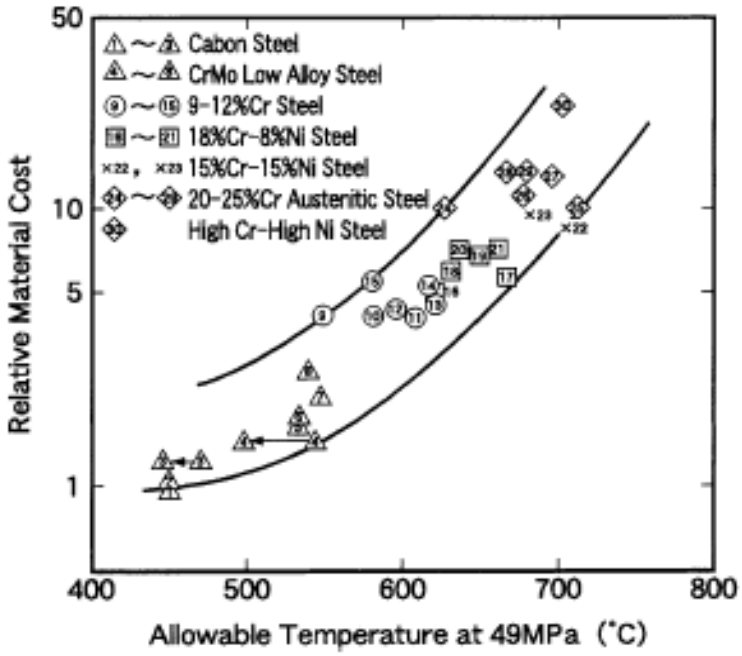

Figure 2.9 Relation between allowable metal temperature at 49 MPa of allowable stress and relative material cost [22].

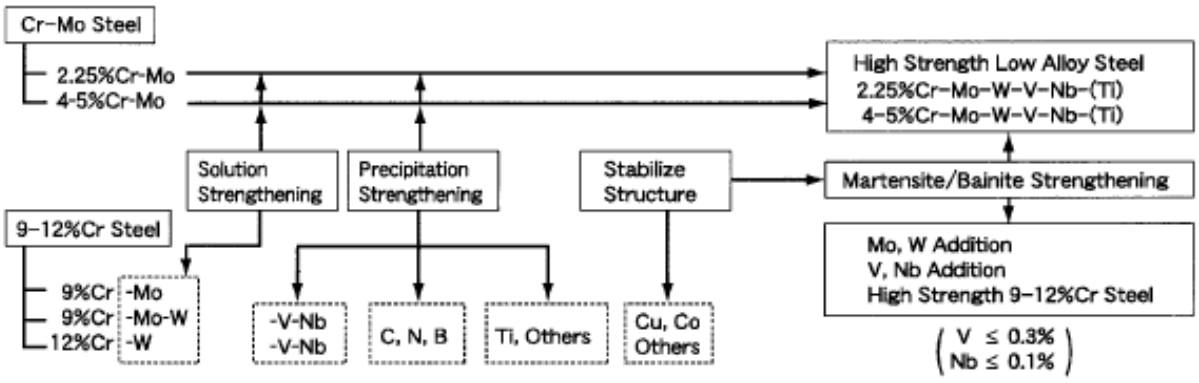

Figure 2.10 General concept of alloy composition design for heat resistant alloy [22].

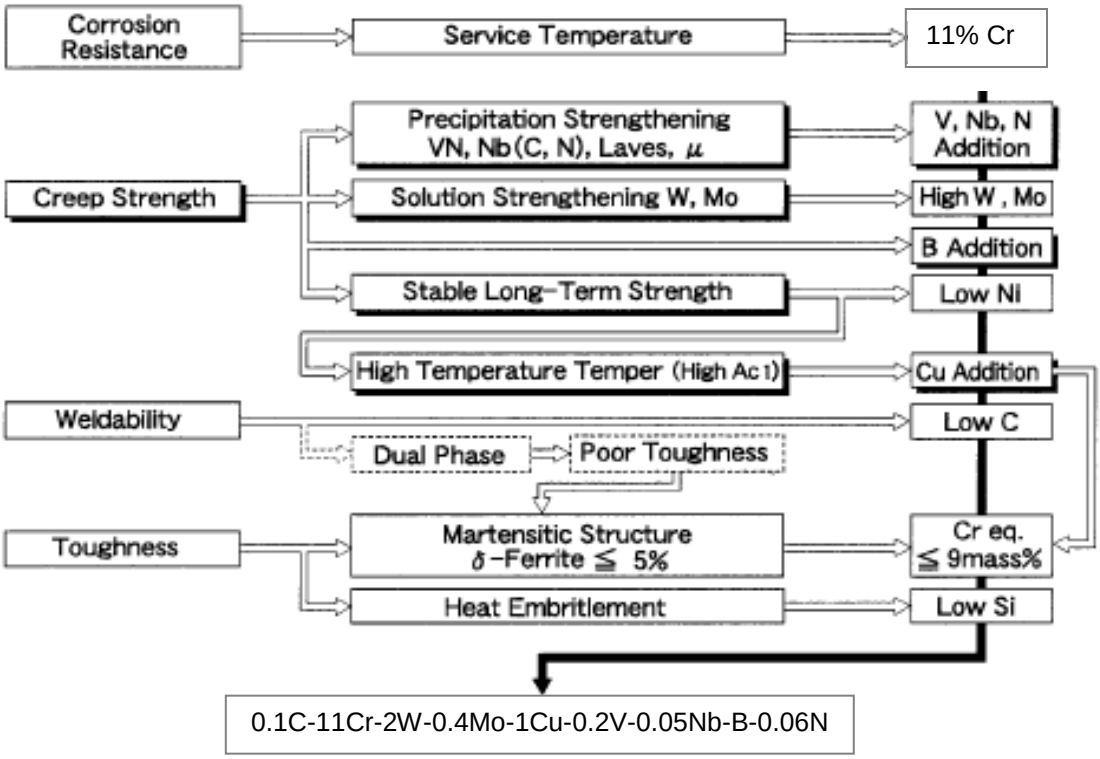

Figure 2.11 Alloy design for HCM12A [27]

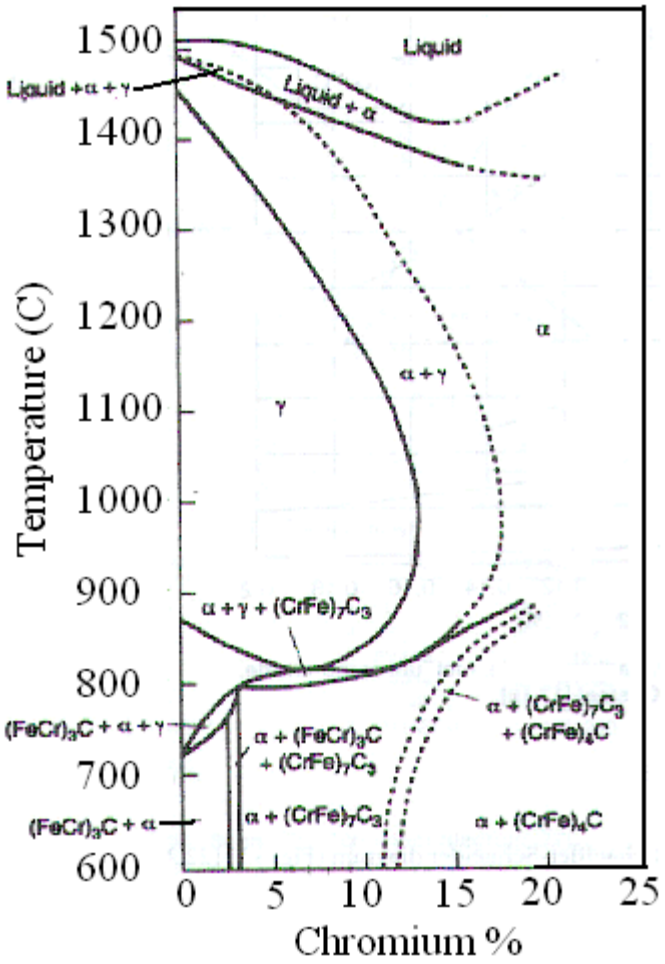

Figure 2.12 Phase diagram of Fe-C-Cr alloys showing the effect of chromium on the constitution of Fe-Cr-C alloys containing 0.1% C [23, 32]; note that $(CrFe)_4C$ is a $M_{23}C_6$ carbide.

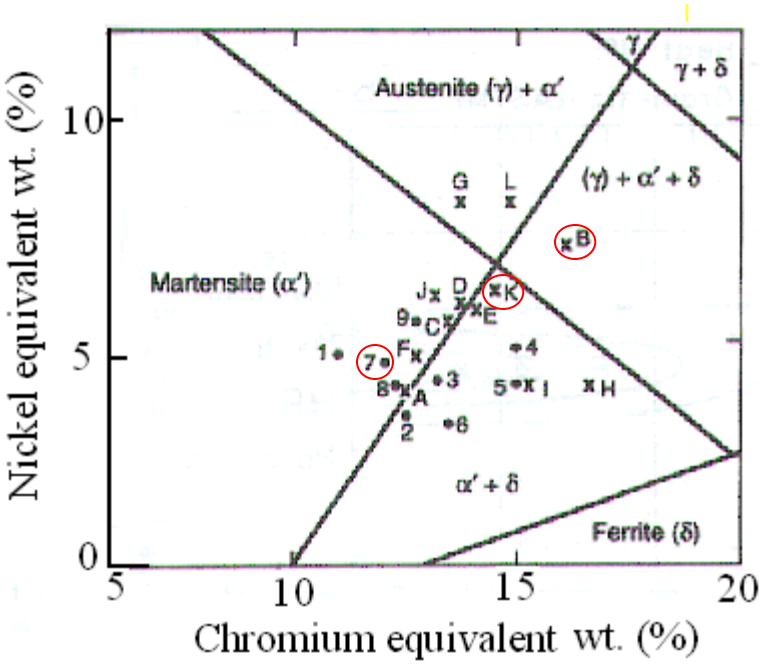

9% Cr alloys (•)
1. EM10
2.HCM9M
3. NSCR9
4. EM12
5. JFMS
6. TEMPALOY F-9
7. T91
8. TB9 (NF616)
9. E911

12% Cr alloys (×)
A. Fl
B. HT-9
C. FV448
D. 1.4914
E. MANET I
F. MANET II
G. GE
H. HCM12
I. TB12
J. TR1150
K. HCM12A
L. HR1200

Figure 2.13 The Schaeffler-Schneider diagram represent the correlation between the phases present to the chromium and nickel equivalent in 9-12%Cr alloys [23].

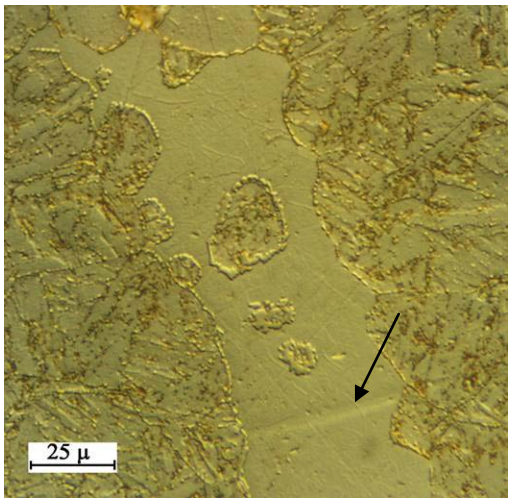

Figure 2.14 Optical micrograph shows a ferrite stringer in HCM12A microstructure. [34]

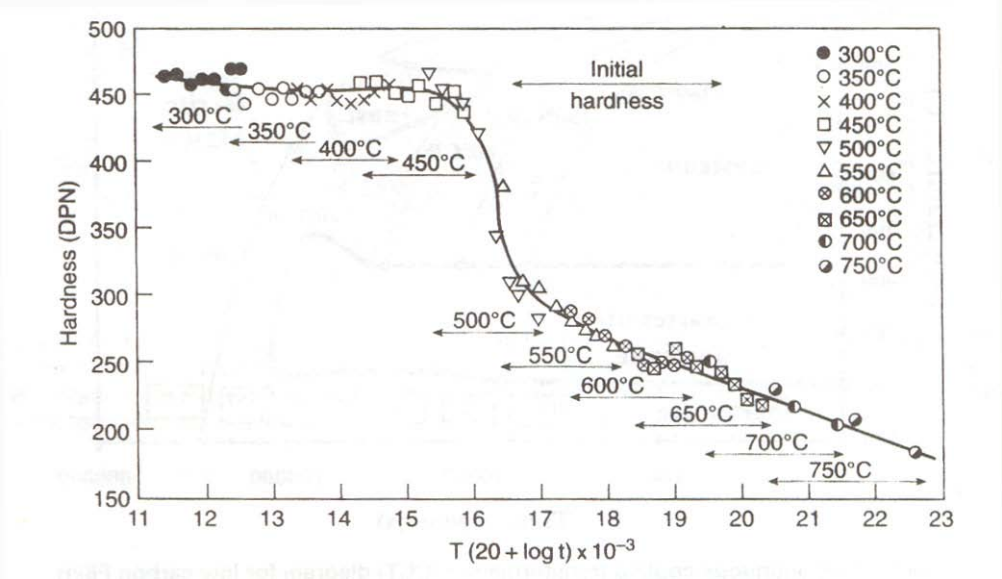

Figure 2.15 Effect of tempering temperature on hardness of a 12Cr-0.14C alloy [23, 37]

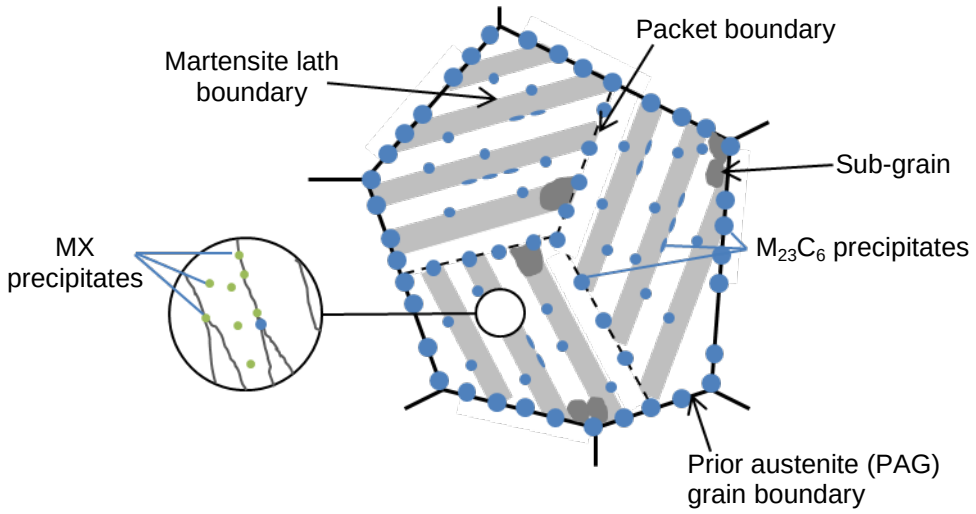

Figure 2.16 Schematic diagram of the microstructure of normalized and tempered F-M alloys.

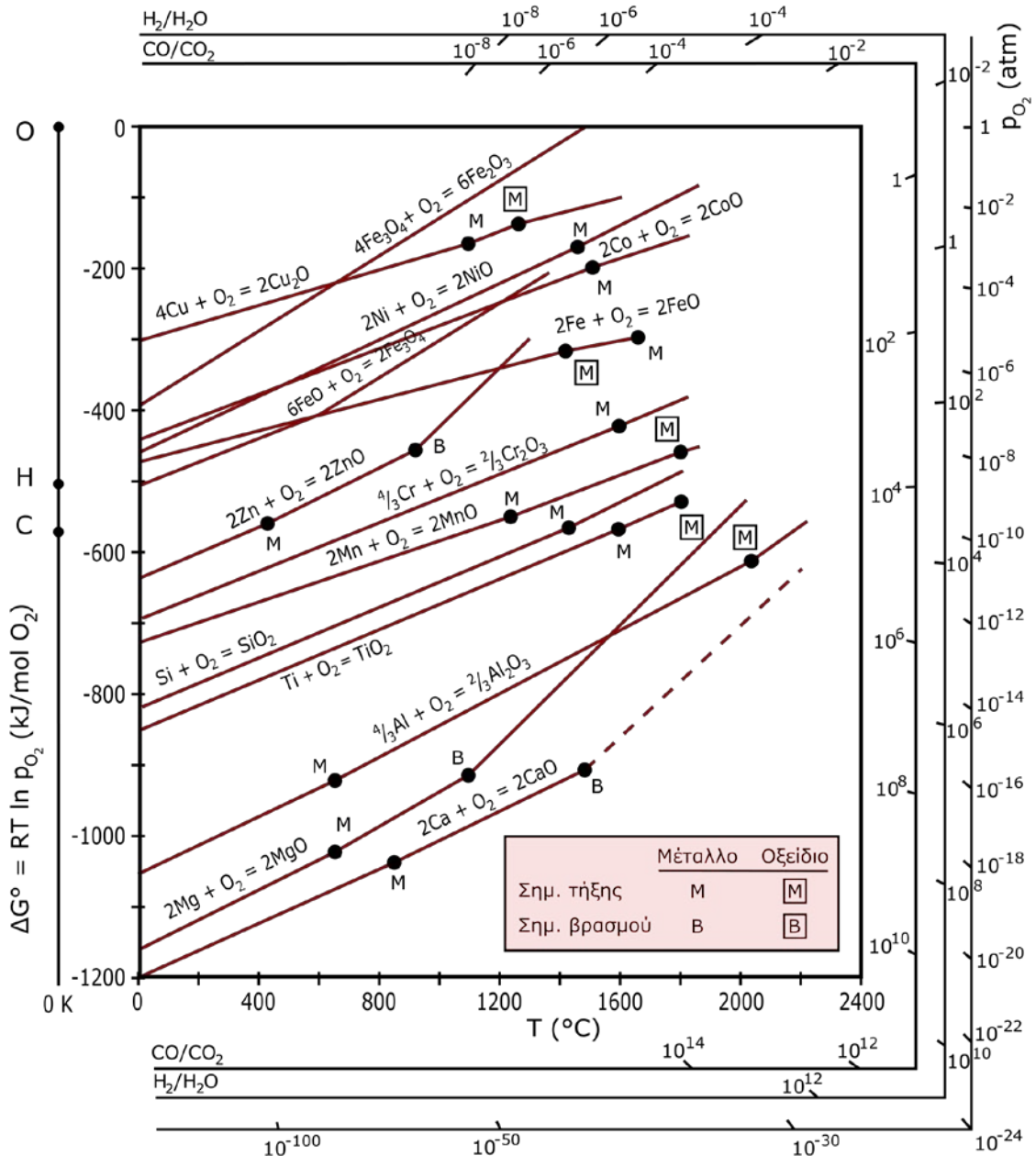

Figure 2.17 Ellingham/Richardson diagram shows plot of free energy with temperature for various oxides [50].

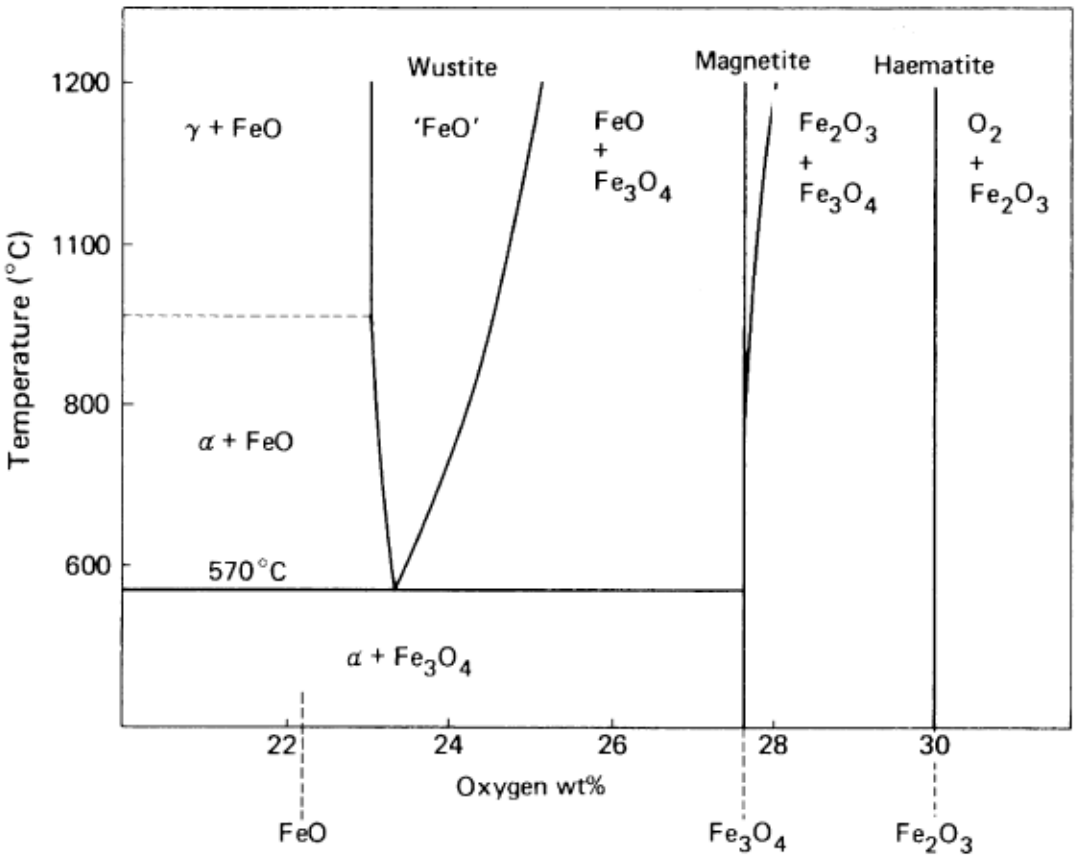

Figure 2.18 Phase diagram of Fe-O [47].

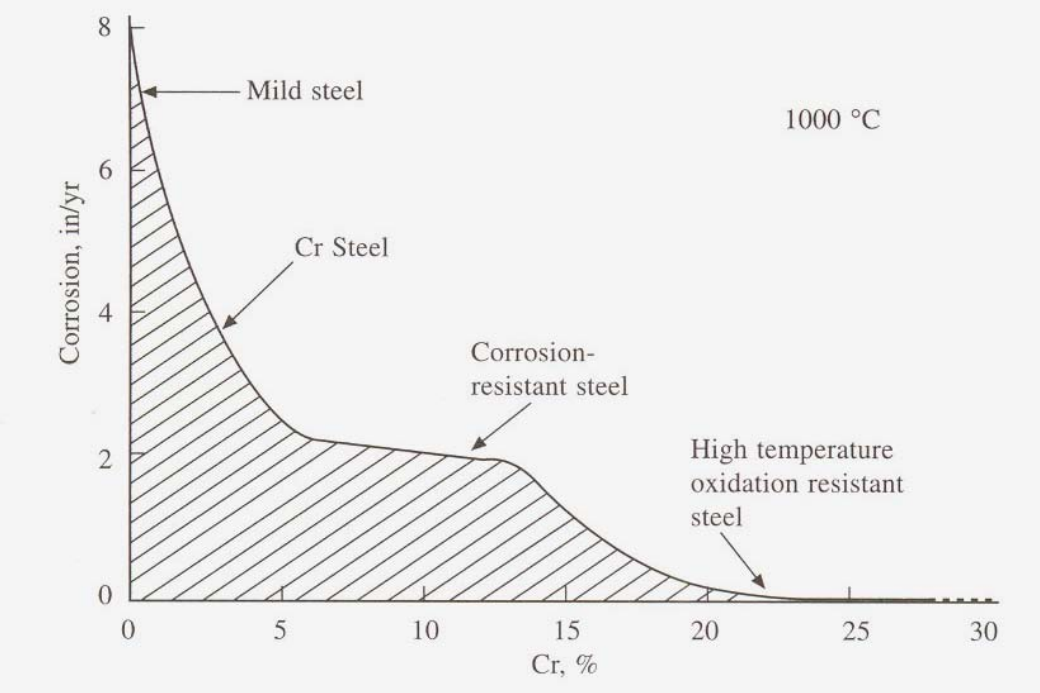

Figure 2.19 Effect of Cr addition on the corrosion rate of alloy at 1000^{o}C [47].

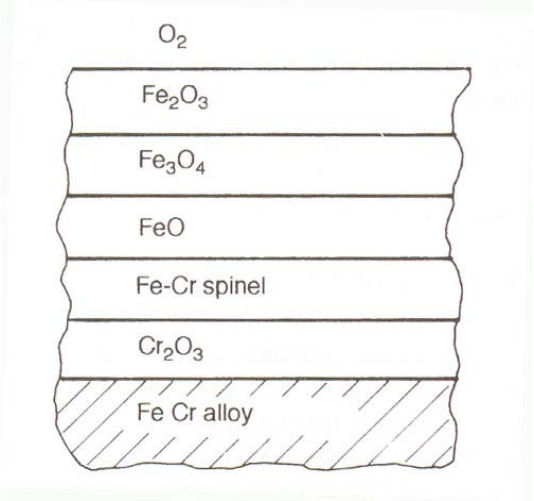

Figure 2.20 Schematic representation of all possible component of oxide layers on Fe-Cr alloy [47].

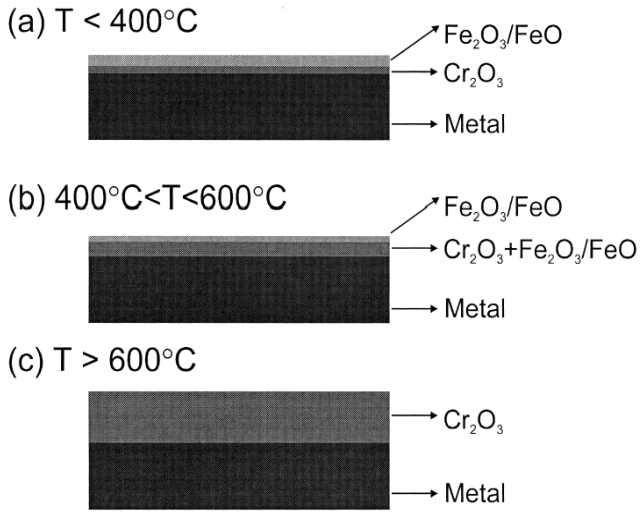

Figure 2.21 Schematic diagram of oxide structure formed on 9Cr-1Mo steel exposed in air at 400-600°C [59]

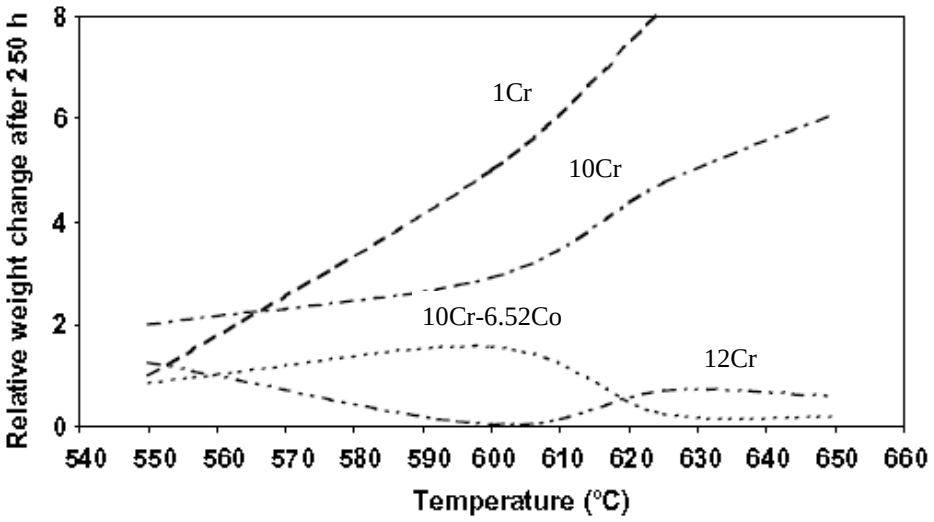

(a)

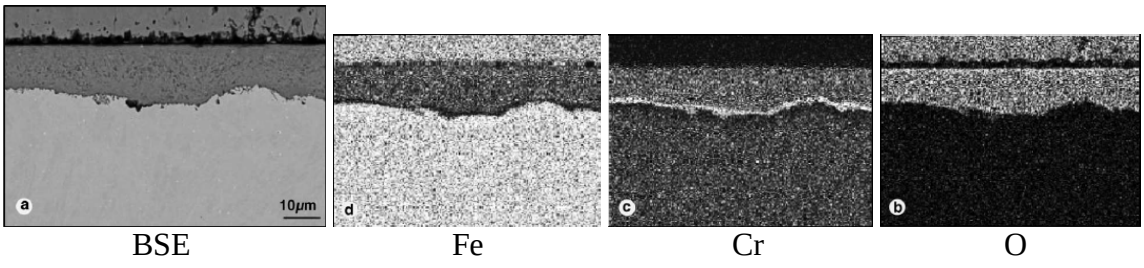

BSE Fe Cr O

(b)

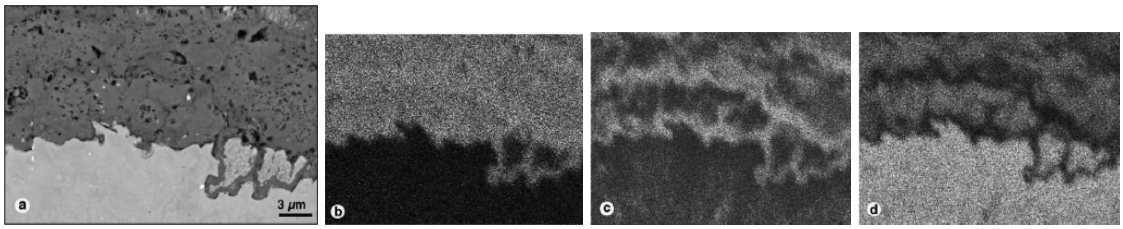

BSE Fe Cr O

(c)

Figure 2.22 Oxidation of 1Cr, 10Cr, 10Cr-6.52Co and 12Cr in Ar-50%H_2O at 550-650°C reported by Zurek et al. (a) Oxidation rate, (b) Composition profiles of 10Cr-6.52Co exposed at 600°C, and (c) Composition profiles of 12%Cr exposed at 625°C. Both composition profiles show enrichment of Cr at the alloy/oxide interface. [62]

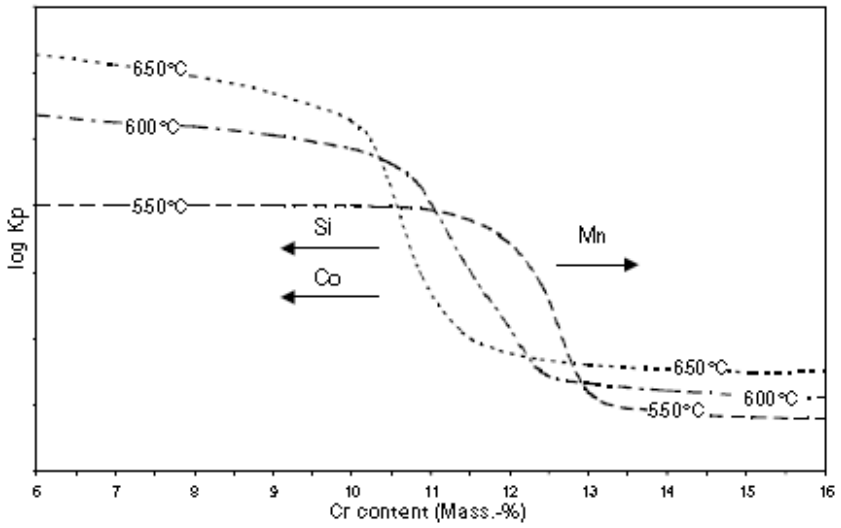

Figure 2.23 Schematic illustration of oxidation rate as function of Cr content for commercial ferritic alloys in steam with the temperature range of 550-650C. Arrows indicate qualitative changes of critical Cr-content by additions of Si, Co, and Mn respectively. [63]

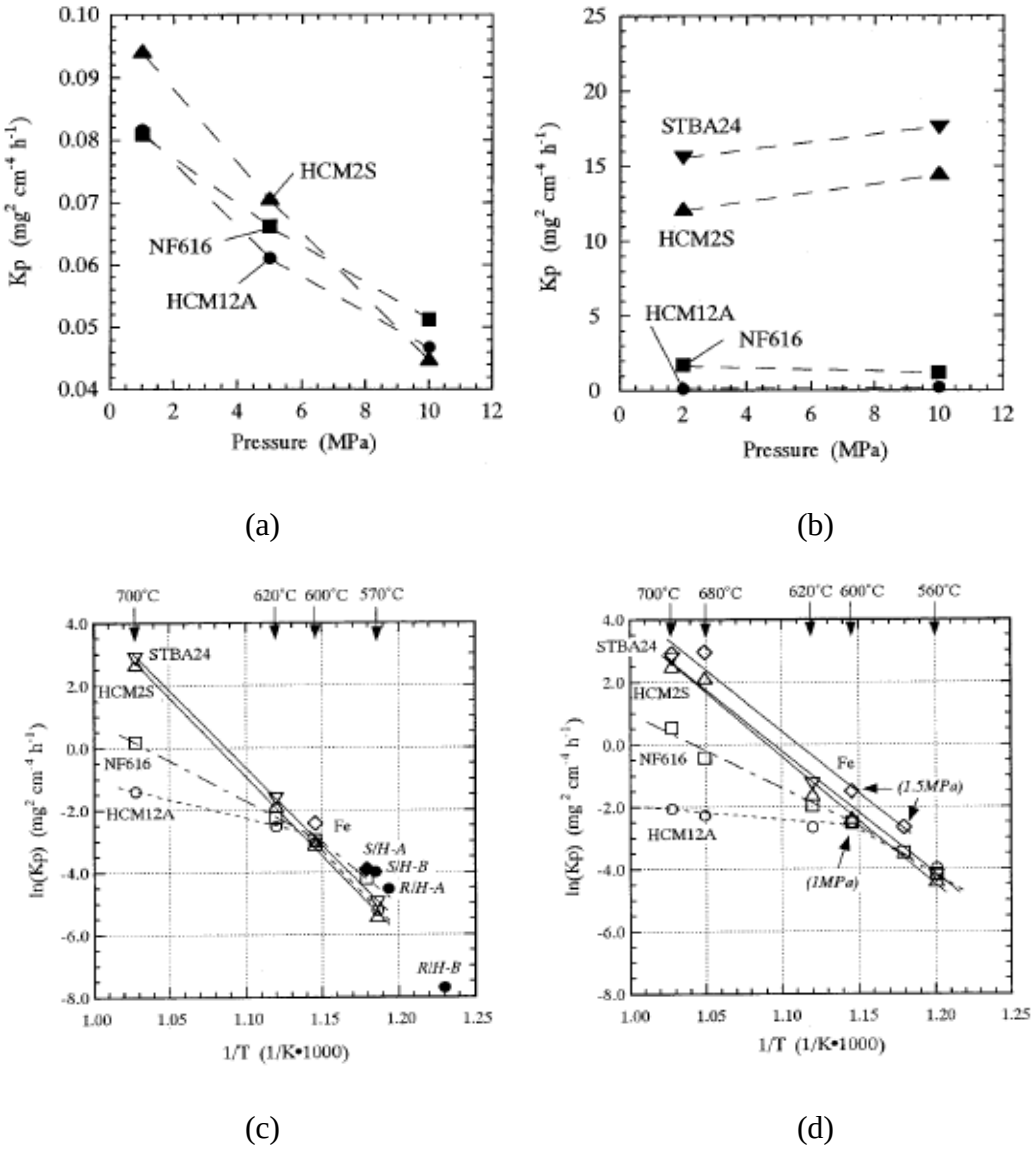

Figure 2.24 Effects of steam pressure: Plots of oxidation rate constants of F-M alloys HCM2S, NF616 and HCM12A versus steam pressure tested at (a) 600°C and (b) 700°C. The Arrhenius plots of k_p measured at (c) 10 MPa and (d) 2 MPa or lower show changes in activation energies trend. [75]

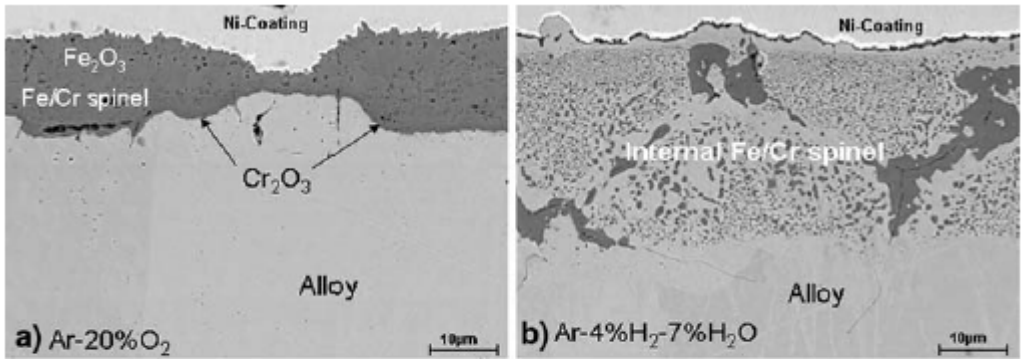

(a) (b)

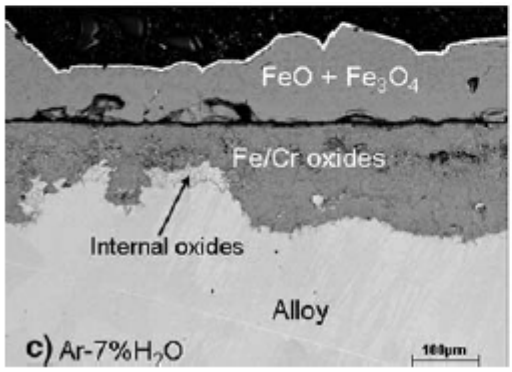

(c)

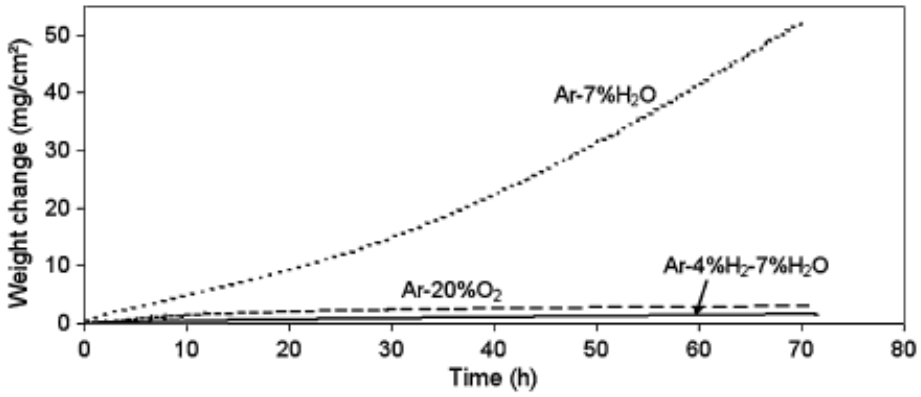

(d)

Figure 2.25 Effect of water vapor and steam composition: Scales formed on Fe-10Cr alloy after exposure in (a) Ar-20%O_2, (b) Ar-4%H_2-7%H_2O, and (c) Ar-7%H_2O and at 900°C for 72 hours, and (d) weight gain. [76]

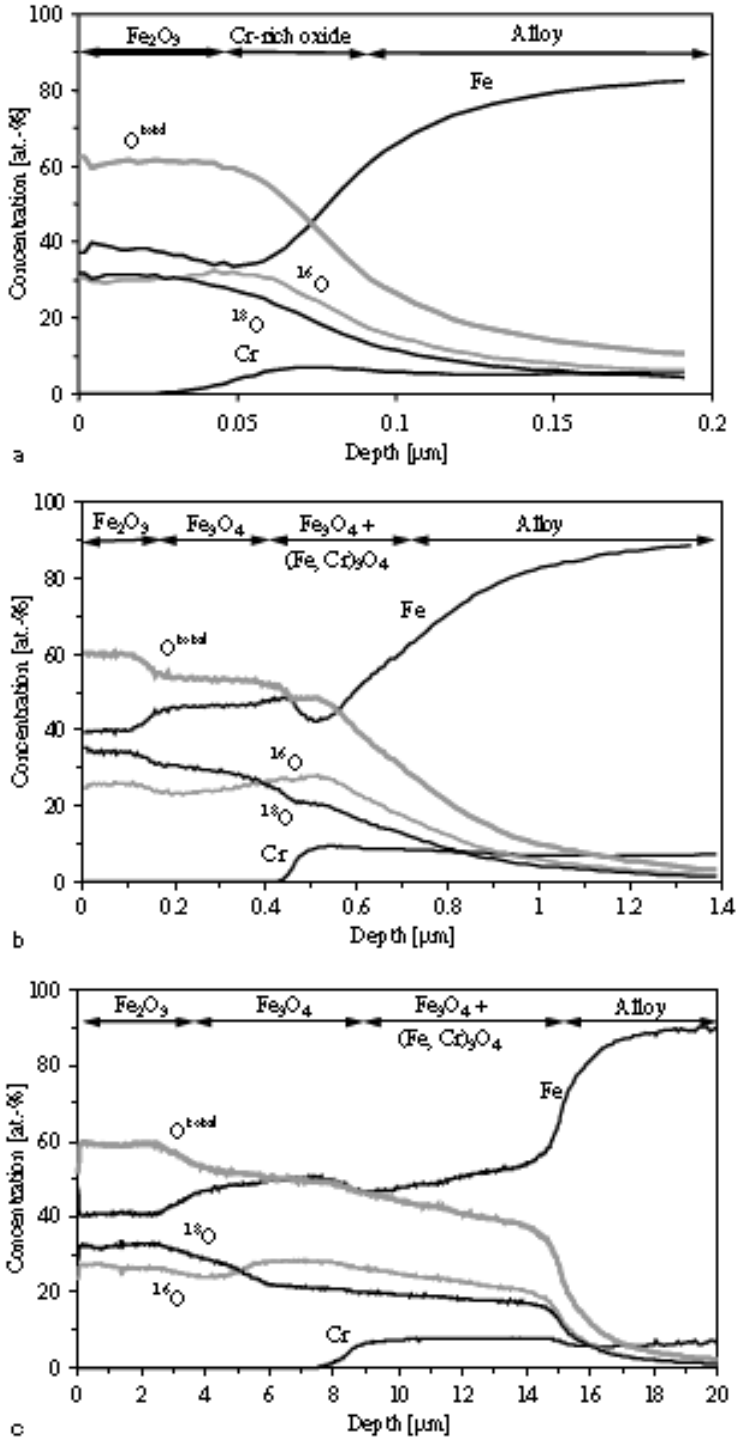

Figure 2.26 Depth profiles of P91 after oxidation in N_2- 1 vol%$^{16}O_2$- 2 vol%$H_2{}^{18}O_2$ at 650°C. The profile after (a) 1 h, (b) 7 h, and 30 h show ^{16}O in the inner layers, and ^{18}O from water molecules distribute in the outer layers. [77]

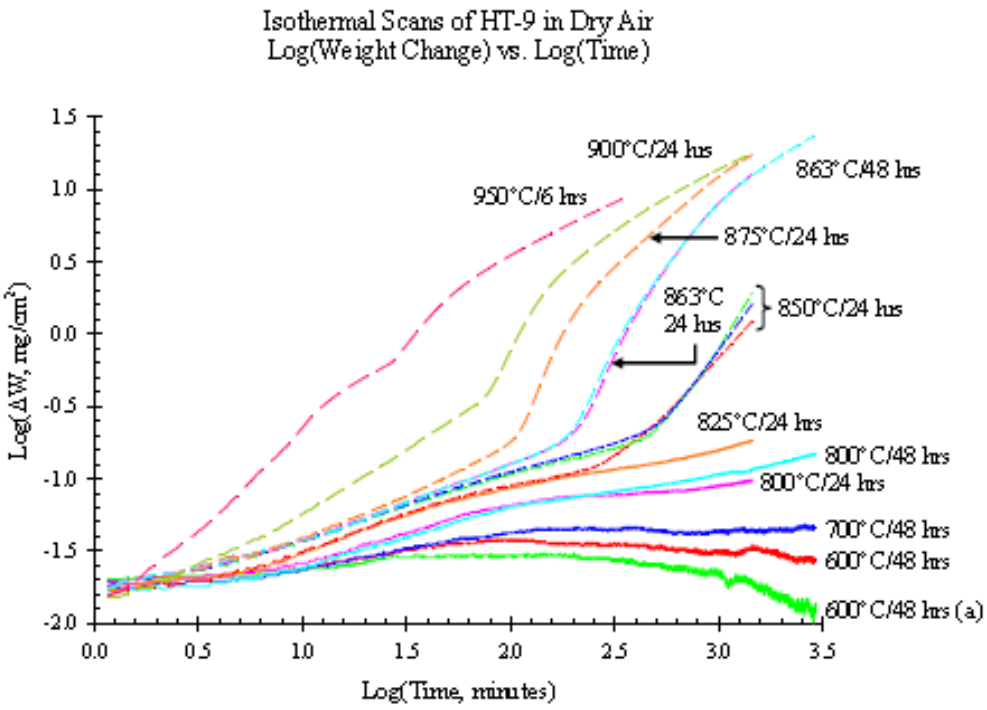

(a)

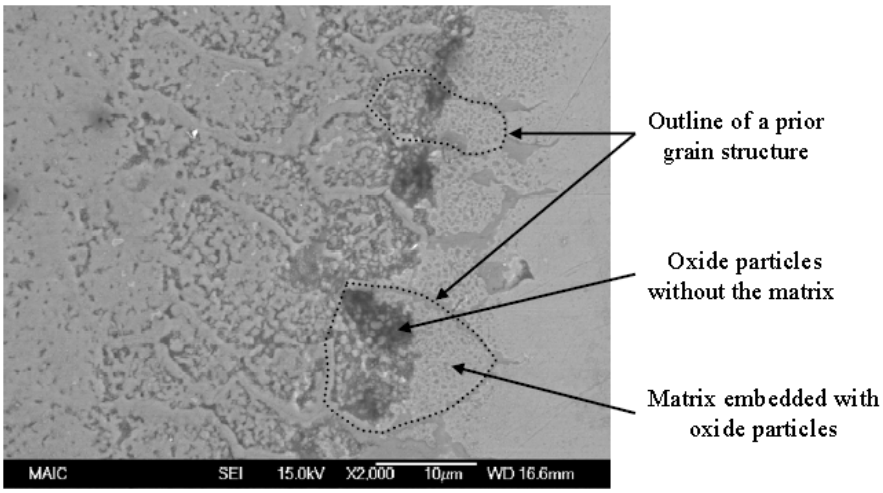

(b)

Figure 2.27 Temperature effect of oxidation in dry air: (a) Double logarithmic plot of weight gain and temperature of HT-9 tested in dry air at 600-950°C. (b) The partial dissolution of grain structure in the internal selective oxidation zone. Grain boundaries are outline with Cr-rich/Fe oxide. [74]

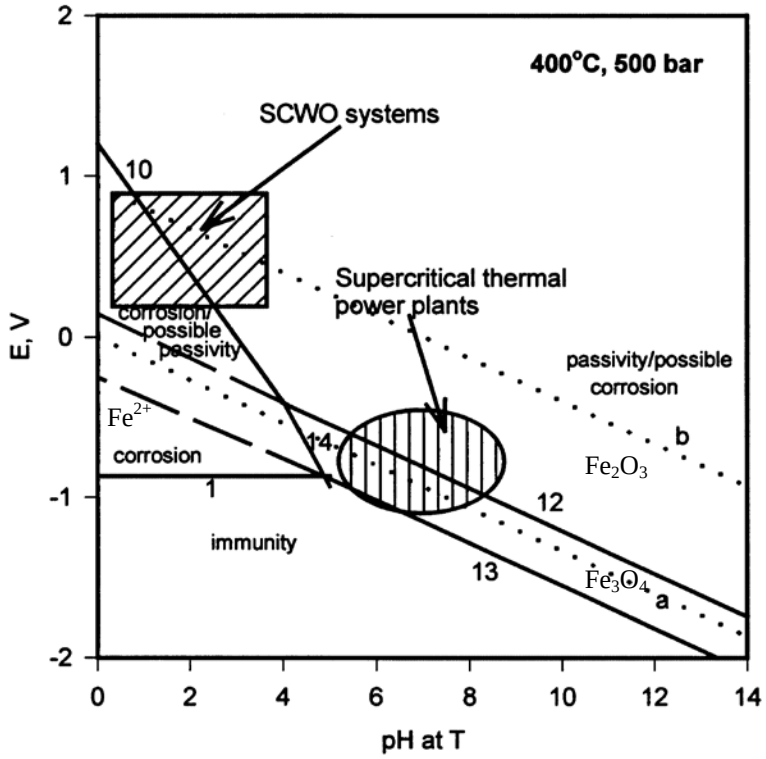

Figure 2.28 Potential-pH diagram for iron in supercritical aqueous solution at 400°C and P = 50 MPa. The diagram shows the approximate regions in potential-pH space for the operation of SCWO reactors and SCW thermal power plants. [6]

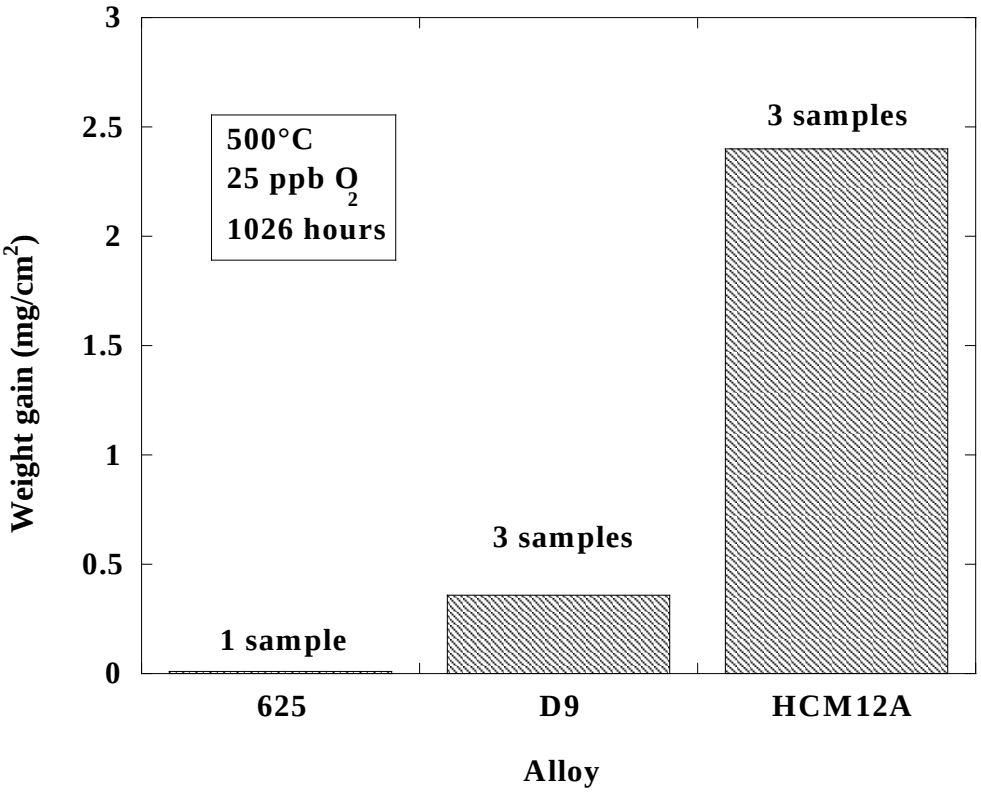

Figure 2.29 Oxidation rates of three alloy classes as represented by 625 (Ni-based alloy), D9 (austenitic alloy), and HCM12A (F-M alloy). The samples were tested in 500°C deaerated SCW (25 ppb O_2) for 1026 hours. [88]

BIBLIOGRAPHY

1. McCreey, G.E., et al. *The INEEL Heat Transfer Flow Loop for Development of Supercritical-Pressure Water Reactors (SCWRs).* in *GENES4/ANP2003*. 2003. Kyoto, Japan.
2. *Black smokers*. 1997 [cited 2010; Available from: http://www.amnh.org/nationalcenter/expeditions/blacksmokers/black_smokers.html.
3. *A Technology Roadmap for Generation IV Nuclear Energy Systems*. 2002 U.S. DOE Nuclear energy research advisory committee and the Generation IV international forum.
4. Haar, L., J.S. Gallagher, and G.S. Kell, *NBS/NRC Steam Tables: Thermodynamic and Transport Properties and Computer Programs for Vapor and Liquid States of Water in SI Units*. 1984, New York: Hemisphere Publishing Corporation.
5. Watanabe, Y., H. Abe, and Y. Daigo. *Environmetally Assisted Cracking of Sensitized Stainless Steel in Supercritical Water: Effects of the Physical Propery of Water*. in *GENES4/ANP2003*. 2003. Kyoto, Japan.
6. Macdonald, D.D. and L.B. Kriksunov, *Probing the Chemical and Electrochemical Properties of SCWO Systems.* Electrochimica Acta, 2001. **47**: p. 775-790.
7. Henrikson, J.T., *Water Density Effects on Supercritical Water Oxidation*, in *Chemical Engineering Department*. 2004, University of Michigan: Ann Arbor. p. 175.
8. Ikushima, Y. *Physical and chemical properties of supercritical water*. in *SCR-2000*. 2000. Tokyo.
9. Koda, S. *Chemical Reactions in Supercritical Water*. in *SCR-2000*. 2000. Tokyo, Japan.
10. Kritzer, P. *Corrosion in High-temperature and Supercritical Water and Aqeous Solutions: Influence of Solution and Material Parameters*. in *SCW-2000*. 2000. Tokyo, Japan.
11. McKinley, J., *Corrosion and Stress Corrosion Cracking of Austenitic Alloys in Supercritical Water*, in *Materials Science and Engineering Department*. 2004, University of Michigan: Ann Arbor. p. 272.
12. Uematsu, M. and E.U. Franck, *Static Dielectric Constant of Water and Steam.* Journal of Physical Chemistry Reference Data, 1980. **9**(4): p. 1291-1306.
13. Marshall, W.L. and E.U. Frank, *Ion Product of Water Substance, 0-1000^{o}C, 1-1000 bar: New International and Its Background.* Journal of Physical Chemistry Reference Data, 1981. **10**: p. 295.
14. Helgeson, H.C., K.D.H. Kirkham, and G.C. Flowers, *Theoretical Prediction of the Thermodynamic Behavior of Aqueous Electrolytes by High Pressures and Temperatures; IV, Calculation of activity coefficients, osmotic coefficients, and apparent molal and standard and relative partial molal properties to 600 degrees C and 5kb.* American Journal of Science, 1981. **281**: p. 1249.
15. Huang, S., et al., *Thermodynamic Analysis of Corrosion of Iron Alloys in Supercritical Water*, in *Supercritical Fluid Science and Technology*. 1989, ACS: Washington DC. p. 276.

16. Kriksunov, L.B. and D.D. Macdonald, *Corrosion in Supercritical Water Oxidation Systems: A phenomenological Analysis.* Journal of Electrochemical Society, 1995. **142**(12): p. 4069-4073.
17. Kriksunov, L.B. and D.D. Macdonald, *Potential-pH Diagrams for Iron in Supercritical Water.* Corrosion, 1997. **53**(8): p. 605-611.
18. Matsubayashi, N., C. Wakui, and M. Nakahara, *NMR Study of Water Structure in Super- and Supercritical Conditions.* Physical Review Letters, 1997. **78**: p. 2573.
19. Mizan, T.I., P.E. Savage, and R.M. Ziff, *Comparison of Rigid and Flexible Simple Point Charge Water Models at Supercritical Conditions.* Journal of Computational Chemistry, 1996. **17**(15): p. 1757-1770.
20. Mizan, T.I., P.E. Savage, and R.M. Ziff, *Fugacity Coeficientts for Free Radiacals in Dense Fluids: HO_2 in Supercritical Water.* An Official Publication of the American Institure of Chemical Engineerings (AIChE) Journal, 1997. **43**(5): p. 1287-1299.
21. Keutsch, F.N. and R.J. Saykally, *Water Clusters: Untangling the Mysteries of the Liquid, one molecule at a time.* Proceedings of the National Academy of Sciences of the United States of America, 2001. **98**(19): p. 10533-10540.
22. Masuyama, F., *History of Power Plants and Porgress in Heat Resistant Steels.* ISIJ International, 2001. **41**(6): p. 612-625.
23. Klueh, R.L. and D.R. Harries, *High chromium ferritic and martensitic steels for nuclear applications*. 2001, PA, U.S.A.: ASTM.
24. Masuyama, F., *New Developments in Steels for Power Generation Boilers*, in *Advanced Heat Resistance Steels for Power Generation*, R.V.a.J.W. Nutting, Editor. 1999, IOM Communications Ltd.: London. p. 33-48.
25. Foldyna, V., *Development of advanced high chromium ferritic steel*, in *Microstructural development and stability in high chromium ferritic power plant steels*, A.S.a.D.J. Gooch, Editor. 1997, The Inst. Of Materials: London. p. 73-92.
26. Klueh, R.L., *Elevated Temperature Ferritic and Martensitic Steels and Their Application to Future Nuclear Reactors.* International Materials Reviews, 2005. **50**(5): p. 287-310.
27. Sawagari, Y., et al. *Development of a High Strength 12Cr Steel (HCM12A).* in *The 1994 Conference on Materials for Advanced Power Engineering*. 1994. Liege, Belgium: Kluwer Academic Publisher.
28. Mukhopadhyay, D.K., F.H. Froes, and D.S. Gelles, *Development of Oxide Dispersive Strengthened Ferritic Steels for Fusion.* Journal of Nuclear Material, 1998. **258-263**: p. 1209-1215.
29. Ukai, S. and M. Fujiwara, *Perspective of ODS Alloys Application in Nuclear Environments* Journal of Nuclear Materials, 2002. **307-311**(1): p. 749-757.
30. Ukai, S., et al., *Alloying Design of Oxide Dispersion Strengthened Ferritic Steel for Long Life FBRs Core Materials* Journal of Nuclear Materials, 1993. **204**: p. 65-73.
31. Ukai, S., et al., *R&D of Oxide Dispersion Strengthened Ferritic Martensitic Steels for FBR* Journal of Nuclear Materials, 1998. **258-263**(2): p. 1745-1749.
32. Tofaute, W., A. Sponheuer, and H. Bennek, Archiv fur Eisenhuttenwesen, 1935. **8**: p. 499.

33. Irvine, K.J., D.J. Crowe, and F.B. Pockering, Journal of Iron and Steel Research International, 1960. **195**: p. 386.
34. Wardle, K.E. and J.I. Cole, *Evaluation of Materials for Advanced Nuclear Reactors.* U.S. Department of Energy Journal of Undergraduate Research, 2003. **3**.
35. Viswanathan, R. and W.T. Bakker. in *2000 International Joint Power Generation Conference*. 2000. Florida, U.S.A.
36. Hättestrand, M., M. Schwind, and H.O. Andrén, *Microanalysis of 9-12% chromium steels P92 and P122*, in *Advanced Heat Resistance Steels for Power Generation*, R.V.a.J.W. Nutting, Editor. 1999, IOM Communications Ltd.: London. p. 199-211.
37. Pickering, F.B., *Historical development and microstructure of high temperature applications*, in *Microstructural development and stability in high chromium ferritic power plant steels*, A.S.a.D.J. Gooch, Editor. 1997, The Inst. Of Materials: London. p. 1-29.
38. Gupta, G., *Role of a Thermo-Mechanical Treatment on the Subgrain Boundary Density and on Creep Behavior of Ferritic-Martensitic Alloy T91*, in *Materials Science and Engineering*. 2007, University of Michigan: Ann Arbor, MI.
39. Hald, J. *Microstructure and Long-Term Creep Properties of 9-12%Cr Steels*. in *ECCC Creep Conference*. 2005. London, U.K.
40. Lu, Z., et al., *Irradiation-induced Grain Boundary Chromium Microchemistry in High Alloy Ferritic Steels.* Scripta Materialia, 2008. **58**: p. 878-881.
41. Takahashi, H., et al., *The Effect of Irradiation and Post-irradiation Annealing on the Yield Stress and Microstructure of Vanadium-carbon Alloys* Journal of Nuclear Materials, 1981. **96**(3): p. 233-242.
42. Neklyudov, I.M. and V.N. Voyevodin, *Features of Structure-phase Transformations and Segregation Processes under Irradiation of Austenitic and Ferritic-martensitic Steels.* Journal of Nuclear Materials, 2003. **212-215**(1): p. 39-44.
43. G. Gupta, et al., *Microstructural evolution of proton irradiated T91*. Journal of Nuclear Materials, 2006. **351**(1-3): p. 162-173.
44. *ASM Handbook* in *Vol. 13A Corrosion: Fundamentals, Testing, and Protection*. 2003, ASM International: Ohio.
45. Birks, N., G.H. Meier, and F.S. Pettit, *Introduction to the High-temperature Oxidation of Metals*. 2nd ed. 2006, New York: Cambride University Press.
46. Jones, D.A., *Principles and Prevention of Corrosion*. 2nd ed. 1996, New Jersey: Prentice-Hll, Inc.
47. Khanna, A.S., *High temperature oxidation and corrosion*. 2002, U.S.A.: ASM International.
48. Kofstad, P., *High Temperature Corrosion*. 1988, London and New York: Elsevier Applied Science.
49. Young, D.J., *High Temperature Oxidation and Corrosion of Metals*. 2008, Great Britain: Elsevier Ltd.
50. *Ellingham diagram*. 2009 [cited 2009; Available from: http://commons.wikimedia.org/wiki/File:Ellingham-diagram-greek.svg.

51. Chen, R.Y. and W.Y.D. Yuen, *Review of the High-temperature Oxidation of Iron and Carbon Steels in Air or Oxygen.* Oxidation of Metals, 2003. **59**(5/6): p. 443-468.
52. Tammann, G., *Über Anlauffarben von Metallen.* Zeitschrift fur Anorganische und Allgemeine Chemie, 1920. **111**: p. 78-89.
53. Fry, A., S. Osgerby, and M. Wright, *Oxidation of alloys in steam environments - Review*, in *NPL Report* 1990.
54. Tsai, S.C., A.M. Huntz, and C. Dolin, *Growth Mechanism of Cr2O3 Scales: Oxygen and chromium diffusion, oxidation kinetics and effect of yttrium.* Materials Science and Engineering, 1996. **A212**: p. 6-13.
55. Kofstad, P., *Defects and transport properties of metal oxides.* Oxidation of Metals, 1995. **44**(1-2): p. 3-27.
56. Sánchez, L., M.P. Hierro, and F.J. Pérez1, *Effect of Chromium Content on the Oxidation Behaviour of Ferritic Steels for Applications in Steam Atmospheres at High Temperatures.* Oxidation of Metals, 2009. **71**(3-4): p. 173-186.
57. Newcomb, S.B., W.M. Stobbs, and E. Metacalfe, *A Microstructural Study of the Oxidation of Fe-Ni-Cr Alloys I. Protective Oxide Growth.* Philosophical Transaction of the Royal Society of London. Series A, Mathematical and Physical Sciences, 1986. **319**(1546): p. 191-218.
58. Newcomb, S.B., W.M. Stobbs, and E. Metacalfe, *A Microstructural Study of the Oxidation of Fe-Ni-Cr Alloys II. Non-protective Oxide Growth.* Philosophical Transaction of the Royal Society of London. Series A, Mathematical and Physical Sciences, 1986. **319**(1546): p. 219-247.
59. Greef, A.P., C.W. Louw, and H.C. Swart, *The Oxidation of Industrial FeCrMo Steel.* Corrosion Science, 2000. **42**: p. 1725-1740.
60. Laverde, D., T. Gómez-Acebo, and F. Castro, *Continuous and Cyclic Oxidation of T91 Ferritic Steel Under Steam.* Corrosion Science, 2004. **46**: p. 613-631.
61. Komai, N., F. Masuyama, and M. Igarashi, *10-year Experience with T23 (2.25Cr-1.6W) and T122 (12Cr-0.4Mo-2W) in a Power Boiler.* Transactions of the American Society of Mechanical Engineers, 2005. **127**: p. 190-196.
62. Zurek, J., et al., *Effect of Alloying Additions in Ferritic 9-12%Cr Steels on the Temperature Dependence of the Steam Oxidation Resistance.* Materials Science Forum, 2004. **461-464**: p. 791-798.
63. Żurek, J., et al., *Anomalous Temperature Dependence of Oxidation Kinetics during Steam Oxidation of Ferritic Steels in the Temperature range 550–650°C.* Corrosion Science, 2004. **46**(9): p. 2301-2317.
64. Wang, G., B. Gleeson, and D.L. Douglass, *A Diffusional Analysis of the Oxidation of Binary Multiphase Alloys.* Oxidation of Metals, 1991. **35**: p. 333-348.
65. Durham, R.N., B. Gleeson, and D.J. Young, *Factors Affecting Chromium Carbide Precipitate Dissolution During Alloy Oxidation.* Oxidation of Metals, 1998. **50**: p. 139-165.
66. Mongomery, M. and A. Karlsson, *Survey of Oxidation in Steamside Conditions.* VGB Kraftwerkstechnik 1995. **75**: p. 235-240.

67. Lepingle, V., et al., *Steam Oxidation Resistance of New 12%Cr Steels: Comparison with some other ferritic steels.* Corrosion Science, 2008. **50**(4): p. 1011-1019.
68. Abe, F., et al. *R&D of Advanced Ferritic Steel of 650^{o}C USC Boilers*. in *The 5th International Charles Parsons Turbine Conference*. 2000: IOM Communications Ltd.
69. Hurst, P. and H.C. Cowen. *The Oxidation of 9Cr-Mo and Other Steels in 6.9 MN/m^{2} Steam at 748 and 823K*. in *International Conference on Ferritic Steels for Fast Reactor Steam Generators*. 1977. London: British Nuclear Energy Society.
70. Chen, Y., et al., *Microstructural examination of oxide layers formed on an oxide dispersion strengthened ferritic steel exposed to supercritical water.* Journal of Nuclear Materials, 2006. **359**(1-2): p. 50-58.
71. Peraldi, R. and B.A. Pint, *Effect of Cr and Ni Contents on the Oxidation Behavior of Ferritic and Austenitic Model Alloys in Air with Water Vapor.* Oxidation of Metals, 2004. **61**(516): p. 463-483.
72. Raman, R.K.S., et al., *Influence of grain size on the oxidation resistance of 2 1/4 Cr-1Mo steel* Oxidation of Metals, 1992. **37**(1-2): p. 1-12.
73. TrindadeI, V.B., et al., *High-Temperature Oxidation of Pure Fe and the Ferritic Steel 2.25Cr1Mo.* Materials Research, 2005. **8**(4): p. 365-369.
74. Vélez, S.B., *Oxidation Kinetics and Mechanisms in HT-9 Ferritic/martensitic Stainless Steel*, in *Materials Science and Engineering*. 2005, University of Florida. p. 134.
75. Yi, Y.-S., et al., *Oxidation Rate of Advanced Heat-Resistant Steels for Ultra-Supercritical Boilers in Pressurized Superheated Steam.* Journal of Pressure Vessel Technology, 2001. **123**(3): p. 391-397.
76. Essuman, E., et al., *The Effect of Water Vapor on Selective Oxidation of Fe-Cr Alloys.* Oxidation of Metals, 2008. **69**: p. 143-162.
77. Ehlers, J., et al., *Enhanced Oxidation of the 9%Cr Steel P91 in Water Vapour Containing Environments.* Corrosion Science, 2006. **48**(11): p. 3428-3454
78. Bertrand, N., et al., *Iron Oxidation at Low Temperature (260–500°C) in Air and the Effect of Water Vapor* Oxidation of Metals, 2010. **73**(1-2): p. 139-162.
79. Opila, E.J., *Volatility of Common Protective Oxides in High-Temperature Water Vapor: Current Understanding and Unanswered Questions.* Materials Science Forum, 2004. **461-464**: p. 765-774.
80. Zhang, L., F. Zhu, and R. Tang, *Corrosion Mechanisms of Candidate Structural Materials for Supercritical Water-cooled Reactor.* Frontier Energy Power Engineering China, 2009. **3**(2): p. 233-240.
81. Surman, P.L., *The Oxidation of Iron at Controlled Oxygen Partial Pressures: I-Hydrogen/Water Vapour.* Corrosion Science, 1973. **13**(113).
82. Surman, P.L. and J.E. Castle, *Gas Phase Transport in the Oxidation of Fe and Steel.* Corrosion Science, 1969. **9**: p. 771.
83. Wambach, J., A. Wokaun, and A. Hiltpold, *Oxidation of Stainless Steel under Dry and Aqueous Conditions: oxidation behavior and composition* Surface and Interface Analysis, 2002. **34**: p. 164-170.

84. Motta, A.T., et al., *Zirconium alloys for supercritical water reactor applications: Challenges and possibilities.* Journal of Nuclear Materials, 2007. **371**(1-3): p. 61-75.
85. Peng, Q., et al., *Corrosion Behavior of Model Zirconium Alloys in Deaerated Supercritical Water at 500°C.* Corrosion, 2007. **63**(6): p. 577-590.
86. Was, G.S. and S. Teysseyre, *Corrosion of Austenitic Alloys in Supercritical Water.* Corrosion, 2006. **62**(11): p. 989-1005.
87. Tan, L., K. Sridharan, and T.R. Allen, *The effect of grain boundary engineering on the oxidation behavior of INCOLOY alloy 800H in supercritical water.* Journal of Nuclear Materials, 2006. **348**(3): p. 263-271.
88. Was, G.S. and T.R. Allen. *Time, Temperature, and Dissolved Oxygen Dependence of Oxidation of Austenitic and Ferritic-martensitic Alloys in Supercritical Water*. in *ICAPP'05*. 2005. Seoul, Korea.
89. Allen, T.R., et al. *Corrosion of Ferritic-Martenistic Alloys in Supercritical Water for GenIV Application*. in *GLOBAL 2005*. 2005. Tsukuba, Japan.
90. Ampornrat, P. and G.S. Was, *Oxidation of Ferritic-martensitic Alloys T91, HCM12A and HT-9 in Supercritical Water.* Journal of Nuclear Materials, 2007. **371**(1-3): p. 1-17.
91. Motta, A.T., et al. *Microbeam Synchrotron Radiation Diffraction and Fluorescence Study of Oxide Layers Formed on 9Cr ODS Steel in Supercritical Water*. in *13th International Conference on Environmental Degradation of Materials in Nuclear Power Systems*. 2007. Whistler, British Columbia.
92. Watanabe, Y. and Y. Diago, *Corrosion Rate and Oxide Scale Characteristics of Austenitic Alloys in Supercritical Water.* Materials Science Forum, 2006. **522-523**: p. 213-220.
93. Dooley, B., et al. *Oxygenated Treatment for Fossil Plants*. in *Proceedings of the International Water Conference*. 1992: Engineers Society of Western Pennsylvavia.
94. Tan, L., Y. Yang, and T.R. Allen, *Porosity prediction in supercritical water exposed ferritic/martensitic steel HCM12A.* Corrosion Science, 2006. **48**(12): p. 4234.

CHAPTER 3

EXPERIMENT

In order to understand mechanisms of the oxidation of F-M alloys in SCW, a series of exposure experiment in SCW were conducted under a temperature range of 400 - 600°C with variations of time and dissolved oxygen concentration. Three conventional F-M alloys, T91, HCM12A, and HT-9, containing different Cr concentration between 9-12% were studied. Another advanced F-M alloy, 9Cr Oxide Dispersive Strengthening (ODS) was also studied at a temperature of 600°C. Following the exposure experiments, samples were analyzed with analysis techniques including Scanning Electron Microscope (SEM), Energy Dispersive Spectrometry (EDS), X-Ray Diffraction (XRD), and Transmission Electron Microscopy (TEM) in order to characterize morphology, phase and composition of oxide scales. This chapter will describe the materials, methodology of the experiments, and analysis procedure that had been used in this thesis.

3.1 Alloy Composition and Process Condition

Three types of F-M alloys, T91, HCM12A, and HT-9, were evaluated in this study. A major difference in these alloys is Cr concentration; T91 contains lower Cr content than HT-9 and HCM12A. In addition, a 9Cr-ODS alloy was also included in a test at temperature 600°C deaerated SCW. Alloys T91 and HT-9 were produced by

American alloy steel, Inc. Alloy HCM12A and 9Cr-ODS were produced in Japan by Sumitomo metal industries, LTD. and Japan nuclear cycle development, respectively. A summary of alloy composition in weight percent is presented in Table 3.1. The first alloy is T91 with a nominal composition of 9Cr-1MoVNb contains 8.37% Cr and major alloying elements of Mo (0.90%), V (0.22%), and Nb (0.08%). The second alloy is HCM12A (11Cr-0.5Mo-2WVNbCu) that contains 10.83% Cr and alloying elements Mo (0.30%), V (0.19%), Nb (0.05%), W (1.89%) with additional of Cu (1.02%). Alloy HT-9 (12Cr-1MoVW) contains the highest Cr among these F-M alloys has composition of 11.63%Cr and Mo (1.00%), V (0.30%), and W (0.52%). A 9Cr-ODS alloy (9Cr-2WTi-0.35Y_2O_3) contains 8.64% Cr with alloying elements of W (1.96%) and Ti (0.02%), and 0.35% of Y_2O_3. In addition to the mentioned alloying elements, Mn (~0.5%), Ni (0.21-0.50%), Si (~0.2%), and C (0.10-0.20%) are also included in these F-M alloys.

All of the F-M alloys were prepared with heat treatments consisted of annealing and tempering. Annealing was performed to austenitize the microstructure and to dissolve the carbides. After annealing, the tempering treatment was done to relieve the stress and enhance toughness. Temperature and time for the tempering and annealing were designed to achieve an optimum microstructure for F-M alloys. The heat treatments of each alloy are shown in Table 3.2. Alloy T91 was annealed at 1066°C for 46 minutes (air cooled) followed by tempering at 790°C for 42 minutes (air cooled). Alloy HCM12A was annealed at 1050°C for 60 minutes (air cooled) and tempered at 770°C for 45 minutes (air cooled). Alloy HT-9 was annealed at 1040°C for 30 minutes (air cooled) and tempered at 760°C for 60 minutes (air cooled). 9Cr-ODS alloy was annealed at 1050°C for 60 minutes and tempering at 800°C for 60 minutes (air cooled).

The typical microstructure of tempered F-M alloys, as described in Chapter 2, consisted of prior austenite grains (PAG). Each PAG contains several equiaxed subgrain packets that have martensite laths align in the same direction. Figure 3.1-Figure 3.4 present SEM images of microstructure of F-M alloys T91, HCM12A, HT-9, and 9Cr-ODS. The PAG sizes of T91, HCM12A, HT-9, and 9Cr-ODS are 9, 13.5, 50, and 10 μm, respectively. The lath size was about 0.2-0.5 μm by 2-5 μm for all four alloys. Precipitate particles decorate the PAG, packet, and lath boundaries. Major type of precipitate is Cr-rich $M_{23}C_6$ (M is Cr, Fe), which are located mainly on PAG and lath boundaries, and occasionally inside the lath matrix. Fine particles of minor alloying elements precipitate at similar locations as $M_{23}C_6$, and these particles are different in each alloy. A list of precipitates found in each alloy is shown in Chapter 2.

3.2 Sample Preparation for Exposure Experiments

After heat treatment the material ingots were machined by Electric Discharge Machining (EDM) with the sample axis aligned along the rolling direction. The specimens were cut ~0.5 mm depth from each surface to avoid oxidized surface. The corrosion coupons were cut into 20 mm × 10 mm × 1 mm as shown in Figure 3.5. A hole with 2 mm diameter was made at one end of the sample for suspending in the autoclave.

Corrosion coupons were mechanically polished using Struers® SiC papers. The coupon was first bonded on a polishing block by melted crystalbond™. The coupon was carefully wet polished from a starting grit of FEPA (European manufacturers of abrasive products standard) P320 (US grit 280), P500 (US grit 360), P800 (US grit 400), P1200

(US grit 600), P2400 (US grit 800), and a final grit of P4000 (US grit 1200), which have SiC particle size varied from ~46 μm to ~5 μm. After each polishing step of SiC grit, the sample was visually inspected to ensure that the scratches from the previous grit SiC had been removed. The polishing removed ~50-100 μm of material from surface to avoid the damaged and oxidized layer from EDM process. The final polished surface appeared smooth and scratch free. After final polishing on one side, the coupon was turn over to another side and was polished by a similar process. The sample was cleaned in acetone to remove the wax, followed by ultrasonic cleaning with methanol, and final rinsing with distilled water.

Dimension and weight of polished corrosion coupons were measured prior loading into the autoclave. Dimension was measured by a micrometer with 1.0 μm precision. Each coupon length and width was measured on two positions as shown in Figure 3.6 (a). The thickness was measure at seven positions on the coupons in order to obtain an accurate measurement in case the surface was not even, Figure 3.6 (b). Width, length, and thickness were averaged from the measurements. Surface area was calculated from width x length x thickness. Table 3.3 presents dimension and surface area of corrosion coupons tested in each experiment.

Weight of the corrosion coupon was measured right before each experiment with a Mettler® micro balance to five digits accuracy (in grams). To start the measurement, a piece of weighing paper was placed on the weighing paper in the scale chamber, and the tare weight was measured. After recording the measurement, the coupon was removed from the chamber. The coupon was re-measured with the same procedure twice. Weight of each coupon reported in Table 3.3 is an average from the three measurements.

3.3 Supercritical Water Test Facilities

The exposure tests were performed in two SCW systems; a single SCW and a multi-sample SCW system in High Temperature Corrosion Laboratory (HTCL) at the University of Michigan. Both systems were built for two specific purposes; i) conduct exposure tests for oxidation study, and ii) conduct constant extension rate tensile tests for stress corrosion cracking study. The single SCW system has a two liter autoclave that can test one tensile specimen and up to eight corrosion coupons. The multi-sample SCW system was designed to test four tensile specimens and up to ten corrosion coupons in a four liter autoclave. Inside the autoclave, tensile specimens can be strained at the same time as corrosion coupons are being exposed. Most of the exposure tests in this thesis were conducted in the multi-sample SCW system, so the following description (unless otherwise stated) will refer to the multi-sample SCW system.

The SCW systems were designed to perform experiments under SCW environment by feeding water from solution make up columns to a pre-heater and to an autoclave, and control temperature and pressure to the SCW condition. A schematic diagram and a picture of the multi-sample SCW system are shown in Figure 3.7, and Figure 3.8. Table 3.4 presents the summary of the specification for the main components of the facility. The test facility is composed of four major sub-systems;

1. Solution makeup system,
2. Preheater and solution feed system,
3. Autoclave,
4. Heat exchanger and cooling system.

In solution makeup system the solution was prepared in two glass columns; one was a main water column and another was a mixing column. Distilled water from an external distillation unit was filled in the mixing column. The water was deionized by circulating through an ion exchange resin with a recirculation pump attached to the column. The test water was deionized for 5-10 hours before transferred with a high pressure pump to the main column, which also has the ion exchanger and recirculation pump attached. The circulation through the ion exchanger ran continuously for both columns. To ensure high purity of the test water, conductivity of the water in main column was monitored at the column outlet throughout experiment. Conductivity of makeup water was controlled at 0.055 ± 0.01 μS/cm (~18.2 MΩ), which is the conductivity of ultra-pure water (deionized water). The Dissolved Oxygen (DO) concentration was controlled by bubbling either pure argon gas (99.99%) for deaeration or a mixture of argon and oxygen into water in the columns. In deaerated condition experiments, the argon gas was purged for ~10 hours before dissolved oxygen went below 10 ppb, which was ready for the test. For controlled oxygen experiment, the ratio of argon and oxygen gas was determined in order to produce 100 and 300 ppb DO concentration, which will be described in section 3.4.4.

The solution feeding system was mainly composed of a water chemistry monitoring system (conductivity and DO sensors), a high-pressure pump and a preheater. The specification of the high-pressure pump and water chemistry monitoring system is described in Table 3.4. Conductivity was measured with Thornton 200CR® conductivity/resistivity sensor. The sensor can measure conductivity in a range of 0.02-600 μS/cm with accuracy of ±1% of reading. DO concentration was measured with

Thornton 367 DO sensor® that has an operating range of 0-10,000 ppb, accuracy 1 ppb within flow rate of 50-2,000 ml/min. Both conductivity and DO sensors were install at outlet of the main water column to monitor the water chemistry before feeding to preheater and test vessel. In addition, another conductivity sensor was installed at outlet of the test vessel to measure the outlet conductivity. DO measurement can be adjusted to measure either inlet or outlet water of test vessel by switching a valve of circulation tube.

The high pressure pump is a major component of solution feeding system. The pump should operate smoothly throughout the experiment. If the pump fails during experiment, it can cause the pressure drop that leads to water phase change to sub-critical region. This will cause damages to test vessel and the experiment. Therefore the pump must be checked and maintained before each experiment. The high pressure pump selected to use in the SCW systems is a dual piston HPLC pump, model Prep 100™ made by Chrom Tech®, Inc. The pump can be operated to a maximum pressure of 27.6 MPa (4,000 psi) with a flow rate range of 0.01-100 ml/min. The dual piston pump has an advantage in low pulsation (±4% at 50 ml/min) that could give continuous pumping across the flow range. The pump required a pair of 2 μm water filters at its inlet, which were installed between the sensors and the pump.

Water from the make up column was pumped through conductivity and DO sensors. If the conductivity and DO reached desired values, the water was fed to heat exchanger then to preheater. Otherwise the water was fed back to the main column through bypass loop and was recirculated until reaching the desired values. After that the water was pumped to the heat exchanger and transferred heat from autoclave outlet water.

Normally the temperature of water at the heat exchanger outlet was ~100 ± 30°C depended on vessel outlet temperature and flow rate.

The preheater considered as a direct contact heater consisted of quartz heating cords that wrapped around water tube and a temperature control unit. The heat generated by the heating cords transferred through tube wall (0.035 inches thick and 0.25 inches outer diameter) to flowing water. Therefore heating by this method depends on two major parameters; water flow rate and specific heat capacity of water (which depends on its temperature). If the flow rate was too high (> 75 ml/min), very high heat was required to increase the water temperature. Thus the heating cords would run continuously, and this could cause failure of the heating cords or the tube. Therefore the optimum flow rate was limited at 50 ± 20 ml/min, which depended on the heat exchanger outlet temperature and the setting temperature.

The autoclave of the multi-sample SCW system was designed to operate at pressure 30 MPa at 600°C (4350 psi) for safety reason. The vessel made of alloy 625 has inside dimension of 5 inches diameter and 12.5 inches high, 1 inch thick wall, and volume 4 liters. It was installed in the inverted position (head at the bottom) on a load frame as briefly represented in Figure 3.9. An inverted geometry has the advantage that the high-pressure fittings and uniform distribution of heat inside the vessel. Both inlet and outlet lines are poses at the bottom of the vessel. Inlet water was brought to upper 1/3 of the vessel through an inlet tube in order to ensure that the water inside was refreshed during experiment. Inside the vessel corrosion coupon sample trees are attached to four support rods located at the center of the vessel, Figure 3.9. (Description of sample loading will be in section 3.4.1.) Three heater bands (1250 W, 480 V Watlow™) were

placed at outer surface of the vessel. These three bands are the main heater that controlled and regulated the water temperature. In case the preheater outlet temperature was low, the main heater would ensure to heat up to the test temperature.

The cooling system consisted of a heat exchanger and a cooling line. The heat exchanger is a helically wound concentric tube (also called parallel-flow or tube-in-tube heat exchanger) made from Inconel® alloy. Outlet water (from vessel) flew in an inner tube (0.25 inches outer diameter) and inlet water (from makeup column) flew in an outer tube (0.50 inches outer diameter) in opposite direction, thus heat from the outlet water transferred to the inlet water. The design has benefits in cooling down the outlet water and pre-heat the inlet water. Length of heat exchanger is ~20.5 feet (614 cm). After heat exchanger, water flew through a cooling line, which is also a concentric tube. Building water was used as coolant at this line. The cooled water was circulated back to the makeup column passing through two of 5 μm filters to eliminate some corrosion products from the test vessel. In order to control pressure of the system, a back pressure regulator was installed at outlet between the cooling line and the water makeup column. The back pressure regulator was adjusted to a desired pressure when performing an experiment. As a result high pressure part begins from the high pressure pump to the back pressure regulator. The rest of the system remained in low pressure.

In summary the process and circulation of water in the SCW system consisted of; 1) conditioning the purified water in solution make up columns to deionize and control DO concentration of inlet water, 2) feeding water to the heat exchanger and the preheater by a high pressure pump (high pressure part started from this section), 3) preheating water flow into the test vessel and its temperature was controlled by the main heater, 4)

cooling outlet water from test vessel by a heat exchanger and a cooling tube, and 5) water was filtered (high pressure part ended at a back pressure regulator) and circulated back to the makeup column.

3.4 Exposure Experiments and Test Conditions

3.4.1. Sample Installation in Autoclave

The samples that had been prepared and measured dimension and weight were ready for loading in the test vessel. Before loading, a wire of Ni-base alloy 600 covered by a zirconia ceramic insulator tube (2 mm outer diameter) was inserted into the 2 mm hole on corrosion coupon. The reason of using the zirconia insulator between the Ni wire and the sample is to avoid galvanic effects. The samples were suspended with the Ni wire on four support rods that that located at center of the vessel, Figure 3.9.

3.4.2. Operation of SCW Systems

After samples were loaded, the vessel was closed and tightened with high torque ~120-200 ft-lbs. Pure Ar gas was purged through an inlet line and was vented at an open valve behind the cooling unit in order to reduce oxygen (or air) concentration in the system. Water was pumped to fill the vessel. After the vessel filled, the system was pressurized by ~0.69-1.4 MPa (100-200 psi) increment steps with a back pressure regulator. Water in the system was running at high pressure (24.1 MPa) for ~5-10 hours to ensure that the autoclave was sealed at high pressure, and the water chemistries were at desired level.

Once the system was pressurized and water condition was suitable, water was heated up by two heating units of preheater and main heater simultaneously. Temperature was monitored at five positions; heat exchanger outlet, preheater, vessel inlet line (preheater outlet), main heater, and inside vessel, using K type thermocouples. First both heaters were set to 100°C. When the temperature inside the vessel reached the set temperature, the set temperature was increased by a 100°C increment. Average time to heat up from room temperature to 300°C was ~1 hour. From 300°C to the target temperature, the temperature was carefully increased by 50°C increment in order to control the system during the phase change. At critical temperature (~374°C), the system pressure slightly increased and recovered after temperature was higher than the critical point. An example of temperature and pressure of the SCW system during an experiment at 500°C deaerated SCW for 10 hours is shown in Figure 3.10. Time to heat up to the target temperature was approximately 2 hours.

During exposure, the temperature inside the autoclave was controlled to within ± 2-10^{o}C (regular 2-5°C) of the target temperature. The autoclave was covered with a thermal insulation blanket made from type E fiberglass. The pressure was maintained at 24.1 ± 0.7 MPa (3,500 ± 100 psi).

After the experiment completed, the system was cooled down with similar process as the heat up. The temperature was decreased by 50°C steps from the test temperature to ~300°C and by 100°C from 300°C to room temperature. It was noticed that at critical point, the system pressure dropped dramatically and recovered after temperature was lower than the critical point, Figure 3.10. The insulation blanket was taken off from the vessel. Time to cool the system down to room temperature was approximately 2 hours.

The water was drained out from the vessel by purging Ar gas through an inlet line and drained at an open valve behind the cooling unit.

3.4.3. Water Chemistry

In deaerated SCW experiments, the DO concentration was controlled by bubbling pure argon gas (99.99%) into water in the makeup columns as described in section 3.3. The inlet DO concentration was controlled at <10 ppb for the deaerated condition. For controlled oxygen experiments, mixed gas of oxygen and argon was purged into the water. In the 100 ppb DO test, Ar and O_2 were mixed manually and purged into the mixing column of the single-sample SCW system. Mixture of 1.2174% oxygen balanced argon gas was used to produce 300 ppb DO concentration in the 300 ppb test in multi-sample SCW system. The DO concentrations were controlled within 100 ± 10 and 300 ± 50 ppb during the experiments. Figure 3.11 and Figure 3.12 present the DO concentration during the experiments 400, 500 and 600°C deaerated SCW, and a test at 500°C containing 300 ppb DO. (Since the 100 ppb test conducted in the single-sample SCW system, the data was not recorded.)

The inlet conductivity was controlled at approximately 0.06 μS/cm, as described in Section 3.3. However, the outlet conductivity was higher than the inlet conductivity due to corrosion products from the samples. The changes in conductivity depended on temperature and duration of the experiment, which can be divided into four regimes. First, during the heat up process the outlet conductivity increased rapidly as a result of oxidation activities inside the system. When the system reached a target temperature, the conductivity rapidly increased then dropped to a lower value and became stable after ~24

hours. It is believed that the oxidation rate reduced after protective oxide formed. Finally the conductivity decreased as a function of temperature at the cooling stage. Figure 3.11 and Figure 3.12 also present the inlet and outlet conductivities from tests in 400, 500 and 600°C deaerated SCW, and a test at 500°C containing 300 ppb DO. Note that in the test at 500°C deaerated SCW (Figure 3.11b), the outlet conductivity was high because the system was being tested for the first time. The outlet conductivities reported in Table 3.5 is the average from starting of heat up to cooling the system.

3.4.4. Experimental Conditions

In order to understand the oxidation mechanisms of F-M alloys in SCW environment, series of exposure experiment were conducted. Effects of SCW temperature, exposure time, and DO concentration were studied. The study was focused on SCW temperature ranging from 400 to 600^{o}C, which is in a range of nominal operation temperature in SCWR. Oxidation behavior as a function of exposure time was evaluated from short (10 hours) to long exposure time (~500 hours) at 400 and 500°C deaerated SCW. Due to limit of the SCW system, the effect of exposure time at 600°C had not been studied. The exposure time for temperature effect study was ~200 hours. Effect of DO concentration in SCW was studied at an intermediate level (<10, 100 and 300 ppb) at temperature 500^{o}C and exposure time ~200 hours. The summary of experiment condition is given in Table 3.5.

3.5 Oxidation Rate Measurements

Weight of corrosion coupons were measured right after the experiments. The coupons were rinsed by distilled water to remove some deposits, and were suspended in air until they were dry. The measurement followed the similar process as that of pre-oxidation. Weight of each coupon after oxidation was an average from three measurements. Weight gain was calculated from difference between pre-oxidation and post-oxidation weights. Weight gain per surface area was calculated from weight gain divided by surface area of the corrosion coupon.

Aside from the weight gain, oxidation rate was determined from oxide thickness. Cross section of corrosion coupons for SEM investigation was prepared followed procedure in Section 3.6.1. The thickness of oxides formed on corrosion coupons were measured in SEM using 20 kV, spot size 40 and Back-Scattered Electrons (BSE) mode. Thicknesses of outer and inner oxides were measured using Scandium® software and were averaged from 10 measurements on different areas. Since transition layer formed in 400 and 500°C SCW are not distinctive from alloy substrate, thickness of this layer was determined in EDS line scan (step size ~0.02 μm, four measurements). The thickness was determined over the points at which the oxygen concentration dropped from the inner oxide level to the background level and the iron concentration increased to alloy substrate. However, the transition layer formed at 600°C SCW is distinct from the alloy and inner oxide. The thicknesses at this temperature were measured from BSE images in addition to determined from EDS line scan. Data reported in Chapter 4 are average of the measurements.

In order to compare results from experiments with different exposure times, the weight gains and oxide thicknesses were normalized to 190 hours using the exponential relations obtained from the time-dependent experiments and fit to the following equation:

$$w^{m_w} = k'_w t \text{ , or } w = k_w t^{n_w} \quad \text{(2.10-2.11)}$$

and,

$$h^{m_h} = k'_h t \text{ , or } h = k_h t^{n_h} \quad \text{(2.8-2.9)}$$

where w is the weight gain (mg/dm^2), h is the oxide thickness of each layer (μm), k'_w and k'_h are oxidation rate constant determined from weight gain (mg/dm^2/hr) and oxide thickness (μm/h) by $k' = k^{1/m}$, t is the time (hours), and n_w and n_h are the exponent on weight gain and thickness ($n=1/m$).

The parameters k'_w and n were determined for each alloy for the exposure in 400°C and 500°C deaerated SCW. The values obtained from 500°C deaerated SCW were used for the normalization of experiments in 500°C SCW containing 100 and 300 ppb DO. The normalization was not applied for an experiment at 600°C because the time-dependence of oxidation rate at was not determined at this temperature. Instead, weight gain at 400 and 500°C were normalized to 190 hours, which matches with the exposure time of 600°C experiment. For the oxide thickness, the exponent used for normalization was 0.40 for both outer and inner oxide layers. The thickness of the transition layer was normalized with the exponent of 0.20.

3.6 Sample Preparation for Characterizations

In order to characterize the oxidation products, corrosion coupons were cut into three parts for surface and cross-section analyses with SEM and TEM. First part was used

for surface oxide analysis by XRD and SEM. There is no special requirement for sample preparation for the surface analysis. Second part was prepared for cross section SEM specimen. Since the oxide layer thicknesses are small compare to analysis resolution of SEM, further characterizations were conducted with TEM. The last part of corrosion coupon was used for cross section TEM specimen.

3.6.1. Cross-sectional SEM Sample Preparation

Cross section SEM specimen was prepared from a part of corrosion coupon with dimension 5 mm x 10 mm. The sample was mounted on edge in conductive filler resin. The ratio (by weight) of epoxy to hardener is 5:1, and was mixed with conductive filler equals to total weight of the mixture. The mixture was poured onto a vertically clipped sample in a 1-inch diameter plastic mold. Air bubbles were pumped out of resin mixture by a vacuum pump to maintain good contact between sample and resin. Hardening time for the epoxy resin was ~10 hours. After the resin settled, sample was polished with SiC paper started with grit P800, P1200, P2400, and P4000 followed by diamond suspension 3, 1, and 0.25 μm. The sample was polished parallel to surface and interface of oxide layers in order to avoid preferential polishing on one side of the coupon. In addition, the sample should be polished gently to avoid damages in oxide grains. A finished cross section sample should have few scratches, oxide grains maintained on the layer, and oxide thicknesses from both side of the coupon are similar.

3.6.2. Cross-sectional TEM Sample Preparation by Focused Ion Beam

Cross section TEM specimens were prepared by mechanical polishing followed by Focused Ion Beam (FIB) cutting. The sample preparation cannot be done by the

conventional methods using a) electropolishing and ion milling (Ar beam with energy 2-5 kV) or b) jet thinning with acid solution by the following reasons;

- Different sputtering rates of oxides and alloy substrate when using ion milling with Ar beam. The sputtering rate of oxides is higher than that of alloy so that the oxide totally removed before the alloy substrate got thinned.
- Different in electrical conductivity of oxides and alloy substrate when using jet thinning technique. The alloy substrate is more conductive than oxides so that the thin area was created only in alloy. This technique also cannot locate a specific thin area, for example, at the interface of oxides and alloy.

Therefore the sample preparation by FIB was selected in this study. The FIB technique gave a better result than the conventional methods because it can produce a large uniform thin area of both scale and alloy substrate, can locate the specific area of interest and also minimizes damage from mechanical polishing.

The sample preparation was conducted in a FEI Nova™ nanolab with dual beam of ultra-high resolution field emission SEM equipped with FIB at 52°. The major difference between SEM and FIB is the use of a different particle to create the primary beam to interact with the sample. FIB uses ions instead of electrons in SEM. In a SEM, electrons are accelerated and focused onto the sample surface to create an image from either secondary electrons or back scattered electrons. Likewise, the ion beam penetrates into the sample surface and creates secondary electrons. The electrons receive energy and will be rejected, and resulted in high amount and energy of secondary electrons produced. Ions also have a property of channeling in crystallographic materials. Therefore, the ion beam images that produced from secondary electrons have a better resolution of surface,

and a better channeling contrast than the electron images. Meanwhile parts of ions deposit into the substrate, and parts of the substrate atoms are sputtered off. Figure 3.13 shows a schematic diagram of interactions of ion beam with the sample surface. Sputtering by FIB gives a better result than ion milling because the beam can be focused and controlled, and has high energy that can remove the heavy element easily. Therefore, the cutting by FIB can produce uniform thin area at the interface of oxide and alloy. In summary FIB can be used for imaging, depositing or sputtering. In this thesis, the FIB was mainly utilized in sputtering process to produce TEM specimens.

Mechanical polishing is required before thinning with FIB. The specimens were first cut into 2 mm x 1 mm coupons and glued to a Si wafer using M-bond™. Specimens were polished with SiC paper grit P800, P1200, P2400, P4000 followed by diamond polishing film with particle size 3, 1, and 0.05 μm for each side. Figure 3.14 demonstrates the mechanical poling steps. First a top part (side A, 1 mm wide) was polished until the surface smooth. Removed thickness was ~0.5 mm. Next the opposite side (side B) that has interested area was polished carefully to remove damages from cutting and to avoid mechanical damage from polishing. After that, the 2 mm long side (side C) was polished to remove ~0.4-0.5 mm from surface. Finally the sample was glued with melted wax on a wedge polisher (T-tool©) by facing the polished side C down. The sample was polished until the thickness was ~50 μm. The tool can be adjusted for wedge polishing by making the interested area (side B) to be the polished side. Polished this side until final thickness was ~20 μm. Glued a piece of molybdenum TEM grid (cut in half to dimensions 3 mm outer diameter, 1x2 mm inner diameter) with M-bond™ at the thick side (side A). Note that the interface of coupon and Si was perpendicular to hemisphere

of the grid (see Figure 3.14 (f)). M-bond™ was cured at 100-120°C for at least 3 hours. To remove the sample that attached to TEM grid from T-tool©, dissolved wax with acetone for 0.5 hour. The sample was final cleaned with ethanol and distilled water before FIB cutting.

Specimens were thinned into an H-bar shape with Ga^+ beam in a FEI Nova™ nanolab in the Electron Microbeam Analysis Laboratory (EMAL) at the University of Michigan. The sample that attached with TEM grid was vertically secured in a cross section TEM holder. The sample was inserted into Nova™ chamber then the chamber was vacuumed. Figure 3.15 shows procedure for TEM sample preparation by FIB. First step was to align the interested area to a eucentric height using SEM mode. The eucentric height is center the position that allows both electron and ion guns (located at 52° apart) operated at the same working distance of 5 mm. The next step is to remove the mechanical damaged area (if any) at the top of interested area by tilting to 0° and cut by ion beam of voltage 30 kV and current 5 nA. Once the mechanically damaged region were removed, the sample was tilted to 52°. Platinum was coated with 20 kV and 0.21 nA beam on the top of interested area in order to avoid ion beam damage, and to mark the interested position. Dimension of Pt was 1-1.5 μm wide, 5-20 μm long (depended on how large of interested area) and ~1-2 μm thick. Note that final thin area could be as large as 20-25 μm. After Pt coating, the sample was thinned by Ga^+ beam. Rough cutting was done using the ion beam voltage of 30 kV with beam current 7 nA to thin the sample down to ~5 μm. The beam current was reduced to 5 and 3 to thin the sample down to ~2 μm. The fine cut was started with the ion beam of current 1 nA to cut through the Pt strip and thinned sample to ~0.5 μm. The beam current was further reduced to 0.5, 0.3 and 0.1

nA, and 50 pA for polishing sample down to ~100 nm thick at topmost part. Since the sputtering rate at the topmost part was high, the lower part of sample was still thick. In order to obtain uniform thin area from top to bottom, the sample was tilted to 52±2° to thin the lower part of sample with 30 pA beam. The final thickness of sample was ~100 nm throughout the area. Using 30 kV Ga^+ beam on F-M alloys, the sputtering depth was ~15-20 µm. Therefore the final thin area was ~20 µm wide and ~15-20 µm long. Figure 3.15 (j) shows the TEM specimen of a HCM12A sample exposed at 500^{o}C and prepared by FIB. The thin area covered two oxide layers and the alloy substrate.

As shown in Figure 3.13, a major concern for sample preparation with FIB is the ion beam damaged layer on sample that caused from two reasons, atomic displacement (can create amorphous or dislocation regions), and ion deposition. Both issues depend on voltage, current, and incident angle of ion beam. In order to evaluate the layer damage by the Ga^+ beam, the ion range in Fe based alloy was simulated by TRIM software [1]. Target density was set at 7.75 g/cm^3, which is the density of HT-9. With energy 30 keV of 1 and 89° incident angle (angle between ion beam and sample surface), the Ga^+ ions range is approximately 4 and 10 nm deep, respectively. The ranges for ions energy 10 and 20 keV at 89° incident angle are ~2 and 4 nm, respectively. The deposition layer from 30 keV beam with 20 pA is <10 nm [2]. Therefore the maximum ion beam damage layer of TEM specimen occurred with 30 keV and 89° was ~10 nm deep from the surface. In order to minimize the damage layer, the sample was final polished using low voltage beam of 20 and 10 kV with beam current 21 pA. The final thickness of sample was ~80-90 nm, and the damage layer expected to be less than 5 nm from both surface. Total preparation time in FIB was ~4-10 hours, which depended on the length of

interested area. For samples tested at 400 and 500°C that have total oxide thickness ~3-12 μm, the thin area can be prepared to cover three regions of outer and inner oxide, and alloy substrate. For the sample exposed at 600^{o}C, three TEM specimens from different regions were prepared because the oxide layers were each 15-20 μm thick.

3.7 Microstructural Characterization

Microstructure characterization of the oxide scales is one of the approaches to understand the oxidation mechanisms. The characterizations were conducted with various techniques based on specific purposes of the analysis. In order to investigate morphology and structure, SEM was employed. In addition to Secondary Electron (SE) images, BSE images were taken to demonstrate better elemental contrast between oxide layers. The surface oxide phase was characterized by XRD technique, which included a glancing angle (3°) XRD for thin oxide film, and a theta-2theta XRD for thick oxide analysis. Composition analysis was conducted by EDS. However, details in terms of structure, composition, and morphology of inner and transition layers cannot be achieved by SEM due to the resolution limit. A high resolution characterization of the layers will be provided by TEM. A summary of sample characterization with analysis techniques is reported in Table 3.6.

3.7.1. Scanning Electron Microscopy

Morphology and structure of samples were examined using SEM, which included a Phillips XL30 Field Emission Gun (FEG) SEM in the EMAL, and a JEOL JSM-6480 SEM in the Irradiated Materials Testing Laboratory (IMTL) at the University of

Michigan. Major difference between two machines is the electron guns in which the XL30FEG equipped with a FEG and the JSM-6480 has a W filament electron source. Operation with the FEG assisted controlling, focusing and increase intensity of the electron beam better than the filament source. Therefore the JSM-6480 was used for low to intermediate magnification (100-5,000x) images, and the XL30FEG was used for high magnification (>5,000x) images. Both SEMs were operated at 20 kV with spot sizes of 5 and 50 in XL30FEG and JSM-6480, respectively.

Images taken from the SEM consisted of two modes of SE and BSE. The SE is a normal operation in the SEM. Electron beam emitted from the electron gun was accelerated and scanned on the sample surface. Interactions of electrons from the gun and electrons of sample atoms produced the secondary electrons, which were detected by an electron detector. The SE images were produced by conversion of electron signals into an image. In addition to the SE, back scattered electrons were bounced back from the sample surface. These electrons can be used to process an image by detection at high angles with an annular back scattered electron detector. Since BSE depended on atomic number of target atoms, BSE images give better elemental contrast than SE images (in current system). Therefore, most of oxides cross section images were taken under BSE mode.

3.7.2. X-ray Diffraction

Analysis of the surface oxide crystal structure was conducted using 1) glancing angle ($\theta = 3°$) XRD, and 2) standard θ-2θ Rigaku© Miniflex™ XRD. A major difference between two machines is that the incoming X-rays was fixed at 3° to sample surface in the glancing angle XRD, but for the Miniflex™ the incoming X-rays was rotated during

measurement. Having a glancing incident angle, the penetration depth of X-ray is less than 2 μm. Therefore the glancing angle XRD is suitable for the thin surface oxide analysis, and Miniflex™ is good for the thick oxide. Comparison of geometries of the glancing angle and the Miniflex™ is shown in Figure 3.16 . Both machines used a similar analysis X-ray of Cu k_α with wavelength approximately 1.54 Å. For the glancing angle XRD, the diffracted X-rays were scanned with step size 0.05° over a range of angles (θ_{det}) from 8 to 40°, which is equivalent to 2θ in range of ~22 to 85°. Conversion of a detected angle to a 2θ was performed in order to compare spectrums with those of Miniflex™ with the following expression;

$$2\theta = 2(\theta_{det} + 3) \qquad (3.3)$$

where, θ is the diffracted angle determined from angle between the incoming beam (3°) and the detected beam, and θ_{det} is the detected angle. For the Rigaku© Miniflex™ XRD, the incoming X-ray beam was rotated from ~7.5 to 40° and the detected beam was scanned over a 2θ range of 15 to 80° with step size 0.02 Å.

After data collection, the patterns were being analyzed. Peaks exhibited in a spectrum corresponded to planes in the crystal, which could be one or several species. The peaks were indexed by converting the diffracted angle (θ) to d-spacing from using Bragg's law;

$$\lambda = 2d\sin\theta \qquad (3.4)$$

where, λ is the wavelength ($CuK_{\alpha 1}$ = 1.541 Å), d is the interplana spacing, θ is the diffracted angle (degree). A set of d-spacing from a pattern was compared with the standard JCPDS (Joint Committee on Powder Diffraction Standard) files for the identified phases. The identification should match most of the peaks within ± 0.05 Å. For

accuracy, the plane (h,k,l) was indexed for each peak, and the lattice parameter for cubic structure was also calculated from the following expression;

$$\frac{1}{d^2} = \frac{h^2}{a^2} + \frac{k^2}{b^2} + \frac{l^2}{c^2} \qquad (3.5)$$

where, *h,k,l* are the plane indices, and *a*, *b*, *c* are the lattice spacing of the crystal (for cubic, $a = b = c$). The standard diffraction patterns of structures observed in this thesis including Fe (bcc), Fe_3O_4, $FeCr_2O_4$, and Cr_2O_3 are listed in Appendix I.

3.7.3. Transmission Electron Microscopy

Microstructural characterization at high special resolution was conducted on the cross section of oxide layers and alloy substrate with the TEM. Two TEM instruments, JEOL 2010F analytical electron microscope and a JEOL 3011 high resolution electron microscope, were used in the present study. The 2010F equipped with a FEG that was operated at 200 kV, but the 3011 has a LaB_6 filament type electron source operated at 300 kV. Both instruments have different advantages. The 2010F is capable of advanced analysis techniques including Scanning Transmission Electron Microscopy (STEM), and Electron Energy Loss Spectroscopy (EELS). Since the electron source in 2010F can be operated in STEM mode, the beam can be controlled for EDS elemental line scan and mapping. The 3011 TEM has advantage in conducting High Resolution (HR) TEM images because the electron source was operated at a higher energy than that of 2010F. As a result electron wavelength in 3011 (0.0197 Å) is shorter than that of 2010F (0.0251 Å), which is suitable for the HRTEM. Both machines are capable for imaging and selected area electron diffraction (SAED) with tilting angles in a range of ± 25° and ± 15° for 2010F and 3011, respectively.

The TEM characterization techniques applied in this study consisted of imaging in bright field (BF) and dark field (DF), SAED for phase identification, STEM for Z-contrast imaging and EDS for composition analysis. The characteristic of each technique will be described here in order to understand the insight information from images. The BF images were taken at regular TEM operation mode that uses the direct transmitted beam (deviation from the direct beam < 5°) to produce an image. The BF images yield good combination of mass, thickness and diffraction contrast, so the BF images are good for structure and morphology characterization. However, the BF images of F-M alloys could not be at their best quality due to interference from magnetic nature of the alloy.

The DF images uses the indirect transmitted beam from either diffracted directions, or high transmitted angles. Two types of DF image were obtained in this study. First is DF images that were produced by selecting a diffracted beam from SAED pattern using an objective aperture. This DF images will show parts of specimen (or grains) that satisfied the diffraction condition. Thus they were used for determining the grain size. Another type of DF image was collected in STEM mode with a High Angle Annular Dark Field (HAADF) detector. So this DF images were formed by collecting high angle scattered electrons (angle from the direct beam ~5-9°). The HAADF images yield very good Z-contrast at high collecting angle (the effects of diffraction contrast can be observed at low collecting angle), which is similar to the BSE images in SEM. Therefore the most of oxide layers images are represented in HAADF mode.

The SAED technique was used for structure and phase determination. Principle of the SAED is similar to the XRD, but the analysis wavelength in TEM is much smaller and the diffracted beam was projected onto an image. In order to take a diffraction pattern

(DP), a selected area aperture was inserted to select an interested area, and the specimen was tilted to one zone axis. Since all of the structures reported in this thesis are crystalline, the DP appeared in two types. If more than one grains were selected by the apperture, the DP was reflected from multiply grains thus can be viewed as a ring pattern, which is similar to the XRD powder diffraction pattern. On the other hand, if the grain size is large, the DP can be viewed as a spot pattern. The spot pattern formed by diffraction of several planes that parallel to beam direction, called zone axis.

Indexing the DP was performed by the following procedure. First, determine d-spacing of diffraction spots with an expression;

$$L\lambda = Rd \tag{3.6}$$

where L is the camera length (cm), λ is the electron wavelength (Å), R is the distance of diffraction spot from direct beam (cm), and d is the interplana spacing (Å). Next, determine plane for each diffraction spots by R ratio method (in case L is unknown), or calculate plane indices (h,k,l) from equation 3.5 (in case of L is known and structure is cubic). In order to verify the plane indexing (in case of spot pattern), the angles between planes were calculated and compared with the DP with equation (for cubic structure);

$$\cos\phi = \frac{h_1h_2 + k_1k_2 + l_1l_2}{\left(h_1^2 + k_1^2 + l_1^2\right)^{1/2}\left(h_2^2 + k_2^2 + l_2^2\right)^{1/2}} \tag{3.7}$$

where, ϕ is the angle between planes, and h, k, l are the plane indices of diffraction spots 1 and 2. Finally a zone axis of the spot DP was determined from at least two or three diffraction planes in the DP. Each diffraction plane (h,k,l) in a [UVW] zone axis must parallel to the beam direction followed Weiss zone law;

$$hU + kV + lW = 0 \tag{3.9}.$$

Thus the cross product of any two planes in a zone axis was used to determine the beam direction;

$$[U,V,W] = (h_1,k_1,l_1) \times (h_2,k_2,l_2) = \begin{bmatrix} i_1 & i_2 & i_3 \\ h_1 & k_1 & l_1 \\ h_2 & k_2 & l_2 \end{bmatrix} \quad (3.10).$$

Once the DP and the zone axis were indexed, a crystal structure of the interested figure was determined followed a rule of structure factor. Most of the structure observed (except Cr_2O_3) are cubic and were determined using the structure factor of cubic systems. Summary of the reflections from cubic system is presented in Table 3.7. For the area that expected to be Cr_2O_3, indexing of the DP was performed by the diffraction image simulation software MacTempas© [3] due to the complex rhombohedral (trigonal) structure. The DPs from at least two zone axes were obtained in order to identify a structure.

In summary, in order to characterize a phase of the interested feature, three parameters consisted of; a) lattice parameter, b) crystal structure, and c) composition must match with the standard information of that phase. The lattice parameter and the crystal structure were determined by SAED. The composition characterization was performed by EDS, which will be explained in next section.

3.7.4. Energy Dispersive Spectroscopy

The microchemistries of oxides and alloy substrate were characterized with EDS technique. Fundamental of the EDS based on interactions of electrons from an electron generator and electrons in sample atoms. The incident electrons penetrate through electron cloud and transfer energy to an electron in an inner shell, which has the lowest

binding energy. As a result the inner electron ejects from the shell while creating an electron hole. An electron from an outer shell, which has a higher binding energy, substitutes the hole. Hence it releases extra energy equals to the difference of energy in the higher and the lower shell in the form of X-ray, called characteristic X-ray. Therefore the characteristic X-ray energy can be used to identify the type of atom, which is called EDS or sometimes called Energy Dispersive X-ray Spectroscopy (EDS).

In this study, the EDS characterization technique was used in both SEM and TEM with the analysis electrons energy of 20 keV and 200-300 keV, respectively. These energy ranges can be used to analyze a wide range of elements from light to heavy elements. Generally the characteristic X-ray energies of elements in four F-M alloys are in a range of 0-15 keV. The characteristic X-ray was detected by an X-ray solid state detector located at ~35° and 34° take off angle from the normal of sample in SEM and TEM, respectively. The EDS spectrums were collected in EDAX® program. Three analysis methods consisted of area scan, line scan, and EDS mapping were applied. The area scan mode analyzed composition in the area of interest. The results are in terms of both qualitative and quantitative analysis. Each of area scan was measured with live time ~120 sec. The line scan mode was performed by controlling the electron beam to scan point by point across the sample. The line scan is useful for a comparison of composition of the oxide layers (in SEM), and between interface (in TEM). The line scan was conducted with dwell time 1,500 - 2,000 µsec in both SEM and TEM. The elemental mapping demonstrated distribution of elements in the interested area, but cannot be use for qualitative analysis. Resolution of EDS mapping was 512 x 400 and dwell time was 200 -

500 μsec. The data collection time for EDS mapping was varied from 0.5 – 1 hour depended on intensity of the elements.

The qualitative analysis of elements was performed using the characteristic X-ray energies from the strongest intensity peaks of K X-ray ($K_{\alpha 1}$, $K_{\alpha 2}$), followed by L and M X-rays. A summary of the characteristic X-rays for all elements in four F-M alloys and oxides is listed in Table 3.8. However, the analysis must be done carefully because there could be peak overlapping between the L or M peaks of one element and the K peak of another element. This could lead to misinterpretation of the results. Such elements are Mn, Si and Nb. Another concern is that elements with K X-ray peak of higher energy than 15 keV cannot be activated by the 20 keV electrons of SEM. In these cases, the minor peaks from L or M X-ray was used to identify the elements. The characteristic X-rays used to identify the elements are listed in Table 3.8.

The quantitative analysis was performed with the EDAX® program, and recalculated by a K-factor method. The analysis results were reported in atomic percent (at%). In both SEM and TEM, the composition profile of oxide layers was measured with major elements along with trace elements. The intensity of characteristic peaks (listed in Table 3.x) was used to determine the concentration of elements. The ratio of atom A to atom B in a material is proportional to the ratio of the measured intensities by the Cliff-Lorimer equation [4]:

$$\frac{C_A}{C_B} = k_{AB}\frac{I_A}{I_B} \tag{3.11}$$

where C_A and C_B are the concentrations of elements A and B, respectively, I_A and I_B are the intensities of characteristic X-rays of A and B, respectively, and k_{AB} is known as the Cliff-Lorimer factor, or *k*-factor of element A and B. The *k*-factor is not a physical

constant and will vary on the geometry basis of the EDS system and beam energy used. Similarly, for a third element (C),

$$\frac{C_A}{C_C} = k_{AC}\frac{I_A}{I_C} \tag{3.12}$$

and,

$$\frac{C_B}{C_C} = k_{BC}\frac{I_B}{I_C} \tag{3.13}$$

This relation can easily be extended to any number of elements. Also, assuming that no other elements are present in the material, then the following is true:

$$C_A + C_B + C_C = 1 \tag{3.14}$$

Equations 3.12 through 3.14 can be solved simultaneously. If the factors k_{AB} and k_{AC} are known, the concentrations of each element can be readily calculated. In STEM-EDS, the *k*-factors are calculated using the matrix area measurements with the bulk composition based on the alloy composition data from Table 3.1. For each matrix area measurement, the set of *k*-factors was calculated, and then the *k*-factors were averaged. These average values were used to determine the concentration for all measurements taken. A set of *k*-factors was calculated for each specimen examined, but the *k*-factors for the same element pair was not necessarily the same for different alloys. The differences were due in part to different absorption arising from differences in bulk compositions between alloys.

3.9 Error Analysis

Measurements of the weight gain, microchemistry, all require some error to be associated with the measured value. The purpose is to provide some level of confidence in the measured value and a range in which one might expect to find the value for a measurement made under identical conditions. In this work, the standard deviation of the data set is provided, described by the following equation:

$$\sigma = \sqrt{\frac{1}{N} \cdot \sum_{i=1}^{N} \left(x_i - \bar{x}\right)^2} \tag{3.15}$$

where N is the total number of measurements in the data set, σ is the standard deviation, x_i is a measurement in the data set, and $\bar{x}$ is the average of the measurements.

In many cases, values are reported that are actually an indirect measurement from two directly measured values. In this case, each directly measured value has a standard deviation, so taking the sum or difference, etc. of the two measured values requires consideration of the standard deviation from each measurement. One must then consider the propagation of error to determine a new standard deviation. The rules for propagation of error analysis are listed in Table 3.9.

Table 3.1 Composition of F-M alloys; T91, HCM12A, HT-9 and 9Cr-ODS.

Alloy	Chemical composition (weight %)															
	C	Mn	P	S	Si	Ni	Cr	Mo	Cu	N	Co	Ti	Nb	Al	V	W
T91	0.10	0.45	0.009	0.003	0.28	0.21	8.37	0.90	0.17	0.048			0.076	0.022	0.216	
HCM12A	0.11	0.64	0.016	0.002	0.27	0.39	10.83	0.30	1.02	0.063			0.054	0.001	0.190	1.89
HT-9	0.20	0.52	0.020	0.006	0.22	0.50	11.63	1.00	0.04	0.047	0.08	<0.01		<0.01	0.300	0.52
9Cr-ODS	0.14	0.05	<0.005	0.004	0.048	0.06	8.64			0.017		0.023				1.96
	Y	0.27	O	0.14	Y_2O_3[a]	0.35	Ex.O[b]	0.065								

Note: a: $[Y_2O_3] = 1.27 \times [Y]$

b: [Ex.O] = [Total O] – [O in Y_2O_3 powder] = [O] – 0.27 x [Y]

Table 3.2 Heat treatment of F-M alloys; T91, HCM12A, HT-9 and 9Cr-ODS.

Alloy	Anneal			Tempering		
	Temp. (^{o}C)	Time (min.)	Cooling	Temp. (^{o}C)	Time (min.)	Cooling
T91	1066	46	Air cooled	790	42	Air cooled
HCM12A	1050	60	Air cooled	770	45	Air cooled
HT-9	1040	30	Air cooled	760	60	Air cooled
9Cr-ODS	1050	60	Air cooled	800	60	Air cooled

Table 3.3 Dimension, surface area, and weight of corrosion coupons tested in each experiment.

Exp.	Temp. (°C)	DO	Time (h)	Alloy	Width (mm)	Length (mm)	Thickness (mm)	Surface area (mm^2)	Weight (g)
1	400	<10*	151	T91	10.027	19.949	0.899	453.963	1.39610
				HCM12A	9.983	19.943	0.966	455.982	1.26278
				HT-9	9.956	19.926	0.923	451.920	1.29869
2a**	400	<10	188	T91	9.970	19.935	0.921	452.560	1.34714
				HCM12A	9.904	19.946	0.856	446.219	1.23513
				HT-9	9.960	19.983	1.009	458.491	1.48815
3	500	<10	182	T91	9.900	19.838	0.910	446.941	1.33394
				HCM12A	9.832	19.886	0.841	441.049	1.19843
4a**	500	<10	195	T91	9.979	19.934	0.876	450.242	1.28928
				HCM12A	10.025	19.959	0.971	458.407	1.44563
				HT-9	9.996	20.015	1.008	460.625	1.44322
				9Cr-ODS	10.062	20.035	1.000	463.383	1.43310
5	500	<10	1	T91	10.000	19.975	0.961	457.112	1.41856
				HCM12A	10.027	19.95	0.906	454.387	1.32765
				HT-9	10.003	19.958	0.976	457.755	1.45009
6	500	<10	10	T91	9.964	19.944	0.922	452.582	1.32172
				HCM12A	10.045	19.959	0.968	459.081	1.47062
				HT-9	9.981	19.951	0.972	456.475	1.43870
7	500	<10	500	T91	9.991	19.974	0.871	451.324	1.27246
				HCM12A	10.056	19.987	0.956	459.400	1.43487
				HT-9	9.983	19.944	0.887	451.254	1.28523
9	500	300	182	T91	9.979	19.932	0.634	435.735	0.91985
				HCM12A	10.027	19.953	0.548	433.013	0.78910
				HT-9	9.974	19.939	0.721	440.886	1.04109
10	600	<10	191	T91	9.972	19.941	0.931	453.398	1.38493
				HCM12A	10.051	19.965	0.972	459.670	1.47273
				HT-9	9.948	19.917	0.939	452.347	1.38602
				9Cr-ODS	10.031	20.025	0.971	460.127	1.46508

* Deaerated condition

** Samples were re-tested for the time dependence experiment

Table 3.4 Specifications for main components of the multi-sample SCW test facility

System	Component Description	Main Specification
Water conditioning	Ion exchange resin	Barnstead® D8902: remove ionic contamination from water
	Filter	2 μm (Swagelock) at pump inlet 5 μm (Swagelock) at back pressure regulator inlet
	Conductivity sensor	Range: 0.02-600 μS/cm Cell constant accuracy: ±1% of reading Max pressure/temp.: 250 psi at 93 ^{o}C Materials: Ti, PEEK
	Dissolved oxygen sensor	Range: 0-10,000 ppb Accuracy: 1 ppb Flow rate: 50-2,000 ml/min Temperature: 5-50 ^{o}C Pressure: <45 psi Materials: 316SS, Polyacetal
Pressurization	High pressure pump	Flow Range: 0.01-100 ml/min Max. Pressure: 4,000 psi Pulsation: ±4% at 50 ml/min Materials: 316SS
	Back pressure regulator	Maximum pressure 41.37 MPa (6000 psi)
Heater	Preheater	4x heating cords wrapped on 0.25″ tube
	Main heater	3x 1250 W 480 V Watlow® heating bands
	Heat exchanger	Concentric tube (inner tube diameter 0.25″, outer tube diameter 0.5″)
Test Vessel		Materials: Inconel® alloy 625 Maximum pressure: 30 MPa (4,350 psi) at 600 ^{o}C 5″ inner diameter and 12.5″ depth

Table 3.5 Summary of SCW experimental conditions

Exp.	Temp. (^{o}C)	Dissolved oxygen (ppb)	Pressure (psi)	Conductivity (μS/cm)		Exposure time (hours)	System	Alloy
				Inlet	Outlet***			
1	400	<10*	3,600±15	0.06	0.07	151.5	MSCW	T91, HCM12A, HT-9
2a**		<10	3,550±15	0.06	0.08	188.0	MSCW	T91, HCM12A, HT-9
2b**		<10	3,550±15	0.06	0.08	136.4	MSCW	T91, HCM12A, HT-9
2c**		<10	3,550±15	0.06	0.08	166.5	MSCW	T91, HCM12A, HT-9
3	500	<10	3,550±10	0.06	0.09	182.2	MSCW	T91, HCM12A
4a**		<10	3,550±10	0.06	0.10	195.0	MSCW	T91, HCM12A, HT-9, 9Cr-ODS
4b**		<10	3,550±10	0.06	0.10	148.0	MSCW	T91, 9Cr-ODS
5		<10	3,580±20	0.07	0.58	1.0	SCW	T91, HCM12A, HT-9
6		<10	3,500±10	0.06	0.43	10.0	SCW	T91, HCM12A, HT-9
7		<10	3,500±10	0.07	0.10	500.0	SCW	T91, HCM12A, HT-9
8		100	3,550±10	0.06	0.13	236.0	SCW	T91, HCM12A
9		300	3,520±10	0.06	0.75	182.0	MSCW	T91, HCM12A, HT-9
10	600	<10	3,550±10	0.06	0.10	191.1	MSCW	T91, HCM12A, HT-9, 9Cr-ODS

* Deaerated condition

** The time dependence experiment

*** Outlet conductivity at stable level

Table 3.6 Summary of sample characterization by the analysis techniques

Exp.	Temp. (°C)	DO (ppb)	Exp. time (hours)	Alloy	Surface oxide		Cross section				
					Morph. (SEM)	Phase (XRD)	Morph. (SEM)	Comp. (SEM-EDS)	Morph. (TEM)	Phase (TEM-SAED)	Comp. (STEM-EDS)
1	400	<10*	151.5	T91, HCM12A, HT-9	all	all	all	all	HCM12A	HCM12A	HCM12A
2a**	400	<10	188.0	T91, HCM12A, HT-9							
2b**	400	<10	136.4	T91, HCM12A, HT-9							
2c**	400	<10	166.5	T91, HCM12A, HT-9							
3	500	<10	182.2	T91, HCM12A	all	all	all	all	HCM12A	HCM12A	HCM12A
4a**	500	<10	195.0	T91, HCM12A, HT-9, 9Cr-ODS	HT-9, 9Cr-ODS	HT-9, 9Cr-ODS	HT-9, 9Cr-ODS	HT-9, 9Cr-ODS			
4b**	500	<10	148.0	T91, 9Cr-ODS							
5	500	<10	1.0	T91, HCM12A, HT-9	all		all	all	HCM12A	HCM12A	
6	500	<10	10.0	T91, HCM12A, HT-9	all		all	all			
7	500	<10	500.0	T91, HCM12A, HT-9	all		all	all			
8	500	100	236.0	T91, HCM12A							
9	500	300	182.0	T91, HCM12A, HT-9	all	all	all	all	HCM12A	HCM12A	HCM12A
10	600	<10	191.1	T91, HCM12A, HT-9, 9Cr-ODS	all	all	all	all	all	all	all

Table 3.7 Summary of reflections from cubic systems

N= $h^2+k^2+l^2$	bcc		fcc		diamond	
	N	*hkl*	N	*hkl*	N	*hkl*
1						
2	2	110				
3			3	111	3	111
4	4	220	4	200	4	200
5						
6	6	211				
7						
8	8	220	8	220	8	220
9						
10	10	310				
11			11	311	11	311
12	12	222	12	222		
13						
14	14	321				
15						
16	16	400	16	400	16	400
17						
18	18	411, 330				
19			19	331	19	331
20	20	420	20	420		
21						
22	22	332				
23						
24	24	422	24	422	24	422
25						
26	26	431				
27			27	511, 333	27	511, 333
28						
29						
30	30	521				
31						
32	32	440	32	440	32	440

Table 3.8 List of characteristic X-ray energies of major compositions in four F-M alloys and oxide.*

Elements	Line	Energy (keV)	T91	HCM12A	HT-9	9Cr-ODS	Note
C	K_α	0.266	✓	✓	✓	✓	
O	K_α	0.515	✓	✓	✓	✓	
Si	K_α	1.739	✓	✓	✓	✓	Si, Nb, Mo energies are close
Nb	L_α	2.164	✓	✓		✓	K energy is too high
Mo	L_α	2.29	✓	✓	✓		K energy is too high
Ti	K_α	4.511	✓			✓	
V	K_α	4.949	✓	✓	✓		
Cr	K_α	5.41	✓	✓	✓	✓	
Mn	K_α	5.893	✓	✓	✓		Mn interferes with Cr K_b because Cr concentration is high.
Fe	K_α	6.396	✓	✓	✓	✓	
Co	K_α	6.928	✓				
Ni	K_α	7.467	✓	✓	✓	✓	
Cu	K_α	8.036	✓	✓	✓		
W	L_α	8.395		✓	✓	✓	K energy is too high
Y	K_α	14.957				✓	Cannot be detected in SEM (low operation voltage)

* Exclude N, P, S, Al

Table 3.9 Relations for calculation of error for two or more quantities which have individual errors

	Relation between Z and (A,B)	Relations between error ΔZ and $(\Delta A,\Delta B)$
1	$Z = A \pm B$	$(\Delta Z)^2 = (\Delta A)^2 + (\Delta B)^2$
2	$Z = AB$	$\left(\frac{\Delta Z}{Z}\right)^2 = \left(\frac{\Delta A}{A}\right)^2 + \left(\frac{\Delta B}{B}\right)^2$
3	$Z = A/B$	$\left(\frac{\Delta Z}{Z}\right)^2 = \left(\frac{\Delta A}{A}\right)^2 + \left(\frac{\Delta B}{B}\right)^2$
4	$Z = A^n$	$\frac{\Delta Z}{Z} = n\frac{\Delta A}{A}$
5	$Z = \ln[A]$	$\Delta Z = \frac{\Delta A}{A}$
6	$Z = e^A$	$\frac{\Delta Z}{Z} = \Delta A$

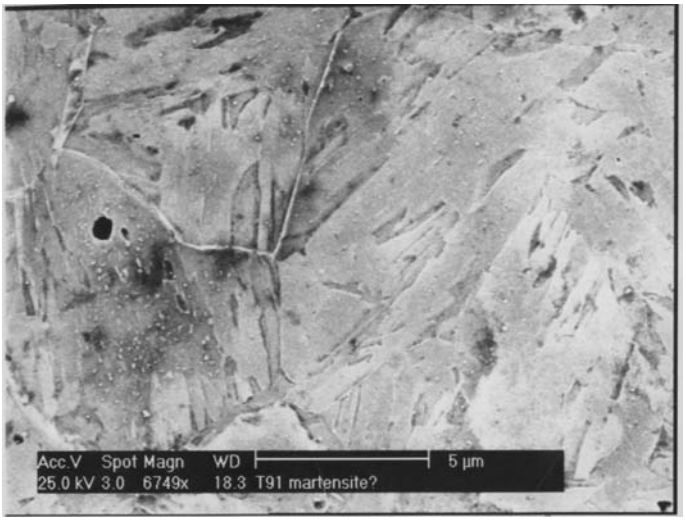

Figure 3.1 Scanning electron microscope image for the microstructure of T91.

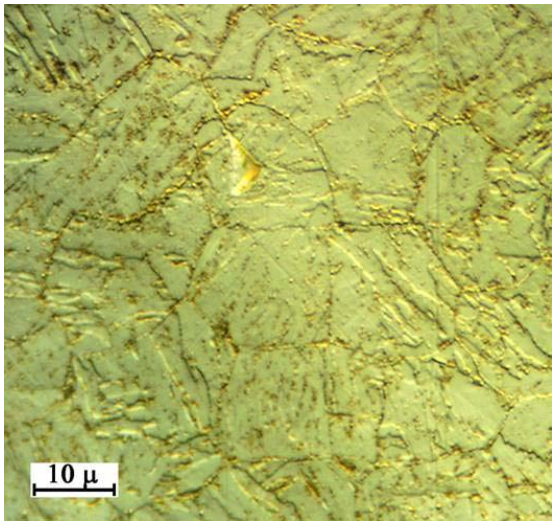

Figure 3.2 Optical micrograph of HCM12A [5].

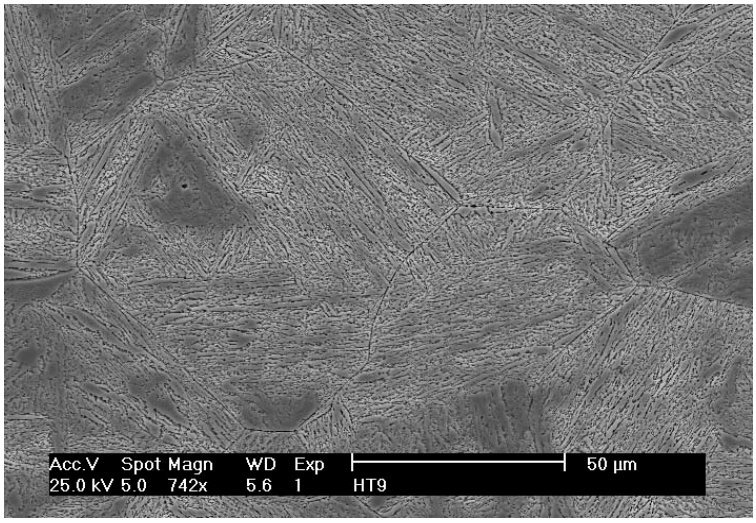

Figure 3.3 Scanning electron microscope image for HT-9.

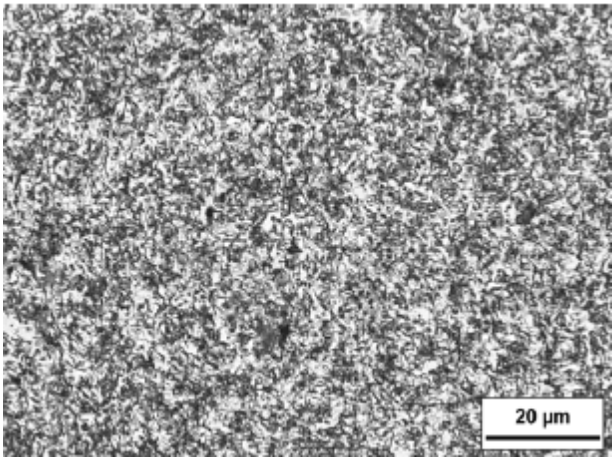

Figure 3.4 SEM images of microstructure of 9Cr-ODS [6].

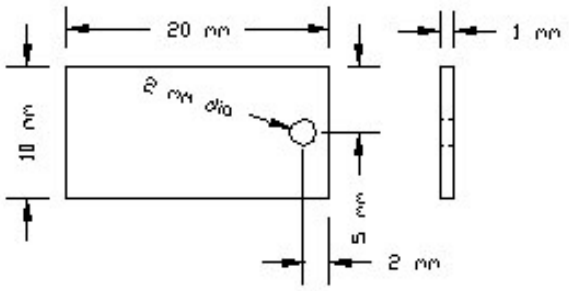

Figure 3.5 Geometry of corrosion coupon before polishing.

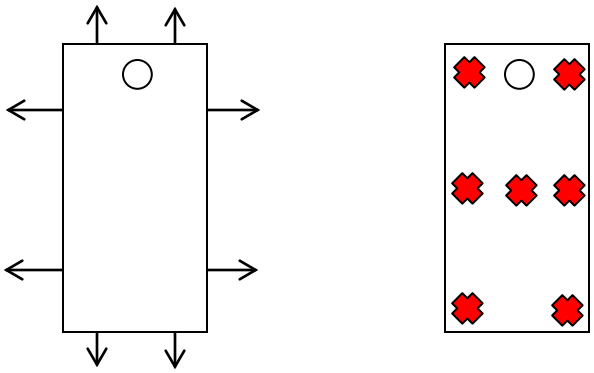

(a) (b)

Figure 3.6 (a) Positions of width and legth measurement of corrosion coupon.
(b) Positions of thickness measurement of corrision coupon.

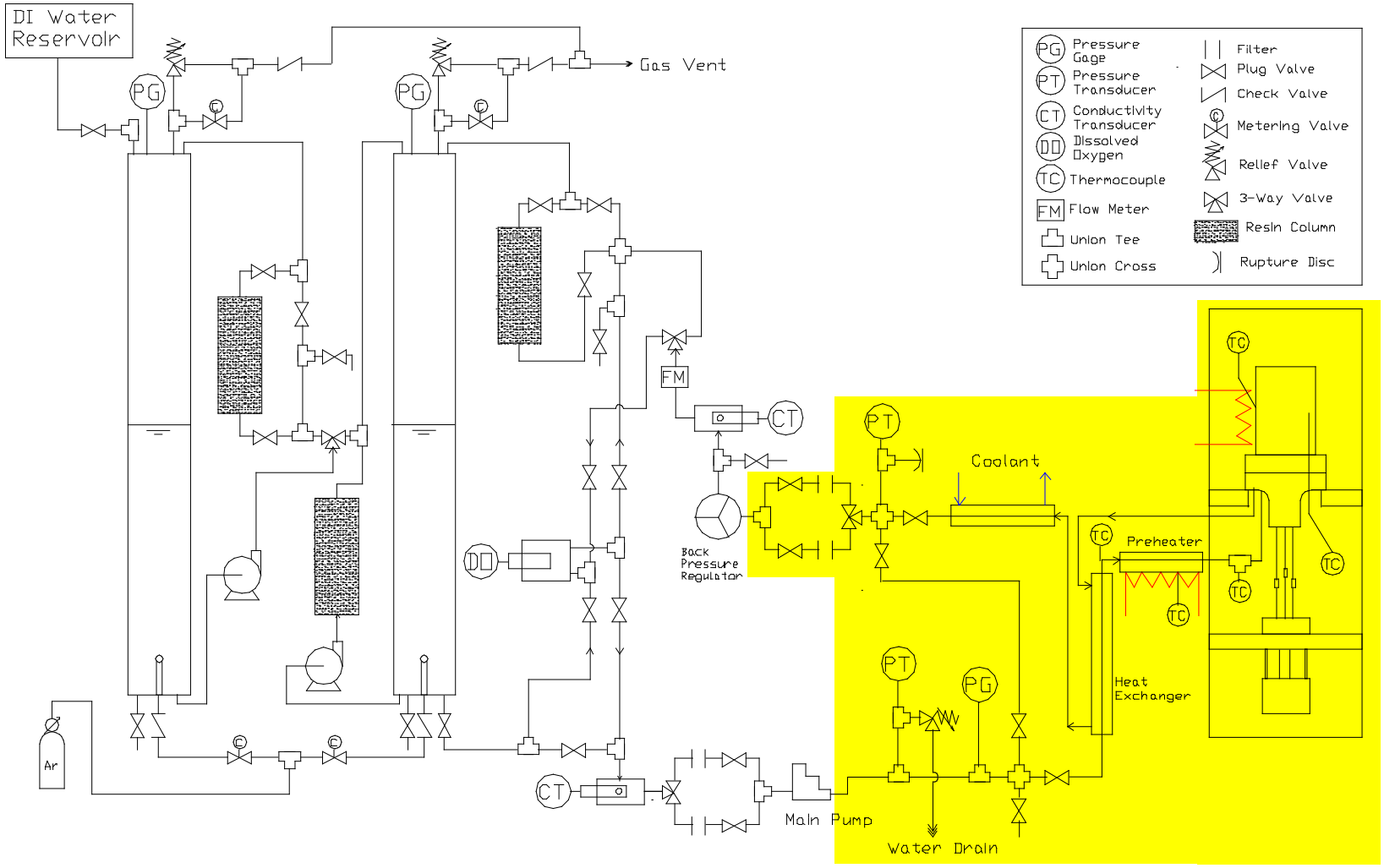

Figure 3.7 Schematic diagram of the multi-sample SCW system. High pressure parts of the system are shown in yellow.

Figure 3.8 The multi-sample SCW system in high temperature corrosion laboratory, University of Michigan

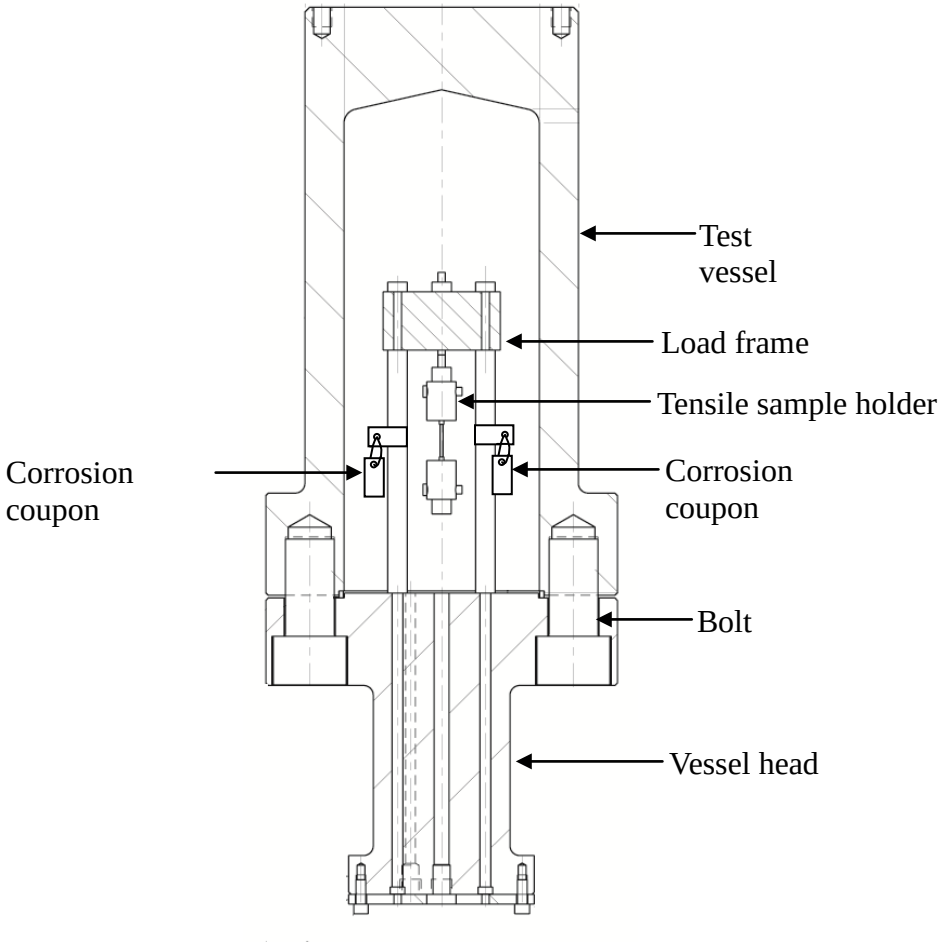

Figure 3.9 Test vessel of the multi-sample SCW system and corrosion coupons suspended inside the test vessel.

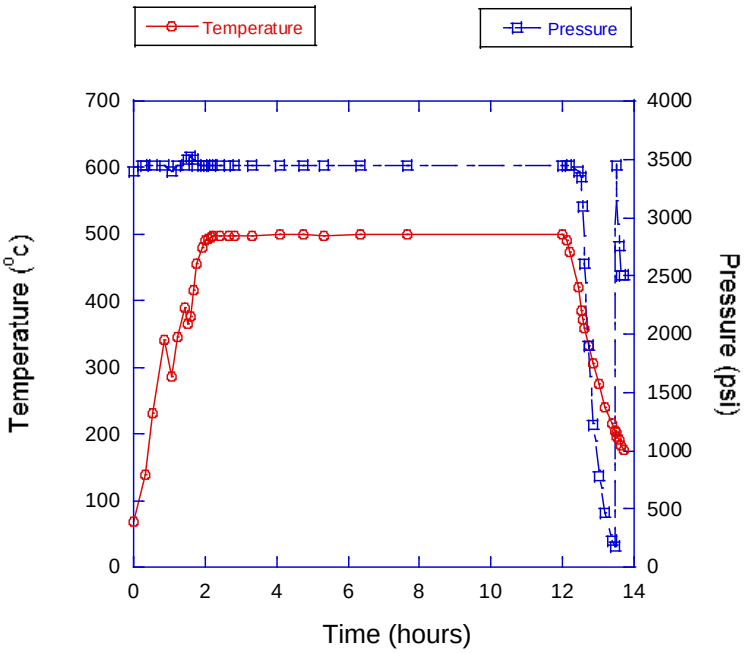

Figure 3.10 Plots of temperature and pressure control during an experiment at 500°C deaerated SCW for 10 hours.

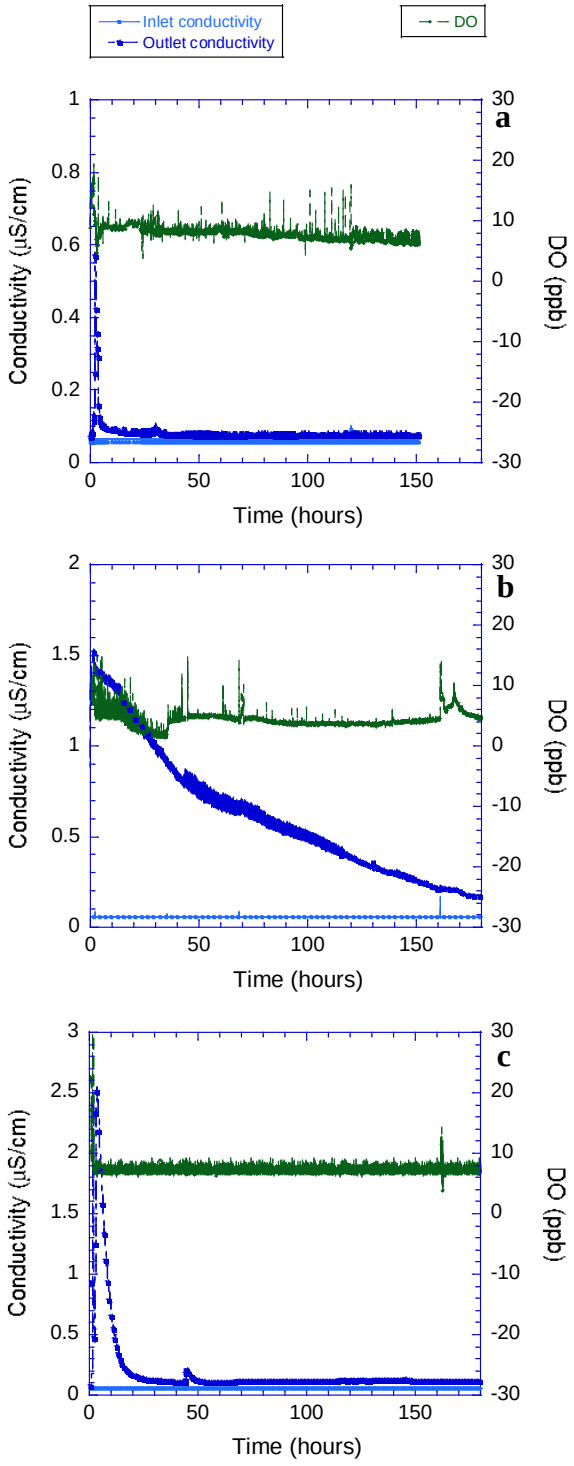

Figure 3.11 Conductivity and DO of experiments in deaerated SCW at (a) 400°C (151 hours), (b) 500°C (182 hours), (c) 600°C (191 hours).
(note: fluctuation of DO signal occurred from switching DO measurement between inlet and outlet lines.)

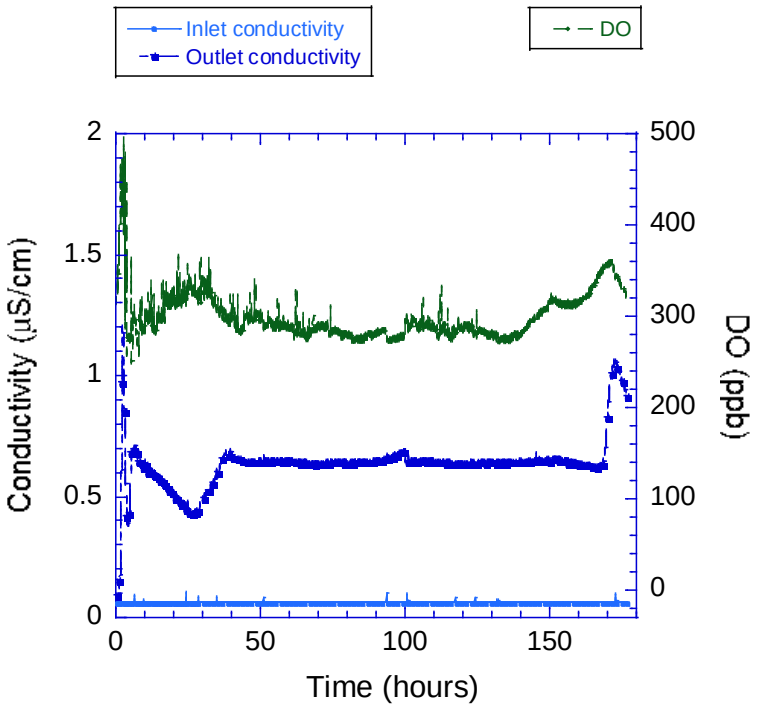

Figure 3.12 Conductivity and DO of experiments in 500°C SCW containing 300 ppb for 182 hours.

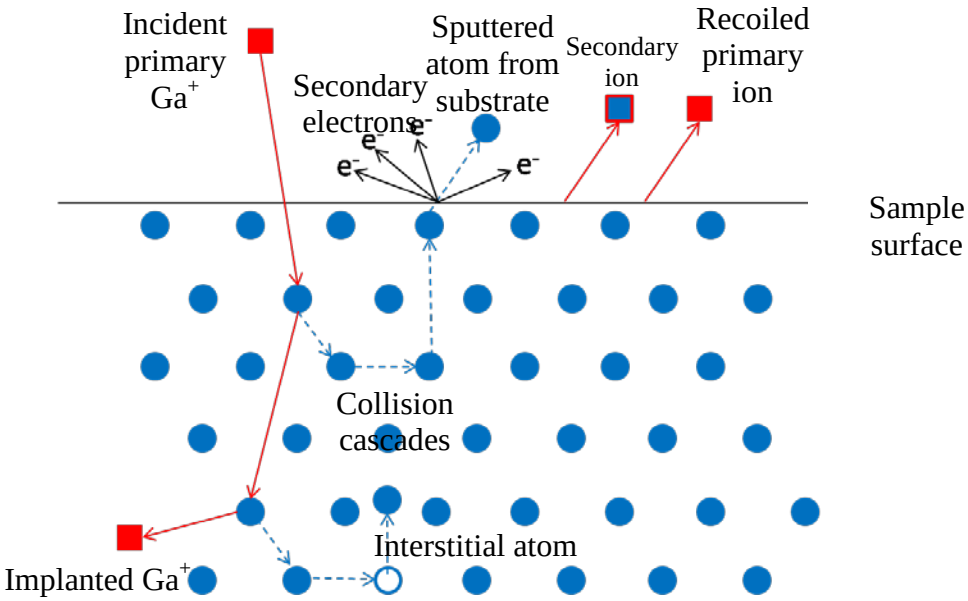

Figure 3.13 A schematic diagram of interactions of ion beam with the target material.

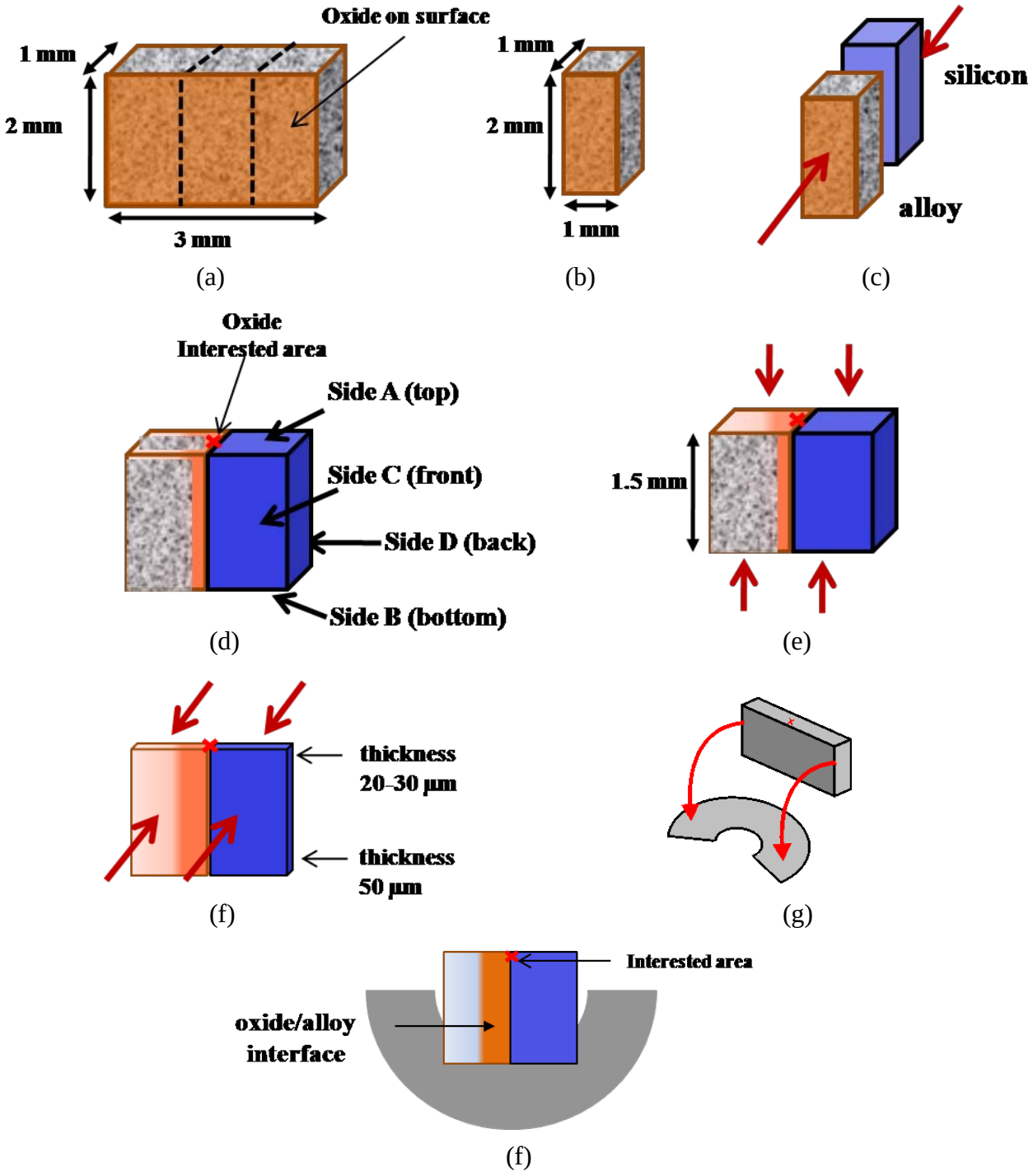

Figure 3.14 Mechanical polishing steps for cross section TEM preparation; (a) a small sample was cut from the exposed corrosion coupon, (b) sample was cut into 1x2x1 mm, (c) oxide surface was protected by gluing it with M-bond™ to silicon, (d) side view of the sample glued with silicon, (e) polished top (side A) and bottom (side B) sides, (f) polished front (side C) and back (side D) sides, (g) glued on Mo TEM grid with M-bong™, (f) finished sample.

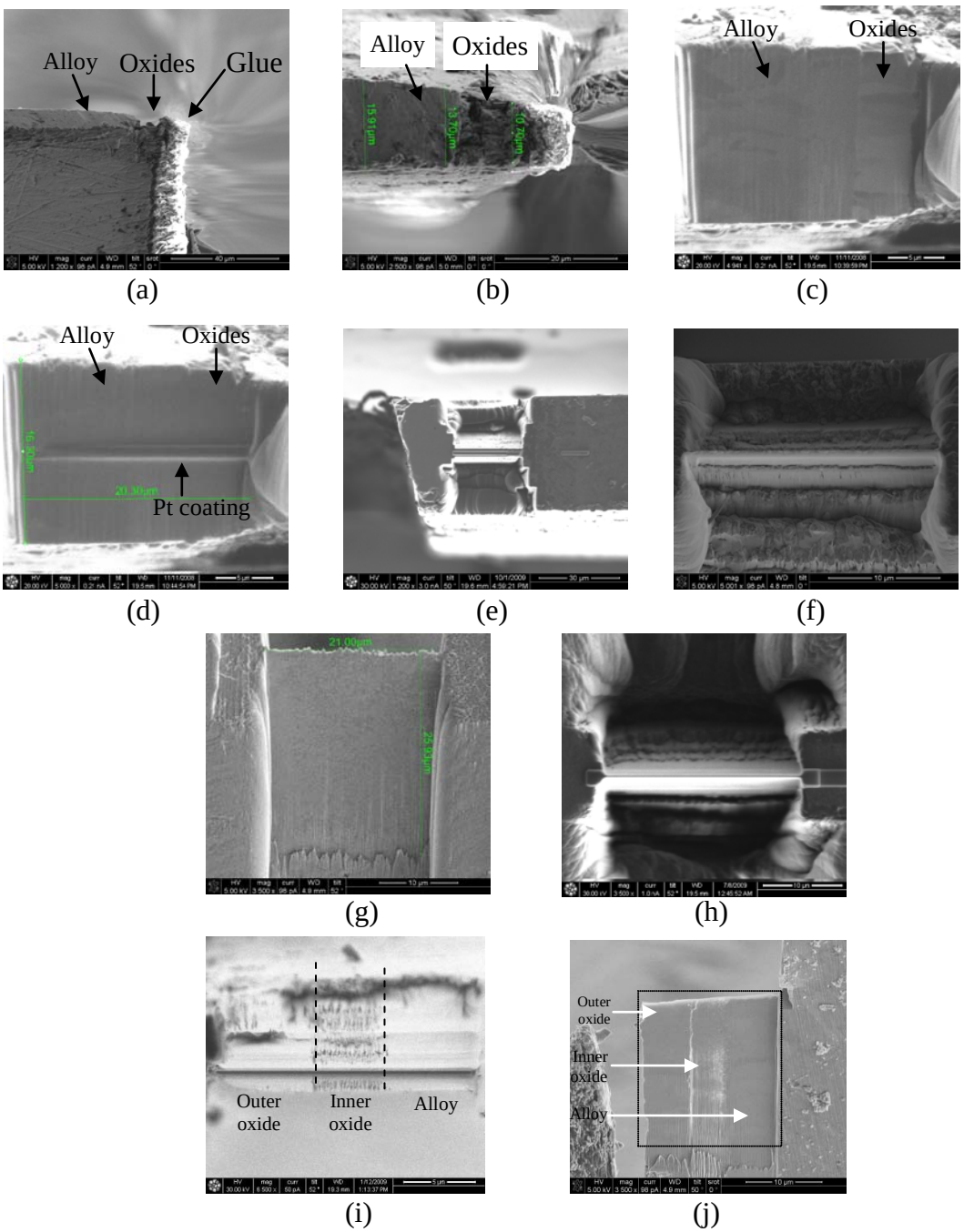

Figure 3.15 Cross section TEM sample preparation in FIB; (a) and (b) Side and top view of sample after mechanical polishing show mechanical damages,
(c) removed the damaged layers by FIB cutting from 0° tilting,
(d) Pt coating at the top of interested area,
(e) thinned interested area into the H-bar shape using 7-3 nA, 30 kV ion beam,
(f) polished interested area with reducing currents from 1 nA to 30 pA, 30 kV ion beam,
(g) side view shows thin area ~20x20 µm,
(h) final polished with 20 and 10 kV.
Top view (i) and side view (j) images of cross section TEM specimen of HCM12A exposed in 500^{o}C SCW for 182 hours.

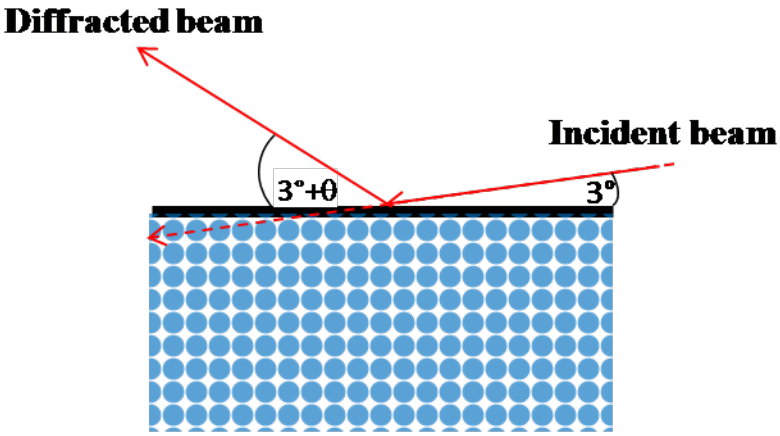

(a)

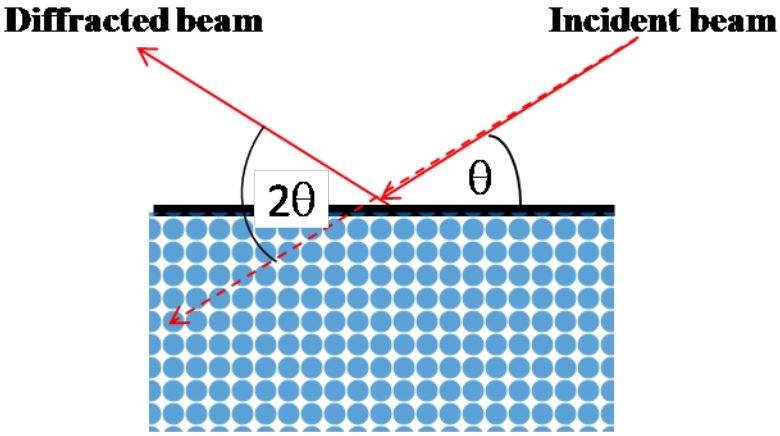

(b)

Figure 3.16 Geometries of (a) the 3° glancing angle XRD compare to (b) the standard theta-2theta XRD.

BIBLIOGRAPHY

1. Ziegler, J.F. *The Stopping and Range of Ions in Matter*. 2008 [cited 2009; Available from: http://www.srim.org/.
2. Giannuzzi, L.A. and F.A. Stevie, *Introduction to Focused Ion Beams: Instrumentation, Theory, Techniques and Practice*. 2005, Boston: Springer Science+Business Media, Inc.
3. *MacTempas*. 2007, Total Resolution LLC: Berkeley, CA.
4. Cliff, G. and G.W. Lorimer, Journal of Microscopy, 1975. **103**: p. 203.
5. Wardle, K.E. and J.I. Cole, *Evaluation of Materials for Advanced Nuclear Reactors.* U.S. Department of Energy Journal of Undergraduate Research, 2003. **3**.
6. Schroer, C., et al., *Oxidation Behaviour of P122 and a 9Cr-2W ODS Steel at 550 °C in Oxygen-containing Flowing Lead-bismuth Eutectic.* Journal of Nuclear Materials, 2010. **398**(1-3): p. 109-115.

CHAPTER 4

EXPERIMENTAL RESULTS

The exposure experiments of four F-M alloys, T91, HCM12A, HT-9, and 9Cr-ODS were conducted in the SCW with conditions described in Chapter 3. The time dependence of oxidation rate was studied in deaerated SCW at temperatures of 400 and 500°C. The temperature dependence of oxidation rate was studied in a temperature range of 400 - 600°C under deaerated SCW. The effect of DO concentration was determined in 500°C SCW containing <10, 100 and 300 ppb with an exposure time of approximately 200 hours. Following the exposure experiments, the oxidized corrosion coupons were analyzed. All of the results are presented in this chapter, which can be classified into two major parts; the oxidation rate and the oxide structure. The oxidation rate was determined from weight gain and oxide thickness. The samples were characterized in terms of oxide phase, morphology, composition, and microstructure. Detailed analysis of oxidation behavior will be described in this chapter.

4.1 Oxidation Rate

The oxidation rates of T91, HCM12A, HT-9, and 9Cr-ODS alloys were evaluated using the weight gain per surface area (mg/dm^2) and the oxide thickness (μm). The weight gain measurements were conducted right after the exposure experiments. Cross sections of corrosion coupons showed that the oxide structure on the F-M alloys exposed in SCW consisted mainly of a three-layer structure, an outer oxide, an inner oxide, and a transition layer. The oxide thickness of each layer was measured on cross sections of corrosion coupon as described in section 3.5. Results of the oxidation rates will be reported as the time dependence, the temperature dependence, and the DO effect.

4.1.1. Time-dependence of Oxidation Rate

The time dependence of the oxidation rate was determined at two temperatures, 400 and 500°C, in deaerated SCW. At 400°C, three of F-M alloys included T91, HCM12A, and HT-9 were tested with the exposure time ranging from approximately 150 – 500 hours. At 500°C, the alloys were exposed in the period of time from 1 – 500 hours in order to observe short and long time oxidation behavior. Additional 9Cr-ODS alloy was studied at 500°C with exposure times of 195 and 351 hours. The weight gain data was obtained in all of experiments. However, the oxide thicknesses were not measured in some of experiments including the experiments at 400°C with exposure times of 188, 324.4 and 491 hours, and at 500°C with exposure times of 195 and 351 hours because the corrosion coupons were reloaded in the next experiment. Therefore, the data of oxidation rate determined from oxide thickness is reported only at 500°C.

Summaries of weight gain and oxide thickness of four F-M alloys exposed at 400 and 500°C are presented in Table 4.1 and Table 4.2. The results show that both weight gain and oxide thickness increased as a function of the exposure time in both SCW temperatures. In order to determine the relation of exposure time and weight gain/ oxide thickness, the functions of parabolic, power, and logarithmic was applied using KaleidaGraph© software [1]. Table 4.3 presents the least square fits to each function. It is found that the best equation to represent the oxidation rate as a function of time is the power-law function. For the weight gain at 400°C, the parabolic and the logarithmic functions yield relatively low least square of fitting. At 500°C, the best fitting is a power function. Therefore, the power law was selected to express a relation of the oxidation rate and the exposure time.

Plots of weight gain versus time, and oxide thickness versus time are shown in Figure 4.1 and Figure 4.2, respectively. The weight gain and oxide thickness fit to the power law ($w = k_w t^{n_w}$ (eqn. 2.11), and $h = k_h t^{n_h}$ (eqn. 2.9)) results in an oxidation rate constant and the time exponent as listed in Table 4.4. The power fitting of oxidation rate from weight gain at 400°C exhibited the oxidation rate constant of 2.35-4.53 mg/dm^2/h and the time exponent of approximately 0.3-0.4. Among three F-M alloys tested at 400°C, HT-9 exhibited the highest weight gain, followed by T91 and HCM12A.

For the 500°C tests, the oxidation rate was determined from short exposure time (1 and 10 hours) to ~500 hours. The purpose of the short exposure times was to observe the early stages of the oxidation. However, it is important to note that the oxides formed were also affected by the heat-up (~2 hours) and the cool-down (~2.5 hours) periods. The results showed that the weight gain and oxide thickness after 1 hour exposure were

observable, which indicated that the oxidation occurred right after the experiment started. The oxidation rate increased rapidly at the short exposure time then gradually increased with increasing exposure time. Fitting by the power function, the oxidation rate constants are in a range of 10.89-11.02 with time exponent of 0.36-0.48. Note that the time exponents at 500°C are slightly higher than those at 400°C. At 500°C, HT-9 exhibited a time exponent of n_w = 0.48 that is close to that of a parabolic law. Figure 4.1 shows that T91, HT-9, and HCM12A exhibited relatively high weight gain compares to 9Cr-ODS alloy. The order of alloy from high to low weight gain is T91, HT-9, HCM12A, and 9Cr-ODS, whereas the 9Cr-ODS exhibited approximately half of weight gain of those of the three alloys. Details of mechanism will be discussed in next chapter.

The oxidation rate determined from the thicknesses of outer and inner oxide layers also can be described by the power law relation, as shown in Table 4.2. The parameters for each of the oxide layers were determined separately. The outer layer oxide was the thickest among the three layers, followed by the inner oxide and the transition layer. The growth rate constants for outer, inner and transition layers are 0.719, 0.464 and 0.470 μm/h, respectively. The exponents of growth rate for the outer and inner oxide layers are 0.37 and 0.41, which are close to that of oxidation rate determined by weight gain (0.43). However, the exponent of the transition layer is 0.20, which is much lower than those of the outer and inner layers. Thus the transition layer could form with a different mechanism from the oxides.

4.1.2. Temperature-dependence of Oxidation Rate

Temperature-dependence of the oxidation rate was determined in deaerated SCW at temperature range of 400-600°C. In order to compare the results from different

exposure times, the weight gain and the total oxide thickness were normalized to 182 hours using a power law of time exponents and oxidation rate constants calculated in Table 4.4. The reason for using normalized time at 182 hours is that most of experiments were conducted with this exposure time. Table 4.5 and Table 4.6 present the oxidation rate from weight gain and oxide thickness for each of the alloys and temperatures. Figure 4.3 is the comparison of weight gain and total oxide thickness at different temperatures for deaerated environments.

The results indicated that all of F-M alloys exhibited similar weight gain / oxide thickness development where the temperature has a significant effect, Figure 4.3 a and b. Both weight gain and oxide thickness increased as a function of temperature by following an exponential relation. The strong temperature dependence of oxidation rate of F-M alloys can be described by an Arrhenius equation (eqn. 2.12). For example, in deaerated SCW, the weight gain at 500^{o}C (~120-140 mg/dm^{2} for T91, HCM12A and HT-9, and ~70 mg/dm^{2} for 9Cr-ODS) is five to six times higher than that of 400^{o}C (~17-24 mg/dm^{2}), and the similar increment employed at 600^{o}C (470-600 mg/dm^{2}). This temperature dependent behavior of oxidation rate is an important key to describe the mechanism of oxidation that will be discussed in the next chapter.

Under conditions where four F-M alloys were tested, the orders of weight gain were slightly different in each temperature. As mention in the previous section, HT-9 and T91 exhibited the highest weight gain at 400 and 500°C, respectively. HCM12A exhibited low weight gains at both temperatures, whereas 9Cr-ODS exhibited an excellent oxidation resistance at 500°C. However, the results were different in the 600°C experiment. T91 presented a highest weight gain, followed by 9Cr-ODS, HCM12A, and

HT-9 was the least. The result at 600°C corresponded to the Cr concentration in alloys. Alloy HT-9 that contains the highest Cr content (~12% Cr) among three alloys presented the least weight gain. HCM12A has 11% Cr presented a slightly higher in weight gain than HT-9. Finally, 9Cr-ODS and T91 contains the least Cr, ~9%, presented the highest weight gain. The effect of Cr content was clearly observed at temperature 500^{o}C and 600^{o}C where the oxidation rates were high.

The temperature dependence of oxidation rate determined from the oxide thickness also followed similar trends as the weight gain, Figure 4.3b. This result implies that the weight gain arose from weight of oxygen adsorbed to form the oxide scales. In addition to the total thickness, thicknesses of each oxide layer as function of temperature also investigated as presented in Table 4.6 and Figure 4.4. The plots demonstrated that the oxide layers, an outer and an inner oxide and a transition layer developed simultaneously. (Since a pore region and a Cr-rich spinel oxide layers were observed only at 600C, the thicknesses of these layers were not included in Figure 4.4.) Under all temperatures where the F-M alloys tested, the outer oxide thickness was highest, followed by the inner oxide and the transition layer. However, formation of the transition layer at 600°C is different from those at 400 and 500°C. Alloys 9Cr-ODS and HCM12A exhibited thick transition layers compared to those of T91 and HT-9. In addition, the thickness of transition layer of 9Cr-ODS at 600°C is relatively large, which is thicker than inner oxide. Detailed analysis of the oxide layer structure will be presented in Section 4.3.

4.1.3. Dissolved Oxygen Effect

The DO effect was determined on three F-M alloys, T91, HCM12A, and HT-9, by controlling the oxygen concentration at 10 (deaerated condition), 100 and 300 ppb in 500°C SCW. Oxidation rates determined from weight gain and oxide thickness in different DO concentrations are presented in Table 4.7Table 4.8 and in Figure 4.5. Similar to the previous section, the weight gain and oxide thickness were normalized to 182 hours using the data in Table 4.4. The result showed that the oxidation rate decreased as the DO concentration increased from 10 (deaerated condition) to 100 and 300 ppb. The effects are more pronounced in T91 and HCM12A than in HT-9. The corresponding alloy effect was observed in this set of experiments where HCM12A presented the lower weight gain than T91 and HT-9.

Data and plots of oxide layer thicknesses as a function of DO are presented in Table 4.8 and Figure 4.6. Results indicated that the thickness of three oxide layers exhibited similar trend as the weight gain. Outer oxide is thickest among three layers, followed by inner oxide and transition layer. It has been observed that the transition layer developed in a faster rate in high oxygen concentrations, which was validated by ratio of transition layer thickness to summation of outer and inner oxide thicknesses, Table 4.8. The thickness ratio revealed higher values (0.21 for T91, 0.19 for HCM12A, and 0.21 for HT-9) in the 300 ppb DO concentration than in the deaerated condition (0.13 for T91, 0.13 for HCM12A, and 0.18 in HT-9).

These results of DO effect on oxidation rate at 10, 100 and 300 ppb DO concentration were reported in the articles by Ampornrat and Was [2], and Was and Allen [3]. Together with results of weight gain of 25 and 2,000 ppb DO concentration

from the University of Wisconsin, the trend of oxidation rate of T91 and HCM12A was demonstrated. The weight gain was clearly the highest at 2000 ppb. The weight gain at 10 ppb DO is next highest, with those at 25, 100 and 300 ppb falling at intermediate values, with a minimum at 300 ppb. This trend of weight gain also agreed with Dooley et al. [4] who found that an oxygenate treatment (OT) with oxygen concentrations of 30-150 ppb in fossil plants resulted in lower weight gains than at either lower or higher oxygen levels.

4.2 Surface Oxide

The first step of the oxide structure characterization is to investigate the surface oxide that directly contacted the SCW. Morphology and structure of that surface oxide were characterized by SEM and XRD techniques. The surface oxide was also characterized by a surface sensitive technique, XPS, which can detect the chemical state of oxide species that formed in the first several hundred nanometers. Summary results of analysis of the surface oxide will be reported in this section.

4.2.1. Surface Oxide Morphology

Planar images of the exposure coupons observed from an optical camera revealed uniform oxide layer cover the surface. There was no evidence of oxide spallation in any alloy or testing condition in this study. The pictures from an optical camera are shown together with the SEM images for all exposure conditions in Figure 4.7 to Figure 4.13. These figures present the surface oxides on T91, HCM12A and HT-9 following exposure

at 400°C, 500°C, and 600°C in deaerated SCW, and at 500°C in SCW containing 100 and 300 ppb DO for ~200 hours. Development of the surface oxide after 1 and 10 hours exposure times at 500°C deaerated SCW also shown in Figure 4.8 and Figure 4.9, respectively.

The SEM images of surface oxide on alloy T91 revealed a rough and porous oxide morphology. The surface oxides formed at 400°C consist of equiaxed grains, with an average size of 1-3 μm, Figure 4.7. At 500°C, development of the oxide surface as a function of exposure time was investigated. The oxide formed after 1 hour exposure appeared as small (~1 μm) equiaxed grains. Pores were observed only on alloy T91. After 10 hours exposure, the oxide grains significantly grew to twice the size of those at 1 hour exposure, Figure 4.8. Pores formed extensively on T91, and started to develop on HCM12A and HT-9, Figure 4.9. After 182 hours exposure, the grain size increased to 2-5 μm and the grain are more porous, as evidenced from the holes in the middle of each grain, Figure 4.10.

The specimens exposed in 500°C SCW containing 100 and 300 ppb DO concentration exhibited similar morphology of those exposed to deaerated SCW at the same temperature, Figure 4.11 and Figure 4.12. At 600°C (Figure 4.13), the oxide grains were about 5 μm in size and the pore size were smaller than that at 500°C. In addition, the samples exposed at 600°C contained numerous cracks on the surface oxide, Figure 4.14a. Most of the cracks propagated along the oxide grain boundaries and penetrated deep into oxide layers and stopped at the transition layer, Figure 4.14b. These cracks could have occurred during the system cooling due to the thermal expansion mismatch between each oxide layers and alloy substrate.

4.2.2. Surface Oxide Phase

The structure of the surface oxide was determined by glancing angle (3° incident angle) XRD in order to confine the analysis to the oxide layer. Because of its greater thickness, the specimens from the 600°C test were investigated using XRD in the θ-2θ mode. Figure 4.15 shows the results for alloys T91, HCM12A and HT-9 before exposing in SCW. All three F-M alloys exhibited iron (BCC) phase with an average lattice constant of a = 2.873 ± 0.005 Å. Comparisons of the observed diffraction peaks from both alloy and surface oxide phases, and the peaks from standard JCPDS are shown in Appendix II.

Figure 4.16 to Figure 4.19 show the results for alloy T91, HCM12A and HT-9 exposed in all environments studied. The XRD results obtained from all three alloys are similar. In all cases at 500°C and 600°C, magnetite (Fe_3O_4, *Fd3m*, a = 8.396 Å) is the only phase detected. In fact, the only other phase detected was BCC iron at 400°C. Because the oxide is considerably thinner at 400°C than at 500°C, the result could be due to the metal from the underlying alloy. The high iron content measured in the surface of the outer layer is likely due to metallic iron. It is important to note that a chromite phase ($FeCr_2O_4$, *Fd3m*, a = 8.379 Å) also has a similar spinel structure with relatively close lattice parameter to magnetite. Nevertheless, the analysis results (will be shown in next section) were concluded from the fact that only Fe and O are present in the surface oxide, thus the surface oxide is magnetite. More detail about characterization of spinel structure oxides will be described in section 4.4.

4.2.3. XPS Analysis of Surface Oxide

Chemical state of the surface oxide was analyzed by the XPS technique. This technique is very sensitive to the chemical state of elements present on the surface with analysis depth of only 1-10 nm. An advantage of the technique is that it can detect the chemical state of surface oxide and has low detection limit. Samples were initially surveyed from high (1100 eV) to low (0 eV) energy with an 89 eV pass energy X-ray. The results from the survey showed iron (Fe2S, Fe2P, FeL3M23), oxygen (O1S, O_{KVV}), and carbon (C1S). Since Fe2S and O1S are considered as major peaks for iron and oxygen, respectively, the multiplex scan was performed with these peaks. Fe2P and O1S spectra were fitted by Auger Scan commercial software.

The fitting process is important because these elements are present in more than one form and are showing different binding energies (e.g., Fe^{2+} and Fe^{3+} in Fe_3O_4). In addition, the binding energy for Fe^{2+} and Fe^{3+} are close in energy. Therefore, the peak of Fe2P is a summation of these two peaks. Using the curve fitting program, these overlap peaks can be distinguished. Table 4.9 shows the peak fitting result compared to data from the literature [5-8] of Fe2P and O1S. The Fe2P spectrum is composed of $Fe2P_{3/2}$ (Fe^{2+}, Fe^{3+}, and satellite) and $Fe2P_{1/2}$ peaks. The O1S spectrum is composed of O^{2-} and OH^- peaks.

In order to characterize the oxide forms, ion compounds in each oxide were considered. The ion compounds for Fe_2O_3 are Fe^{3+} and O^{2-}. Fe_3O_4 is composed of Fe^{3+}, Fe^{2+} and O^{2-}. Moreover, OH^- could combine with Fe^{2+}, Fe^{3+} and O^{2-} to form FeOOH, $Fe[OH]_2$, or $Fe[OH]_3$. The binding energy of Fe^{3+} from Fe_2O_3 for $2P_{3/2}$ and $2P_{1/2}$ is located at 711 eV and 723.3 eV, respectively [6]. The Fe^{3+} from Fe_2O_3 also exhibits the

satellite peak at 716 eV [7]. The binding energies of Fe^{3+} in Fe_3O_4 and FeOOH are located at same positions as Fe^{3+} from Fe_2O_3 but it does not exhibit the satellite peak [5]. Fe_3O_4 has another chemical state Fe^{2+} located at 710 eV [5, 8]. These facts help to distinguish the oxide types on the sample surface. The oxygen chemical states, O^{2-} and OH^- display peaks at 529.90 eV and 531.80 eV respectively.

Figure 4.19 and Figure 4.20 present the XPS spectra from T91 and HCM12A exposed in 500°C SCW with deaerated condition and containing 100 ppb DO. The results suggested that the oxide types observed on T91 and HCM12A in SCW are Fe_2O_3, Fe_3O_4, FeOOH, $Fe[OH]_2$, and $Fe[OH]_3$. There are not clear conclusions for the different between two SCW environments. Since the analysis depth of XPS is from 1 nm to 10 nm from the surface, it is possible that there is a thin layer of oxide film or small cluster of hematite (Fe_2O_3), FeOOH, $Fe[OH]_2$, and $Fe[OH]_3$, that, by virtue of its thickness, would go undetected by X-ray analysis. However, the quantitative ratio of Fe_2O_3, Fe_3O_4, FeOOH, $Fe[OH]_2$, and $Fe[OH]_3$ cannot be determined due to the coincidence in binding energy for Fe^{3+} from Fe_2O_3 and Fe^{3+} from Fe_3O_4 at 711 eV.

4.3 Oxide Scale Structure and Composition

The results from SEM investigation of cross sections of corrosion coupons showed that the layers of oxide formed beneath the surface oxide. The oxide scale structure, composition, and thickness are different in each of the alloys and exposure environments. Analysis of the oxide structure will lead to an understanding of the oxidation mechanisms of these alloys in SCW. This section will describe the structure and the composition of oxide scales formed on the F-M alloys in different conditions of SCW.

Cross sections of corrosion coupons showed that the oxide structure on the F-M alloys exposed in SCW presented mainly a three-layer structure, an outer oxide, an inner oxide, and a transition layer. Figure 4.21 to Figure 4.29 show cross-section images of T91, HCM12A, HT-9, and 9Cr-ODS coupons exposed to all environments. Composition profiles from EDS line scans are shown opposite the SEM image for each of the three alloys. The composition profiles determined by EDS line scans show two distinct oxide/metal ratios that correspond to the two oxide layers. The oxygen content is similar in both outer and inner oxide layers. The outer oxide is predominantly iron oxide whereas the inner layer contains a significant amount of chromium. The transition layer is characterized by a sharp drop in the oxygen content with distance from the inner oxide. In addition to these three layers, a porous Cr-rich spinel oxide and a porous zone were observed in the samples exposed in 600°C. Figure 4.30 shows the oxide scale structure on four F-M alloys exposed in 600°C deaerated SCW, which also represents all of oxide characteristics observed in this study.

4.3.1. Outer oxide

The outer oxide is a layer that was in contact with SCW. As described in the previous section, the outer oxide phase is magnetite and the surface morphology was very rough. Composition analysis showed that the outer oxide consisted of Fe and O, and has an oxygen-to-metal (O/M, M is metal) ratio ~1.3. The composition is consistent with a Fe_3O_4 structure that was confirmed by XRD. The scale consisted of columnar grains of magnetite. The surface pores (or roughness) were located only at the oxide/ water interface, and did not penetrate throughout the layer. (The porosity that was observed in Figure 4.21 to Figure 4.29 resulted from mechanical polishing damage since the magnetite grains are very brittle. Cross section samples that were carefully polished are shown Figure 4.30.) Small voids were observed inside some of magnetite grains, Figure 4.30b. Void size measured in TEM mode was ~100 – 500 nm. Interface of the outer/inner oxides is smooth and flat, possible exhibiting the original surface of alloy substrate.

4.3.2 Inner Oxide

Morphology of inner oxide was distinguished from the outer oxide in which the inner layer appeared to be rough with a lot of small particles and precipitates but the outer oxide consisted of big grains of magnetite, Figure 4.30. Composition of the inner oxide consisted of Fe, Cr, O and minor alloying elements, and exhibited an O/M ratio of ~1.1 to 1.3, which corresponds to an oxide with a nominal composition of $(Fe,Cr)_3O_4$. In order to determine the ratio of Fe and Cr in the oxide, the compositions were averaged from a line scan across the inner oxide layer where the composition profile was flat, Figure 4.21 to Figure 4.29. Table 4.10 reports atomic percent and atomic fraction in $(Fe,Cr)_3O_4$. The results showed that the ratios of Fe and Cr are slightly different in each environment.

However, a significant trend of the Fe:Cr ratios was observed in each alloy. The averaged Cr concentrations in the inner oxide of T91, 9Cr-ODS, HCM12A and HT-9 from all tests are 9.5, 10.4, 11.8 and 13.3 at%, respectively. It was observed that the Cr concentrations in the inner layer are relatively close to that in the original alloy substrate, and slight enrichment was observed. Corresponding Fe:Cr:O ratios of inner oxide in T91, 9Cr-ODS, HCM12A and HT-9 are 2.4: 0.7: 4.0, 2.4: 0.7: 3.9, 2.1: 0.9: 4.0, and 2.1: 1.0: 4.0, respectively. From all alloys and environments the averaged Fe:Cr:O ratio is ~2.2: 0.8: 4.0, which possibly represents a stoichiometry of Fe_2CrO_4, or a solid solution of oxide Fe_3O_4 and $FeCr_2O_4$. Since the thickness of this layer is small, the oxide phase cannot be determined by XRD. The phase characterization determined by TEM will be reported in next section.

The major precipitate observed in the inner oxide is Cr-rich $M_{23}C_6$, where M is metal elements Cr, Fe, Mo, etc. This precipitate type was observed mainly at PAG boundaries, Figure 4.31. Trends of minor elements were also observed in the inner layer from the EDS scans, Figure 4.21 to Figure 4.29. In T91, the Mo content in the inner layer is slightly higher than in the outer layer and is closer to the bulk metal value. The same is true for Cu and W in HCM12A, and Ni in HT-9. In the tests at 500°C, a peak in the Cr level can be observed at the inner/outer oxides interface.

4.3.3. Transition Layer and Cr-enriched Oxide

Transition layer is a region between the inner oxide and the alloy substrate, where the metal content increases to bulk values and the oxygen content decreases to nearly zero. The transition layer is difficult to image but appears in BSE mode in the SEM as it showed better Z-contrast in image. It was found that the distinctive morphology of the

transition layer was observed on alloys exposed in 500 and 600°C SCW. In 500°C SCW, the distinguished morphology of transition layer can be observed on HT-9 tested with deaerated condition and in 100 ppb DO (Figure 4.22 - Figure 4.25), and HCM12A tested in 300 ppb DO (Figure 4.25). Since the transition layer at 400°C test was difficult to observed, the layer thicknesses reported in Table 4.2 - Table 4.6 were measured from the EDS composition line scans.

At 600^{o}C the transition region became more apparent in BSE images as rough morphology between the inner oxide and the alloy substrate, Figure 4.26 to Figure 4.29. Aside the transition layer, two structures of Cr rich oxide and porous region were observed in samples tested at 600°C, Figure 4.30. The Cr enriched oxide regions were observed at the interface of the transition layer and the alloy substrate in some parts of coupon. The porous regions were observed in the inner oxide and transition interface of T91 and HT-9.

The Cr-rich oxide appears as a dark area in images of 600^{o}C samples in Figure 4.26 - Figure 4.29. Two EDS line scans were performed for these samples; the first line scan ws through a regular transition layer, the second line was through the dark area in Figure 4.26 - Figure 4.29. The second line shows a Cr-enriched region that consisted of Fe, Cr and O. Composition maps of 9Cr-ODS tested at 600°C (Figure 4.32) show a Cr rich region at the transition/alloy interface with enrichments of Cr, O, W and Si. The Cr-enriched area in the 600^{o}C test has an Fe:Cr ratio of 1.0 in an oxide compound of $(Fe,Cr)_3O_4$. However, the exact composition cannot be determined with SEM-EDS due to the Cr-rich oxide areas are too small, thus the area was characterized with STEM-EDS.

4.3.4. Alloy Effect on Oxide Structure at 600°C

In 600°C SCW, the F-M alloys exhibited a four layer oxide structure; (i) an outer layer of magnetite (Fe_3O_4), (ii) an inner layer of Fe-Cr oxide ($(Fe,Cr)_3O_4$), (iii) a transition layer formed at the interface of inner oxide and alloy substrate, and (iv) a Cr-enriched oxide formed in some regions between the transition layer and alloy substrate, Figure 4.30. In addition, a porous region was observed in the inner oxide and transition interface of T91 and HT-9. There are major differences in the oxide layer thicknesses between these four F-M alloys exposed at 600°C, Figure 4.33. The outer oxide is the thickest in all cases and was consistent with measured weight gains. However, the thickness of the inner oxide and the transition layer do not follow the trend of either weight gain or Cr concentration. T91 exhibited the thickest inner oxide, followed by HT-9, HCM12A, and 9Cr-ODS. The transition layers formed on 9Cr-ODS are much thicker than those of other alloys. The porous Cr-rich spinel oxide partially formed on 9Cr-ODS, HCM12A and T91, but it was rarely found on HT-9.

In order to compare the thicknesses of oxide layers in each alloy, ratios of (inner oxide + transition layer + Cr-rich)/ outer oxide were determined. It was found that The values for T91 and HCM12A are close to 1 while that for HT-9 is less than 1, and for 9Cr-ODS is higher than 1, Table 4.6.

4.4 Microstructure of Alloy and Oxide

Due to spatial resolution limits of the SEM, detailed microstructure of the inner oxide and the transition layer was still indeterminate in terms of phase and chemical composition. A better characterization of the scales was provided by TEM techniques. The microstructure of alloy and oxides were characterized with the TEM by focusing on phase, morphology, and microchemistry of the oxide scales. In the first part, microstructure of alloys will be reported in brief in order to compare with microstructure of the oxides. Alloy HCM12A, which contains an intermediate level of Cr content, was examined in all environments and used to represent the oxide microstructure of F-M alloys. Specimens of HCM12A oxidized in 400, 500, and 600°C deaerated SCW were characterized to investigate effects of the SCW temperature. The DO effect was observed on HCM12A tested in 500°C SCW containing 300 ppb DO concentration. All of F-M alloys from a test at 600°C were characterized in order to determine the alloy effect on formation of the oxides. Summary of the characteristic of the oxides of all alloys and environments is listed in Table 4.11 and Table 4.12.

4.4.1. Microstructure of Alloys

The microstructure of the F-M alloys after heat treatment consisted of a prior austenite grain (PAG) size of ~9, 13.5, 50 and 10 μm for T91, HCM12A, HT-9 and 9Cr-ODS, respectively. Figure 4.34 shows the microstructure of HCM12A before oxidation test. Each PAG contains several equiaxed sub-grain packets (packet size ~4 μm) that have martensite laths aligned in the same direction. The lath size was about 0.2-0.5 μm

by 2-5 μm. Selected area electron diffraction (SAED) from a lath (Figure 4.34 c and d) showed that the alloy has BCC structure with a = 2.86 ± 0.2 Å, which matches with Fe ($Im\bar{3}m$, a = 2.866 Å). Note that the slight tetragonal elongation in martensite cannot be distinguished due to the limited resolution of SAED of TEM. Chromium is distributed uniformly in the lath matrix as solid solution. Precipitate particles decorate the PAG, sub-grain, and lath boundaries. Coarse precipitate particles of Cr-rich $M_{23}C_6$ (M is metal elements of Cr, Fe, Mo, etc.) are located mainly on PAG and lath boundaries with size ~50-100 nm, Figure 4.35. SAED from the Cr-rich $M_{23}C_6$ precipitates exhibited $Fm3m$ structure with a = 10.30 ± 0.3 Å, Figure 4.36. Another precipitate with size ~10-30 nm and major elements V and Nb are located near $M_{23}C_6$ and inside the lath matrix. These V and Nb rich precipitates are likely carbides or nitrides, i.e., NbC, NbN, VN, or (NbV)C [9]. Due to the detection limit of the energy dispersive spectrometer (EDS) in which the light elements are difficult to detected, the exact composition of V and Nb rich particles cannot be determined. Copper-rich particles were also found at lath boundaries. Precipitate particles of Cr-rich $M_{23}C_6$ and V-Nb are shown in Figure 4.37, and a Cu-rich precipitate is shown in Figure 4.38. The microstructure of T91 is shown in Figure 4.39.

4.4.2. HCM12A Oxidized in 400°C Deaerated SCW

Oxides formed on HCM12A tested in 400°C deaerated SCW consisted of outer and inner layer oxides. It was found that the transition layer that exhibits distinct morphology was not observed in the specimen exposed at this temperature. Total oxides thickness was only ~2.29 μm so that every layer can be shown in one TEM image. Figure 4.40 a and b illustrate bright field (BF) and high angle annular dark field (HAADF)

images of two oxide layers and alloy substrate. Outer layer oxide consisted of columnar grains of magnetite, Figure 4.41. The grain size of magnetite formed at this temperature was ~0.2 to 0.5 μm wide and ~0.8 to 1.5 μm long. SAED from magnetite grains (Figure 4.41b and c) showed single diffraction of FCC structure with a = 8.295 ± 0.15 Å matched with that of magnetite ($Fd\bar{3}m$, a = 8.396 Å), and agreed with results from XRD. No void or precipitates were observed in the magnetite layer.

The morphology of the inner layer oxide is different from that of the outer layer in that the grains were much smaller. Figure 4.42 a and b present BF and HAADF images of the inner layer oxide. It was observed that the layer contains small equiaxed oxide grains, precipitates and microcracks. The small oxide grain size was reflected in a ring pattern in SAED, which occurred from diffractions of multiple random-oriented small grains, Figure 4.42c. The oxide grain size was determined from a dark field (DF) image indicating that the grain size of the oxide was 83 ± 41.95 nm, Figure 4.42d. The SAED was interpreted as a spinel structure ($Fd\bar{3}m$) with a lattice parameter of 8.59 ± 0.14 Å, Figure 4.43. This result is close to the structure of Fe-Cr oxide of the composition $Fe^{2+}(Fe^{3+}_{2-x}Cr^{3+}_{x})O^{2-}_{4}$, where $0<x<2$. When x is 0, the oxide phase is magnetite (a = 8.396 Å). If x is 2, the oxide phase is chromite ($FeCr_2O_4$, a = 8.378 Å). The oxide remains a spinel structure as long as Cr^{3+} is substituted for Fe^{3+} in the range $0<x<2$, and the lattice parameter ranged between 8.378 to 8.405 Å [10, 11]. Due to a resolution limit of ~0.1 Å in SAED, the lattice parameter difference in this system cannot be determined. Composition analysis by EDS from the previous section indicates that the ratio of Fe to Cr in the inner layer was ~2.2 to 0.8.

An important observation of the inner layer oxide is the presence of precipitate particles. Precipitates of Cr-rich $M_{23}C_6$ were observed in some regions of inner oxide. Images in Figure 4.44 show precipitate particles and a SAED pattern. Analysis revealed a $Fm3m$ structure with a = 11.35 ± 0.5 Å with major compositions of Cr, Figure 4.45. The structure is close to that of Cr-rich $M_{23}C_6$ particle found in the alloy. Aside from the Cr-rich carbide, precipitates of V-Nb enrich particles (Nb map is not shown in the figure) were also observed in the inner oxide, Figure 4.45. From the same figure, Cu precipitates tend to agglomerate in the inner layer. This implies that the inner oxide was the original alloy substrate that was subsequently oxidized. Oxygen ions diffused into the alloy matrix and formed a Fe-Cr oxide without interacting with the precipitates. As shown in Figure 4.44a, the precipitates outlined the PAGB and subgrain boundaries of the original alloy.

Another feature observed in the inner oxide is microcracks between oxide grains as shown in Figure 4.42a, Figure 4.42b and Figure 4.44b, with some cracks aligned perpendicular to the surface. These cracks possibly arose from stress during growth of the oxide or during the cooling process. Thus the inner oxide layer is considered very porous because it consisted of small oxide grains, pores, and cracks.

High resolution transmission electron microscope (HRTEM) image was taken at grain boundary in magnetite layers, at outer - inner oxide interface, and at inner oxide – alloy interface, Figure 4.46. It is found that magnetite grains attached to each other with small angle orientation in which (111) on the left grain attached with (112) on the right one. A series of dislocations were observed at the grain boundary. No voids were observed at the magnetite boundary.

4.4.3. HCM12A Oxidized in 500°C Deaerated SCW

Oxides formed on HCM12A in 500°C deaerated SCW consisted of an outer oxide, an inner oxide, and a transition layer. Figure 4.47 presents SEM and TEM images of three layers of the oxide formed on HCM12A tested in deaerated SCW at 500°C. The outer layer oxide consisted of columnar grains of magnetite, Figure 4.48. The grain size of magnetite formed at this temperature was ~0.8 ± 0.3 μm wide and 2 ± 0.5 μm long. SAED from magnetite grains showed single diffraction of FCC structure matched with that of magnetite (a = 8.342 ± 0.04 Å), which agreed with results from XRD and 400°C test. No precipitate particles were observed in the magnetite layer. Voids are present in some magnetite grains, Figure 4.48a. Void size was approximately 0.5 μm.

The inner layer oxide formed in this temperature exhibits similar morphology as that in 400°C, which consisted of small equiaxed oxide grains, precipitate particles, microcracks and micropores. TEM images that show the microcracks and precipitate particles of the inner layer oxide are Figure 4.49 a and b. SAED exhibits spinel structure with lattice parameter of 8.41 ± 0.02 Å, Figure 4.49c, which matches with that of $Fe^{2+}(Fe^{3+}_{2-x}Cr^{3+}_{x})O^{2-}_{4}$, where x ~ 0.8 (result from EDS of SEM). Grain size of spinel oxide which measured from DF image was 54.30 ± 24.02 μm, Figure 4.50. Along with Fe-Cr spinel oxide, precipitate particles were observed throughout the layer. A large precipitate particle of Cr-rich $M_{23}C_6$ were observed in this layer, Figure 4.49a and Figure 4.51. SAED analysis revealed a $Fm3m$ structure with a = 11.00 ± 0.3 Å. Other types of particle are Cu and V-Nb, which were detected in composition mapping, Figure 4.52. These particles are small so that they can be observed only at high magnification. Cu particles tend to segregate in the inner oxide. The particle size of Cu varied from 20-100

nm. V-Nb particles were found near $M_{23}C_6$ precipitates. The distribution of V-Nb particles was similar to that in the alloy.

Located between the inner oxide and the alloy substrate, a transition layer was observed in specimens tested at 500°C. The transition layer appeared to be inhomogeneous and of different morphology from that of the inner oxide and alloy substrate. At low magnification of BSE (SEM) image, the inner layer-transition layer appeared rough with dark lines penetrating to the alloy substrate. A similar feature was observed in HAADF images of the transition layer (Figure 4.53 a and b). Note that no voids or pores were observed in the transition layer, which distinguished it from the inner oxide. The boundary of transition layer and the alloy substrate is not clearly defined.

In order to characterize the transition layer, SAED and composition mapping in STEM mode were used. It was observed that the dark lines were spinel oxide formed along lath and PAG boundaries. Composition mapping (Figure 4.53) showed that oxygen diffused into the area between the lath boundaries, where precipitate particles were located. The morphology of intra-lath in the transition layer appeared rough and different from the alloy matrix, as shown in Figure 4.53 a and b. SAED taken from an area inside a lath of Figure 4.53c (circled) exhibited two diffraction patterns at once. One pattern consisted of single diffraction of Fe (BCC) (bright spots) and spinel oxide (ring pattern), indicating that the grain size of spinel oxide was relatively small compared to that of iron. Indexing diffraction patterns from the $[\bar{1}11]$ (Figure 4.53e) and from the [012] (Figure 4.53f) zone axes confirmed that the bright spots are Fe (BCC), a = 2.93 Å. A ring pattern was also observed, that corresponded to spinel oxide, a = 8.56 Å. Indexing of the diffraction pattern is shown in Figure 4.54. A dark field image (Figure 4.53d) was

produced from spots of ring pattern in Figure 4.53f showed that the oxide nucleated inside the lath in the transition layer. Similar feature also observed in Figure 4.50b.

4.4.4. HCM12A Oxidized in 500°C SCW Containing 300 ppb DO

Microstructure of scales formed on HCM12A exposed in 500°C SCW containing 300 ppb DO is similar to that of 500°C deaerated SCW. The scales consisted of an outer layer of magnetite, an inner layer of $Fe^{2+}(Fe^{3+}_{2-x}Cr^{3+}_{x})O^{2-}_{4}$, where x ~ 1 (result from EDS in SEM), and a transition layer. Figure 4.55 and Figure 4.56 present BF and HAADF images of oxide scales on HCM12A exposed in 500°C SCW containing 300 ppb DO. A major difference between samples is that sample exposed in 300 ppb DO formed a thicker transition layer than that of deaerated SCW, as presented in Figure 4.55d. The outer oxide consisted of magnetite grains. The inner oxide consisted of equiaxed Fr-Cr spinel oxides. Figure 4.57 shows BF and DF images of the inner layer oxide exhibiting oxide grain size ~55.80 μm. Composition maps reveals Cr-rich carbide, Cu, and V-Nb rich precipitates in this oxide layer, Figure 4.58. Micropores were found mostly near the inner oxide-alloy interface, Figure 4.59a.

The transition layer where oxide grains nucleated in the lath structure became more noticeable in this environment, Figure 4.59a. Similar to sample tested in deaerated condition, the transition layer on sample tested in 300 ppb DO consisted of Fe-Cr spinel oxide at major grain boundaries, and small oxide grains precipitated inside the lath. The thickness of this layer is ~1.5 μm. SAED was taken from circled area in Figure 4.59a exhibited two patterns at once. Analyses of the diffraction pattern showed that the phase shows bright region matched with Fe (BCC) of a = 2.89 Å from $[\bar{1}11]$ (Figure 4.59b),

[$\bar{1}$12] (Figure 4.59c) and [$\bar{1}$13] (Figure 4.59d). The weak ring pattern can be indexed as FCC spinel structure with a = 8.48 Å.

4.4.5. HCM12A Oxidized in 600°C Deaerated SCW

Scales formed on HCM12A exposed in 600°C deaerated SCW consisted of three layers; outer oxide, inner oxide, and transition layer. In addition porous Cr-rich regions were also observed the between transition layer and alloy substrate in some locations. Figure 4.60 shows SEM and TEM images of the layers and a Cr-rich region formed on HCM12A after exposure at 600°C for 190 hours. The thicknesses of the outer, inner, and transition layers were 20.53, 15.50, and 6.35 μm, respectively. Since microstructure of outer and inner oxides are similar to those at 400 and 500°C, analysis of the specimen exposed at this temperature focused on transition layer and porous Cr-rich region.

The outer oxide consisted of the magnetite phase with grain size 0.7±0.5 μm wide and ~3±1.5 μm long as shown in Figure 4.60b and Figure 4.61. Comparison of magnetite grain sizes in Table 4.11 and 4.12 showed that the grain size increased as a function of temperature. A few voids were observed in some magnetite grains. The inner oxide consisted of small grains of spinel oxide $Fe^{2+}(Fe^{3+}_{2-x}Cr^{3+}_{x})O^{2-}_{4}$, where x ~ 0.9 and precipitate particles embedded in the layer, Figure 4.60c. The inner oxide exhibited higher porosity than that observed at 500°C. Spinel oxide grain size determined from DF was 50.79±28.56 μm, which is the smallest among the three test temperatures, Table 4.11 and 4.12. Pores and cracks are observed throughout the inner layer, Figure 4.60c, providing evidence of a short circuit diffusion path for oxygen toward the inner oxide-transition interface.

The microstructure of the transition layer formed at 600°C was complex and distinct from that at 500°C. The transition layer at 500°C was described as the alloy in which oxygen had gradually diffused. Oxygen penetrated along lath boundaries forming spinel near the interface between the transition and inner oxide layers. For the specimen tested at 600°C, the morphology of the transition layer consisted of a lath structure with fine oxide precipitates, precipitate particles at lath boundaries, and a strip of Cr_2O_3 along the lath boundaries, Figure 4.60d, Figure 4.62, and Figure 4.63. It was observed that the laths in the transition layer are different from the laths in the alloy matrix with fine oxide precipitates distributed throughout the laths, Figure 4.62a and b. In addition, big oxide particles (or strips) formed around the laths in the transition layer. Figure 4.62c and d illustrate the interface of transition layer-alloy with BF and DF images, which clearly shows the difference in morphology of the transition layer and alloy substrate. A HAADF image in Figure 4.63 presents the detailed microstructure of the transition layer. The image shows; (i) small oxide grains nucleated in lath matrix, (ii) Cr_2O_3 formed at lath boundaries, and (iii) precipitates of V, Nb, W, Mo and Cu enriched compounds.

Due to the complex structure of the transition layer, SAED was taken from various specific areas. SAED from inside the laths exhibited two diffraction patterns; Fe (BCC) appeared as a bright spot pattern and spinel oxide as a weak spot pattern, Figure 4.64. The bright pattern can be indexed by a [012] zone axis by assuming a structure of Fe (BCC), and the weak pattern can be indexed by [013] and $[\bar{2}33]$ zone axes of spinel oxide. Detail of indexing the diffraction pattern is shown in Figure 4.65. The result exhibited fine oxides inside the lath with a preferred orientation that related to Fe matrix. The lattice parameter of the spinel oxide is approximately 8.50 ± 0.01 Å, which is close

to that of $Fe^{2+}(Fe^{3+}_{2-x}Cr^{3+}_{x})O^{2-}_{4}$, where 0<x<2 (the exact composition cannot be determined because the particles are very small). Dark field image from Fe and spinel oxide diffraction spots showed that the lath remained in the iron structure (Figure 4.64c), and the oxide partially formed around and inside the lath (Figure 4.64d). These results indicate that selective oxidation occured in the transition layer, both inside the laths and at lath boundaries.

Another oxide phase, chromia (Cr_2O_3) was detected at two locations; (i) the lath boundary, and (ii) the interface of the transition layer and the alloy. This phase appeared as a dark strip when observed in dark field mode, Figure 4.66a. The feature was observed as bright strip by tilting near a zone axis in bright field mode, Figure 4.66b. The Cr_2O_3 formed as equiaxed grains or thin ribbons at lath boundaries, but as a thick ribbon at the interface between the transition layer and alloy. Investigation found that the Cr_2O_3 did not form continuously at the interface of the transition layer and the alloy substrate. Figure 4.67 shows HAADF images of the interface where (a) Cr_2O_3 strip formed, and (b) the interface without Cr_2O_3. The average width of Cr_2O_3 grains was 240±63 nm.

In order to verify the oxide phase, SAED was taken in four different directions using a grain at the transition layer - alloy interface, Figure 4.66c. Due to the complex rhombohedral (trigonal) structure, indexing of the diffraction patterns was performed by the diffraction image simulation software MacTempas© [12]. The diffraction pattern in Figure 4.66c was indexed as a [241] zone axis by assuming an $R\bar{3}C$ structure. The lattice parameters of Cr_2O_3 are; a = b = 4.959 Å, c = 13.594 Å, and $\alpha = \beta = 90°$, $\gamma = 120°$. The result agreed with synchrotron analysis results reported by Motta, et. al. [13] in which

they observed Cr_2O_3 formed in the transition layer and at the transition and alloy interface of 9Cr ODS F-M alloy exposed at 600°C SCW.

Elemental mapping in Figure 4.68 shows that the dark strips in the HAADF image have high concentration of Cr and O, which agrees with SAED results. The element maps shown in this figure consisted of Fe, Cr, O, Cu, V, Nb, Mo, and W. Iron was present in the lath structure, which was similar to those in the alloy substrate. Chromium was concentrated at the lath boundaries in the forms of Cr_2O_3 ribbon, and perhaps including $Cr_{23}C_6$ precipitates. Chromium was also distributed inside the laths in solid solution. Oxygen appeared in the transition layer in the form of a solid solution, and as an oxide at particular locations. In the form of a solid solution, the oxygen concentration was high at inner oxide - transition interface and dropped to very low levels at the transition layer – alloy interface. Oxygen was also concentrated at the lath boundaries as Cr_2O_3. Copper was found at the lath boundaries and was not associated with oxygen, implying that Cu precipitates were not oxidized. Other precipitates included V, Nb, Mo, and W enriched particles were observed at the lath boundaries.

In addition to the two oxide layers and the transition layer, a porous chromium rich region was observed at the interface of the transition layer and alloy substrate. The region appeared as a dark area in BSE (SEM) image, Figure 4.60a. The chromium rich region was not continuous, and was found only in some locations. The morphology of the chromium rich region was characterized by high porosity (Figure 4.60e and Figure 4.69) and was easily damaged during sample preparation with mechanical polishing and ion beam cutting. TEM images reveal that the region consists of small grains of oxide (50-100 nm). Pores and cracks were observed between oxide grains, which were confirmed

by two methods of tilting and focused-defocused techniques. An selected area was first focused then tilted to ±9.9°. The feature that is expected to be a pore will disappear when specimen was tilted, as shown by arrows in Figure 4.70 a and b. The presence of pores was re-confirmed by focused-defocused technique. Fresnel fringes at the feature's edge will be visible in an over-focused TEM image if the pores are exist. Figure 4.70c and d show the under-focused and the over-focused images, respectively. SAED taken from this region indicated a ring pattern of FCC structure and a = 8.48±0.02 Å, Figure 4.71. The lattice parameter matched to that of spinel oxide $Fe^{2+}(Fe^{3+}_{2-x}Cr^{3+}_{x})O^{2-}_{4}$, where 0<x<2. The composition analysis found that the region contains high Cr concentration than those of alloy substrate and intra-lath in transition layer, as shown in EDS spectrum in Figure 4.72. Major compositions of the porous Cr-rich consisted of Fe (~17.9 at %), Cr (~23.6 at %) and O (~53.8 at %). Corresponding atomic ratio of Fe:Cr:O is ~ 1.2:1.8:4. Therefore it is possible that the porous Cr-rich region consists of chromite ($FeCr_2O_4$).

4.4.6. T91 Oxidized in 600°C Deaerated SCW

T91 exposed in 600°C deaerated SCW exhibited similar oxide scale structure as HCM12A tested in the same condition. The scales consisted of an outer layer of magnetite, an inner layer of $Fe^{2+}(Fe^{3+}_{2-x}Cr^{3+}_{x})O^{2-}_{4}$, where x ~0.7 (results from EDS-SEM), a transition layer, and a porous Cr-rich region. The characterization for this alloy focused on microstructure and microchemistry in the transition layer. Figure 4.73 shows characteristic of the transition layer formed on T91, which consisted of fine oxide precipitates inside lath, precipitates of Cu rich particle, and Cr-rich Fe-Cr oxide around laths and at interface of transition layer and alloy substrate (parallel to the interface).

Morphologies of alloy, transition layer and inner oxide are distinct as shown in Figure 4.73a. Figure 4.74 presents the interface of transition layer and alloy substrate. The figure clearly shows that the Cr-rich Fe-Cr oxide formed at lath/ subgrain boundaries that perpendicular to the interface of scale. Simultaneously, the Cr-rich Fe-Cr oxide formed at the interface of transition-alloy substrate, which is not dependent to grain boundary or orientation. Figure 4.74b shows that the formation of Cr-rich oxide can occur inside lath.

Figure 4.75 presents the interface of inner oxide and transition layer, which clearly shows the difference in the microstructure of these layers. The inner oxide is very porous with micro-voids, Figure 4.75c. In a high contrast image (Figure 4.75 a), dark strips of Cr-rich oxide that connect to the Cr-rich oxide in the transition layer can be observed in the inner oxide. Pores in the inner layer oxide were observed as clusters of micro-voids, Figure 4.75c. The size of micro-voids is approximately less than 100 nm, and size of the cluster is ~300-500 nm. Precipitates of Mo-rich and Cu-rich particles distributed throughout the layer.

The major difference of the transition layer on T91 and HCM12A is that the oxides around lath and at transition-alloy interface is Cr-rich Fe-Cr oxide, whereas the major oxide in HCM12a is Cr_2O_3. Figure 4.76a presents BF image of the Cr-rich oxide, which appeared as bright strip in the middle of a lath at the transition-alloy interface. SAED was taken from this feature (in circle) exhibiting a FCC spinel structure with a ~8.20 Å, Figure 4.76b and c. Again, the structure matches to that of $Fe^{2+}(Fe^{3+}_{2-x}Cr^{3+}_{x})O^{2-}_{4}$, where $0<x<2$. DF image was taken from the DP in order to confirm that the interested area is the Cr-rich strip, Figure 4.76d and e. The DF image shows that width of Cr-rich strip is ~100-200 nm. Composition analysis of the Cr-rich oxide indicated that the

Fe:Cr:O is 1.5:1.5:4, Table 4.12. Figure 4.77 shows the composition line scan across the Cr-rich oxide. In summary the Cr-rich oxide strips in the transition layer of T91 is $Fe^{2+}(Fe^{3+}_{2-x}Cr^{3+}_{x})O^{2-}_{4}$, where x ~ 1.5.

Composition maps of transition layer of T91 are presented in Figure 4.78. The maps show that Cr and O enriched at the Cr-rich oxide strips. Ni is likely to enrich in the transition layer in a form of solid solution. A Cu precipitate was observed in the layer. Si enriched at the lath boundaries associating with Cr and O.

4.4.7. HT-9 Oxidized in 600°C Deaerated SCW

Structure of oxide scales formed on HT-9 exposed in 600°C is different from those on HCM12A and T91. The oxide scales consisted of thick outer and inner layers, whereas the transition layer formed only in some regions as shown in Figure 4.30 and plots in Figure 4.33. Therefore the characterization of this alloy focused on the interface of inner oxide and alloy. Figure 4.79 and Figure 4.80 presents BF and DF images of the inner oxide and the alloy substrate of HT-9, respectively. The transition layer cannot be observed clearly in the BF mode, but it can be observed better under HAADF mode. Characteristic of the interface of inner oxide and alloy substrate consisted of pores, Cr-rich oxide band (non-porous), and transition region, Figure 4.80. Pores were observed right between the inner oxide and the alloy substrate with size ~200-500 nm. In the inner oxide next to the pores, Cr-rich oxide region was observed. This Cr-rich oxide formed as solid band with approximately 0.5-1 μm wide. No voids were observed in this Cr-rich region. The transition region in HT-9 was observed only in small area, Figure 4.80b. The transition region consisted of fine oxides precipitated inside alloy lath and Cr-rich oxide at the lath boundaries.

Similar to the other alloys, the inner oxide can be described as porous oxide layer of $Fe^{2+}(Fe^{3+}_{2-x}Cr^{3+}_{x})O^{2-}_{4}$, where x = 1.0. Pores were observed as clusters of micro-voids, Figure 4.81a. SAED from the inner oxide exhibits a FCC spinel structure of a = 8.96 Å, Figure 4.81b. The Cr-rich oxide region was discovered via the composition mapping, Figure 4.82 and Figure 4.83. It was found that concentrations of Cr and O are high in the inner oxide near the interface with alloy substrate. Fe tends to deplete in the same region. Composition of the Cr-rich strips was determined by EDS line scans and spot scans, Figure 4.84. The results agreed with composition mapping. It was found that the atomic ratio of Cr-rich oxide is Fe:Cr:O ~1.1:1.9:4, which is close to the chromite phase with a composition of $Fe^{2+}(Fe^{3+}_{2-x}Cr^{3+}_{x})O^{2-}_{4}$, where x ~ 2. The SAED was taken from this region in order to verify the oxide phase, Figure 4.85. The DP exhibited ring pattern of a FCC spinel structure. The results of composition and electron diffraction indicated that the Cr-rich oxide is chromite phase, $FeCr_2O_4$.

From the composition maps (Figure 4.82 and Figure 4.83), precipitate particles of Ni, V and Mo was observed. Ni is major precipitate observed in the HAADF images as bright particles with size ~200-500 nm, Figure 4.81c and d. Composition analysis showed that the particle is a compound of Ni (~25at%), Fe (~30at%) and O (~40at%), Figure 4.81e & f, and Figure 4.84a. However, the measurement could have some interference from the oxide matrix. Therefore the exact composition of the Ni-rich particle is still unclear. Other types of precipitate found are Mo and V. Si segregated in some regions near the interface of inner oxide and alloy substrate.

4.4.8. 9Cr-ODS Oxidized in 600°C Deaerated SCW

The oxide scales formed on 9Cr-ODS alloy are similar to those of T91 and HCM12A in which the scales consisted of an outer oxide, an inner oxide, a transition layer, and a porous Cr-rich oxide region. However the 9Cr-ODS exhibits relatively large transition layer, Figure 4.30. The oxide formation in this layer is important because the alloy exhibited low oxidation rate (by weight gain), which could be a result of the protective oxide formation in the layer. Therefore the characterization was focused on the transition layer and its interface with inner oxide and alloy substrate. Figure 4.86 presents HAADF images of transition layer, inner oxide, and alloy substrate of 9Cr-ODS exposed in 600°C deaerated SCW. Figure 4.87a shows the typical microstructure of the transition layer, which consisted of laths with fine oxide grains nucleated inside, Cr-rich Fe-Cr oxide formed between laths, and precipitates of W, Ti and Y enriched particles at the lath boundaries. Figure 4.87b shows the fringes of intra-lath small oxide grains (arrows).

Interface of the transition layer with the alloy substrate and the inner oxide are shown in Figure 4.88. Unlike T91 and HCM12A, the Cr-rich oxide strip that formed at the interface of transition layer and alloy substrate was not observed. However, the transition layer is distinct from the alloy substrate by formation of large Cr-rich oxide strips between laths. Precipitates observed in alloy are Ti-rich particle (Figure 4.88b) and Y_2O_3. Ti can be observed as small particle with size ~10-50 nm, Figure 4.88b. Since the size of Y_2O_3 particles is in nano-scale, this type of particle was only detected in the composition maps. On the inner oxide side, a large amount of pores and precipitates was observed, Figure 4.88c. Similar to other three alloys, the pores consisted of micro-voids

and nano-size particles inside, Figure 4.88d. The pore size varies from 200 to 500 nm. Precipitates in the inner oxide were found as the same types as in the transition layer.

Composition maps of the transition layer are presented in Figure 4.89 and Figure 4.90. The images clearly show enrichment of Cr and O, and depletion of Fe at the lath boundaries. Precipitates in the transition layer are W, Ti, and Y-rich particles. W is the biggest precipitate found in the layer with size up to 500 nm. Figure 4.89 shows several W-rich precipitates distributed inside lath and at lath boundaries. High magnification composition maps in Figure 4.90 show that W particle consisted of Cr and Fe. Precipitates of Ti were also observed with the similar size as in alloy substrate. Y_2O_3 nanoparticles are detected in the map as groups of particle, Figure 4.90f. Composition of the Cr-rich oxide was determined by EDS line scan and area scan, Figure 4.91. It was found that the Cr-rich oxide has Fe:Cr:O ~ 0.7: 2.1: 4.2, which also matches to that of chromite. Trace of Si was observed in some regions of chromite. Composition analysis of the W-rich particle found that the particle possible is an oxide compound of W (~25at%), Fe (~27at%) and O (~30%).

Figure 4.92 present BF images of Cr-rich oxide strips, which appeared as bright features. It was found that the Cr-rich strip composed of several oxide grains. Size of the grains is approximately 100 to 300 nm. SAED was taken from the oxide in order to characterize phase. The diffraction pattern (Figure 4.92c) exhibited a FCC spinel structure with a = 8.92 Å. DF image was taken from the diffraction spot in order to confirm the feature, Figure 4.92e. Together with the composition analysis, the Cr-rich oxide formed at the lath boundaries in transition layer is chromite ($FeCr_2O_4$).

Summary of microstructure analysis

In summary, microstructure of oxides formed on three F-M alloys; T91, HCM12A, HT-9 and 9Cr-ODS consisted of two oxide layers and a transition layer. The microstructure changes with the SCW temperature and the alloy type. At 400°C, only two layers of oxide were observed. At 500 and 600°C, three layers of an outer oxide, an inner oxide and a transition layer formed. In addition, a porous Cr rich region was found at 600°C. Figure 4.93 illustrates schematic diagram of oxides formed on T91, HCM12A, HT-9 and 9Cr-ODS in 600°C SCW. The outer oxide consisted of columnar grains of magnetite. Voids were found in some of magnetite grains. The inner oxide consisted of small equiaxed grains of Cr substitution in $Fe^{2+}(Fe^{3+}_{2-x}Cr^{3+}_{x})O^{2-}_{4}$, where x = 0.7, 0.9, 1.0 and 0.7 for T91, HCM12A, HT-9 and 9Cr-ODS respectively. A lot of defects including micropores and microcracks were observed in the inner oxide. The transition layer consisted of grain boundary oxidation and fine oxide grains precipitated inside the laths. Chromia and chromite formed at the lath boundaries and at interface of alloy – transition layer. Dense chromite layer also found at interface of transition layer – inner oxide interface of HT-9 (600°C). Precipitate particles of minor alloying elements also distributed throughout the inner layer and the transition layer. Enrichment of Si and Mo (in T91 and HT-9) was observed in the $FeCr_2O_4$ strips.

Table 4.1 The time-dependence of weight gain of T91, HCM12A, HT-9, and 9Cr-ODS exposed in deaerated SCW at 400 and 500°C.

Exp.	Temp. (^{o}C)	Exp. time (hours)	Acc. Exp. time (hours)	Weight gain (mg/dm^2)			
				T91	HCM12A	HT-9	9Cr-ODS
1	400	151.5		19.525 ± 1.993	16.043 ± 2.289	22.947 ± 2.246	
2a*		188.0	188.0	20.549 ± 1.881	17.331 ± 2.320	23.701 ± 2.219	
2b*		136.4	324.4	24.306 ± 1.982	22.261 ± 2.371	27.481 ± 2.265	
2c*		166.5	490.9	27.326 ± 2.059	25.398 ± 2.401	30.244 ± 2.320	
3	500	182.2		137.301 ± 1.949	119.940 ± 1.660	129.890 ± 1.705	
4a*		195.0	195.0	146.070 ± 2.264	133.142 ± 1.789	140.968 ± 2.313	73.229 ± 2.437
4b*		148.0	351.0	177.090 ± 2.294	168.573 ± 1.823		90.566 ± 2.520
5		1.0		15.824 ± 0.602	12.618 ± 0.751	9.612 ± 0.953	
6		10.0		38.151 ± 1.876	37.757 ± 0.566	41.988 ± 0.669	
7		477.0		195.499 ± 2.544	187.781 ± 0.820	204.393 ± 1.898	

* Samples were re-loaded in the next experiment

Table 4.2 The time-dependence of oxide thickness of T91, HCM12A, HT-9 exposed in deaerated SCW at 400 and 500°C.

Exp.	Temp. (°C)	Exp. time (hours)	Acc. Exp. time (hours)	Oxide layer thickness (μm)											
				T91				HCM12A				HT-9			
				Tot.	O	I	T	Tot.	O	I	T	Tot.	O	I	T
1	400	151.5		2.88 ± 0.36	1.39 ± 0.30	0.89 ± 0.20	0.60 ± 0.05	2.39 ± 0.25	1.14 ± 0.20	0.85 ± 0.14	0.40 ± 0.05	2.69 ± 0.22	1.21 ± 0.18	0.83 ± 0.12	0.65 ± 0.05
2a*		188.0	188.0												
2b*		136.4	324.4												
2c*		166.5	490.9												
3	500	182.2		12.12 ± 0.31	6.37 ±0.26	4.35 ±0.11	1.40 ± 0.08	10.57 ±0.22	5.31 ± 0.15	4.06 ± 0.12	1.20 ± 0.07				
4a*		195.0	195.0									12.69 ± 0.61	6.03 ± 0.33	4.74 ± 0.48	1.92 ± 0.41
4b*		148.0	351.0												
5		1.0						1.63 ± 0.13	0.71 ± 0.07	0.54 ± 0.09	0.38 ± 0.06				
6		10.0						3.28 ± 0.33	1.52 ± 0.24	1.16 ± 0.21	0.60 ± 0.10				
7		477.0		15.83 ±0.56	8.21 ±0.46	6.08 ±0.23	1.53 ±0.24	14.84 ±0.65	7.00 ±0.53	5.88 ±0.39	1.96 ±0.40	14.72 ±0.86	7.21 ±0.58	5.34 ±0.43	2.17 ±0.46

* Samples were re-loaded in the next experiment

O : outer layer oxide

I : inner layer oxide

T : transition layer

Table 4.3 Relations of weight gain vs. time fitted by parabolic, power and logarithmic equation.

Temperature (°C)	Alloy	R^2		
		Parabolic	Power	Logarithmic
400	T91	0.4994	0.9992	0.8493
	HCM12A	0.9282	0.9928	0.6938
	HT-9	0.0840	0.9991	0.9253
500	T91	0.9815	0.9965	0.9239
	HCM12A	0.9907	0.9976	0.9267
	HT-9	0.9915	0.9961	0.9409
	9Cr-ODS	0.8598	1.0000	0.7495

Table 4.4 Oxidation rate constant and power from the power equation ($w = k_w t^{nw}$ and $h = k_h t^{nh}$) of time-dependence of oxidation rate determined from weight gain at 400 and 500°C, and oxide thickness at 500°C deaerated SCW.

Temp. (°C)	Alloy	Oxidation rate from	Oxidation rate const. ($mg/dm^2/h$) or ($\mu m/h$)	power	R^2
400	T91	Weight gain	4.53	0.29	0.9992
	HCM12A	Weight gain	2.35	0.39	0.9928
	HT-9	Weight gain	5.44	0.28	0.9991
500	T91	Weight gain	15.43	0.42	0.9965
	HCM12A	Weight gain	13.07	0.43	0.9976
	HT-9	Weight gain	11.02	0.48	0.9961
	9Cr-ODS	Weight gain	10.89	0.36	1.0000
500	T91	Outer oxide	0.846	0.38	0.9872
		Inner oxide	0.518	0.40	0.9973
		Transition	0.389	0.23	0.9599
		Total oxide thickness	1.710	0.37	0.9916
500	HCM12A	Outer oxide	0.719	0.37	0.9944
		Inner oxide	0.464	0.41	0.9984
		Transition	0.470	0.20	0.9018
		Total oxide thickness	1.548	0.36	0.9989
500	HT-9	Outer oxide	0.749	0.37	0.9807
		Inner oxide	0.405	0.44	0.9545
		Transition	0.417	0.27	0.9779
		Total oxide thickness	1.584	0.37	0.9759

Table 4.5 The temperature-dependence of weight gain of T91, HCM12A, HT-9, and 9Cr-ODS exposed in deaerated SCW at 400, 500 and 600°C.

Exp.	Temp. (^{o}C)	Exp. time (hours)	Weight gain (mg/dm^2)			
			T91	HCM12A	HT-9	9Cr-ODS
1	400	151.5	19.525 ± 1.993	16.043 ± 2.289	22.947 ± 2.246	
		Norm.*	20.678 ± 2.303	17.157 ± 2.302	23.824 ± 2.392	
3	500	182.2	137.301 ± 1.949	119.940 ± 1.660		
4a		195.0			140.968 ± 2.313	73.230 ± 2.437
		Norm.*	137.301 ± 1.949	119.940 ± 1.660	129.890 ± 1.705	71.240 ± 1.950
10	600	190	614.398 ± 2.903	491.077 ± 2.343	475.226 ± 2.488	502.977 ± 3.076
		Norm.*	602.651 ± 2.137	481.690 ± 1.918	466.142 ± 1.975	493.361 ± 2.205

* Normalized to 182 hours using the power law equation

Table 4.6 The temperature-dependence of oxide thickness of T91, HCM12A, HT-9, and 9Cr-ODS exposed in deaerated SCW at 400, 500 and 600°C. (continued on next page)

Exp.	Temp. (°C)	Exp. time (hours)	Oxide layer thickness (μm)													
			T91							HCM12A						
			Tot.	O	I	T	Pore[a]	Cr-rich[b]	(I+T+C)[c] / O	Tot.	O	I	T	Pore[a]	Cr-rich[b]	(I+T+C)[c] / O
1	400	151.5	2.88 ± 0.36	1.39 ± 0.30	0.89 ± 0.20	0.60 ± 0.05				2.39 ± 0.25	1.14 ± 0.20	0.85 ± 0.14	0.40 ± 0.05			
		Norm.*	3.10 ± 0.33	1.50 ± 0.28	0.96 ± 0.19	0.65 ± 0.05				2.57 ± 0.23	1.23 ± 0.19	0.91 ± 0.13	0.43 ± 0.05			
3	500	182.2	12.12 ± 0.31	6.37 ± 0.26	4.35 ± 0.11	1.40 ± 0.08			0.90	10.57 ± 0.22	5.31 ± 0.15	4.06 ± 0.12	1.20 ± 0.07			0.99
10	600	190.0	44.18 ± 2.31	22.70 ± 0.88	16.57 ± 1.08	4.35 ± 1.36	0.45 ± 1.23	0.11 ± 0.22	0.95	37.97 ± 3.05	19.22 ± 1.46	12.22 ± 0.78	6.35 ± 2.55	0.00	0.19 ± 0.24	0.98
		Norm.*	43.34 ± 0.76	22.27 ± 0.35	16.25 ± 0.42	4.27 ± 0.53				37.07 ± 1.19	18.85 ± 0.57	11.99 ± 0.31	6.22 ± 1.00			

* Normalized to 182 hours using the power law equation
O : outer layer oxide, I : inner layer oxide, T : transition layer
a Pore region at inner oxide/transition interface
b Cr-rich spinel region at transition/alloy interface
c Thickness ratio of (inner oxide + transition layer)/ outer oxide for 500°C test
c Thickness ratio of (inner oxide + transition layer + Cr-rich layer)/ outer oxide for 600°C test

Table 4.6 (continue)

Exp.	Temp. (°C)	Exp. time (hours)	Oxide layer thickness (μm)													
			HT-9							9Cr-ODS						
			Tot.	O	I	T	Pore[a]	Cr-rich[b]	(I+T+C)[c] / O	Tot.	O	I	T	Pore[a]	Cr-rich[b]	(I+T+C)[c] / O
1	400	151.5	2.69 ± 0.22	1.21 ± 0.18	0.83 ± 0.12	0.65 ± 0.05										
		Norm.*	2.89 ± 0.20	1.30 ± 0.17	0.89 ± 0.11	0.70 ± 0.05										
4a	500	195.0	12.69 ± 0.61	6.03 ± 0.33	4.74 ± 0.48	1.92 ± 0.41			1.10							
		Norm.*	12.34 ± 0.28	5.86 ± 0.13	4.61 ± 0.19	1.86 ± 0.16										
10	600	190.0	34.87 ± 1.44	18.83 ± 0.67	14.26 ± 0.72	1.74 ± 1.05	0.02 ± 0.06	0.02 ± 0.06	0.85	46.53 ± 1.44	20.28 ± 0.51	11.23 ± 0.55	14.82 ± 1.09	0.00	0.21 ± 0.55	1.29
		Norm.*	34.16 ± 0.56	18.47 ± 0.26	13.99 ± 0.28	1.71 ± 0.41				45.44 ± 0.49	19.89 ± 0.20	11.02 ± 0.22	14.54 ± 0.39			

* Normalized to 182 hours using the power law equation

O : outer layer oxide, I : inner layer oxide, T : transition layer

a Pore region at inner oxide/transition interface

b Cr-rich spinel region at transition/alloy interface

c Thickness ratio of (inner oxide + transition layer)/ outer oxide for 500°C test

c Thickness ratio of (inner oxide + transition layer + Cr-rich layer)/ outer oxide for 600°C test

Table 4.7 Dissolved oxygen effects on weight gain of T91, HCM12A, and HT-9 exposed at 500°C SCW containing <10 ppb (deaerated), 100 ppb, and 300 ppb DO concentration.

Exp.	Temp. (^{o}C)	D.O. (ppb)	Exp. time (hours)	Weight gain (mg/dm^2)		
				T91	HCM12A	HT-9
3	500	<10	182.2	137.301 ± 1.949	119.940 ± 1.660	
4a			195.0			140.968 ± 2.313
			Norm.*	137.301 ± 1.949	119.940 ± 1.660	129.890 ± 1.705
8	500	100	236.0	165.000 ± 2.012	143.000 ± 2.437	
			Norm.*	123.410 ± 1.602	112.150 ± 1.765	
9	500	300	182.0	115.131 ± 5.178	105.386 ± 3.480	126.412 ± 4.603

* Normalized to 182 hours using the power law equation

Table 4.8 Dissolved oxygen effects on oxide thickness of T91, HCM12A, and HT-9 exposed at 500°C SCW containing <10 ppb (deaerated), 100 ppb, and 300 ppb DO concentration.

Exp.	Temp. (°C)	D.O. (ppb)	Exp. time (hours)	Oxide layer thickness (μm)														
				T91					HCM12A					HT-9				
				Tot.	O	I	T	T/(O+I)**	Tot.	O	I	T	T/(O+I)**	Tot.	O	I	T	T/(O+I)**
3	500	<10	182.2	12.12 ± 0.31	6.37 ± 0.26	4.35 ± 0.11	1.40 ± 0.08		10.57 ± 0.22	5.31 ± 0.15	4.06 ± 0.12	1.20 ± 0.07						
4a			195.0											12.69 ± 0.61	6.03 ± 0.33	4.74 ± 0.48	1.92 ± 0.41	
			Norm.*	12.12 ± 0.31	6.37 ± 0.26	4.35 ± 0.11	1.40 ± 0.08	0.13	10.57 ± 0.22	5.31 ± 0.15	4.06 ± 0.12	1.20 ± 0.07	0.13	12.34 ± 0.28	5.86 ± 0.13	4.61 ± 0.19	1.86 ± 0.16	0.18
8	500	100	236.0	12.60 ± 0.55	6.65 ± 0.38	4.31 ± 0.19	1.50 ± 0.07		11.36 ± 0.31	5.76 ± 0.25	4.35 ± 0.18	1.25 ± 0.07						
			Norm.*	11.36 ± 0.16	5.99 ± 0.14	4.01 ± 0.07	1.35 ± 0.03	0.14	10.24 ± 0.11	5.19 ± 0.09	3.92 ± 0.06	1.27 ± 0.03	0.14					
9	500	300	182.0	10.66 ± 0.31	5.25 ± 0.19	3.58 ± 0.23	1.83 ± 0.10	0.21	9.55 ± 0.28	4.68 ± 0.23	3.32 ± 0.14	1.55 ± 0.06	0.19	11.50 ± 0.45	5.59 ± 0.34	3.91 ± 0.28	2.00 ± 0.10	0.21

* Normalized to 182 hours using the power law equation

** Thickness ratio of transition layer to summation of outer and inner oxides

Table 4.9 The XPS results of surface oxide formed on T91 and HCM12A exposed in 500°C SCW under deaerated condition and containing 100 ppb DO.

Peak	Suggested oxide	Data from [5-8] (eV)	T91 500°C DSCW				T91 500°C,100 ppb				HCM12A 500°C DSCW				HCM12A 500°C,100 ppb			
			eV	area	int	FWHM	eV	area	int	FWHM	eV	area	int	FWHM	eV	area	int	FWHM
Fe2P$_{3/2}$																		
Fe^{2+}	Fe_3O_4, $Fe[OH]_2$	709.7	710	1209	343	3.31	710	1607	411	3.82	710	2357	578	3.83	709.3	821	277	2.79
Fe^{3+}	Fe_2O_3, Fe_3O_4, FeOOH, $Fe[OH]_3$	711.0 ± 0.1	711	3144	655	4.51	711	2467	447	5.19	711	3425	457	7.04	711	3251	666	4.59
Satellite	Fe_2O_3	714.5, 716.0	715.9	1513	307	4.63	716	985	235	3.94	716	860	213	3.80	715.5	1545	324	4.49
Fe2P$_{1/2}$	Fe_2O_3, Fe_3O_4, FeOOH, $Fe[OH]_2$, $Fe[OH]_3$	723.3, 724.0	723.3	1847	357	4.86	723.3	2620	321	7.67	723.3	2564	371	6.50	723.4	2823	335	7.92
O1S	Fe_2O_3, Fe_3O_4	530 ± 1																
O^{2-}	FeOOH	531.2, 531.8	530.3	1430	1128	1.19	529.9	1880	1113	1.59	529.9	2772	1624	1.60	530.4	1295	948	1.28
OH^-	FeOOH, $Fe[OH]_2$, $Fe[OH]_3$	709.7	531.8	1259	474	2.49	531.8	749	285	2.47	531.8	1486	511	2.73	531.8	1762	468	3.54

Note: eV = binding energy (eV)
area = peak area (counts)
int = peak intensity (counts)
FWHM = full width at half maximum (eV)

Table 4.10 Compositions of the inner oxide ($(Fe,Cr)_3O_4$) of T91, HCM12A, HT-9, and 9Cr-ODS exposed in SCW. The data was determined in EDS of SEM.

Exp.	Temp. (^oC)	DO (ppb)	Exp. time (hours)	Alloy	Atomic %*			Atomic fraction			Note
					Fe	Cr	O	Fe	Cr	O	
1	400	<10	151.5	T91	32.55	10.40	56.35	2.3	0.7	4.0	
				HCM12A	31.69	11.16	56.43	2.2	0.8	4.0	
				HT-9	28.92	13.04	54.21	2.1	0.9	3.9	
5	500	<10	1.0	HCM12A							Oxide scales are too small.
6	500	<10	10.0	HCM12A	24.36	10.16	60.29	1.8	0.8	4.4	
3	500	<10	182.2	T91	31.17	9.35	58.14	2.2	0.7	4.1	
				HCM12A	28.87	11.71	56.03	2.1	0.8	4.1	
4a	500	<10	195.0	HT-9	30.86	14.43	49.21	2.2	1.1	3.7	
7	500	<10	477.0	T91	35.86	9.23	52.99	2.5	0.7	3.8	
				HCM12A	30.03	13.73	54.54	2.1	1.0	3.9	
				HT-9	27.00	13.74	58.33	2.1	1.0	3.9	
8	500	100	236.0	T91	30.46	8.90	59.39	2.2	0.6	4.2	
				HCM12A	27.87	11.55	57.08	2.0	0.8	4.1	
9	500	300	182.0	T91	33.45	9.77	55.39	2.4	0.7	3.9	
				HCM12A	30.22	11.68	53.47	2.2	0.9	3.9	
				HT-9	29.36	12.16	54.98	2.1	0.9	4.0	
10	600	<10	191.1	T91	38.40	10.38	50.09	2.7	0.7	3.5	
				HCM12A	30.79	12.01	53.93	2.2	0.9	3.9	
				HT-9	28.78	13.31	55.55	2.0	1.0	4.0	
				9Cr-ODS	32.96	10.43	54.46	2.4	0.7	3.9	
			average	T91	33.65	9.67	55.39	2.4	0.7	3.9	
					±3.00	±0.62	±3.42	±0.2	±0.0	±0.2	
				HCM12A	29.12	11.71	55.97	2.1	0.9	4.0	
					±2.44	±1.07	±2.33	±0.1	±0.1	±0.2	
				HT-9	28.98	13.34	54.46	2.1	1.0	3.9	
					±1.38	±0.84	±3.32	±0.1	±0.1	±0.1	
				9Cr-ODS	32.96	10.43	54.46	2.4	0.7	3.9	

Table 4.11 Summary of microstructure characterizations of the oxides formed on HCM12A exposed in 400 and 500°C deaerated SCW, and in 500°C containing 300 ppb DO SCW for 188, 182.2, and 182 hour, respectively.

Exposure condition	400°C deaerated SCW	500°C deaerated SCW	500°C 300 ppb DO
Alloy	HCM12A	HCM12A	HCM12A
Outer layer			
Morphology	Packed columnar grains	Packed columnar grains with few voids	Packed columnar grains with few voids
Thickness (μm)	1.50	5.31	4.68
Phase, structure	Magnetite, $Fd\bar{3}m$	Magnetite, $Fd\bar{3}m$	Magnetite, $Fd\bar{3}m$
Lattice parameter (Å)	a = 8.295 ± 0.15	a = 8.342 ± 0.04	a = 8.401 ± 0.08
Chemical composition	Fe_3O_4	Fe_3O_4	Fe_3O_4
Grain size (μm)	0.5 ± 0.1wide 1.4 ± 0.3 long	0.5 ± 0.3 wide 2 ± 0.5 long	0.7 ± 0.5wide 2 ± 1.0 long
Void size (μm)	N/A	0.5 ± 0.1	0.5 ± 0.2
Precipitate	None	None	None
Inner layer			
Morphology	Equiaxed oxide grains with precipitates and micro-cracks.	Porous equiaxed oxide grains with precipitates, micro-pores and micro-cracks.	Porous equiaxed oxide grains with precipitates, micro-pores and micro-cracks.
Thickness (μm)	0.97	4.06	3.32
Phase, structure	Fe-Cr oxide, $Fd\bar{3}m$	Fe-Cr oxide, $Fd\bar{3}m$	Fe-Cr oxide, $Fd\bar{3}m$
Lattice parameter (Å)	a = 8.59 ± 0.14	a = 8.41 ± 0.02	a = 8.50 ± 0.20
Chemical composition	$Fe^{2+}(Fe^{3+}_{2-x}Cr^{3+}_{x})O^{2-}_{4}$, where x = 0.8	$Fe^{2+}(Fe^{3+}_{2-x}Cr^{3+}_{x})O^{2-}_{4}$, where x = 0.8	$Fe^{2+}(Fe^{3+}_{2-x}Cr^{3+}_{x})O^{2-}_{4}$, where x = 0.9
Grain size (nm)	83.00 ± 41.95	54.30 ± 24.02	55.07 ± 42.03
Precipitate	$Cr_{23}C_6$, Cu, V-Nb	$Cr_{23}C_6$, Cu, V-Nb	$Cr_{23}C_6$, Cu, V-Nb
Transition layer			
Morphology	Clear interface of inner oxide and alloy substrate.	Mixed characteristics of alloy and oxide. Spinel oxide formed at lath boundary.	Mixed characteristics of alloy and oxide. Spinel oxide formed at lath boundary.
Thickness (μm)	0.67	1.20	1.55
Precipitate	Similar to inner oxide	Similar to inner oxide	Similar to inner oxide
Phase, structure, a (Å)			
a. Inside lath			
Fe	N/A	Fe, $Im\bar{3}m$, a = 2.93	Fe, $Im\bar{3}m$, a = 2.90
Fe-Cr oxide	N/A	Fe-Cr oxide, $Fd\bar{3}m$, a = 8.56	Fe-Cr oxide, $Fd\bar{3}m$, a = 8.50
b. Oxide at lath boundaries	N/A	Fe-Cr oxide, $Fd\bar{3}m$, a = 8.40	Fe-Cr oxide, $Fd\bar{3}m$, a = 8.40
c. Porous Cr-rich region	N/A	N/A	N/A

Table 4.12 Summary of the microstructure of oxides formed on T91, HCM12A, HT-9 and 9Cr-ODS exposed in 600°C deaerated SCW for 191 hours.

Exposure condition	600°C deaerated SCW	600°C deaerated SCW
Alloy	T91	HCM12A
Outer layer		
Morphology	Packed columnar grains with few voids and cracks	Packed columnar grains with few voids and cracks
Thickness (μm)	22.27	18.85
Phase, structure	Magnetite, $Fd\bar{3}m$	Magnetite, $Fd\bar{3}m$
Lattice parameter (Å)	a = 8.40 (by XRD)	a = 8.364 ± 0.06
Chemical composition	Fe_3O_4	Fe_3O_4
Grain size (μm)	Not determined	0.7 ± 0.5wide 3 ± 1.5 long
Void size (μm)	Not determined	0.5 ± 0.1
Precipitate	None	None
Inner layer		
Morphology	Porous equiaxed oxide grains with precipitates	Porous equiaxed oxide grains with precipitates
Thickness (μm)	16.25	11.99
Phase, structure	Fe-Cr oxide, $Fd\bar{3}m$	Fe-Cr oxide, $Fd\bar{3}m$
Lattice parameter (Å)	a = 8.45 ± 0.20	a = 8.38 ± 0.20
Chemical composition	$Fe^{2+}(Fe^{3+}_{2-x}Cr^{3+}_{x})O^{2-}_{4}$, where x = 0.7	$Fe^{2+}(Fe^{3+}_{2-x}Cr^{3+}_{x})O^{2-}_{4}$, where x = 0.9
Grain size (nm)	Not determined	50.79 ± 28.56
Precipitate	$Cr_{23}C_6$, Cu, Mo	$Cr_{23}C_6$, Cu, V-Nb, Mo
Transition layer		
Morphology	Mixed characteristics of alloy and oxide. Small oxide grains distributed inside lath. Cr-rich oxide formed at lath boundaries. Porous Cr-rich spinel oxide was observed at some locations between transition and alloy.	Mixed characteristics of alloy and oxide. Small oxide grains distributed inside lath. Cr oxide formed at lath boundaries. Porous Cr-rich spinel oxide was observed at some locations between transition and alloy.
Thickness (μm)*	4.27	6.22
Precipitate	$Cr_{23}C_6$, Cu, Si, Mo	$Cr_{23}C_6$, Cu, V-Nb, Mo, W
Phase, structure, a (Å)	Ni-enriched in this layer.	
a. Inside lath		
Fe	Fe, $Im\bar{3}m$, a = 2.89	Fe, $Im\bar{3}m$, a = 2.90
Fe-Cr oxide	Fe-Cr oxide, $Fd\bar{3}m$, a = 8.38	Fe-Cr oxide, $Fd\bar{3}m$, a = 8.50
b. Oxide at lath boundaries	$Fe^{2+}(Fe^{3+}_{2-x}Cr^{3+}_{x})O^{2-}_{4}$, where x = 1.5, a = 8.20	Cr_2O_3, $R\bar{3}C$, a=b= 4.96, c = 13.59
c. Porous Cr-rich region	$Fe^{2+}(Fe^{3+}_{2-x}Cr^{3+}_{x})O^{2-}_{4}$, where $x \sim 2$	$Fe^{2+}(Fe^{3+}_{2-x}Cr^{3+}_{x})O^{2-}_{4}$, where x = 1.8, a = 8.48

Table 4.12 (continue)

Exposure condition	600°C deaerated SCW	600°C deaerated SCW
Alloy	HT-9	9Cr-ODS
Outer layer		
Morphology	Packed columnar grains with few voids and cracks	Packed columnar grains with few voids and cracks
Thickness (μm)	18.47	19.89
Phase, structure	Magnetite, $Fd\bar{3}m$	Magnetite, $Fd\bar{3}m$
Lattice parameter (Å)	a = 8.40 (by XRD)	a = 8.40 (by XRD)
Chemical composition	Fe_3O_4	Fe_3O_4
Grain size (μm)	Not determined	Not determined
Void size (μm)	Not determined	Not determined
Precipitate	None	None
Inner layer		
Morphology	Porous equiaxed oxide grains with precipitates. Cr-rich Fe-Cr oxide formed at inner oxide-alloy interface.	Porous equiaxed oxide grains with precipitates
Thickness (μm)	13.99	11.02
Phase, structure	Fe-Cr oxide, $Fd\bar{3}m$	Fe-Cr oxide, $Fd\bar{3}m$
Lattice parameter (Å)	a = 8.96 ± 0.20	a = 8.51 ± 0.20
Chemical composition	$Fe^{2+}(Fe^{3+}_{2-x}Cr^{3+}_{x})O^{2-}_{4}$, where x = 1.0 for inner oxide, and x = 2.0 for Cr-rich region	$Fe^{2+}(Fe^{3+}_{2-x}Cr^{3+}_{x})O^{2-}_{4}$, where x = 0.7
Grain size (nm)	Not determined	Not determined
Precipitate	$Cr_{23}C_6$, Ni+Fe+O, V, Mo, Si	$Cr_{23}C_6$, Ti, W, Y_2O_3
Transition layer		
Morphology	Mixed characteristics of alloy and oxide. Small oxide grains distributed inside lath. Cr-rich oxide formed at lath boundaries. Porous Cr-rich spinel oxide was observed at some locations between transition and alloy.	Mixed characteristics of alloy and oxide. Small oxide grains distributed inside lath. Cr-rich oxide formed at lath boundaries. Porous Cr-rich spinel oxide was observed at some locations between transition and alloy.
Thickness (μm)*	1.71	14.54
Precipitate	Not determined	$Cr_{23}C_6$, Ti, W, Y_2O_3
Phase, structure, a (Å)		
a. Inside lath		
Fe	Not determined	Fe, $Im\bar{3}m$, a = 2.90
Fe-Cr oxide	Not determined	Fe-Cr oxide, $Fd\bar{3}m$, a = 8.38
b. Oxide at lath boundaries	Not determined	$Fe^{2+}(Fe^{3+}_{2-x}Cr^{3+}_{x})O^{2-}_{4}$, where x = 2.1, a = 8.92
c. Porous Cr-rich region	$Fe^{2+}(Fe^{3+}_{2-x}Cr^{3+}_{x})O^{2-}_{4}$, where $x \sim 2$	$Fe^{2+}(Fe^{3+}_{2-x}Cr^{3+}_{x})O^{2-}_{4}$, where $x \sim 2$

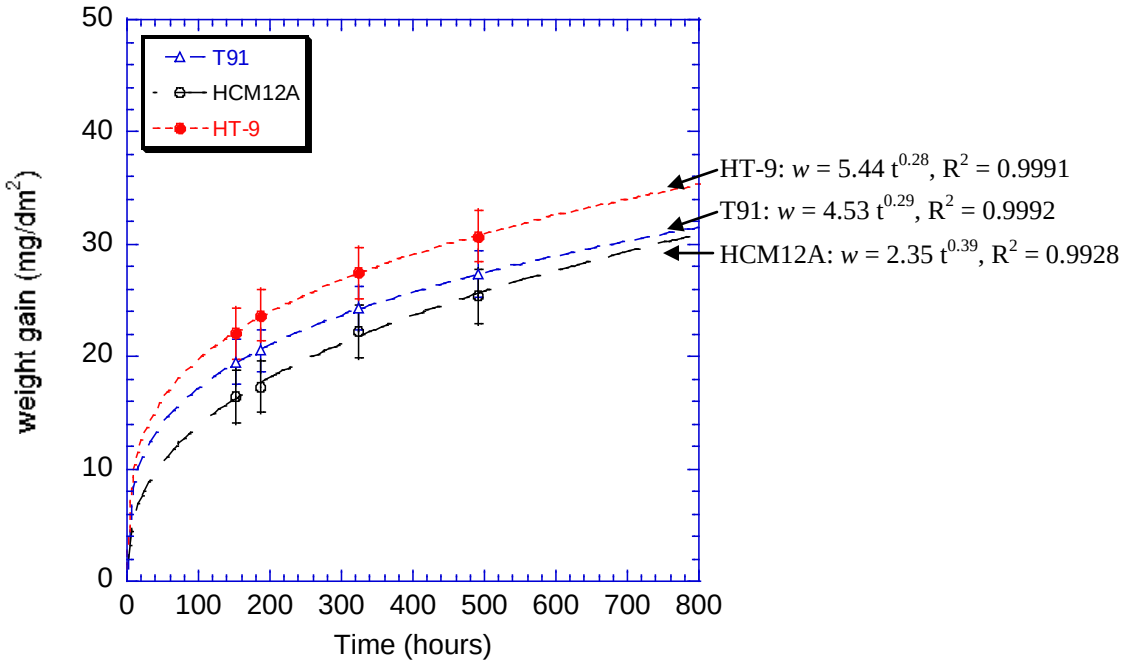

(a) 400°C

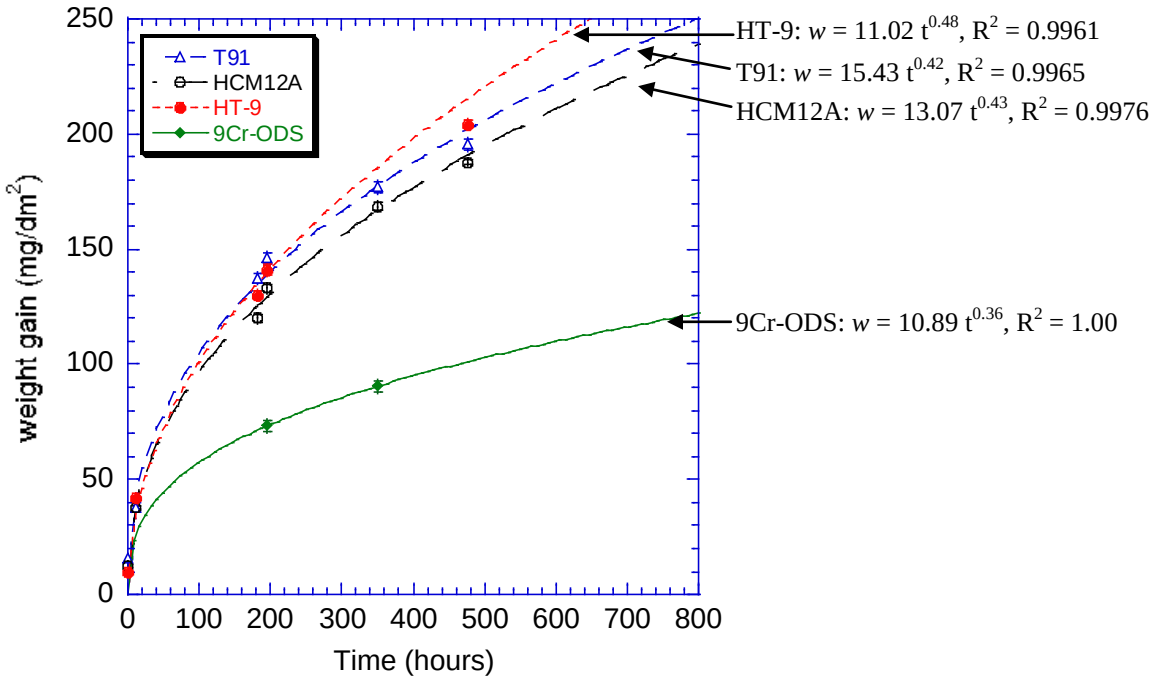

(b) 500°C

Figure 4.1 Plots of the time-dependence of weight gain of T91, HCM12A, HT-9, and 9Cr-ODS exposed in deaerated SCW at 400 and 500°C. (Note that the unit of oxidation rate constant from fitting equation is mg/dm^2/h.)

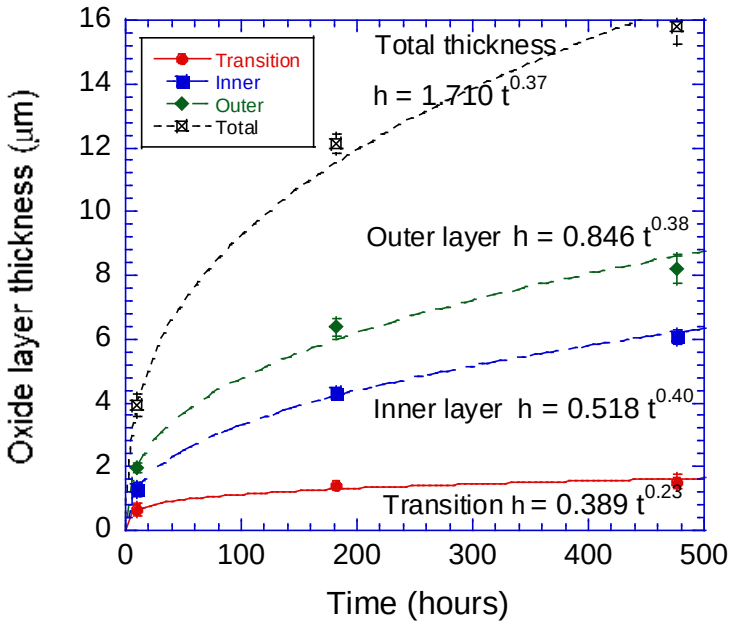
Oxide layer thickness (μm)
Time (hours)
Transition
Inner
Outer
Total
Total thickness
h = 1.710 t^0.37
Outer layer h = 0.846 t^0.38
Inner layer h = 0.518 t^0.40
Transition h = 0.389 t^0.23

(a)

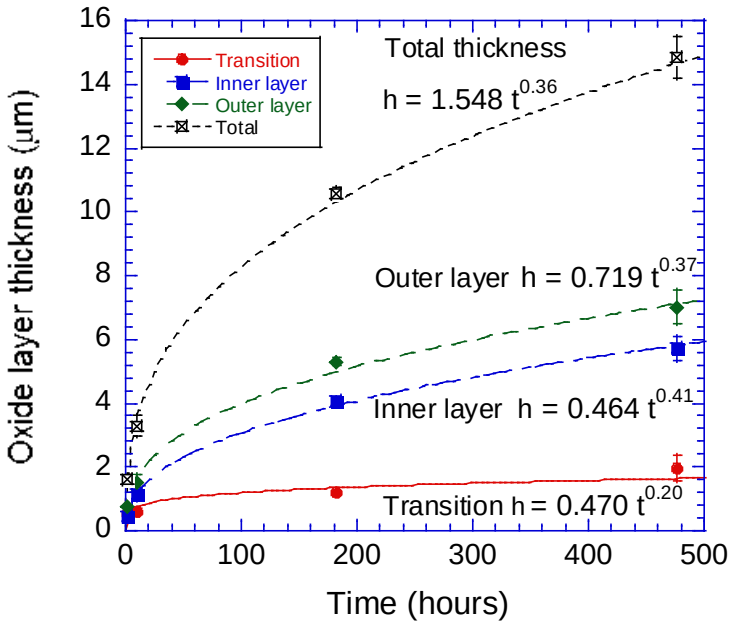
Oxide layer thickness (μm)
Time (hours)
Transition
Inner layer
Outer layer
Total
Total thickness
h = 1.548 t^0.36
Outer layer h = 0.719 t^0.37
Inner layer h = 0.464 t^0.41
Transition h = 0.470 t^0.20

(b)

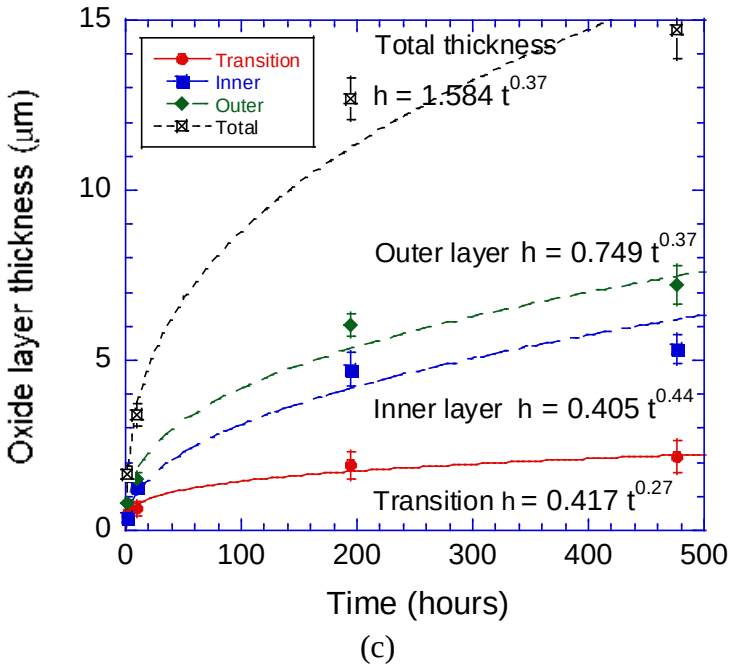

(c)

Figure 4.2 Plots of the time-dependence of oxide thickness of (a) T91, (b) HCM12A and (c) HT-9 exposed in deaerated SCW at 500°C. (Note that the unit of oxidation rate constant from fitting equation is μm/h.)

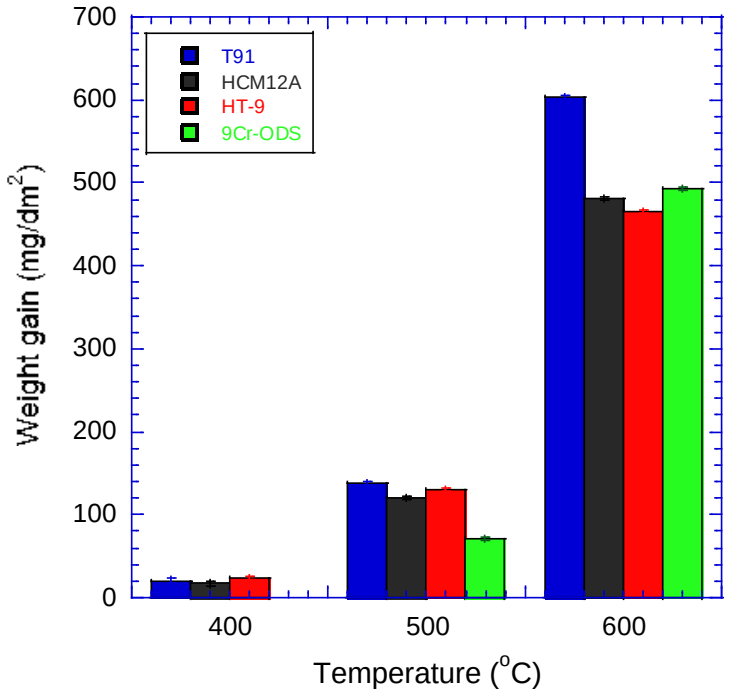

(a) weight gain

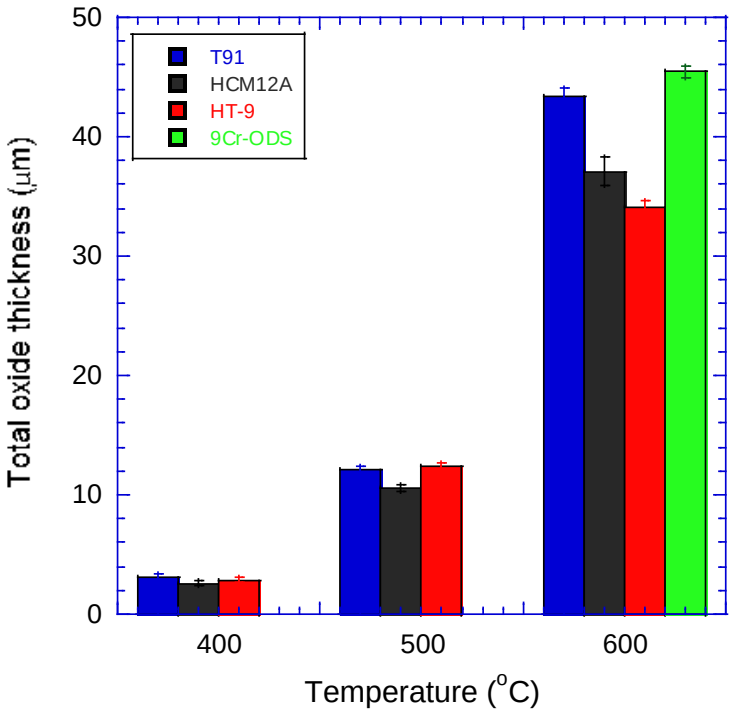

(b) oxide thickness

Figure 4.3 Temperature-dependence of weight gain and total oxide thickness of T91, HCM12A, HT-9, and 9Cr-ODS exposed in deaerated SCW at 400, 500 and 600°C. The weight gain was normalized to 182 hours.

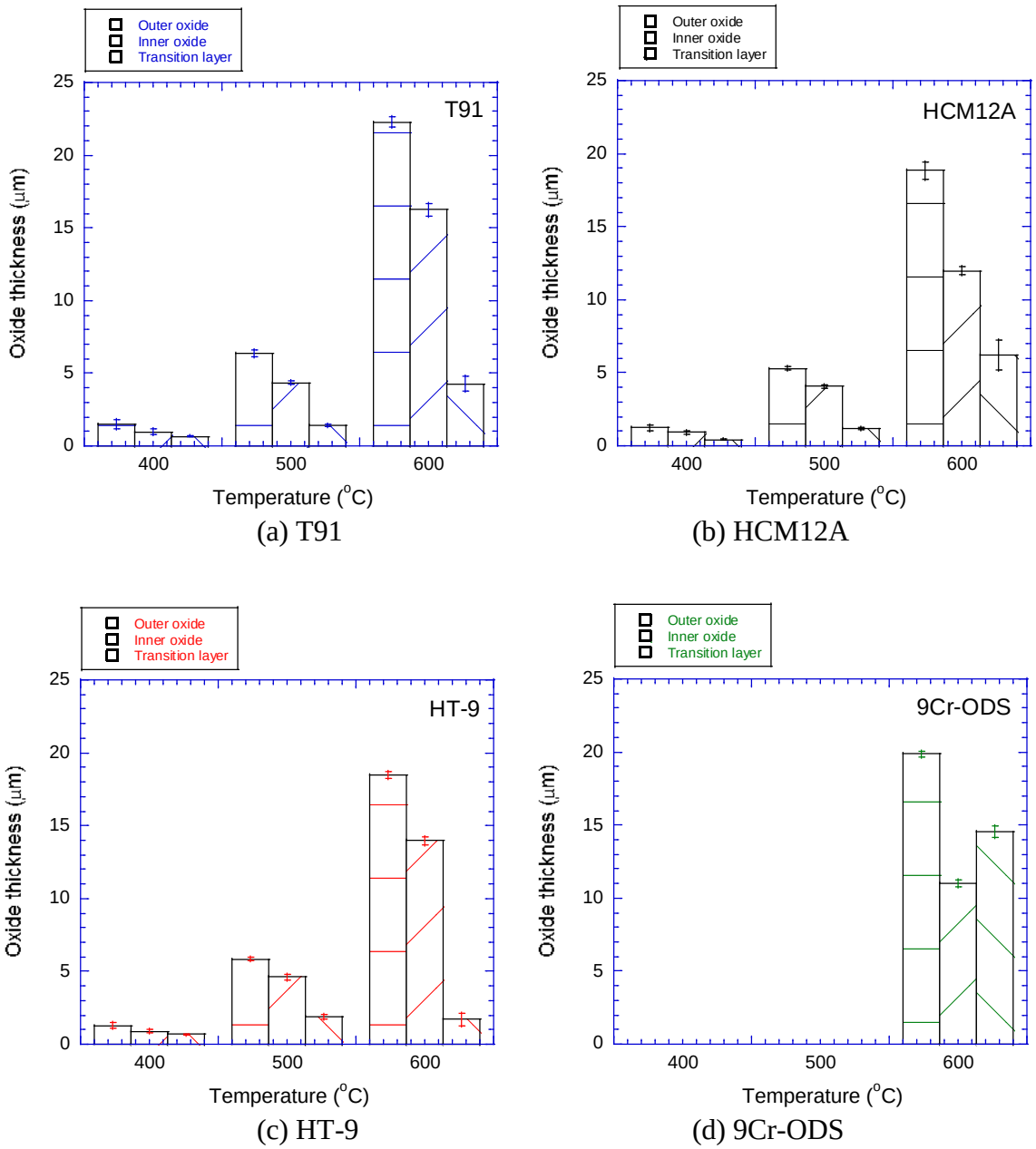

(a) T91 (b) HCM12A

(c) HT-9 (d) 9Cr-ODS

Figure 4.4 Temperature-dependence of oxide layer thickness of T91, HCM12A, HT-9, 9Cr-ODS exposed in deaerated SCW at 400, 500 and 600°C. The oxide thickness was normalized to 182 hours.

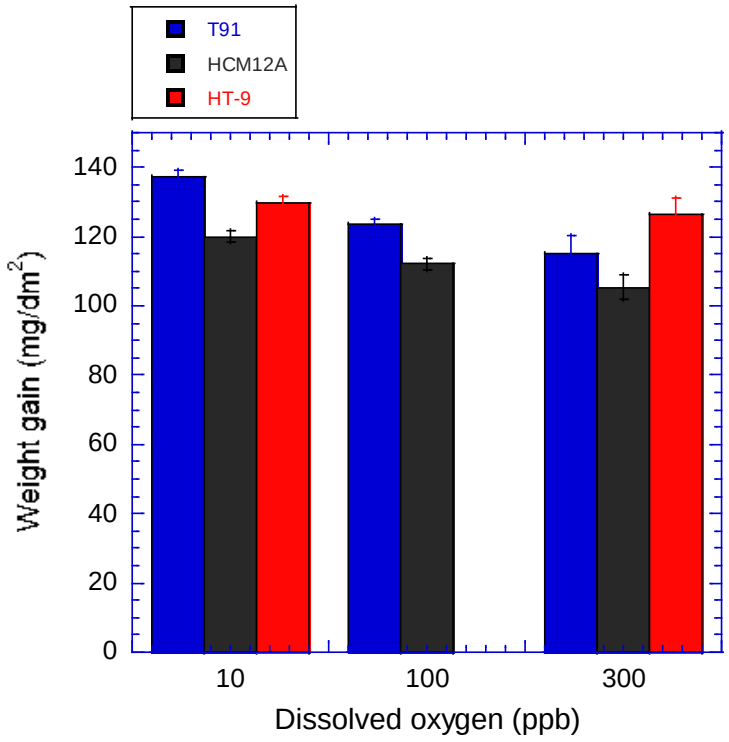

(a) weight gain

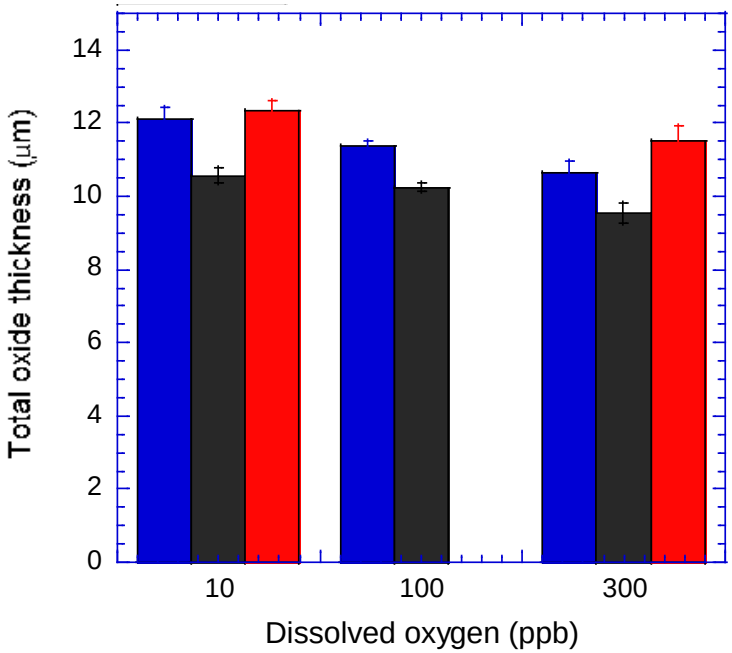

(b) Oxide thickness

Figure 4.5 Dissolved oxygen effect on the weight gain and total oxide thickness of T91, HCM12A, and HT-9 in 500°C SCW containing <10 (deaerated), 100 and 300 ppb DO concentration. The weight gain was normalized to 182 hours.

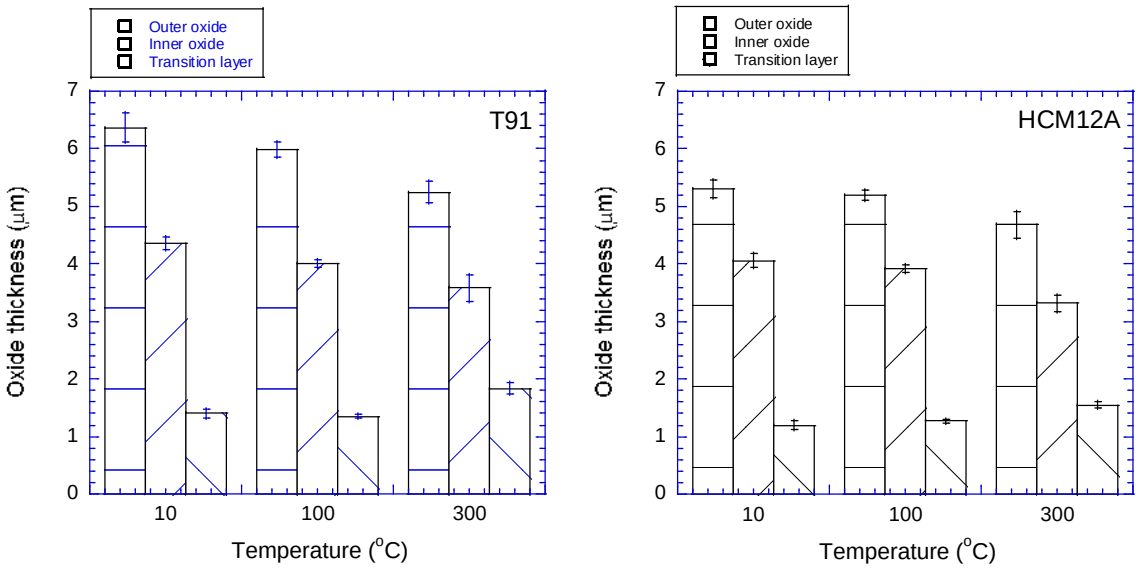

(a) T91

(b) HCM12A

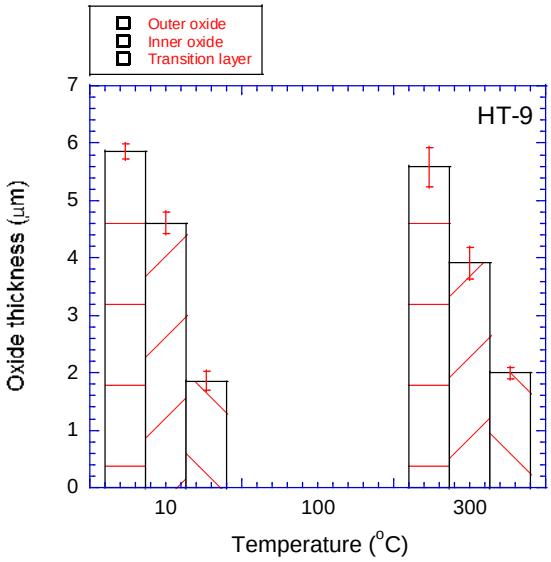

(c) HT-9

Figure 4.6 Dissolved oxygen effect on the oxide layer thickness of T91, HCM12A, and HT-9 in 500°C SCW containing <10 (deaerated), 100 and 300 ppb DO concentration. The weight gain was normalized to 182 hours.

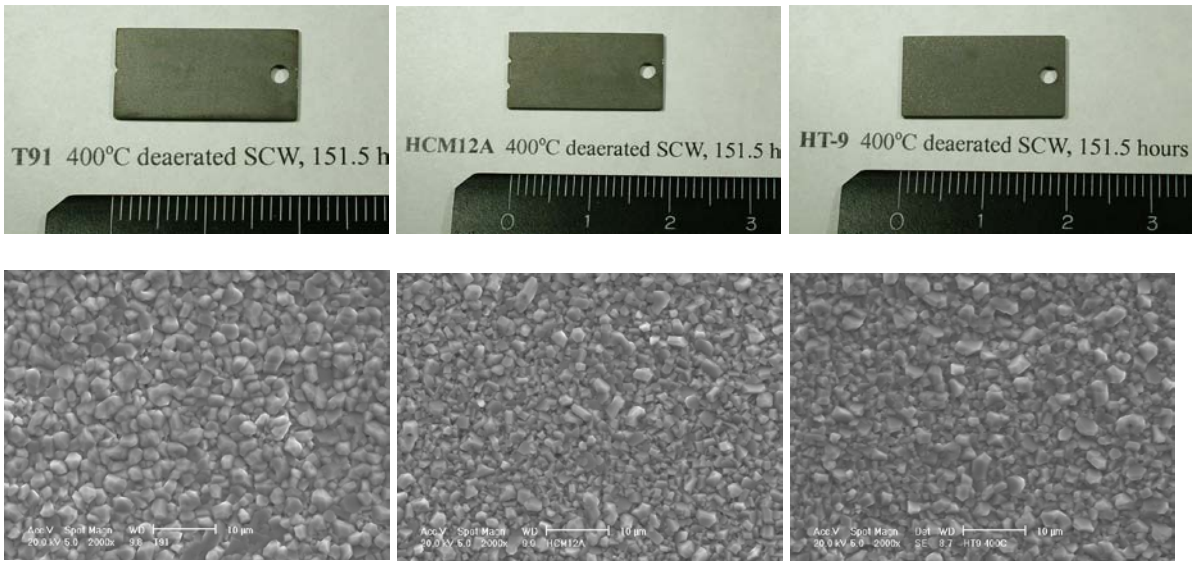

(a) T91 (b) HCM12A (c) HT-9

Figure 4.7 SEM images showing morphology of oxide on T91, HCM12A, and HT-9 corrosion coupon exposed in 400°C deaerated SCW for 151.5 hours.

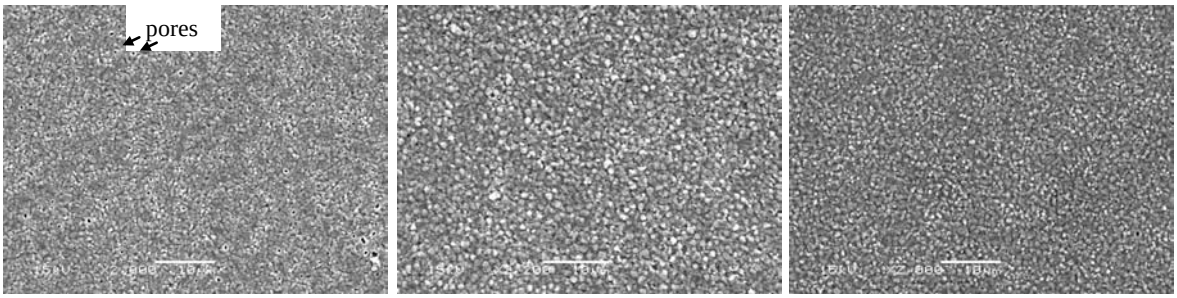

(a) T91 (b) HCM12A (c) HT-9

Figure 4.8 SEM images showing morphology of oxide on T91, HCM12A, and HT-9 corrosion coupon exposed in 500°C deaerated SCW for 1 hour.

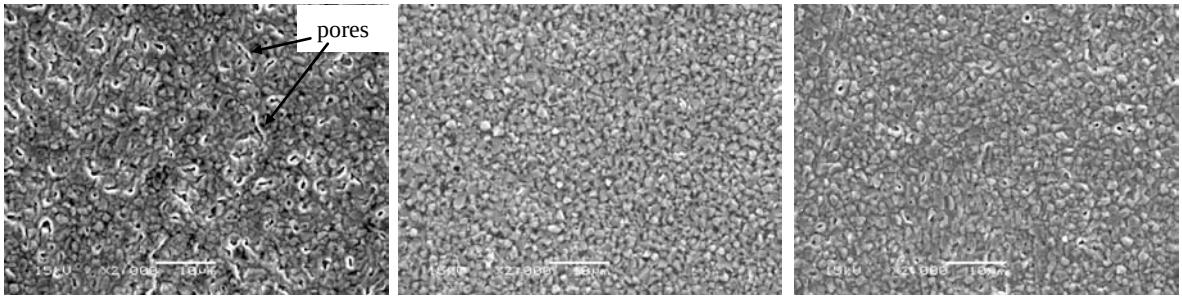

(a) T91 (b) HCM12A (c) HT-9

Figure 4.9 SEM images showing morphology of oxide on T91, HCM12A, and HT-9 corrosion coupon exposed in 500°C deaerated SCW for 10 hours.

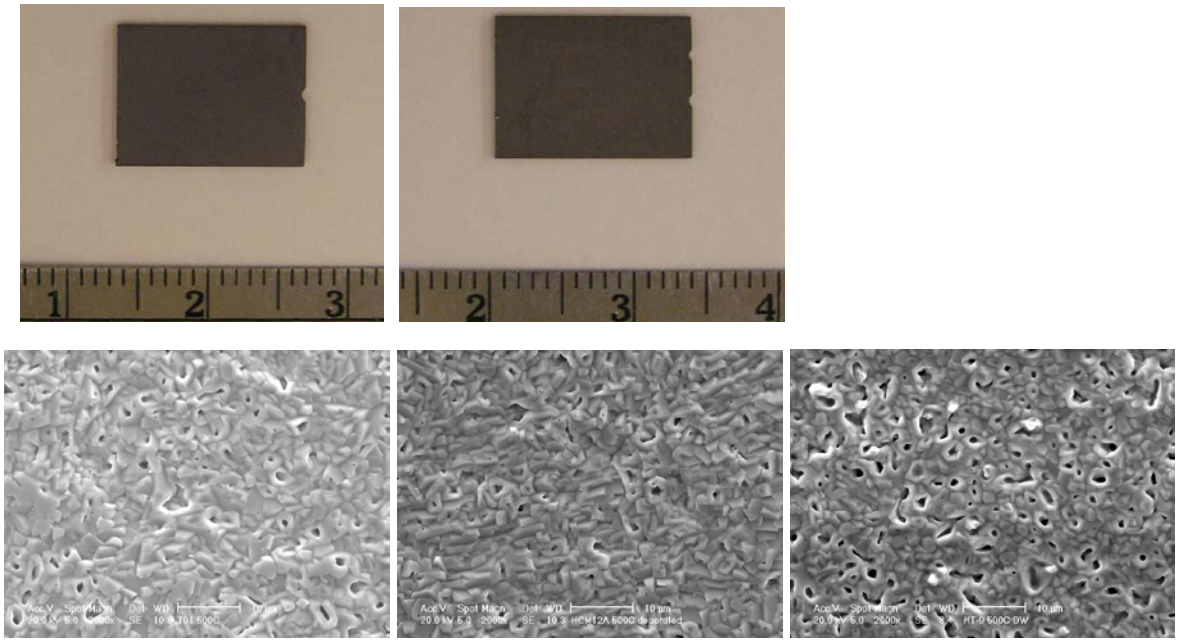

(a) T91 (b) HCM12A (c) HT-9

Figure 4.10 SEM images showing morphology of oxide on T91, HCM12A, and HT-9 corrosion coupon exposed in 500°C deaerated SCW for 182.2 hours (T91 and HCM12A) and 195 hours (HT-9).

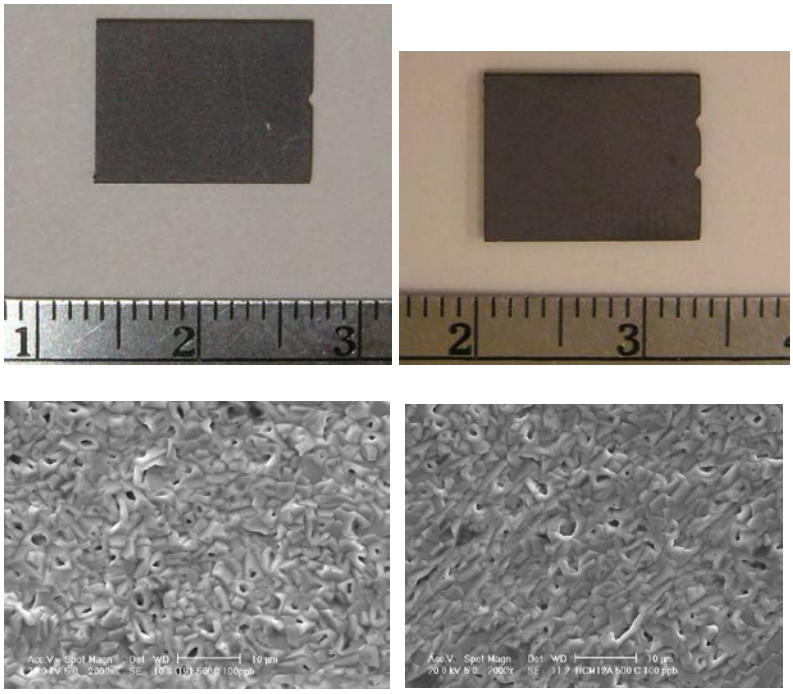

(a) T91 (b) HCM12A

Figure 4.11 SEM images showing morphology of oxide on T91 and HCM12A corrosion coupon exposed in 500°C SCW containing 100 ppb DO concentration for 236 hours.

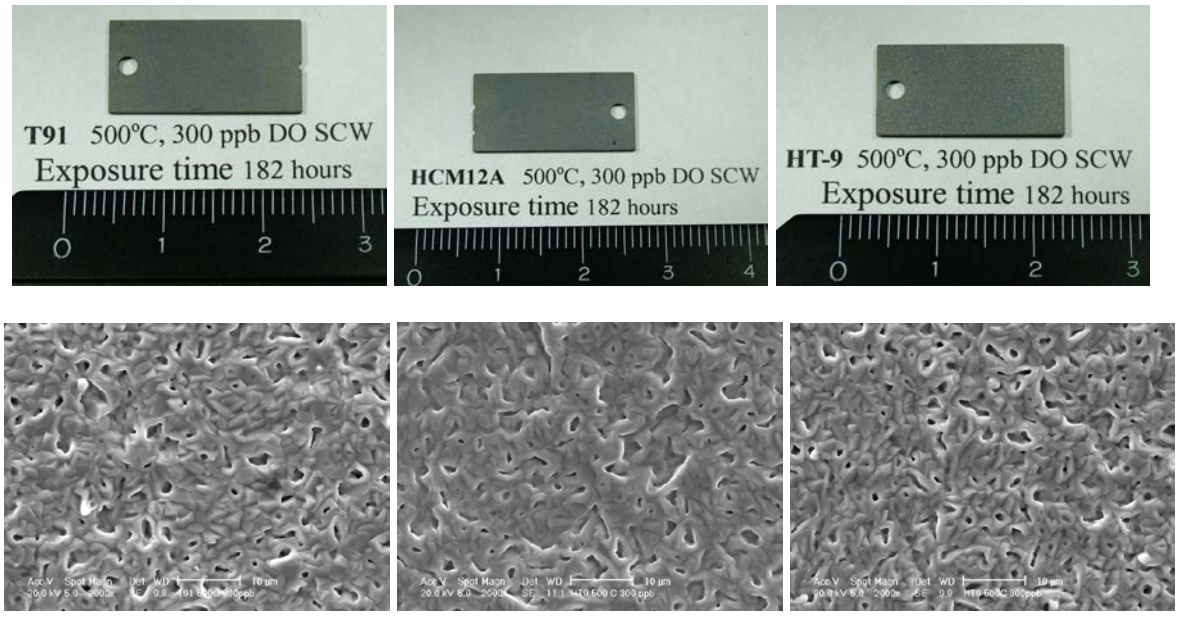

(a) T91 (b) HCM12A (c) HT-9

Figure 4.12 SEM images showing morphology of oxide on T91, HCM12A, and HT-9 corrosion coupon exposed in 500°C SCW containing 300 ppb DO concentration for 182 hours.

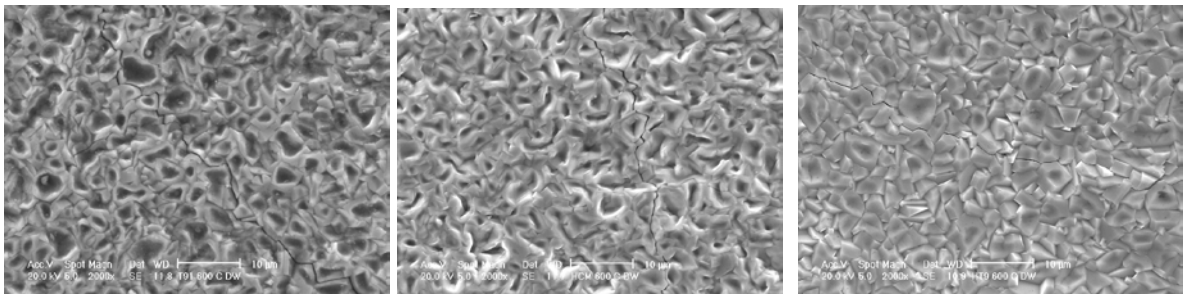

(a) T91 (b) HCM12A (c) HT-9

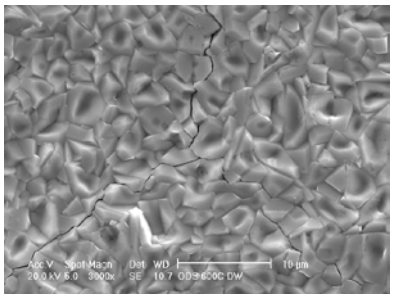

(d) 9Cr-ODS

Figure 4.13 SEM images showing morphology of oxide on T91, HCM12A, HT-9, and 9Cr-ODS corrosion coupon exposed in 600°C deaerated SCW for 191 hours.

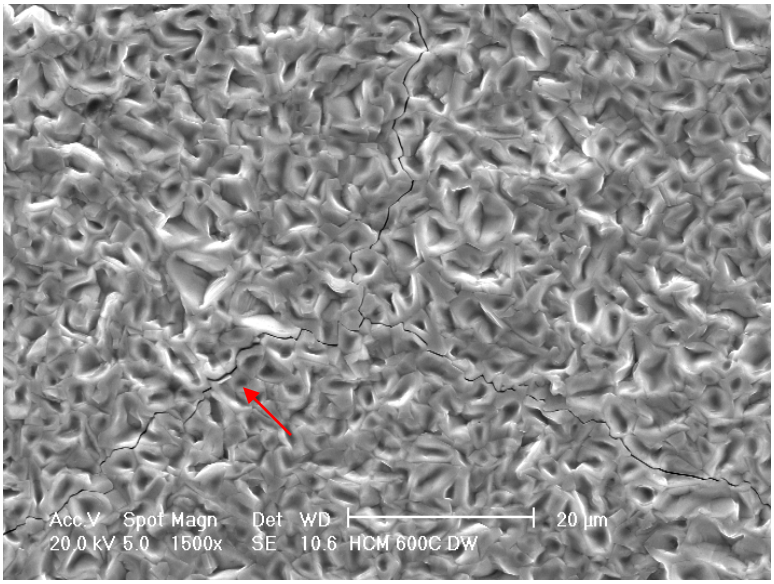

(a)

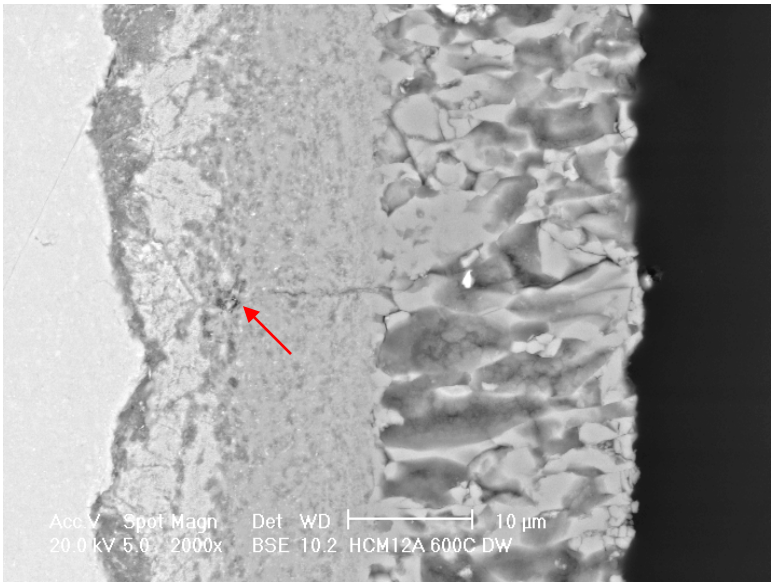

(b)

Figure 4.14 SEM images showing microcracks on (a) surface oxide and (b) cross section of HCM12A exposed in 600^{o}C deaerated SCW for 191 hours. Cross sectional BSE image shows a crack penetrates across outer and inner oxide layers.

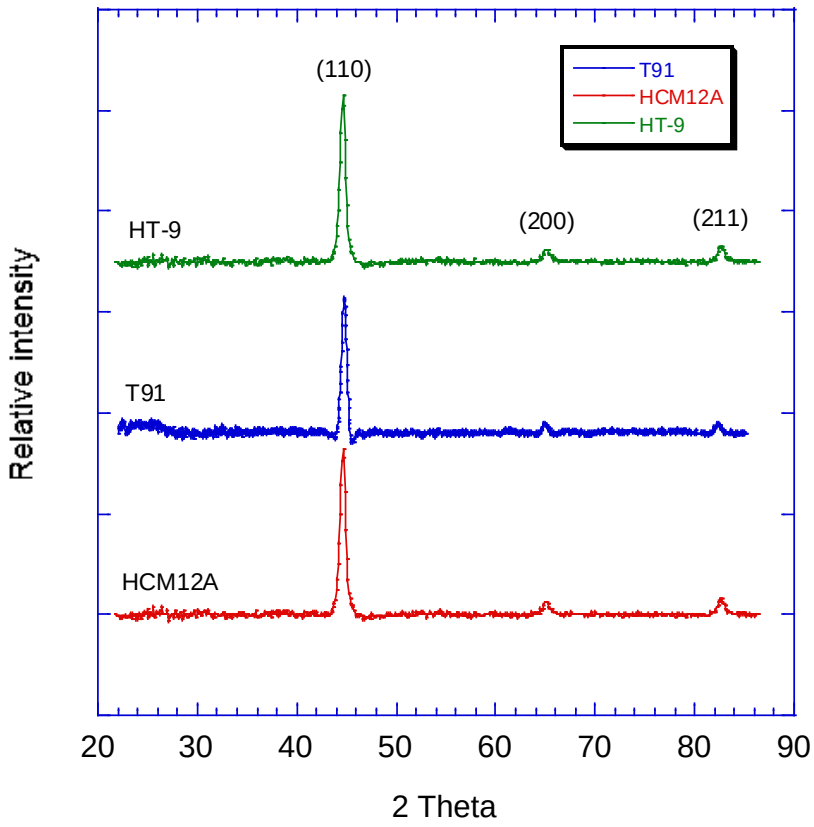

Figure 4.15 Glancing angle XRD spectrum of alloy T91, HCM12A, and HT-9 before exposure in SCW showing iron phase (BCC).

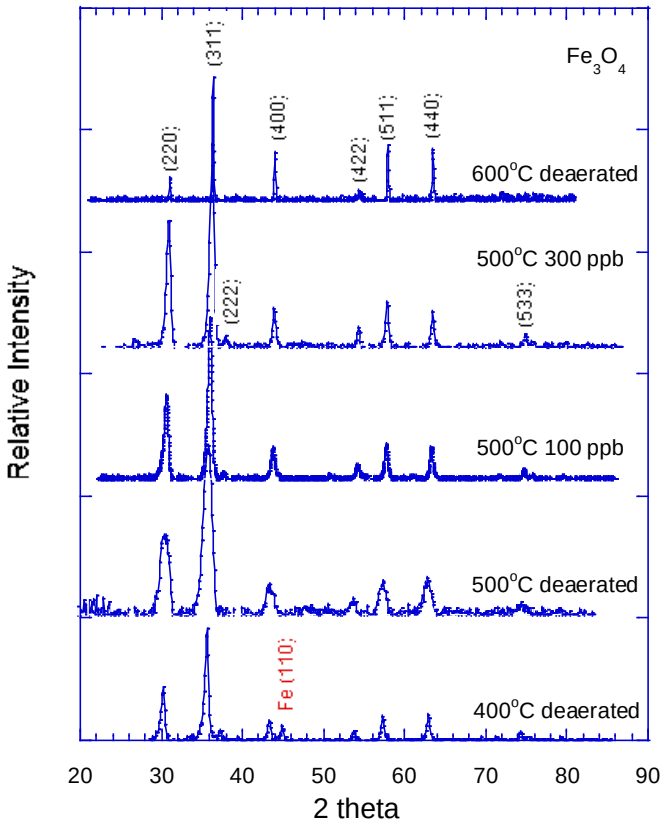

Figure 4.16 The XRD spectra of the outer oxide layer of T91 tested in SCW at 400, 500, and 600°C deaerated SCW, and at 500°C containing 100 and 300 ppb DO concentration.

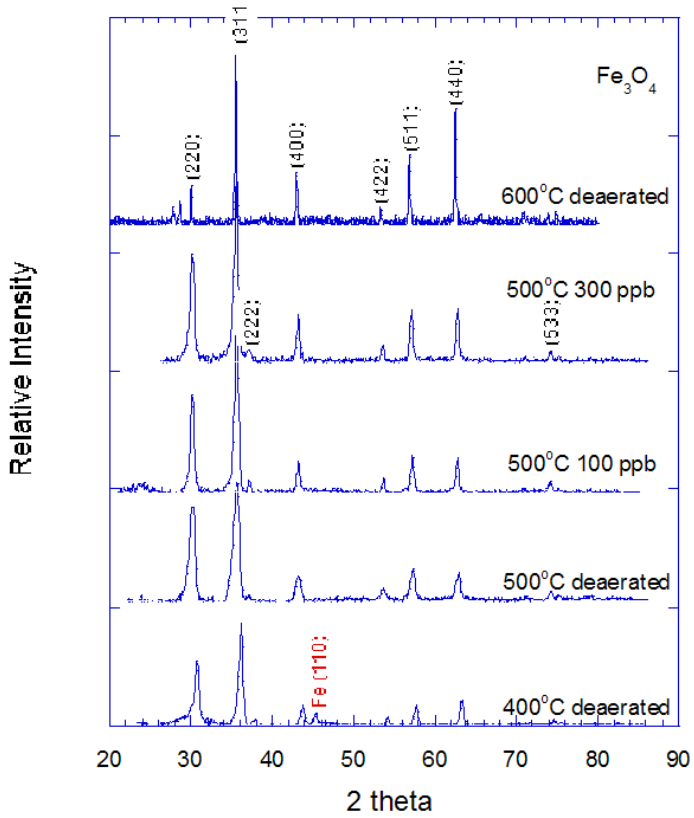

Figure 4.17 The XRD spectra of the outer oxide layer of HCM12A tested in SCW at 400, 500, and 600°C deaerated SCW, and at 500°C containing 100 and 300 ppb DO concentration.

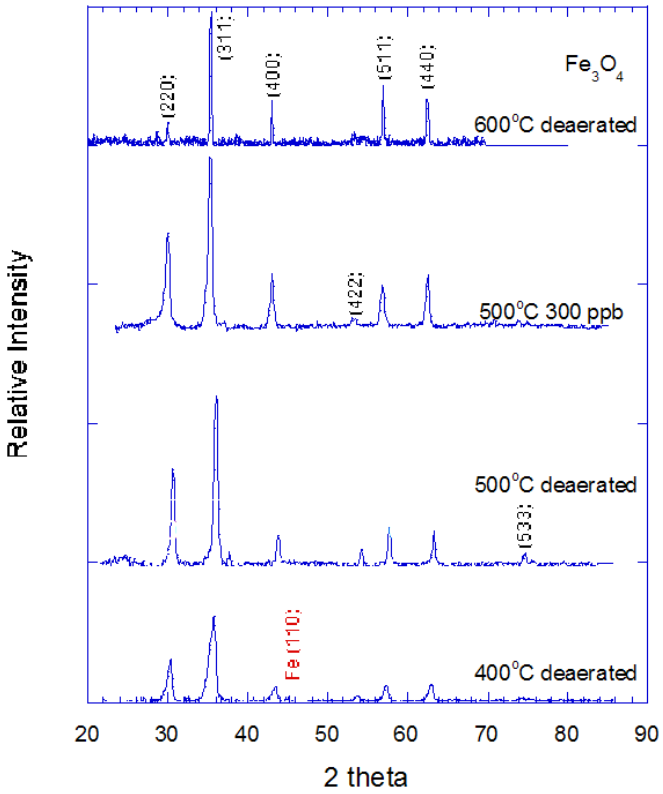

c) HT-9

Figure 4.18 The XRD spectra of the outer oxide layer of HT-9 tested in SCW at 400, 500, and 600°C deaerated SCW, and at 500°C containing 100 and 300 ppb DO concentration.

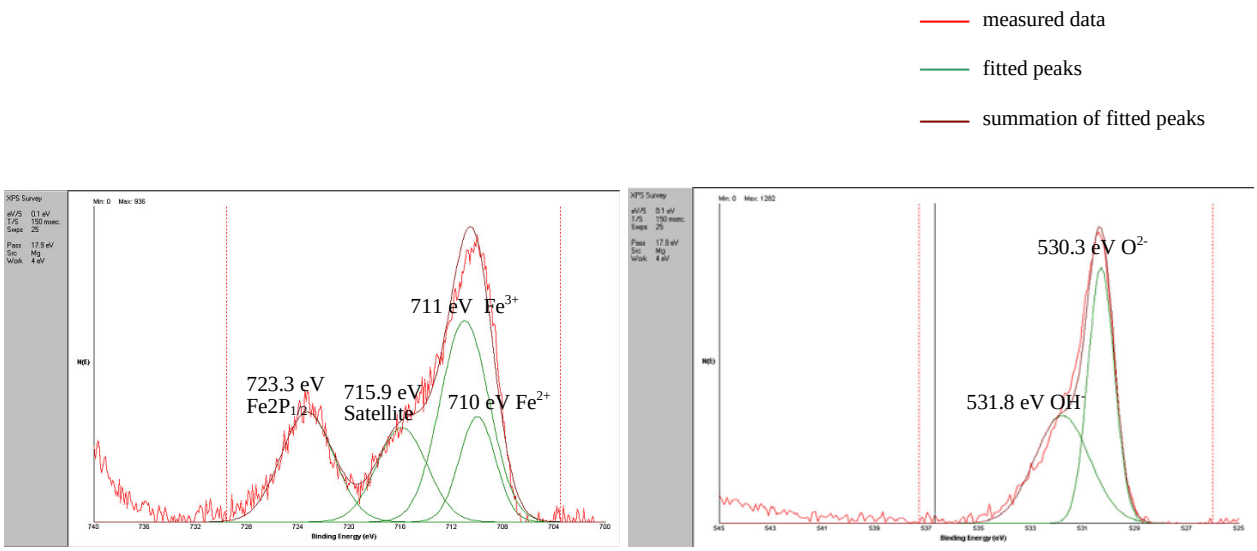

Fe2P O1S

(a)

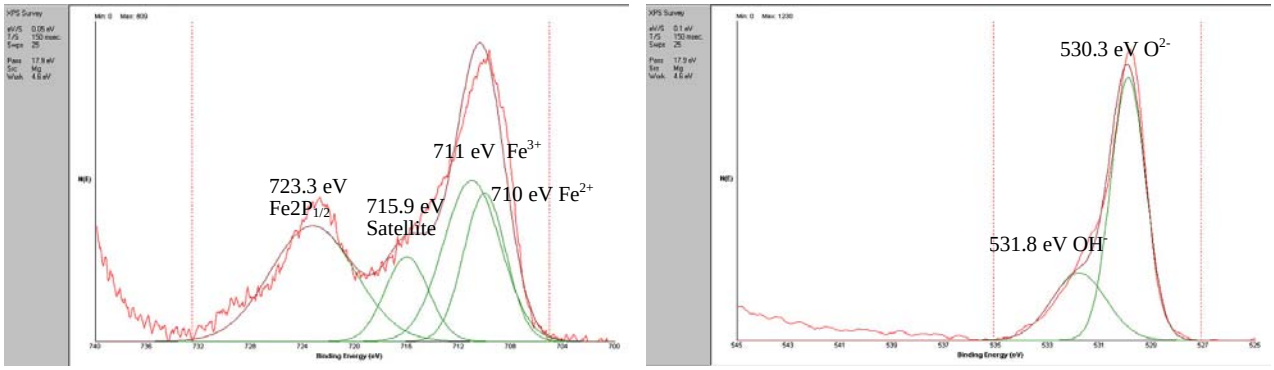

Fe2P O1S

(b)

Figure 4.19 The XPS spectra from T91 exposed in 500°C SCW under (a) deaerated condition, and (b) 100 ppb DO concentration. Peak fitting of Fe2P is shown on the left side, and O1S is shown on the right side.

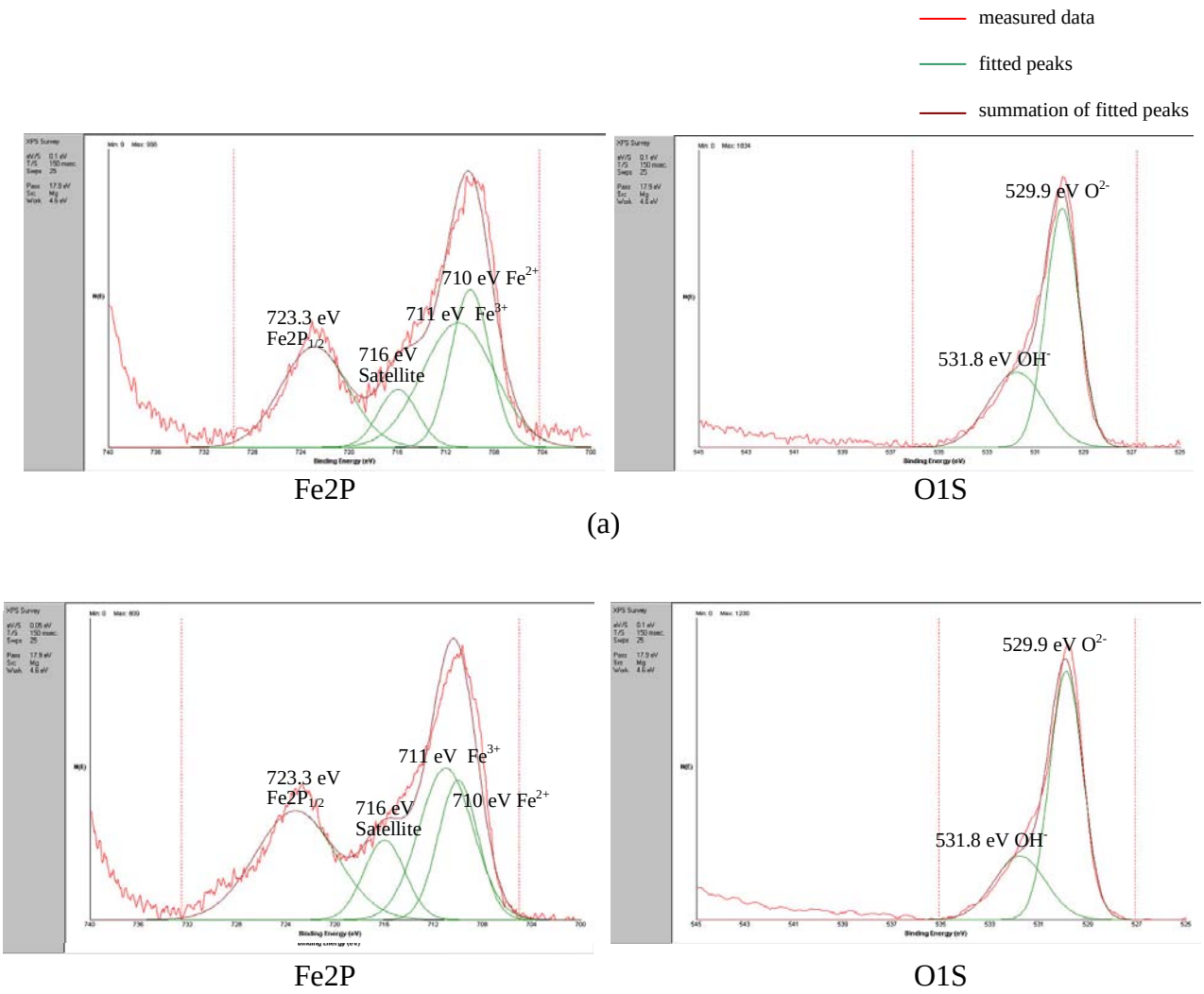

Figure 4.20 The XPS spectra from HCM12A exposed in 500°C SCW under (a) deaerated condition, and (b) 100 ppb DO concentration. Peak fitting of Fe2P is shown on the left side, and O1S is shown on the right side.

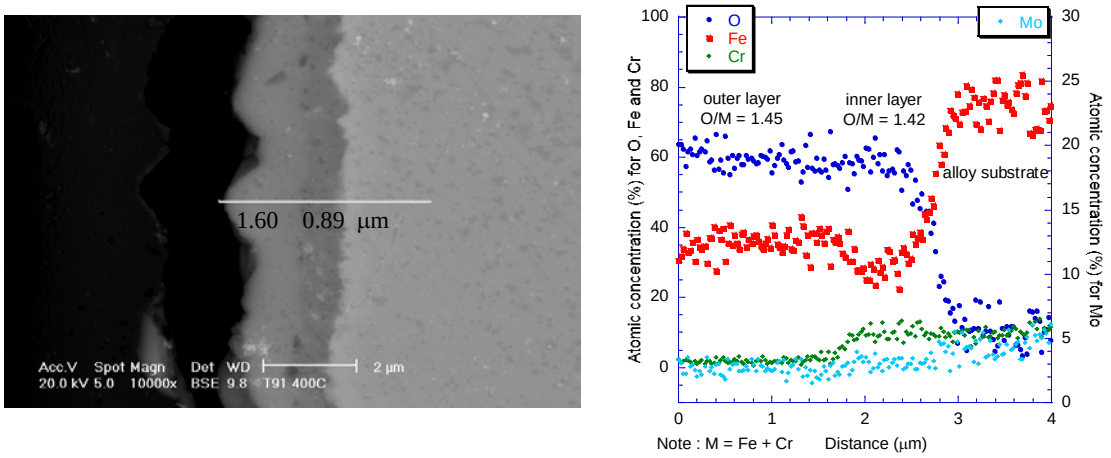

a) T91

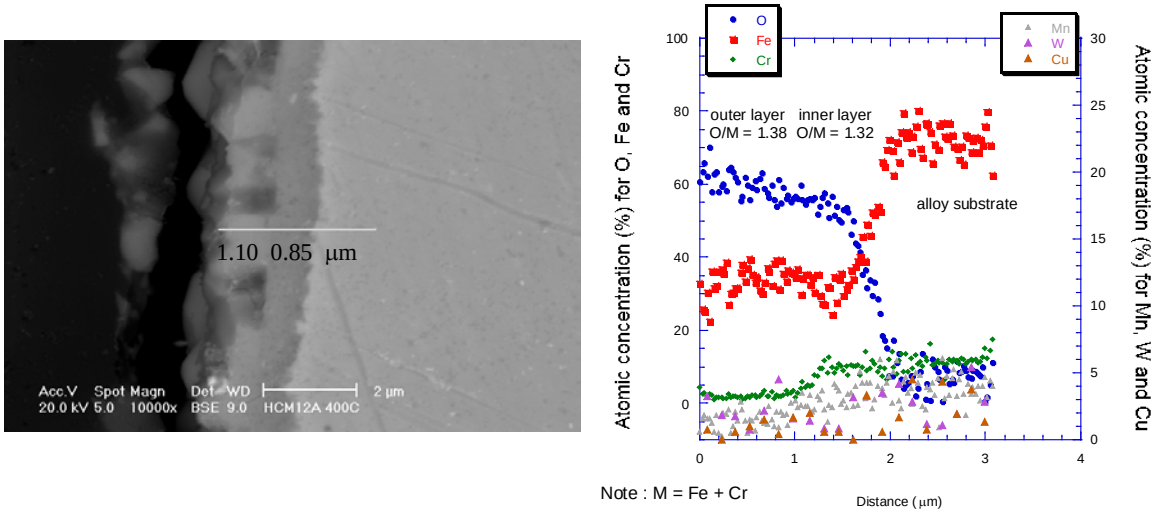

b) HCM12A

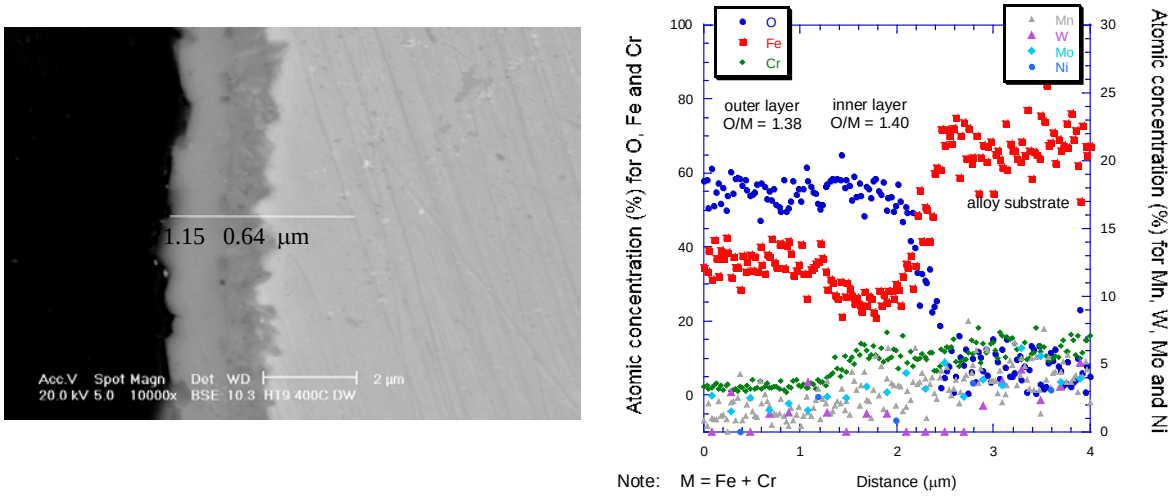

c) HT-9

Figure 4.21 Corrosion coupon cross-section BSE image and composition profile of T91, HCM12A, and HT-9 tested in 400°C deaerated SCW, 151.5 hours.

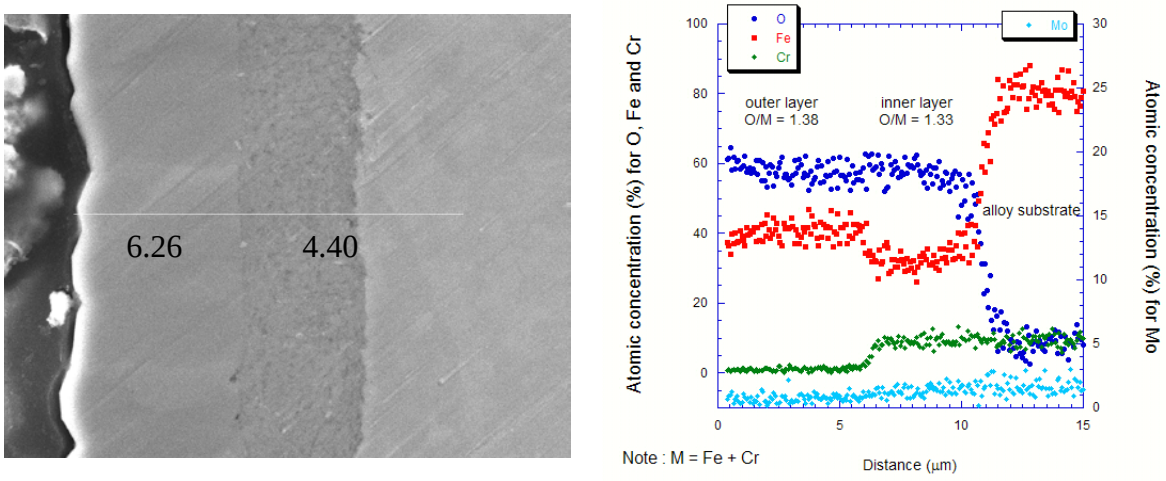

a) T91

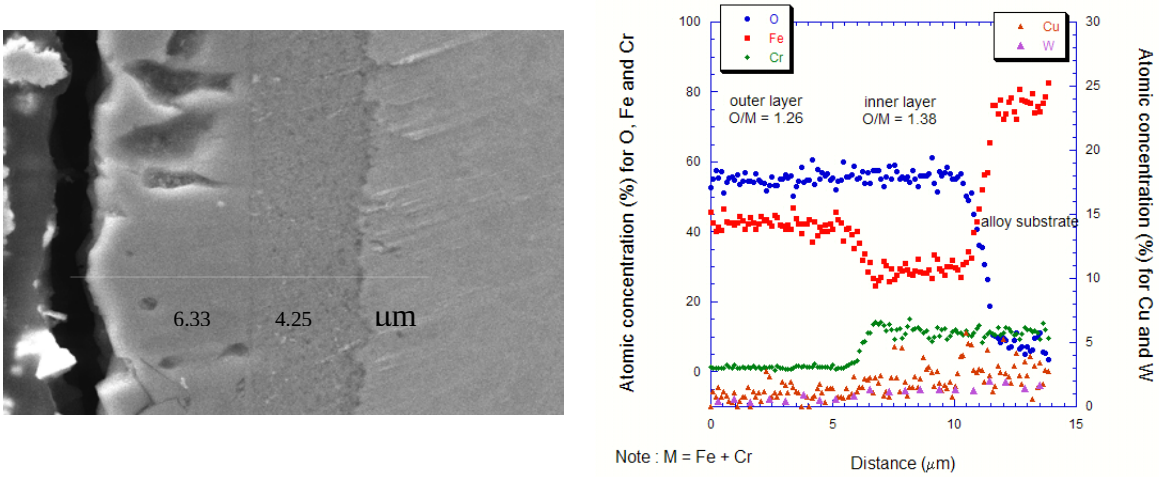

b) HCM12A

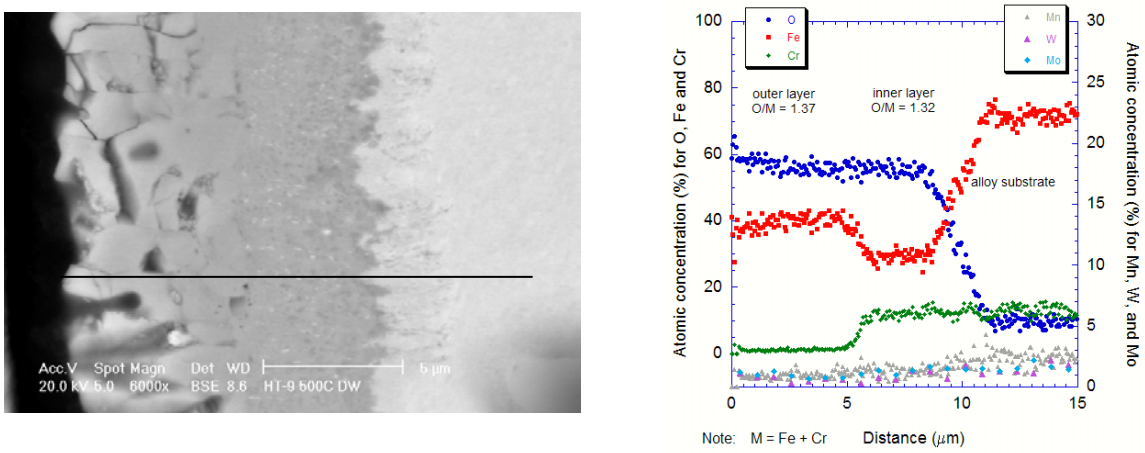

c) HT-9

Figure 4.22 Corrosion coupon cross-section BSE image and composition profile of T91 and HCM12A (exposure time 182.2 hours), and HT-9 (exposure time 195 hours) tested in 500°C deaerated SCW.

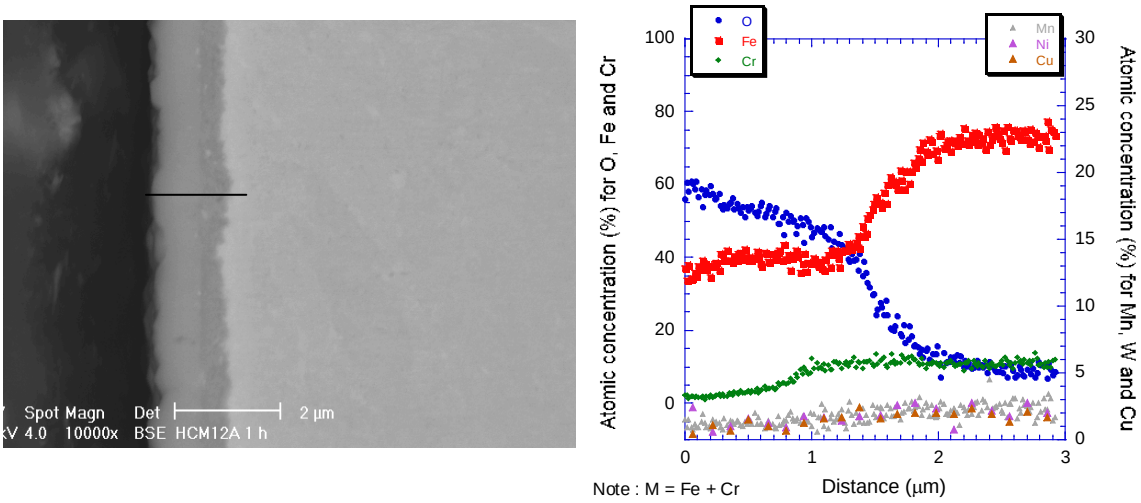

(a) 1 hour

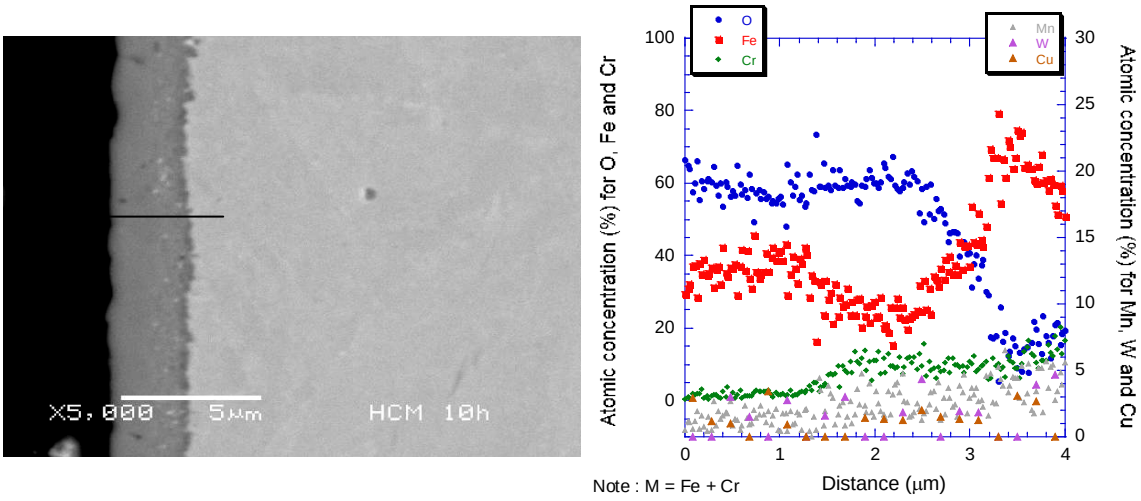

(b) 10 hours

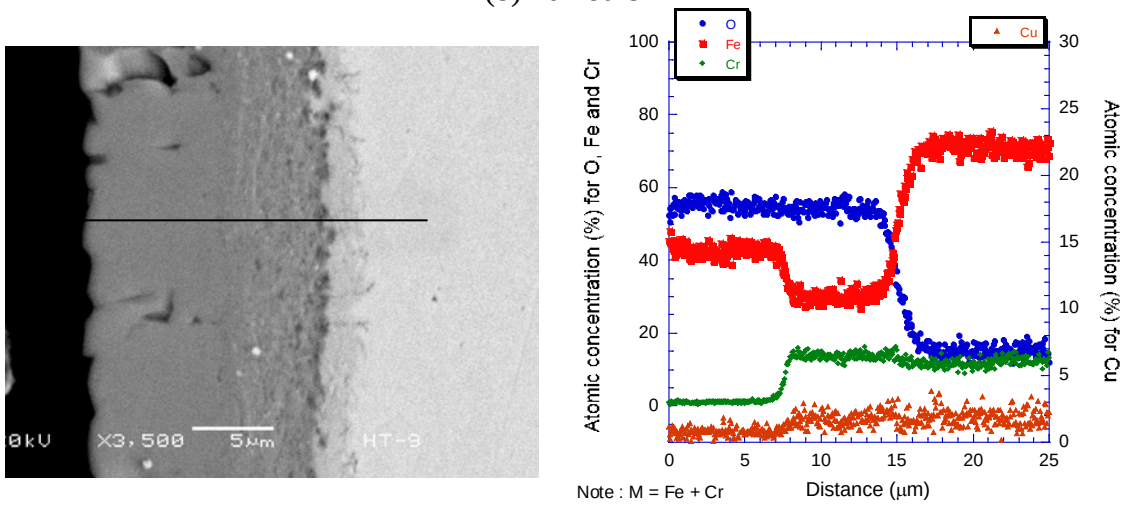

(c) 477 hours

Figure 4.23 Corrosion coupon cross-section BSE image and composition profile of HCM12A exposed in 500°C deaerated SCW for (a)1, (b) 10 and (c) 477 hours.

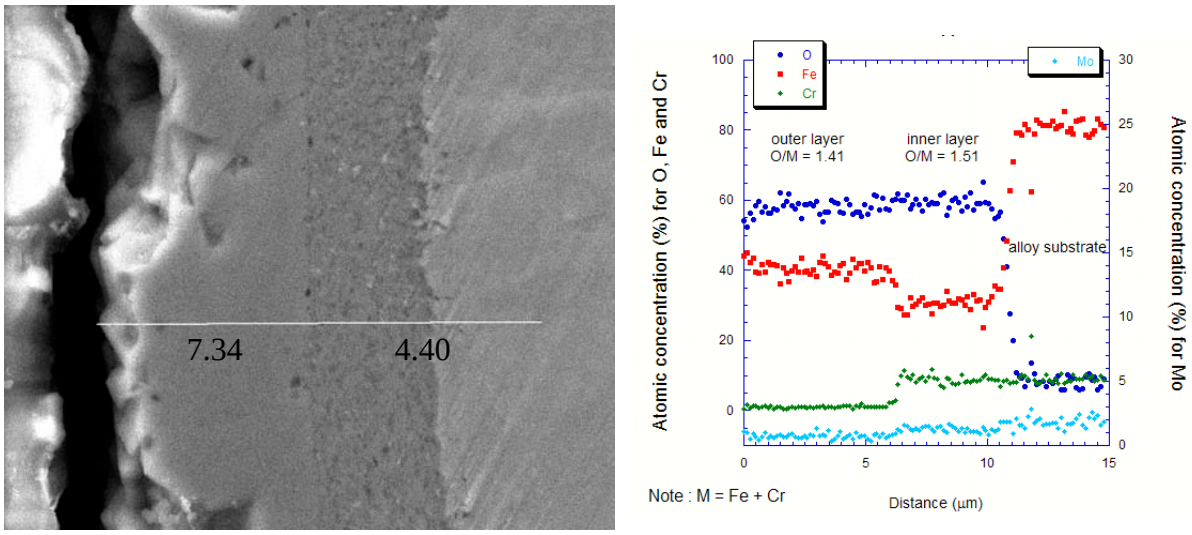

a) T91

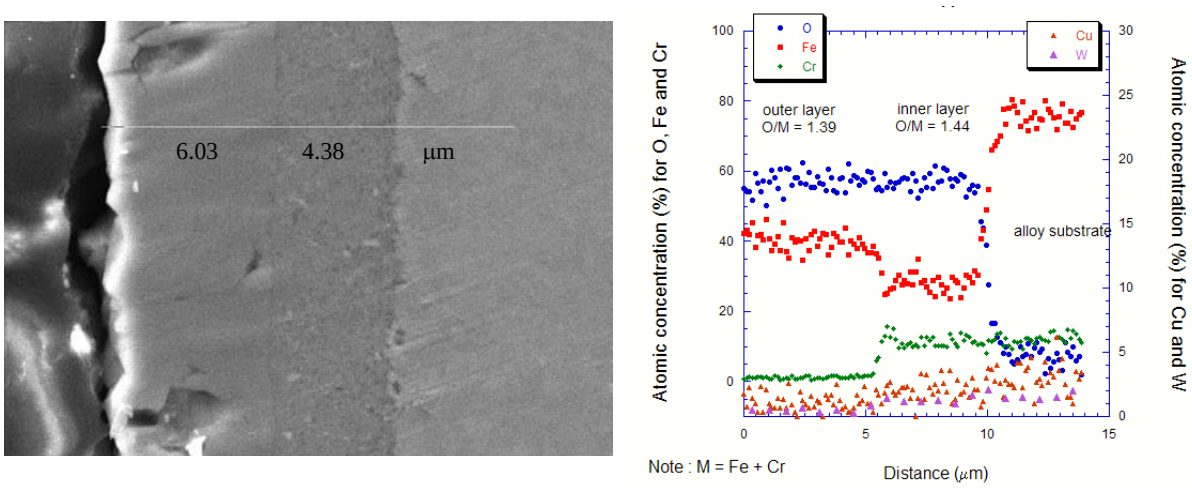

b) HCM12A

Figure 4.24 Corrosion coupon cross-section BSE image and composition profile of T91 and HCM12A tested in 500°C and 100 ppb SCW, 236 hours.

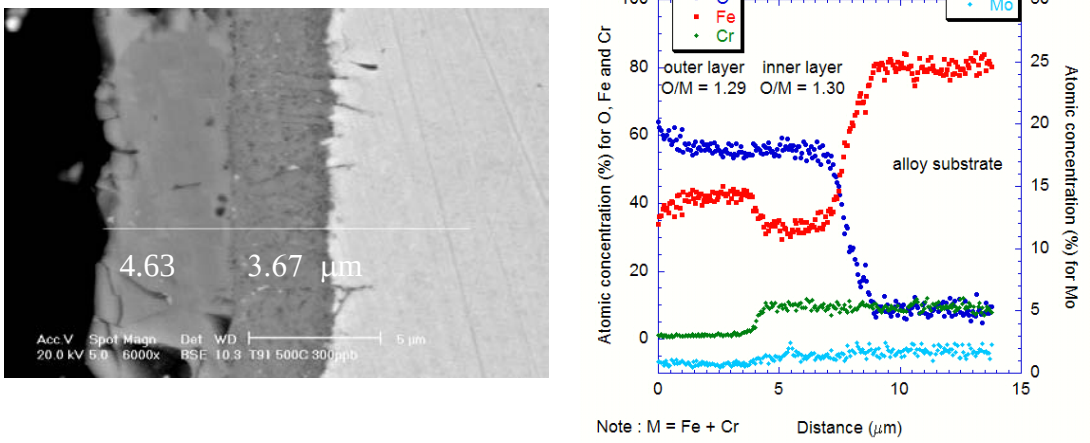

a) T91

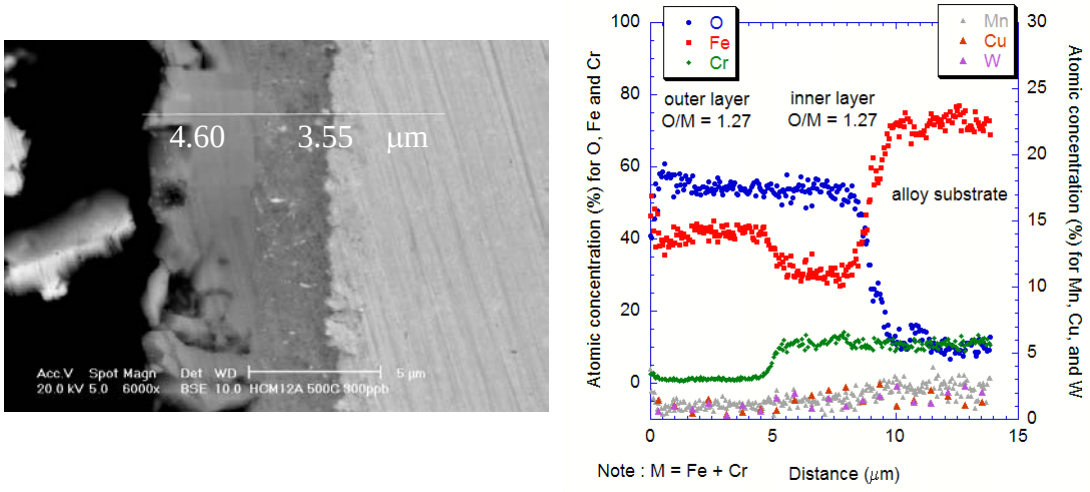

b) HCM12A

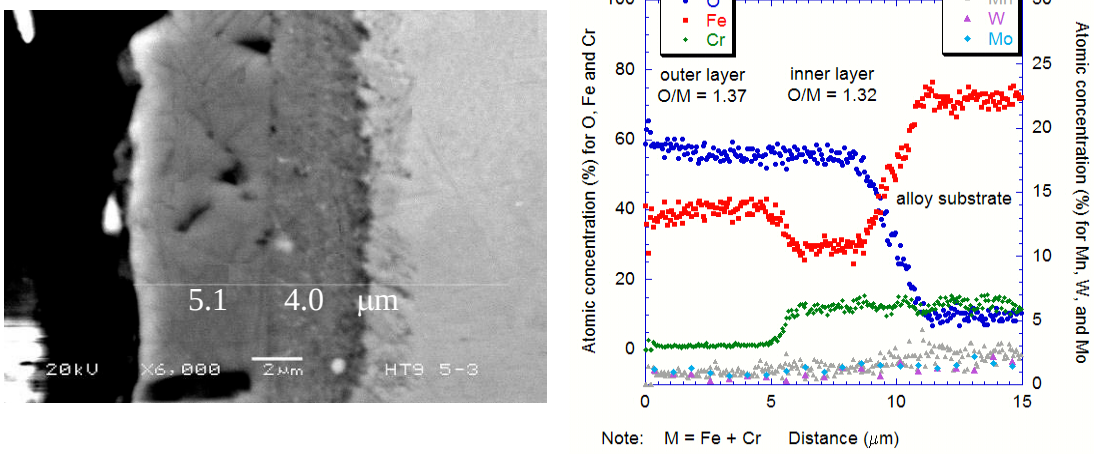

c) HT-9

Figure 4.25 Cross-section BSE images and composition profiles of alloys T91, HCM12A and HT-9 in 500C SCW containing 300 ppb dissolved oxygen, exposure time 182 hours.

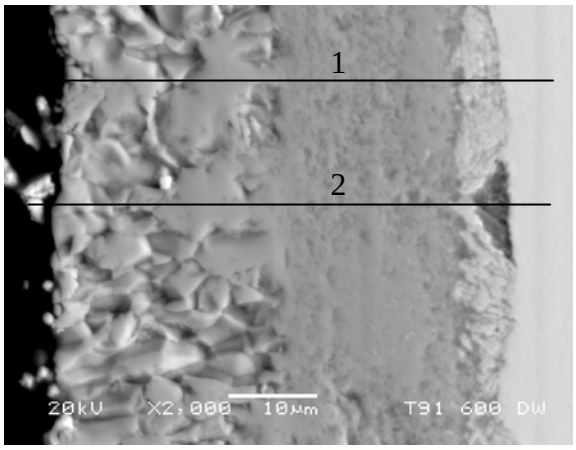

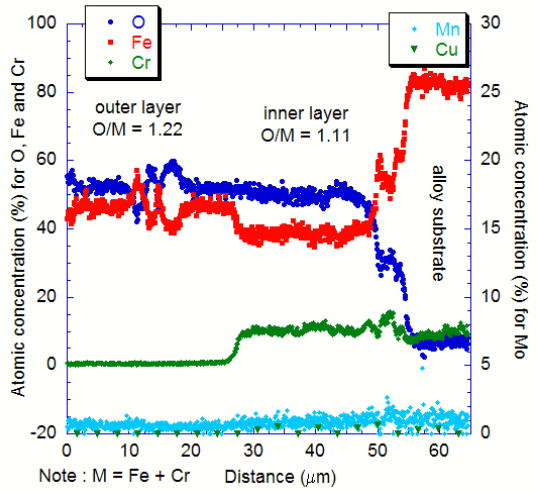

EDS line scan across line (1)

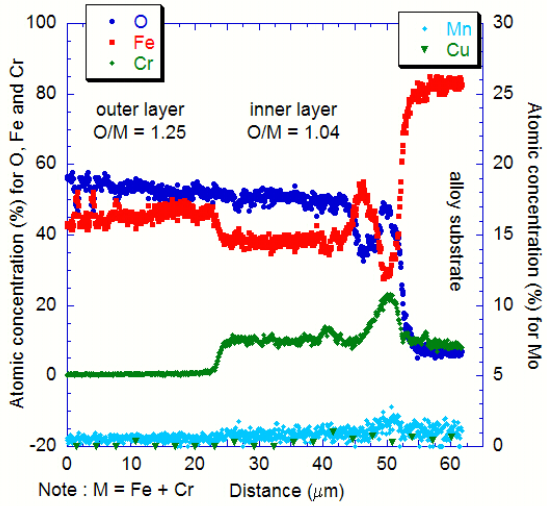

EDS line scan across line (2) passes Cr-enriched region

Figure 4.26 Corrosion coupon cross-section BSE image and composition profile of T91 tested in 600^{o}C deaerated SCW, 191 hours.

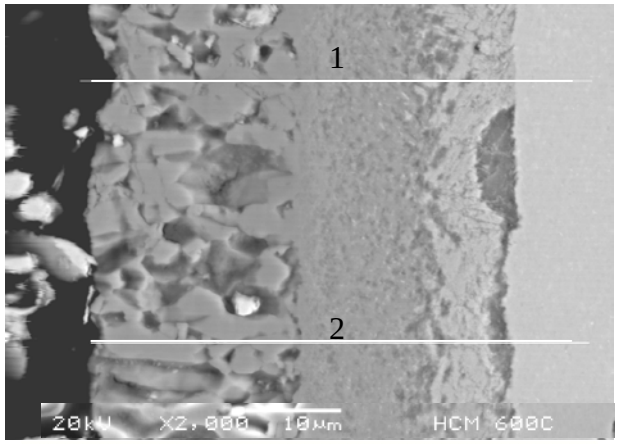

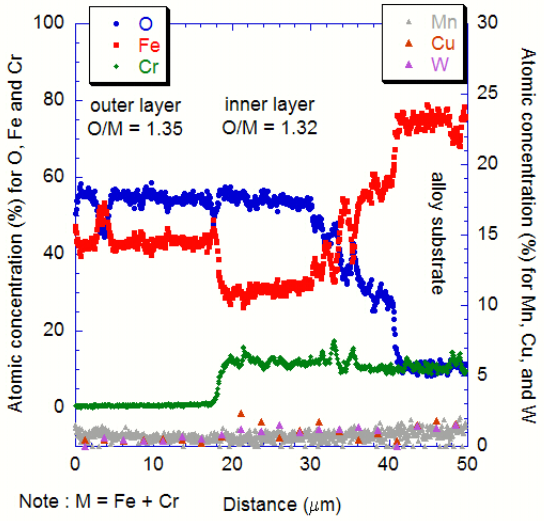

EDS line scan across line (1)

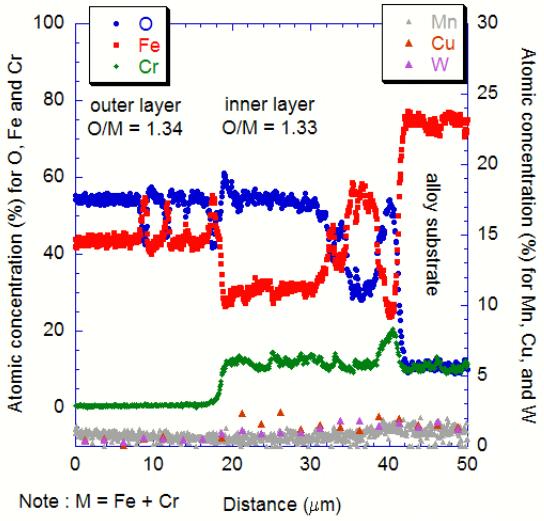

EDS line scan across line (2) passes Cr-enriched region

Figure 4.27 Corrosion coupon cross-section BSE image and composition profile of HCM12A tested in 600^{o}C deaerated SCW, 191 hours.

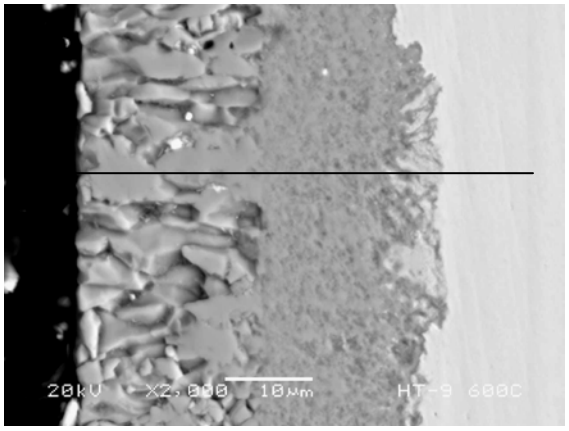

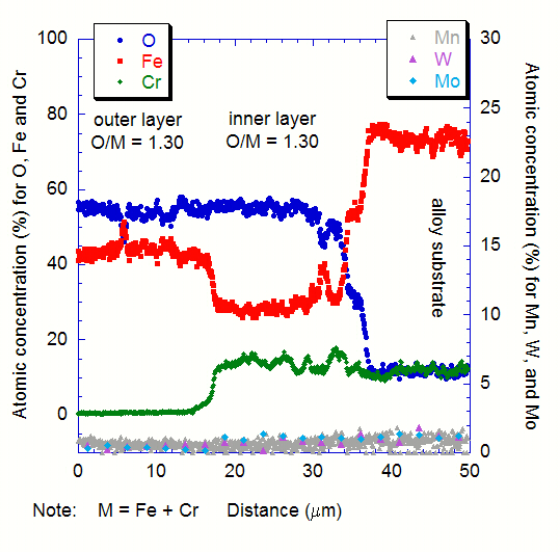

EDS line scan

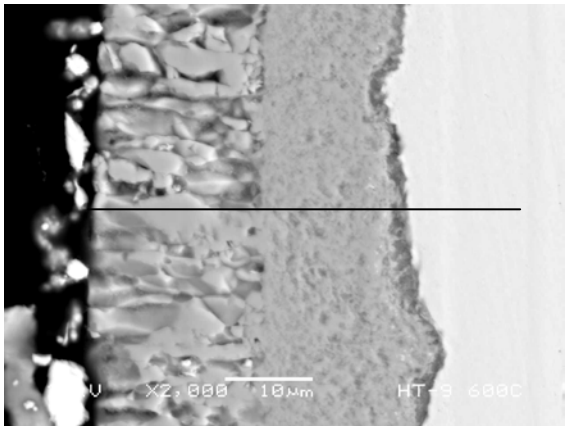

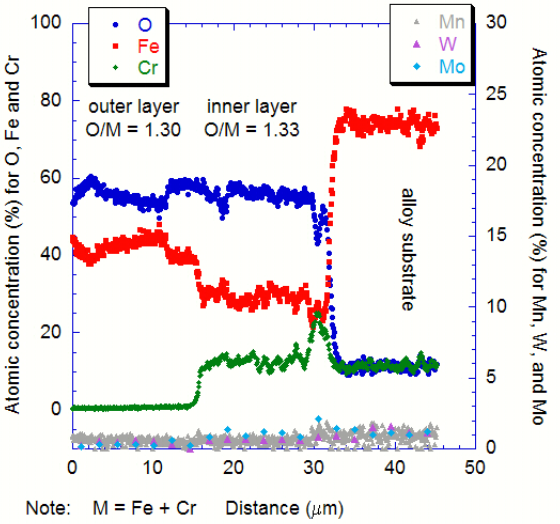

EDS line scan across line passes Cr-enriched region

Figure 4.28 Corrosion coupon cross-section BSE image and composition profile of HT-9 tested in 600°C deaerated SCW, 191 hours.

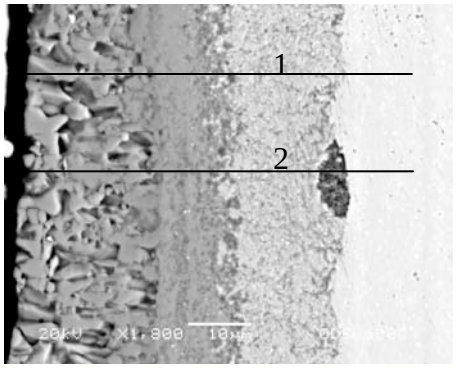

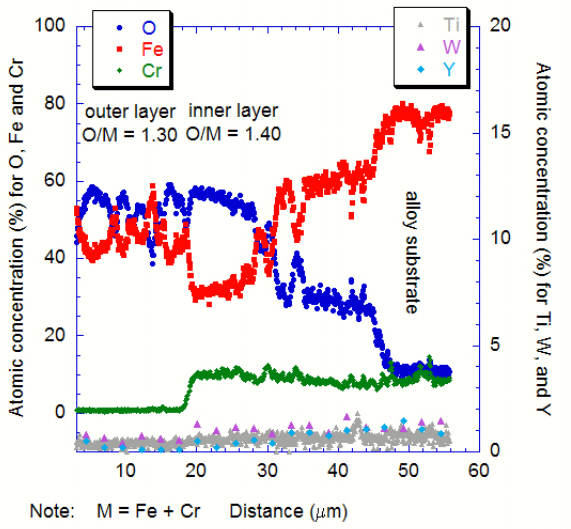

EDS line scan across line (1)

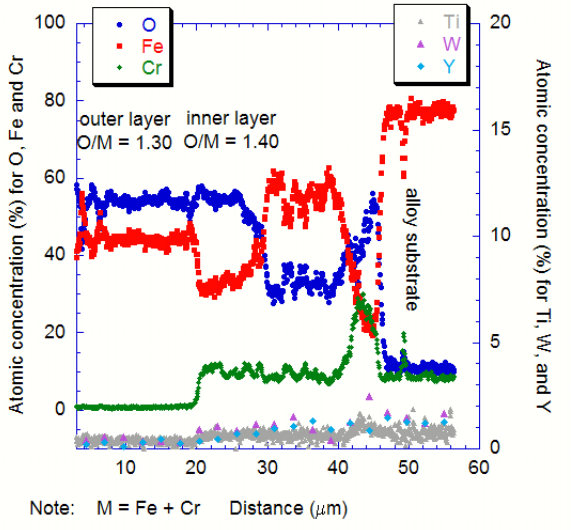

EDS line scan across line (2)

Figure 4.29 Corrosion coupon cross-section BSE image and composition profile of 9Cr-ODS tested in 600^{o}C deaerated SCW, 191 hours.

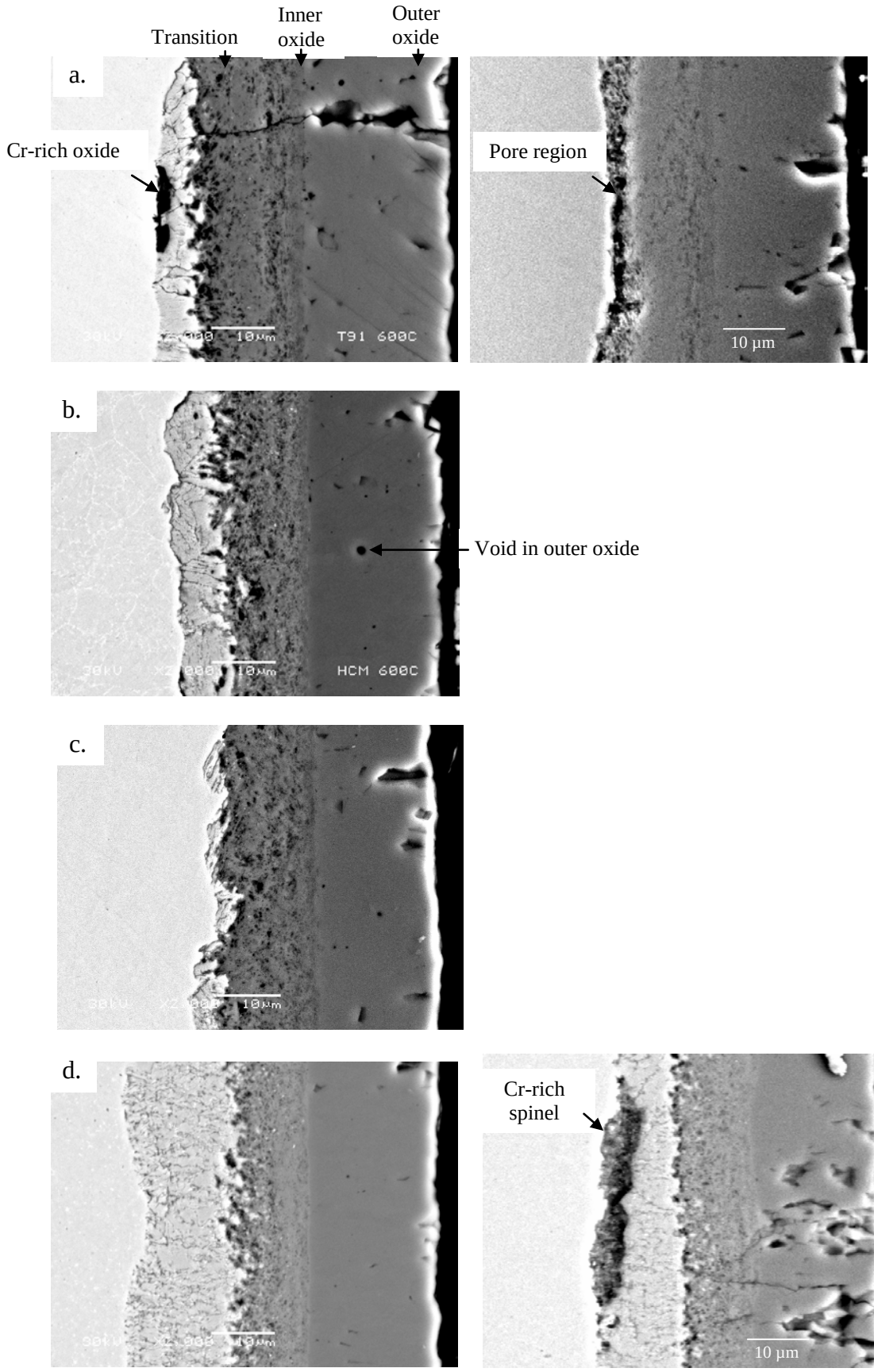

Figure 4.30 BSE images showing oxide structure of a) T91, b) HCM12A, c) HT-9 and d) 9Cr-ODS exposed in 600°C SCW for 191 hours.

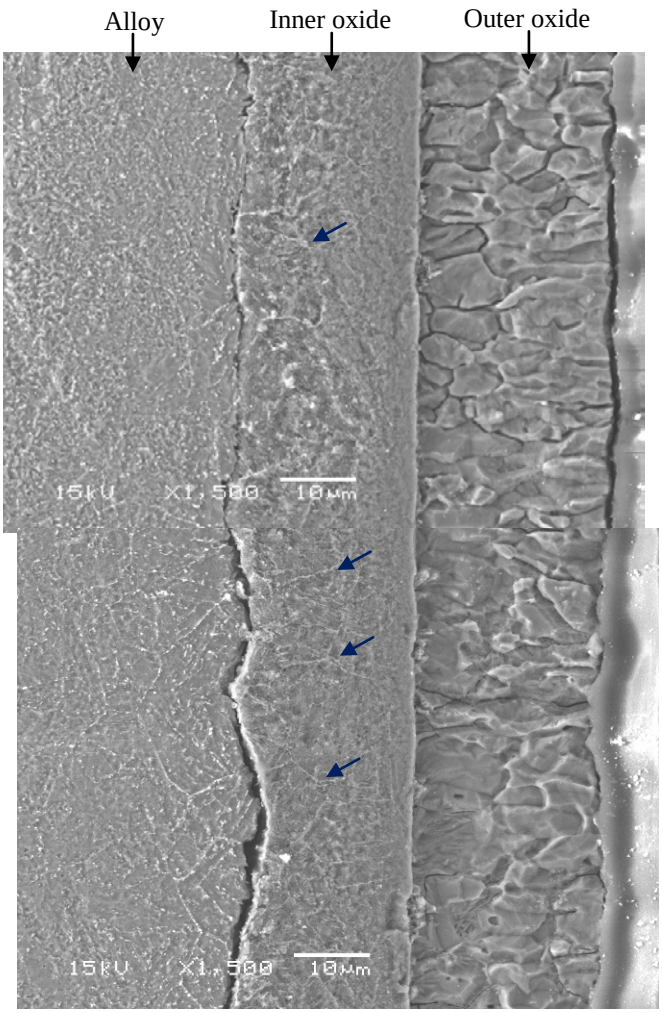

Figure 4.31 Cross section BSE images of etched T91 exposed in 600C deaerated SCW for 191 hours. The image shows Cr-rich $M_{23}C_6$ outline PAG boundaries.

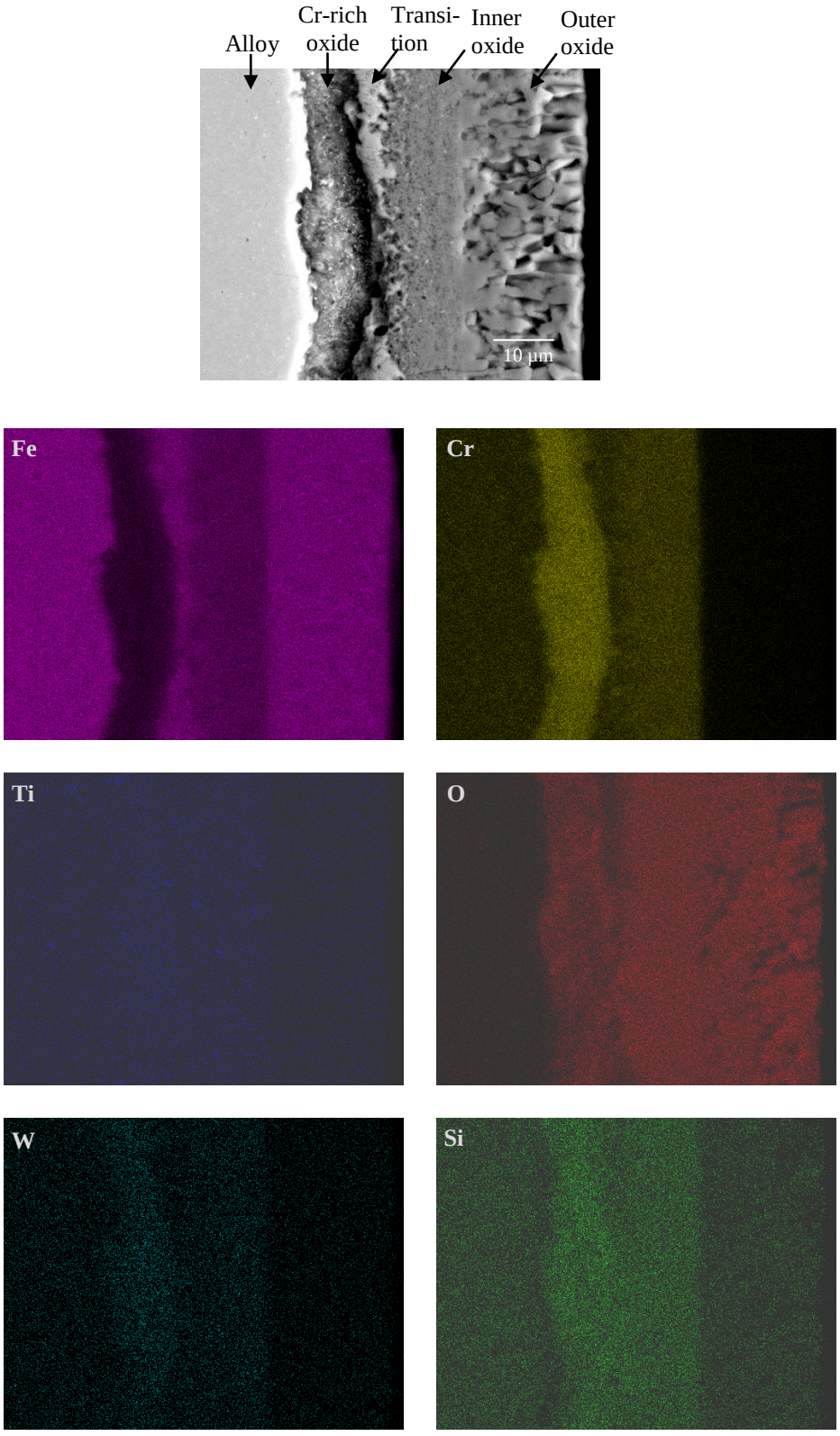

Figure 4.32 BSE image and elemental mapping of 9Cr-ODS exposed in 600°C SCW for 191 hour. The maps show Cr-enriched oxide at transition/alloy interface.

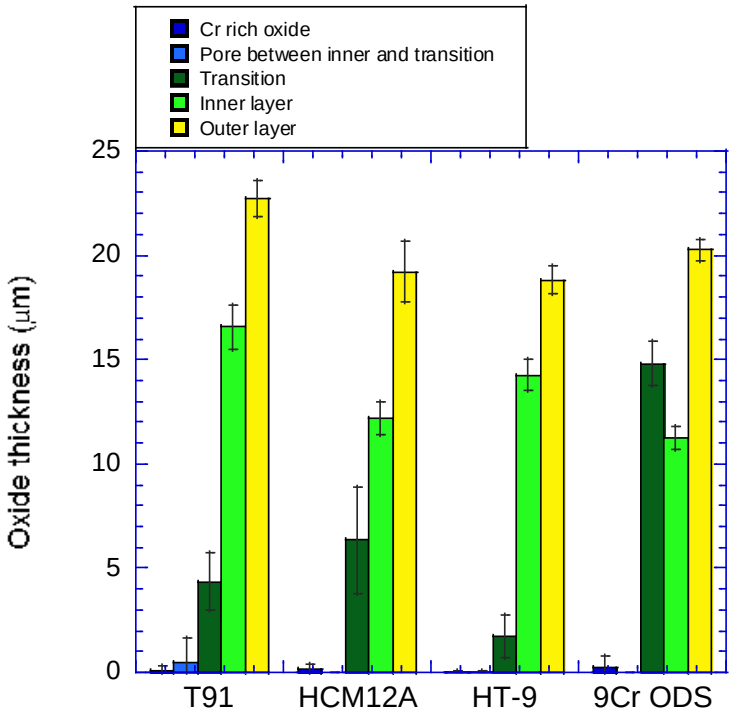

Figure 4.33 Comparison of oxide thickness formed on T91, HCM12A, HT-9 and 9Cr-ODS exposed in 600°C deaerated SCW for 191 hours.

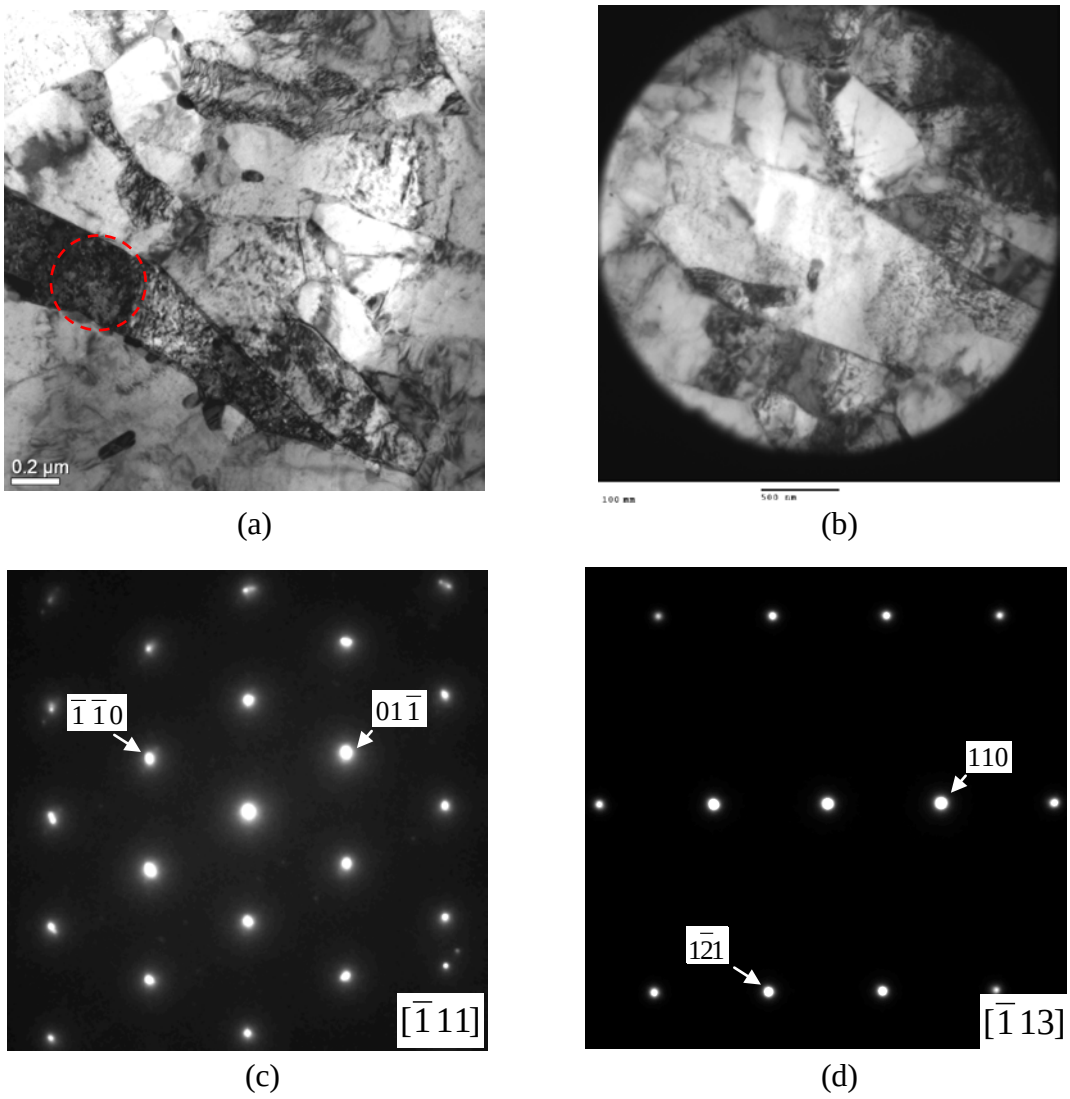

Figure 4.34 TEM images showing microstructure of HCM12A before exposure in SCW. (a) and (b) Martensite laths, and SAED from a lath (circled) in (a) from (c) $[\bar{1}11]$ and (d) $\bar{1}13$ zone axes exhibited BCC structure of Fe.

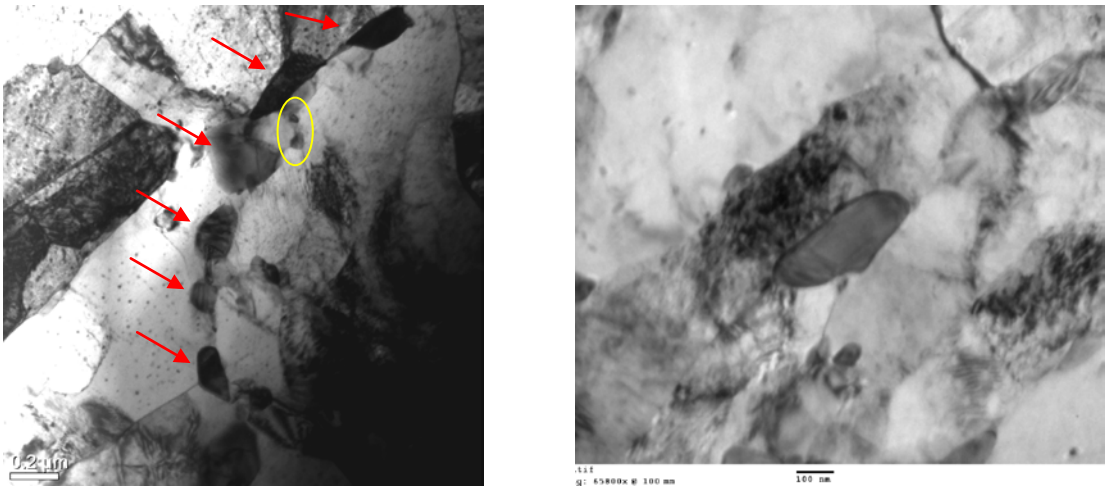

(a) (b)

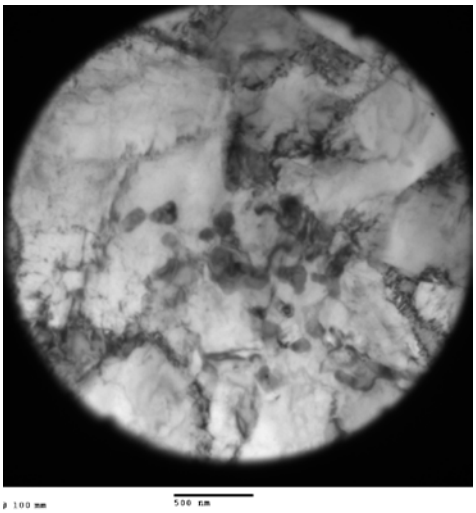

(c)

Figure 4.35 TEM images showing precipitate particles of Cr-rich $M_{23}C_6$ in pre-oxidized HCM12A. (a) The particles outline the PAG boundary, (b) a particle at lath boundary, and (c) clusters of precipitates inside alloy matrix.

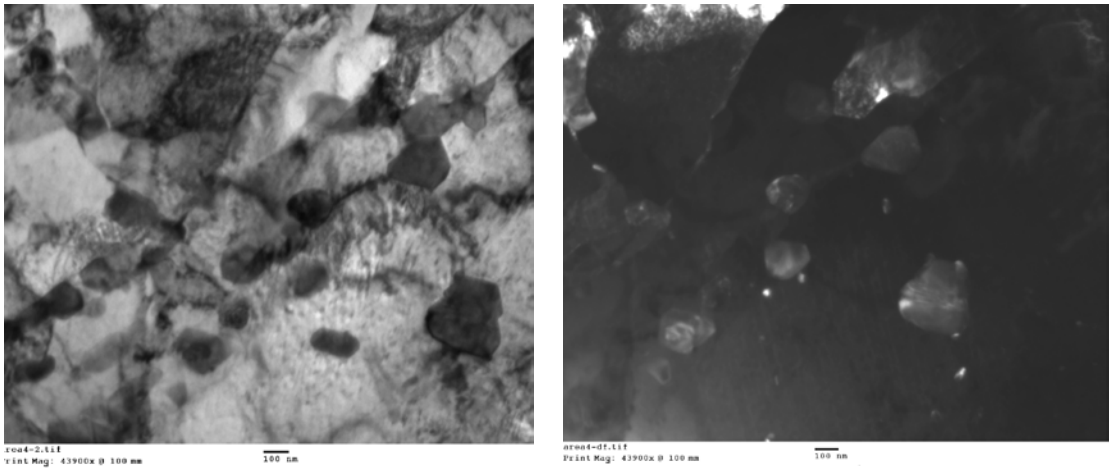

(a) (b)

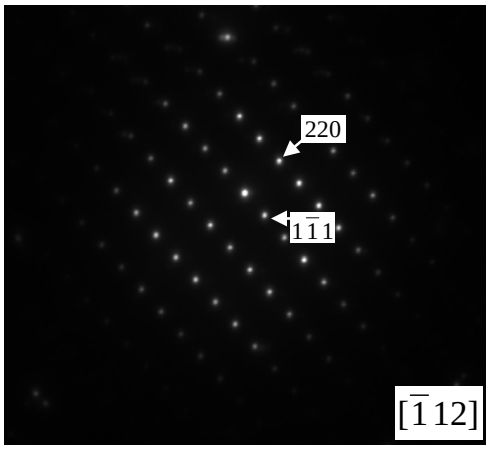

(c)

Figure 4.36 (a) BF and (b) DF of Cr-rich $M_{23}C_6$ precipitates, and (c) SAED of the precipitates from $[\bar{1}12]$ zone axes exhibiting FCC structure.

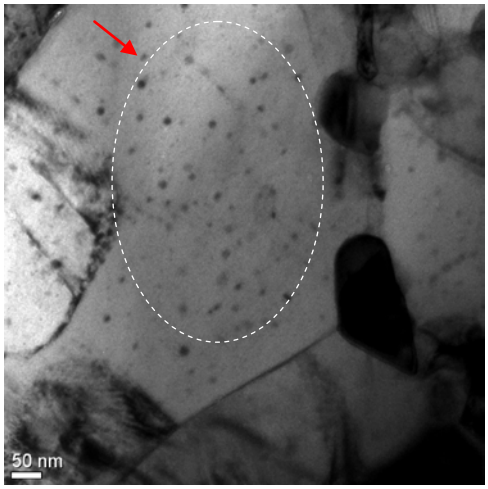

Figure 4.37 TEM image showing precipitate particles of V-Nb compound in pre-oxidized HCM12A.

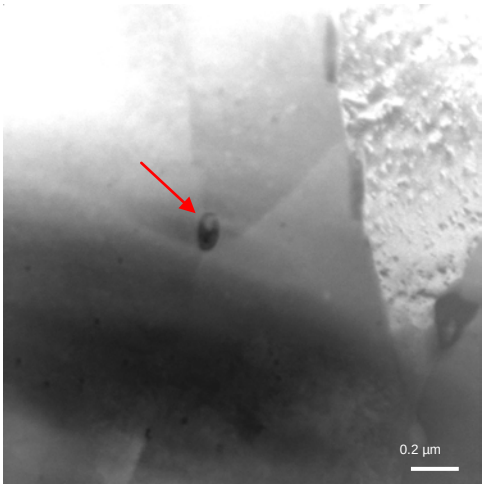

Figure 4.38 TEM image showing precipitate particles of Cu in pre-oxidized HCM12A.

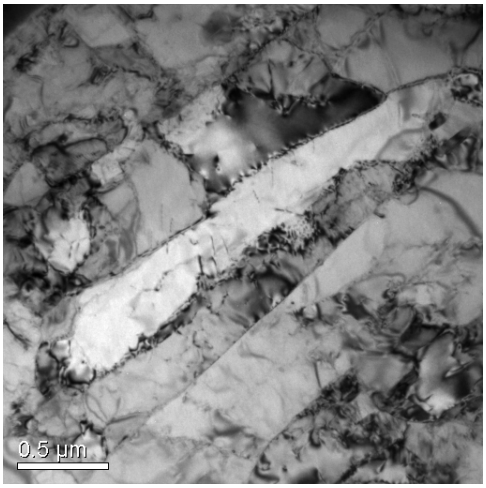

(a)

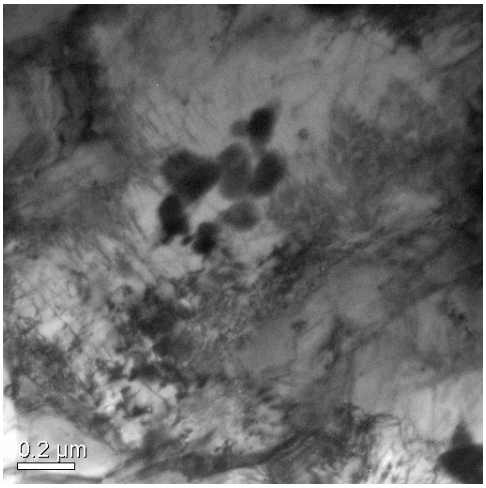

(b)

Figure 4.39 TEM images of microstructure of pre-oxidized T91 showing (a) the martensite laths, and (b) cluster of Cr-rich $M_{23}C_6$ precipitates.

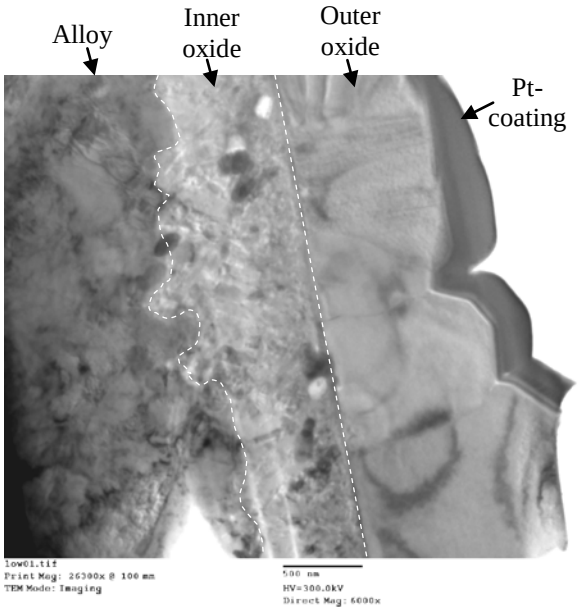

(a)

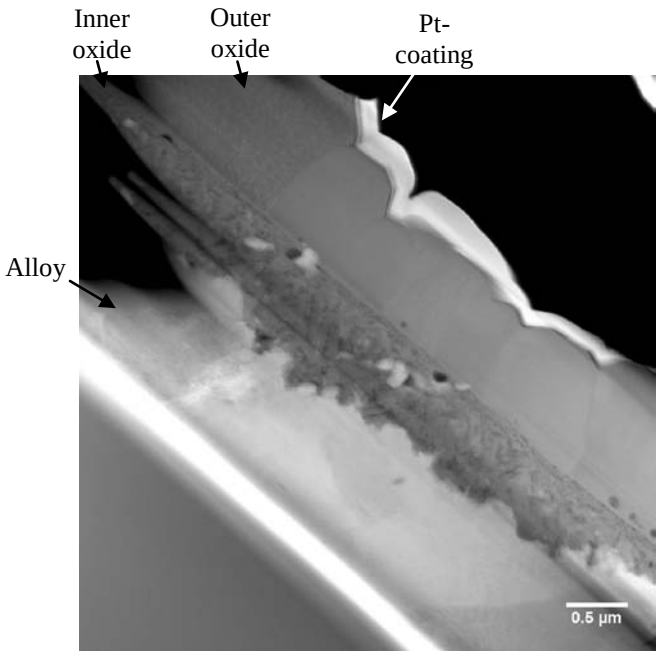

(b)

Figure 4.40 (a) Bright field and (b) HAADF images of oxides formed on HCM12A exposed in 400°C deaerated SCW for 151 hours. The images show two distinct layers of oxide.

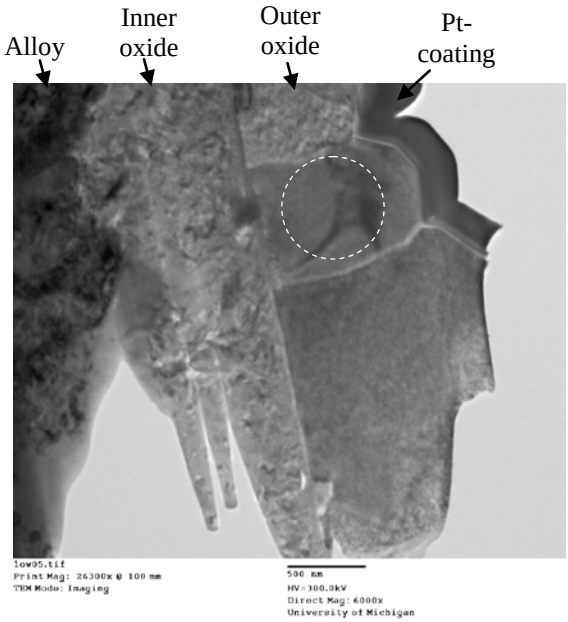

(a)

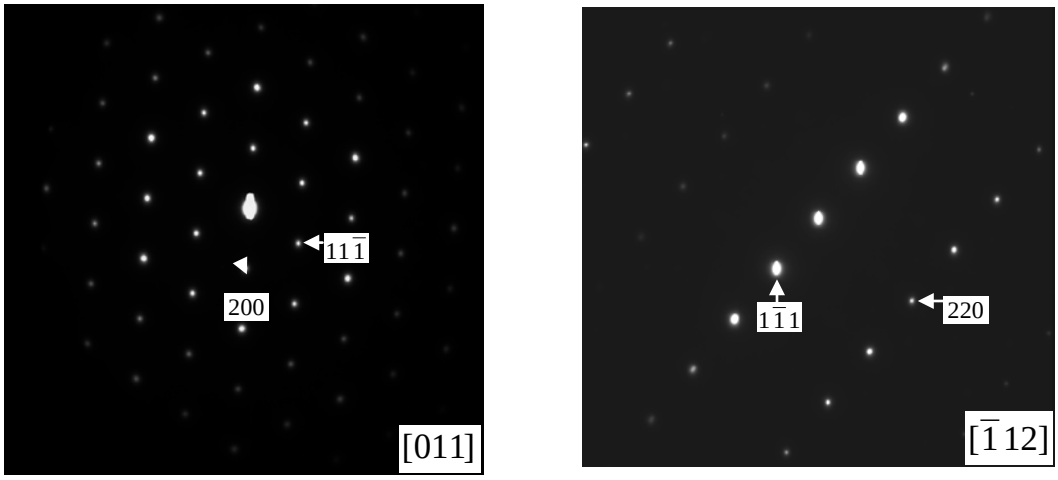

(b) (c)

Figure 4.41 TEM image of oxides formed on HCM12A exposed in 400°C deaerated SCW for 151 hours present magnetite grains in the outer layer. (a) Bright field image, and SAED of a magnetite grain (circled) from (b) [011] and (c) $[\bar{1}12]$ directions.

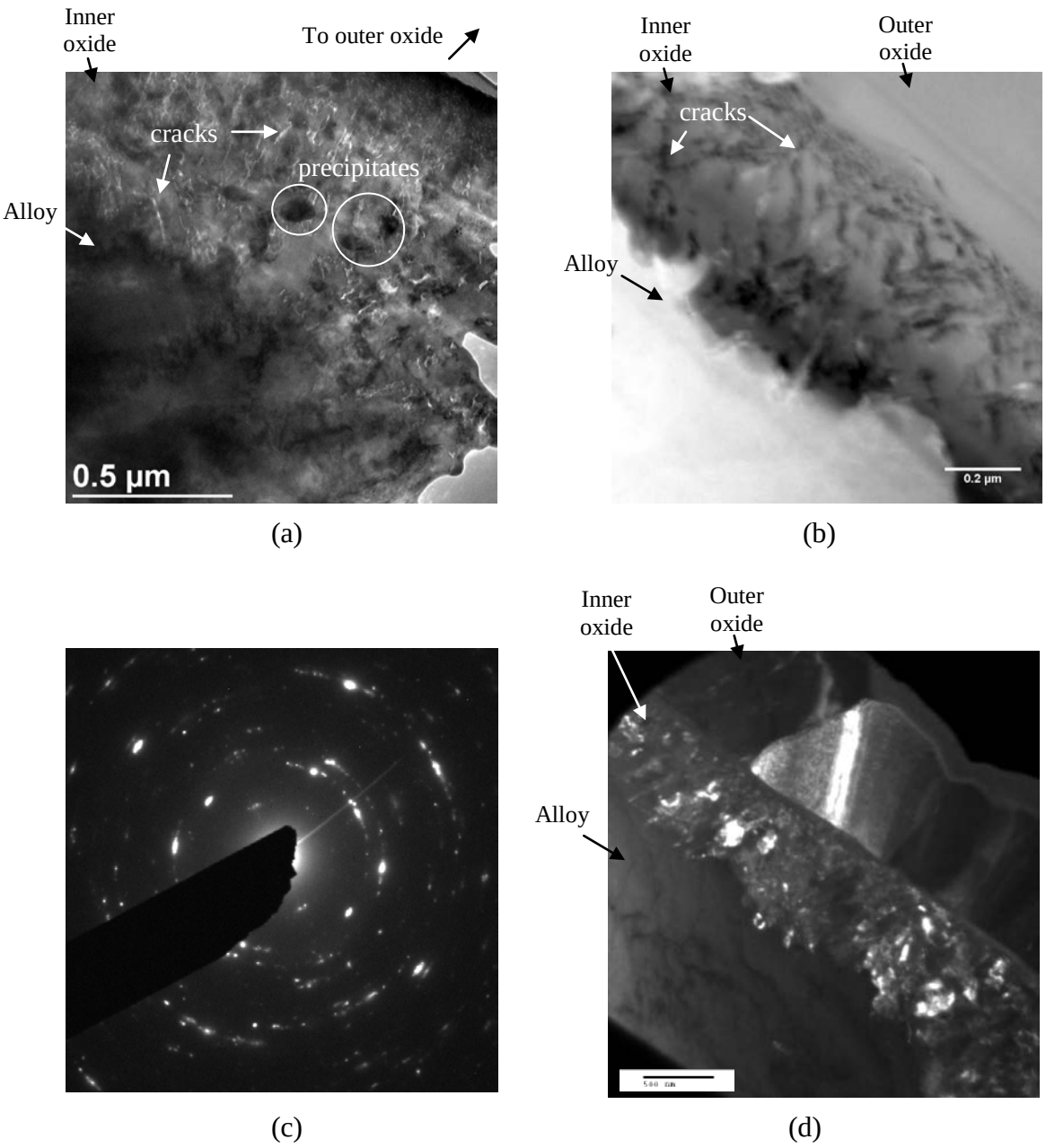

Figure 4.42 TEM images of oxides formed on HCM12A exposed in 400°C deaerated SCW for 151 hours. (a) BF and (b) HAADF images of inner layer oxide shows precipitates and microcracks in the layer, (c) SAED from the inner oxide shows ring pattern, and (d) DF image exhibits grain size of the inner oxide < 100 nm.

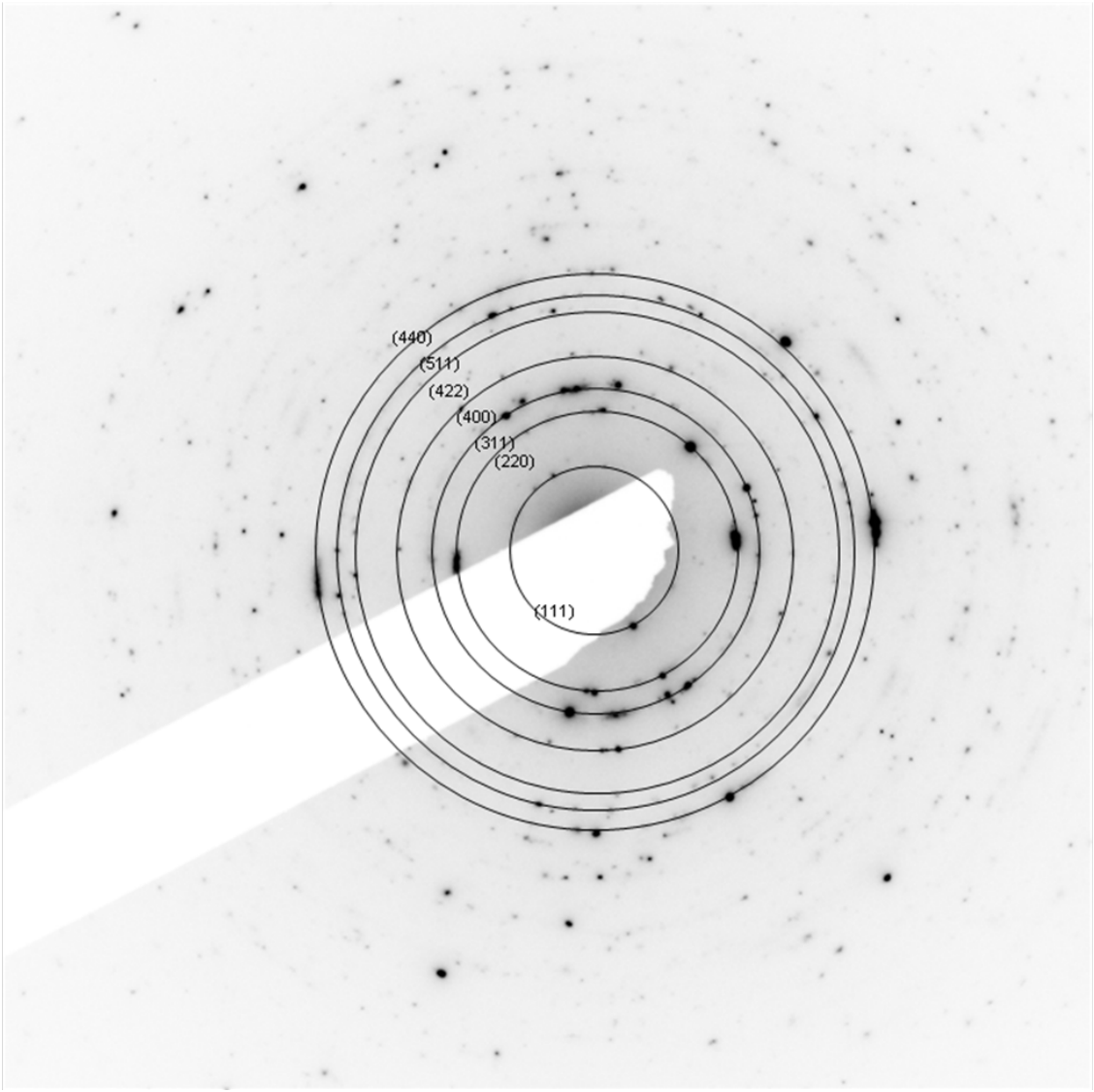

Figure 4.43 Indexing SAED pattern from the inner oxide of HCM12A exposed in 400°C deaerated SCW for 151 hours. The pattern exhibited FCC spinel structure.

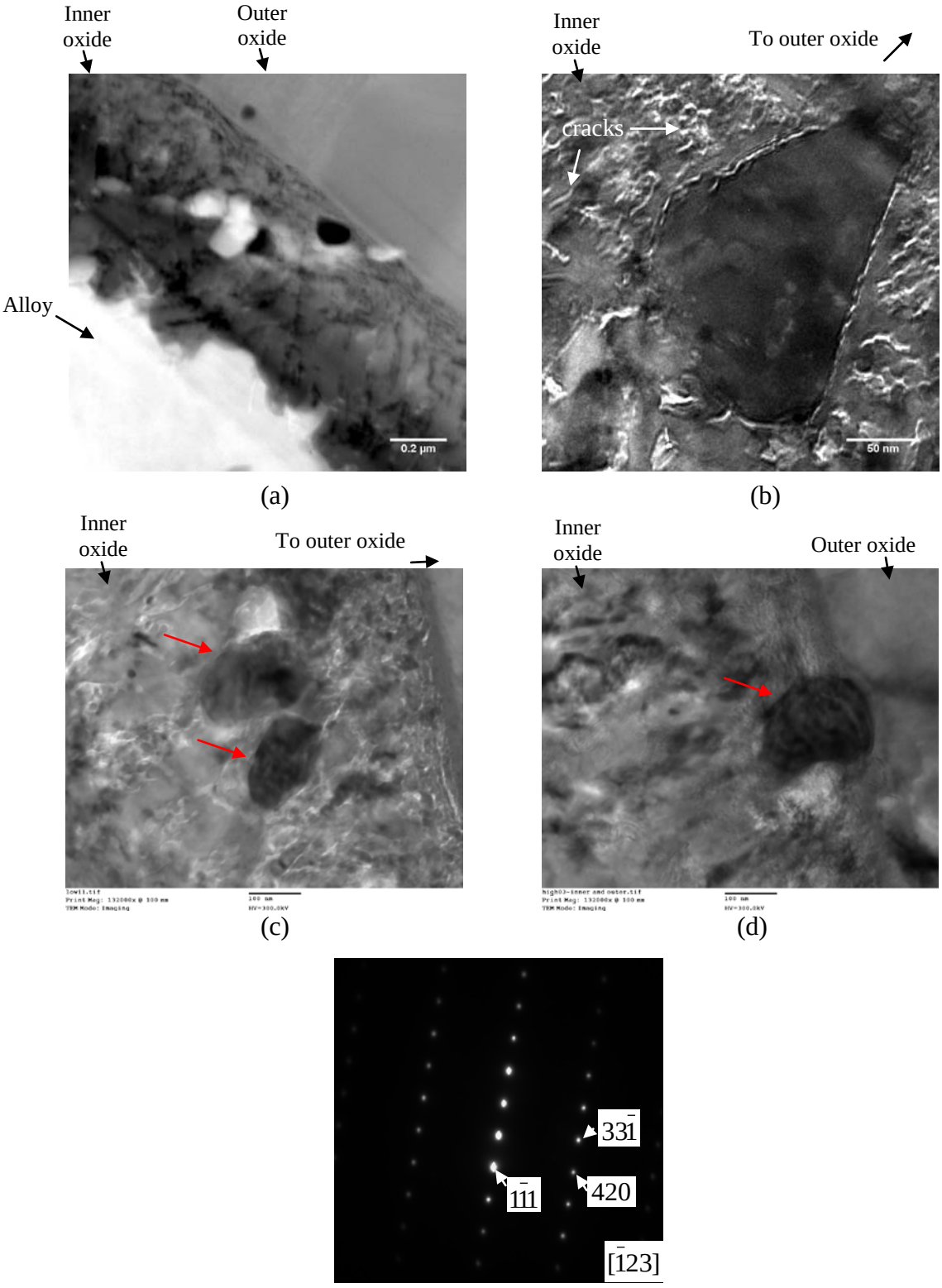

Figure 4.44 TEM images of oxides formed on HCM12A exposed in 400°C deaerated SCW for 151 hours. (a) - (d) Precipitate particles of Cr-rich $M_{23}C_6$ observed in the inner layer oxide. (e) SAED of precipitate from fcc $[\bar{1}23]$ zone axis.

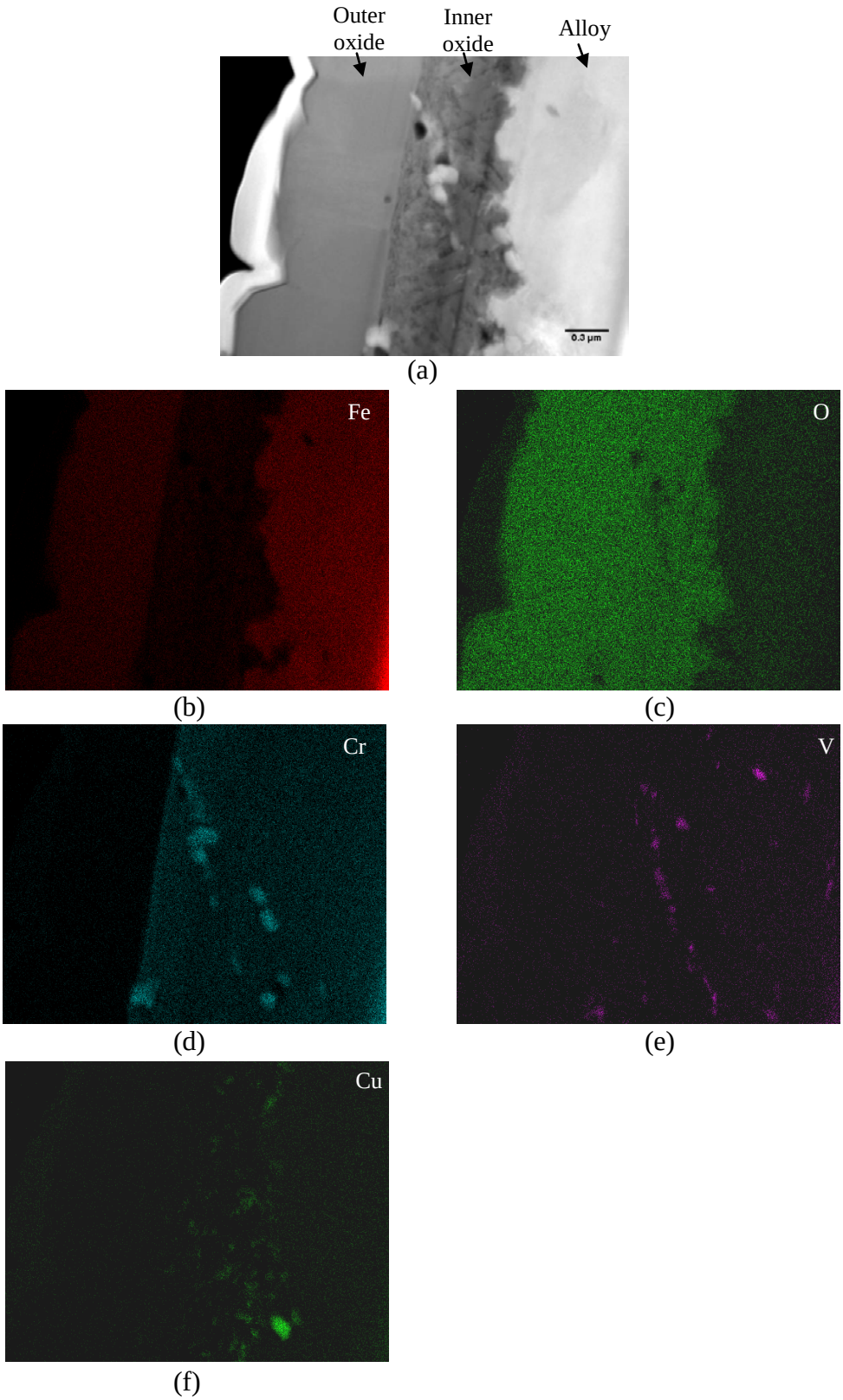

Figure 4.45 Composition mapping of oxides formed on HCM12A exposed in 400°C deaerated SCW for 151 hours. (a) HAADF image and composition maps of (b) Fe, (c) O, (d) Cr, (e) V, and (f) Cu. The results show Cr, V and Cu precipitated in the inner layer oxide.

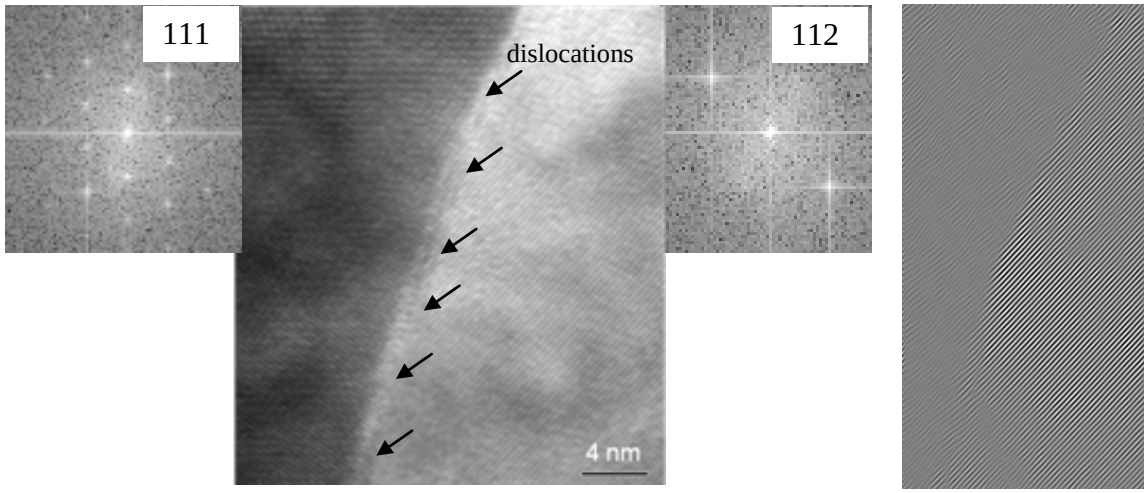

(a)

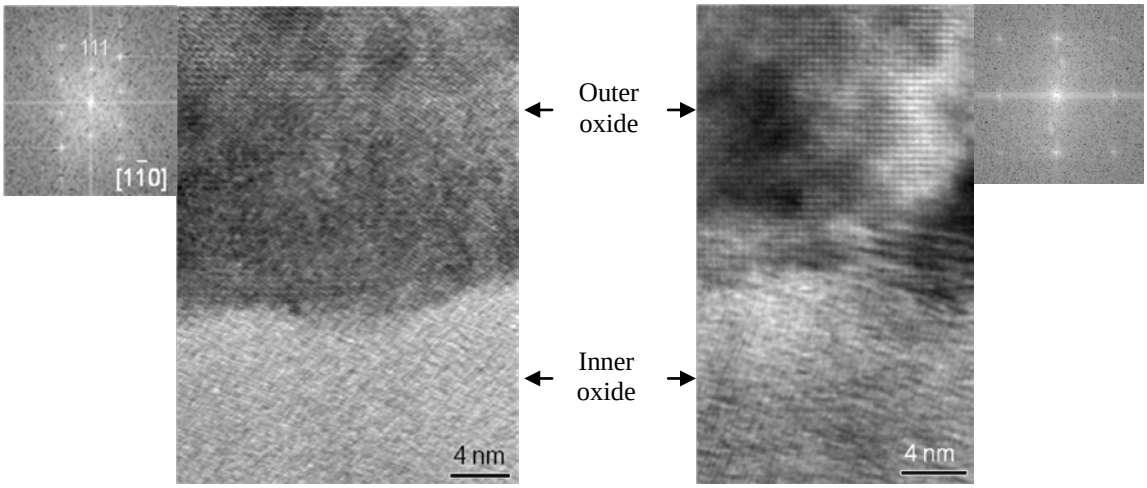

(b)

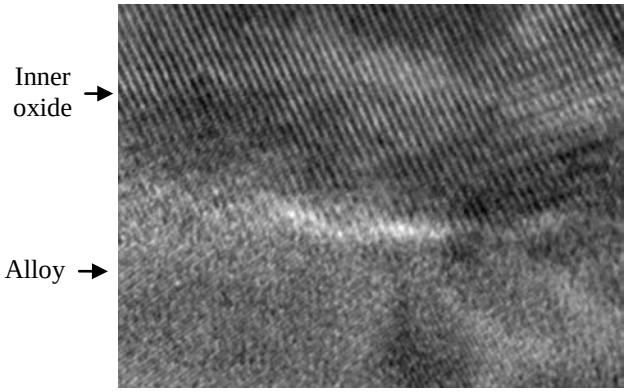

(c)

Figure 4.46 HRTEM images of oxides formed on HCM12A exposed in 400°C deaerated SCW for 151 hours. (a) Interface of magnetite grains and Fourier transformed image (right), (b) the outer-inner oxides interface, and (c) the inner oxide – alloy interface.

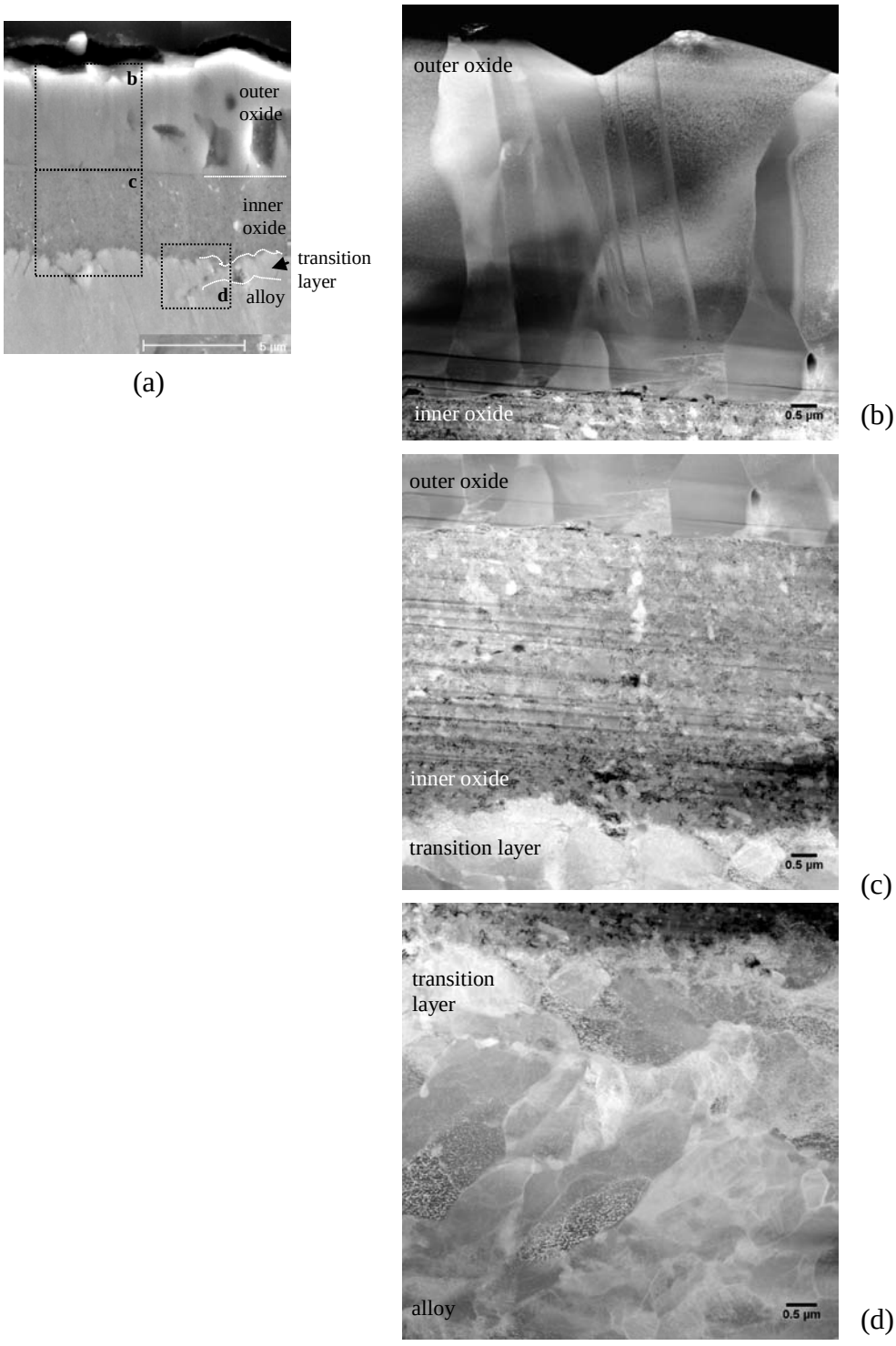

Figure 4.47 Images of oxides formed on HCM12A exposed in 500°C deaerated SCW for 182 hours. (a) Cross sectional BSE image shows oxide layers in (b) – (c). HAADF images of (b) outer layer oxide, (c) inner layer oxide, and (d) transition layer and alloy substrate.

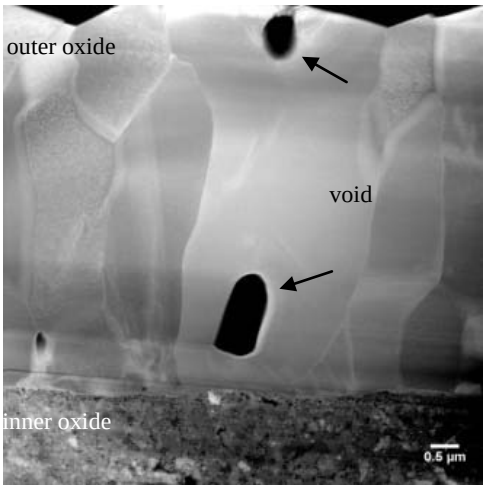

(a)

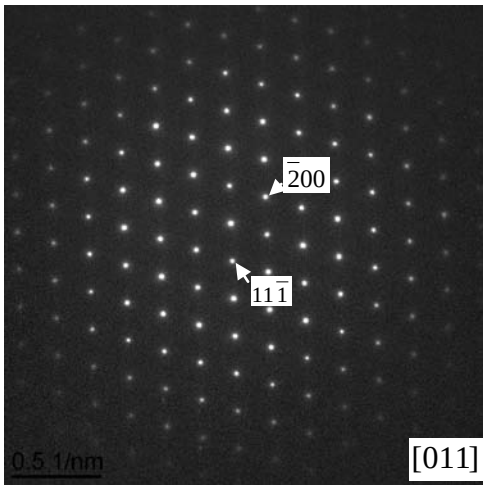

(b)

Figure 4.48 TEM images of the outer layer oxide formed on HCM12A exposed in 500°C deaerated SCW for 182 hours. (a) HAADF image shows magnetite grains with voids inside the grain. (b) SAED pattern from [011] zone axis.

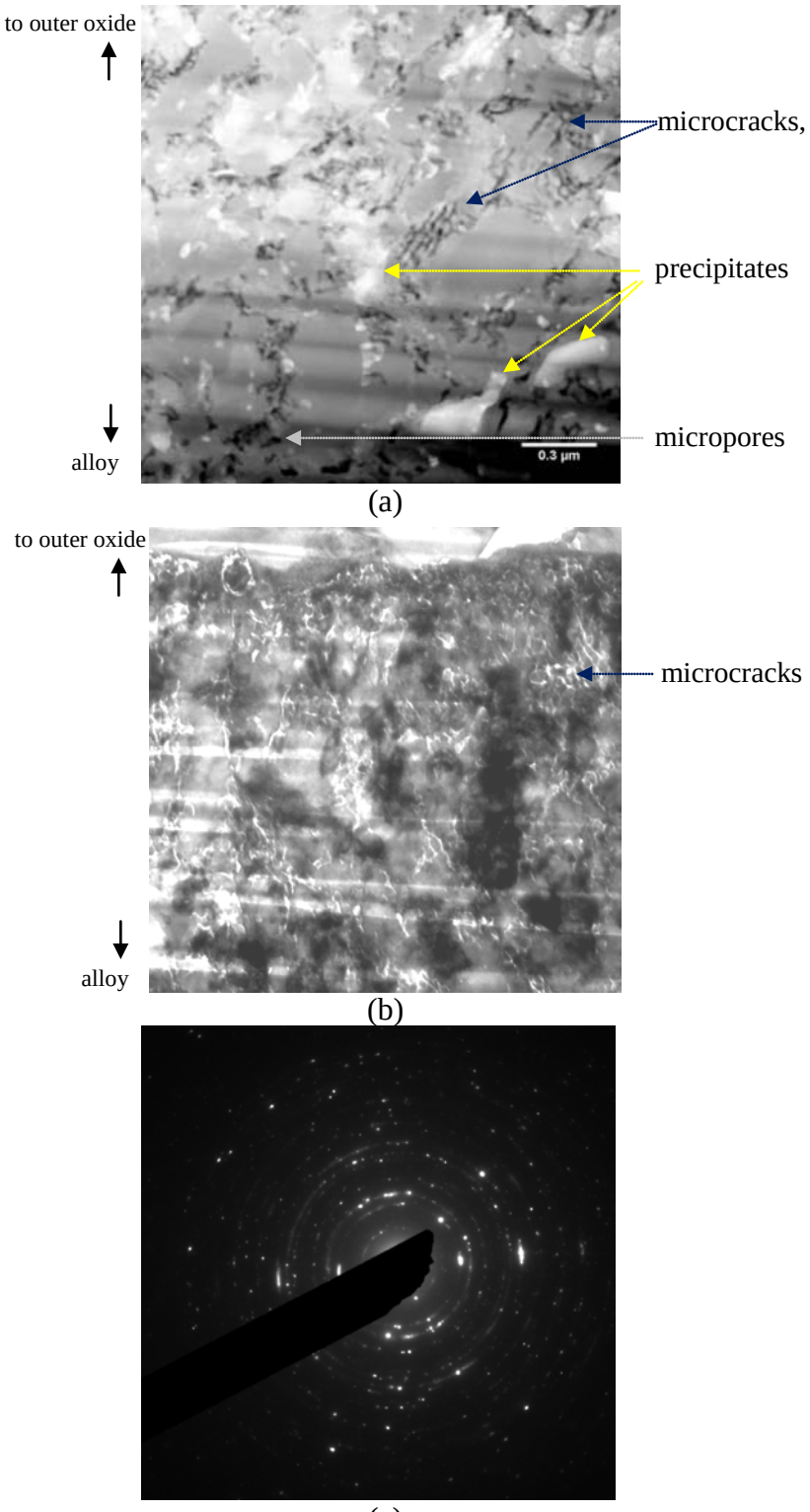

Figure 4.49 TEM images of the inner layer oxide formed on HCM12A exposed in 500°C deaerated SCW for 182 hours. (a) HAADF and (b) BF images shows morphology of the inner oxide that consisted of small grains of $(Fe,Cr)_3O_4$, precipitates, and microcracks. (c) SAED pattern from the inner oxide exhibited FCC spinel structure.

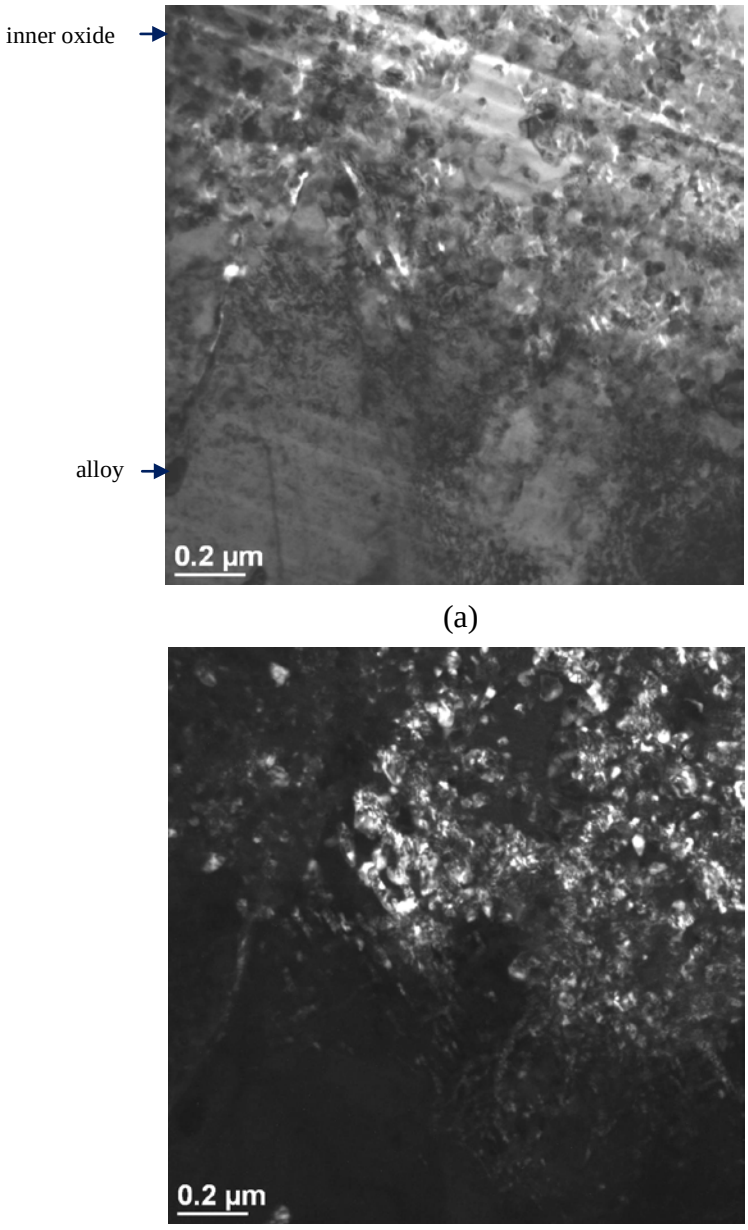

Figure 4.50 TEM images of the inner layer oxide formed on HCM12A exposed in 500°C deaerated SCW for 182 hours. (a) BF and (b) DF image shows small grain size of Fe-Cr spinel structure oxides.

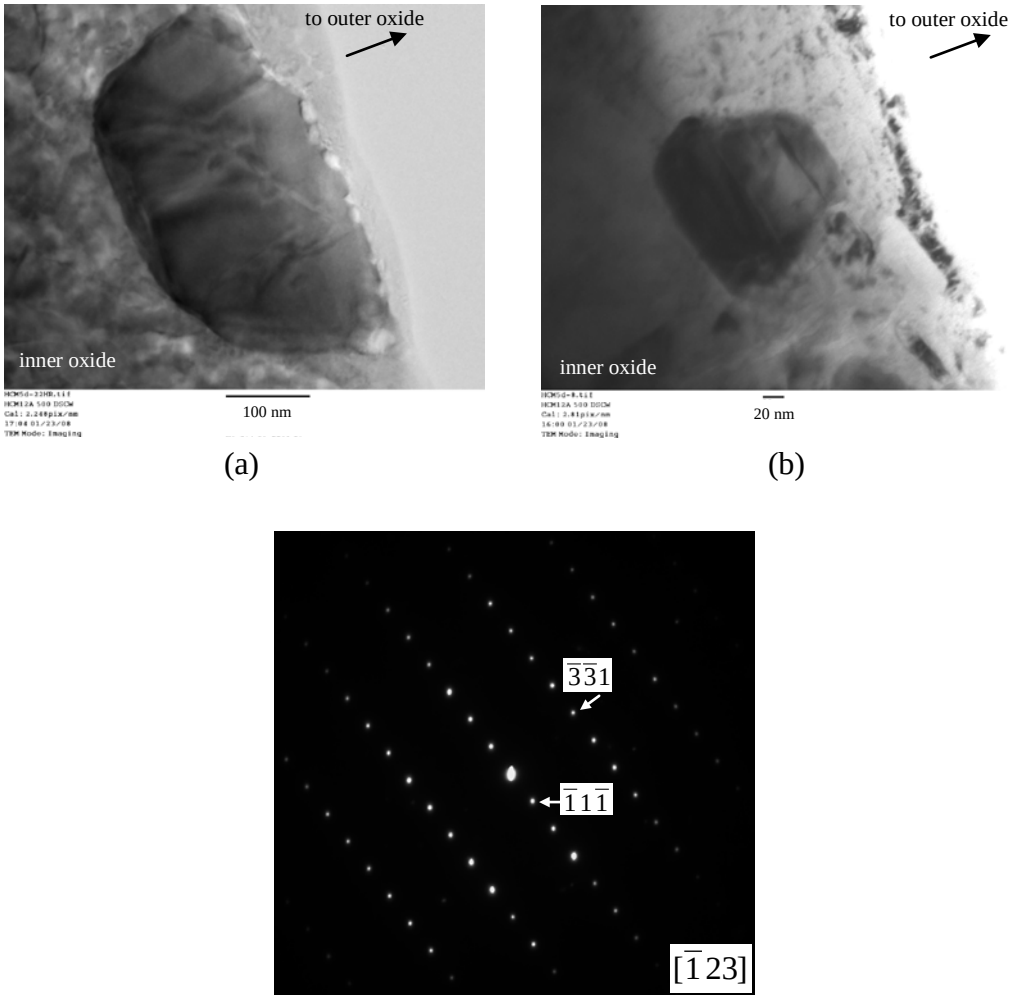

Figure 4.51 (a) and (b) TEM images of precipitate particles in the inner layer oxide formed on HCM12A exposed in 500°C deaerated SCW for 182 hours. (c) SAED from a particle in (a) exhibited FCC structure of $Cr_{23}C_6$ with a = 10.69 Å.

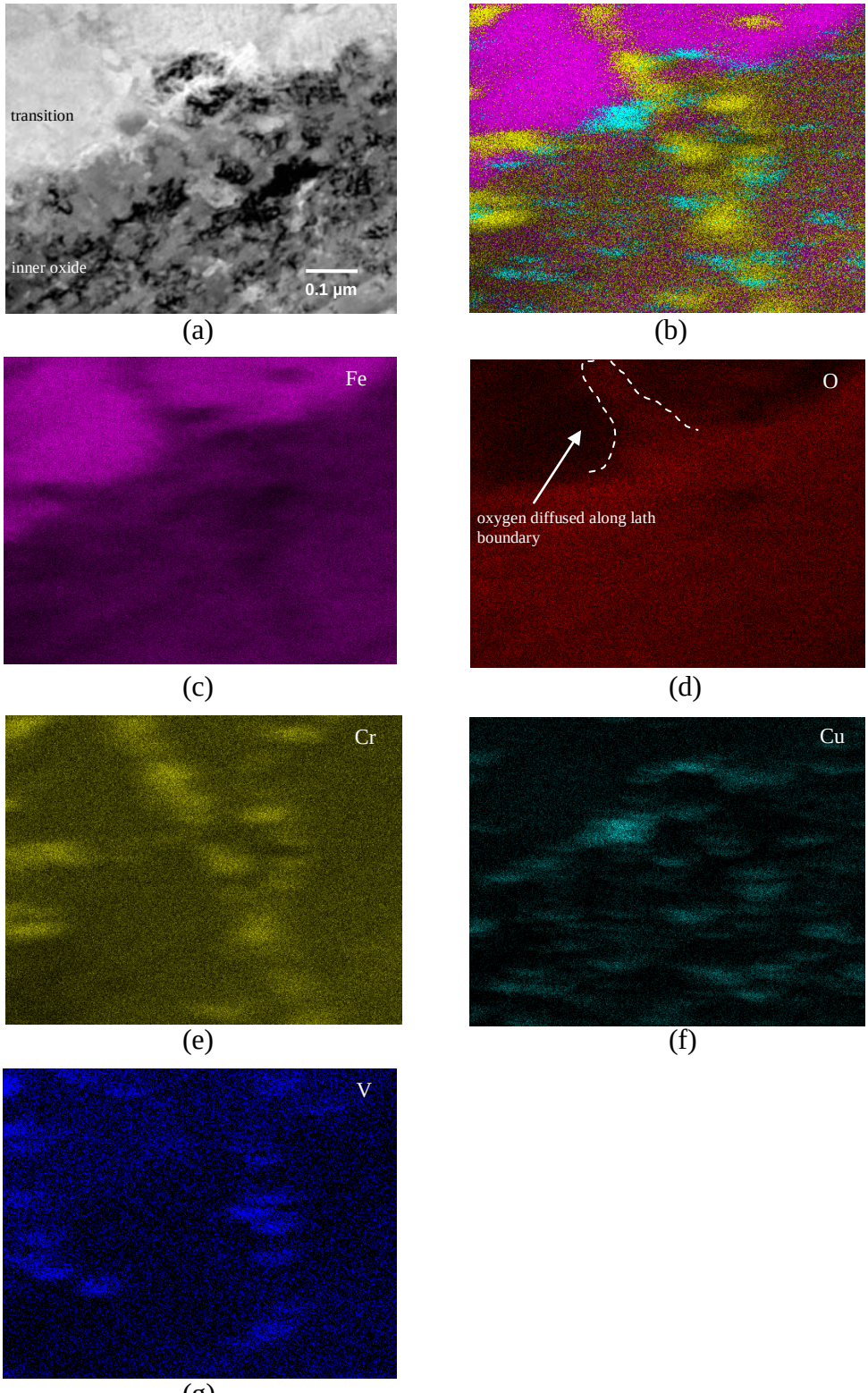

Figure 4.52 Composition maps of an interface of the inner oxide - transition layer of HCM12A exposed in 500°C deaerated SCW for 182 hours. (a) HAADF image, and composition maps of (b) all elements, (c) Fe, (d) O, (e) Cr, (f) Cu and (g) V.

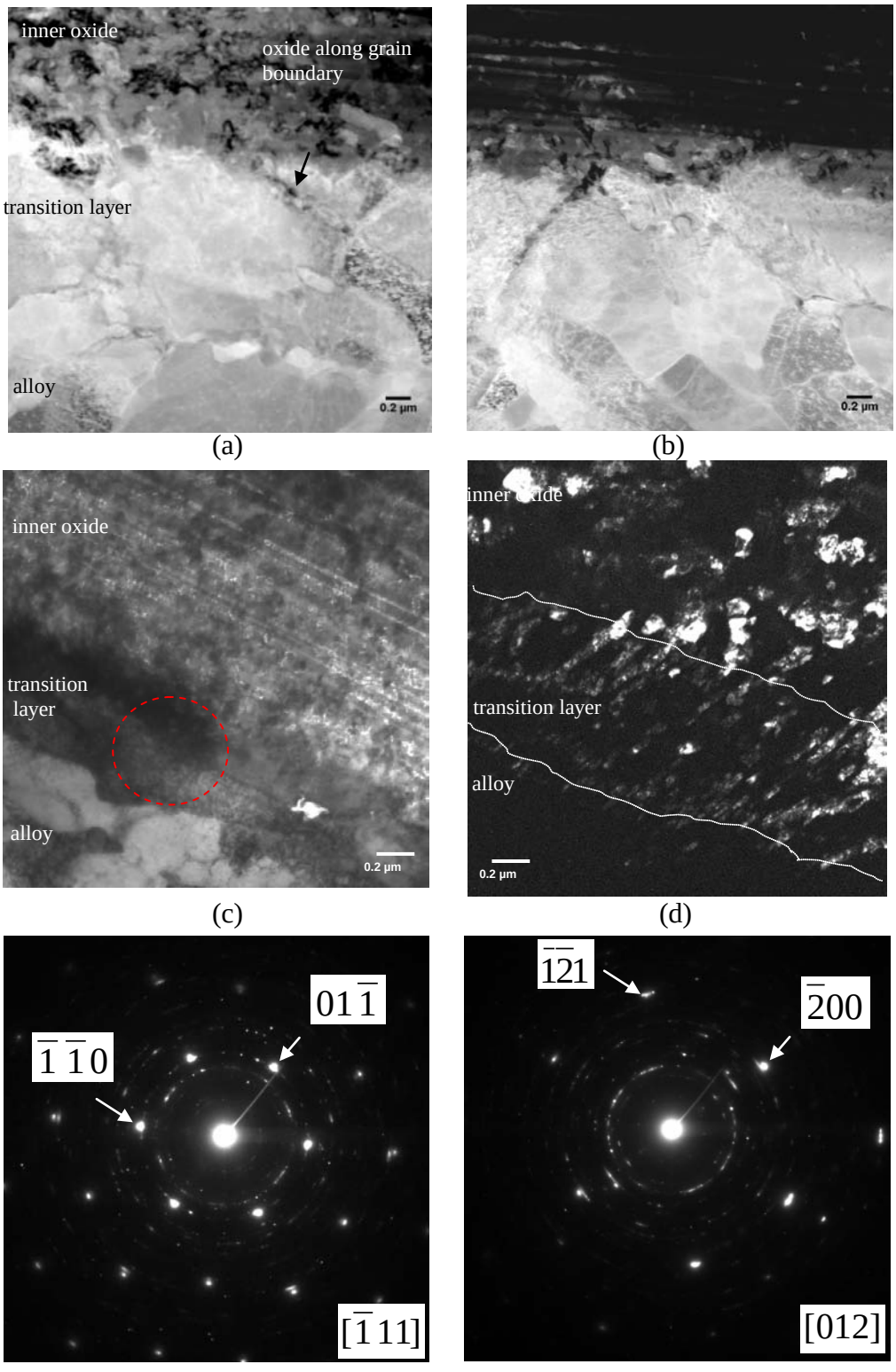

Figure 4.53 Images of the transition layer formed on HCM12A exposed in 500°C deaerated SCW for 182 hours. (a) and (b) HAADF images. (c) and (d) BF and DF images show oxide formation in the layer. (e) and (f) SAED patterns taken from transition layer.

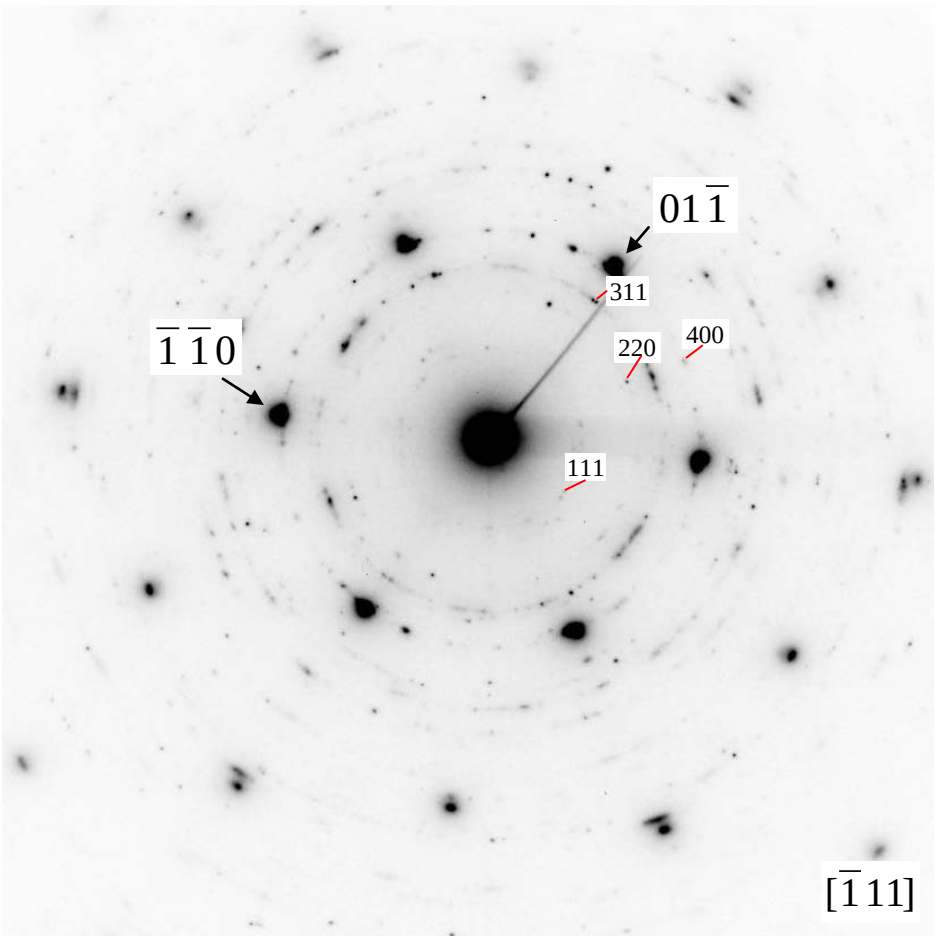

Figure 4.54 Indexing SAED pattern from the transition layer of HCM12A exposed in 500°C deaerated SCW for 182 hours. The pattern exhibited BCC structure (bright spots) of alloy matrix from $[\bar{1}11]$ zone axis, and polycrystal of FCC spinel structure (ring pattern) from the oxides.

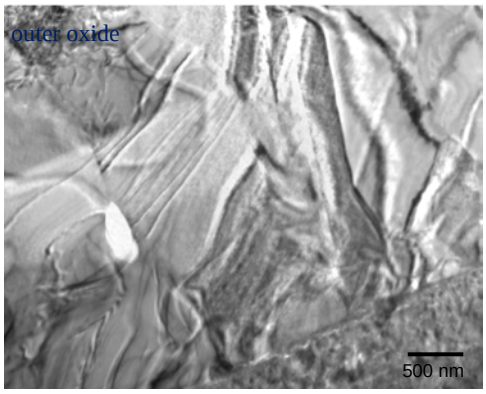

(a)

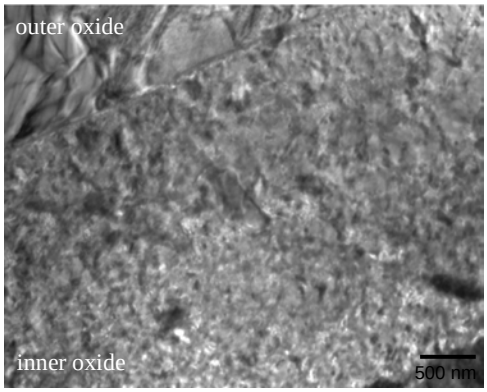

(b)

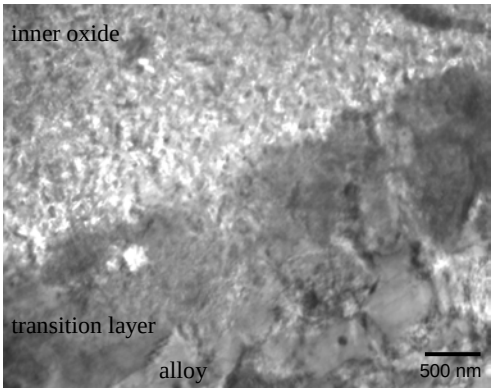

(c)

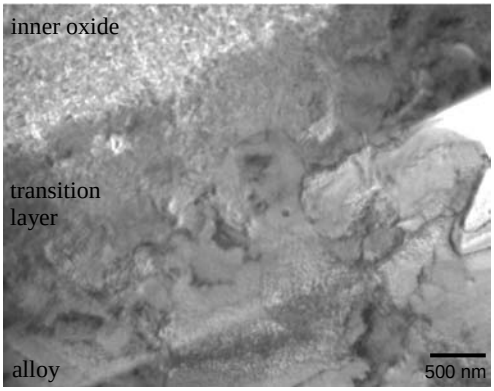

(d)

Figure 4.55 TEM images of oxides formed on HCM12A exposed in 500°C SCW containing 300 ppb DO for 182 hours. (a) outer oxide, (b) inner oxide, (c) transition layer, and (d) transition layer and alloy interface.

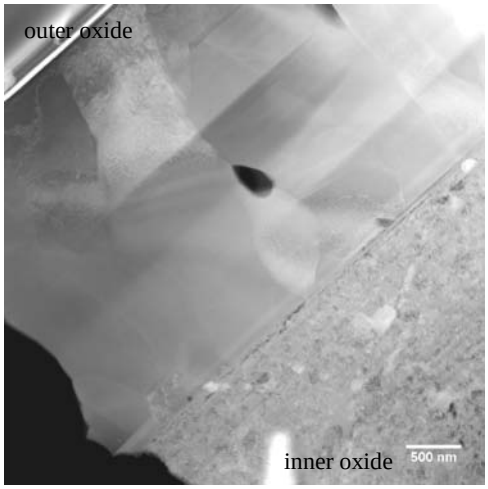

(a)

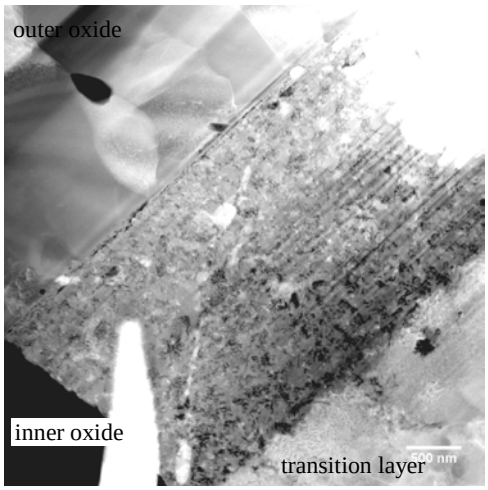

(b)

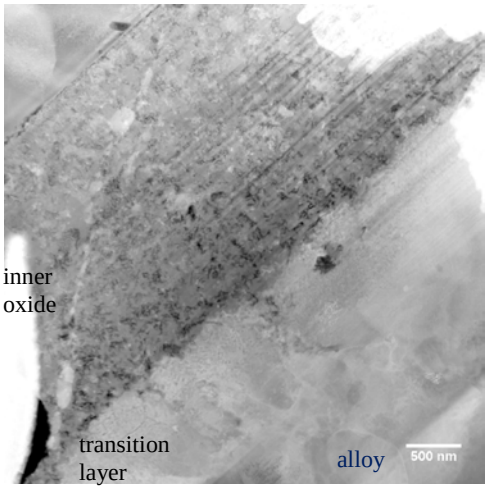

(c)

Figure 4.56 HAADF images of oxides formed on HCM12A exposed in 500°C SCW containing 300 ppb DO for 182 hours. (a) outer oxide, (b) inner oxide, (c) transition layer and alloy interface.

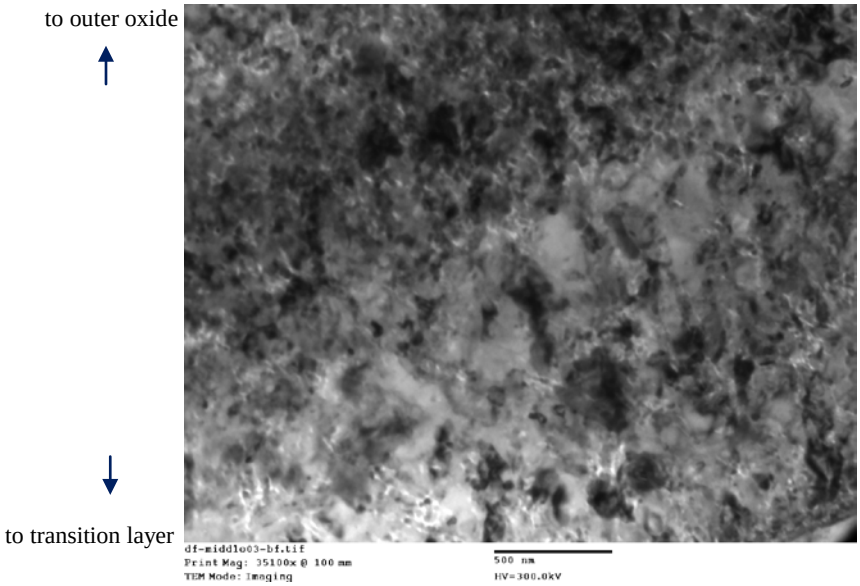

(a)

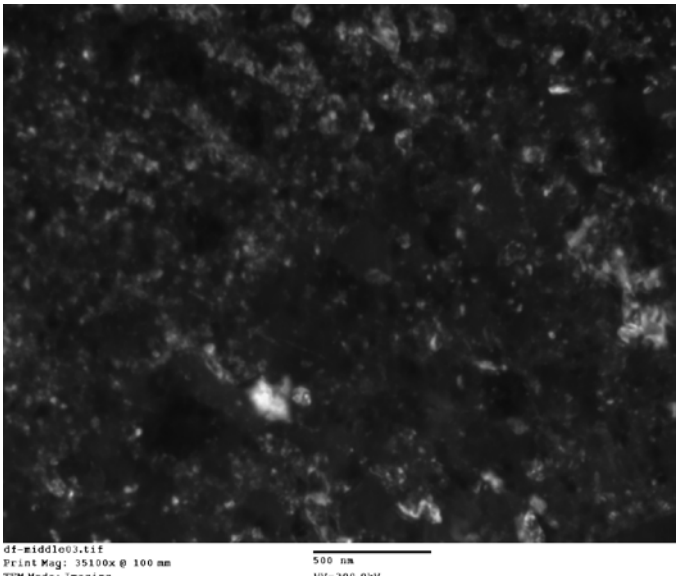

(b)

Figure 4.57 (a) BF and (b) DF images of inner oxide formed on HCM12A exposed in 500°C SCW containing 300 ppb DO for 182 hours. The images show small grain size of oxides in this layer.

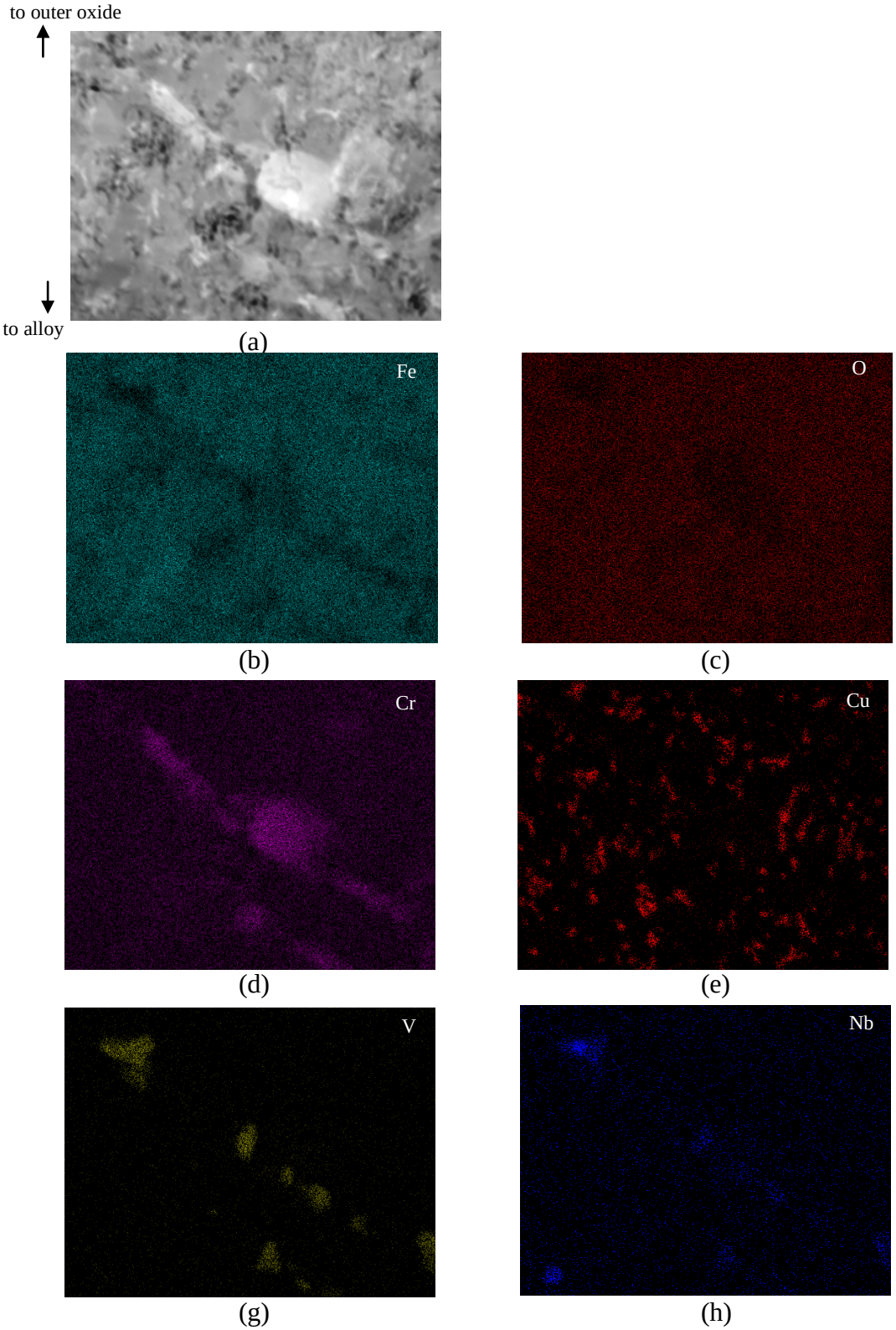

Figure 4.58 Composition maps of the inner oxide formed on HCM12A exposed in 500°C SCW containing 300 ppb DO for 182 hours. (a) HAADF image, and composition maps of (b) Fe, (c) O, (d) Cr, (e) Cu, (f) V and (g) Nb.

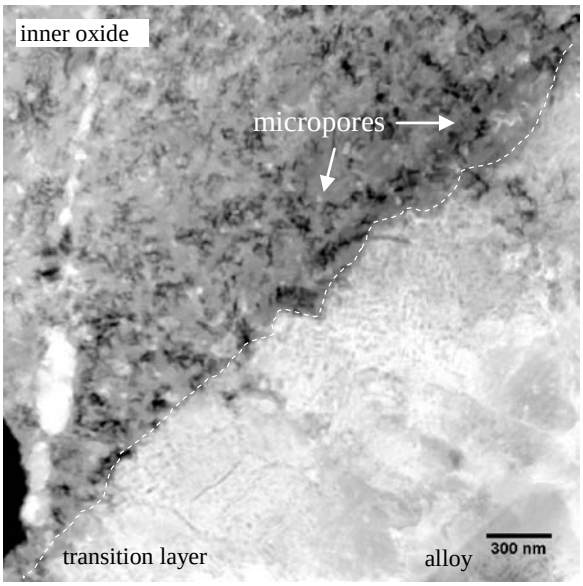

(a)

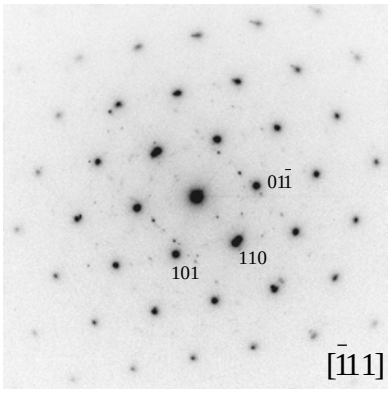

(b)

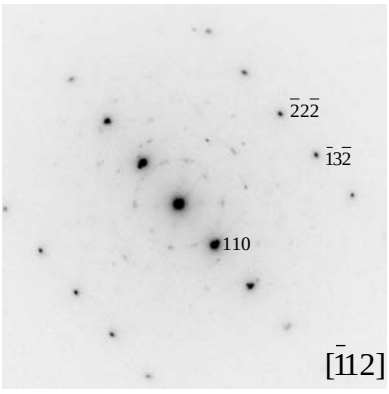

(c)

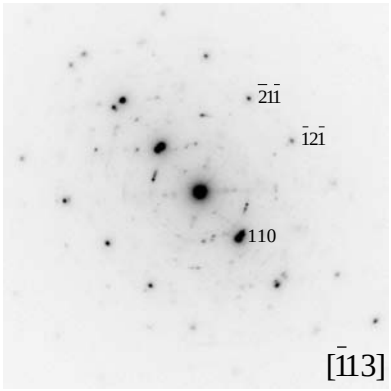

(d)

Figure 4.59 Transition layer formed on HCM12A exposed in 500°C SCW containing 300 ppb DO for 182 hours. (a) HAADF image shows distinct morphology of transition layer from inner oxide and alloy substrate, (b) – (d) SAED from the transition layer exhibits two DP. The bright spots are DP of alloy from (b) $[\bar{1}11]$, (c) $[\bar{1}12]$ and (d) $[\bar{1}13]$ zone axes and the ring pattern diffracted from spinel oxide.

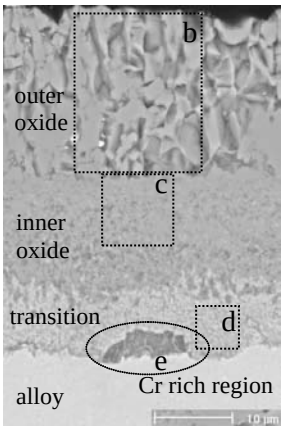

(a)

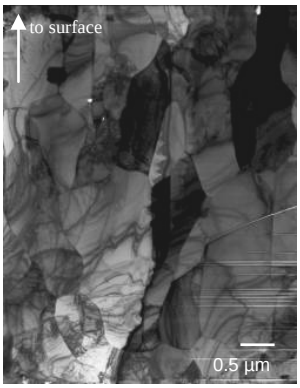

(b)

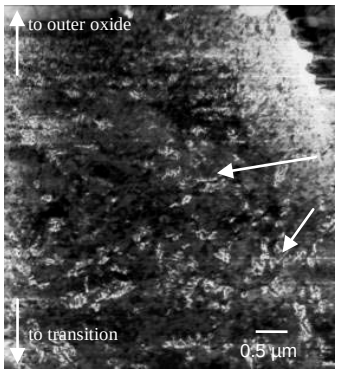

micro
pores

(c)

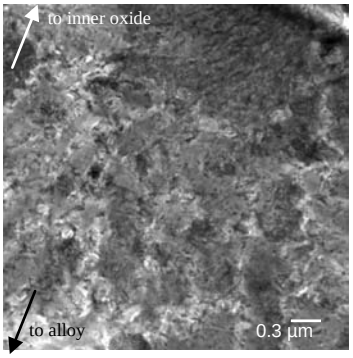

(d)

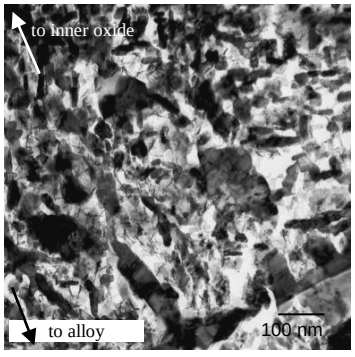

(e)

Figure 4.60 Images of oxides formed on HCM12A exposed in 600°C deaerated SCW for 191 hours. (a) Cross sectional SEM image shows oxide layers in (b) – (c). TEM images of (b) outer layer oxide, (c) inner layer oxide, (d) transition layer and (e) porous Cr-rich region.

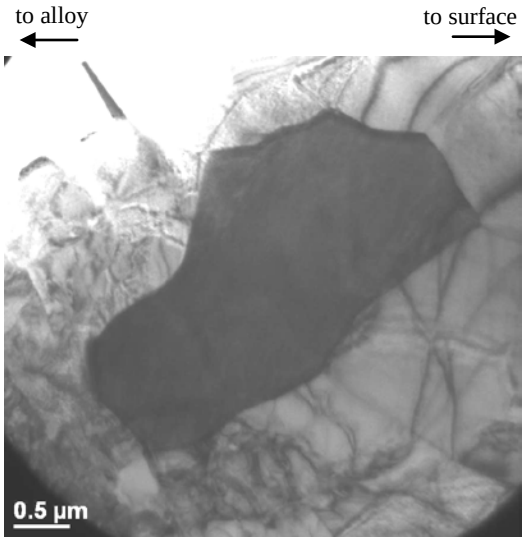

(a)

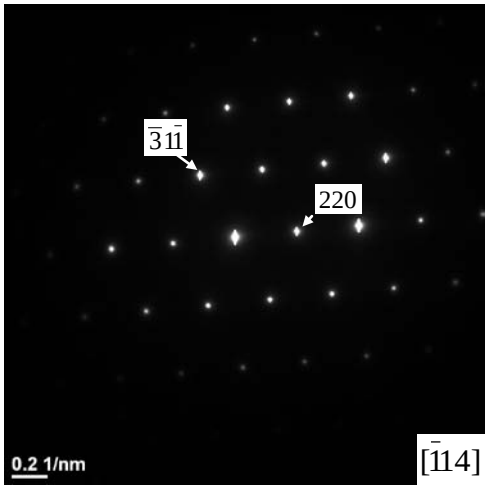

(b)

Figure 4.61 (a) BF image of a magnetite grain in the outer layer and (b) SAED from $[\bar{1}14]$ direction.

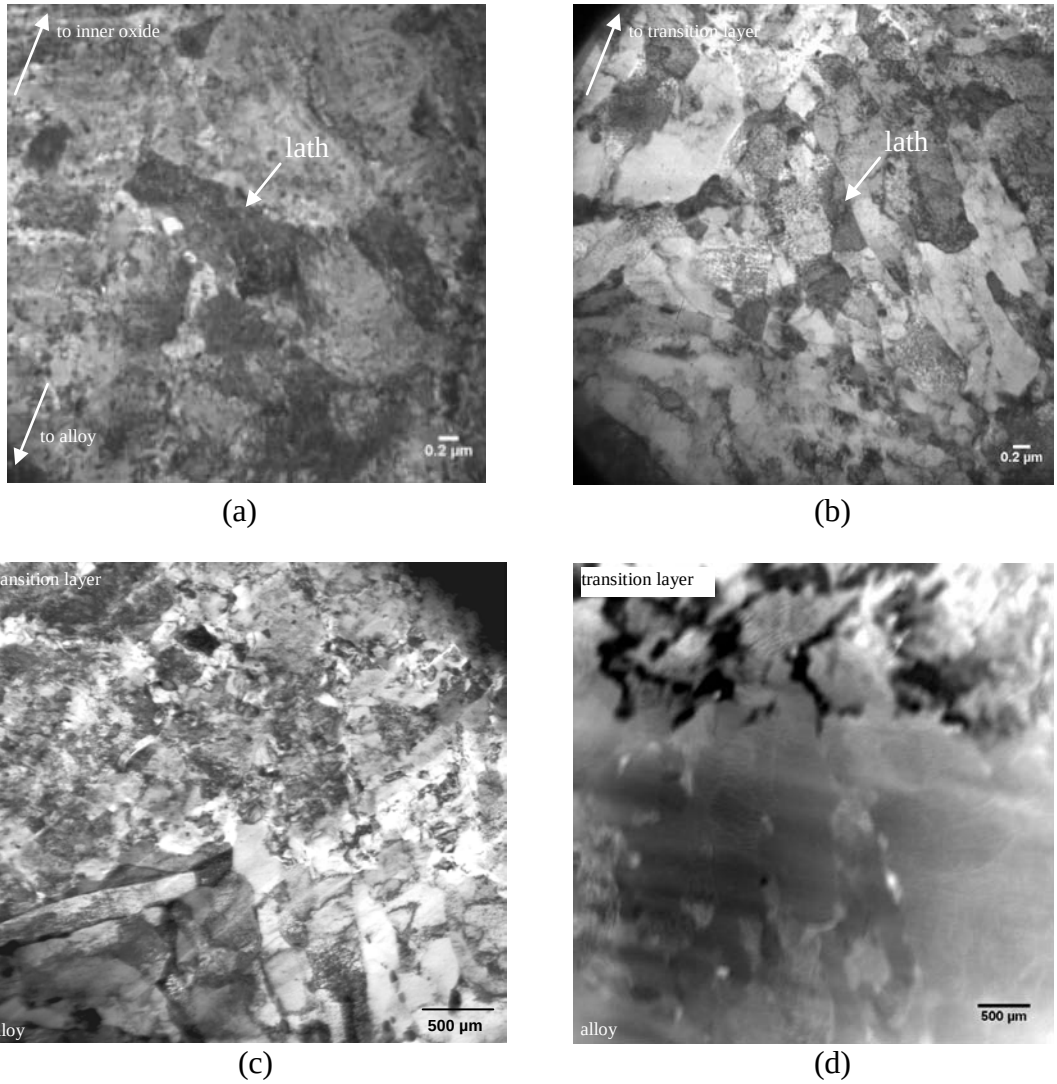

Figure 4.62 Comparison of microstructure of transition layer and alloy substrate on HCM12A exposed in 600°C deaerated SCW for 191 hours. BF images of (a) transition layer, (b) alloy, (c) interface of transition layer and alloy, and (d) HAADF images of the interface.

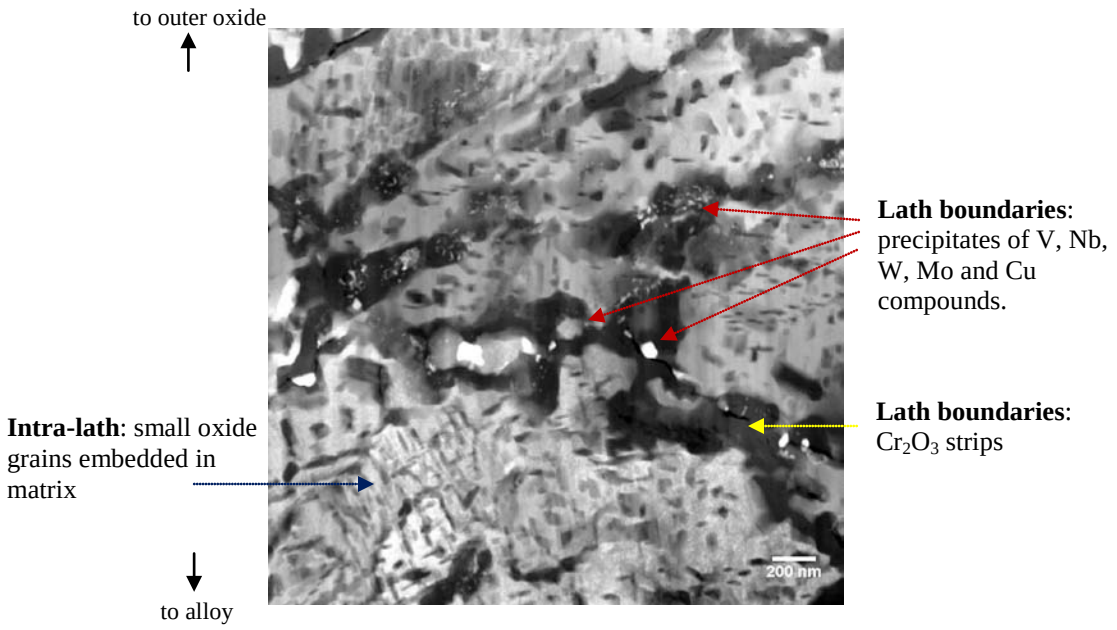

Figure 4.63 HAADF image presents the detailed microstructure of transition layer of HCM12A exposed in 600°C deaerated SCW for 191 hours.

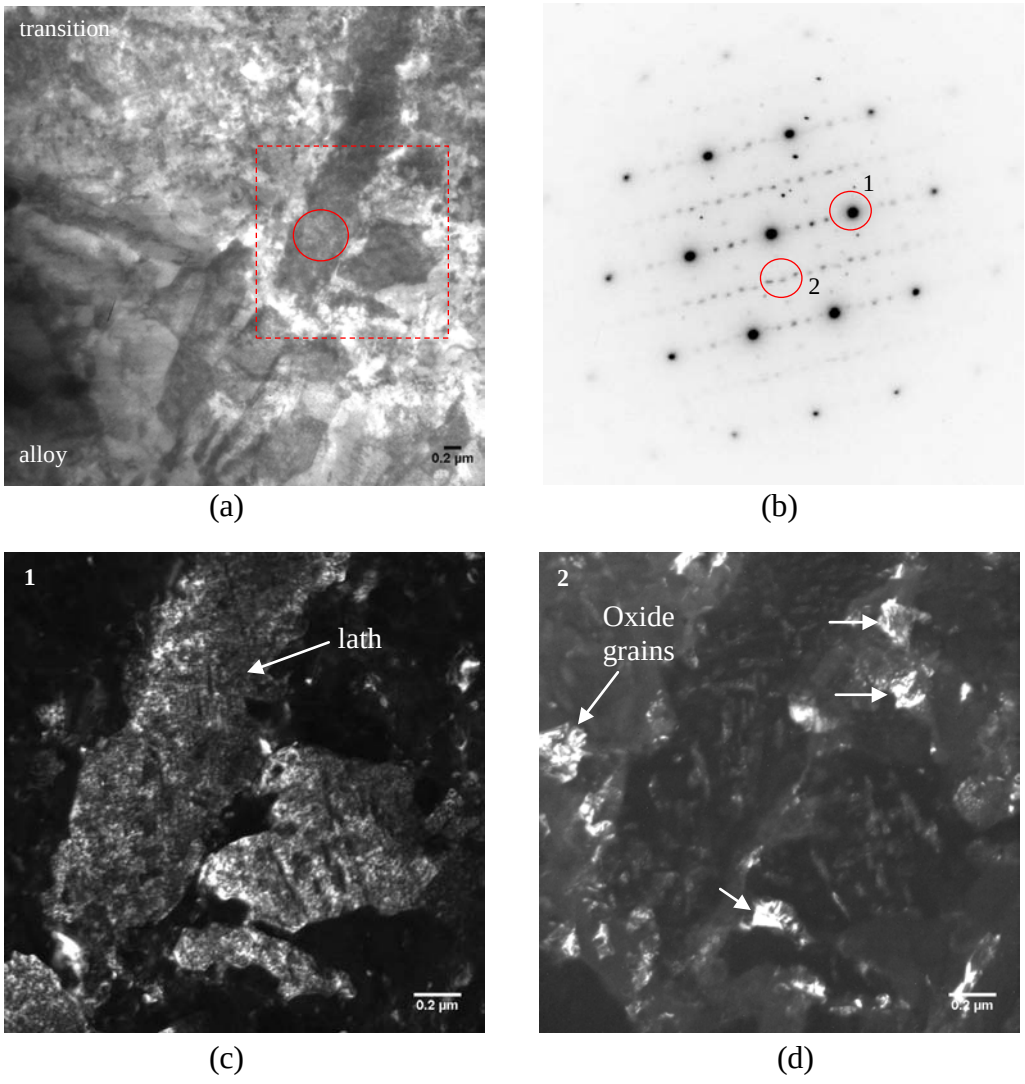

Figure 4.64 Images of transition layer of HCM12A exposed in 600°C deaerated SCW for 191 hours. (a) BF image shows area of analysis in red-dashed box and SAED in circled area, (b) SAED pattern of intra-lath exhibited two diffraction sets of Fe BCC (bright spots) and FCC spinel structure of oxide (weak spots). DF image taken from (c) bright spot #1 shows lath structure, and (d) weak spots #2 shows formation of oxide grains.

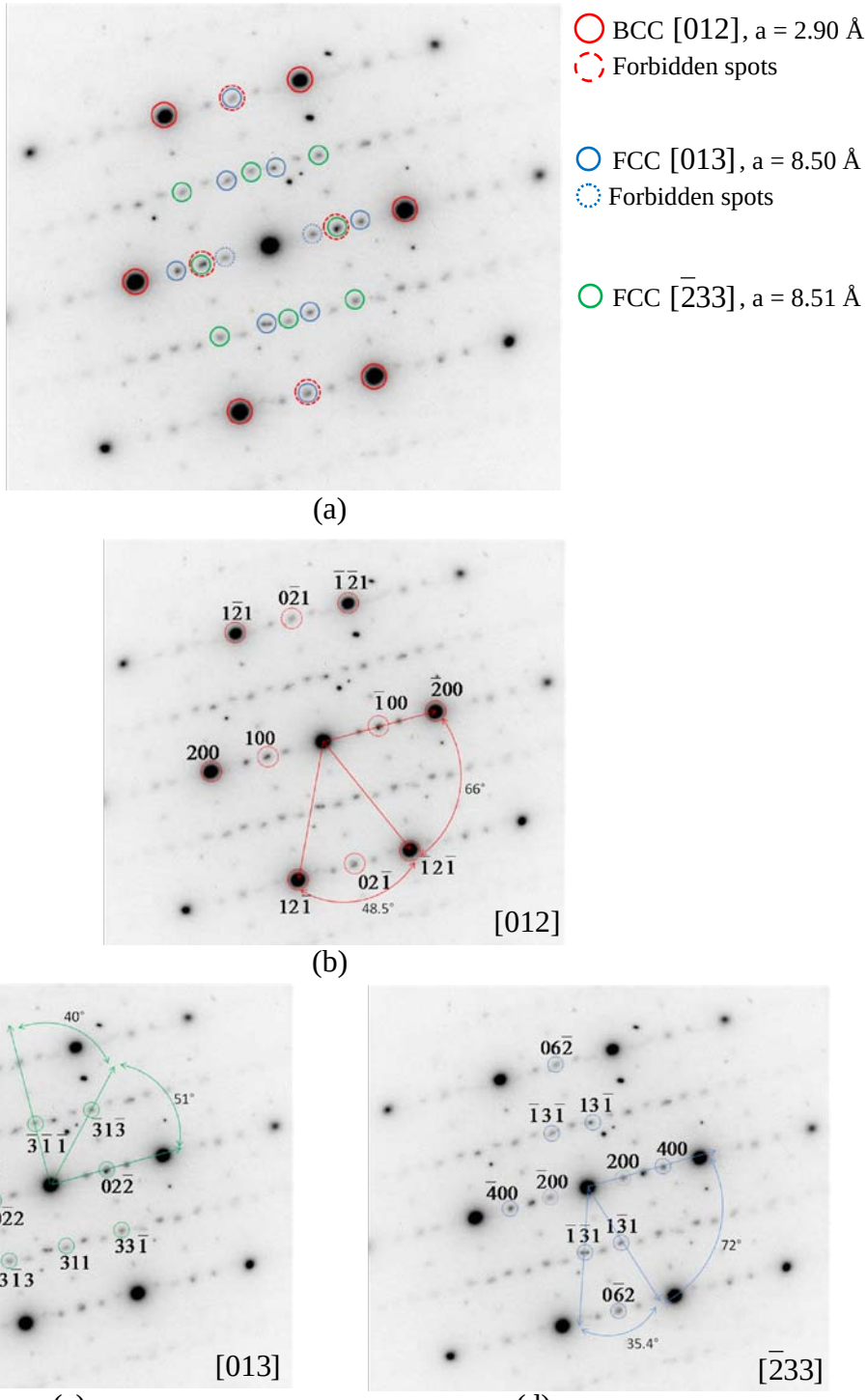

Figure 4.65 (a) Indexing SAED pattern from intra-lath of the transition layer of HCM12A exposed in 600°C deaerated SCW for 191 hours. The pattern exhibited three DP; (b) BCC structure from [012] of alloy matrix (a=2.90 Å), and FCC spinel structure from (c) [013] and (d) [$\bar{2}$33] from the oxides (a=8.50±0.01 Å).

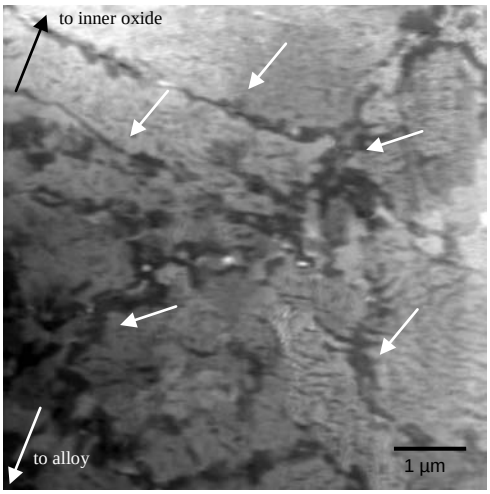

(a)

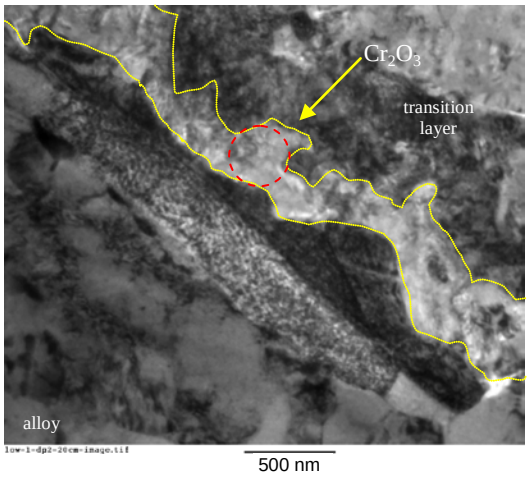

(b)

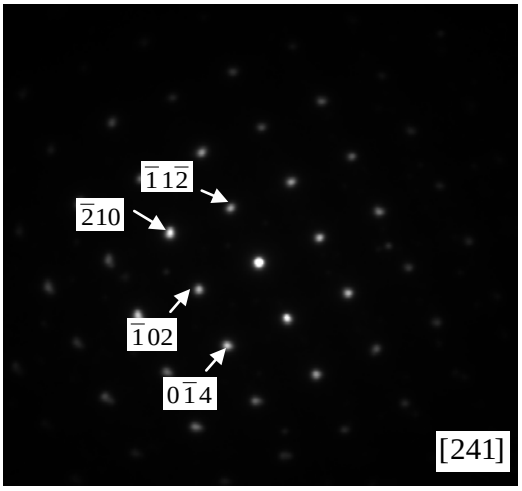

(c)

Figure 4.66 TEM images of Cr_2O_3 formed in the transition layer of HCM12A exposed in 600°C deaerated SCW for 191 hours. (a) HAADF image shows dark strips (arrows) of Cr_2O_3 between laths, (b) BF shows Cr_2O_3 strip at transition layer- alloy interface, and (c) SAED pattern can be indexed as the $[241]$ zone axis with $R\bar{3}C$ of Cr_2O_3.

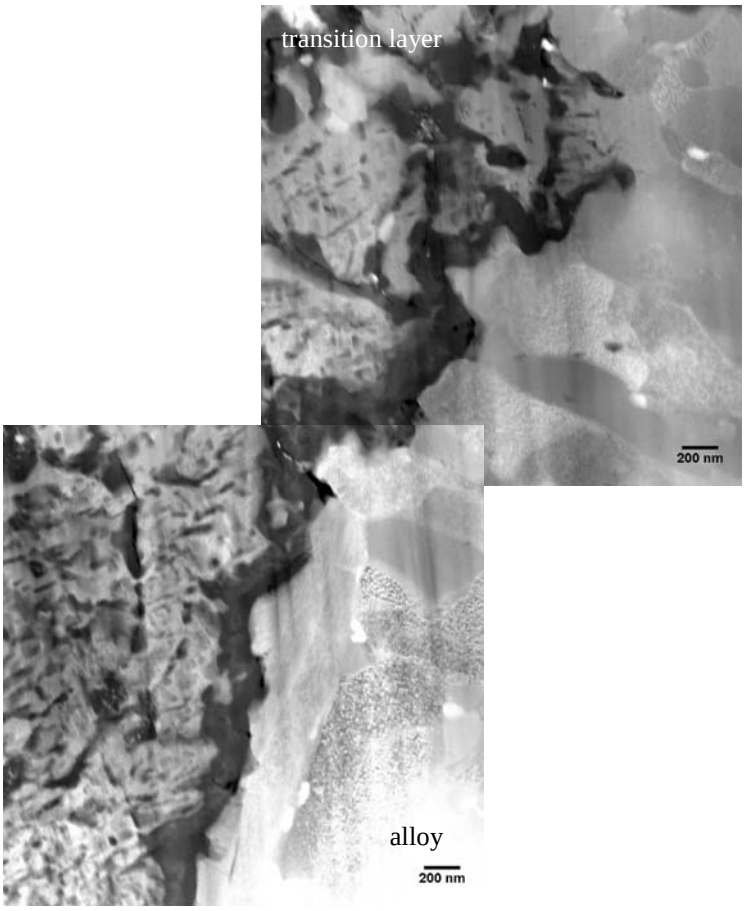

(a)

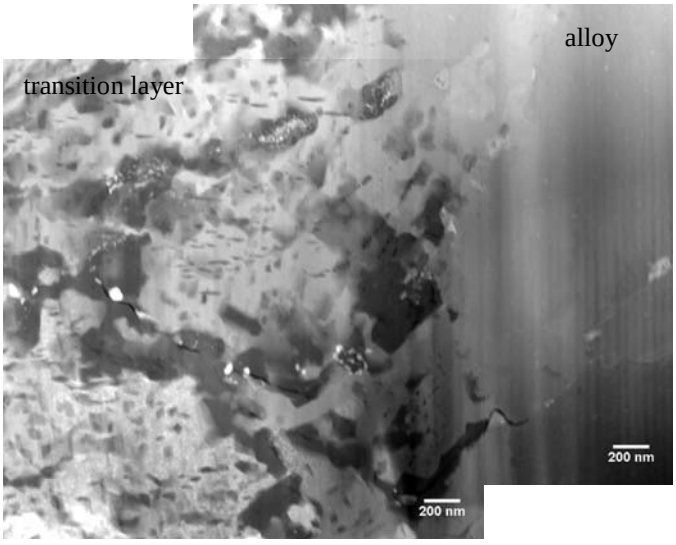

(b)

Figure 4.67 HAADF images of interface of transition layer and alloy substrate of HCM12A exposed in 600°C deaerated SCW for 191 hours. (a) Cr_2O_3 formed at the interface, and (b) the interface without Cr_2O_3.

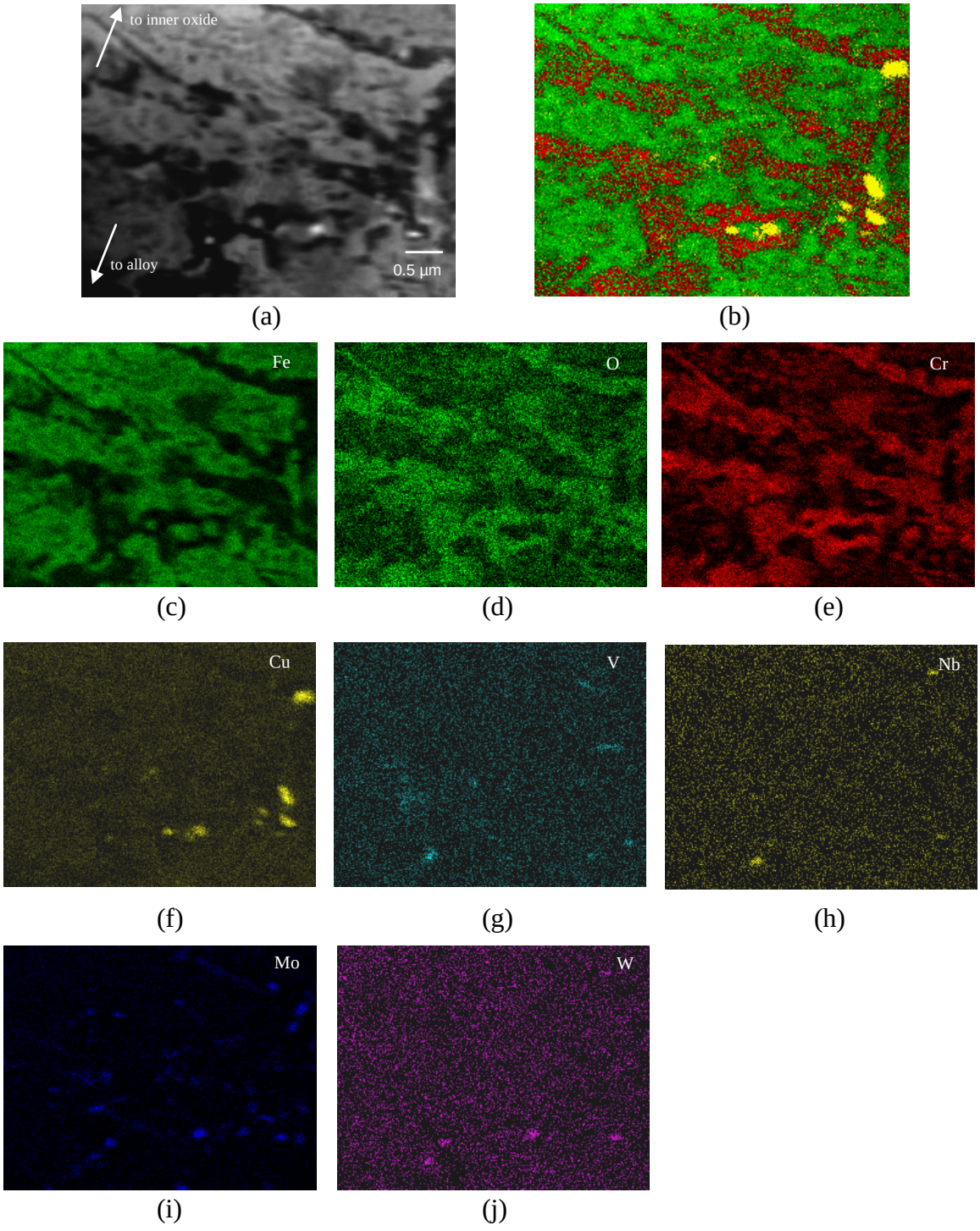

Figure 4.68 Composition maps of the transition layer of HCM12A exposed in 600°C deaerated SCW for 191 hours. (a) HAADF image and composition maps of (b) Fe-Cr-O-Cu, (c) Fe, (d) O, (e) Cr, (f) Cu, (g) V, (h) Nb, (i) Mo and (j) W. The result revealed that Cr and O enriched between laths, and precipitates of compound of Cu, V, Nb, Mo and W formed at the lath boundaries.

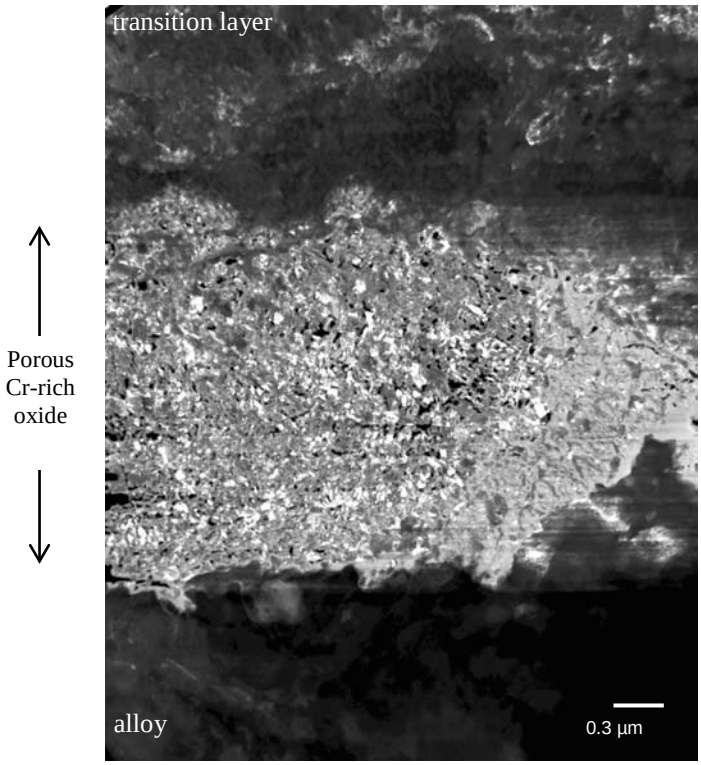

(a)

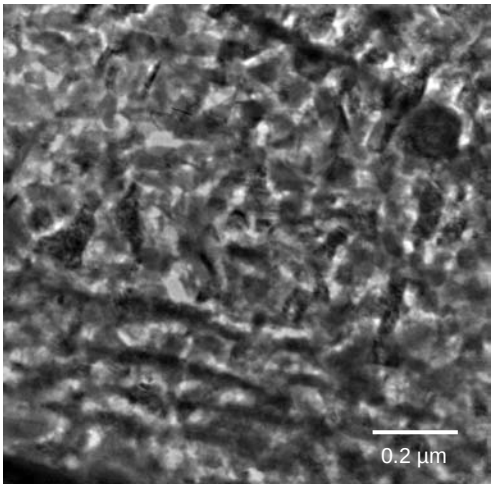

(b)

Figure 4.69 (a) DF and (b) BF images show morphology of porous Cr-rich oxide formed between transition layer and alloy of HCM12A exposed in 600°C deaerated SCW for 191 hours.

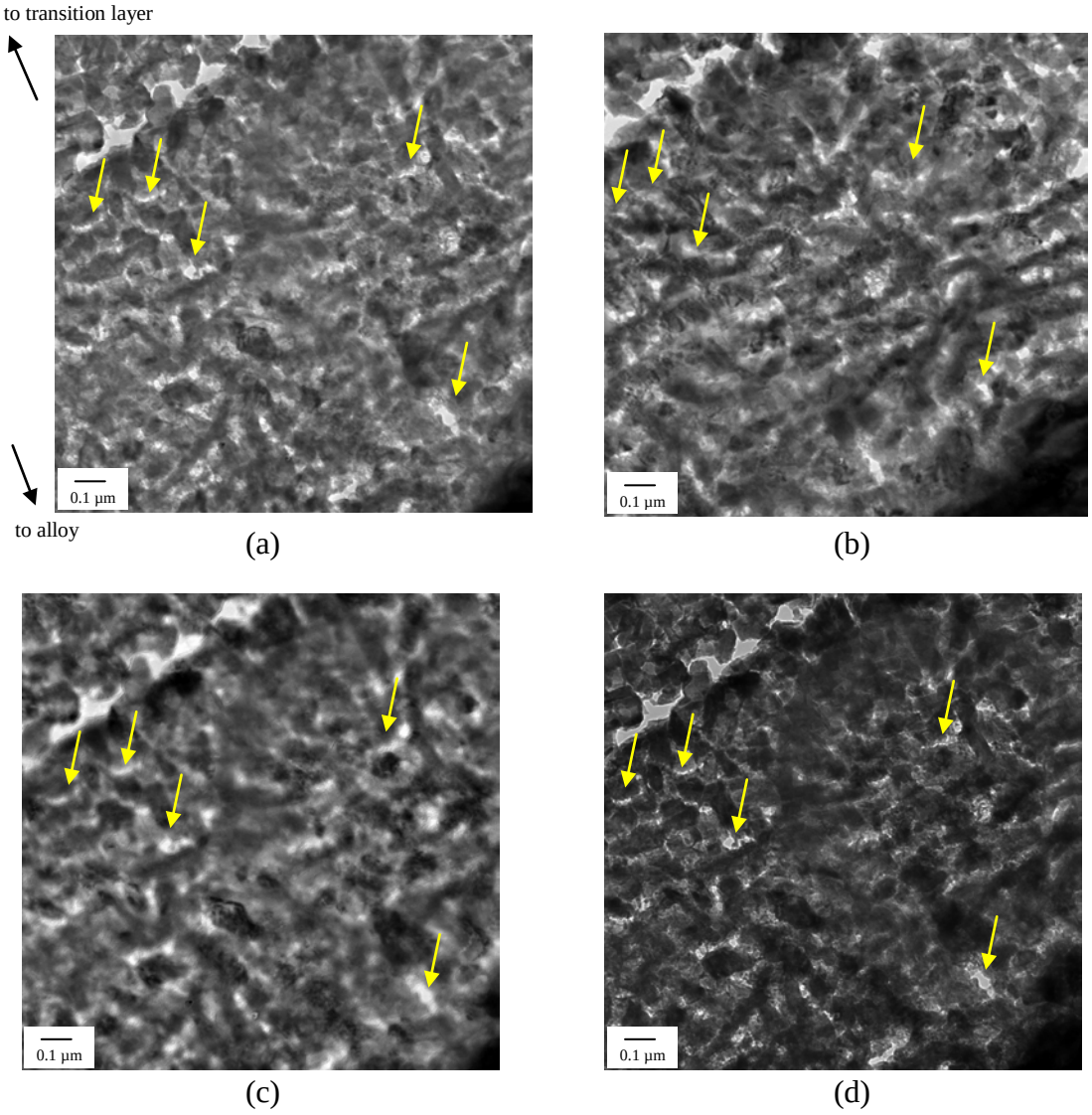

Figure 4.70 Series of TEM images verifying porosity of the Cr-rich oxide of HCM12A exposed in 600°C deaerated SCW for 191 hours. Specimen was first focused (a) and was tilted to 9.9° (b). Both images showed different morphology of pore (arrows), which confirmed that the pores are exist. (c) Under-focused and (d) over-focused images show fringes at pore and crack's edge (arrows).

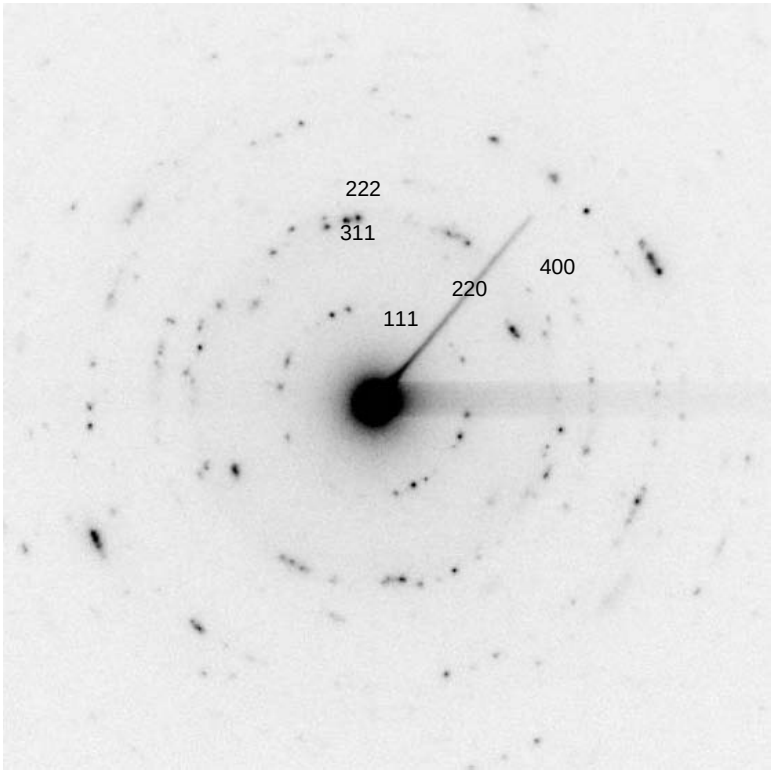

Figure 4.71 Indexing SAED of porous Cr-rich oxide formed on HCM12A exposed in 600°C deaerated SCW for 191 hours. The DP exhibited FCC spinel structure of a = 8.48 Å.

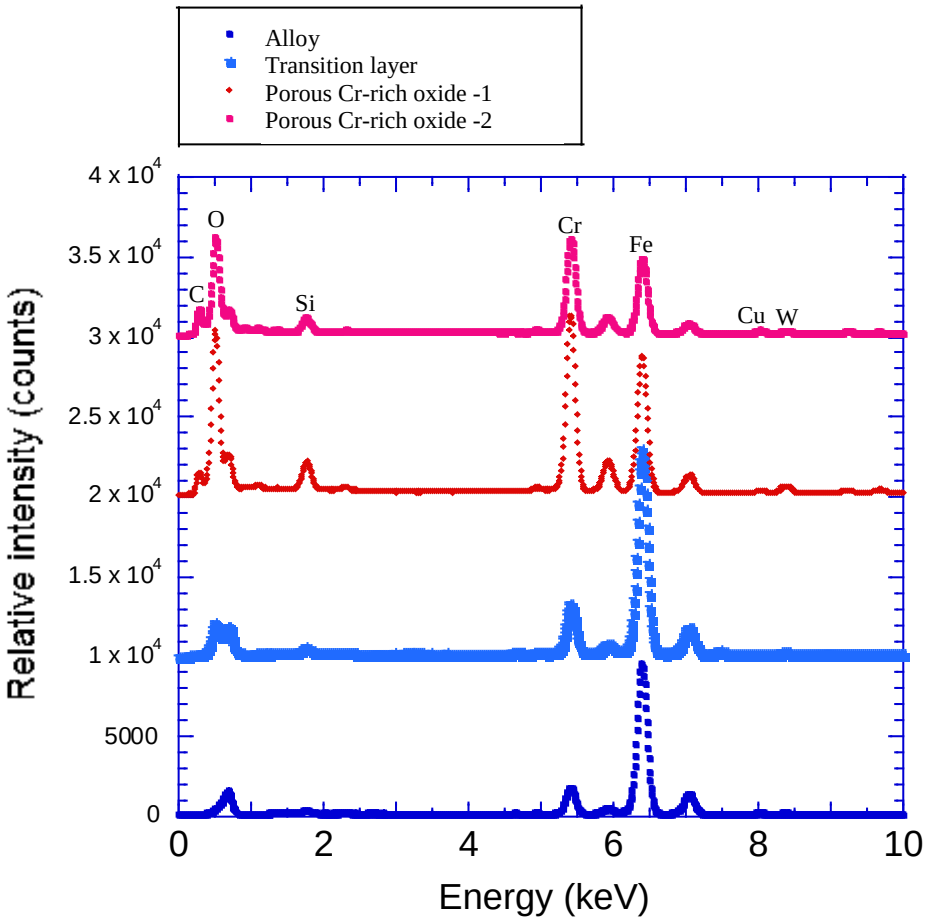

Figure 4.72 Comparison of EDS spectrum of alloy, transition layer and porous Cr-rich oxide from HCM12A exposed in 600°C deaerated SCW for 191 hours.

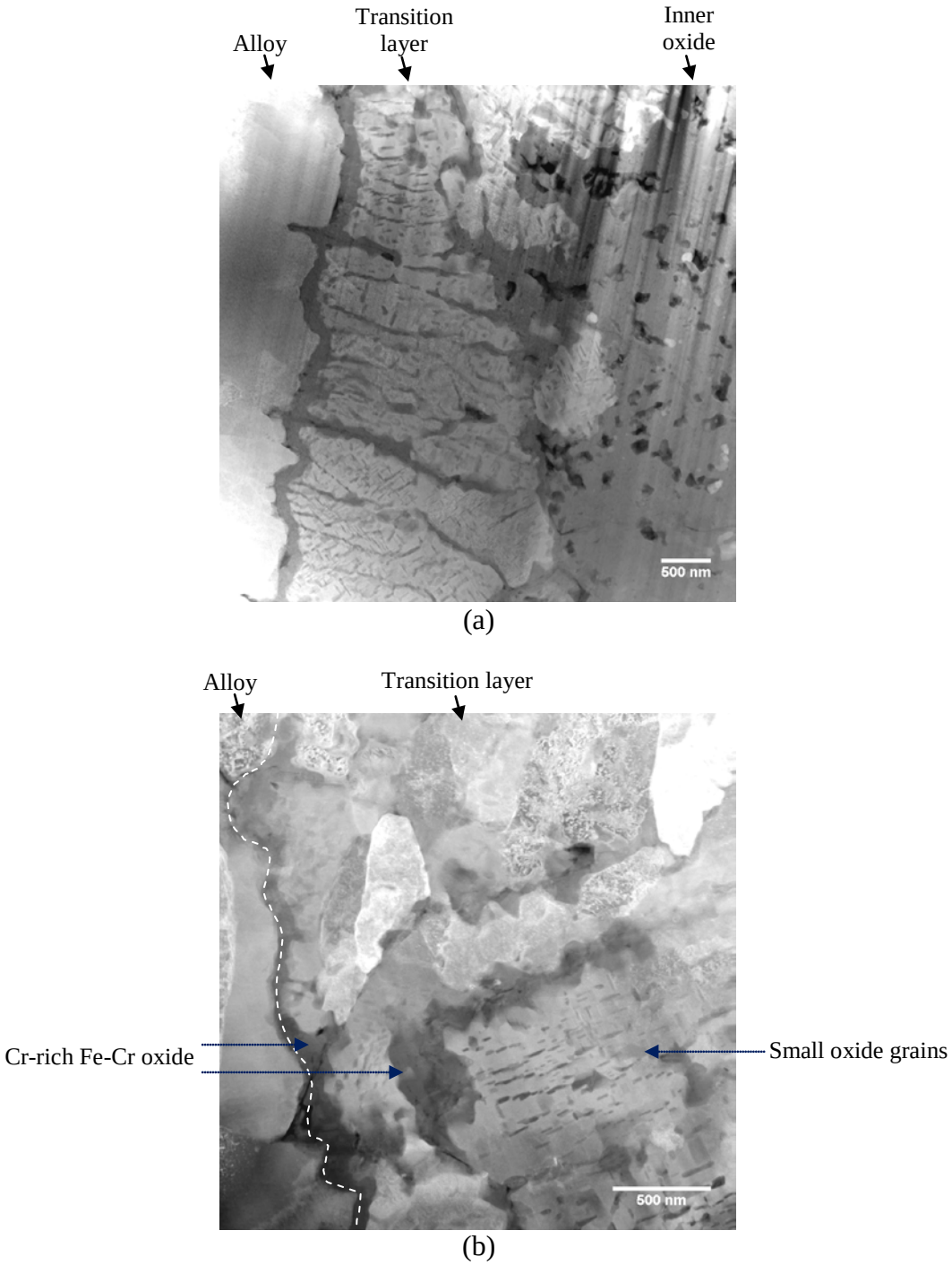

Figure 4.73 HAADF images T91 exposed in 600°C deaerated SCW for 191 hours. (a) Inner oxide - transition layer – alloy substrate. (b) Typical structure of transition layer of T91 that consisted of Cr-rich Fe-Cr oxide at lath boundaries and at transition - alloy interface. Small oxide grains embedded in the laths.

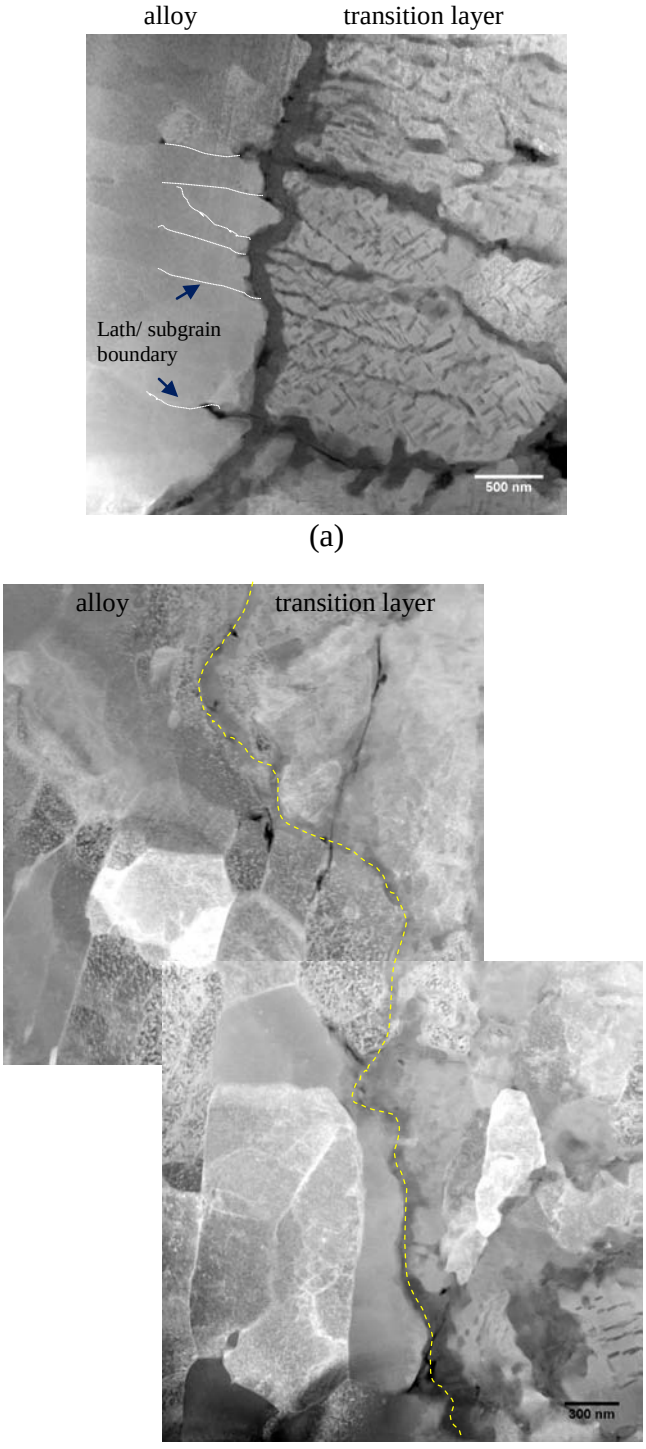

Figure 4.74 HAADF images of interface of transition layer and alloy of T91 exposed in 600°C deaerated SCW for 191 hours. Figure (a) shows that Cr-rich Fe-Cr oxide formed at lath/ subgrain boundaries of alloy (perpendicular to the interface) and an oxide strip formed in the middle of lath (interface). (b) Continuous Cr-rich Fe-Cr oxide at the interface of transition layer and alloy substrate.

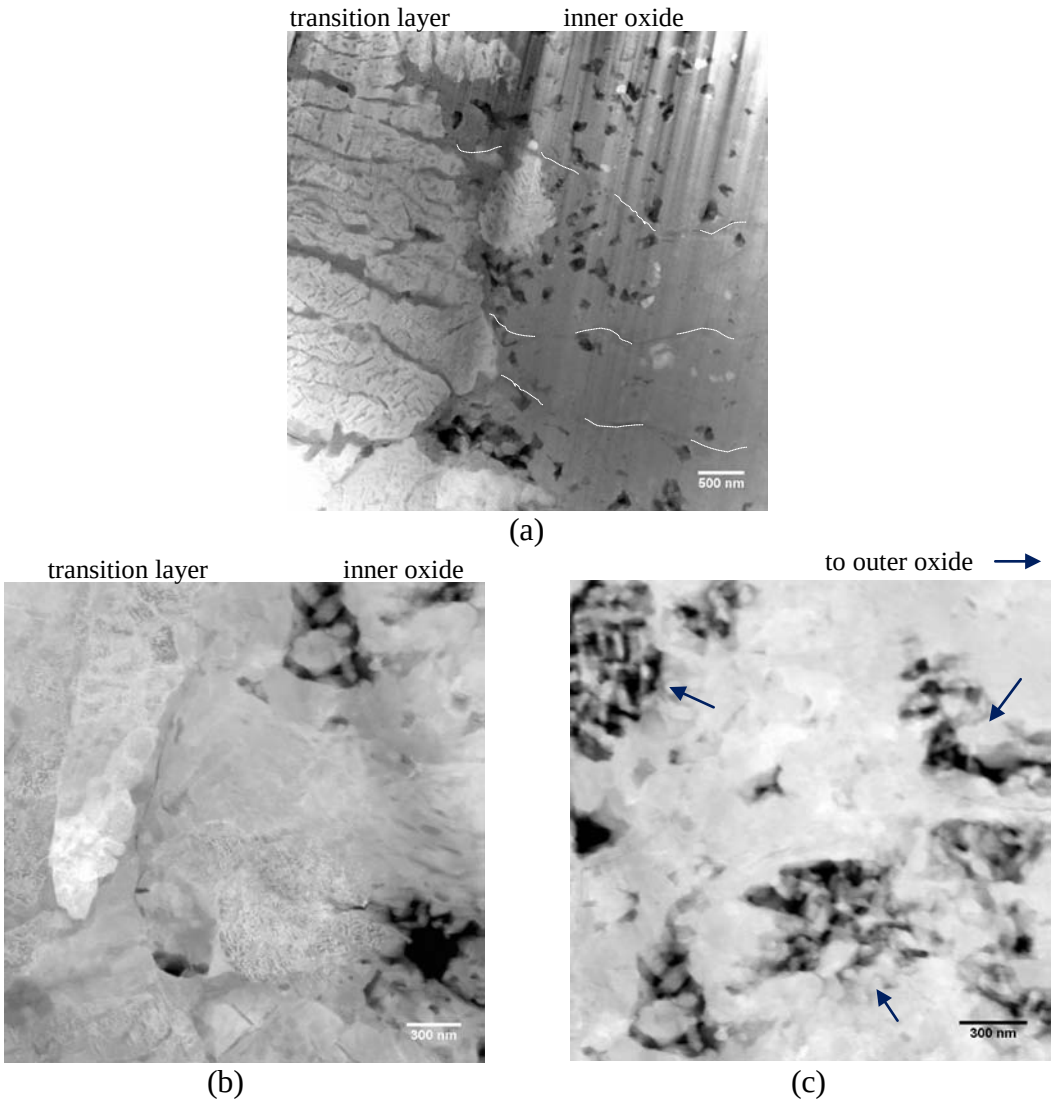

Figure 4.75 HAADF images of the inner oxide – transition layer interface of T91 exposed in 600°C deaerated SCW for 191 hours. Figure (a) shows z-contrast and difference in morphology of the transition layer and the inner oxide. Cr-rich Fe-Cr oxide strips can be observed in the inner oxide (white lines). (b) High magnification of the interface. (c) Pores in the inner layer oxide.

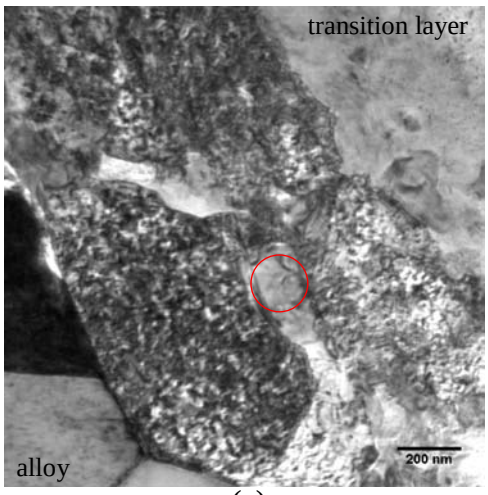

(a)

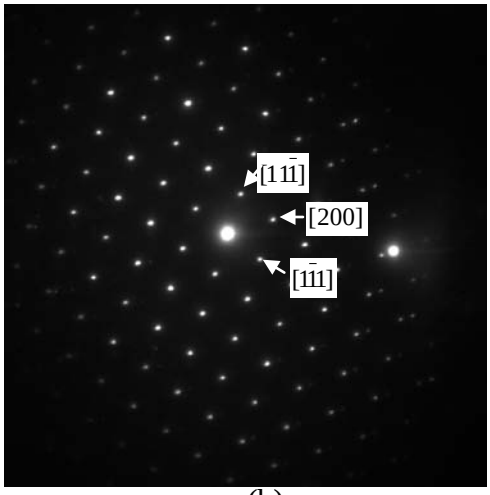

(b)

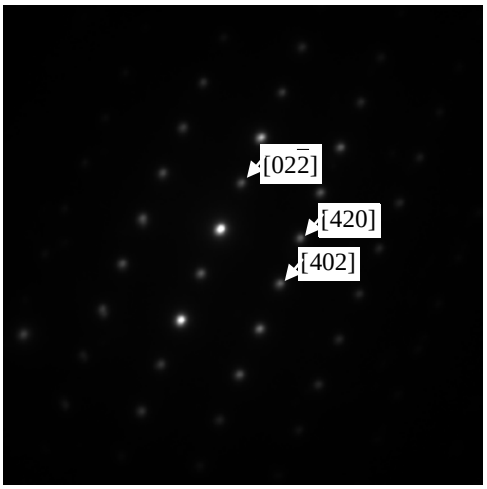

(c)

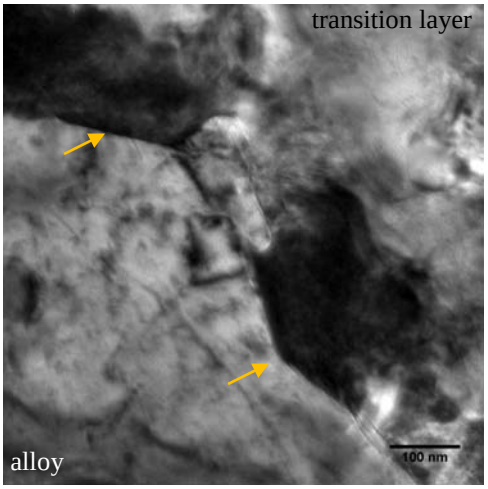

(d)

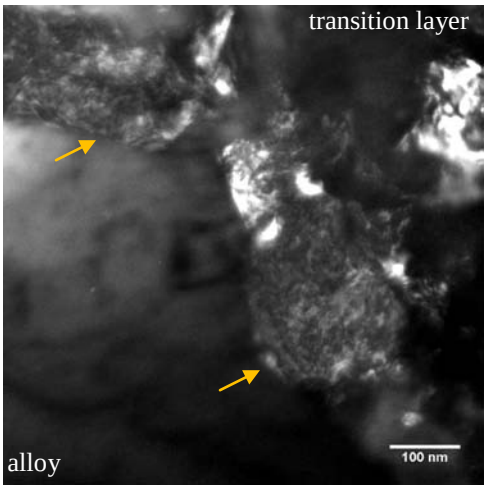

(e)

Figure 4.76 Characterization of Cr-rich strip of T91 exposed in 600°C deaerated SCW for 191 hours. (a) BF image shows of Cr-rich strip at interface of transition layer and alloy. (b) and (c) SAED from circled area in (a) exhibit FCC structure with a ~ 8.20 Å from (b) [011] and (c) $[\bar{1}22]$ directions. (d) BF and (e) DF images from SAED in (b).

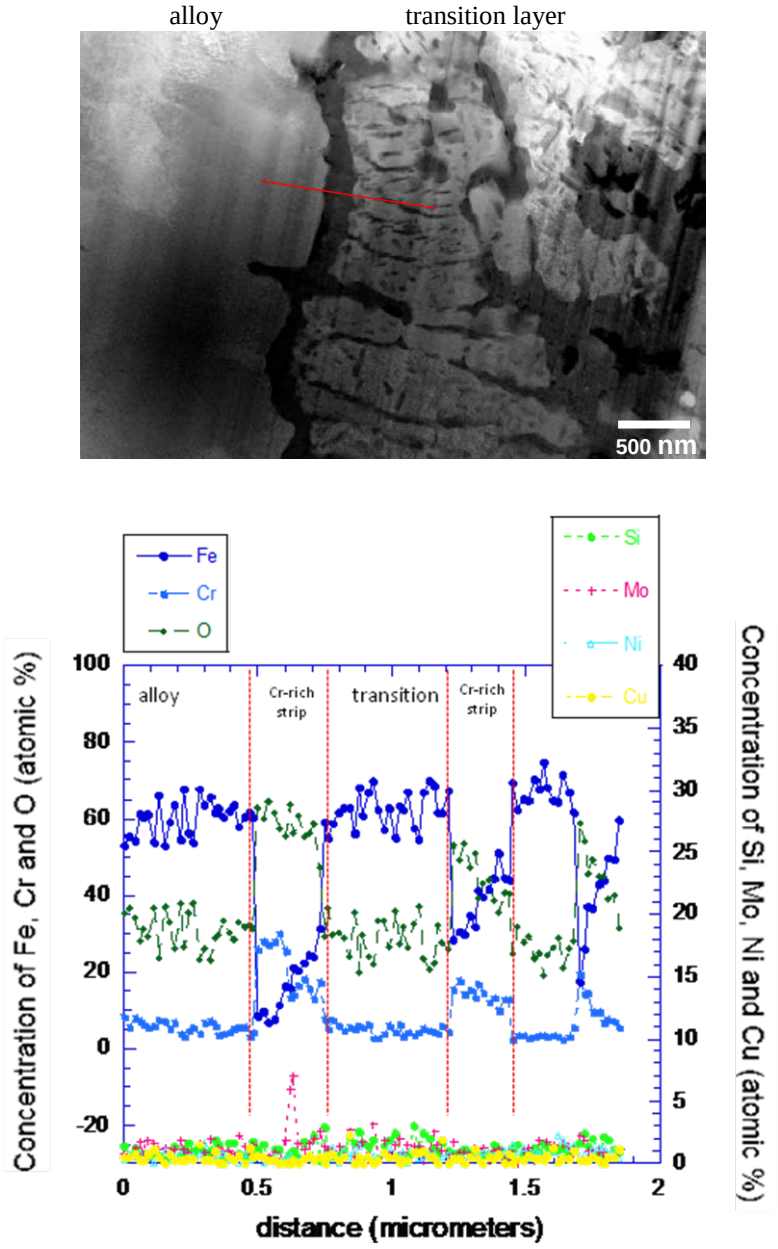

Figure 4.77 HAADF image and composition line scan across Cr-rich oxide at the interface of transition and alloy substrate of T91 exposed in 600°C deaerated SCW.

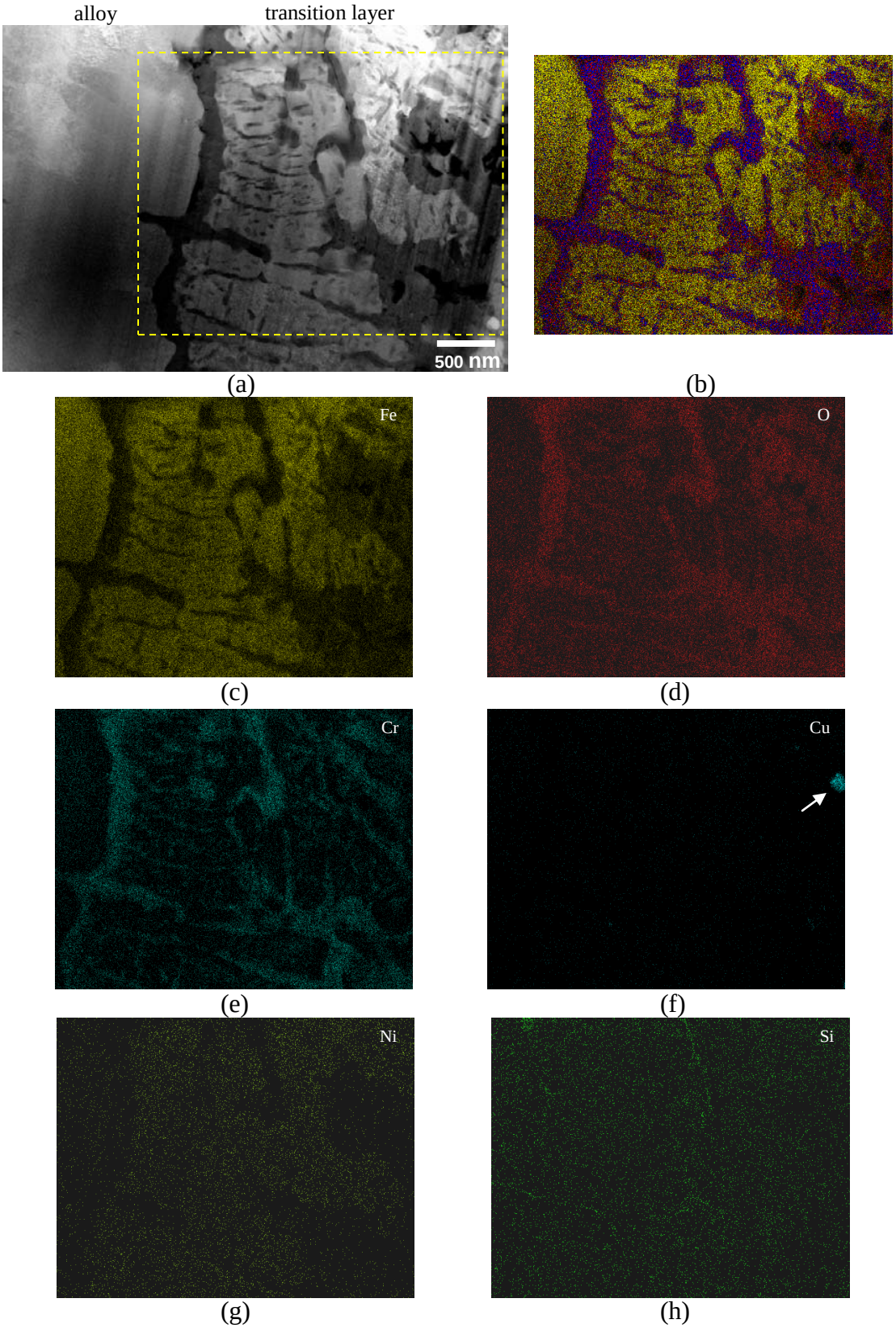

Figure 4.78 Composition maps of the transition layer of T91 exposed in 600°C deaerated SCW for 191 hours. (a) HAADF image and composition maps of (b) Fe-Cr-O, (c) Fe, (d) O, (e) Cr, (f) Cu, (g) Ni and (h) Si.

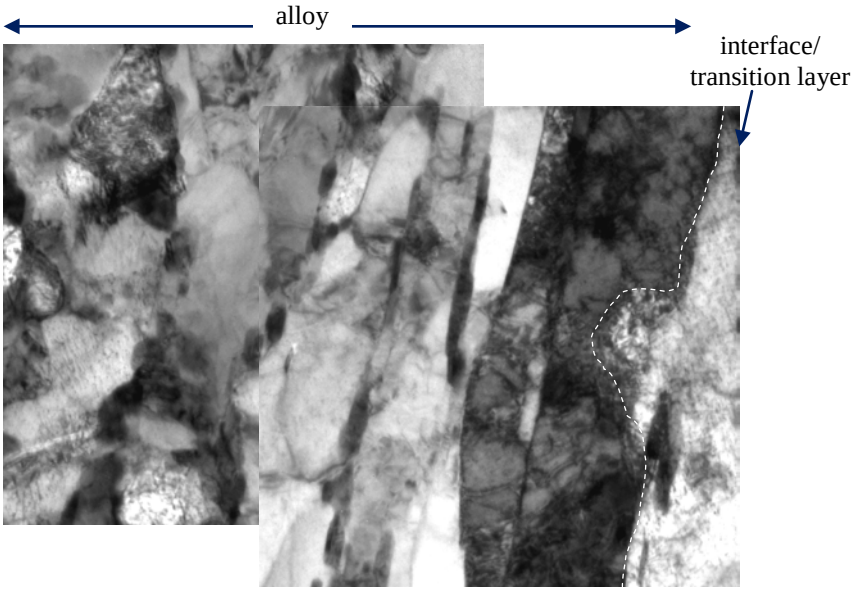

(a)

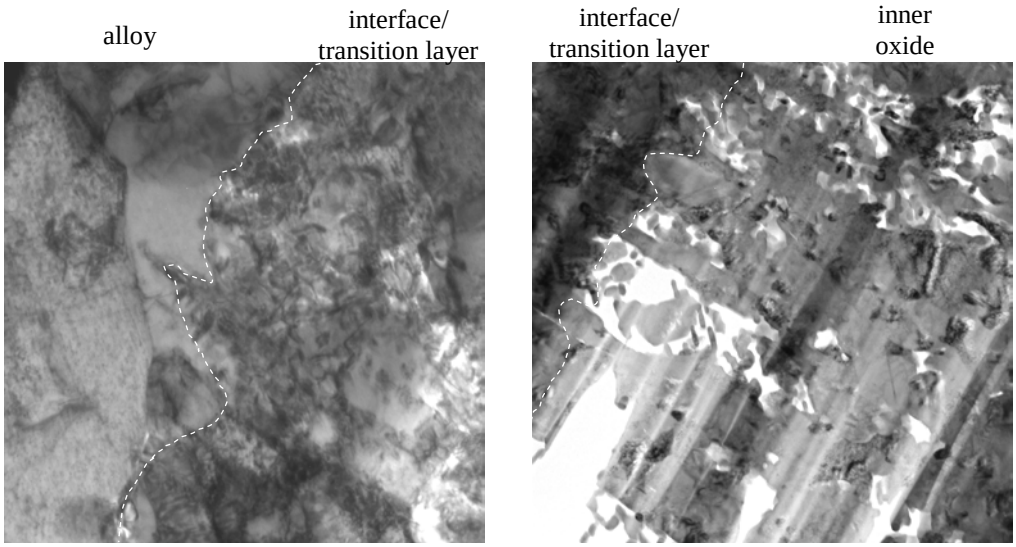

(b) (c)

Figure 4.79 TEM images of HT-9 exposed in 600°C deaerated SCW for 191 hours. (a) Alloy substrate, (b) interface of alloy and inner oxide, and (c) inner layer oxide.

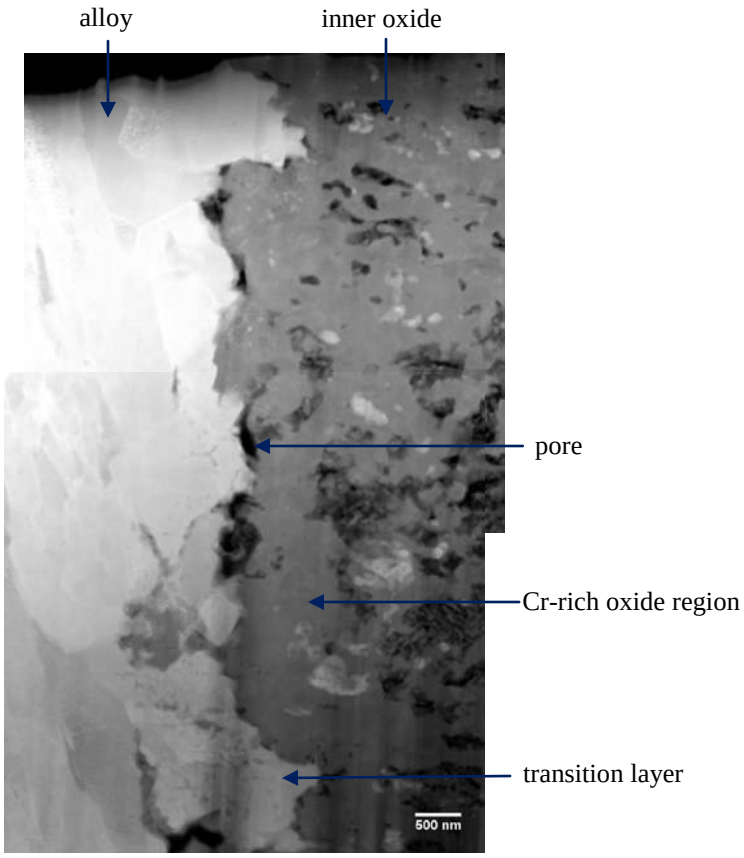

(a)

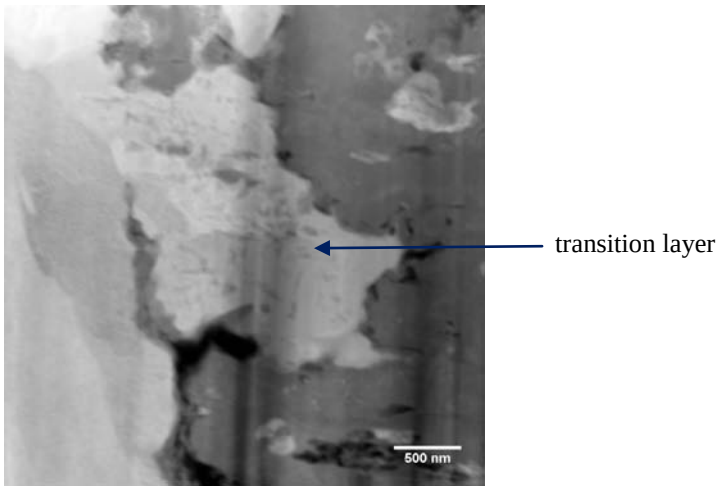

(b)

Figure 4.80 HAADF images of interface of alloy and inner layer oxide of HT-9 exposed in 600°C deaerated SCW for 191 hours. (a) Images show characteristic of the interface that consisted of Cr-rich oxide region, pores, and transition region. (b) Transition region formed between alloy and inner oxide.

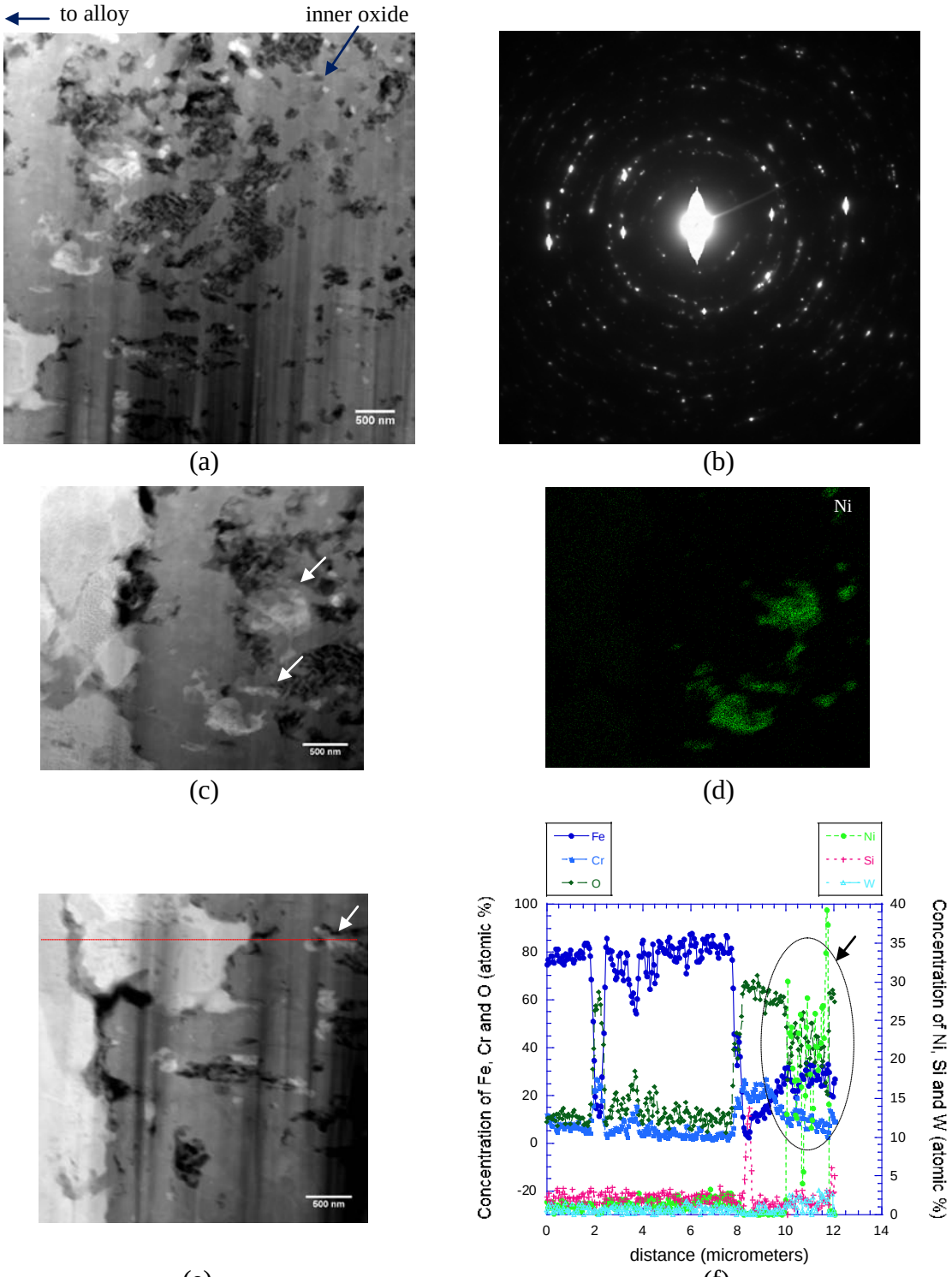

Figure 4.81 HAADF image of inner layer oxide of HT-9 exposed in 600°C deaerated SCW for 191 hours. (a) The inner oxide consisting of spinel structure oxide, pores and precipitates. (b) SAED from the inner oxide exhibits spinel structure. (c) and (d) Major precipitate type is Ni-rich particle. (e) and (f) Composition line scan shows Ni, Fe and O enriched in the particle (circled).

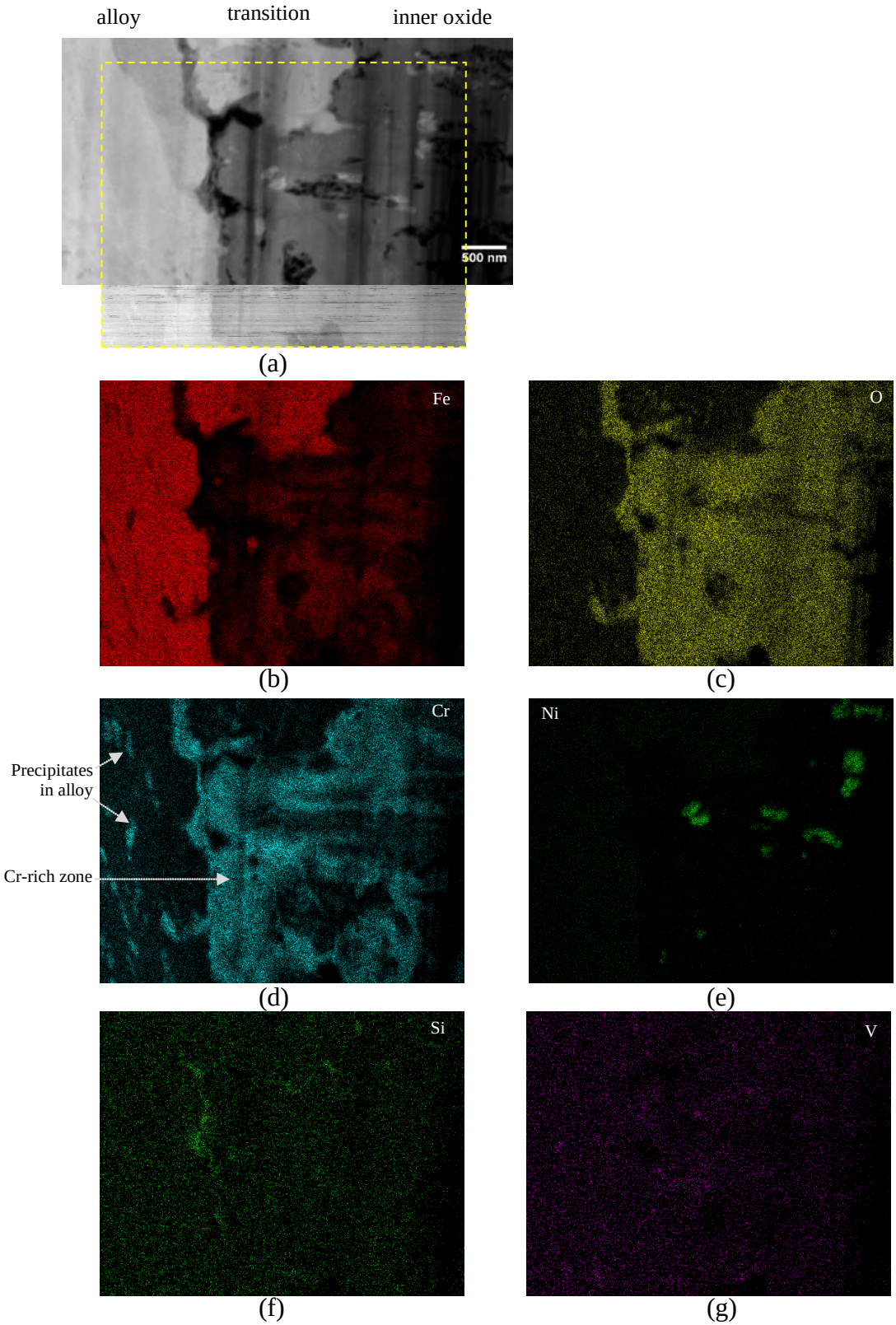

Figure 4.82 Composition maps of Cr-rich oxide region at interface of inner oxide and alloy on HT-9 exposed in 600°C deaerated SCW for 191 hours. (a) HAADF image and composition maps of (b) Fe, (c) O, (d) Cr, (e) Ni, (f) Si and (g) V. (W and Ti are omitted from this figure)

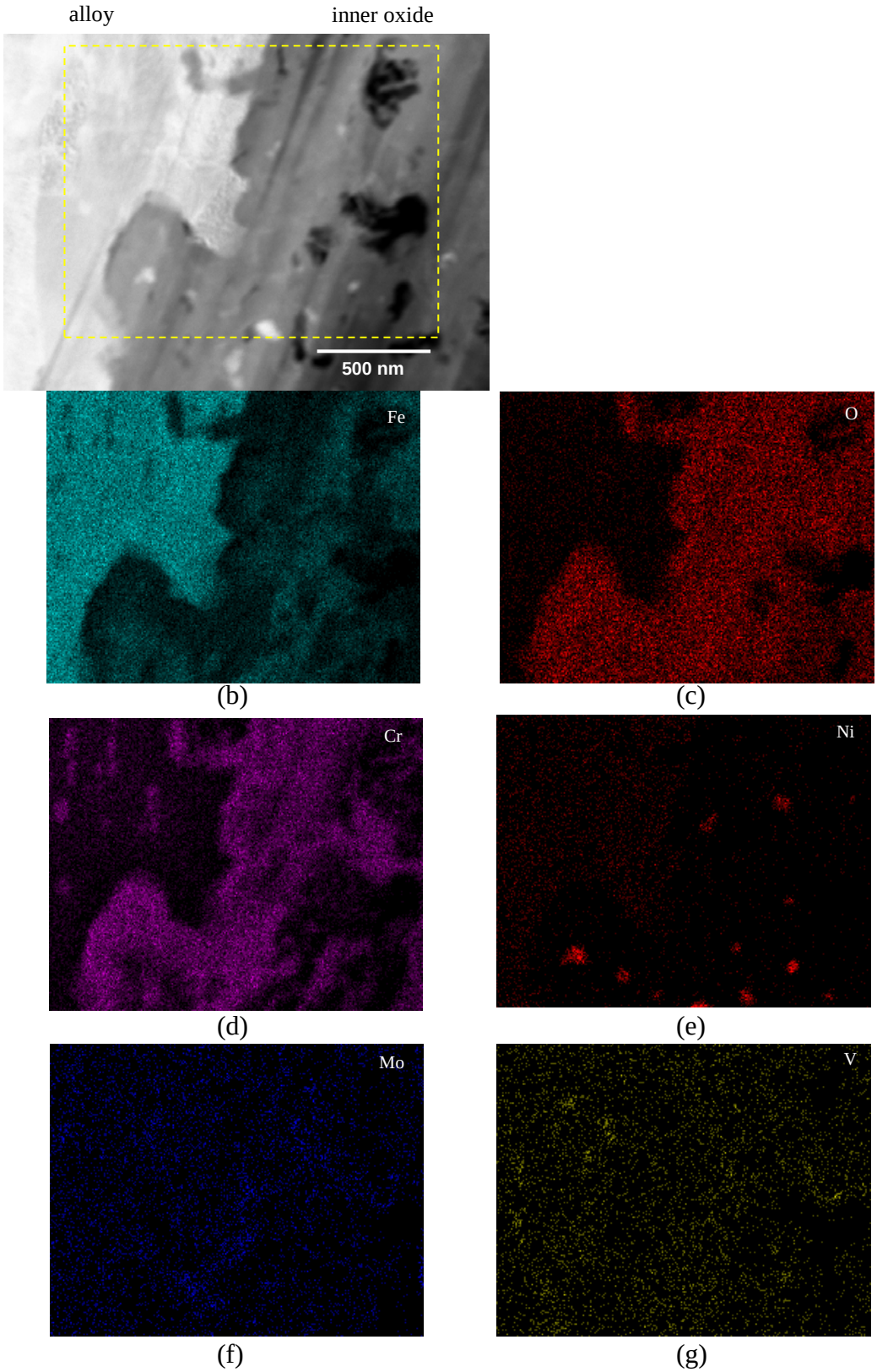

Figure 4.83 Composition maps of Cr-rich oxide region at interface of inner oxide and alloy on HT-9 exposed in 600°C deaerated SCW for 191 hours. (a) HAADF image and composition maps of (b) Fe, (c) O, (d) Cr, (e) Ni, (f) Mo and (g) V.

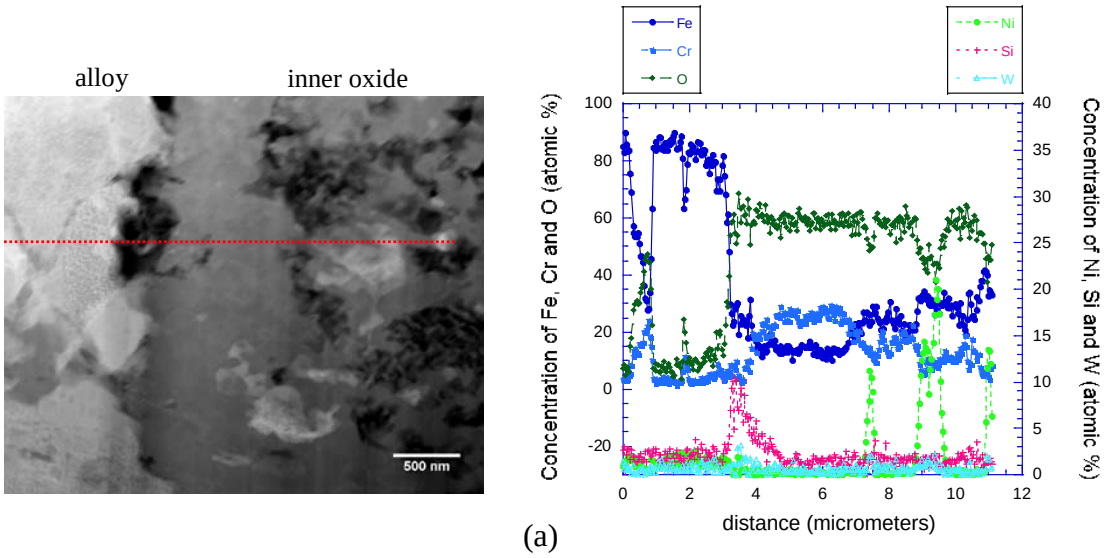

(a)

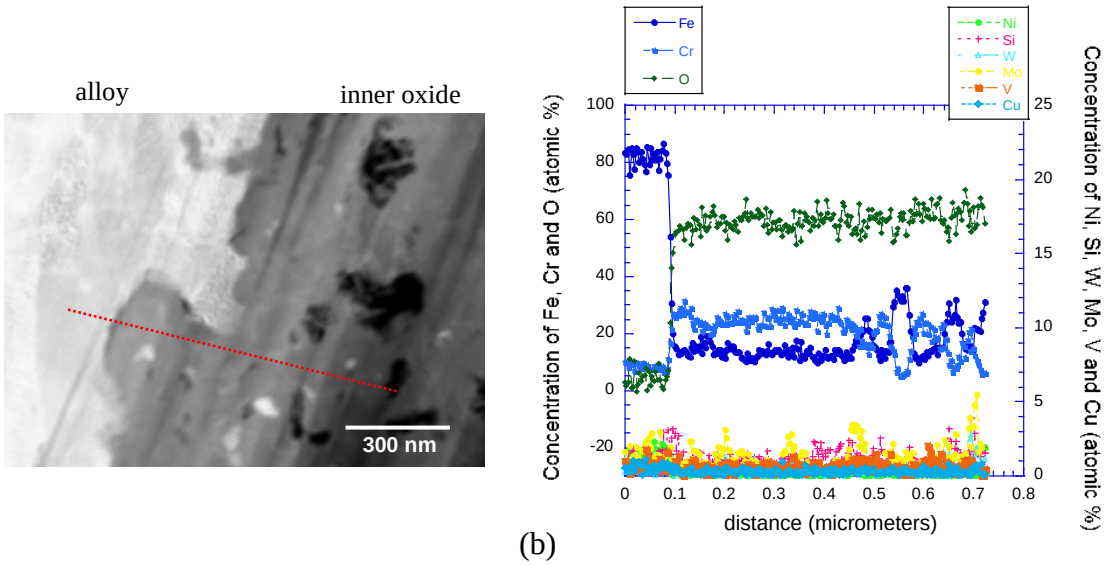

(b)

Figure 4.84 (a) and (b) Composition line scans of Cr-rich oxide region at interface of inner oxide and alloy on HT-9 exposed in 600°C deaerated SCW for 191 hours. The scans show Cr-rich spinel oxide at the interface with Fe:Cr:O of approximately 1:2:4.

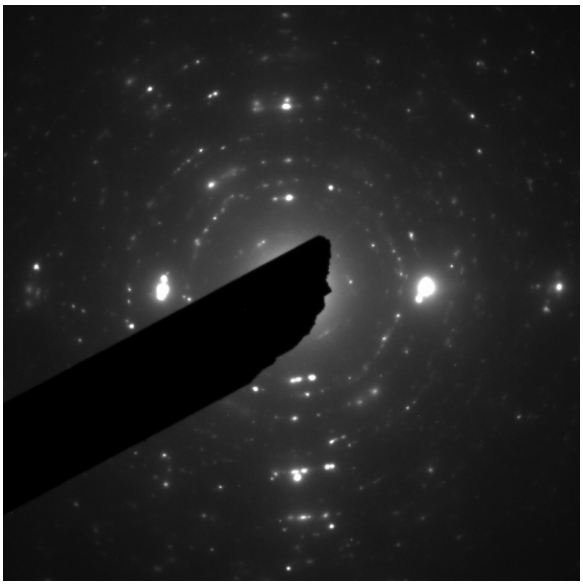

Figure 4.85 SAED pattern of Cr-rich oxide region at interface of inner oxide and alloy on HT-9 exposed in 600°C deaerated SCW for 191 hours. The pattern exhibits spinel structure.

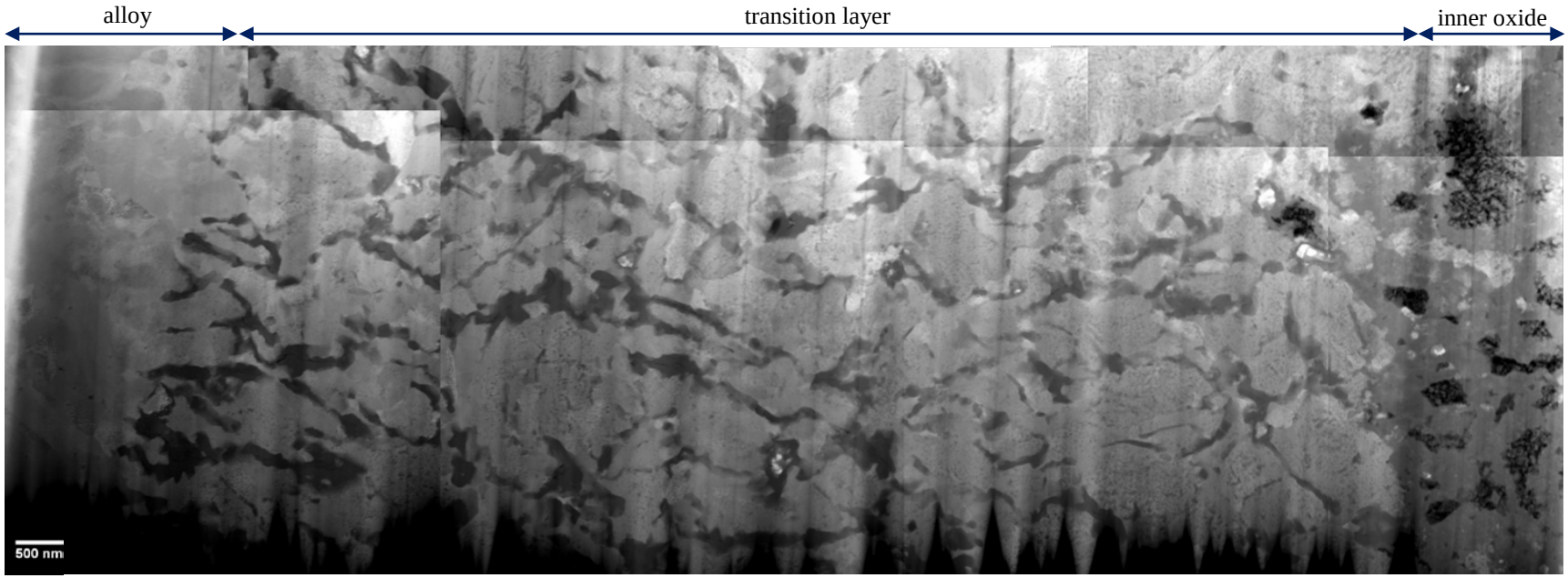

Figure 4.86 HAADF image of inner layer oxide, transition layer and alloy substrate of 9Cr-ODS exposed in 600°C deaerated SCW for 191 hours.

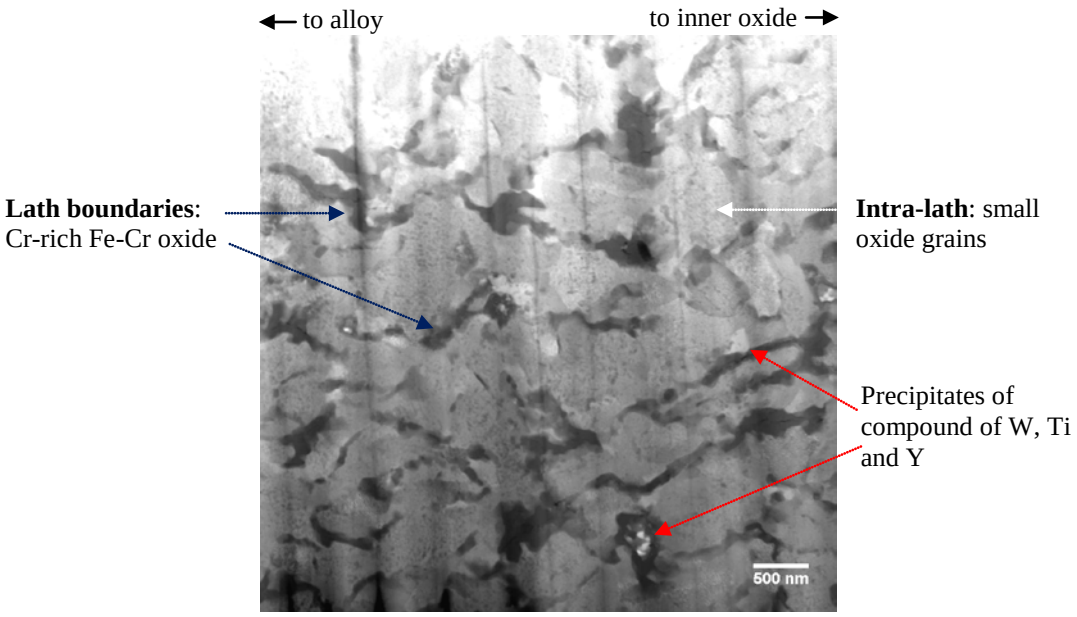

(a)

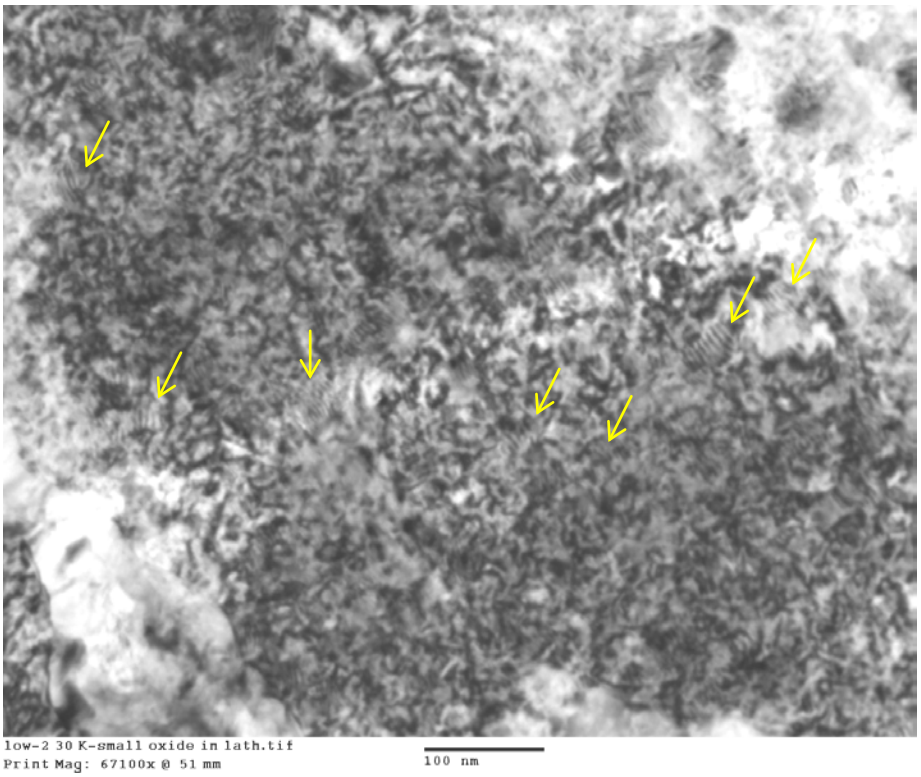

(b)

Figure 4.87 Characteristic of transition layer formed on 9Cr-ODS exposed in 600°C deaerated SCW for 191 hours. (a) HAADF image of transition layer. (b) BF image of intra-lath in the transition layer shows lattice fringes of small oxide grains.

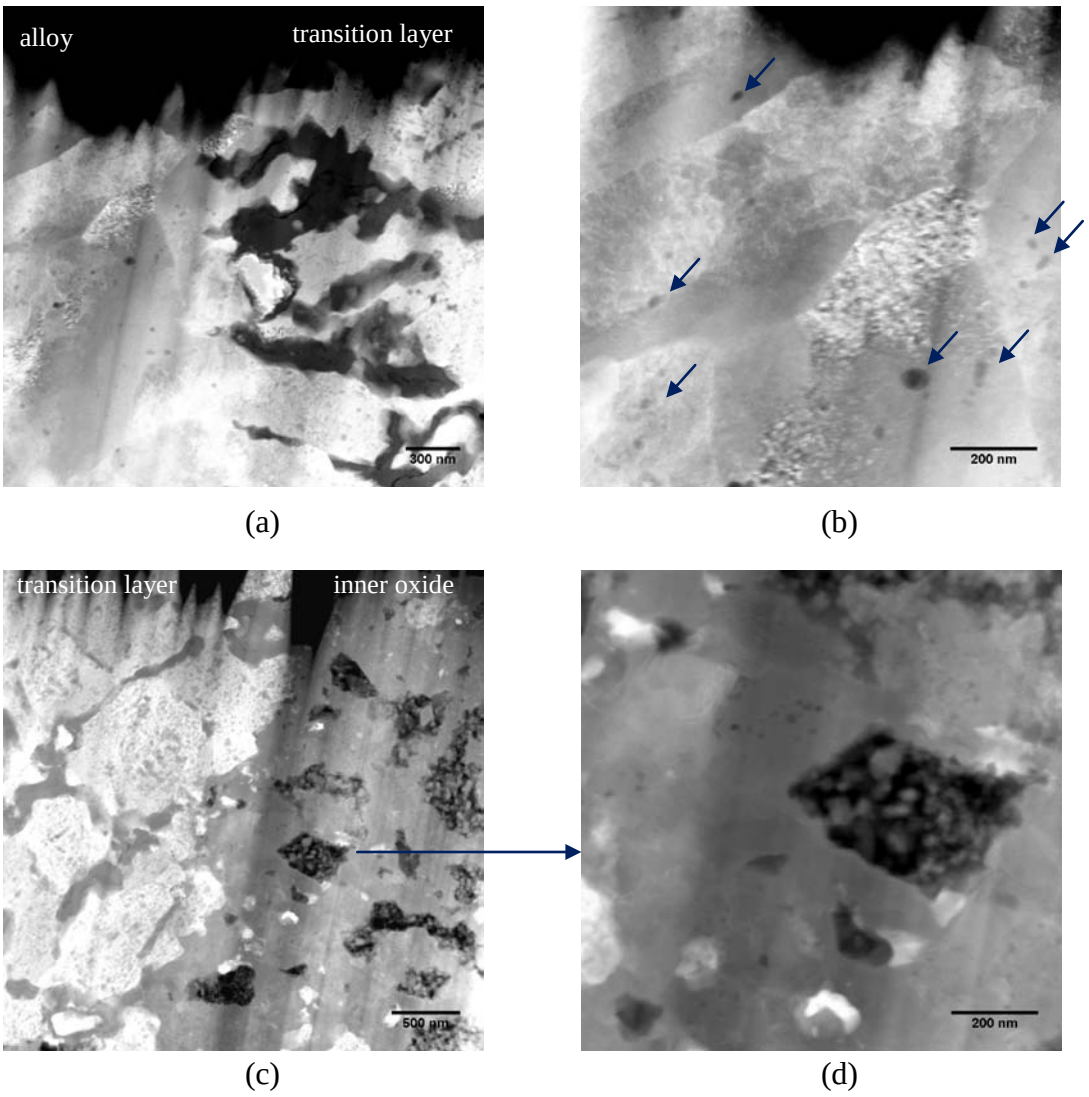

Figure 4.88 HAADF images of 9Cr-ODS exposed in 600°C deaerated SCW for 191 hours. (a) Interface of transition layer and alloy, and (b) small precipitates of Ti in the alloy substrate. (c) Interface of inner oxide and transition layer, and (d) high magnification image shows large pore in the inner oxide.

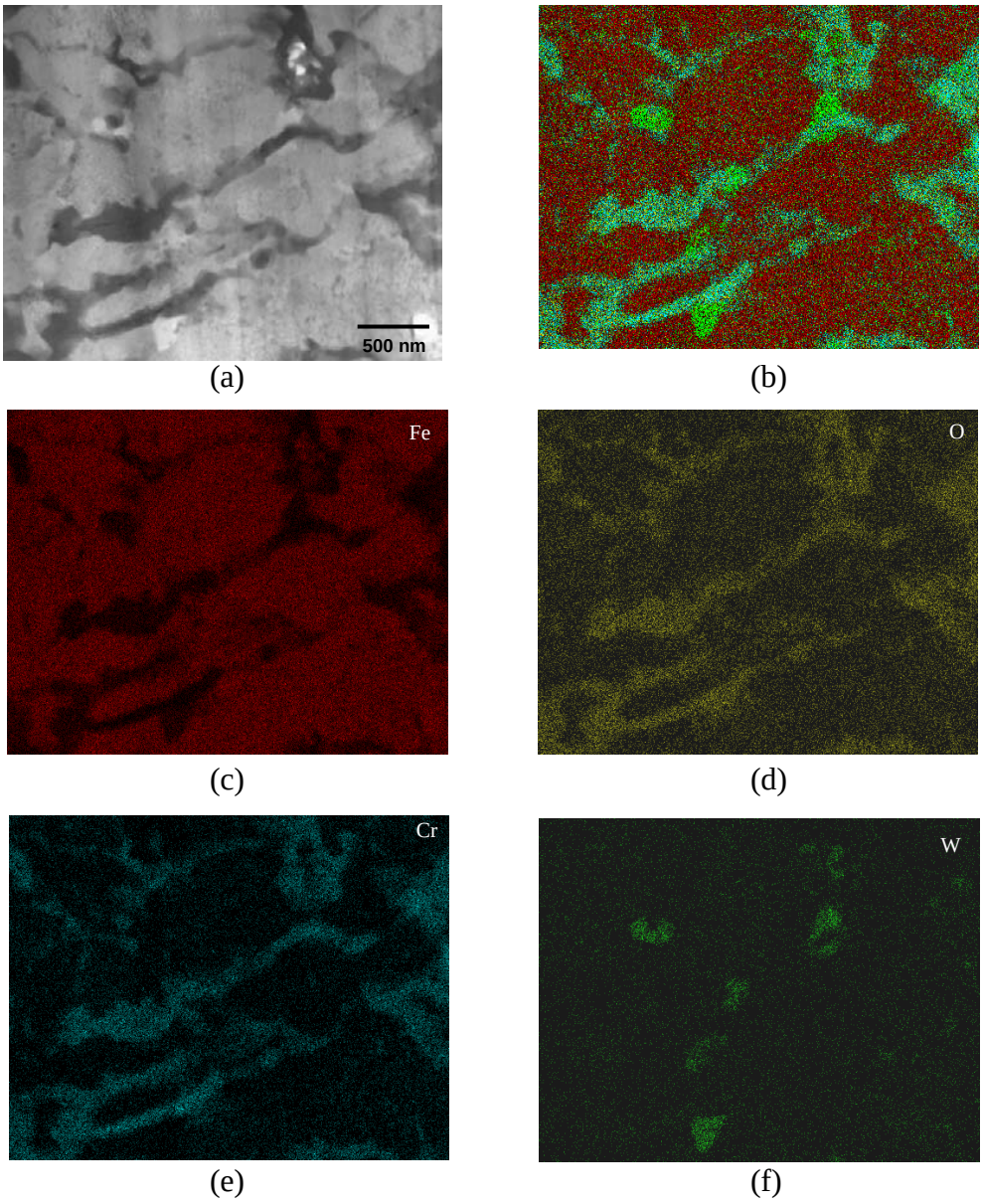

Figure 4.89 Composition maps of transition layer of 9Cr-ODS exposed in 600°C deaerated SCW for 191 hours. (a) HAADF image and composition maps of (b) all elements, (c) Fe, (d) O, (e) Cr and (f) W. The results show Cr-rich oxide at lath boundaries and W-rich particles as a major precipitate in the transition layer.

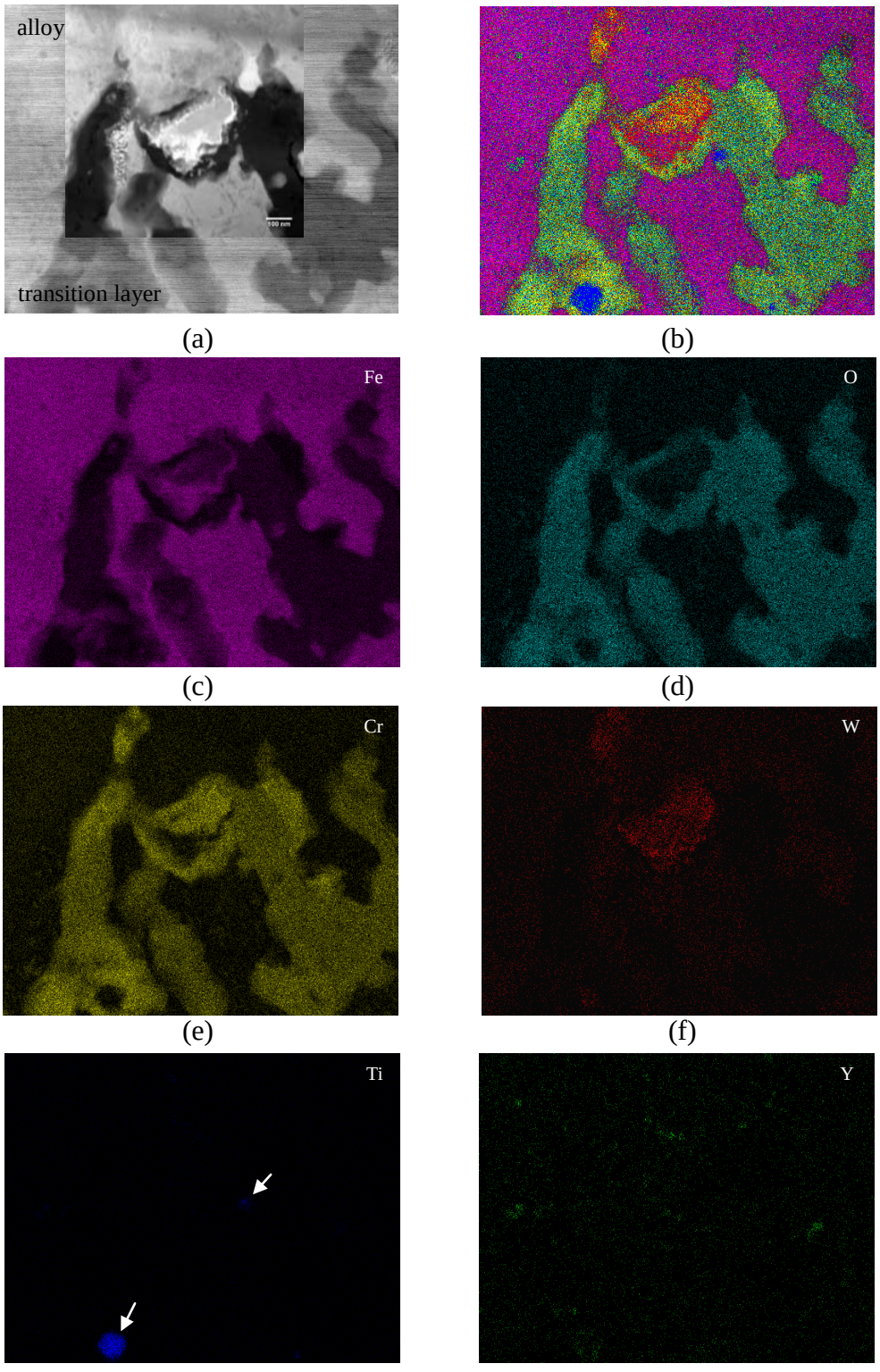

Figure 4.90 Composition maps show W, Ti and Y enriched precipitates formed in transition layer of 9Cr-ODS exposed in 600°C deaerated SCW for 191 hours. (a) HAADF image and composition maps of (b) all elements, (c) Fe, (d) O, (e) Cr, (f) W, (g) Ti and (h) Y.

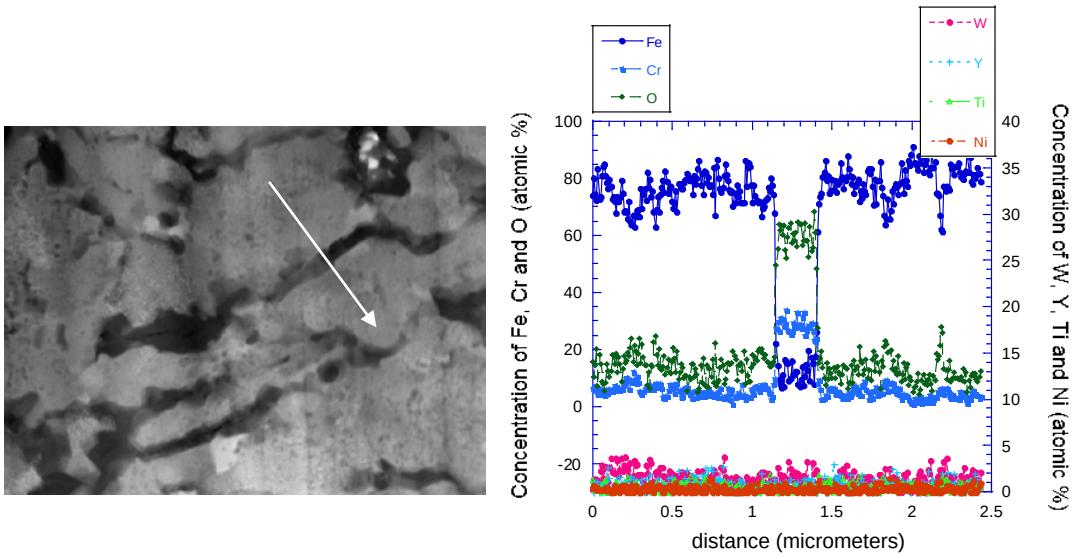

(a)

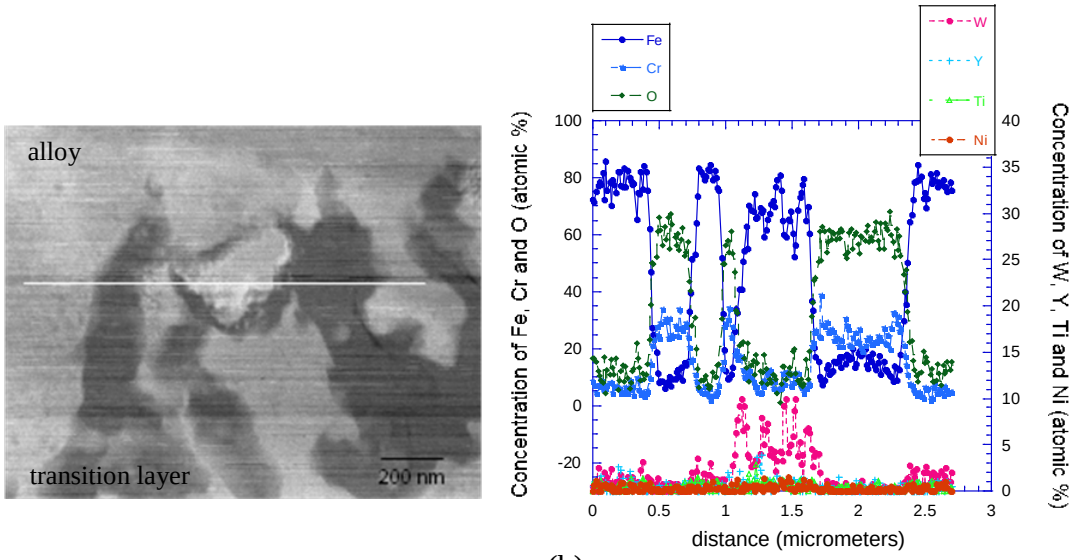

(b)

Figure 4.91 HAADF images and composition line scans across (a) the Cr-rich oxide and (b) the W-rich particle in the transition layer of 9Cr-ODS exposed in 600°C deaerated SCW for 191 hours.

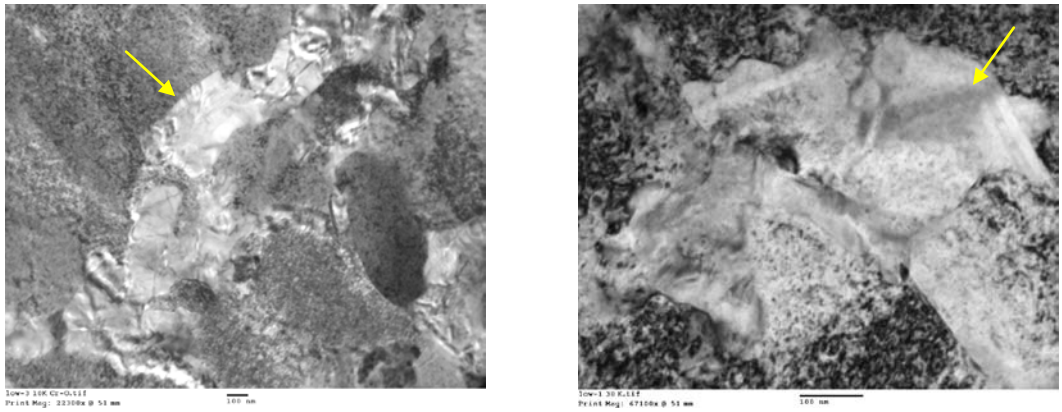

(a) (b)

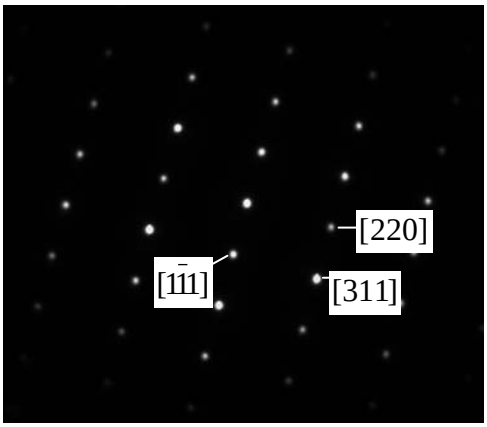

(c)

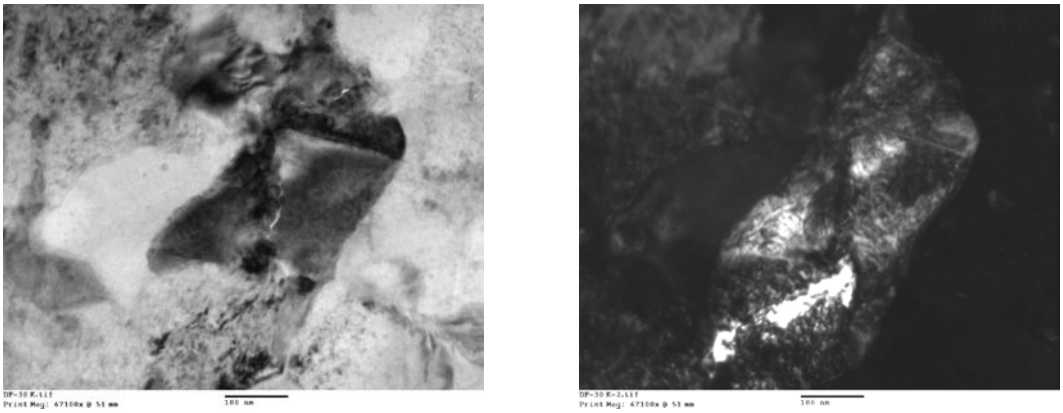

(d) (e)

Figure 4.92 (a) and (b) BF images illustrate Cr-rich oxide bands in the transition layer of 9Cr-ODS exposed in 600°C deaerated SCW for 191 hours. (c) SAED from a Cr-rich oxide band in (d). The pattern from [112] exhibits FCC structure with a = 8.92 Å, and (e) DF image from the pattern in (c).

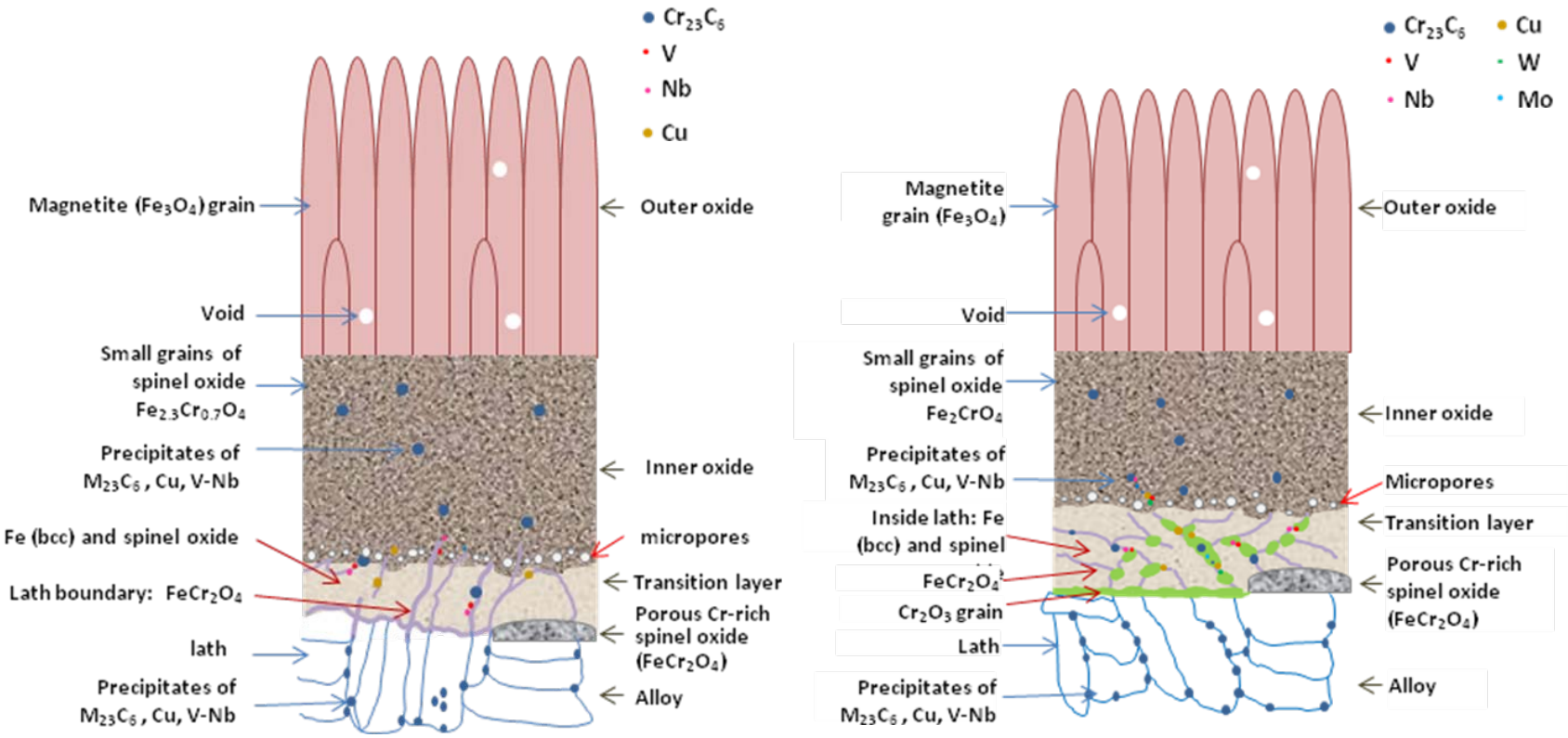

(a) T91 (b) HCM12A

Figure 4.93 Schematic diagram of oxides formed on (a) T91, (b) HCM12A, (c) HT-9 and (d) 9Cr-ODS alloy exposed in 600°C deaerated SCW for 191 hours.

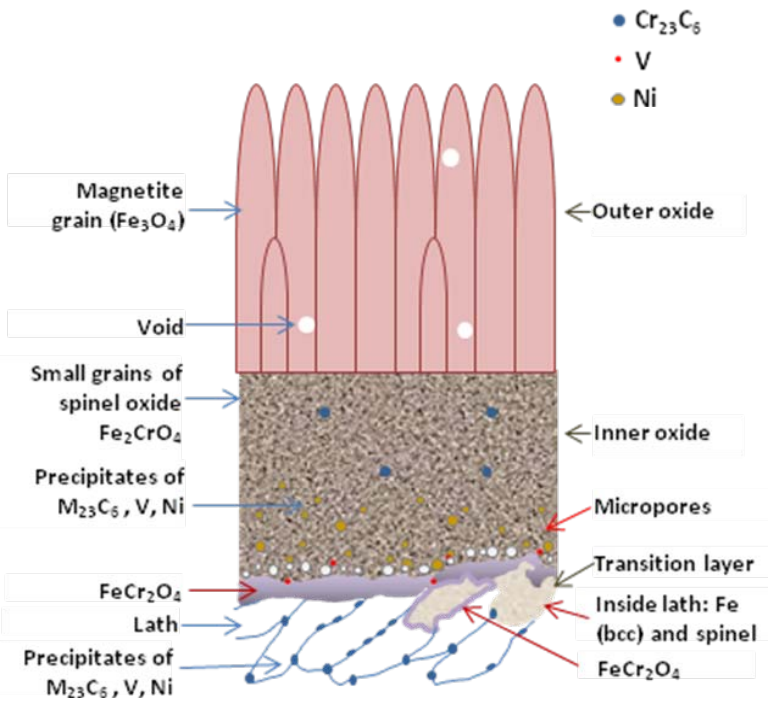

(c) HT-9

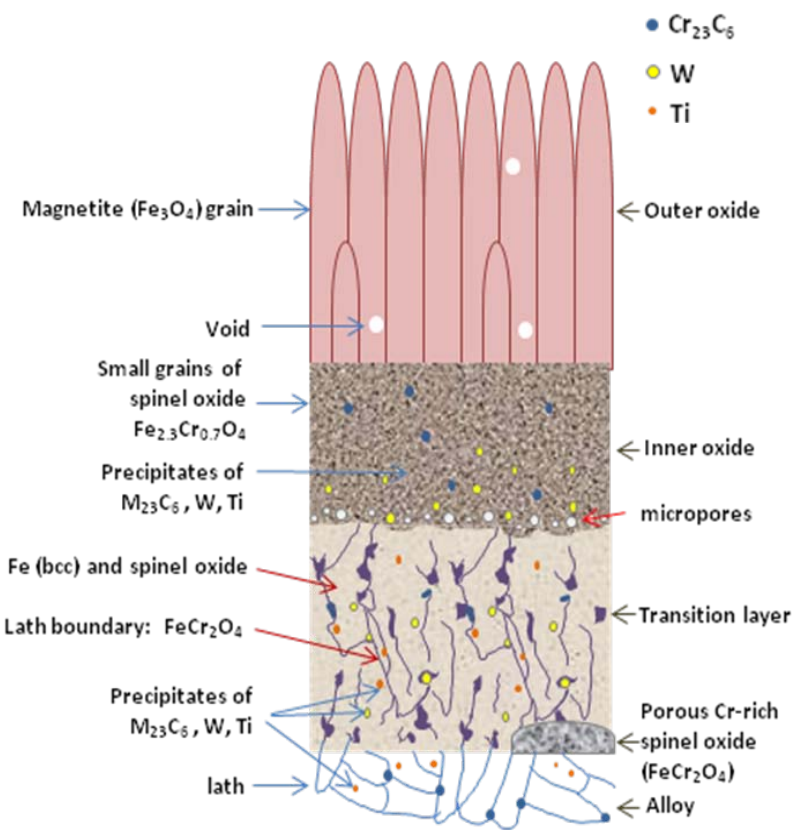

(d) 9Cr-ODS

Figure 4.93 (cont.) Schematic diagram of oxides formed on (a) T91, (b) HCM12A, (c) HT-9 and (d) 9Cr-ODS alloy exposed in 600°C deaerated SCW for 191 hours.

BIBLIOGRAPHY

1. *KaleidaGraph*. 2006, Synergy Software.
2. Ampornrat, P. and G.S. Was, *Oxidation of Ferritic-martensitic Alloys T91, HCM12A and HT-9 in Supercritical Water.* Journal of Nuclear Materials, 2007. **371**(1-3): p. 1-17.
3. Was, G.S. and T.R. Allen. *Time, Temperature, and Dissolved Oxygen Dependence of Oxidation of Austenitic and Ferritic-martensitic Alloys in Supercritical Water*. in *ICAPP'05*. 2005. Seoul, Korea.
4. Dooley, B., et al. *Oxygenated Treatment for Fossil Plants*. in *Proceedings of the International Water Conference*. 1992: Engineers Society of Western Pennsylvavia.
5. Asami, K. and K. Hashimoto, *The X-ray Photo-electron Spectra of Several Oxides of Iron and Chromium.* Corrosion Science, 1977. **17**(7): p. 559-570.
6. Lin, T.-C., G. Seshadri, and J.A. Kelber, *A Consistent Method for Quantitative XPS Peak Analysis of Thin Oxide Films on Clean Polycrystalline Iron Surfaces.* Applied Surface Science, 1997. **119**(1-2): p. 83-92.
7. Ruby, C., J. Fusy, and J.-M.R. Génin, *Preparation and Characterization of Iron Oxide Films Deposited on MgO (100).* Thin Solid Films, 1999. **352**: p. 22-38.
8. Wandely, K., *Photoemission Studies of Adsorbed Oxygen and Oxide Layers.* Surface Science Reports, 1982. **2**(1): p. 1-121.
9. Klueh, R.L. and D.R. Harries, *High chromium ferritic and martensitic steels for nuclear applications*. 2001, PA, U.S.A.: ASTM.
10. Gillot, B., et al., *Availability of Fe2+ ions in Cr- or Al-substituted magnetites with relevance to the process of oxidation in defect phase [gamma]*. Journal of Solid State Chemistry, 1982. **45**(3): p. 317-323.
11. Magalhães, F., et al., *Cr-containing magnetites Fe3-xCrxO4: The role of Cr3+ and Fe2+ on the stability and reactivity towards H2O2 reactions.* Applied Catalysis A: General, 2007. **332**(1): p. 115-123.
12. *MacTempas*. 2007, Total Resolution LLC: Berkeley, CA.
13. Motta, A.T., et al. *Microbeam Synchrotron Radiation Diffraction and Fluorescence Study of Oxide Layers Formed on 9Cr ODS Steel in Supercritical Water*. in *13th International Conference on Environmental Degradation of Materials in Nuclear Power Systems*. 2007. Whistler, British Columbia.

CHAPTER 5

DISCUSSION

The oxidation behavior of F-M alloys exposed in SCW was presented in Chapter 4. It was found that the exposure time, the SCW temperature, the dissolved oxygen concentration and the alloy type affect the oxidation rate. Microstructure characterization showed that the F-M alloys exposed in SCW formed a complex scale structure that consisted of an outer oxide, an inner oxide, and a transition layer. Each layer has distinct morphology, phase and composition. In this chapter, the results will be explained and interpreted to understand the oxidation mechanism(s). The discussion will be focused under four major topics. The first topic involves interpretation of the weight gain and oxide growth as a function of time and temperature. The oxidation rate results will be compared with the literature data and diffusion-related mechanisms will be discussed to determine the rate controlling mechanism. The second topic describes the formation of the outer and inner layer oxides and transition layer in terms of diffusion processes and phase formation of each layer. Calculation of oxygen partial pressure will be done for inner oxide – outer oxide – water interface. Finally, the defect formation as a driving force for cation transport will be discussed and the oxidation mechanisms will be proposed.

5.1 Time and Temperature Dependence of the Weight Gain and Oxide Growth

This section will interpret results of oxidation rate that leads to an understanding of the oxidation mechanism. The results showed that the time-dependence of oxidation rate obeys a power law function, and the SCW temperature has strong effects on the oxidation rate. The experimental results will be compared with theoretical and literature data. Determination of activation energy from the temperature dependence of oxidation rate, and comparison of diffusivities of Fe and O ions in magnetite and in Fe-Cr spinel oxide will give a clue of the rate controlling mechanism. A calculation of mass balance between the outer and the inner oxides will be performed in order to determine the original alloy surface and ion species that influence the oxidation mechanism.

5.1.1. Time Dependence of the Weight Gain and Oxide Growth

The time dependence of weight gain and oxide thickness was evaluated in 400 and 500°C deaerated SCW. Results showed that the weight gain and oxide thickness increases as a function of the exposure time, and can be expressed by a power law;

for oxide thickness, $h = k_h t^{n_h}$, (2.9)

and for weight gain $w = k_w t^{n_w}$, (2.11).

The oxidation rate constant determined from weight gain (k_w) at 400°C SCW is in the range 2.35-5.44 mg/dm^2/h and the time exponent (n_w) is 0.28-0.39. In 500°C SCW, the k_w is 10.89-15.43 mg/dm^2/h and the n_w is 0.36-0.48, Table 4.4. Comparison of the k_w and n_w from this thesis and literature data [1-7] is shown in Table 5.1. The table lists the data for various F-M alloys containing Cr content in a range of 8.37 to 12.12 tested in

400, 500, 550, 600 and 627°C SCW. It is shown that results of k_w and n_w from this thesis agree with those reported in the literature where the ranges of k_w is 8-29 mg/dm^2/h and n_w is 0.24-0.50 at 500°C SCW. In this thesis, the time dependence of the oxidation rate was not determined at 600°C (due to limitation of the SCW system). However, the literature data suggests that the oxidation rate constant at 600°C is approximately in a range of 49-70 mg/dm^2/h and n_w is ~0.31-0.45. Note that the time exponent is in the similar range as that for the data at 400 and 500°C.

The oxidation rate constants are affected by alloy type and temperature, but the time dependence did not depend on these parameters. The value of n_w falls in a range between ~0.3 to 0.5, which confirms that the weight gain can be expressed as a power law. Generally the weight gain should follow a parabolic law if the oxidation process satisfies the ideal conditions as suggested in section 2.3.1b. However, the weight gain resulted from total oxygen absorbed in three oxide layers. Determining the oxide growth from each oxide layer will provide more specific details about growth behavior of the layers.

The growth oxide thickness was determined only in 500°C deaerated SCW. The results showed that the oxide scale growth can be expressed as a power law, similar to that of the oxidation rate from weight gain, Table 4.4. The growth rate for the outer oxide is the highest among three layers, follows by the inner oxide and the transition layer. The mass balance equation, which determines relation of oxide concentration and thickness of each layer will be discussed in the next section (5.2).

The time exponents (n_h) of the outer and inner oxide are close to each other in a range of 0.37-0.44, and agree with that of total oxide thickness. The n_h determined from

inner oxide, outer oxide and total thickness also agrees with n_w determined from weight gain. However, the time exponent of transition layer is relatively low as ~0.20-0.27. This could imply different formation mechanisms between the transition layer, and the outer and inner oxides.

Oxide scale growth occurs by diffusion of ions through a barrier of oxide layers with the chemical potential is the driving force. As the oxide grows thicker the diffusion distance increases, resulted in decreasing of the oxidation rate. As mentioned in the background section, deviation of the oxidation rate from a parabolic law usually observed in oxidation of most of metal elements. For the oxidation of F-M alloys under SCW condition, the deviation also exists. The reason could be attributed to the microstructure of oxide. First, porosity was observed in the oxide layers, both the outer and inner oxides. Porosity affects transport of ions through the oxide scale. Diffusion of cations requires solid state diffusion paths, either by volume diffusion or by grain boundary diffusion. Therefore the formation of porosity in the scale results in reduction of diffusion rate of cations. Conversely, diffusion of oxygen could accelerate if pores or any microcracks are in the scale. Second, it is found that the short-circuit diffusion of ions is the rate controlling mechanism (will be described in next section). Third, establishment of thermodynamic equilibrium at each interface is uncertain, due to the fact that the oxide grows continuously. The assumption that the oxide slightly deviates from the stoichiometry is rarely observed. The spinel structure of both outer (magnetite) and inner (Fe-Cr oxide) oxides is reported to be highly defective [8, 9] in which the defect structure in the oxide varies with oxygen activity and the amount of Cr^{3+}, Fe^{3+} and Fe^{2+}. Next,

evidence of oxygen distribution in alloy lath of the transition layer generally showed that there is oxygen solubility in alloy.

Theoretically, oxidation should follow parabolic behavior if; (i) the oxide scale is compact and adherent, (ii) diffusion of ions through the compact scale is the rate controlling process, (iii) thermodynamic equilibrium exists at both the metal/oxide and oxide/gas interfaces, (iv) the oxide deviates only slightly from stoichiometry, and (v) oxygen solubility in the metal may be neglected. An exponent that is below that for the parabolic law suggests that the controlling mechanism is deviated from the ideal processes. The deviation from a parabolic law can be explained from the above reasons.

5.1.2. Temperature Dependence of the Weight Gain and Oxide Growth

Results showed that the temperature has a great influence on the oxidation rate of F-M alloys in SCW. Both weight gain and oxide thickness increased dramatically at higher test temperatures. Figure 4.3 and 4.4 show that the temperature dependence of the weight gain and oxide thickness growth can be fitted by an exponential function, called an Arrhenius equation;

$$k' = k'_0 \exp(-Q / RT), \qquad (2.12)$$

where k' and k'_0 are the oxidation rate constants (mg/dm^2/h or μm/h), Q is the activation energy of oxidation (J/mol), R is the gas constant (8.314 J/mol-K) and T is temperature (K). Relation of weight gain or oxide thickness and temperature can be expressed as;

$$h = k_{eff,h} t^{n_h} e^{-\frac{n_h Q}{RT}}, \qquad (2.13)$$

$$w = k_{eff,w} t^{n_w} e^{-\frac{n_w Q}{RT}}, \qquad (2.14)$$

where h is the oxide thickness (μm), w is the weight gain (mg/dm^2), $k_{eff,h}$ and $k_{eff,w}$ are the effective oxidation rate constant from thickness (μm/h) and weight gain (mg/dm^2/h), respectively, t is time (hours), and n_h and n_w are the exponent on weight gain and thickness.

For a constant exposure time the activation energy for oxidation, Q, can be calculated from the slope of a plot of *ln h* vs. *1/T*, and *ln w* vs. *1/T*; $slope = -\frac{nQ}{R}$.

Calculation of activation energies was done with the weight gain, and oxide thickness including total thickness, outer oxide, inner oxide, and transition layer. The time exponent, n, has strong effect on the Q value. For the weight gain, the time exponent is in a range of 0.28-0.48 from results at 400 and 500°C. The literature data at 600°C showed that $n_w \sim 0.31$-0.45 for 9Cr-ODS, P92 and HCM12A. Since the activation energy is calculated with an assumption of that the oxidation mechanism remains unchanged within the temperature range. The averaged n_w from three temperatures is used to calculate the activation energy. Therefore, the averaged value of $n_w = 0.40$ from is used to calculate activation energy from weight gain rate.

Since the oxide thickness growth was determined only at 500°C, the activation energies were calculated based on an assumption that the time exponents are in a similar range for each temperature, and used the time exponents from the 500°C test. The time dependence of oxidation in the outer and inner oxide are quite similar (and close to that of weight gain), thus an average of $n_h = 0.40$ is used for these oxide layers. The time exponent from the transition layer is less than that of the outer and inner oxides ($n_h = 0.23$). An averaged value of $n_h = 0.37$ is used for the total oxide thickness.

Figure 5.1 shows plots of *ln w* vs. 1/*T* for the four F-M alloys following tests in deaerated 400°C, 500°C and 600°C SCW. The fitting parameters and activation energies of the F-M alloys calculated from weight gain and oxide thickness of this study, and literature data are listed in Table 5.2. It was found that the activation energies determined from weight gain of T91 (206 ± 6 kJ/mol), HCM12A (199 ± 6 kJ/mol) and HT-9 (181 ± 4 kJ/mol) in SCW are very close and below that of 9Cr-ODS (287 kJ/mol). (Standard deviation of Q was estimated from error propagation from 2σ of slope (B) of linear regression using GraphPad Software© [10]. Since data of 9Cr-ODS is limited only two temperatures, the standard deviation cannot be determined.) Moreover, the values for a given alloy are in quite similar in both steam and SCW.

Activation energies determined from the oxide thickness are calculated from i) total oxide thickness, ii) outer oxide, iii) inner oxide and iv) transition layer, Table 5.2. Figure 5.2-Figure 5.4 present plots of *ln x* vs. 1/*T* for T91, HCM12A and HT-9 following tests in 400°C, 500°C and 600°C deaerated SCW. (The activation energy of 9Cr-ODS alloy was not determined because only one data at 600°C is available.) The fitting parameters and activation energies are also reported in Table 5.2. The activation energies determined from the total oxide thickness are 173 ± 14, 175 ± 12 and 164 ± 10 kJ/mol for T91, HCM12A and HT-9, respectively. These values are slightly less than those from the weight gain, but they still fall in the same range. Outer layer oxide yields the activation energies in a range of 166 – 162 kJ/mol, and the inner layer oxide yield slightly lower values of 158 – 172 kJ/mol.

The activation energies of transition layer are different from other oxide layers, and are distinct for each alloy. The results for T91, HCM12A and HT-9 are 196 ± 41, 277

± 66 and 101 ± 55 kJ/mol, respectively. (Standard deviations of these values are very large perhaps due to high measurement error from composition profiles.) The reason for the difference from the other oxide layers could be attributed to the difference in power n_h of the time-dependence oxidation rate equation, where n_h of outer and inner oxide is ~0.4 and n_h for transition layer is ~0.2. This result also implied to a different formation mechanism of the transition layer, which will be determined in the next step.

Oxidation can occur by one of two processes; diffusion of Fe cations through the oxide to the oxide-water interface, or diffusion of O anions through the oxide to the metal-oxide interface. (Diffusion of Cr is too slow to influence the oxidation mechanism, thus it is negligible.) The activation energy provides a clue as to which process is rate controlling. Table 5.3 lists selected diffusion data including D_0 (frequency factor) and Q (activation energy) of Fe and O ions in oxides from literature. In addition, diffusion coefficients of Fe and O in oxides at particular temperatures also reported in Table 5.4.

It is important to note that there are two major parameters influencing the diffusion coefficients and activation energies reported in the literature. The first parameter is the short circuit diffusion along grain boundaries that allows fast diffusion of ions through the oxide specimen. Experiments conducted with polycrystal oxide specimens provided higher diffusivities than those of single-crystal oxide specimen. Therefore, information of single crystal or polycrystal, and experimental method will be given in the table. Another parameter involves oxygen partial pressure in the spinel structure oxide, which included magnetite and Fe-Cr spinel oxide. Generally, the diffusivities of cation and anion in spinel structure oxide are influenced by its defect structure. (Detail will be explained in Section 5.4) Vacancy diffusion mechanism

dominates under high oxygen partial pressure, whereas interstitial mechanism dominates at low oxygen partial pressure [8, 11]. Therefore the diffusivities of cations and anions change as a function of oxygen partial pressure. Most of the sources of data listed in Table 5.3 did not specify the oxygen partial pressure, so this could be a reason for the variation in the diffusion data.

The activation energies shown in Table 5.3 are classified into three groups; diffusion of O and Fe in Fe_3O_4, diffusion of O, Fe and Cr in Cr_2O_3 (will be used in later section), and diffusion of O, Fe and Cr in spinel oxides. The activation energy of oxygen diffusion in magnetite is in the range of 71.1 – 264 kJ/mol. The data from hydrothermal experiments showed particularly low values of Q of ~ 71 and 188 kJ/mol. Because the nature of the hydrothermal condition may change the defects in magnetite, the Q values from these experiments may be affected (hydrothermal experiments were conducted under water pressures of 10, 100, or 200 MPa). It is noted that the activation energies obtained from experiments conducted with single crystal have lower values than that of polycrystal. In addition, the activation energy from grain boundary diffusion (167 kJ/mol) is lower than that from polycrystal (264 kJ/mol) in the experiments of Crouch and Robertson [12].

Experimental values for the diffusion coefficient and activation energy of iron in magnetite also vary considerably. Overall the activation energies of Fe diffusion are higher than O diffusion in magnetite (87.9 – 351.5 kJ/mol), thus exhibiting that diffusion of O occurs easier than Fe. Although the activation energies of Fe do not show a difference between single crystal and polycrystal, the data from nanoparticle experiments exhibited the lowest value.

Data on the diffusion of ions in the spinel structure oxides is very rare. O diffusions in spinel oxide of $FeCr_2O_4$, $Fe_{2.32}Ni_{0.68}O_4$ and $NiCr_2O_4$ exhibit the values of *Q* in a range of 138 - 295 kJ/mol. Only data reported on diffusions of Fe and Cr in spinel oxides of $MnCr_2O_4$ with *Q* of 255.40 kJ/mol for Fe and 188 kJ/mol for Cr. Another data reported on diffusion of Fe and Cr in $Fe_{3-x}Cr_xO_4$, where *x* is 0.3, 0.6, 0.99 and 1.2 by Töpfer et al. [9]. However, only data set was reported from the tests at temperature 1200°C so that the activation energy is not determined. However, the trend is expected to be similar for Fe and Cr diffusion in other spinel oxide.

In summary, the activation energies for diffusion of O and Fe in bulk magnetite are not distinguished and likely to be greater than 200 kJ/mol. The average activation energy for O diffusion is slightly lower than Fe diffusion in magnetite and those of spinel oxide. An important fact is that the short circuit diffusion has a major effect on activation energy as observed from results of polycrystal and grain boundary diffusion. Due to the large variability of activation energy reported in the literature data, it is difficult to determine on the basis of activation energy alone, which ion controls the oxidation rate. The measured activation energies form weight gain and total oxide thickness of the F-M alloys in this study are ~163 - 206 kJ/mol, which are less than those of oxygen and iron diffusion in bulk oxide. The data that close to the Q in this study are the grain boundary diffusion of O [12], diffusion in polycrystalline of Fe in magnetite [8], and O diffusion in spinel oxide [13]. The activation energies determined from the outer and inner oxide thickness also fall in the same range. However, the higher activation energies of transition layer could be attributed to other diffusion mechanisms.

The activation energies determined from weight gain are slightly higher than those of oxide thickness. The values possibly indicate difference in mechanism of each determination method or oxide layer, or it possibly occurred from errors of measurement. The activation energy determined from weight gain that accounted from mechanism involving oxygen absorption in outer oxide, inner oxide, transition layer and dissolved oxygen in alloy substrate. The activation energy determined from oxide thickness involved growth mechanism of each individual oxide layer, which could be different for each layer. Therefore the activation energy from weight gain should be higher or equals to that of oxide thickness. Major reason is that the Q from weight gain included the activation energy of oxygen dissolution in alloy, which was not included in the oxide thickness.

Comparison between alloys, the activation energies determined from both weight gain and oxide thickness (except transition layer) of T91, HCM12A and HT-9 are in the same range. This implies that the rate controlling mechanism of oxidation in these three F-M alloys are similar. However, the activation energy determined from weight gain of 9Cr-ODS is much higher than those of other three alloys. Thus, it could imply that the rate controlling mechanism in the 9Cr-ODS is different from the other. This implication is not unexpected because the 9Cr-ODS consisted of nanoparticles of Y_2O_3 in the alloy matrix. Diffusion mechanism of anions and cations could be affected from these nanoparticles. (Effect of the nanoparticles is explained in section 5.2.4.) However, the activation energy of 9Cr-ODS was determined from only two data points, and no data from oxide thickness. Further research should be conducted for a better understanding of mechanism in this alloy.

In conclusion, the activation energies suggest, i) the occurrence of short circuit diffusion along grain boundaries or defects in the oxide scale, and ii) the difference in growth mechanisms of the inner and outer oxide, and the transition layer. Therefore, microstructure of oxides was thoroughly investigated. In order to clarify the rate controlling mechanism, the diffusion rates of Fe and O are determined in section 5.1.4.

5.1.3. Determination of Location of Original Alloy Substrate and Mass Balance Equation

It is important to consider about the oxide structure before determinate the rate limiting mechanism in the next section. Assumption of the oxidation mechanism is that the outer oxide grew by outward diffusion of Fe ions, and the inner oxide grew by inward diffusion of O ions. Important piece of information required to prove this assumption is the location of the original alloy surface. The original alloy surface was determined from the microstructure of oxide and the mass balance between the outer and inner oxides.

The microstructure of the outer oxide consisted of columnar grains of magnetite with voids formed in some of magnetite grains, and no precipitates were found in the layer, Figure 4.48. These features distinguish from the microstructure of the F-M alloys, which consisted of PAG that contains packets with martensite laths and precipitate particles locate at the boundaries. Further, the columnar shape of magnetite also shows that the grains grew along the direction of Fe diffusion. Therefore, the outer layer is not the original alloy substrate, and could form only by outward diffusion of Fe.

The inner oxide consisted of small equiaxed grains of Fe-Cr spinel oxide. Precipitates of Cr-rich $M_{23}C_6$ and minor alloying elements were observed in the layer. In

the samples tested at 400 and 500°C, the precipitate alignment was observed as the same shape as PAG in alloy substrate, Figure 5.11. Although the precipitates in 600°C samples were not observed as the PAG, they distributed throughout the inner oxide. The presence of these precipitates indicates that the inner oxide is the original alloy substrate. Additional evidence is the Cr concentration in the inner oxide, which has the same level as that of alloy substrate. Cr is a slow diffuser element compared to Fe. As reported by Töpfer et al. [9], the self diffusion coefficient of Cr in Fe-Cr spinel oxide at 1200°C is approximately three order of magnitude slower than that of Fe, Table 5.4. The diffusion of Cr is almost negligible. While Fe diffused outward, Cr remained in the inner oxide. These facts lead to the conclusion that the inner oxide is the original alloy substrate that grew by inward diffusion of oxygen.

If the outer oxide grew by outward diffusion of Fe and the inner oxide is the original alloy substrate, the original alloy surface is the same location as the interface of outer and inner oxides. The entire cross section SEM images also show the flat interface between the outer and inner oxides, which is consistent with polished surface of alloy before oxidation. This conclusion agrees with most of reports involved the oxidation of iron based alloys [4, 14-17]. Soraya [18] conducted a marker experiment in a study of oxidation in air of HT-9 at 600-800°C by painting liquid Pt as a marker on the surface of alloy before oxidation. After oxidation, it was found that the outer oxide did not grow on the area of Pt, indicating that the interface of outer – inner oxide is the original alloy surface.

Mass balance equation

In addition to the observation of microstructure of oxides, the mass balance of Fe between the outer and inner oxide is demonstrated. Determination of the oxide thickness ratio shows that the inner/outer layer ratio is less than one, Table 4.6 and Figure 4.33. However, the thickness ratio of (inner oxide + transition + Cr-rich oxide)/outer oxide is close to one. These discrepancies could be accounted from the differences of oxide density and elemental concentrations in the oxides. Calculation of mass balance equation was developed by Tomlinson and Cory [19], and Martinelli et al. [15-17]. The equations in this study were derived based on these works in order to apply with the current oxide microstructure.

First, the mass conservation of Fe and Cr is determined. Three assumptions are proposed; i) the original alloy surface is the interface of outer – inner oxides, iii) the outer oxide grows by outward diffusion of Fe, and ii) Cr concentration in the inner oxide equals to that of alloy substrate. From the assumptions, amount of Fe in the outer oxide should equal to amount of Fe in the original alloy after subtracting the Fe in the inner oxide;

$$\#\ \text{Fe in outer oxide} = \#\ \text{Fe in alloy} - \#\ \text{Fe in inner oxide} \qquad (5.1)$$

and,

$$\#\ \text{Cr in inner oxide} = \#\ \text{Cr in alloy.} \qquad (5.2)$$

It is important to note that the outward diffusion of Fe should also account for sources from lath boundaries in the transition layer, and from porous Cr-rich oxide (in 600°C test). In addition, there are possible volatile / soluble corrosion products and oxide phases (i.e., $Fe(OH)_2$) produced at the oxide – water interface. These terms are considered very small amount comparing to the terms listed in equation **5.1**. Therefore the mass balance equation is first determined by neglecting these terms.

Equations **5.1 and 5.2** can be expressed in terms of concentration and molar volume (assuming the same surface area);

$$C_{Fe,mag} h_{mag} = C_{Fe,alloy} h_{alloy} - C_{Fe,sp} h_{sp} \quad (5.3)$$

$$C_{Cr,sp} h_{sp} = C_{Cr,alloy} h_{alloy} \quad (5.4)$$

where, h_{mag}, h_{sp} and h_{alloy} are the thicknesses (in μm) of outer oxide (*mag*), inner oxide (*sp*) and alloy. $C_{Fe,mag}$, $C_{Fe,sp}$ and $C_{Fe,alloy}$ are the concentration of Fe in magnetite, spinel oxide and alloy substrate (mol/cm^3). The mole concentration of metal (M) in oxide (M_mO_n) can be determined from numbers of mole of M in oxide divided by molar volume of oxide;

$$C_{M,M_mO_n} = \frac{m}{V_{M_mO_n}} \quad (5.5),$$

where, *m* is the numbers of mole of *M* in one mole of oxide, V_{MmOn} is the molar volume of the oxide (cm^3).

The outer oxide is magnetite (Fe_3O_4). The inner oxide is Fe-Cr spinel oxide with a composition of $Fe^{2+}(Fe^{3+}_{2-x}Cr^{3+}_x)O^{2-}_4$, where *x* is approximately 0.7, 0.9, 1.0 and 0.7 for T91, HCM12A, HT-9 and 9Cr-ODS, respectively. (The composition of inner oxide depends on Cr concentration in alloy. The test conditions have only small effect on the composition.) The molar volume of Fe_3O_4 is 44.6 cm^3/mol [20]. Since the lattice parameter of Fe-Cr spinel oxide is close to that of magnetite (a = 8.396 Å for Fe_3O_4, and a = 8.378 – 8.405 Å for Fe-Cr spinel oxide), the molar volume approximately equals that of magnetite. Therefore, the molar volumes of Fe_3O_4 and Fe-Cr spinel oxide used in the calculation are both 44.6 cm^3/mol. The molar volume of the alloy substrate is 6.82 cm^3/mol (Fe, bcc) [21]. The concentrations of Fe and Cr in oxide are;

Fe in magnetite, $$C_{Fe,mag} = \frac{3}{V_{Fe_3O_4}} = \frac{3}{44.6} = 0.067 \text{ mol/cm}^3,$$

Fe in Fe-Cr spinel, $$C_{Fe,sp} = \frac{3-x}{V_{(Fe,Cr)_3O_4}} = \frac{3-x}{44.6} \text{ mol/cm}^3,$$

Cr in Fe-Cr spinel, $$C_{Cr,sp} = \frac{x}{V_{(Fe,Cr)_3O_4}} = \frac{x}{44.6} \text{ mol/cm}^3.$$

Relation of the Cr concentration (x) in Fe-Cr spinel oxide and the oxide layer thickness can be derived by dividing equation **5.3** with **5.4**, then substitute C.

5.3/5.4, $$\frac{C_{Fe,alloy}}{C_{Cr,alloy}} = \frac{C_{Fe,sp}h_{sp} + C_{Fe,mag}h_{mag}}{C_{Cr,sp}h_{sp}} = \frac{C_{Fe,sp}}{C_{Cr,sp}} + \frac{C_{Fe,mag}h_{mag}}{C_{Cr,sp}h_{sp}}.$$

Substitute C, $$\frac{C_{Fe,alloy}}{C_{Cr,alloy}} = \frac{3-x}{x} + \frac{3h_{mag}}{xh_{sp}}.$$

Therefore, $$x = 3\frac{\left(1+\frac{h_{mag}}{h_{sp}}\right)}{\left(1+\frac{C_{Fe,alloy}}{C_{Cr,alloy}}\right)} \qquad (5.6).$$

Calculation of Cr concentration in Fe-Cr spinel oxide from oxide thickness for each alloy and environment is shown in Table 5.5. The calculation was conducted with oxide thicknesses from tests in 400 (151 hours), 500 (182 and 195 (for HT-9) hours) and 600°C (191 hours) deaerated SCW, and at 500°C with 100 (236 hours) and 300 ppb (182 hours). The results show that the Cr concentrations calculated from eqn. **5.11** agree with that from the experiments. The discrepancy could be accounted for the measurement error.

In order to determine the thickness of alloy that was consumed to produce the outer layer oxide (h_{alloy}), equations **5.8** and **5.9** were derived as;

Eqn. **5.8-5.9**, $$\left(C_{Fe,alloy} - C_{Cr,alloy}\right)h_{alloy} = \left(C_{Fe,sp} - C_{Cr,sp}\right)h_{sp} + C_{Fe,mag}h_{mag},$$

substitute C, $$\left(C_{Fe,alloy} - C_{Cr,alloy}\right)h_{alloy} = \left(\frac{3-2x}{V_{Fe_3O_4}}\right)h_{sp} + \frac{3}{V_{Fe_3O_4}}h_{mag},$$

therefore, $$h_{alloy} = \frac{(3-2x)h_{sp} + 3h_{mag}}{\left(C_{Fe,alloy} - C_{Cr,alloy}\right)V_{Fe_3O_4}}. \qquad (5.7)$$

Calculation of h_{alloy} is shown in Table 5.6. The results show that the thickness of alloy that was consumed is close to the inner oxide thickness (h_{sp}). It was concluded that the inner oxide grew only inside the consumed alloy thickness. The difference of h_{alloy}-h_{sp} that is always positive indicating that the thickness of consumed alloy is slightly greater than the inner oxide. The discrepancy could be accounted from the porosity of inner oxide, the transition layer and the porous Cr-rich oxide.

Using the criteria of $h_{alloy} \approx h_{sp}$, relation of the outer and inner oxide thicknesses (eqn. **5.8**) can be simplified as;

$$h_{mag} = \left(\frac{C_{Fe,alloy} - C_{Fe,sp}}{C_{Fe,mag}}\right)h_{sp} \qquad (5.8).$$

Determination of mass balance between outer oxide and inner oxide confirms hypothesis of that the outer oxide grew by outward diffusion of Fe and inner oxide grew by inward diffusion of oxygen. Concentration of Cr in the inner oxide is correlated to the ratio of outer to inner oxide thicknesses. The determination also confirms that the original alloy surface locates at the interface of inner – outer oxide.

5.1.4. Determination of Rate Limiting Process from Diffusion Coefficients

In addition to the activation energy, determination of diffusing rates of Fe and O in oxide layers will provide a clue for which ion specie is the rate limiting mechanism of oxidation. Since the growth of oxide is controlled by diffusion of ion in the oxide layer,

the ion specie that has lowest diffusion coefficient is the rate limiting mechanism. From the previous section, two species of diffuser play important role in the oxide formation; Fe ions and O ions. Diffusion media are the outer oxide of magnetite and the inner oxide of Fe-Cr spinel. Therefore the determination focused on four diffusion processes; i) Fe and ii) O diffusion in magnetite, and iii) Fe and iv) O diffusion in Fe-Cr spinel oxide. Using the diffusion data of D, D_0 and Q in Table 5.3 and Table 5.4, the diffusion coefficients of Fe and O in oxides at the test temperatures can be evaluated.

As mentioned previously, one of the parameters that affect the diffusion of Fe and O ions in magnetite and Fe-Cr spinel oxide is the oxygen partial pressure. The reason is that the defect structure of the spinel structure oxides including magnetite and Fe-Cr spinel oxide changes as a function of oxygen partial pressure. Vacancy diffusion dominates at high oxygen partial pressure, whereas interstitial diffusion dominates at low oxygen partial pressure. Therefore, the diffusivities as a function of oxygen partial pressure are also considered in addition to the diffusion data in Table 5.3. Before determining the rate limiting mechanism, the diffusivities as a function of oxygen partial pressure were determined and compared with the diffusivities in Table 5.3.

According to the literature, function of diffusion coefficient and oxygen partial pressure were reported for three diffusion systems; i) Fe diffusion in magnetite, ii) O diffusion in magnetite, iii) cations (Co, Cr, Fe and Mn) diffusion in Fe-Cr spinel oxide. There is no report for O diffusion in spinel oxide as a function of oxygen partial pressure. Note that these diffusivities are determined for single crystal or lattice diffusion. Diffusivity of iron in magnetite was proposed by Dieckmann and Schmalzried in 1975

[22]. The oxygen partial pressure dependence of tracer diffusion coefficient of Fe in Fe_3O_4 at 900-1400°C can be expressed as [8];

$$D_{Fe,Fe_3O_4} = 4\times10^{-11}\exp\left(\frac{1.45(eV)}{k_BT}\right)P_{O_2}^{2/3} + 8\times10^{7}\exp\left(-\frac{6.37(eV)}{k_BT}\right)P_{O_2}^{-2/3} \qquad (5.9)$$

where, D_{Fe,Fe_3O_4} is the diffusivity of Fe in Fe_3O_4 (cm^2/s), k_B is the Boltzmann constant (8.617 x 10^{-5} eV/K), P_{O_2} is the oxygen partial pressure (atm) and T is temperature (K). Note that the equation included the temperature-dependence of the diffusivity. Although the temperature range for this equation limits at 900-1400°C, Atkinson [8] and Maruyama [23] verified that it can be applied at lower temperatures of 500 and 550°C, respectively. Maruyama et al. [23] reported the diffusivity of Fe in magnetite at 550°C in a different term;

$$D_{Fe,Fe_3O_4} = aP_{O_2}^{-2/3} + \frac{bP_{O_2}^{2/3}}{1+2K_VP_{O_2}^{2/3}} \qquad (5.10),$$

where, D_{Fe,Fe_3O_4} is in m^2/s, a = 8.0 x 10^{-36} m^2/s and b = 2.9 x 10^{-6} m^2/s are parameters depending on temperature, and K_V = 4.4 x 10^7 is a dimensionless constant correlating with the contribution Fe ions through a vacancy mode. Plots of Fe diffusivity at 400, 500 and 600°C are shown in Figure 5.5. Trend of the diffusivity can be observed as a V-shape, where the lowest value of diffusivity indicates equilibrium of vacancy and interstitial defects. The diffusion on left-hand side (low oxygen partial pressure) of V-shape is controlled by interstitial mechanism, while the right-hand side is controlled by vacancy mechanism.

Likewise, diffusion coefficient of O in Fe_3O_4 can be expressed as a function of oxygen partial pressure [23, 24]. Maruyama extrapolated the function to 550°C;

$$D_{O,Fe_3O_4} = cP_{O_2}^{-1/2} + FP_{O_2}^{1/6} \qquad (5.11)$$

where, D_{O,Fe_3O_4} is in m^2/s, c = 1.3 x 10^{-34} m^2/s and F = 5.1 x 10^{-22} m^2/s are parameters depending on temperature. Plot of O diffusivity in Fe_3O_4 at 550°C is shown in Figure 5.6. Note that the diffusion coefficient of O in Fe_3O_4 is lower than those of Fe diffusions in Fe_3O_4 and Fe-Cr spinel oxide. At 550°C and P_{O_2} ~10^{-25} atm (at lowest value of D), D_{Fe,Fe_3O_4} and $D_{Fe,sp}$ are in order of 10^{-15} cm^2/s comparing to D_{O,Fe_3O_4} ~ 10^{-21} cm^2/s. This is due to the fact that concentration of anion defect is lower than that of cation defect.

The diffusion coefficients of cations in Fe-Cr spinel were determined at 1200°C by Töpfer et al. [9]. The authors reported cation tracer diffusion coefficients of Fe, Cr, Co and Mn of five different Fe:Cr ratios of Fe-Cr spinel oxide with slightly deviation from stoichiometry (δ), $(Fe_{1-x}Cr_x)_{3-\delta}O_4$, where x varied from 0, 0.1, 0.2, 0.33 to 0.4, and δ ~ 10^{-4}. The diffusivities of vacancy and interstitial defects were also reported in this work. However, the author did not show the equation of diffusivity. The data was extracted from figures in the article using Datathief software© [25]. Averaged diffusivities of each chemical composition from oxygen partial pressure ~10^{-9} – 10^{-3} atm are reported in Table 5.4.

The diffusion coefficients in Fe-Cr spinel oxide were calculated following the procedure of Martinelli et al. [15]. Assuming the same temperature and oxygen partial pressure dependence of Fe diffusion in magnetite (by Dieckmann and Schmalzried [22]) and in Fe-Cr spinel, the Fe diffusivities in Fe-Cr spinel oxide can be calculated using the diffusivities of vacancy and interstitial reported by Töpfer et al. [9]. The Fe diffusion coefficient in Fe-Cr spinel (in cm^2/sec) can be calculated from;

$$D_{Fe,sp} = \left(\frac{D_{Fe,sp}^{Töpfer}}{D_{Fe,Fe_3O_4}^{Töpfer}}(V) \right) \frac{D_V K_V P_{O_2}^{2/3}}{12\left(1 + 2K_V P_{O_2}^{2/3}\right)} + \left(\frac{D_{Fe,sp}^{Töpfer}}{D_{Fe,Fe_3O_4}^{Töpfer}}(I) \right) \frac{4}{3} D_I K_I P_{O_2}^{-2/3} \qquad (5.12)$$

where, D_V and D_I are the partial cation diffusion coefficients of the cation diffusion via vacancies (V) and interstitials (I) in Fe_3O_4. K_V and K_I are the reaction constants leading to the formation of a vacancy and an interstitial. $\frac{D_{Fe,sp}^{Töpfer}}{D_{Fe,Fe_3O_4}^{Töpfer}}(V)$ and $\frac{D_{Fe,sp}^{Töpfer}}{D_{Fe,Fe_3O_4}^{Töpfer}}(I)$ are the ratios of D_V and D_I of Fe-Cr spinel oxide to that of Fe_3O_4 from Töpfer et al. [9]. (*sp* denoted Fe-Cr spinel oxide) The equations of D_V, D_I, K_V and K_I and calculated values at 400, 500 and 600°C are listed in Table 5.7.

Fe diffusivity was calculated for the Fe-Cr spinel oxide with composition of Fe_2CrO_4, $Fe_{1.8}Cr_{1.2}O_4$ as they are close to the composition of the inner oxide. The D_v ratio of Fe_2CrO_4 is 0.468, and 1.349 for $Fe_{1.8}Cr_{1.2}O_4$. The D_I ratio of Fe_2CrO_4 is 0.028, and 0.022 for $Fe_{1.8}Cr_{1.2}O_4$. Plots of diffusion coefficients of Fe in Fe_3O_4, Fe_2CrO_4, $Fe_{1.8}Cr_{1.2}O_4$ as a function of oxygen partial pressure at 400, 500 and 600°C are shown in Figure 5.7. The plot shows that diffusion coefficients Fe_2CrO_4, $Fe_{1.8}Cr_{1.2}O_4$ are lower than that of Fe_3O_4 by approximately 1-2 orders of magnitude.

It should be noted that the plots of diffusion coefficient of Fe in magnetite from equations **5.9, 5.10 and 5.12** (used ratios of D_V and D_I = 1 for Fe_3O_4) are in good agreement although the equations are in different forms. In addition to these equations that were determined for diffusion in single crystal of magnetite or Fe-Cr spinel oxide, recent works by Ueda et al. [26] determined the effective diffusion coefficients of Fe and O in magnetite on polycrystalline sample. They found that the oxygen potential dependence of cation diffusivity is similar in both grain boundary and lattice of magnetite. The effective diffusion coefficients exhibited the V-shaped behavior similar to

that of lattice diffusion reported by Dieckman et al. [Dieckman]. The effective diffusion coefficient of Fe was one order, and O was four orders of magnitude higher than that of lattice diffusion. As a result of this finding, the effective diffusion coefficient in Fe-Cr spinel oxide is believed to obey the similar oxygen dependence behavior.

It is difficult to compare the diffusivities calculated from eqn. **5.9 – 5.12**, and the data in Table 5.3 because of data depends on the oxygen partial pressure. However, the lowest value of diffusivity can be determined from the plots where interstitial and vacancy defects are in equilibrium. From plots in Figure 5.5, the lowest diffusivities of Fe in Fe_3O_4 at 400, 500 and 600°C are ~10^{-19}, 10^{-17} and 10^{-15} cm^2/s, respectively. These values are in good agreement with the diffusivities determined from data in Table 5.3. Similar to the oxygen diffusivity from eqn. **5.11**, the values are in good agreement with the data obtained from single crystal in Table 5.3. Therefore, the determination of rate controlling mechanisms was conducted using the data from Table 5.3. The diffusivity as a function of oxygen potential will be used for determination of the oxygen partial pressure in next section.

From the previous section, it was determined that the short circuit diffusion of either cation or anion is the rate controlling mechanism. Besides that, the nature of oxide structure consisted of multiple grains. Therefore only diffusion data of ions in poly-crystalline samples was determined. The diffusivities of Fe and O in magnetite are evaluated for the outer oxide, and the diffusivities in Fe-Cr spinel oxide with ratio of Fe:Cr ~ 2:1 are determined. Due to limited data of Fe and O diffusion in the spinel oxide , the diffusivity of O in $FeCr_2O_4$ [13] is used because it has a closest composition.

Diffusivity data of Fe in spinel oxide (Fe_2CrO_4) is available only at 1200°C [9], and was extrapolated to 400-600°C with the diffusivities determined from eqn. **5.12**.

Diffusivities of Fe and O in polycrystal of magnetite and spinel oxide at 400-600°C were calculated using equation $D = D_0 e^{-\frac{Q}{RT}}$ and diffusion data (D_0 and Q) from Table 5.3. Comparison of diffusivities of O and Fe in magnetite and Fe-Cr spinel oxide is shown in Figure 5.8. It is found that the diffusivity of O in polycrystalline magnetite at 400 – 600°C is higher than that of Fe. The oxygen diffusion in Fe-Cr spinel oxide is slower than that in magnetite, but still higher than that for Fe. The diffusion of Fe in Fe-Cr spinel oxide tends to be lower than the Fe diffusion in magnetite. Comparison in Figure 5.7 shows that the diffusivity of Fe decreases as the Cr content in Fe-Cr spinel oxide increases. The diffusivities of Fe in magnetite and Fe-Cr spinel are slower than that of O. Finally, it can be estimated that the Fe diffusion in Fe-Cr spinel oxide is the slowest process. Therefore, this fact implies that Fe diffusion is the rate limiting mechanism in the oxidation of the alloy.

Results of the oxidation rate support the conclusion of the rate limiting mechanism. Under the same environment, the oxidation rate is directly dependent with Cr concentration in alloy. Composition analysis results showed that Cr concentration in the inner oxide is relatively close to that of alloy substrate, and Cr fraction in Fe-Cr spinel oxide increases following the Cr content in alloy. Work of Töpfer et al. [9] indicates that the diffusivities of Fe in Fe-Cr spinel oxide decreases as Cr content increases. The effect of Cr concentration is more pronounced at a higher temperature.

In addition to magnetite in the outer oxide and Fe-Cr spinel (with Fe:Cr ~ 2:1) in the inner oxide, characterization results showed that $FeCr_2O_4$ and Cr_2O_3 formed at lath

boundaries in transition layer, and at the oxide – alloy interface at 600°C. Presence of these oxides may change the rate limiting mechanism since the diffusivities of Fe and O are very low in these oxides, Table 5.3 and Table 5.4. However, the results showed that these oxides are discontinuous and formed very small fraction comparing to the outer and inner oxides. Therefore, the rate limiting mechanism remains unchanged in the current result.

Diffusion distances of Fe and O in oxides were evaluated using diffusion data (in polycrystalline) from Table 5.3 - Table 5.4 and compared to the oxide layer thicknesses after exposure for 182 hours. The diffusion distances were calculated by;

$$s = \sqrt{4Dt} \qquad (5.13),$$

where s is the diffusing distance (cm), D is the diffusion coefficient (cm^2/s) and t is the time (s). The evaluation was separated into two oxide layers. The diffusion distance in the outer oxide calculated from diffusivities of Fe and O in polycrystalline magnetite. In the inner oxide, the diffusion distance was calculated from O diffusion in polycrystal of $FeCr_2O_4$ and Fe in polycrystal of Fe_2CrO_4. Figure 5.9 and Figure 5.10 display the diffusion distances compared with thickness of the outer and inner oxides. The plots show that all of diffusion distances of ions are smaller than the oxide thickness, but the diffusion of O via grain boundaries is closet. This fact implies that the short-circuit diffusion plays an important role on the effective diffusivity of ions in these oxide scales.

Conclusively, interpretation of the oxidation rate reveals important information of the oxidation mechanism. First, the power relation of the oxidation rate shows that the oxidation occurred by diffusion controlled mechanism. Deviation from parabolic law indicates that the diffusion occurred through defects in oxides. This agrees with the result

of activation energy determined from the temperature dependence of the oxidation rate. The activation energy that is lower than that of lattice diffusion suggests the occurrence of short circuit diffusion along grain boundaries and defects in the oxide. Determination of original alloy substrate and mass balance equation confirm that diffusion of two ion species, Fe and O, play an important role in oxidation mechanism. The outer oxide grew by outward diffusion of Fe and the inner oxide grew by inward diffusion of oxygen. Determination of the diffusion coefficients indicates that Fe diffusion is the rate limiting mechanism in the alloy.

5.2 Formation of Oxide Structure

Characterization showed that oxide microstructure consisted of three major layers, an outer layer of magnetite, an inner layer of Fe-Cr spinel oxide and a transition layer of grain boundary oxidation. The oxidation rate determined from scale thickness indicated that the outer layer and the inner layer oxides grew simultaneously. This result implies that the formation of these two layers is correlated. The assumption is that the outer oxide grew by outward diffusion of Fe ions, and the inner oxide grew by inward diffusion of O ions. In this section, the formation of the duplex oxide structure will be discussed. The first topic is the determination of oxygen partial pressure at the alloy-oxide-water interface will be determined. Next, the formation of the outer and inner oxides will be discussed in terms of transport processes and thermodynamic stability of the oxide phase.

5.2.1. Determination of Oxygen Partial Pressure at Inner oxide-Outer oxide-Alloy Interfaces

In this study, most of experiments were conducted under the deaerated condition, which was produced by purging Ar gas into water. The dissolved oxygen was controlled below 10 ppb. Therefore, the maximum oxygen partial pressure from the dissolved oxygen in water can be determined using Henry's law;

$$P_{O_2} = k_H^{px} C_{O_2} \qquad (5.14),$$

where, P_{O_2} is the oxygen partial pressure in solution (atm), k_H^{px} is the Henry's law constant (atm/mole) and C_{O_2} is the concentration of oxygen in water (mole). Both k_H^{px} and C_{O_2} change as a function of temperature.

However, there are several concerns about solubility of oxygen in the SCW state. As mentioned in background section, the solubility of low polarity compound (such as O_2 and N_2) increases when the water phase transforms from liquid to SCW. In opposite, the solubility of high polarity compound (such as salts or metallic ions) is diminished in the SCW. These are affected from the changes in density, viscosity and hydrogen bonding of SCW. Oxygen is considered completely miscible in the SCW [27]. Therefore, the Henry's constant used for the solubility of oxygen in SCW should be different from that of water or steam phases. Macdonald et al. determined the Henry's law constants for hydrogen in SCW [28]. They reported that the values decrease exponentially as a function of temperature. Henry's constant of oxygen is expected to follow a similar trend as that of hydrogen.

The oxygen partial pressure from dissolved oxygen was evaluated using Henry's constants from both steam and SCW for a comparison. The data for SCW was estimated using the exponential relation as a function of temperature similar to that of hydrogen from Macdonald's work [28]. The Henry's constant of oxygen (O_2) in steam at temperature 25, 400, 500 and 600°C are 769.23, 12709.71, 16957.35 and 21178.36 atm/mole, respectively [29]. For SCW, Henry's constant are approximately 295, 12 and 7 atm/mole for 400, 500 and 600°C, respectively. Note that the reduction of Henry's constants indicates increase of solubility at high temperature.

For deaerated water, dissolved oxygen was controlled below 10 ppb. Water concentrations are 3.12×10^{-7}, 4.68×10^{-8}, 2.50×10^{-8} and 2.34×10^{-8} mol/L at 25, 400, 500 and 600°C, respectively. Calculated oxygen partial pressures with 10 ppb DO from Henry's constant for steam are 2.40×10^{-4}, 5.95×10^{-4}, 4.24×10^{-4} and 4.96×10^{-4} atm at

25, 400, 500 and 600°C, respectively. Using Henry's constant data for SCW, the oxygen partial pressures are 1.38 x 10^{-5}, 3.07 x 10^{-7} and 1.80 x 10^{-7} atm for 400, 500 and 600°C, respectively. The oxygen partial pressures at 500°C for 100 ppb DO are 4.24 x 10^{-3} atm (used steam data) and 3.07 x 10^{-6} atm (used SCW data). The values for 300 ppb DO are 1.27 x 10^{-2} atm (used steam data) and 9.21 x 10^{-6} atm (used SCW data).

The estimated oxygen partial pressure using Henry's constant of SCW is lower than that of steam. The values also are still quite high compare to a dissociation P_{O_2} of surface oxide phase (magnetite) observed in this study. It can be assumed that the oxygen was almost totally removed from water under deaerated condition, and oxygen was miscible under SCW. Therefore, the oxygen partial pressure at specimen surface was very low, and was resulted from dissociation of water molecules only. Indirect evaluation of oxygen partial pressure can be done by measurement of oxidation potential, can be determined using the oxidation rate relation.

The oxidation rate constant can be expressed in term of diffusivities of metal and oxygen ions. Most of theories for the oxidation rate were derived based on an assumption of the parabolic rate law. Although the results of oxidation rate equations in this thesis deviate from that of a parabolic law, the parabolic law still provides a better estimation for the oxidation rate than that for linear or logarithmic functions. Therefore, determination of diffusivities in oxide layers is performed following equations derived from the parabolic law.

Wagner's theory of oxidation expresses the parabolic oxidation rate (k_p'' in eqn. (2.5)) in terms of two major driving forces for oxidation; the chemical potential, and the electronic and ionic conductivity. Parabolic oxidation rate constant of magnetite was

derived from Wagner's theory by Garnaud and Rapp [30] using Dieckmann and Schmalzried's [22] diffusion data of Fe in magnetite at 900-1400°C. The theory was confirmed by Atkinson [8] who measured diffusivity of Fe in magnetite at 500°C, and used the diffusivity to calculate the oxidation rate constant (from oxide thickness) compared to experimental data. Results from their works are in good agreement. The parabolic rate constant can be expressed as a function of diffusivities of Fe and oxygen partial pressure as [8];

$$k_p'' = \frac{4}{3}\int_{P_{O_2}^{in}}^{P_{O_2}^{out}} f^{-1} D_{Fe}\, d\ln P_{O_2}\,, \qquad (5.15)$$

where, k_p'' is the parabolic constant from oxide thickness (from eqn (2.5)) in cm^2/sec, $P_{O_2}^{out}$ and $P_{O_2}^{in}$ are the oxygen partial pressure at oxide - environment interface (out) and at oxide – substrate interface (in), f^{-1} is the correlation factor for the diffusion mechanism, $f \approx 0.5$ when transport occurs by vacancies mechanism, and $f \approx 0.4$-1 when transport occurs by interstitial mechanism (for convenient, use $f = 0.5$ for both mechanisms), and D is the diffusion coefficient of Fe in oxide.

As introduced in section 5.1.4, the diffusion coefficient of Fe in spinel structures changes as a function of oxygen partial pressure and temperature. Therefore, the rate constant in equation **5.15** was detemined using the diffusion coefficient from Dieckman and Schmalzried's equation [22]. Equation for Fe diffusion in Fe_3O_4 is [15];

$$D_{Fe,Fe_3O_4} = \frac{D_V K_V P_{O_2}^{2/3}}{12\left(1 + 2K_V P_{O_2}^{2/3}\right)} + \frac{4}{3} D_I K_I P_{O_2}^{-2/3} \qquad (5.16)$$

where, D_V and D_I are the partial cation diffusion coefficients of the cation diffusion via vacancies (V) and interstitials (I) in Fe_3O_4. K_V and K_I are the reaction constants leading

to the formation of a vacancy and an interstitial. Equations of D_V, D_I, K_V and K_I and values at 400, 500 and 600°C are listed in Table 5.7.

The diffusion coefficient of Fe in Fe-Cr spinel oxide is modified from equation **5.16**, and was written as equation **5.12**. Simplification of equations **5.16** and **5.12** yields;

$$D_{Fe,Fe_3O_4} = \frac{AP_{O_2}^{2/3}}{\left(1+2K_V P_{O_2}^{2/3}\right)} + BP_{O_2}^{-2/3} \qquad (5.17)$$

$$D_{Fe,sp} = R_V \frac{AP_{O_2}^{2/3}}{\left(1+2K_V P_{O_2}^{2/3}\right)} + R_I BP_{O_2}^{-2/3} \qquad (5.18)$$

where, $A = \frac{D_V K_V}{12}$, $B = \frac{4}{3} D_I K_I$, $R_V = \frac{D_{Fe,sp}^{Töpfer}}{D_{Fe,Fe_3O_4}^{Töpfer}}(V)$, and $R_I = \frac{D_{Fe,sp}^{Töpfer}}{D_{Fe,Fe_3O_4}^{Töpfer}}(I)$. Parameters A and B are the function of temperature, and R_V and R_I are the function of oxide composition. The inner oxide composition of T91 and 9Cr-ODS alloys is ~$Fe_{2.4}Cr_{0.6}O_4$, and is ~Fe_2CrO_4 for HCM12A and HT-9, Table 4.10. Fortunately, the diffusion data for vacancies and interstitials in these oxide compositions are reported by Töpfer et al. [9]. The R_V of $Fe_{2.4}Cr_{0.6}O_4$ and Fe_2CrO_4 are 0.589 and 0.468, respectively. The R_I ratio of $Fe_{2.4}Cr_{0.6}O_4$ and Fe_2CrO_4 are 0.263 and 0.028, respectively.

In order to determine the oxygen partial pressure from oxidation rate equations of inner and outer oxide, the following assumptions have been made;

- Oxide scales grew under a quasi-steady state and obeyed parabolic law.
- Fe ions diffused through both layers.
- Oxygen activities are constant at the interface of inner – outer oxide.
- Deviation from stoichiometry of oxide considered very small.

In order to determine the oxidation rate equation of the outer oxide, the diffusion of Fe in Fe_3O_4 (eqn. **5.17**) is substituted into **5.15**, and integrated;

for outer oxide,
$$k''_{p,outer} = \frac{4}{3}\int_{P_{O_2}^{inner-outer}}^{P_{O_2}^{outer-water}} f^{-1} D_{Fe,Fe_3O_4}\, d\ln P_{O_2}\ , \qquad (5.19)$$

$$k''_{p,outer} = \frac{4}{3} f^{-1}\int_{P_{O_2}^{inner-outer}}^{P_{O_2}^{outer-water}} \left[\frac{AP_{O_2}^{2/3}}{\left(1+2K_V P_{O_2}^{2/3}\right)} + BP_{O_2}^{-2/3}\right] d\ln P_{O_2}\ ,$$

$$k''_{p,outer} = \frac{4}{3} f^{-1}\left[\frac{3A\ln\left(2K_V P_{O_2}^{2/3}+1\right)}{4K_V} - \frac{3B}{2P_{O_2}^{2/3}}\right]\Bigg|_{P_{O_2}^{inner-outer}}^{P_{O_2}^{outer-water}}\ . \qquad (5.20)$$

Likewise, the oxidation rate of the inner oxide is determined from diffusion coefficient of Fe in Fe-Cr spinel oxide;

for inner oxide,
$$k''_{p,inner} = \frac{4}{3}\int_{P_{O_2}^{trans-inner}}^{P_{O_2}^{inner-outer}} f^{-1} D_{Fe,sp}\, d\ln P_{O_2} \qquad (5.21),$$

$$k''_{p,inner} = \frac{4}{3} f^{-1}\left[\frac{3R_V A\ln\left(2K_V P_{O_2}^{2/3}+1\right)}{4K_V} - \frac{3R_I B}{2P_{O_2}^{2/3}}\right]\Bigg|_{P_{O_2}^{trans-inner}}^{P_{O_2}^{inner-outer}}\ . \qquad (5.22)$$

where, $P_{O_2}^{outer-water}$, $P_{O_2}^{inner-outer}$ and $P_{O_2}^{trans-inner}$ are the oxygen partial pressures at the outer oxide – water interface, the inner – outer oxide interface, and the transition – inner oxide interface, as described in Figure 5.11.

It is important to note that the oxidation rate constants used in equations **5.20** and **5.22** were derived from a parabolic equation of oxidation rate from oxide thickness. The k''_p is defined in equation **2.5**, and was determined from slope of a plot of x^2 and t. k''_p has unit of cm^2/sec. Calculated k''_p from inner and outer oxide thickness is listed in Table 5.8.

The calculation of the oxygen partial pressure was performed separately for the outer and the inner oxides. The oxygen partial pressures at the outer oxide – water interface and at the inner – outer oxide interface are unknown. Oxygen partial pressure at

the transition – inner oxide interface can be determined from the phase boundary partial pressure between Fe_3O_4 + M_3O_4 (oxide phases in the inner oxide) and Fe + M_3O_4 (phases in the transition layer) in the phase diagrams, Figure 5.12 - Figure 5.14. The calculation started from the inner oxide by substituted the partial pressure at transition – inner oxide interface in equation **5.22** then calculated the partial pressure at inner – outer oxide interface. The calculated partial pressure at inner – outer oxide interface was substituted in equation **5.20** of the outer oxide to calculate the partial pressure at outer oxide – water interface. As a result, the oxygen partial pressures at three interfaces of transition – inner oxide – outer oxide – alloy could be determined.

An example of calculation is demonstrated with HCM12A tested at 500°C deaerated SCW.

For the inner oxide, $P_{O_2}^{trans-sp}$ = 10^{-29} atm and k_p'' = 9.92 x 10^{-14} cm^2/s. Parameters used in the calculation (eqn. **5.22**) are;

- R_V = 0.468, R_I = 0.028 (for Fe_2CrO_4),

- at 500°C, k_V = 3.75 x 10^8, A = 4.8 x 10^{-1} cm^2/sec and B = 4.98 x 10^{-33} cm^2/sec.

Calculated $P_{O_2}^{inner-outer}$ is 2.73 x 10^{-19} atm.

For the outer oxide, substituted $P_{O_2}^{inner-outer}$ = 2.73 x 10^{-19} atm and k_p'' = 1.52 x 10^{-13} cm^2/s in eqn. **5.20**. Parameters of k_V, A and B used in the calculation are similar to those of inner oxide. The calculated $P_{O_2}^{iouter-water}$ = 6.27 x 10^{-19} atm.

Likewise, the oxygen partial pressure of T91 and HT-9 can be determined with a similar method. However, the time dependence of oxidation rates from oxide thickness at 400 and 600°C were not determined. In order to evaluate the oxygen partial pressure at

these temperatures, an estimation of k_p'' at these temperatures were calculated from $k_p'' = \frac{h^2}{2t}$ (h is oxide thickness (cm) and t is time (sec)). Table 5.8 reports the calculated oxygen partial pressure of the F-M alloys tested in this study at 400, 500 and 600°C.

The calculation shows that the oxygen partial pressures at three interfaces of each temperature agree with the oxygen partial pressures where magnetite and Fe-Cr spinel oxide are stable. At 400°C, the averaged $P_{O_2}^{trans-sp}$, $P_{O_2}^{inner-outer}$ and $P_{O_2}^{inner-water}$ are ~3.0 x 10^{-35}, 1.7 x 10^{-23} and 5.1 x 10^{-23} atm, respectively. At 500°C, the averaged $P_{O_2}^{trans-sp}$, $P_{O_2}^{inner-outer}$ and $P_{O_2}^{inner-water}$ are ~1.0 x 10^{-29}, 2.3 x 10^{-19} and 6.3 x 10^{-19} atm, respectively. At 600°C, the averaged $P_{O_2}^{trans-sp}$, $P_{O_2}^{inner-outer}$ and $P_{O_2}^{inner-water}$ are ~2.0 x 10^{-25}, 4.5 x 10^{-16} and 1.8 x 10^{-15} atm, respectively.

However, the oxygen partial pressure gradient (difference between $P_{O_2}^{trans-sp}$ and $P_{O_2}^{inner-outer}$) is very high in the inner layer spinel oxide, whereas the $P_{O_2}^{inner-outer}$ and $P_{O_2}^{outer-water}$ are close to each other. Note that this could reflect limitations of the calculation method, or it could imply to defect behavior in the oxide. The assumptions that were made for this calculation could deviate from the real process. The diffusion equations were used by neglecting the short circuit diffusion effect. However, this behavior could imply to the change of dominant diffusion mechanism in the oxide, which represent the location of void formation. The interstitial diffusion dominates at low oxygen partial pressure, whereas the vacancy diffusion dominates at the higher values. The plots of diffusion coefficient of Fe in Figure 5.5 and Figure 5.7 show that the equilibrium points of vacancy and interstitial diffusion (the minimum point of D_{Fe}) occur at oxygen partial

pressure ~ 10^{-30}, 10^{-25} and 10^{-20} atm at 400, 500 and 600°C, respectively. It is found that the range of oxygen partial pressure in the inner oxide covers these defect equilibrium points, indicating both interstitial and vacancy diffusion influence the mechanism in inner oxide. The difference in diffusivities of vacancy and interstitial leads to a large oxygen potential gradient where the dominate mechanism changes from interstitial to vacancy mechanism. The plots of oxygen partial pressure as a function of oxide thickness reported by Martinelli et al. and Maruyama et al. [15, 23] also showed similar trend as our current result, which the oxygen partial pressure rapidly increases from the interstitial-dominated region to the vacancy-dominated region.

Plots of oxygen partial pressure and relative position in total oxide thickness at each temperature are shown in Figure 5.15. The relative position is the position of three interfaces in total oxide thickness. Assuming that the interface of inner – outer oxide is at zero position, the relative thickness of inner oxide has negative sign and positive sign for the outer oxide. Relative position of the transition – inner oxide interface is the inner oxide thickness divided by the total thickness, and the position of the outer oxide – water interface is the outer oxide thickness divided by the total thickness. The oxygen partial pressure where the dominate mechanism changes are drawn as dashed horizontal lines. If the oxygen partial pressure is higher than these lines, the vacancy diffusion mechanism dominates. Alternatively, the interstitial diffusion dominates at the lower oxygen partial pressure.

As described previously, the diffusion in inner oxide was controlled by both interstitial and vacancy mechanisms, whereas the diffusion in the outer oxide was controlled by vacancy mechanism. To determine the position in oxide where the

dominate mechanism changes, the oxygen partial pressures in the oxide were determined for HCM12A at 400, 500 and 600°C, and were added into the plot. (Calculation detail will be presented in Section 5.4.) It is found that the position where the dominate mechanism changes is located near the transition layer – inner oxide interface. More details about mechanism will be discussed in Section 5.4.

5.2.2. Formation of Outer Oxide

Analysis results from XRD, SEM and TEM showed that the outer layer oxide consisted of columnar grains of magnetite with rough exterior. Voids were observed in some magnetite grains. Results from XPS revealed that small amount of Fe_2O_3, FeOOH, $Fe[OH]_2$ and $Fe[OH]_3$ possibly formed on the outermost surface. In order to understand the formation of oxide in the outer layer, two major processes including transport of Fe and oxidation of magnetite need to be determined.

Results from the composition profile (Figure 4.21 – 4.29) shows that the outer oxide formed by outward diffusion of Fe ions from the transition layer – inner oxide interface to the oxide – water interface. The fact that Fe concentration remains in lath matrix in the transition layer, and decreased at the transition – inner oxide interface indicates that Fe started to diffuse outward from this interface. Depletion of Fe content at lath boundaries in the transition layer also showed that the grain boundary is an important diffusion path. Fe concentration reduced in the inner layer, but Cr concentration remained similar to that of the alloy substrate. This evidence reveals that Fe is the only element that diffused outward because the diffusivity of Cr in oxide is much slower than that of Fe (Table 5.4). The Fe ions diffused through Fr-Cr spinel oxide (inner oxide) and magnetite

(outer oxide) to the outer oxide – water interface. Diffusion of Fe in the inner oxide is controlled by both interstitial and vacancy mechanisms, whereas the diffusion in outer oxide is dominated by vacancy mechanism, as described in the previous section. Transport of Fe proceeded through both lattice and short circuit diffusion path. Evidences of the time dependence of oxidation rate that deviated from parabolic law and the activation energy that exhibited relatively low value indicated that the short diffusion has a major influence on the oxidation rate.

Formation of magnetite occurred at the outer oxide – water interface. Reactions governing the magnetite formation can be described as;

$$Fe + \frac{1}{2}O_2 = FeO \tag{5.23}$$

$$3FeO + \frac{1}{2}O_2 = Fe_3O_4 \tag{5.24}$$

$$H_2 + \frac{1}{2}O_2 = H_2O \tag{5.25}$$

Summation of these three equations gives;

$$3Fe + 4H_2O = Fe_3O_4 + 4H_2 \tag{5.26}$$

Phase formation of oxide in SCW can be determined from a predominance diagram of Fe-Cr-O at each temperature, Figure 5.12 - Figure 5.14. These diagrams were constructed with FactSage© software [31] demonstrating the stability of oxide at different oxygen partial pressure and ratio of moles Cr/(Fe-Cr) at 400, 500 and 600°C. For the outer oxide that consisted of Fe and O, possible oxide phases at temperature range of 400-600°C with variation of oxygen partial pressure from high to low are Fe_2O_3, Fe_3O_4, and FeO (at 600°C). The ranges of $P_{O_2}^{inner-outer}$ to $P_{O_2}^{outer-water}$ determined from the previous

section are 1.7 x 10^{-23} – 5.1 x 10^{-23} atm, 2.3 x 10^{-19} – 6.3 x 10^{-19} atm, and 4.5 x 10^{-16} – 1.8 x 10^{-15} atm at 400, 500 and 600°C, respectively. These results matched well with the oxygen partial pressures for the phase region of magnetite in the predominance diagram. From the diagrams in Figure 5.12 - Figure 5.14, the oxygen partial pressures of the magnetite phase region are approximately 3 x 10^{-35} – 5 x 10^{-23} atm, 1 x 10^{-29} – 2 x 10^{-19} atm and 2 x 10^{-25} – 1 x 10^{-15} atm for 400, 500 and 600°C, respectively. The $P_{O_2}^{inner-outer}$ and $P_{O_2}^{outer-water}$ are high enough for magnetite to be stable, but hematite cannot be stable. At 600°C, the oxygen partial pressure in the outer oxide is much higher than the phase region of wustite (~10^{-25} atm) so that only magnetite is stable. The position of oxygen partial pressures & composition of the outer oxide are marked in the phase diagram.

5.2.3. Formation of Inner Oxide

Analysis results showed that the inner layer oxide consisted primarily of small equiaxed grains of Fe-Cr spinel oxide, Figure 4.93. The chemical formula of oxide can be represented as $Fe^{2+}(Fe_{2-x}^{3+}Cr_x^{3+})O_4$, where x is the concentration of Cr in oxide that changes with alloy type. For alloys T91, HCM12A, HT-9 and 9Cr-ODS, x is approximately 0.7, 0.9, 1.0 and 0.7, respectively. The chromite phase ($FeCr_2O_4$) was also observed in some regions of the inner oxide – alloy interface in HT-9 exposed at 600°C, and at former lath boundaries in alloys exposed at 600°C. Crystalline structure of the inner oxide, for all variations of the Cr concentration, was identified by electron diffraction as a spinel structure ($Fd\bar{3}m$). However, the lattice constants (a_o) that could slightly change with the composition cannot be distinguished due to low analysis

resolution of the method. Morphology of the layer is considered very porous with micro-voids and micro-cracks. Precipitates of carbide and minor alloying elements distribute throughout the inner oxide. At 400 and 500°C, the precipitate alignment was observed like PAG and package boundaries. However, the precipitate alignment in specimen tested at 600°C did not outline the boundaries. The hypothesis for the inner oxide is that this layer formed by inward diffusion of O, and also by outward diffusion of Fe. In order to understand the mechanisms in the inner layer, three major phenomena including elemental transport, formation of Fe-Cr spinel oxide, and possible causes of the scale defects of micropores and microcracks will be discussed.

Formation of the inner oxide occurred spontaneously as the outer oxide formed. As Fe ions diffused outward, oxygen diffused inward and reacted with Fe and Cr in the original alloy substrate. The observation that the Cr concentration in the inner oxide approximately equals to the original alloy substrate indicates that Cr is a slow diffuser. The oxygen concentration in the inner oxide equals to that of the outer oxide and gradually decreases in the transition layer to the background level. In the transition layer, oxygen diffused through lath boundaries of alloy forming Cr-rich oxide, and also dissolved in lath matrix forming the fine oxide precipitates in lath matrix. However, the Fe concentration still remains in the lath matrix. It can be seen that the oxygen diffused inward from the oxide – water interface to the transition – alloy interface.

As the Fe diffused outward Cr became enriched in the inner layer. Therefore the oxygen reacted with Fe and Cr forming Fe-Cr spinel oxide. Concentration of Cr in the oxide followed trend of Cr content in the alloy substrate as mentioned previously. Since the interface of outer – inner oxide is the original alloy surface, it could be determined

that the Fe-Cr spinel oxide grew toward the alloy substrate with reaction occurred at the transition layer – inner oxide interface. The oxygen partial pressure at this interface could be determined from the phase boundary between Fe+M_3O_4 and M_3O_4+Fe_3O_4 (M is Fe and Cr) in the predominance diagram, Figure 5.12 - Figure 5.14. At interface of transition layer – inner oxide, the oxygen partial pressures are ~ 3 x 10^{-35}, 1 x 10^{-29} and 2 x 10^{-25} atm for 400, 500 and 600°C, respectively. The $P_{O_2}^{inner-outer}$ determined from the oxidation rate equation are ~ 1.7 x 10^{-23}, 2.3 x 10^{-19} and 4.5 x 10^{-16} atm at 400, 500 and 600°C, respectively. The ranges of $P_{O_2}^{trans-inner}$ to $P_{O_2}^{inner-outer}$ are quite broad, however, they are still in the phase region of M_3O_4+Fe_3O_4. The calculated oxygen partial pressures are in good agreement with the results of oxide phase found in the inner layer oxide.

Formation of the Fe-Cr spinel oxide is quite complicated due to; i) the concentration ratio of Cr in the oxide cannot be represented as an integer, ii) the Cr concentration changed upon alloy type, and iii) the Cr concentration changed upon local chemistry (i.e., in HT-9 exposed at 600°C). Based on standard free energies of reactions from Ellingham diagram (Figure 2.17), typical oxides formed are Cr_2O_3, Fe_3O_4, and FeO (above 570°C). Further reaction of these oxides produces $(Fe,Cr)_3O_4$. Reactions governing to the Fe-Cr spinel oxide formation can be described as;

$$Fe + \frac{1}{2}O_2 = FeO \tag{5.27}$$

$$3FeO + \frac{1}{2}O_2 = Fe_3O_4 \tag{5.28}$$

$$\frac{2}{3}Cr + \frac{1}{2}O_2 = \frac{1}{3}Cr_2O_3 \tag{5.29}$$

$$FeO + Cr_2O_3 = FeCr_2O_4 \tag{5.30}$$

$$FeCr_2O_4 + 4FeO = 2Fe_2CrO_4 + Fe \qquad (5.31)$$

Slightly deviation from stoichiometry of Fe_2CrO_4 or $FeCr_2O_4$ can occur if concentration of Cr in alloy is limited. Within the range of Cr concentration observed in the inner oxide, these phases exhibit spinel structure. Therefore the chemical composition of the oxide can be best described as Cr substitution in magnetite based structure. Since valency state of Cr is usually present as 3+ [11], the composition can be written as $Fe^{2+}(Fe^{3+}_{2-x}Cr^{3+}_{x})O^{2-}_{4}$, where $0 < x < 2$. In the F-M alloys, the Cr concentration in the inner oxide depends on that of alloy substrate, which exhibits $x \sim 1$. Formation of this Fe-Cr spinel oxide could be explained better from the crystallographic point of view. First it is important to understand basic of the spinel structure, which is found in both outer oxide (magnetite) and inner oxide (Fe-Cr spinel oxide).

Spinel structure is in a space group of $Fd\bar{3}m$, #227. Spinel is basically FCC with general composition of AB_2O_4, where A is a divalent (2+) cation and B is a trivalent (3+) cation. Crystallographic model of the spinel structure is shown in Figure 5.16. Divalent ions (A^{2+}) form into a big FCC lattice, and oxygen ions form into FCC close packing. Inside the big FCC structure, there are two types of cubic structure locating in 8 subcells, Figure 5.16 a. First type of subcell has 4 oxygen ions at 4 of lattice points (drum shape) and one A^{2+} locates in a tetrahedral site inside the cubic. Another type has 4 oxygen ions at 4 lattice points (drum shape) and 4 of B^{3+} locate at octahedral sites at the other four corners of the cubic. There are totally 32 oxygen ions, 8 Fe^{2+} ions and 16 Fe^{3+} ions in unit cell. However, there are 32 octahedral and 64 tetrahedral interstices within unit cell available for cations. Therefore only one half of the octahedral and 1/8 of the tetrahedral

sites are filled with cations. Figure 5.16 b illustrates tetrahedral and octahedral sites in unit cell of spinel.

Arrangement of cation in spinel unit cell can be classified into three types; a normal structure, an inverse structure and a random structure. The normal spinel structure has the divalent (A^{2+}) ions occupy 1/8 of tetrahedral sites and trivalent (B^{3+}) ions on one half of the octahedral sites (as shown in Figure 5.16). The inverse structure all of the A^{2+} ions and 1/2 of the B^{3+} ions have changed places in random order, where 4 of B^{3+} atoms will be on the tetrahedral sites, and 4 of A^{2+} and 4 of B^{3+} will be at the octahedral sites. The random arrangement is mixed between the normal and the inverse structures. Temperature also affects cation arrangement by gradually transforms into a normal spinel at temperature higher than ~1000°C [32].

In magnetite, A ions are Fe^{2+} and B ions are Fe^{3+}, and exhibits an inverse spinel structure. In Fe-Cr spinel oxide, a Cr^{3+} ion with ionic radius of 61 pm can substitute a Fe^{3+} ion with similar ionic radius of 65 pm in octahedral site. If amount of Cr^{3+} ions increases, they can substitute Fe^{2+} (78 pm) in octahedral sites and Fe^{3+} in tetrahedral sites (49 pm) [33]. Additional of Cr^{3+} in the structure influence the arrangement of cations resulting in the decrease of degree of inversion. Gillot et al. [34] stated that additional of Cr in a range of 0 – 0.4, 0.4 – 1.4 and 1.4 – 2, the structure transforms from totally inverse spinel, partially inverse spinel to normal spinel, respectively. The transformation resulted in physical and chemical properties of the oxide. Lattice parameter (a_0) decreases with increasing Cr content (for $x = 0$, $a_0 = 8.397$ Å, a_0 decreases to 8.386 Å for $x = 0.8$), but also slightly increases at $x \sim 1.2$-1.5 ($a_0 = 8.405$ Å) [34]. The changes in lattice parameter depend on the sites that Cr^{3+} ions are substituting. Grain size of the particle

also tends to decrease with increasing Cr content. Most important, the diffusion coefficient of cation diminishes due to two major reasons; substitution of Cr^{3+} ions onto Fe^{3+} octahedral sites, and crystalline size. The diffusion coefficients of Fe in Fe-Cr spinel with variation of Cr content were reported by Töpfer et al. [9], Table 5.4.

Porosity in inner oxide

Porosity of the inner oxide is another phenomenon that required attention because it can affect the diffusion mechanism of anions and cations through the scale. Moreover, porosity can limit adhesion of scale and alloy substrate resulting in spallation of the scales. Results from microstructure characterization shows that there are defects existing in the inner oxide including nano- and micro-size pores and microcracks. These pores have size ranging from around <100 nm to 500 nm. The pores were observed throughout the inner layer. However, the pore density is very high at interface of transition layer – inner oxide, Figure 5.17, whereas the pores at other locations are smaller in size and density. The assumption is that the micropores occurred from coalescence of Fe vacancies that are created by outward diffusion of Fe ions. In other word, the cation vacancies were injected inward when Fe diffused outward. If high amount of the vacancies is produced, they can coalesce into a pore. Microcracks were observed between Fe-Cr spinel oxide grains and between transition layer and outer oxide as longitudinal lines. The assumption of microcracks formation is the growth stress developed during the scales growth, and thermal expansion mismatch during cooling process.

From the mass balance equation involved the thickness of consumed alloy, **eqn. 5.17**. The result of calculation shown in Table 5.6 indicates that the thickness of

consumed alloy from calculation is always higher than the thickness of inner oxide + transition layer from measurement. It is possible that the inner oxide that contains micropores supplied higher amount of Fe ions for magnetite formation more than dense spinel oxide. Quantity of micropores in the inner oxide can be evaluated using a Pilling-Bedworth ratio (PBR). The ratio determines volume of oxide per volume of metal that transforms into oxide (M_mO_n);

$$PBR = volume\ of\ oxide\ /\ volume\ of\ m\ moles\ of\ M \qquad (5.32)$$

The PBR has a few restrictions, for example, the oxide should form by inward diffusion of oxygen, and the texture and direction of scale growth are neglected [35]. Thus the method can be applied well for the inner oxide. The PBR of spinel grows on Fe-Cr alloy is 2.1, and the value is similar to that of magnetite grows on Fe-Cr alloy [36].

The inner oxide grew by inward diffusion of oxygen forming Fe-Cr spinel oxide. The outer oxide grew by outward diffusion of Fe ions from the inner oxide. Therefore, volume of inner oxide contains volume of alloy that transformed to oxide plus volume of pores (or vacancies) that were created by outward diffusion of Fe;

$$V_{sp} = V_{alloy,sp} + V_{pore} \qquad (5.33)$$

where, V_{sp} is the volume of inner oxide, $V_{alloy,sp}$ is the volume of alloy that transformed into the spinel oxide and V_{pore} is the volume of pores. Since the PBR of spinel/Fe-Cr = 2.1, then $V_{sp}/V_{alloy,sp}$ = 2.1. Substitutes $V_{alloy,sp} = V_{sp}$ /2.1 into **eqn. 5.33**. The volume of pore is;

$$V_{sp} = 1.9V_{pore} \qquad (5.34)$$

This gives the volume of pore ~34% of the volume of inner oxide. However, this number is the maximum porosity that was created. Not all of these pores are stable. Two

mechanisms can occur to maintain scale and alloy adhesion [14]. First, the vacancies created will inject into alloy substrate (or, outward diffusion of cations), mostly through fast diffusion path such as grain boundaries or dislocations. Second, the cations diffuse from the substrate can fill these pores by interacting with oxygen ions forming oxide inside the pores. When these pores filled up, new pores develop near the transition – inner oxide interface due to outward diffusion of the cations. Therefore, it is difficult to evaluate the porosity of the inner layer at particular time. In addition, note that this mechanism allows the inner oxide to grow inward. The hypothesis involved the growth of inner oxide through the nano-pores (or, nano-cavities), created by outward diffusion of cations, was proposed by Roberson and Manning [37-40] called "available space model".

Microcracks in the inner oxide perhaps occurred from two major reasons; first is the growth stress developed during the scales growth, and the thermal expansion mismatch during cooling process. Outer oxide cracking was observed after exposure to 600°C deaerated SCW. The cracking likely resulted from the thermal expansion (α) mismatch of oxide and alloy on cooling. The calculated volume change of magnetite after cooling from 600°C is ~1.28%, which is twice that for the alloy, ~0.69%. (α for magnetite = 20.6 x 10^{-6}/K (293-843 K) and 50.1 x 10^{-6}/K (843-1273 K) [41], and F-M alloy =11.9 x 10^{-6}/K [42]. Since the samples from this test exhibited very thick oxides, the tensile stress generated in oxides, the tensile stress generated in oxide will be high enough to cause the microcracks.

5.2.4. Formation of Transition Layer

Besides outer and inner oxides, the transition layer developed between the inner oxide and alloy substrate of the F-M alloys exposed in SCW. The transition layer is first identified from a composition profile where oxygen concentration decreased from the inner oxide level to background level, and Fe increased from that of the inner oxide level to alloy level. Initially only little is known about microstructure and oxide phases in this layer. Characterization results showed that the transition layer exhibited the alloy structure with selective oxidation at lath boundary and fine oxide grains nucleated inside lath matrix, as shown in the schematic diagram of oxide scales in Figure 4.93. Two major factors affected the microstructure in the transition layer including the test temperature and the alloy type.

At 400 and 500°C, the transition layer consisted of Fe-Cr spinel oxide (with composition close to that of the inner oxide) at the lath boundaries and also fine grains of Fe-Cr spinel oxide inside the lath matrix. At 600°C, the layer is quite thick and the Cr-rich oxide phases of $FeCr_2O_4$ (chromite) and Cr_2O_3 (chromia) was found at the lath boundaries. Both Cr-rich oxides also observed as strips at the alloy – transition layer interface of T91, HCM12A and 9Cr-ODS. Instead, a dense layer of $FeCr_2O_4$ formed at the transition layer – inner oxide interface in HT-9. In addition to the transition layer, porous Cr-rich oxide nodules of $FeCr_2O_4$ formed at the transition layer-alloy interface on alloys T91, HCM12A and 9Cr-ODS tested at 600°C. It was found that dissolved oxygen in SCW also influences formation of the transition layer. Samples exposed in SCW containing 300 ppb DO at 500°C exhibit large transition layer compared to those of deaerated water.

The results of oxide phase characterization agreed with those reported in literature [43-45]. Characterization results from synchrotron radiation indicated that $FeCr_2O_4$ is a major phase formed in the transition layer of 9Cr-ODS alloy exposed in 600°C SCW. The Cr_2O_3 was observed in some regions, i.e., near the interface of transition layer and inner, and near the interface of transition layer and alloy. Combining with our current results, it can be confirmed that these Cr-rich oxide phases formed at the lath boundaries in the transition zone.

Formation of oxide phase in the transition layer depends on the oxygen potential and local chemistry, which can be described following the diffusion path in Fe-Cr-O phase diagrams (Figure 5.12 - Figure 5.14). It is clear that the major diffusion path in transition layer is the alloy lath boundaries. Fe diffused outward and O diffused inward along the lath boundaries. Inside lath, Fe content gradually decreased and O gradually increased. Diffusion of Cr, which plays an important role in the oxide formation in this layer, cannot be easily explained. At the lath boundaries where Fe diffused outward, Cr became enrich and oxide phases of $FeCr_2O_4$ and Cr_2O_3 are stable. Further, both Cr-rich oxides were also observed at the interfaces of alloy – transition, and transition – inner oxide in the samples exposed at 600°C. Reactions governing the formation of oxides can be described using similar equations as that of the inner oxide. Basically, oxidation started with the most reactive elements, Cr and Fe to form Cr_2O_3 and FeO. Further reaction of Cr_2O_3 and FeO developed $FeCr_2O_4$ and $(Fe,Cr)_3O_4$ to become stable as described previously (eqn. **5.29 – 5.32)**. However, Cr_2O_3 is stable under either one of the following conditions; i) chromium concentration (mole Cr/(Fe+Cr)) greater than ~0.65 at oxygen partial pressure ~10^{-28} to 10^{-12} atm, or ii) low oxygen partial pressure (<10^{-28} atm)

in which it is too low to oxidize Fe so that Cr_2O_3 is the only stable phase. The first reason seems to be practical in our case more than the latter case. Evidence of $FeCr_2O_4$ formed together with Cr_2O_3 indicates that oxygen partial pressure is high enough to oxidize Fe. Therefore the second hypothesis could be ruled out.

Development of chromia and chromite at the lath boundaries is desirable because these oxides can reduce diffusions of both Fe and oxygen ions, which could affect the oxidation rate. However, the mechanism of grain boundary Cr-rich oxide formation in 600°C samples is still unclear. First question involves the source of Cr that supplied enough Cr content to form Cr_2O_3 and $FeCr_2O_4$. Second question involves the alloy effect on the oxide type and formation of the transition layer. Third question is the dissolved oxygen effect on formation of the Cr-rich oxides. Based on current results, they may not provide enough information to answer all of these questions, but they can lead to basic understanding of the mechanism in this layer.

First, the source of Cr for formation of Cr_2O_3 and $FeCr_2O_4$ should be determined. Since $FeCr_2O_4$ transformed by reaction of Cr_2O_3 and FeO, the formation of Cr_2O_3 is the key for these two oxides to be stable. In pre-oxidized alloy, there is no segregation of Cr at the lath boundaries (determined in region without precipitates) [46]. Therefore possible sources of Cr could be;

i) Cr diffused from alloy matrix, or

ii) Cr dissociated from chromium carbide precipitates.

Microstructure and composition profile in the transition layer were investigated in order to prove the hypotheses. Composition profiles were measured across two regions; a) at the interface of alloy – transition layer and b) at the lath boundary where Cr-rich

oxide formed. The results show that there is Cr depletion zone at the interface of alloy – transition layer. On HT-9 tested at 600°C, the Cr depletion zone is present in a width of approximately 1.5-2 μm and concentration of Cr dropped from ~11-12 at% to ~3-8 at%, Figure 4.28a. For T91 and HCM12A, the Cr depletion zone was observed only in small region near the interface of alloy – transition layer next to the $FeCr_2O_4$ strip, ~0.2 μm wide and Cr concentration dropped to only 2 at%. Similar result was observed on 9Cr-ODS alloy in which Cr dropped to ~6-7 at% at the interface of alloy – transition layer. Inside lath matrix in the transition layer, Cr concentration decreased to ~3-5 at% for T91, HCM12A and 9Cr-ODS, Figure 4.91. These results imply that the major source of Cr for Cr-rich oxide formation is the lath matrix.

Microstructure investigation of carbide precipitates does not show significant carbide free zone. Figure 5.18 a and b show cross section images of etched T91 and HCM12A tested in 600°C deaerated SCW for 191 hours. The images show carbide precipitates outline PAG boundaries in alloy and in some regions of inner layer. This result is contradict to a work of J. Jang, et al. [3] who reported the carbide free zone in the alloy region near interface of alloy – transition layer on T91 tested in 627°C SCW without deaeration for 200 hours. The major difference could be accounted for the DO concentration in SCW in which our experiment was conducted in deaerated condition but theirs was conducted in non-deaerated condition. (Effect of DO will be discussed later in this section.) Despite of carbide free zone in the alloy, the carbides in transition layer and inner layer of 600°C sample were not observed clearly as that of 400 and 500°C samples, Figure 5.18 c and d. Evidence of big carbides at PAG boundary indicates that they were

not dissociated. However, the absences of carbides in some regions on the inner oxide and small carbides inside the PAG were also observed.

From above results, it can be concluded that Cr diffused from the lath matrix to lath boundaries to form Cr-rich oxides in the transition zone. In order to prove that the Cr-rich oxide can develop by diffusion of Cr from alloy matrix, determination of oxygen partial pressure is conducted. Evaluation of oxygen partial pressure for the formation of Cr_2O_3 in the alloy phase can be performed by equation [14];

$$P_{O_2} > \left(\frac{a_{BO_\upsilon}}{a_B} \right)^{2/\upsilon} \exp\left(\frac{2\Delta G^0(BO_\upsilon)}{\upsilon RT} \right) \qquad (5.35)$$

where, BO_υ is the oxide, υ is the ratio of moles of oxygen per metal, a_{BO_υ} is the activity of oxide (if the oxide is formed as pure BO_υ, a_{BO_υ}=1), a_B is the activity of element B in alloy, and $\Delta G^0(BO_\upsilon)$ is the standard Gibbs free energy of formation of oxide at temperature T (K) as listed in **Table 2.4**. Using activity of Cr in Fe-9Cr-1Mo calculated by A. Saltelli et al. [47], a_{Cr} = 5.86 at 600°C. The oxygen partial pressure required for Cr_2O_3 formation in F-M alloys at 600°C is ~2.09 x 10^{-29} atm, which agrees with the value from phase diagram, Figure 5.14.

Microstructure effect

Microstructure of alloy also affected oxidation mechanism and oxidation rate. The effect of microstructure can be observed clearly in the transition layer. Microstructure parameters that affect the oxidation consisted of alloy grain size, grain alignment and precipitates. First parameter is the alloy grain size, which includes PAG, packet and lath size. Characterization results of the transition layer showed that Cr-rich oxide formed at all grain boundaries including smallest structure of alloy, which is the lath boundary. This

result implies that the lath size has the most influence on oxidation mechanism. In this study, the lath sizes of four F-M alloys are similar, ~ 0.2-0.5 μm wide and 2-5 μm long. Therefore the effect of lath size could not be observed in this study.

However, current results showed that the lath boundaries of alloy acted like short circuit diffusion path for inward diffusion of O ions and outward diffusion of Fe ions. At the same time, Cr became enrich at the lath boundaries and form Cr-rich oxides. These mechanisms possibly lead to opposite effects on the oxidation rate. For an alloy that has small lath size, the inward diffusion of O and the outward diffusion of Fe can increase the oxidation rate because it contains large area of short circuit diffusion. On the other hand, Cr diffusion to the lath boundaries will form Cr-rich protective oxide that can reduce the oxidation rate. These competitive mechanisms lead to the conclusion that effect of small lath size by itself can increase the oxidation rate. However, if the alloy contains Cr concentration high enough to form Cr-rich oxide, the small lath size could have positive effect on oxidation resistance.

Other two parameters are grain alignment and precipitates. Grain alignment also has an influence on the oxidation. Results of microstructure of transition layer showed that laths that align perpendicular to specimen surface tend to have more oxide formed at their boundaries than laths that align in other direction, Figure 4.73 and 4.80. Precipitate particles do not have direct effect on the oxidation. However, dislocation around the precipitate allowed short circuit diffusion paths for inward diffusion of O ions and outward diffusion of Fe ions. Microstructure results showed that the oxide grains usually observed along with precipitates.

In summary, the effects of microstructure cannot be seen by comparison among four different alloys in the current study. The main reason is that they exhibit similar lath size, precipitate and random grain alignment. However, evidences of lath boundary oxides in the transition layer revealed that the microstructure also plan an important role on the oxidation mechanism.

Role of Cr on oxidation

Cr concentration plays an important role on oxidation resistance of the F-M alloys. The main reason is that Cr can substitute metal elements (i.e., Fe, Ni or Mn) in the oxide structure, or form into Cr_2O_3. These oxides are considered as protective oxide that can reduce the diffusion rate of cations and anions. Formation of these oxides depends on alloy composition and exposure conditions, i.e., oxygen potential and temperature.

For the exposure conditions in this study, Cr exhibited in two regions, the inner oxide and the transition layer. The inner layer oxide is $Fe_{2-x}Cr_xO_4$ ($x \approx 0.7 - 1.0$). Cr concentration of Fe-Cr spinel oxide in this layer is dependent on Cr in alloy substrate. Addition of Cr in Fe-Cr spinel oxide can decrease diffusion rate of O and Fe in the oxide. Diffusion data in Table 5.4 shows that diffusion coefficient of Fe in $Fe_{2-x}Cr_xO_4$, decreases when Cr concentration increases from $x = 0.3 - 1.2$. Since the inner oxide formed into thick layer, the effect of Cr is more pronounce in this layer (regardless of microstructure). Thus this fact indicated that the increase of alloy Cr content will lead to an increase of Cr content in the Fe-Cr spinel oxide of the inner layer, and lead to the reduction of the diffusion rate of Fe and O ions in this layer. As a result, the oxidation rate will decrease.

In the transition layer, Cr formed Cr-rich protective oxides of $FeCr_2O_4$ and Cr_2O_3 at lath boundaries. $FeCr_2O_4$ can reduce diffusion rate of O and Fe more than the inner

oxide because of its higher Cr concentration. Additional phase of Cr_2O_3 is desirable because it can diminish the diffusion rate of ions through the oxide. The alloy with high Cr content tends to form Cr_2O_3 more than the lower Cr alloy. For example, the major oxide phase in the transition layer of HCM12A is Cr_2O_3, whereas the major oxide phase in T91 is $FeCr_2O_4$. If these oxide form at the lath boundaries, it can reduce the outward diffusion of Fe ions and inward diffusion of O ions to that lath. However, if these oxides formed into continuous layer, it will have more effect on the oxidation rate. For example, continuous layer of $FeCr_2O_4$ in HT-9 exposed at 600°C results in lowest oxidation rate among four F-M alloys. In conclusion, Cr has strong influence on the oxidation resistance of alloy by forming Cr-rich protective oxide. Thus it is an important alloying element in the F-M alloys.

Alloy effect

Next discussion involves the alloy effect on the transition layer formation. From the results, it is found that the transition layer on T91, HCM12A and HT-9 exhibited similar microstructure at 400 and 500°C. Difference in the transition layer microstructure can be observed at 600°C test. T91, HCM12A and 9Cr-ODS alloys exhibited thick transition layer. In HT-9 case, Cr diffused from the alloy matrix to the interface of alloy – inner oxide to form $FeCr_2O_4$ band. The difference between these alloys could be attributed to Cr concentration in alloy. Cr was added into Fe-based alloy in order to form protective oxide layer. Minimum amount of Cr in the Fe-Cr alloy that can form external scale of Cr_2O_3 is ~20% at temperature above 600ºC of steam oxidation [48]. However, alloys with low Cr content tend to form Cr-rich scale at grain boundary or in the inner oxide instead. Among four F-M alloys in this experiment, HT-9 contain the highest Cr

(11.63 wt% and 12.34 at%) so that it has potential to form continuous layer of $FeCr_2O_4$ at the interface of alloy and inner oxide. For other three alloys, the preferential site for Cr-rich oxide formation is at the lath boundaries. Understanding of critical Cr concentration for the continuous Cr-rich oxide formation should be considered in the future works.

Alloy 9Cr-ODS exhibited thickest transition layer among four tested F-M alloys tested at 600°C. The result is coincidence with relative low weight gain of this alloy comparing to T91 that has the similar Cr concentration. The reason for this alloy to form large transition layer could be attributed to effect of minor alloying elements, i.e., Y_2O_3, W or Ti, in 9Cr-ODS. From literature data, there are two major assumptions. First is the dispersion of Y_2O_3 may have contributed to scale formation by promoting a fine grain size in the matrix that increased the diffusion of Cr to the scale-metal interface or to the lath boundaries [49]. Second, the fine particles of Y_2O_3 could trap vacancies to suppress Fe diffusion [50]. The real mechanism is still under consideration. However, analysis results from our current study showed that nano-particles of Y_2O_3 distributed throughout the alloy matrix and nearby the Cr-rich oxide strip. Ti and W were observed as bigger particles than that of Y_2O_3. The precipitates of Ti-rich are ~10-50 nm diameters, which distributed in the transition and the inner oxide and did not associate with the Cr-rich oxide. The W-rich particles also have large size of ~ 50 – 500 nm distributed throughout the transition and inner layers. Therefore, the results support hypothesis of that the nano-particles that distributed in the alloy matrix may affect the diffusion of either Fe or Cr, or both of them. Suppression of Fe diffusion could result in Fe remained in lath matrix. Diffusion of Cr to lath boundaries may be increased, and promoted Cr enrichment at the lath boundaries forming the Cr-rich oxides. As a result, the 9Cr-ODS alloy formed large

transition layer and relatively thin inner oxide. Further study of effects of nano-particles of Y_2O_3 needed to be investigated.

Formation of Cr-rich oxides of the transition layer has a positive effect to the oxidation resistance. Compared to T91, the 9Cr-ODS alloy that formed large transition layer exhibited a lower weight gain. Cr-rich oxides in this alloys majorly consisted of Fe, Cr, O and trace of Si. Some literature reported that the Cr-rich oxide also contains other elements such as Y [44], and Si [49]. Due low statistical analysis in current study, further investigation should be done. However, formation of Cr-rich oxides in the transition layer could reduce outward diffusion of Fe and inward diffusion of O resulting in reduction of the oxidation rate.

Dissolved oxygen concentration was found to have effects in the increase of transition layer thickness and the reduction of oxidation rate in the 500°C tests. T91, HCM12A and HT-9 exposed in 500°C SCW containing 300 ppb DO exhibited significantly higher T/(O+I) ratio (~0.21) than those of deaerated SCW (~0.13) and 100 ppb DO (~0.14). (T, O and I are the transition layer, outer oxide and inner oxide thickness, respectively.) Weight gain also decreased as DO was increased from deaerated water to 300 ppb, Figure 4.5. The results could be explained using water vapor (H_2O^{18}) and O_2 mixture test on P91 reported by Ehlers et al. [51], Figure 2.26. The authors suggested that the oxygen from DO can penetrate through the inner oxide and promote formation of the transition layer. Formation of Cr-rich oxide decreased the oxidation rate.

5.3 Oxidation Mechanism

The hypotheses of the oxidation mechanism have been proven for each oxide layer in section 5.1-5.3. The oxidation kinetic suggested that diffusion of Fe ions is the rate controlling mechanism, and diffusion of ions along defect structure of oxide plays an important role on the growth of oxide scales. The outer oxide grew by outward diffusion of Fe ions. The inner oxide grew by inward diffusion of oxygen, and outward diffusion of Fe created cation vacancies that can develop into pores. The transition layer grew by grain boundary diffusion of O, Fe and Cr. Oxide phases developed in each layer depend on oxygen partial pressure and element concentration. One last question involves the driving force for these ions to diffuse through oxide scale. This section will discuss about defects formation in oxide, which plays an important role in ions transport through the scales. Finally, the complete picture of oxidation mechanisms will be demonstrated in the last topic.

5.3.1. Defect Formation in Oxide

Composition profiles across oxide layers clearly show that the diffusions of Fe and O are driven with the chemical potential difference between the outer oxide – water interface and the alloy – oxide interface. However, transport of cations through oxide scale occurs via solid state diffusion, which was assisted by defect structure of oxide. This section will describe the formation of cation defect in the oxide structure, which is important to the transport of Fe ions as a rate controlling mechanism.

Reactions governing the formation of magnetite and Fe-Cr spinel oxide are described in section 5.2. However, defects or deviation from stoichiometry of these oxides can be created if oxygen or metal atoms are adding or removing from the oxide structure. As described in **section 2.3.1a**, the oxide can be classified as n-type (anion defects), p-type (cation defects) and amphoteric type (both anion and cation defects). Spinel structure oxide ($Fd\bar{3}m$), the crystal structure of both magnetite and Fe-Cr spinel oxide, exhibits the amphoteric defect behavior. It shows non-stoichiometry under either cation or anion deficit, and the mechanism is dependent on the oxygen partial pressure at the ambient environment [11, 52]. Under high oxygen partial pressure, the defects are created by either deficit of cations or excess of anions (mostly deficit of cations). This leads to the p-type oxide behavior. Transport of cations under this condition is dominated by vacancies diffusion. Meanwhile, the defects of cation excess or anion deficient are created under low oxygen partial pressure leading to the n-type oxide behavior. The transport of cations under this condition is dominated by interstitials diffusion.

Derivation of cation defect equation of spinel structure oxide was explained in works of Dieckman and Töpfer [9, 11], which is included in Appendix D. The deviation from stoichiometry due to the cation defects in the spinel structure oxide $M_{3-\delta}O_4$ (M is metal) as a function of oxygen partial pressure can be written as;

$$\delta = [V]^0 a_{O_2}^{2/3} - [I]^0 a_{O_2}^{-2/3} \qquad (5.36)$$

where, δ is the deviation from stoichiometry due to cation defects. (δ was determined quantitatively from mass changed per initial mass of spinel oxide samples ($Fe_{3-x}Cr_xO_4$, $0<x<1.5$) during exposure in different oxygen activities. δ is unitless and has value in a range of 10^{-5} to 10^{-2} at 1200°C [9].), a_{O_2} is activity of oxygen, $[V]^0$ and $[I]^0$ are the defect

constants denote cation vacancy and interstitial concentrations that are normalized to a_{O_2} = 1. Given $a^0_{O_2} = \frac{P_{O_2}}{P^0_{O_2}}$, where $P^0_{O_2}$=1 bar, the deviation from stoichiometry can be written as a function of oxygen partial pressure;

$$\delta = [V]^0 P_{O_2}^{2/3} - [I]^0 P_{O_2}^{-2/3} \qquad (5.37)$$

Further, tracer diffusion of cation in a spinel oxide depends on partial diffusivities of cation vacancies and interstitials, which also can be expressed as a function of oxygen partial pressure [9, 11];

$$D_M \approx D^0_{M(V)} P_{O_2}^{2/3} - D^0_{M(I)} P_{O_2}^{-2/3} \qquad (5.38)$$

where, $D^0_{M(V)}$ and $D^0_{M(I)}$ are the partial cation tracer diffusion coefficients of *M* ions via vacancies and interstitials, respectively. The diffusivities of Fe and Cr that expressed in this form are shown in eqn. **5.2** – **5.5** and **5.18**. Therefore, corresponding plots of diffusion coefficient of Fe in magnetite and in Fe-Cr spinel oxide as a function of P_{O_2} (Figure 5.5 and Figure 5.7) can demonstrate the oxygen partial pressure range in which vacancy and interstitial diffusion dominates.

Determination of oxygen partial pressure in section 5.2 indicates that the dominate cation defect in oxide structure changes from vacancies dominate in high P_{O_2} (> 10^{-30}, 10^{-25} and 10^{-20} atm at 400, 500 and 600°C, respectively) to interstitials dominate in low P_{O_2}. The changing point is locating somewhere in the inner oxide. This result indicates that the entire outer oxide is a p-type oxide. Most of the inner oxide is a p-type, whereas it changes to an n-type near the transition layer – inner oxide interface.

At the outer oxide – water interface

Magnetite in outer oxide has cation vacancy as a major defect type (p-type oxide). It can be assumed that the outer oxide grew at the interface of outer oxide – water, and the inner oxide grew at the interface of transition layer – inner oxide. The defect reactions of magnetite at the outer oxide – water interface are first formulated using Kroger-Vink notation[1]. When oxygen dissociated from water is incorporated in an oxide lattice in the oxygen positions, an equivalent number of Fe vacancies on the Fe positions must be allocated in order to maintain the ratio of Fe to O lattice sites in the magnetite. Formation of vacancies can be written as;

$$\frac{1}{2}O_2 = O_O + V''_{Fe} + 2h^{\bullet} \qquad (5.39)$$

Vacancies diffused inward to the transition layer – inner oxide interface. The reaction of vacancy and Fe in alloy results in Fe^{2+} and electrons.

$$Fe_{metallic} + V''_{Fe} = Fe_{Fe} + 2e^{-} \qquad (5.40)$$

This equation is equivalent to traditional charge balance equation $Fe_{metallic} = Fe^{2+} + 2e^{-}$. Both Fe_{Fe} and electrons diffuse outward by cation vacancies to the outer oxide – water interface.

In addition, two electron holes formed in equation 5.39 can receive electrons from two of Fe^{2+}, resulting in formation of two of Fe^{3+}.

[1] Kröger-Vink notation describes point defects and regular atoms in a lattice. Major symbol indicate defect type or atom specie. A site that it occupies is denoted by subscript, and its charge is denoted by superscript.

- M_M and O_O are the metal atom on a normal metal lattice site and the oxygen atom on a normal oxygen site in the oxide M_xO_y, respectively.
- V_M and V_O are the vacancies of metal and oxygen in the oxide lattice.
- Subscript "i" denotes an interstitial position of metal (M_i) and oxygen (O_i)
- Superscript of a dot ($^{\bullet}$) is the positive charge and a prime ($'$) is the negative charge.

$$2Fe^{\bullet\bullet} + 2h^{\bullet} = 2Fe^{\bullet\bullet\bullet} + 2e^{-} + 2h^{\bullet} = 2Fe^{\bullet\bullet\bullet} \qquad (5.41)$$

Therefore, the reaction of Fe ions and adsorbed oxygen ions at the outer oxide – water interface can be written as;

$$O_{adsorbed} + 2e^{-} = O^{2-} \qquad (5.42)$$

$$3Fe^{\bullet\bullet} + \frac{2}{3}O_2 = 2Fe^{\bullet\bullet\bullet} + V_{Fe} + \frac{1}{3}Fe_3O_4 \qquad (5.43)$$

At the transition layer – inner oxide interface

According to $P_{O_2}^{trans-inner}$ and $P_{O_2}^{tinner-outer}$, the Fe-Cr spinel oxide in inner layer has both p-type and n-type oxide ranges. Interstitial diffusion mechanism dominates near the interface of transition layer – inner oxide, and vacancy diffusion dominates on another interface of inner oxide. Cation defect reaction at the interface of transition layer – inner oxide can be written as the n-type oxide reaction. Interstitial metal ions are created at transition layer – inner oxide interface;

$$Fe_{metallic} = Fe_i^{\bullet\bullet} + 2e^{-} \text{ and } Fe_{metallic} = Fe_i^{\bullet\bullet\bullet} + 3e^{-} \qquad (5.44)$$

$$Cr_{metallic} = Cr_i^{\bullet\bullet} + 2e^{-} \text{ and } Cr_{metallic} = Cr_i^{\bullet\bullet\bullet} + 3e^{-} \qquad (5.45)$$

At this point, it is important to concern about oxygen diffusion though oxide scales. Oxygen can diffuse through the oxide lattice via anion vacancies and interstitials with similar trend as the cations [24]. However, the anion defect is considered as minor defect in the spinel lattice. Lattice diffusion of oxygen ions through these minor defects are slower compared to that of cations, Table 5.3. In order for oxygen to reach the transition layer – inner oxide interface, only short circuit diffusion via defects in scale or grain boundaries could permit this long range of diffusion. Plots of diffusion distance of oxygen in polycrystal of magnetite and in Fe-Cr spinel oxide in Figure 5.9 and Figure

5.10 also support this assumption. Therefore, major diffusion path of oxygen is via grain boundaries and defect in the oxide scale. The adsorbed oxygen atoms from the water interface receive electrons and become oxygen ions ($O_{adsorbed} + 2e^- = O^{2-}$). Interaction of cation interstitials and oxygen ions can be written as;

$$Fe_i^{\bullet\bullet} + (2-x)Fe_i^{\bullet\bullet\bullet} + xCr_i^{\bullet\bullet\bullet} + 4O^{2-} = (3-x)Fe_{Fe} + xCr_{Cr} + 4O_O$$
$$= Fe_{3-x}Cr_xO_4 \qquad (5.46)$$

where, x is moles of Cr in the Fe-Cr spinel oxide.

It should be noted that determination of the cation interstitial defects in Dieckman and Töpfer's works was done by conservation of defects in oxide structure. When cation interstitials are formed, the M^{n+} ion moves to a nearest interstice site, creating a Frenkel defect pair;

$$M^{n+} + V_I = M_I^{n+} + V_M \qquad (5.47)$$

where n can be 2+ or 3+, V_I is the interstice site. Thus the defect concentration can be evaluated as noted in Appendix D [9, 11].

Determination of location of defect equilibrium in the inner oxide

Position in the inner oxide where dominate defect type changes can be determined from oxygen partial pressure of defect equilibrium. From plots of diffusion coefficient of Fe and O in Figure 5.5 - Figure 5.7, the defect equilibrium occurs at a particular oxygen partial pressure, which yields a lowest value of the V-shape diffusion coefficient. At this oxygen partial pressure, the dominate defect type changes from vacancy at high P_{O_2} to interstitial at low P_{O_2}. The oxygen partial pressures of defect equilibrium are ~10^{-30}, 10^{-25} and 10^{-20} atm at 400, 500 and 600°C, respectively. The location in oxide that has the

oxygen partial pressure of defect equilibrium can be calculated from flux equation of Fe under the assumption of; i) oxide growth rate follows parabolic law, ii) the flux of Fe is the rate controlling mechanism and constant throughout the scale, iii) the chemical potential of O is fixed by that of Fe with the thermodynamic constraint of $3\mu_M + 4\mu_O = \mu^0_{M_3O_4}$ (M is metal), and iv) the oxygen ions diffuse under chemical potential of O as a driving force [23, 53]. Flux of Fe is expressed as;

$$J_{Fe} = -\frac{C_{Fe}D_{Fe}}{RT}\frac{d\mu_{Fe}}{dx} \tag{5.48}$$

where, C_{Fe} is the concentration of Fe ion (mol/cm^3), D_{Fe} is the diffusion coefficient of Fe in Fe-Cr spinel oxide, R is the gas constant, T is temperature (K), and μ_{Fe} is the chemical potential of Fe (J/mol). Using thermodynamic constraint (condition iii)) and relation of chemical potential and oxygen partial pressure, $\mu_{O_2} = \mu^0_{O_2} + RT\ln P_{O_2}$, the d$\mu_{Fe}$ can be written as;

$$d\mu_{Fe} = -\frac{2}{3}RTd\ln P_{O_2} \tag{5.49}$$

Substituted into eqn. **5.48**, the flux of Fe can be expressed in term of the oxygen partial pressure;

$$J_{Fe} = \frac{2C_{Fe}D_{Fe}}{3}\frac{d\ln P_{O_2}}{dx} \tag{5.50}$$

Assumed constant flux of Fe and integrated over the entire scale;

$$J_{Fe}H = \frac{2C_{Fe}}{3}\int_{P^{in}_{O_2}}^{P^{out}_{O_2}} D_{Fe}d\ln P_{O_2} \tag{5.51}$$

where H is the oxide layer thickness.

Likewise, for any position h in the scale;

$$J_{Fe}h = \frac{2C_{Fe}}{3}\int_{P_{O_2}^{in}}^{P_{O_2}^{h}} D_{Fe}\, d\ln P_{O_2} \qquad (5.52)$$

Divided eqn. **5.52** by **5.51**,

$$\frac{h}{H} = \frac{\int_{P_{O_2}^{in}}^{P_{O_2}^{h}} D_{Fe}\, d\ln P_{O_2}}{\int_{P_{O_2}^{in}}^{P_{O_2}^{out}} D_{Fe}\, d\ln P_{O_2}} \qquad (5.53)$$

Given diffusion coefficient of Fe in Fe-Cr spinel and *h*/*H*, the oxygen partial pressure at any position *h* in the scale can be determined.

Position of the defect equilibrium is the position that oxygen partial pressure equals to ~10^{-30}, 10^{-25} and 10^{-20} atm at 400, 500 and 600°C, respectively. Calculation was done using oxide thickness data of HCM12A exposed in 400, 500 and 600°C deaerated SCW and diffusion coefficient of Fe in Fe_2CrO_4 (composition of inner oxide of HCM12A). It was found that the relative positions of defect equilibrium from the interface of transition layer – inner oxide, *h/H*, are 0.0315, 0.0350 and 0.1355 for 400, 500 and 600°C, respectively. Corresponding distances from the transition layer – inner oxide interface are 0.0267, 0.1421 and 1.6558 μm for 400 (151 hours), 500 (182 hours) and 600°C (190 hours), respectively. Plots of oxygen partial pressure versus relative position in oxide are shown in Figure 5.15. It is found that the relative position of defect equilibrium locates near the transition layer – inner oxide interface. The relative position shifted to a further position from the interface at 600°C. This implies that the dominate cation defects in the inner oxide mostly is vacancy defects. Only small region of near the transition layer – inner oxide that has interstitial defect dominates.

Further implication of defect equilibrium position could be referring to the position of void formation in the oxide. Works of Maruyama et al. [23, 53], Ueda et al.

[26], and Tan et al. [54] proposed that location of void formation in magnetite grew on iron, Fe-Cr alloy and HCM12A is consistent with the location of the dominate defect type changes from vacancies to interstitials. At the transition point, outward flow of interstitial cations changes to inward flow of cation vacancies. Reaction of both defect types at the transition is not widely understood. However, the change of dominate diffusion mechanism causes divergence of the Fe and O flux from equations 5.51 and 5.52. Thus it allows preferential site for vacancy condensation that leads to the void formation. These defects and diffusion behavior should also be applied for the Fe-Cr spinel oxide of the inner layer oxide. Evidence is that high density of micropores is observed near the interface of transition layer – inner oxide (Figure 5.17), which also agrees with the calculated location of defect equilibrium. However, a major difference between the outer and inner oxide is that grain size of Fe-Cr oxide in the inner layer is much smaller than magnetite of the outer layer. The vacancies formation in the inner oxide is also influenced by outward diffusion of Fe ions. Therefore, further research should be conducted for this issue.

5.3.2. Summary of Oxidation Mechanisms

All of information obtained from this research should fulfill the understanding for the oxidation mechanism of F-M alloys in SCW. Overall picture of oxidation mechanisms is illustrated in Figure 5.19, which showed by schematic diagram of oxide structure of HCM12A exposed in 600°C deaerated SCW. In this figure, the transport of Fe and O is demonstrated by conservation of charges of Fe^{2+}, Fe^{3+}, e^{-} and O^{2-}. (Due to unknown interaction at defect equilibrium point in the inner oxide, the conservation of

defects is not demonstrated in this diagram.) The phenomena occurred at each oxide layer can be described as followed;

Outer layer oxide

The outer layer oxide consisted of columnar grains of magnetite that formed by outward diffusion of Fe ions. The magnetite grains grow at interface of outer oxide – water. Calculating from oxidation rate constant (k_p'') and D_{Fe} in magnetite, oxygen partial pressures at the outer oxide – water interface are approximately in the orders of 10^{-23}, 10^{-19} and 10^{-15} atm at 400, 500 and 600°C, respectively. These values are consistent with the oxygen partial pressure at phase boundary between Fe_3O_4 and Fe_2O_3 in the phase diagram, Figure 5.12 - Figure 5.14. Transport of Fe ions in the outer oxide is dominated by vacancy diffusion mechanism.

Inner layer oxide

The inner layer oxide consisted of fine grains of Fe-Cr spinel oxide ($Fe_{3-x}Cr_xO_4$, $x \approx 0.7$ for T91 and 9Cr-ODS, 0.9 for HCM12A and 1.0 for HT-9). Existence of precipitate particles in the layer indicates that the inner layer is the alloy substrate that was oxidized. Micro and nano-size pores occurred from outward diffusion of Fe ions to form the outer oxide. Calculated oxygen partial pressures at the inner – outer oxide interface are approximately in the orders of 10^{-23}, 10^{-19} and 10^{-16} atm at 400, 500 and 600°C, respectively. The values are much higher than those of at the transition – inner oxide interface, which determined from the phase diagram, 10^{-35}, 10^{-29} and 10^{-25} atm at 400, 500 and 600°C, respectively. The reason is that the dominate diffusion mechanism changes in the inner layer oxide. This phenomena possibly leads to the formation of porosity region in the inner oxide near its interface with the transition layer. Transport of Fe ions occurs

via the vacancy diffusion in most of the layer, but the interstitial diffusion mechanism dominates near the transition layer – inner oxide interface. Transport of O ions occurs mostly via the short circuit diffusion.

Transition layer

The transition layer consisted of grain boundary Cr-rich oxides of $FeCr_2O_4$ and Cr_2O_3, and alloy laths with fine spinel structure oxide precipitates. In this layer, Fe diffused outward from intra-laths and at grain boundaries, similar to oxygen that diffused into lath matrix and at grain boundaries. Cr diffused from the lath matrix forming Cr-rich oxides at the lath boundaries. In HT-9 exposed at 600°C, Cr concentration is high enough to form chromite layer at the interface of transition layer – inner oxide. Diffusion mechanism dominates in the transition layer is the short circuit diffusion along grain boundaries.

Table 5.1 Comparison of oxidation rate constants and powers determined from weight gain of F-M alloys in SCW from this thesis and from literature.

Temp (°C)	Alloy	Cr	DO (ppb)	Oxidation rate*		Ref.
				k ($mg/dm^2/h$)	Power (n)	
400	T91	8.37	<10	**4.53**	**0.29**	**This study**
	HCM12A	10.83	<10	**2.35**	**0.39**	**This study**
	HT-9	11.63	<10	**5.44**	**0.28**	**This study**
500	T91	8.37	<10	**15.43**	**0.42**	**This study**
	T91	8.37	25	11.56	0.45	[1]
	9Cr-ODS (0.35 Y_2O_3)	8.64	<10	**10.89**	**0.36**	**This study**
	9Cr-ODS (0.35 Y_2O_3)	8.64	25	29.48	0.24	[2]
	P92 (NF616)	8.82	25	9.11	0.49	[4]
	P92 (NF616)	9.50	25	29.84	0.28	[6]
	HCM12A	10.83	<10	**13.07**	**0.43**	**This study**
	HCM12A	10.83	25	8.31	0.50	[4]
	HCM12A	10.83	25	20.57	0.35	[4]
	HT-9	11.63	<10	**11.02**	**0.48**	**This study**
550	T91b (0.2Ni)	8.37	NDA**	79.24	0.24	[3]
	P92 (NF616)	8.82	N/A***	27.21	0.33	[7]
	T92	9.00	NDA**	40.88	0.35	[3]
	K1 (9Cr-0.25Y_2O_3)	9.00	N/A***	39.13	0.32	[7]
	T91a (0.1Ni)	9.38	NDA**	71.39	0.24	[3]
	P92 (NF616)	9.50	25	27.75	0.32	[6]
	K2 (12Cr-0.25Y_2O_3)	12.00	N/A***	37.10	0.36	[7]
	T122 (HCM12A)	12.12	NDA**	65.36	0.11	[3]
600	9Cr-ODS (0.35 Y_2O_3)	8.64	25	56.24	0.39	[2]
	P92 (NF616)	8.82	25	53.40	0.45	[4]
	P92 (NF616)	9.50	25	89.86	0.31	[6]
	HCM12A	10.83	25	49.80	0.42	[4]
	HCM12A	10.83	25	70.80	0.37	[4]
627	T91b (0.2Ni)	8.37	NDA**	59.37	0.46	[3]
	T92	9.0	NDA**	59.37	0.46	[3]
	T91a (0.1Ni)	9.38	NDA**	47.41	0.48	[3]
	T122 (HCM12A)	12.12	NDA**	113.66	0.13	[3]

Note: * : Oxidation rate is expressed as power law (eqn 2.11)
** : NDA = Non-deaerated water
*** : N/A = Water chemistry was not given in the paper

Table 5.2 Activation energies determined from weight gain and oxide thickness of T91, HCM12A, HT-9 and 9Cr-ODS, and from literature data.

Alloy	Oxidation rate from	# of data	Temp. (°C)	n_w, n_h*	Y = A + BX**			**Q (kJ/mol)**
					A	B	R^2	
T91	Weight gain	3	400-600	0.40	17.7	-9886.6	0.9990	**206 ± 6**
HCM12A	Weight gain	3	400-600	0.40	17.4	-9803.1	0.9999	**199 ± 1**
HT-9	Weight gain	3	400-600	0.40	16.2	-8726.0	0.9995	**181 ± 4**
9Cr-ODS	Weight gain	2	500-600	0.40	22.2	-13821.0		**287**
T91	Tot. thickness	3	400-600	0.37	12.5	-7694.5	0.9933	**173 ± 14**
	Outer oxide	3	400-600	0.40	12.1	-7887.3	0.9964	**164 ± 10**
	Inner oxide	3	400-600	0.40	12.2	-8268.2	0.9961	**172 ± 11**
	Transition	3	400-600	0.23	7.6	-5421.6	0.9573	**196 ± 41**
HCM12A	Tot. thickness	3	400-600	0.37	12.5	-7796.6	0.9955	**175 ± 12**
	Outer oxide	3	400-600	0.40	12.1	-7980.5	0.9964	**166 ± 10**
	Inner oxide	3	400-600	0.40	11.2	-7575.0	0.9999	**158 ± 2**
	Transition	3	400-600	0.23	10.4	-7671.9	0.9459	**277 ± 66**
HT-9	Tot. thickness	3	400-600	0.37	11.9	-7264.4	0.9999	**163 ± 1**
	Outer oxide	3	400-600	0.40	11.8	-7787.0	0.9994	**162 ± 4**
	Inner oxide	3	400-600	0.40	12.0	-8111.3	0.9999	**169 ± 2**
	Transition	3	400-600	0.23	3.9	-2781.5	0.7696	**101 ± 55**
Literature data								
T91 [55]	Weight gain	N/A	300-600 (in steam)					199.0
T91 [56]	Weight gain	3	400-650 (in steam)					207.9
HCM12A [55]	Weight gain	N/A	300-600 (in steam)					166
P92 [6]	Weight gain	3	500-600 (in SCW)					234
HT-9 [57]	Weight gain	9	600-950 (in air)					305

Note: * n_h and n_w from equation 2.9 and 2.11

** Linear equation from plots of; ln (weight gain/ oxide thickness) versus 1/T (K^{-1}).
Y = ln (weight gain/ oxide thickness), X = 1/T,
A is y-intercept, and B is slope.

Table 5.3 Frequency factor (D_o) and activation energy (Q) of Fe, Cr and O in Fe_3O_4, Cr_2O_3 and miscellaneous oxides

Oxide	Ions	Temp. (°C)	D_o (cm^2/s)	Q (kJ/mol)	Note (S) Single crystal, (P) Polycrystal	Ref.
Fe_3O_4	O	302-550	3.20×10^{-14}	71.1	(S) hydrothermal with O^{18}	[58]
Fe_3O_4	O	480-1100	1.20×10^{-9}	264	(P) Creep measurement	[12]
Fe_3O_4	O	505-660	4.30×10^{-7}	211 ± 20	(S) Natural isotope O^{18} measurement	[59]
Fe_3O_4	O	500-800	3.50×10^{-6}	188.4	(S) 20-200 MPa hydrothermal with O^{18}	[60]
Fe_3O_4	O	480-1100	1.20×10^{-2}	167	G.B.* (P) Creep measurement	[12]
Fe_3O_4	Fe	350-1200	4.51×10^{-5}	149	(P) Fe^{55} in Fe_3O_4, averaged from $P_{O2} = 10^{-28} – 10^{-18}$ atm	[8]
Fe_3O_4	Fe	0- 80	7.2×10^{-5}	87.86	(P) aqueous nano particles	[61]
Fe_3O_4	Fe	770-1200	0.25	225.52	(P) Fe^{59} in Fe_3O_4	[62, 63]
Fe_3O_4	Fe	750-1000	5.2	230.12	(P) oxidation in $Fe_{2.993}O_4$	[62, 64]
Fe_3O_4	Fe	850-1075	104	312.54 ± 18	(S) Fe^{55} in Fe_3O_4	[62, 65]
Fe_3O_4	Fe	850-1075	6.0×10^{5}	351.46 ± 25	(P) Fe^{55} in Fe_3O_4	[62, 65]
Cr_2O_3	O	1100-1450	15.9	422	(P) O^{18} mass spectroscopy	[62, 66]
Cr_2O_3	Fe	740-1100	4.30×10^{-9}	181	(P) secondary ion mass spectrometry (SIM)	[67]
Cr_2O_3	Fe	740-1100	1.20×10^{4}	347	G.B. (S) SIM measured on film	[67]
Cr_2O_3	Cr	900-1100	4.29×10^{-8}	92	(P) Cr^{51} radiotracer	[62, 68]
Cr_2O_3	Cr	1045-1550	0.137	256	(P) Cr^{51} radiotracer	[62, 69]
Cr_2O_3	Cr	1100-1250		371	(P) film evaporation	[62, 70]
$FeCr_2O_4$	O	600-1000	1.61×10^{-5}	138	(P) O^{18} radiotracer on Fe-Cr alloy	[13]
$NiCr_2O_4$	O	1200-1500	2.60×10^{-8}	295	(P) O^{18} radiotracer	[71]
$Fe_{2.32}Ni_{0.68}O_4$	O	1140-1340	5.00×10^{-7}	255	(P)	[72]
$MnCr_2O_4$	Fe	1000-1200	1.35×10^{-3}	255.40	(P) Fe^{59} radio tracer	[73]
	Cr	900-1100	2.03×10^{-5}	187.56	(P) Cr^{51} radio tracer	[73]
Fe_3O_4	vacancy	1300-1450	0.14	135.98	(P) Measurement of P_{O2}	[74]

Table 5.4 Diffusion coefficients of Fe, Cr and O in Fe-Cr spinel oxide and Cr_2O_3.

Oxide	Ions	Temperature (°C)	Diffusion coefficient (D) (cm^2/s)	Note (S) Single crystal, (P) Polycrystal	Ref.
Fe_3O_4	Fe	1200	6.71×10^{-9}	(P) Fe^{59} tracer	[9]
	Cr	1200	1.54×10^{-11}	(P) Cr^{51} tracer	[9]
$Fe_{2.7}Cr_{0.3}O_4$	Fe	1200	5.33×10^{-9}	(P) Fe^{59} tracer	[9]
	Cr	1200	7.73×10^{-12}	(P) Cr^{51} tracer	[9]
$Fe_{2.4}Cr_{0.6}O_4$	Fe	1200	2.50×10^{-9}	(P) Fe^{59} tracer	[9]
	Cr	1200	4.61×10^{-12}	(P) Cr^{51} tracer	[9]
$Fe_{2.01}Cr_{0.99}O_4$	Fe	1200	1.09×10^{-9}	(P) Fe^{59} tracer	[9]
	Cr	1200	1.49×10^{-12}	(P) Cr^{51} tracer	[9]
$Fe_{1.8}Cr_{1.2}O_4$	Fe	1200	1.73×10^{-9}	(P) Fe^{59} tracer	[9]
	Cr	1200	1.22×10^{-12}	(P) Cr^{51} tracer	[9]
Cr_2O_3	Cr	1197.6	1.00×10^{-18}		[75]
		1289.5	5.00×10^{-18}		[75]
		1339.9	6.00×10^{-18}		[75]
		1393.7	9.00×10^{-17}		[75]
		1451.0	8.00×10^{-16}		[75]
Cr_2O_3	Cr	800	5.90×10^{-18}	Bulk	[76]
Cr_2O_3	Cr	900	2.00×10^{-17}	Bulk	[76]
Cr_2O_3	Cr	800	1.10×10^{-12}	Grain boundary	[76]
Cr_2O_3	Cr	900	9.30×10^{-12}	Grain boundary	[76]
Cr_2O_3	O	800	2.60×10^{-18}	Bulk	[76]
Cr_2O_3	O	900	4.40×10^{-17}	Bulk	[76]
Cr_2O_3	O	800	5.90×10^{-13}	Grain boundary	[76]
Cr_2O_3	O	900	1.60×10^{-12}	Grain boundary	[76]

Table 5.5 Calculation of Cr concentration in inner oxide from the oxide thicknesses. The results agree with Cr concentration from experiments.

Temp. (^oC)	DO (ppb)	Alloy	$C_{Fe,alloy}$ (mol/cm^3)	$C_{Cr,alloy}$ (mol/cm^3)	h_{sp} (μm)	h_{mag} (μm)	x_{cal} (mole)	x_{exp} (mole)	different (x_{cal}- x_{exp})
400	<10	T91	0.130	0.013	0.89	1.39	0.70	0.73	-0.03
		HCM12A	0.123	0.017	0.85	1.14	0.85	0.79	0.07
		HT-9	0.122	0.018	0.83	1.21	0.95	0.95	0.00
500	<10	T91	0.130	0.013	4.35	6.37	0.67	0.66	0.01
		HCM12A	0.123	0.017	4.06	5.31	0.84	0.85	-0.01
		HT-9	0.122	0.018	4.74	6.03	0.87	1.00	-0.13
500	100	T91	0.130	0.013	4.31	6.65	0.69	0.60	0.09
		HCM12A	0.123	0.017	4.35	5.76	0.85	0.80	0.05
500	300	T91	0.130	0.013	3.58	5.25	0.67	0.69	-0.02
		HCM12A	0.123	0.017	3.32	4.68	0.88	0.86	0.02
		HT-9	0.122	0.018	3.91	5.59	0.93	0.88	0.05
600	<10	T91	0.130	0.013	16.57	22.70	0.65	0.74	-0.09
		HCM12A	0.123	0.017	12.22	19.22	0.94	0.87	0.07
		HT-9	0.122	0.018	14.26	18.83	0.89	0.95	-0.06
		9Cr-ODS	0.130	0.014	11.23	20.28	0.79	0.75	0.05

Table 5.6 Calculation of thickness of alloy that was consumed to produce the inner oxide (h_{alloy}).

Temp. (^{o}C)	DO (ppb)	Alloy	h_{sp} (μm)	h_{mag} (μm)	x_{exp} (mole)	h_{alloy} (μm)	different (h_{alloy}- h_{sp})
400	<10	T91	0.89	1.39	0.73	1.06	0.17
		HCM12A	0.85	1.14	0.79	0.98	0.13
		HT-9	0.83	1.21	0.95	0.97	0.14
500	<10	T91	4.35	6.37	0.66	5.06	0.71
		HCM12A	4.06	5.31	0.85	4.47	0.41
		HT-9	4.74	6.03	1.00	4.88	0.14
500	100	T91	4.31	6.65	0.60	5.31	1.00
		HCM12A	4.35	5.76	0.80	4.92	0.57
500	300	T91	3.58	5.25	0.69	4.13	0.55
		HCM12A	3.32	4.68	0.86	3.85	0.53
		HT-9	3.91	5.59	0.88	4.62	0.71
600	<10	T91	16.57	22.70	0.74	17.91	1.34
		HCM12A	12.22	19.22	0.87	15.40	3.19
		HT-9	14.26	18.83	0.95	15.39	1.13
		9Cr-ODS	11.23	20.28	0.75	14.98	3.75

Table 5.7 List of parameters in equations **5.5 and 5.17**, and calculated values at 400, 500 and 600°C.

Parameters	Equation*	Temperature (°C)		
		400	500	600
D_V (cm^2/s)	$D_V = 0.177\eta \exp\left(-\frac{14600}{T}\right) + 1.16\times10^{-3}(1-\eta)\exp\left(-\frac{8670}{T}\right)$	$2.95\text{x}10^{-9}$	$1.56\text{x}10^{-8}$	$5.64\text{x}10^{-8}$
η	$\eta = \frac{1}{1+3\times10^{-3}\exp\left(\frac{11900}{T}\right)}$	$6.98\text{x}10^{-6}$	$6.87\text{x}10^{-5}$	$4.01\text{x}10^{-4}$
D_I (cm^2/s)	$D_I = 1.22\times10^{4}\exp\left(-\frac{27700}{T}\right)\left(1+1.56\times10^{6}\exp\left(-\frac{20100}{T}\right)\right)^{-1}$	$1.63\text{x}10^{-14}$	$3.34\text{x}10^{-12}$	$2.02\text{x}10^{-10}$
K_V	$K_V = 2.04\times10^{-7}\exp\left(\frac{27170}{T}\right)$	$6.96\text{x}10^{10}$	$3.75\text{x}10^{8}$	$6.70\text{x}10^{6}$
K_I	$K_I = 1.93\times10^{3}\exp\left(-\frac{43140}{T}\right) + 3.01\times10^{9}\exp\left(-\frac{63270}{T}\right)$	$2.80\text{x}10^{-25}$	$1.12\text{x}10^{-21}$	$6.68\text{x}10^{-19}$
A (cm^2/s)	$A = \frac{D_V K_V}{12}$	17.1	$4.88\text{x}10^{-1}$	$3.15\text{x}10^{-2}$
B (cm^2/s)	$B = \frac{4}{3} D_I K_I$	$6.07\text{x}10^{-39}$	$4.98\text{x}10^{-33}$	$1.80\text{x}10^{-28}$

* T is temperature in Kelvin

Table 5.8 Oxygen partial pressure of T91, HCM12A and HT-9 determined by oxidation rate equation.

Exp.	alloy	k_p'' (cm^2/s)		Oxygen partial pressure (atm)		
		Inner oxide	Outer oxide	$P_{O_2}^{trans-inner}$	$P_{O_2}^{inner-outer}$	$P_{O_2}^{outer-water}$
400°C DSCW	T91	$6.26x10^{-15}$	$1.17x10^{-14}$	$3.00x10^{-35}$	$1.46x10^{-23}$	$4.58x10^{-23}$
	HCM12A	$5.62x10^{-15}$	$1.19x10^{-14}$	$3.00x10^{-35}$	$1.85x10^{-23}$	$5.22x10^{-23}$
	HT-9	$5.32x10^{-15}$	$1.34x10^{-14}$	$3.00x10^{-35}$	$1.71x10^{-23}$	$5.50x10^{-23}$
500°C DSCW	T91	$1.12x10^{-13}$	$2.11x10^{-13}$	$1.00x10^{-29}$	$1.57x10^{-19}$	$6.16x10^{-19}$
	HCM12A	$9.92x10^{-14}$	$1.52x10^{-13}$	$1.00x10^{-29}$	$2.73x10^{-19}$	$6.27x10^{-19}$
	HT-9	$9.43x10^{-14}$	$1.67x10^{-13}$	$1.00x10^{-29}$	$2.53x10^{-19}$	$6.39x10^{-19}$
600°C DSCW	T91	$1.58x10^{-12}$	$3.77x10^{-12}$	$2.00x10^{-25}$	$3.43x10^{-17}$	$1.49x10^{-15}$
	HCM12A	$1.09x10^{-12}$	$2.70x10^{-12}$	$2.00x10^{-25}$	$5.11x10^{-16}$	$1.83x10^{-15}$
	HT-9	$1.49x10^{-12}$	$2.59x10^{-12}$	$2.00x10^{-25}$	$8.70x10^{-16}$	$2.28x10^{-15}$
	9Cr-ODS	$9.22x10^{-13}$	$3.01x10^{-12}$	$2.00x10^{-25}$	$3.81x10^{-16}$	$1.81x10^{-15}$

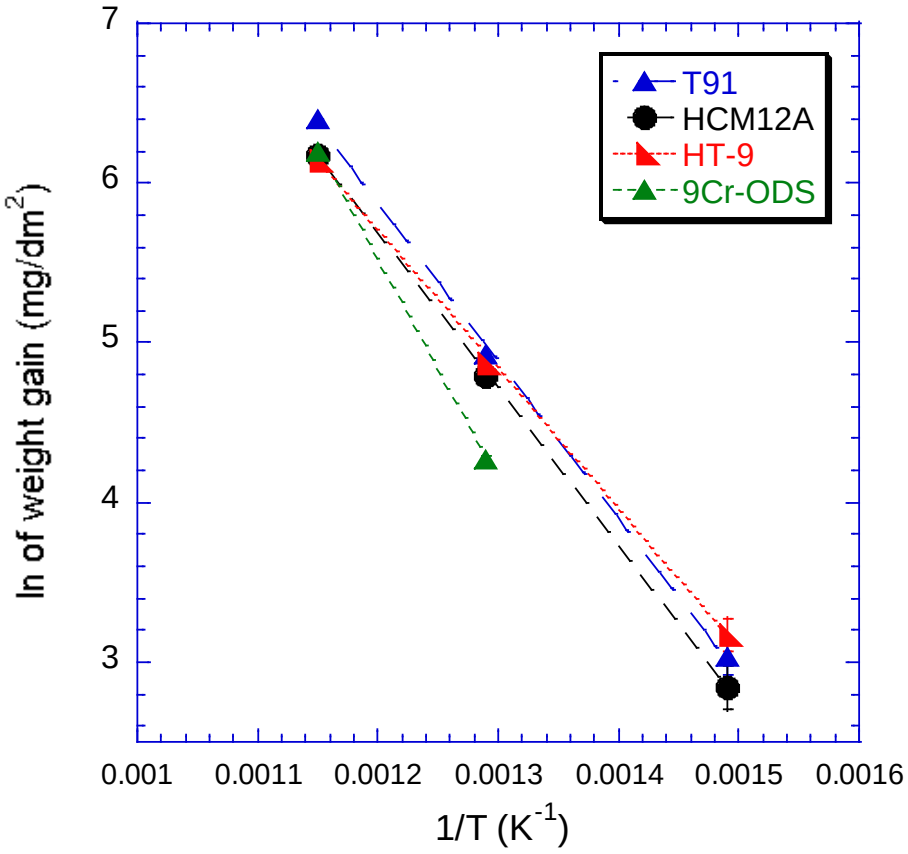

Figure 5.1 Plot of natural logarithmic of weight gain and 1/T of T91, HCM12A, HT-9 and 9Cr-ODS.

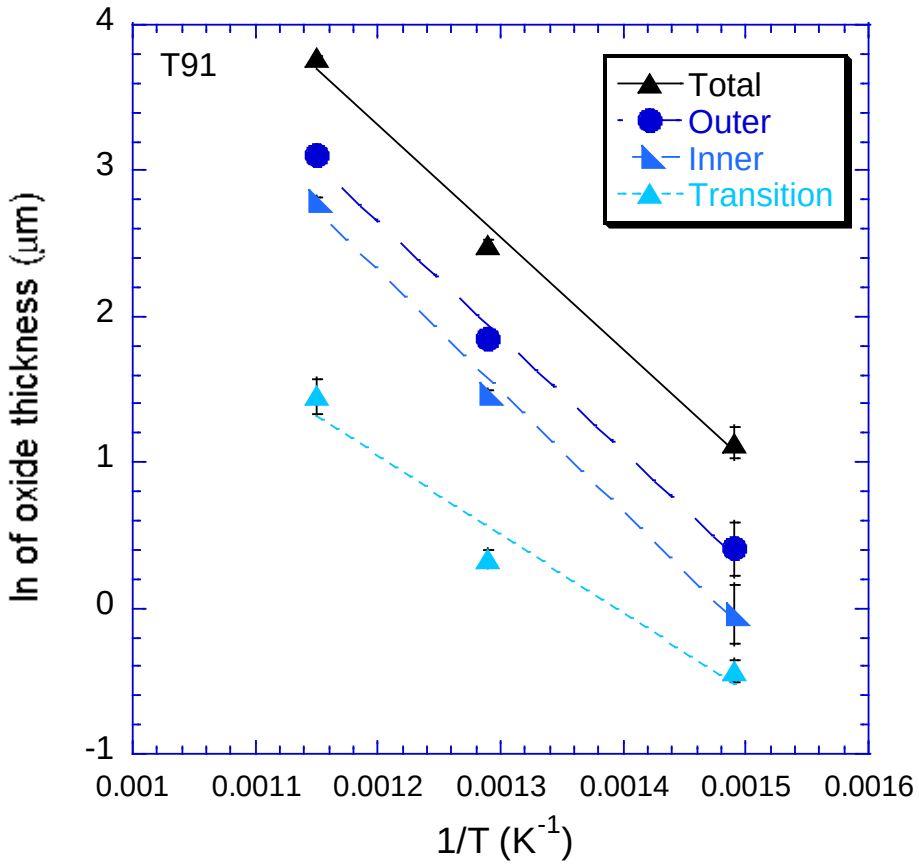

Figure 5.2 Plot of natural logarithmic of oxide thickness and 1/T of T91 tested in 400, 500 and 600°C deaerated SCW. The thickness was normalized to 182 hours.

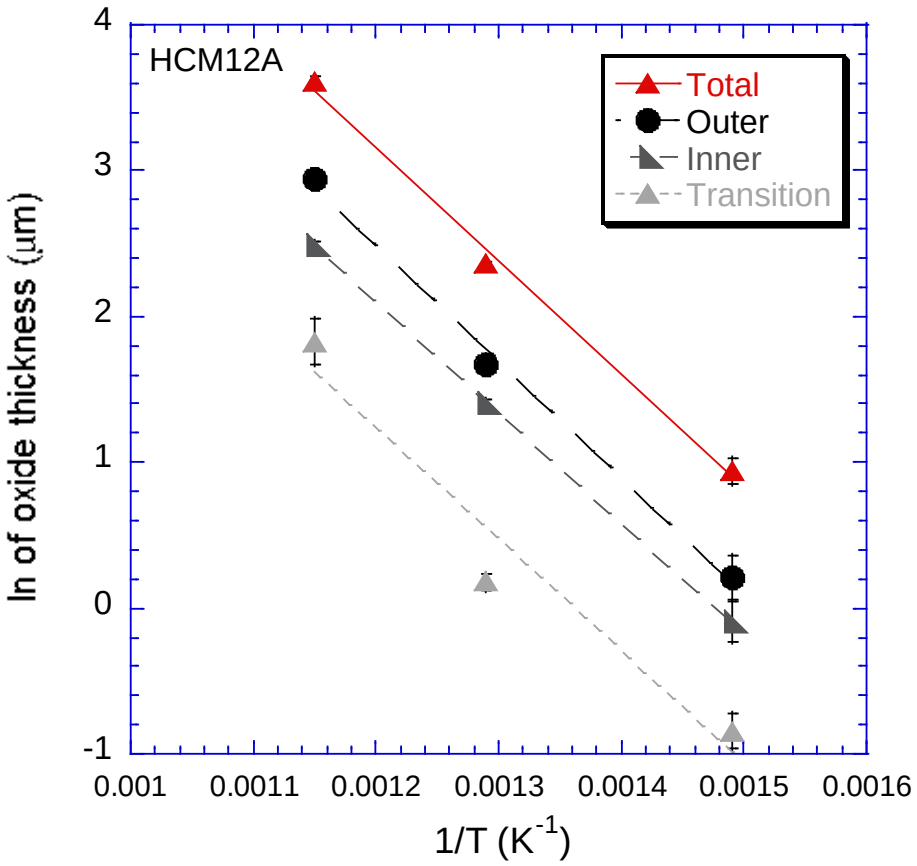

Figure 5.3 Plot of natural logarithmic of oxide thickness and 1/T of HCM12A tested in 400, 500 and 600°C deaerated SCW. The thickness was normalized to 182 hours.

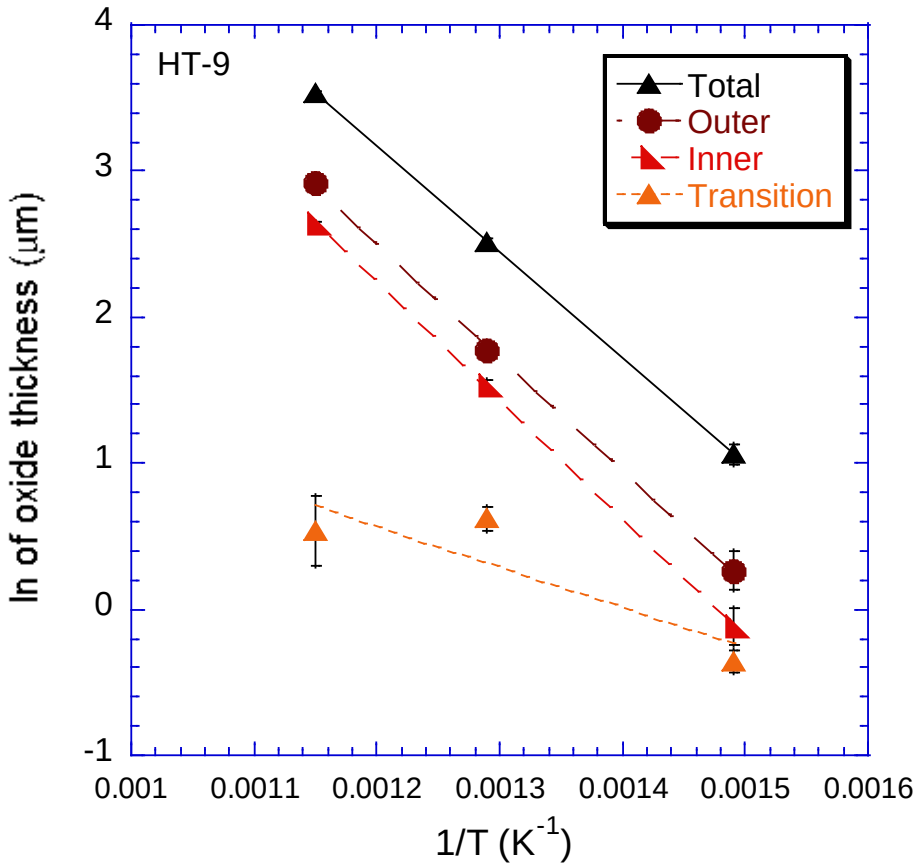

Figure 5.4 Plot of natural logarithmic of oxide thickness and 1/T of HT-9 tested in 400, 500 and 600°C deaerated SCW. The thickness was normalized to 182 hours.

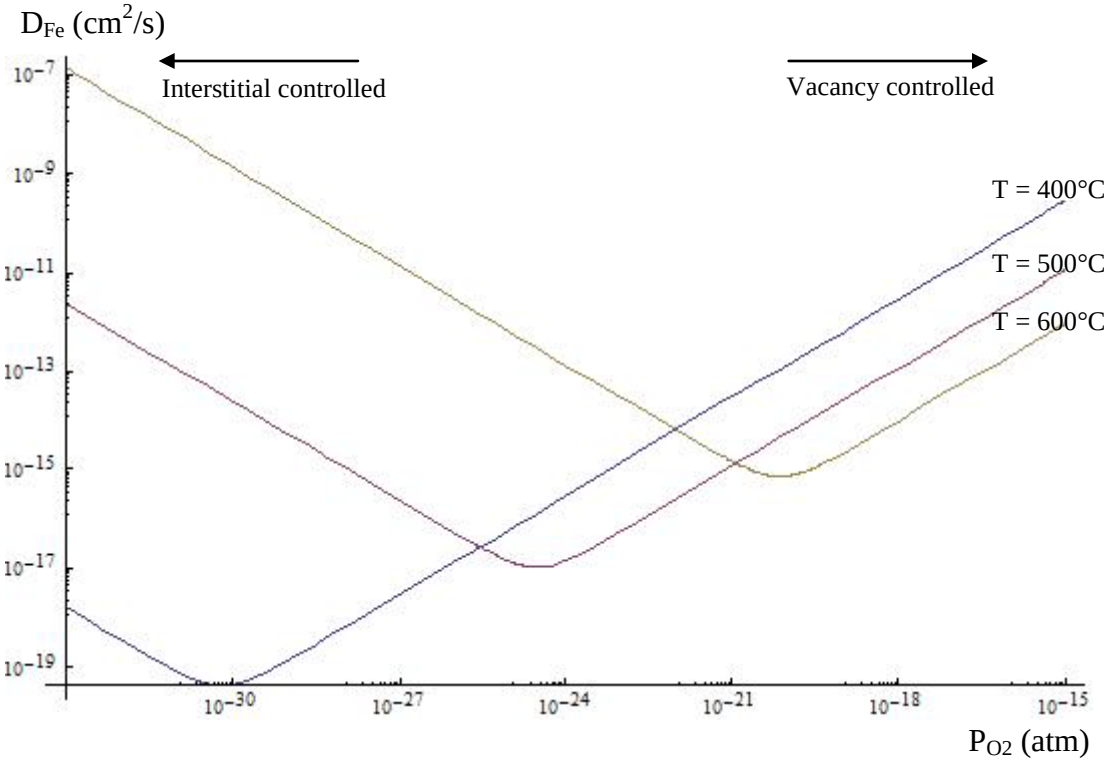

Figure 5.5 Plots of diffusivity of Fe in Fe_3O_4 as a function of oxygen partial pressure.

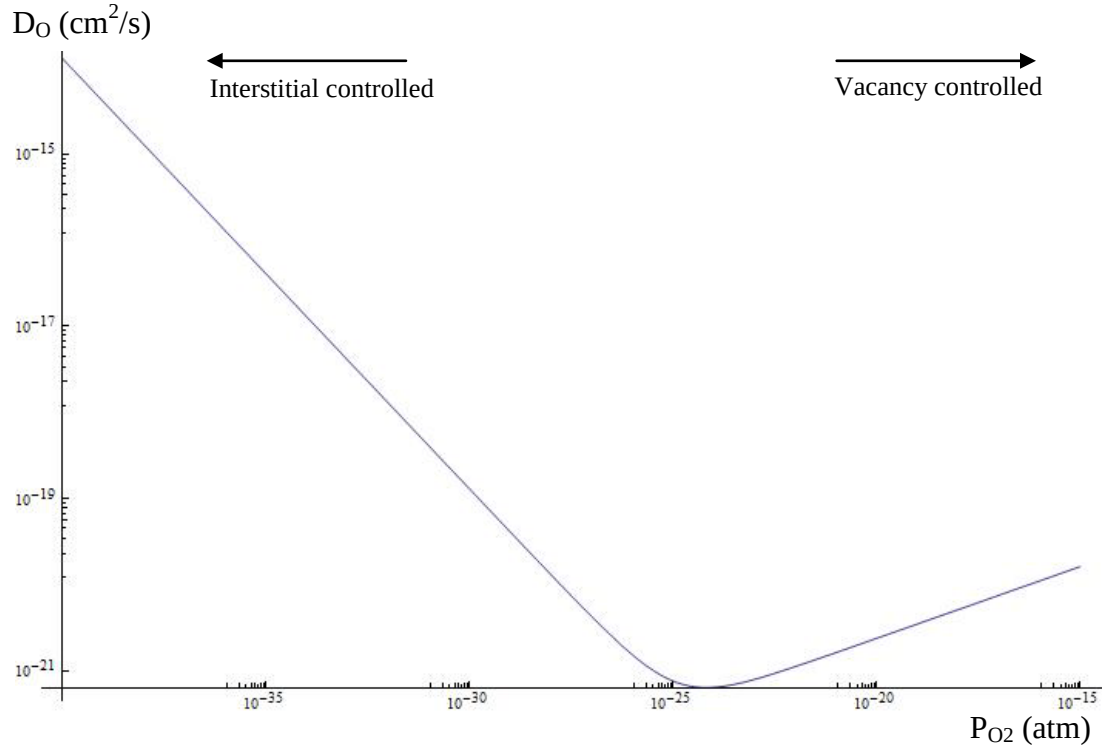

Figure 5.6 Plots of diffusivity of O in Fe_3O_4 as a function of oxygen partial pressure at 550°C.

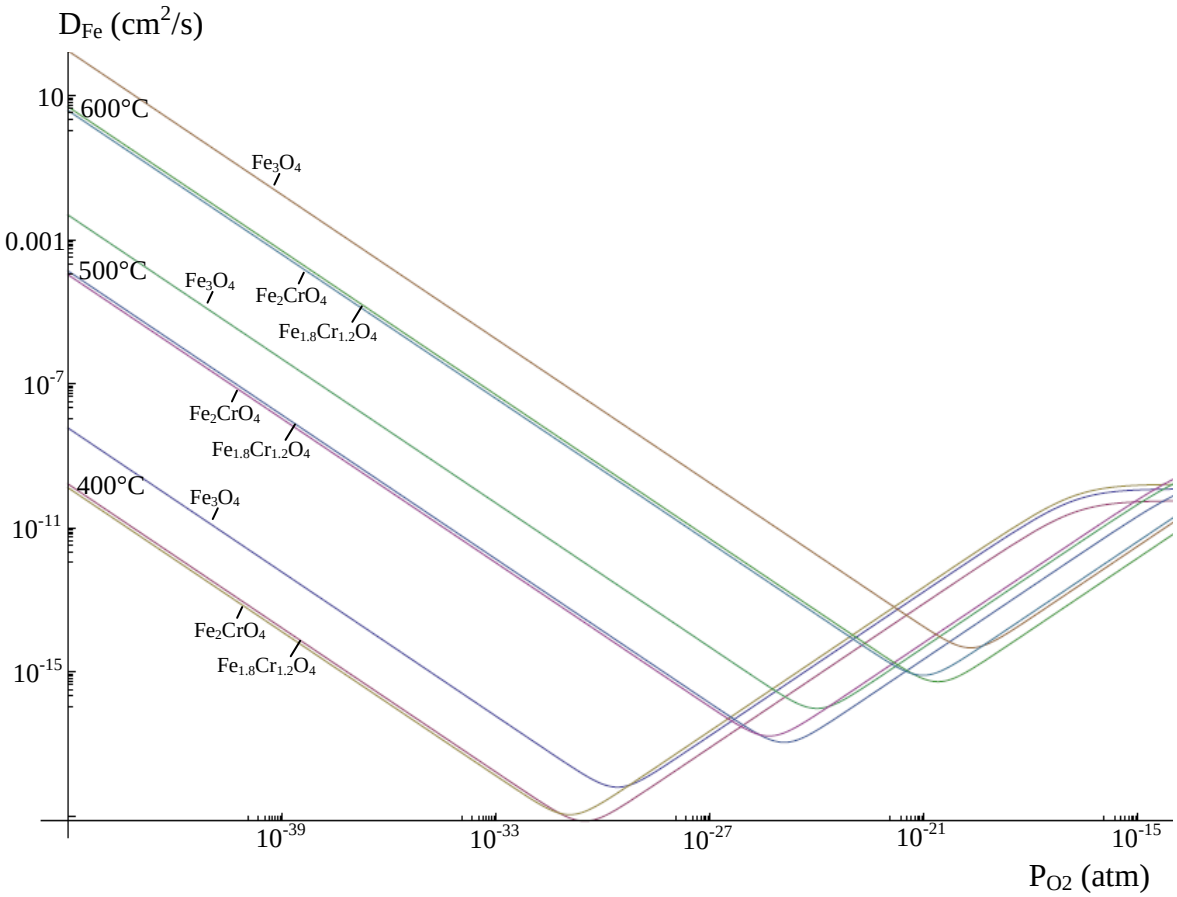

Figure 5.7 Plots of diffusivity of Fe in Fe_3O_4, Fe_2CrO_4, $Fe_{1.8}Cr_{1.2}O_4$ as a function of oxygen partial pressure at 400, 500 and 600°C.

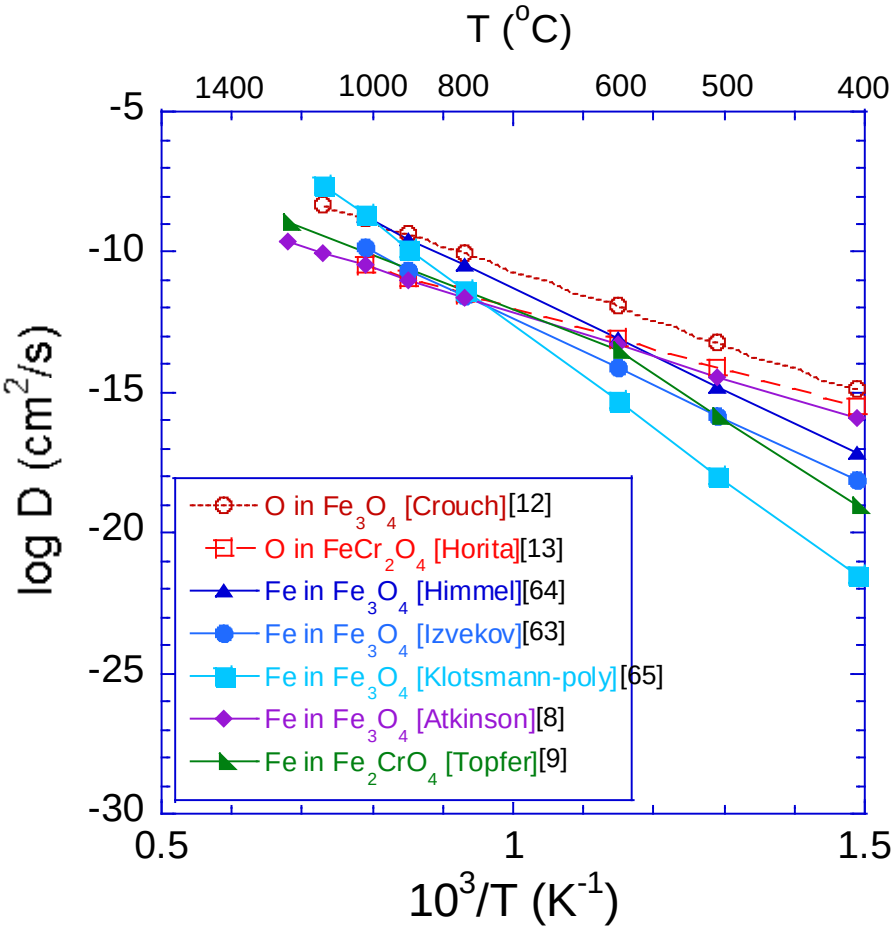

Figure 5.8 Comparison of the diffusion coefficients of Fe and O in Fe_3O_4 and $FeCr_2O_4$. The data was obtained from the experiment with poly-crystal.

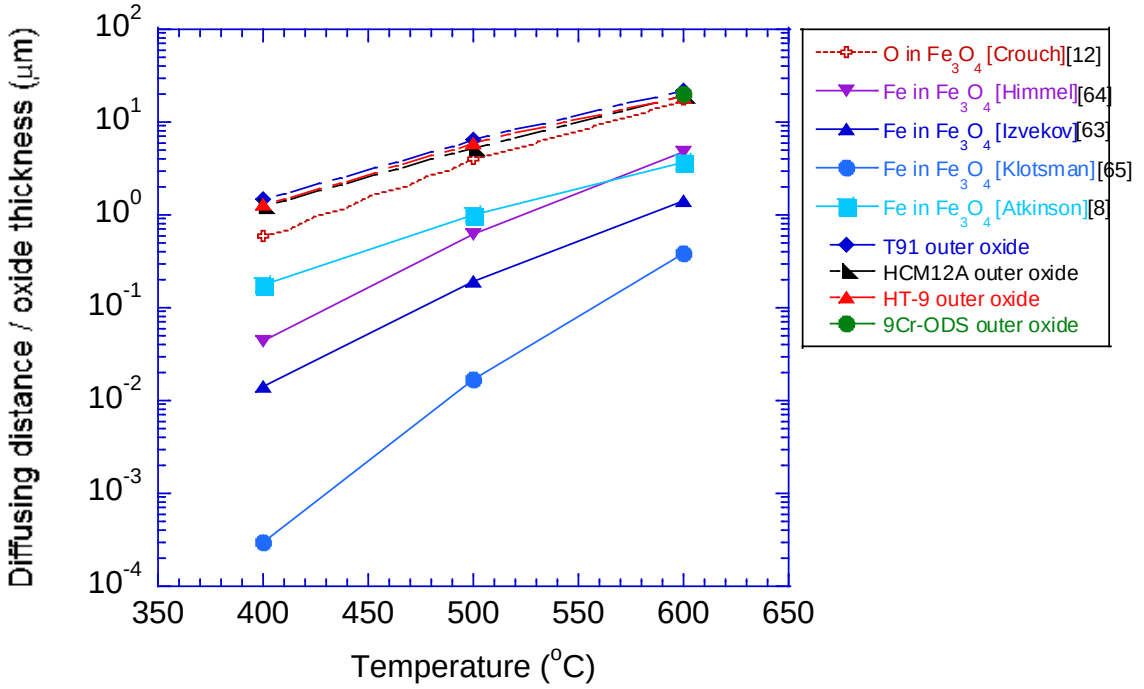

Figure 5.9 Calculated diffusing distance of Fe and O in Fe_3O_4 compared with outer oxide thickness.

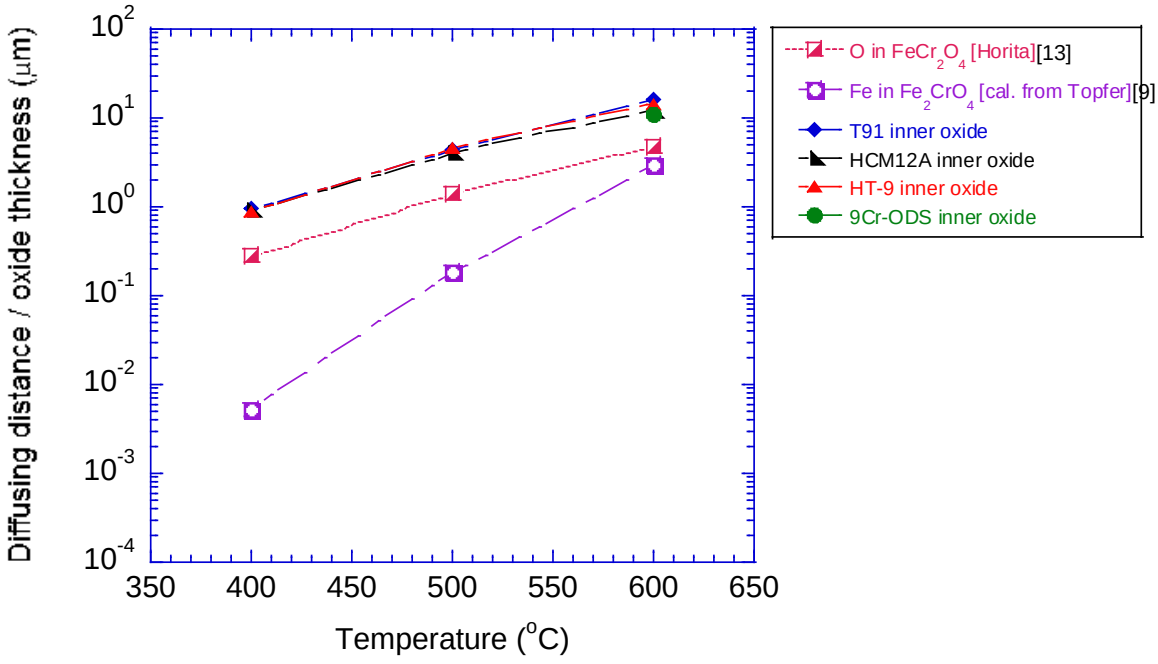

Figure 5.10 Calculated diffusing distance of O in $FeCr_2O_4$ and Fe in Fe_2CrO_4 compared with inner oxide thickness.

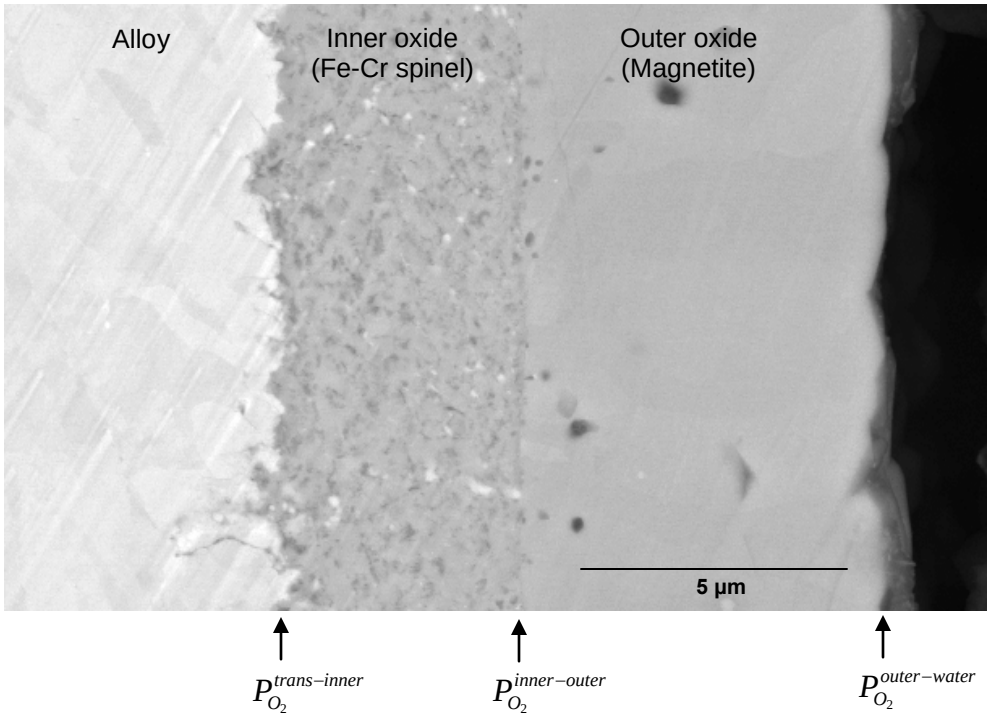

Figure 5.11 A BSE image of HCM12A illustrating position of oxygen partial pressure determined by the oxidation rate equation. The alloy was exposed in 500°C deaerated SCW for 182 hours.

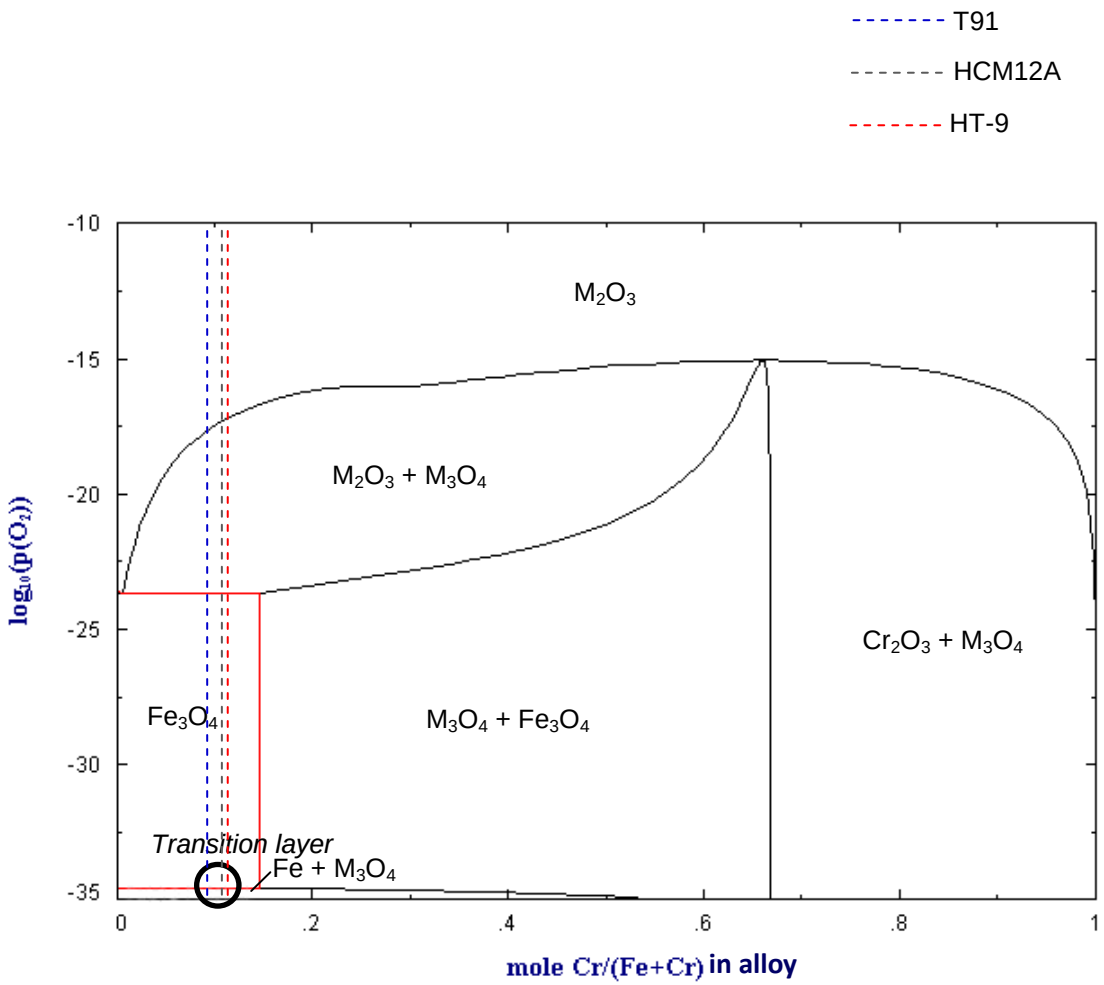

Figure 5.12 Predominance diagram of the Fe-Cr-O system at 400°C. M is Fe and Cr.

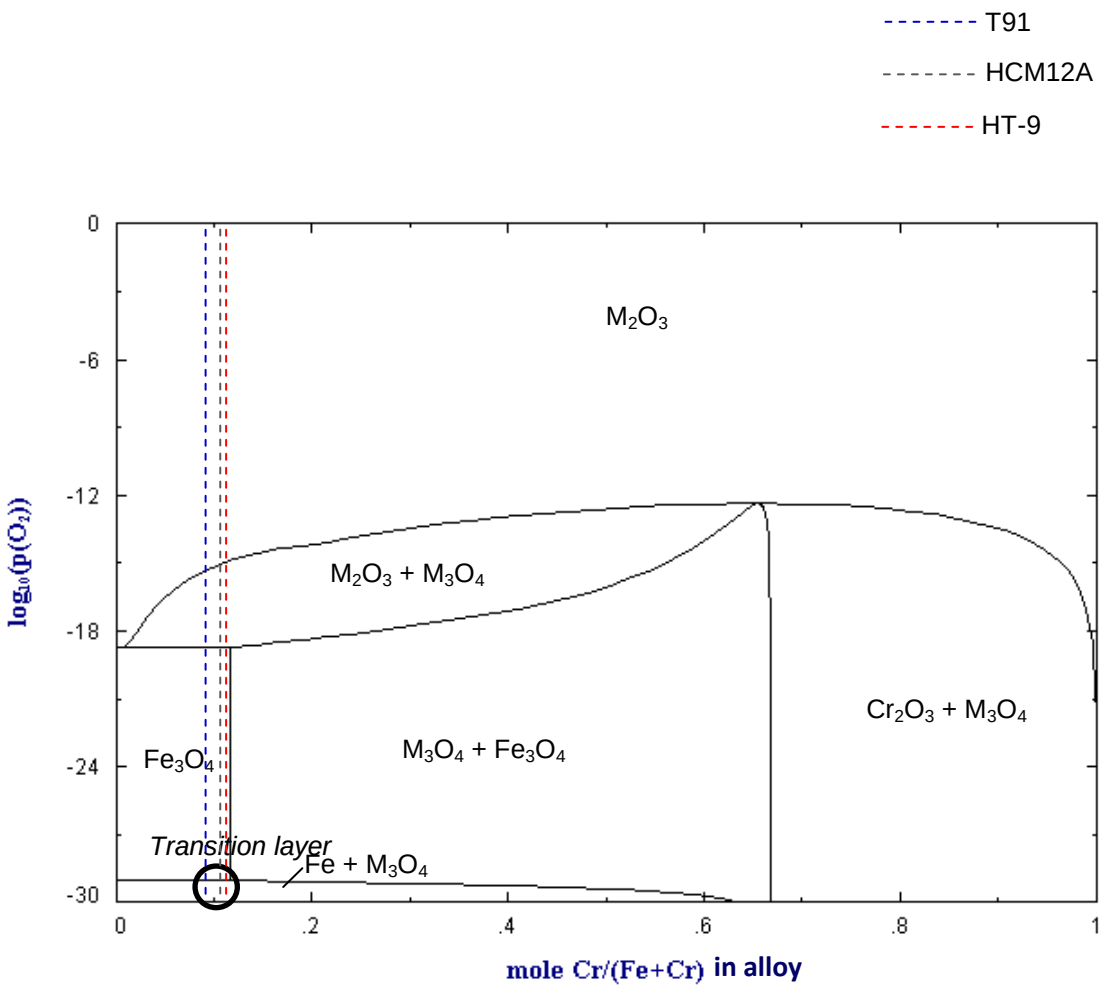

Figure 5.13 Predominance diagram of the Fe-Cr-O system at 500°C. M is Fe and Cr.

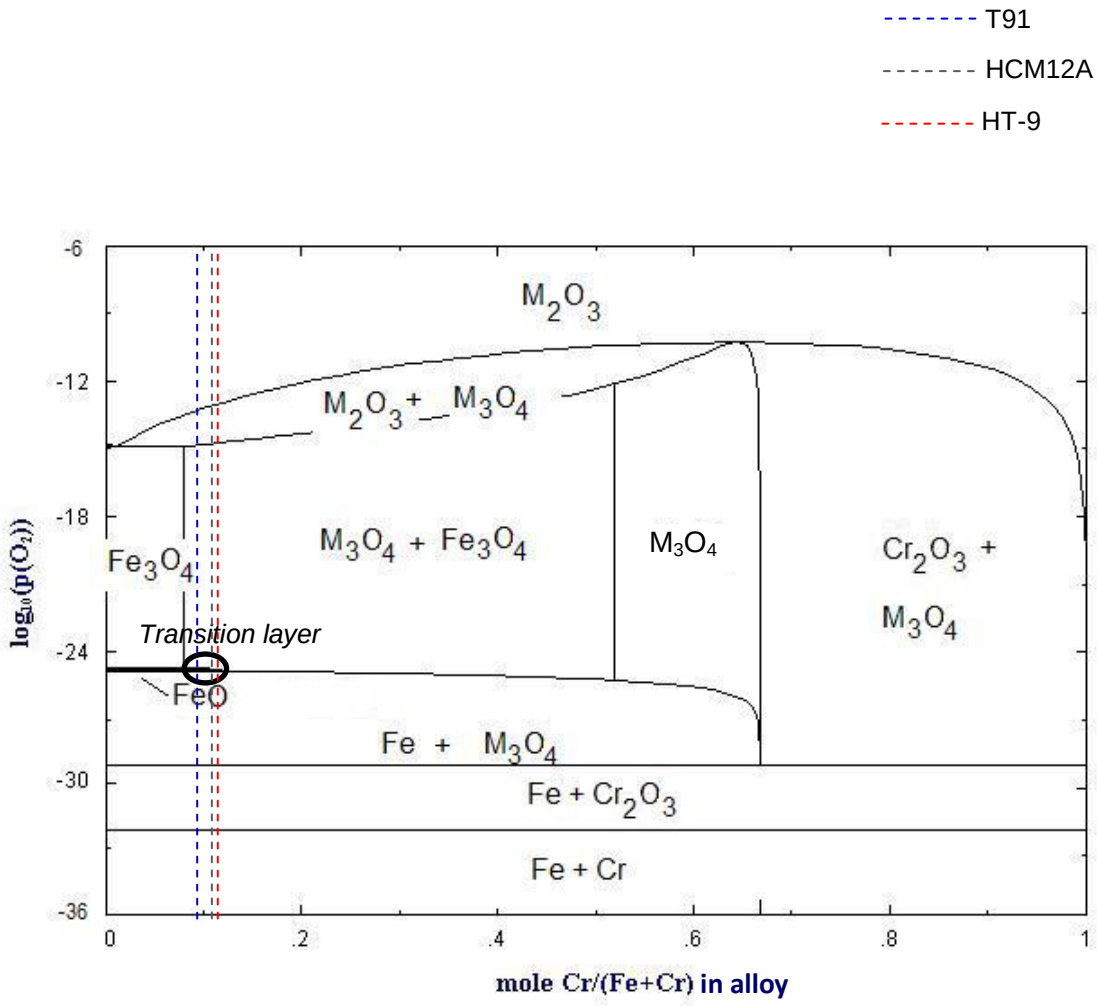

Figure 5.14 Predominance diagram of the Fe-Cr-O system at 600°C. M is Fe and Cr.

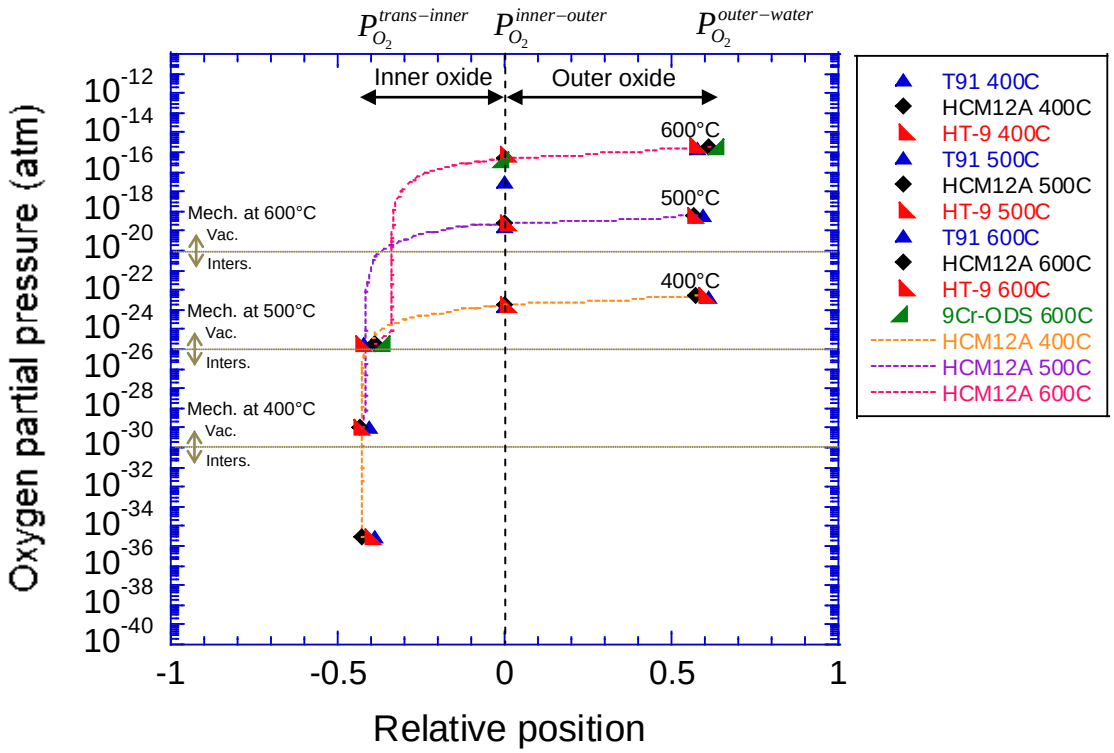

Figure 5.15 Plot of $P_{O_2}^{trans-inner}$, $P_{O_2}^{inner-outer}$ and $P_{O_2}^{outer-water}$ versus relative position in total oxide of T91, HCM12A, HT-9 and 9Cr-ODS exposed in 400-600°C SCW. The relative position is the position of three interfaces in total oxide thickness. Assuming that the interface of inner – outer oxide is at zero position, the relative position in the inner oxide has negative sign and positive sign for the outer oxide. The oxygen partial pressure in the oxide layers of HCM12A was added to demonstrate the trend.

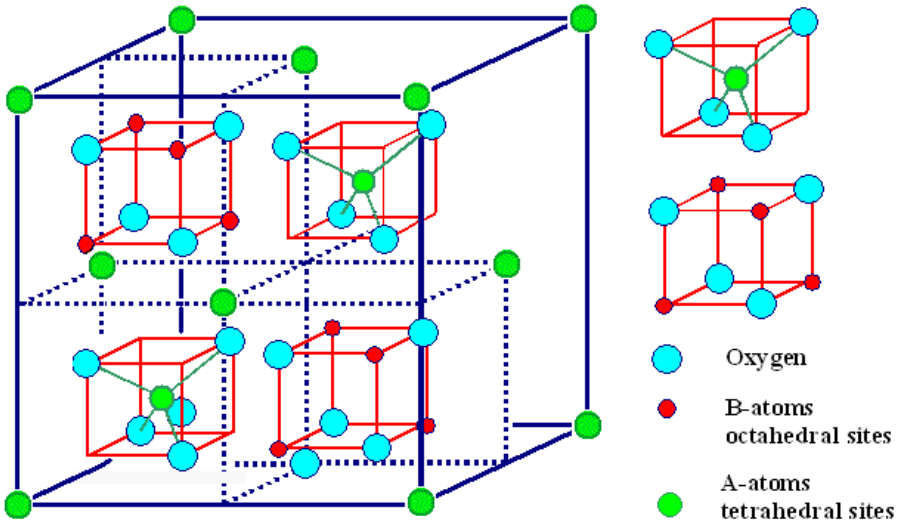

AB_2O_4 spinel The red cubes are also contained in the back half of the unit cell

(a)

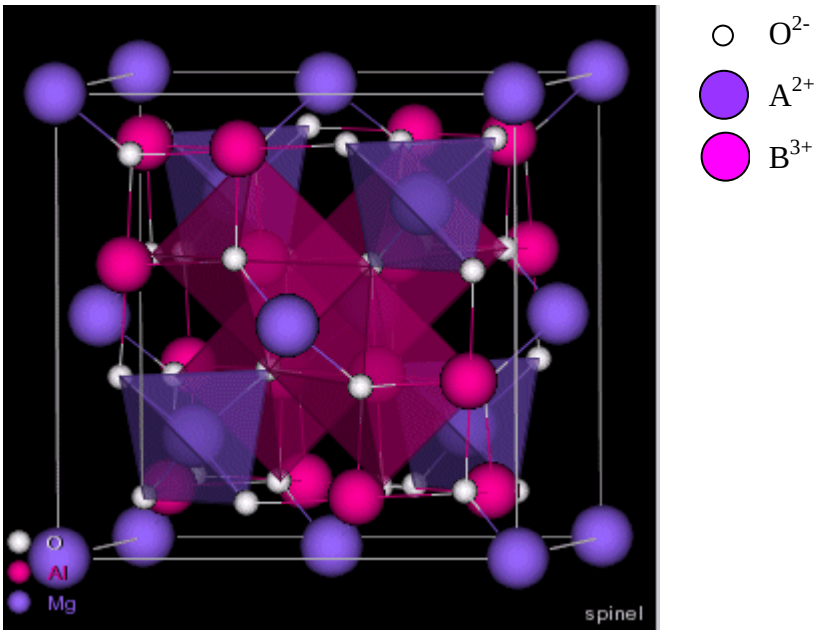

(b)

Figure 5.16 Crystallographic models of spinel structure showing (a) two types of sub-lattice that contain A^{2+} in tetrahedral site and B^{3+} in octahedral sites [77]. (b) Unit cell of spinel with tetrahedral sites (blue) and octahedral sites (pink).

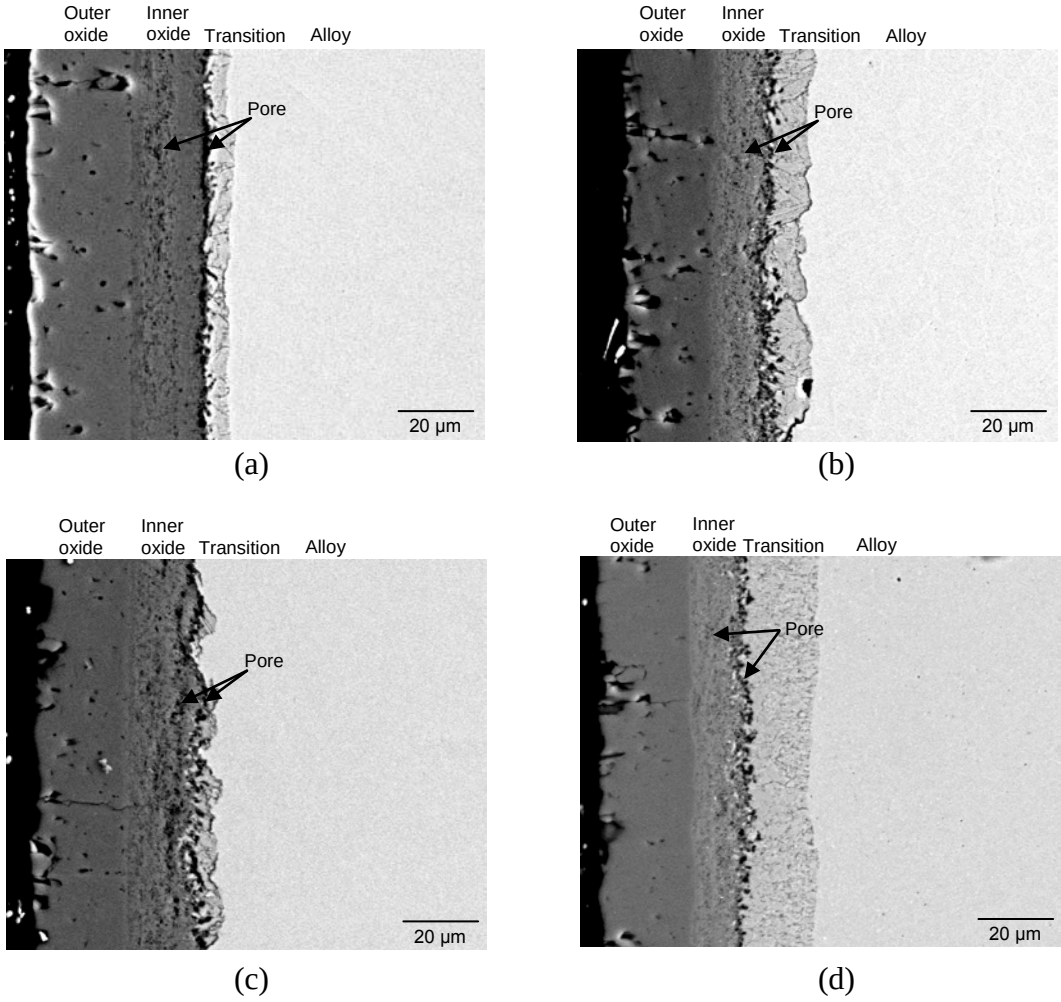

Figure 5.17 Cross section BSE images of (a) T91, (b) HCM12A, (c) HT-9 and (d) 9Cr-ODS show pore formation in inner oxide at i) the interface inner oxide and transition layer, and ii) in the inner oxide. The samples were exposed in 600°C deaerated SCW.

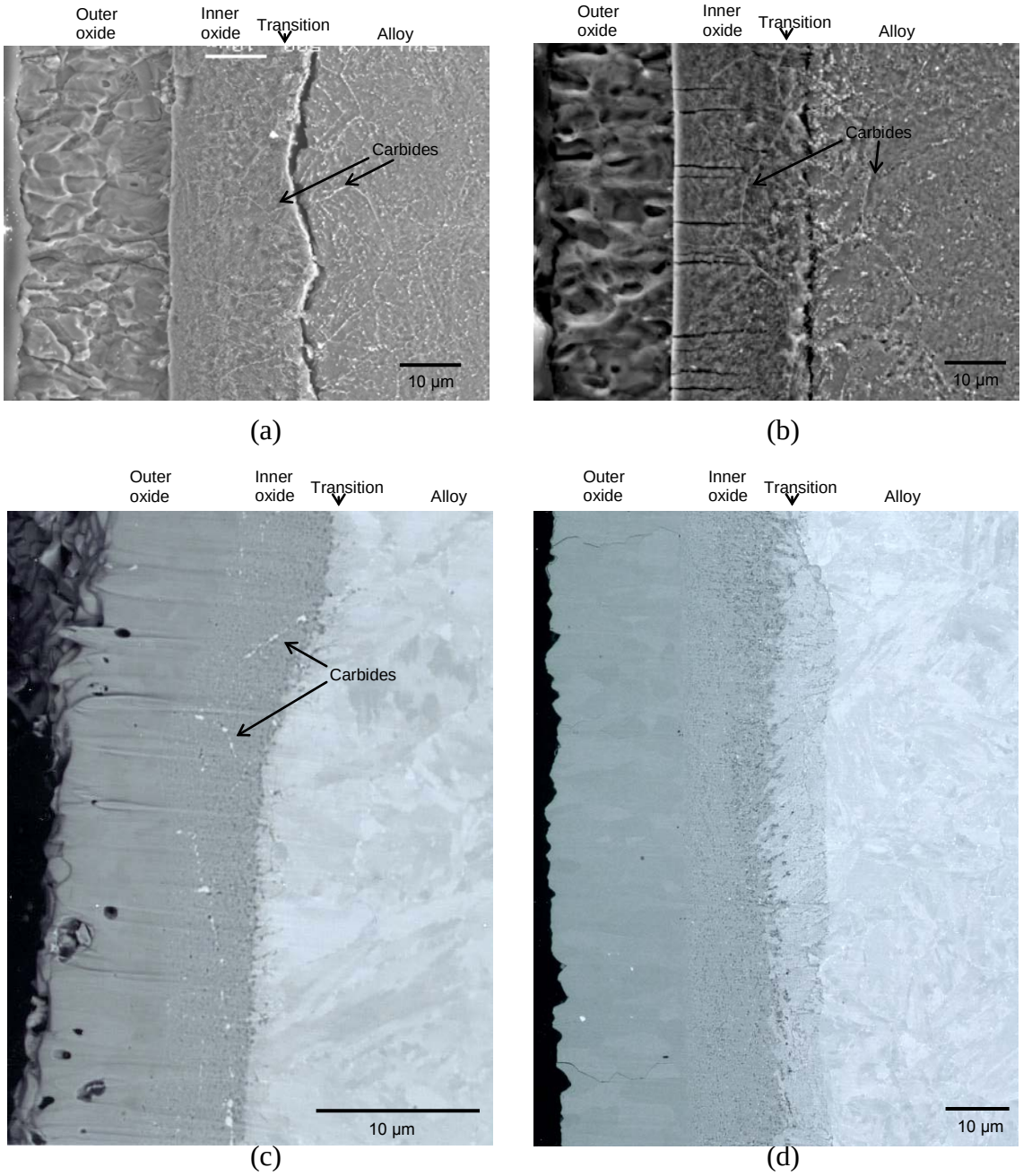

Figure 5.18 SEM cross section images of etched samples of (a) T91 and (b) HCM12A exposed in 600°C SCW for 191 hours. BSE images of HCM12A exposed in (c) 500°C SCW for 182 hours and (d) 600°C SCW for 191 hours. The samples in (c)-(d) were polished by Ar beam technique to avoid mechanical damage.

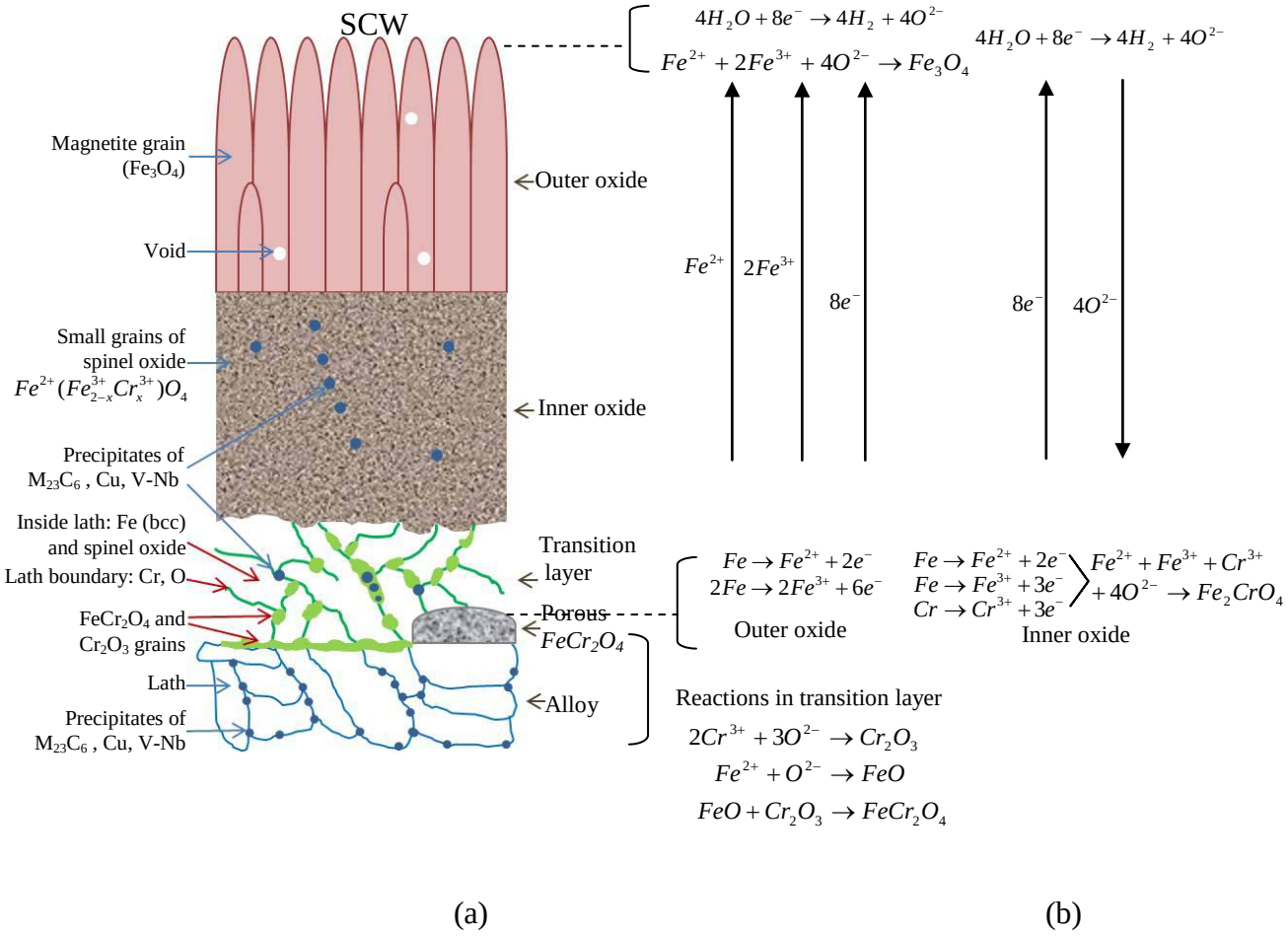

Figure 5.19 (a) Schematic diagram of oxide layer formed on HCM12A exposed in 600°C SCW. (b) Model of reactions and transport processes of ions involved in the growth of the outer oxide (Fe_3O_4), the inner oxide ($Fe_{3-x}Cr_xO_4$, assumed x = 1), and the transition layer.

BIBLIOGRAPHY

1. Chen, Y., K. Sridharan, and T. Allen, *Corrosion behavior of ferritic-martensitic steel T91 in supercritical water.* Corrosion Science, 2006. **48**(9): p. 2843-2854.
2. Chen, Y., et al., *Oxidation of 9Cr oxide dispersion strengthened steel exposed in supercritical water.* Journal of Nuclear Materials, 2007. **371**(1-3): p. 118-128.
3. Jang, J., et al., *Effect of Cr Content on Supercritical Water Corrosion of High Cr Alloys.* Materials Science Forum, 2005. **475-479**: p. 1483-1486.
4. Tan, L., X. Ren, and T.R. Allen, *Corrosion behavior of 9-12% Cr ferritic-martensitic steels in supercritical water.* Corrosion Science, 2010. **52**(4): p. 1520-1528.
5. Was, G.S. and T.R. Allen. *Time, Temperature, and Dissolved Oxygen Dependence of Oxidation of Austenitic and Ferritic-martensitic Alloys in Supercritical Water*. in *ICAPP'05*. 2005. Seoul, Korea.
6. Yin, K., et al., *Corrosion behavior of ferritic/martensitic steel P92 in supercritical water.* The Journal of Supercritical Fluids, 2009. **50**(3): p. 235-239.
7. Zhang, L., F. Zhu, and R. Tang, *Corrosion Mechanisms of Candidate Structural Materials for Supercritical Water-cooled Reactor.* Frontier Energy Power Engineering China, 2009. **3**(2): p. 233-240.
8. Atkinson, A., M.L. O'Dwyer, and R.I. Taylor, *^{55}Fe Diffusion in Magnetite Crystal at 500^{o}C and its Relevance to Oxidation of Iron.* Journal of materials science, 1983. **18**: p. 2371-2379.
9. Töpfer, J., S. Aggarwal, and R. Dieckmann, *Point defects and cation tracer diffusion in (CrxFe1 - x)3 - [delta]O4 spinels.* Solid State Ionics, 1995. **81**(3-4): p. 251-266.
10. GraphPad Software, I., *GraphPad InStat*, H. Motulsky, Editor. 2009, GraphPad Software, Inc.: La Jolla, CA.
11. Dieckmann, R., *Point defects and transport in non-stoichiometric oxides: Solved and unsolved problems.* Journal of Physics and Chemistry of Solids, 1998. **59**(4): p. 507-525.
12. Crouch, A.G. and J. Robertson, *Creep and Oxygen Diffusion in Magnetite.* Acta metall. mater., 1990. **38**(12): p. 2567-2572.
13. Horita, T., et al., *Diffusion of oxygen in the scales of Fe-Cr alloy interconnects and oxide coating layer for solid oxide fuel cells.* Solid State Ionics, 2008. **179**(38): p. 2216-2221.
14. Kofstad, P., *High Temperature Corrosion*. 1988, London and New York: Elsevier Applied Science.
15. Martinelli, L., et al., *Oxidation mechanism of a Fe-9Cr-1Mo steel by liquid Pb-Bi eutectic alloy (Part III).* Corrosion Science, 2008. **50**(9): p. 2549-2559.
16. Martinelli, L., et al., *Oxidation mechanism of an Fe-9Cr-1Mo steel by liquid Pb-Bi eutectic alloy at 470 °C (Part II).* Corrosion Science, 2008. **50**(9): p. 2537-2548.
17. Martinelli, L., et al., *Oxidation mechanism of a Fe-9Cr-1Mo steel by liquid Pb-Bi eutectic alloy (Part I).* Corrosion Science, 2008. **50**(9): p. 2523-2536.

18. Bene´tez Ve´lez, S., *Oxidation kinetics and mechanisms in HT-9 ferritic/martensitic stainless steel*, in *Materials Science and Engineering Department*. 2005, University of Florida: Gainesville, FL. p. 134.
19. Tomlinson, L. and N.J. Cory, *Hydrogen emission during the steam oxidation of ferritic steels: Kinetics and mechanism.* Corrosion Science, 1989. **29**(8): p. 939-965.
20. *http://database.iem.ac.ru*. 2009 [cited 2010 September, 2010].
21. *http://webelements.com*. 1993 [cited 2010 September, 2010].
22. Dieckmann, R. and H. Schmalzried, *Point Defects and Cation Diffusion in Magnetite.* Zeitschrift fur Anorganische und Allgemeine Chemie, 1975. **96**(3-4): p. 331-333.
23. Maruyama, T., et al., *Chemical Potential Distribution and Void Formation in Magnetite Scale Formed in Oxidation of Iron at 823K* Materials Science Forum, 2004. **461-464**: p. 807-814.
24. Millot, F. and N. Yan, *Diffusion of O_{18} in Fe_3O_4: An experimental approach to study the behavior of minority defects in oxides.* Journal of Physics and Chemistry of Solids, 1997. **58**(1): p. 63-72.
25. Tummers, B., J.v.d. Laan, and K. Huyser, *Data Thief III*. 2008, http://www.datathief.org.
26. Ueda, M. *Quantitative prediction of void formation in growing magnetite scale formed on iron at 823 K*. in *Materials Science and Technology Conference and Exhibition, MS and T'07 - "Exploring Structure, Processing, and Applications Across Multiple Materials Systems"*. 2007.
27. Seminario, J.M., et al., *Theoretical Analyses of O_2/H_2O Systems under Normal and Supercritical Conditions.* Chemical Physics Letters, 1994. **222**: p. 25-32.
28. Macdonald, D.D., et al., *Supercritical Water Oxidation Studies: Understanding the chemistry and electrochemistry of SCWO systems*. 1997, Pennsylvania State University: University Park, PA. p. 328.
29. Sander, R., *Compilation of Henry's Law Constants for Inorganic and Organic Species of Potential Importance in Environmental Chemistry*. 1999, http://www.mpch-mainz.mpg.de/~sander/res/henry.html. p. 107.
30. Garnaud, G. and R.A. Rapp, *Thickness of the oxide layers formed during the oxidation of iron.* Oxidation of Metals, 1977. **11**(4): p. 193-198.
31. *FactSage*©. 1976 - 2004, ThermFact Inc. & GTT-Technologies.
32. O'Neill, H.S.C. and W.A. Dollase, *Crystal Structures and Cation Distributions in Simple Spinels from Powder XRD Structural Refinements: $MgCr_2O_4$, $ZnCr_2O_4$, Fe_3O_4 and the Temperature Dependence of the Cation Distribution in $ZnAl_2O_4$.* Physics and Chemistry of Minerals, 1994. **20**(8): p. 541-555.
33. Magalhães, F., et al., *Cr-containing magnetites $Fe_{3-x}Cr_xO_4$: The role of Cr^{3+} and Fe^{2+} on the stability and reactivity towards H_2O_2 reactions.* Applied Catalysis A: General, 2007. **332**(1): p. 115-123.
34. Gillot, B., et al., *Study of the Oxidation Kinetics of Finely-divided Manetites. II-Influence of Chromium Substitution.* Materials Research Bulletin, 1976. **11**: p. 843-850.
35. *ASM Handbook* in *Vol. 13A Corrosion: Fundamentals, Testing, and Protection*. 2003, ASM International: Ohio.

36. Schütze, M., *Protective Oxide Scales and Their Breakdown*. 1997, NY: John Wiley & Sons, Inc.
37. Robertson, J., *The mechanism of high temperature aqueous corrosion of steel.* Corrosion Science, 1989. **29**(11-12): p. 1275-1291.
38. Robertson, J., *The mechanism of high temperature aqueous corrosion of stainless steels.* Corrosion Science, 1991. **32**(4): p. 443-465.
39. Robertson, J. and M.I. Manning, *Criteria for Formation of Single Layer, Duplex, and Breakaway Scales on Steels.* Materials Science and Technology, 1988. **4**(12): p. 1064-1071.
40. Robertson, J. and M.I. Manning, *Healing Layer Formation in Fe-Cr-Si Ferritic Steels.* Materials Science and Technology, 1989. **5**(8): p. 741-753.
41. *A Handbook of Physical Constants, Mineral Physics and Crystallography*. AGU reference. 1995: The Americal Geophysical Union.
42. Robertson, J. and M.I. Manning, *Limits to Adherence of Oxide Scales.* Materials Science and Technology, 1990. **6**: p. 81-91.
43. Bischoff, J., A.T. Motta, and R.J. Comstock, *Evolution of the oxide structure of 9CrODS steel exposed to supercritical water*. Journal of Nuclear Materials, 2009. **392**(2): p. 272-279.
44. Chen, Y., et al., *Microstructural examination of oxide layers formed on an oxide dispersion strengthened ferritic steel exposed to supercritical water.* Journal of Nuclear Materials, 2006. **359**(1-2): p. 50-58.
45. Motta, A.T., et al. *Microbeam Synchrotron Radiation Diffraction and Fluorescence Study of Oxide Layers Formed on 9Cr ODS Steel in Supercritical Water*. in *13th International Conference on Environmental Degradation of Materials in Nuclear Power Systems*. 2007. Whistler, British Columbia.
46. Lu, Z., et al., *Irradiation-induced Grain Boundary Chromium Microchemistry in High Alloy Ferritic Steels.* Scripta Materialia, 2008. **58**: p. 878-881.
47. Saltelli, A., O.K. Chopra, and K. Natesan, *An Assessment of Carburization-decarburization Behavior of Fe-9Cr-Mo Steels in a Sodium Environment.* Journal of Nuclear Materials, 1982. **110**: p. 1-10.
48. Wright, I.G. and B.A. Pint. *An Assessment of the High-temperature Oxidation Behavior of Fe–Cr steels in Water Vapor and Steam*. in *NACE Corrosion*. 2002. Denver, CO: NACE.
49. Hoelzer, D.T., B.A. Pint, and I.G. Wright, *A microstructural study of the oxide scale formation on ODS Fe-13Cr steel.* Journal of Nuclear Materials, 2000. **283-287**(Part 2): p. 1306.
50. Kimura, A., et al. *Super ODS Steels R&D for Cladding of Highly Efficient Nuclear Plants*. in *ICAPP'07*. 2007. Nice, France.
51. Ehlers, J., et al., *Enhanced Oxidation of the 9%Cr Steel P91 in Water Vapour Containing Environments.* Corrosion Science, 2006. **48**(11): p. 3428-3454
52. Kofstad, P., *Defects and transport properties of metal oxides.* Oxidation of Metals, 1995. **44**(1-2): p. 3-27.
53. Maruyama, T., M. Ueda, and K. Kawamura, *Void Formation in the Growing Scale Induced by the Divergence of the Diffusive Ionic Flux in High Temperature Oxidation of Metals.* Defect and Diffusion Forum, 2009. **289-292**: p. 1-13.

54. Tan, L., Y. Yang, and T.R. Allen, *Porosity prediction in supercritical water exposed ferritic/martensitic steel HCM12A.* Corrosion Science, 2006. **48**(12): p. 4234.
55. Klueh, R.L., *Elevated Temperature Ferritic and Martensitic Steels and Their Application to Future Nuclear Reactors.* International Materials Reviews, 2005. **50**(5): p. 287-310.
56. Laverde, D., T. Gómez-Acebo, and F. Castro, *Continuous and Cyclic Oxidation of T91 Ferritic Steel Under Steam.* Corrosion Science, 2004. **46**: p. 613-631.
57. Vélez, S.B., *Oxidation Kinetics and Mechanisms in HT-9 Ferritic/martensitic Stainless Steel*, in *Materials Science and Engineering*. 2005, University of Florida. p. 134.
58. Castle, J.E. and P.L. Surman, *The Self-diffusion of Oxygen in Magnetite. Techniques for Sampling and Isotopic Analysis of Micro Quantities of Water*. Journal of physical chemistry, 1967. **71**(13).
59. Sharp, Z.D., *Determination of Oxygen Diffusion Rates in Magnetite from Natural Isotopic Variations.* Geology, 1991. **19**(6): p. 653-656.
60. Giletti, B.J. and K.C. Hess, *Oxygen diffusion in magnetite.* Earth and Planetary Science Letters, 1988. **89**: p. 115-122.
61. Tang, J., et al., *Magnetite Fe3O4 Nanocrystals: Spectroscopic observation of aqueous oxidation kinetics.* Journal of Physical Chemistry B, 2003. **107**(30): p. 7501-7506.
62. Harrop, P.J., *Self-Diffusion in Simple Oxides (A Bilbliography).* Journal of Materials Science, 1968. **3**: p. 206-222.
63. Izvekov, V.I. and K.M. Gorbunova. *Study of Iron Diffusion in Corundum, Magnetite, and Rutle with the Help of Fe^{59} Indicator*. in *The use of radioactive and stable isotopes and radiation in the national economy and in science*. 1958. Moscow, USSR: Acad. Sci.
64. Himmel, L., R.T. Mehl, and C.E. Birchenall, *Self-diffusion of Iron in Iron Oxides and Wagner Theory of Oxidation.* J. Metals, 1953. **5**(6): p. 827-843.
65. Klotsmann, S.M. and A.N. Timofeyev, *The Problem of the Measurement of Diffusion Coefficients in Oxide Phases (in Russian).* Fitz. Merall. i merallov (Phys. Metals Metallogr.), 1969. **10**: p. 93.
66. Hagel, W.C., *Anion Diffusion in α-Cr_2O_3.* Journal of American Ceramic Society, 1965. **48**: p. 70.
67. Sabioni, A.C.S., et al., *Diffusion of Iron in Cr_2O_3: Polycrystals and Thin Films.* Materials Science and Engineering: A, 2005. **392**(1-2): p. 254-261.
68. Ignatov, D.V., I.N. Belokurova, and I.N. Belganin. *An Investigation of the Diffusion Processes of Iron and Chromium in the Oxides of α-Al_2O_3, α-Cr2O3, $NiCr_2O_4$ and $NiAl_2O_4$.* in *The Use of Radioactive and Stable Isotopes and Radiation in the National Economy and in Science*. 1958. USSR.
69. Hagel, W.C. and A.U. Seybolt, *Cation Diffusion in Cr_2O_3.* Journal of Electrochemical Society, 1961. **108**: p. 1146.
70. Fedorchenko, I.M. and Y.B. Ermolovich, *Diffusion of Chromium Through its Oxide.* Chemical Abstract, 1960. **55**: p. 7219b.

71. Kingery, W.D., D.C. Hill, and R.P. Nelson, *Oxygen Mobility in Polycrystalline $NiCr_2O_4$ and α-Fe_2O_3.* Journal of the American Ceramic Society, 1960. **43**(9): p. 473-475.
72. O'Bryan, H.M. and F.V. DiMarcello, J. Am. Ceram. Soc., 1970. **53**: p. 413.
73. Belokurova, I.N. and D.V. Ignatov, *Investigation of the Processes of Iron and Chromium Diffusion in the Spinels $NiCr_2O_4$ and $NiAl_2O_4$ using Fe^{59} and Cr^{51}.* Atomic Energy, 1958. **4**(3): p. 399-400.
74. Nakamura, A., et al., *Vacancy diffusion in magnetite.* Journal of Physics and Chemistry of Solids, 1978. **39**(11): p. 1203-1206.
75. Sabioni, A.C.S., et al., *Measurement of Iron Self-diffusion in Hematite Single Crystal by Secondary Ion-mass Spectrometry (SIMS) and Comparison with Cation Self-diffusion in Corundum-structure Oxides.* Philosophical Magazine, 2005. **85**(31): p. 3643 - 3658.
76. Tsai, S.C., A.M. Huntz, and C. Dolin, *Growth Mechanism of Cr_2O_3 Scales: Oxygen and chromium diffusion, oxidation kinetics and effect of yttrium.* Materials Science and Engineering, 1996. **A212**: p. 6-13.
77. Föll, H. *Ionic Crystals*. Available from: http://www.tf.uni-kiel.de/matwis/amat/def_en/kap_2/basics/b2_1_6.html.

CHAPTER 6

CONCLUSION

The study of oxidation mechanisms of F-M alloys, T91, HCM12A, HT-9 and 9Cr-ODS exposed in at 400 – 600°C supercritical water leads to the understanding of oxidation mechanisms. The conclusions of this thesis are;

1. Microstructure of oxide formed on four F-M alloys; T91, HCM12A, HT-9 and 9Cr-ODS, exposed in 400 – 600°C SCW consisted of two oxide layers and a transition layer. The microstructure changes with the SCW temperature and the alloy type. The outer oxide consisted of columnar grains of magnetite. The inner oxide consisted of small equiaxed grains of Fe-Cr spinel oxide $Fe^{2+}(Fe^{3+}_{2-x}Cr^{3+}_{x})O^{2-}_{4}$, where x = 0.7, 0.9, 1.0 and 0.7 for T91, HCM12A, HT-9 and 9Cr-ODS, respectively. Defects including micropores and microcracks were observed in the inner oxide. The transition layer consisted of grain boundary oxidation and fine oxide grains precipitated inside the laths. Chromia and chromite formed at the lath boundaries. Precipitate particles of minor alloying elements distributed in the inner oxide and the transition layer.
2. Oxidation rate was determined from weight gain and oxide thickness for each alloy. The weight gain and oxide thickness increased as a function of exposure time, and obey the power law. The time exponents of weight gain are ~0.31 –

0.45. The time exponents of outer oxide, inner oxide and total thickness are ~0.37 – 0.44. The exponent is different for the transition layer, n ~0.20-0.27. This implies that the mechanisms in the outer and inner oxide are different from that of transition layer. Deviation from n = 0.5 (parabolic law) indicates short circuit diffusions along grain boundaries or defects in oxide scales.

3. The SCW temperature has a great effect on oxidation. Weight gain and oxide thickness increased exponentially as a function of temperature, which can be expressed as an Arrhenius equation. Activation energies were determined from relation of weight gain and oxide layer thicknesses versus temperature. Oxide phases in the outer and inner layer remain unchanged for exposure temperature 400 – 600°C. For the transition layer, Cr-rich oxide of $FeCr_2O_4$ formed at lath boundaries at three temperatures, but additional phases of Cr_2O_3 and porous $FeCr_2O_4$ was observed at 600°C.
4. The oxide microstructure shows that the original alloy surface is the interface of inner and outer oxide. Mass balance between the inner and outer oxide also proved this hypothesis. It is concluded that two major ion species that play an important role in oxidation mechanism are Fe and O ions. This confirms the hypotheses of; i) the outer oxide grows by outward diffusion of Fe, iii) the inner oxide grows by inward diffusion of O and iii) Cr diffusion is negligible.
5. Rate limiting processes was determined using activation energy of oxidation and diffusion coefficients of Fe and O in magnetite and Fe-Cr spinel oxide. The activation energy of oxidation indicates occurrence of short circuit diffusion. It

was found that the rate limiting process is Fe diffusion. Diffusion of oxygen mostly occurred along short circuit diffusion paths.

6. Determination of oxygen partial pressure can be achieved using Wagner's equation for spinel structure oxide (magnetite and Fe-Cr spinel oxide), which is expressed in terms of k_p'', D_{Fe} and P_{O_2}. For the spinel structure oxide, the diffusion coefficient of Fe depends on P_{O_2}. Using the P_{O_2} at transition layer – inner oxide obtained from phase diagram, the P_{O_2} at the inner – outer oxide interface and the outer oxide – water interface can be calculated.
7. Formation of the outer oxide occurs by outward diffusion of Fe ions. The oxide phase depends on the P_{O_2}. The calculated P_{O_2} at the outer oxide – water interface are approximately in the orders of 10^{-23}, 10^{-19} and 10^{-15} atm at 400, 500 and 600°C, respectively. These values are consistent with the P_{O_2} that Fe_3O_4 is stable in the phase diagram. Transport of Fe ions in the outer oxide is dominated by vacancy diffusion mechanism.
8. Formation of the inner oxide occurs by inward diffusion of oxygen. Micro and nano-size pores are resulted from outward diffusion of Fe ions to the outer oxide. Calculated P_{O_2} at the inner – outer oxide interface are approximately in the orders of 10^{-23}, 10^{-19} and 10^{-16} atm at 400, 500 and 600°C, respectively. The values are much higher than those of at the transition – inner oxide interface, which determined from the phase diagram. The reason is that the dominate diffusion mechanism changes in the inner layer oxide. However, the P_{O_2} values are consistent with those from phase diagram in which Fe-Cr spinel oxide is stable.

9. Transition layer formed by grain boundary oxidation. In this layer, Fe diffused outward and O diffused inward primarily at grain boundaries, and partly at intra-laths. Cr diffused from the lath matrix forming Cr-rich oxides at the lath boundaries. The effect of Cr is more pronounce at 600°C. In HT-9 exposed at 600°C, Cr concentration is high enough to form chromite layer at the interface of transition layer – inner oxide.
10. Transport of Fe ions mostly assisted by cation vacancy diffusion. Only small region near the transition layer – inner oxide interface that the interstitial diffusion dominates. Oxygen transport occurred primarily by the short-circuit diffusion.

CHAPTER 7

FUTURE WORK

The study in this thesis is sufficient to provide insight into the oxidation mechanisms of F-M alloys in SCW. However, there are several options of future work that can gain more understandings for the oxidation mechanisms. Suggested future works included; determinate the oxidation potential in SCW, understand the diffusion mechanism of O and Fe ions through the short circuit diffusion paths in oxides, determine the effects of minor alloying elements in the ODS alloys.

First of all, study in this thesis focused on understanding of the formation of oxide on the F-M alloys exposed in SCW through studies of the oxide microstructure and the oxidation rate. However, a part of information on the SCW side is not yet clearly understood. Oxygen partial pressure on the specimen surface cannot be determined directly from the oxygen partial pressure of dissolved oxygen. One major challenge is to understand the SCW properties involve solubility of oxygen and dissociation of water molecules. As mentioned in the background section, oxygen is considered miscible in SCW. Dissociation of water molecules of, which considered from the dielectric constant, is relatively low compared to that of liquid phase but higher than that of gaseous phase. Understanding of these properties is necessary to monitor the oxidation potential in SCW, which will be very useful in the SCWR.

Next suggested work involves the understanding of the diffusion mechanism of Fe and O through the short circuit diffusion paths in oxide scales. Current knowledge of diffusion mechanism is limited only for the lattice diffusion cases. The oxygen partial pressure dependence of diffusivities of Fe and O ions in a spinel structure oxide needs to be modified by including the short circuit diffusion effect. Diffusion of O ions is also not quite well understood in terms of diffusing ion species and their diffusion processes. Understand these mechanisms will provide the information for the oxidation rate model.

Last additional suggested work involves the study of effect of minor alloying elements on the oxidation mechanism. Results from 9Cr-ODS alloy showed that the minor alloying element of Y_2O_3 nano-particles has a major influence on the oxidation rate and the oxide microstructure. The oxidation resistance of this alloy is higher than that of T91 with a similar Cr content. The oxide microstructure consisted of a large transition layer, which resulted in large area that contained Cr-rich oxide. The effect of these nano-particles is not quite well understood. Determination of this issue will provide an idea to improve an oxidation resistance alloy in the future.

APPENDIX I

Diffraction pattern from Joint committee on powder diffraction standard (JCPDS)

I.1 Fe, Iron (BCC)

PDF # 06-0696
Structure: $Im\bar{3}m$ Space group: 229
Lattice parameter: a = 2.8664 Å
Analysis X-ray: Cu $K\alpha_1$ Wavelength: 1.5406 Å
Strong lines (d)[1]: $2.03_X\ 1.17_3\ 1.43_2$

Table I.1 List of interplana spacing (d), relative intensity (I), diffraction planes (hkl) and angles (2-theta) for Fe (BCC)

d(Å)	Int.[2]	h	k	l	2-theta[3]
2.0268	100	1	1	0	44.673
1.4332	28	2	0	0	65.021
1.1702	52	2	1	1	82.333
1.0134	20	2	2	0	98.945
0.9064	27	3	1	0	116.385
0.8275	15	2	2	2	137.136

[1] Strong lines are three highest intensity peaks in diffraction pattern. Subscript denotes intensity of that peak divided by 10, and subscript X =100%.
[2] Relative intensity of each peak to highest peak. The highest peak is assigned as 100%.
[3] 2-theta from analysis X-ray listed for each structure.

I.2 Fe_3O_4, Magnetite

PDF # 75-0449

Structure: $Fd\bar{3}m$ Space group: 227

Lattice parameter: a = 8.3970 Å

Analysis X-ray: Cu $K\alpha_1$ Wavelength: 1.5406 Å

Strong lines (d): 2.51_X 1.47_6 1.60_4

Table I.2 List of interplana spacing (d), relative intensity (I), diffraction planes (hkl) and angles (2-theta) for Fe_3O_4

d(Å)	Int.	h	k	l	2-theta
4.7978	4	1	1	1	18.478
2.9380	25	2	2	0	30.398
2.5056	100	3	1	1	35.809
2.3989	8	2	2	2	37.459
2.0775	24	4	0	0	43.527
1.9064	1	3	3	1	47.662
1.6963	12	4	2	2	54.014
1.5993	38	5	1	1	57.586
1.4690	56	4	4	0	63.249
1.4046	2	5	3	1	66.512
1.3139	4	6	2	0	71.782
1.2673	12	5	3	3	74.866
1.2528	4	6	2	2	75.883
1.1995	4	4	4	4	79.911
1.1636	2	5	5	1	82.900
1.1105	5	6	4	2	87.840

I.3 Fe_2O_3, Hematite

PDF # 72-0469

Structure: $R\bar{3}c$ (rhombohedral) Space group: 167

Lattice parameter: a = 5.0380, c = 13.7720 Å, 90.0 x 90.0 x 120.0

Analysis X-ray: Cu $K\alpha_1$ Wavelength: 1.5406 Å

Strong lines (d): 2.70_X 2.52_8 1.70_7

Table I.3 List of interplana spacing (d), relative intensity (I), diffraction planes (hkl) and angles (2-theta) for Fe_2O_3

d(Å)	Int.	h	k	l	2-theta
3.6855	23	0	1	2	24.128
2.7028	100	1	0	4	33.117
2.5190	75	1	1	0	35.611
2.2953	2	0	0	6	39.216
2.2084	23	1	1	3	40.828
2.0796	3	2	0	2	43.479
1.8428	50	0	2	4	49.417
1.6966	65	1	1	6	54.002
1.6374	2	2	1	1	56.125
1.6014	14	0	1	8	57.504
1.4873	45	2	1	4	62.385
1.4543	45	3	0	0	63.962
1.4149	2	1	2	5	65.969
1.3514	6	2	0	8	69.499
1.3133	19	1	0	10	71.819
1.3078	4	1	1	9	72.169
1.2638	2	2	1	7	75.104
1.2595	11	2	2	0	75.407
1.2285	4	0	3	6	77.659
1.2146	2	2	2	3	78.718
1.2054	2	1	3	1	79.435
1.1909	9	1	2	8	80.606
1.1645	9	0	2	10	82.820
1.1477	2	0	0	12	84.315
1.1416	14	1	3	4	84.865
1.1042	15	2	2	6	88.469

I.4 $FeCr_2O_4$, Chromite

PDF # 00-034-0140

Structure: $Fd\bar{3}m$ Space group: 227

Lattice parameter: a = 8.3790 Å

Analysis X-ray: Cu $K\alpha_1$ Wavelength: 1.5406 Å

Strong lines (d): 2.53_X 1.48_5 1.61_4

Table I.4 List of interplana spacing (d), relative intensity (I), diffraction planes (hkl) and angles (2-theta) for $FeCr_2O_4$

d(Å)	Int.	h	k	l	2-theta
4.8390	13.0	1	1	1	18.3192
2.9620	33.0	2	2	0	30.1471
2.5260	100.0	3	1	1	35.5099
2.4180	7.0	2	2	2	37.1526
2.0943	22.0	4	0	0	43.1607
1.7105	11.0	4	2	2	53.5301
1.6125	39.0	5	1	1	57.0709
1.4812	48.0	4	4	0	62.6709
1.4162	2.0	5	3	1	65.9013
1.3247	3.0	6	2	0	71.1103
1.2777	10.0	5	3	3	74.1523
1.2632	5.0	6	2	2	75.1496
1.2095	3.0	4	4	4	79.1177
1.1734	1.0	7	1	1	82.0615
1.1197	4.0	6	4	2	86.9357
1.0907	12.0	7	3	1	89.8595
1.0476	5.0	8	0	0	94.6643
0.9873	2.0	6	6	0	102.5584
0.9675	10.0	7	5	1	105.5319
0.9612	2.0	6	6	2	106.5259
0.9367	2.0	8	4	0	110.6414
0.8931	1.0	6	6	4	119.1959
0.8783	5.0	9	3	1	122.5722
0.8552	12.0	8	4	4	128.5055
0.8217	1.0	10	2	0	139.2522
0.8101	7.0	9	5	1	143.9287
0.8063	<1	10	2	2	145.6260

I.5 Cr_2O_3, Eskolaite

PDF # 00-038-1479

Structure: $R\bar{3}c$ (rhombohedral) Space group: 167

Lattice parameter: a = 4.9588, c = 13.5942 Å, 90.0 x 90.0 x 120.0

Analysis X-ray: Cu $K\alpha_1$ Wavelength: 1.5406 Å

Strong lines d): 2.67_X 2.48_9 1.67_9

Table I.5 List of interplana spacing d), relative intensity I), diffraction planes hkl) and angles 2-theta) for Cr_2O_3

d(Å)	Int.	h	k	l	2-theta	d(Å)	Int.	h	k	l	2-theta
3.6313	73	0	1	2	24.4939	1.0875	13	2	2	6	90.2016
2.6653	100	1	0	4	33.5969	1.0602	1	0	4	2	93.1924
2.4797	93	1	1	0	36.1958	1.0421	9	2	1	10	95.3273
2.2659	7	0	0	6	39.7487	1.0306	1	1	1	12	96.7329
2.1752	35	1	1	3	41.4798	1.0238	2	4	0	4	97.5902
2.0477	6	2	0	2	44.1938	0.975	<1	2	3	2	104.3842
1.8152	38	0	2	4	50.2198	0.9583	<1	2	2	9	106.9942
1.6724	87	1	1	6	54.8518	0.9463	6	3	2	4	108.9842
1.6115	<1	2	1	1	57.1107	0.937	5	4	1	0	110.5872
1.579	7	1	2	2	58.3966	0.9177	<1	4	1	3	114.144
1.4649	28	2	1	4	63.4484	0.8958	7	1	3	10	118.607
1.4316	39	3	0	0	65.1057	0.8883	3	3	0	12	120.266
1.2959	14	1	0	10	72.9437	0.8847	1	2	0	14	121.0799
1.29	6	1	1	9	73.3283	0.866	10	4	1	6	125.6229
1.2394	9	2	2	0	76.8502	0.8426	3	4	0	10	132.1725
1.2103	6	3	0	6	79.0552	0.8363	1	2	2	12	134.1626
1.1959	1	2	2	3	80.1992	0.8332	6	1	2	14	135.1724
1.1731	4	3	1	2	82.0913	0.8327	3	0	5	4	135.3616
1.1485	7	0	2	10	84.2381	0.8265	4	3	3	0	137.5024
1.1329	2	0	0	12	85.6813	0.7978	5	3	2	10	149.8418
1.1238	7	1	3	4	86.5382						

I.6 $Cr_{23}C_6$, Chromium carbide

PDF # 35-0783

Structure: $Fm\bar{3}m$ Space group: 225

Lattice parameter: a = 10.6599 Å

Analysis X-ray: Cu $K\alpha_1$ Wavelength: 1.5406 Å

Strong lines (d): 2.05_X 2.18_2 2.38_2

Table I.6 List of interplana spacing (d), relative intensity (I), diffraction planes (hkl) and angles (2-theta) for $Cr_{23}C_6$

d(Å)	Int.	h	k	l	2-theta
6.1481	1	1	1	1	12.5291
3.2136	1	3	1	1	23.9701
3.0772	1	2	2	2	25.0326
2.6657	4	4	0	0	28.8968
2.4452	1	3	3	1	31.5027
2.3830	23	4	2	0	32.3250
2.1761	24	4	2	2	35.3984
2.0519	100	5	1	1	37.5411
1.8840	20	4	4	0	40.8868
1.8016	22	5	3	1	42.7568
1.7766	12	6	0	0	43.3585
1.6857	2	6	2	0	45.6966
1.6260	2	5	3	3	47.3745
1.6066	6	6	2	2	47.9465
1.4930	<1	5	5	1	51.5948
1.4787	<1	6	4	0	52.0938
1.3326	2	8	0	0	57.8053
1.2927	2	8	2	0	59.5895
1.2560	12	8	2	2	61.3308
1.2307	6	7	5	1	62.5916
1.2227	15	6	6	2	63.0012
1.1919	2	8	4	0	64.6293
1.1698	4	9	1	1	65.8503
1.1174	1	9	3	1	68.9385
1.0878	6	8	4	4	70.8145
1.0712	3	7	7	1	71.9119
1.0452	<1	10	2	0	73.7008
1.0259	1	10	2	2	75.0874

APPENDIX II

Analysis of X-ray diffraction pattern

X-ray diffraction pattern listed in this appendix are measured by glancing angle X-ray diffractometer. The analyses were done by calculating d-spacing of each peak and comparing with standard diffraction pattern of expected phase listed in Appendix I. The diffraction patterns that are not listed here were measured by a regular θ-2θ diffractometer and analyzed using computer software from the machine.

II.1 T91 alloy

Phase	plane			standard			measured		Δd
	h	k	l	Int.	$2\theta_{std.}$ (degree)	$d_{std.}$ (Å)	$2\theta_{meas.}$ (degree)	$d_{meas.}$ (Å)	$d_{meas.}$-$d_{std.}$
Fe (bcc)	1	1	0	100	44.673	2.0268	44.72	2.0267	-0.0001
	2	0	0	20	65.021	1.4332	64.80	1.4389	0.0057
	2	1	1	30	82.333	1.1702	82.24	1.1724	0.0022
	2	2	0	10	98.945	1.0134	ND		
	3	1	0	12	116.385	0.9064	ND		
	2	2	2	6	137.136	0.8275	ND		

ND : not detected

II.2 T91 exposed in 400°C DSCW for 151 hours

Phase	plane			standard			measured		Δd
	h	k	l	Int.	$2\theta_{std.}$ (degree)	$d_{std.}$ (Å)	$2\theta_{meas.}$ (degree)	$d_{meas.}$ (Å)	$d_{meas.}$-$d_{std.}$
Fe_3O_4	1	1	1	7	18.478	4.7978	ND		
	2	2	0	29	30.398	2.938	30.22	2.9559	0.0179
	3	1	1	100	35.809	2.5056	35.68	2.5150	0.0094
	2	2	2	8	37.459	2.3989	37.30	2.4100	0.0111
	4	0	0	20	43.527	2.0775	43.34	2.0860	0.0085
	3	3	1	1	47.662	1.9064	ND		
	4	2	2	8	54.014	1.6963	53.69	1.7060	0.0097
	5	1	1	24	57.586	1.5993	57.29	1.6070	0.0077
	4	4	0	33	63.249	1.4690	62.88	1.4770	0.008
	5	3	1	1	66.512	1.4046	ND		
	6	2	0	2	71.782	1.3139	ND		
	5	3	3	6	74.866	1.2673	74.32	1.2760	0.0087
	6	2	2	2	75.883	1.2528	ND		
	4	4	4	2	79.911	1.1995	79.28	1.208	0.0085

	6	4	2	2	87.84	1.1105	ND		
Fe	1	1	0	100	44.673	2.0268	44.85	2.0196	-0.0072
	2	0	0	20	65.021	1.4332	ND		
	2	1	1	30	82.333	1.1702	ND		

II.3 T91 exposed in 500°C DSCW for 182 hours

Phase	plane			standard			measured		Δd
	h	k	l	Int.	$2\theta_{std.}$ (degree)	$d_{std.}$ (Å)	$2\theta_{meas.}$ (degree)	$d_{meas.}$ (Å)	$d_{meas.}$-$d_{std.}$
Fe_3O_4	1	1	1	7	18.478	4.7978			
	2	2	0	29	30.398	2.938	30.44	2.9351	-0.0029
	3	1	1	100	35.809	2.5056	35.89	2.5005	-0.0051
	2	2	2	8	37.459	2.3989			
	4	0	0	20	43.527	2.0775	43.55	2.0771	-0.0004
	3	3	1	1	47.662	1.9064			
	4	2	2	8	54.014	1.6963	53.98	1.6977	0.0014
	5	1	1	24	57.586	1.5993	57.68	1.5974	-0.0019
	4	4	0	33	63.249	1.469	63.07	1.4733	0.0043
	5	3	1	1	66.512	1.4046	ND		
	6	2	0	2	71.782	1.3139	ND		

II.4 T91 exposed in 500°C SCW containing 100 ppb DO for 236 hours

Phase	plane			standard			measured		Δd
	h	k	l	Int.	$2\theta_{std.}$ (degree)	$d_{std.}$ (Å)	$2\theta_{meas.}$ (degree)	$d_{meas.}$ (Å)	$d_{meas.}$-$d_{std.}$
Fe_3O_4	1	1	1	7	18.478	4.7978			
	2	2	0	29	30.398	2.938	30.42	2.938737	0.000737
	3	1	1	100	35.809	2.5056	35.78	2.509843	0.004243
	2	2	2	8	37.459	2.3989	ND		
	4	0	0	20	43.527	2.0775	43.48	2.08156	0.00406
	3	3	1	1	47.662	1.9064	ND		
	4	2	2	8	54.014	1.6963	53.82	1.703527	0.007227
	5	1	1	24	57.586	1.5993	57.42	1.604991	0.005691
	4	4	0	33	63.249	1.469	62.96	1.476443	0.007443
	5	3	1	1	66.512	1.4046	ND		
	6	2	0	2	71.782	1.3139	ND		
	5	3	3	6	74.866	1.2673	74.48	1.274054	0.006754

II.5 HCM12A exposed in 400°C DSCW for 151 hours

Phase	plane			standard			measured		Δd
	h	k	l	Int.	$2\theta_{std.}$ (degree)	$d_{std.}$ (Å)	$2\theta_{meas.}$ (degree)	$d_{meas.}$ (Å)	$d_{meas.}$-$d_{std.}$
Fe_3O_4	1	1	1	7	18.478	4.7978	ND		
	2	2	0	29	30.398	2.938	30.66	2.9144	-0.0236
	3	1	1	100	35.809	2.5056	36.06	2.4891	-0.0165
	2	2	2	8	37.459	2.3989	37.5	2.3971	-0.0018
	4	0	0	20	43.527	2.0775	43.55	2.0772	-0.0003
	3	3	1	1	47.662	1.9064	47.87	1.8992	-0.0072
	4	2	2	8	54.014	1.6963	54.19	1.6917	-0.0046
	5	1	1	24	57.586	1.5993	57.69	1.5970	-0.0023
	4	4	0	33	63.249	1.469	63.28	1.4687	-0.0003
	5	3	1	1	66.512	1.4046	ND		
	6	2	0	2	71.782	1.3139	ND		
	5	3	3	6	74.866	1.2673	74.62	1.2712	0.0039
	6	2	2	2	75.883	1.2528	ND		
	4	4	4	2	79.911	1.1995	ND		
	6	4	2	2	87.84	1.1105	ND		
Fe	1	1	0	100	44.673	2.0268	45.46	2.0102	-0.0166
	2	0	0	20	65.021	1.4332	ND		
	2	1	1	30	82.333	1.1702	ND		

II.6 HCM12A exposed in 500°C DSCW for 182 hours

Phase	plane			standard			measured		Δd
	h	k	l	Int.	$2\theta_{std.}$ (degree)	$d_{std.}$ (Å)	$2\theta_{meas.}$ (degree)	$d_{meas.}$ (Å)	$d_{meas.}$-$d_{std.}$
Fe_3O_4	1	1	1	7	18.478	4.7978	ND		
	2	2	0	29	30.398	2.938	30.49	3.0052	0.0672
	3	1	1	100	35.809	2.5056	35.96	2.5499	0.0443
	2	2	2	8	37.459	2.3989	ND		
	4	0	0	20	43.527	2.0775	43.52	2.1145	0.0370
	3	3	1	1	47.662	1.9064	ND		
	4	2	2	8	54.014	1.6963	53.87	1.7242	0.0279
	5	1	1	24	57.586	1.5993	57.67	1.6176	0.0183
	4	4	0	33	63.249	1.469	63.36	1.4834	0.0144
	5	3	1	1	66.512	1.4046	ND		
	6	2	0	2	71.782	1.3139	ND		
	5	3	3	6	74.866	1.2673	74.61	1.2829	0.0156

II.7 HCM12A exposed in 500°C SCW containing 100 ppb DO for 236 hours

Phase	plane			standard			measured		Δd
	h	k	l	Int.	$2\theta_{std.}$ (degree)	$d_{std.}$ (Å)	$2\theta_{meas.}$ (degree)	$d_{meas.}$ (Å)	$d_{meas.}$-$d_{std.}$
Fe_3O_4	1	1	1	7	18.478	4.7978	ND		
	2	2	0	29	30.398	2.938	30.58	2.9222	-0.01581
	3	1	1	100	35.809	2.5056	35.94	2.4977	-0.00790
	2	2	2	8	37.459	2.3989	37.55	2.3938	-0.00501
	4	0	0	20	43.527	2.0775	43.60	2.0749	-0.00264
	3	3	1	1	47.662	1.9064	ND		
	4	2	2	8	54.014	1.6963	54.04	1.6961	-0.00025
	5	1	1	24	57.586	1.5993	57.54	1.6009	0.00157
	4	4	0	33	63.249	1.4690	63.38	1.4667	-0.00233
	5	3	1	1	66.512	1.4046	ND		
	6	2	0	2	71.782	1.3139	ND		
	5	3	3	6	74.866	1.2673	74.57	1.2719	0.00464

II.8 HT-9 exposed in 400°C DSCW for 151 hours

Phase	plane			standard			measured		Δd
	h	k	l	Int.	$2\theta_{std.}$ (degree)	$d_{std.}$ (Å)	$2\theta_{meas.}$ (degree)	$d_{meas.}$ (Å)	$d_{meas.}$-$d_{std.}$
Fe_3O_4	1	1	1	7	18.478	4.7978	ND		
	2	2	0	29	30.398	2.938	30.32	2.9460	0.008
	3	1	1	100	35.809	2.5056	35.78	2.5080	0.0024
	2	2	2	8	37.459	2.3989	ND		
	4	0	0	20	43.527	2.0775	43.34	2.086	0.0085
	3	3	1	1	47.662	1.9064	ND		
	4	2	2	8	54.014	1.6963	53.59	1.709	0.0127
	5	1	1	24	57.586	1.5993	57.39	1.6050	0.0057
	4	4	0	33	63.249	1.469	62.88	1.4770	0.008
	5	3	1	1	66.512	1.4046	ND		
	6	2	0	2	71.782	1.3139	ND		
	5	3	3	6	74.866	1.2673	ND		
	6	2	2	2	75.883	1.2528	ND		
	4	4	4	2	79.911	1.1995	ND		
	6	4	2	2	87.84	1.1105	ND		
Fe	1	1	0	100	44.673	2.0268	44.85	2.0196	-0.0072
	2	0	0	20	65.021	1.4332	ND		
	2	1	1	30	82.333	1.1702	ND		

APPENDIX III

Derivation of defect concentration in spinel structure oxide

In the spinel structure, there are 96 interstices available for cations, but only one half of octahedral and 1/8 of tetrahedral sites are occupied. Therefore a lot of unoccupied positions exist in the lattice. Cation vacancies are created by reaction of the cation and oxygen [1, 2];

$$3M^{2+} + \frac{2}{3}O_2 = 2M^{3+} + V_M + \frac{1}{3}M_3O_4 \qquad (1)$$

where m is the cation, V_M is the cation vacancy. Meanwhile, cation interstitials are formed by the M^{n+} ion moves to a nearest interstice site, creating a Frenkel defect pair;

$$M^{n+} + V_I = M_I^{n+} + V_M \qquad (2)$$

where n can be 2+ or 3+, V_I is the interstice site.

Concentration of cation vacancies and interstitial can be determined using the concept of point defect thermodynamic, and substitution of V_M into eqn. 4 [1, 2];

$$[V_M] = \frac{[M^{2+}]^3}{[M^{3+}]^2} K_V \frac{a_{O_2}^{2/3}}{a_{M_3O_4}^{1/3}} \approx \frac{K_V}{4} a_{O_2}^{2/3} = [V]^0 a_{O_2}^{2/3} \qquad (3)$$

and

$$[M_I^{n+}] = \frac{K_{Fr}}{[V_M]} = \frac{4K_{Fr}}{K_V} a_{O_2}^{-2/3} = 4K_I a_{O_2}^{-2/3} = [I]^0 a_{O_2}^{-2/3} \qquad (4)$$

where, K_V and K_{Fr} (Fr = Frankel) are the equilibrium constants for the reactions in eqn. 3 and 4, respectively, $K_I = K_{Fr}/K_V$, and $[V]^0$ and $[I]^0$ are the defect constants denote cation vacancy and cation interstitial concentration which are normalized to $a_{O_2} = 1$.

The deviation from stoichiometry of oxide (vacancies and interstitials) can be expressed as;

$$\delta = [V_M] - [M_I^{n+}] = \frac{K_V}{4} a_{O_2}^{2/3} - 4K_I a_{O_2}^{-2/3}$$
$$= [V]^0 a_{O_2}^{2/3} - [I]^0 a_{O_2}^{-2/3} \qquad (5)$$

Therefore, the vacancies and interstitials are created as a function of oxygen activity. Given, $a_{O_2}^0 = \frac{P_{O_2}}{P_{O_2}^0}$, where $P_{O_2}^0$ =1 bar. The deviation from stoichiometry can be written as;

$$\delta = [V]^0 P_{O_2}^{2/3} - [I]^0 P_{O_2}^{-2/3} \qquad (6)$$

The tracer diffusion of cation in a spinel oxide depends on diffusivities of vacancies and interstitials, which can be expressed as a function of oxygen partial pressure [1, 2];

$$D_M \approx D_{M(V)}^0 P_{O_2}^{2/3} - D_{M(I)}^0 P_{O_2}^{-2/3} \qquad (7)$$

where, $D^0_{M(V)}$ and $D^0_{M(I)}$ are the partial cation tracer diffusion coefficients of *M* ions via vacancies and interstitials. Therefore, the diffusivities of Fe and Cr can be described in terms of oxygen partial pressure, as shown in eqn. **5.2** – **5.5** and **5.18**.

Reference

1. Dieckmann, R., *Point defects and transport in non-stoichiometric oxides: Solved and unsolved problems.* Journal of Physics and Chemistry of Solids, 1998. **59**(4): p. 507-525.
2. Töpfer, J., S. Aggarwal, and R. Dieckmann, *Point defects and cation tracer diffusion in (CrxFe1 - x)3 - [delta]O4 spinels.* Solid State Ionics, 1995. **81**(3-4): p. 251-266.